Clumped Isotope Thermometry Techniques and their Application to Fossil Teeth and Pedogenic Carbonates

Dissertation
Zur Erlangung des Doktorgrades
der Naturwissenschaften

vorgelegt beim Fachbereich 11
der Johann Wolfgang Goethe-Universität
in Frankfurt am Main

von
Niklas Maximilian Löffler
aus Mechernich

Frankfurt am Main, 2020
(D 30)

Vom Fachbereich 11 der Johann Wolfgang Goethe-Universität als Dissertation angenommen.

Dekan: Prof. Dr. Georg Rümpker

Gutachter: Prof. Dr. Andreas Mulch

Senckenberg Biodiversität und Klima Forschungszentrum,
Senckenberganlage 25, 60325 Frankfurt (Main), Deutschland
und
Institut für Geowissenschaften, Johann Wolfgang Goethe-Universität,
Altenhöferallee 1, 60438 Frankfurt (Main), Deutschland

Prof. Dr. Jens Fiebig

Institut für Geowissenschaften, Johann Wolfgang Goethe-Universität,
Altenhöferallee 1, 60438 Frankfurt (Main), Deutschland

Datum der Disputation: 27.04.2021

For ma blonde Cherry, in endless appreciation of her patience and support

and

my family for their love and encouragement.

TABLE OF CONTENTS

Chapter **Page**

List of tables

List of figures

List of equations

Page

Abbreviations

25G	25 °C gas
4D-MB	mountain building processes in 4D
AEMET	Agencia Estatal de Meteorología
AFF	acid fractionation factor
AGU	American Geophysical Union
av	average
approx.	approximately
BiK-F	Biodiversity and Climate Research Centre Frankfurt (Main)
CDB	Calatayud-Daroca Basin
CDES	carbon dioxide equilibrium scale
CD-ROM	compact disc read-only
CEDEX	Centro de Estudios y Experimentación de Obras Públicas
CHAP	carbonated hydroxylapatite
CI	confidence interval
CMMT	cold month mean temperature
comp.	compare
CRD	cavity-ring-down
DFG	Deutsche Forschungsgemeinschaft
DIC	dissolved inorganic carbon
DJF	December, January, February
DOI	Digital Object Identifier
DSDP	Deep Sea Drilling Project
e.g.	*exempli gratia*
eq.	equation
ETF	empirical transfer function
ETH	Eidgenössische Technische Hochschule Zürich
EU	European Union
Fig.	figure
FTIR	Fourier-transform infrared spectroscopy
GC	gas chromatograph
GNIP	Global Network of Isotopes in Precipitation

GSA	Geological Society of America
HAL	Hofmann's auto line
HAP	hydroxylapatite
HG	heated gas
HMWK	Hessisches Ministerium für Wissenschaft und Kunst (State of Hesse)
incl.	including
prep.	preparation
IODP	Integrated Ocean Drilling Program
ITU	International Telecommunication Union (United Nations)
IUPAC	International Union of Pure and Applied Chemistry
IRMS	gas source isotope ratio mass spectrometer
JGU	Johann Wolfgang Goethe University Frankfurt Main
JJA	June, July, August
K-Pg	Creteaceous-Paleogene
LA-ICP-MS	laser ablation inductive coupled plasma mass spectrometer
LIDAR	light detection and ranging
LOEWE	Landes-Offensive zur Entwicklung Wissenschaftlich ökonomischer Exzellenz (HMWK)
LWIA	Liquid-Water Isotope Analyzer
MAP	mean annual precipitation (≠ "map")
MAT	mean annual temperature (≠ "MAT 253")
max.	maximum
MCO	Middle Miocene Climatic Optimum
MMCT	Middle Miocene Climatic Transition
MMT	mean monthly temperatures
MMP	mean monthly precipitation
MOR	Museum of the Rockies (U.S.A.)
N	North
NAFB	Northern Alpine Foreland Basin
n.a.	not applicable
n.d.	not defined
NIST	National Institute of Standards and Technology

NE	Northeast
ORCID	Open Researcher Contributor Identification
PETM	Paleocene–Eocene Thermal Maximum
Ph.D.	Doctor of Philosophy (*doctor philosophiae*)
ppb	parts per billion
ppm	parts per million
PTFE	Polytetrafluoroethylene
RGM	Rijksmuseum van Geologie en Mineralogie (The Netherlands)
RSM	Royal Saskatchewan Museum (Canada)
S	South
SARS-CoV-2	Severe Acute Respiratory Syndrome Coronavirus 2
S-BiK-F	Senckenberg Biodiversity and Climate Research Centre Frankfurt (Main)
sd	standard deviation
se	standard error
subm.	submitted
SW	Southwest
SEM-EDX	scanning electron microscope with energy dispersive X-ray analysis
SRM	standard reference material
SSW	South-southwest
SVP	Society of Vertebrate Paleontology
Tab.	table
TC-EA	high temperature conversion elemental analyzer
TIC	Total inorganic carbon
TLDAS	tunable laser direct absorption spectroscopy
TOC	Total organic carbon
U.S.A.	United States of America
VPDB	Vienna-Pee Dee Belemnite
vs.	*versus*
VSMOW	Vienna-Standard Mean Ocean Water
W	West
WMMT	warmest month mean temperature
wt.	weight

X-ray	Röntgen radiation
z.B.	zum Beispiel (*e.g.)*

Acknowledgements

I would hereby like to acknowledge all of the individuals who made this Ph.D. thesis possible:

- The working groups at the S-BiK-F and JGU including the administrative assistants, technicians, master students, Ph.D. students, Postdocs, and Professors for the professional and fruitful collaboration over years.
- My supervisors Prof. Dr. Andreas Mulch and Prof. Dr. Jens Fiebig for their constant support and contributions to this scientific work.
- All co-authors of my first author studies who trustfully shared extensive information on sample sites, sample material, data, and valuable feedback.
- My life partner Chèr Chislett and our furry canine children Mariposa and Olive for enriching my life.

Thank you all so much for your support and companionship!

Namely:

(in alphabetic order of the surnames)

Cornelia Anhalt, Nicolò Ardenghi, David Bajnai, Michael E. Böttcher, Geanina-Adriana Butiseaca, Chèr Chislett, Mariposa Chislett-Löffler, Olive Chislett-Löffler, Anika C. Conrad, Jens Fiebig, Laura Fink, Sven Hofmann, Wout Krijgsman, Emilija Krsnik, Tina Lüdecke, Maud Meijers, Katharina Methner, Andreas Mulch, Charlotte Prud'homme, Martin Rosner, Vanessa Schlidt, Burkhard C. Schmidt, Christoph Schreiber, Manuel Schumann, Ulrich Treffert, Ulrike Wacker, Iuliana Vasiliev-Popa, Thomas Tütken, Iryna Yashchenko.

I would also like to thank you, dear reader, for taking the time to work through this Ph.D. thesis. I sincerely hope that it will provide useful information and insights into the complex topic of clumped isotope thermometry and its application for studying paleoclimate and paleothermophysiology. Please feel free to contact me if you have any questions or feedback. Please refer to the *curriculum vitae* at page 155 for contact information.

Abstract

Measuring formation temperatures of minerals offers the potential to derive information on environmental conditions, thermophysiology of extinct animals, and diagenesis. Stable isotope geochemistry on carbonate and phosphate oxygen has previously shown that it can yield reliable temperature estimates if *e.g.* the initial oxygen isotopic composition ($\delta^{18}O$) of the precipitating fluid is known and *vice versa*. However, initial $\delta^{18}O$ of fluids frequently cannot be obtained for extinct taxa or abiotic samples from the geological past if mineral formation temperatures are unknown. This limit has been overcome since the introduction of clumped isotope (Δ_{47}) thermometry in the early 2000s. Δ_{47} thermometry has proven its applicability for carbonates, especially since Δ_{47} temperature calibrations from different laboratories started to converge and overall precision increased in the late 2010s. This, in turn, enabled the identification of biasing effects on Δ_{47} such as the contribution of secondary ions within the measuring system, the choice of isotopic parameters for data calculation, and reaction kinetics. As a consequence, it has become increasingly important to refine and verify the temperature dependence of Δ_{47} for various carbonate-bearing minerals including (bio)apatite and to develop a method that allows for an independent verification of kinetic effects during the precipitation of samples. Because the overall performance of the analytical setups had to be increased in order to achieve the aforementioned goals, established methods of Δ_{47} analysis now routinely reach a higher accuracy when compared to a few years ago (*ca.* 2015). This enables high precision reconstructions of *e.g.* important climatic events in Earth history such as the Middle Miocene Climatic Transition which is a potential analogue for future climate projections and whose continental thermal structure has not yet been constrained in full detail.

This Ph.D. thesis focuses on the refinement of the geochemical methods of clumped isotope analysis on abiogenic and biogenic materials (Δ_{47} and Δ_{48} on carbonate; Δ_{47} on apatite) and the application of Δ_{47}-based paleothermometry on fossil samples from the Miocene and Cretaceous (*Carcharodon megalodon* and *Tyrannosaurus rex*). This allows for the reconstruction of both mineral formation temperatures and the $\delta^{18}O$ of their respective parental fluids. The resulting Δ_{47} and $1{,}000\ln(\alpha_{CHAP\text{-}water})$ temperature calibration for (bio)apatite give comparable temperature sensitivities when compared to previously published calibrations for calcite:

$$\Delta_{47\ CDES\ 110} = 0.0325\ (\pm\ 0.0012) \times 10^6/\ T^2 + 0.2137\ (\pm\ 0.0124)$$

(with T in K and Δ_{47} in ‰; $R^2 = 0.9924$, *p*-value < 0.0001, n = 122; 8 samples)

and

$1{,}000\ln(\alpha_{CHAP\text{-}water}) = 17.23\ (\pm\ 0.59) \times 10^3 \times T^{-1} - 27.28\ (\pm\ 1.73)$

(with T in K; $R^2 = 0.997$, *p*-value < 0.04 n = 17, 3 samples)

Applying these calibrations to tooth enamel from an adult *T. rex* (RGM 792.000; *ca.* 66.5 Ma old) results in a body temperature of 38 ± 3 °C and a body water $\delta^{18}O$ of -8.4 ± 0.1 ‰$_{VSMOW}$. The palaeohabitate temperature derived from *Carcharodon megalodon* tooth enameloid (5.75 ± 0.06 Ma) is 19 ± 4 °C with a seawater $\delta^{18}O$ of -1.3 ± 1.0 ‰$_{VSMOW}$. The measured paleotemperatures are thereby in agreement with the thermophysiological concepts of endothermy and gigantothermy (for *T. rex*), and the preferred habitat temperature of the great white shark (for *C. megalodon*) – which is seen as the modern analogue of *C. megalodon*.

This thesis further includes the description of a new geochemical method for dual clumped isotope analyses (Δ_{47} and Δ_{48}) that allows future studies on reaction kinetics and the highly precise determination of carbonate formation temperatures. The dual Δ_{47} and Δ_{48} analysis is applied to carbonate reference materials, whereas the Upper Cretaceous ETH-3 from Northern Germany yields a mineral precipitation temperature of 15 ± 3 °C. Established Δ_{47} thermometry is applied to Middle Miocene pedogenic carbonates from Southern Europe (Spain). The measured soil temperatures reveal a high continental climate variability during the MMCT with both short termed temperature swings that coincide with potential changes of seasonality and events defined by the marine record (*e.g.* Mi3a and Mi3b), as well as overall declining temperatures across the MMCT with a statistical cooling of 12 °C.

Collectively, it can be concluded that clumped isotope analyses of carbonate and (bio)apatite has become an invaluable proxy that can successfully be applied to a wide range of fields of research including paleothermometry, thermophysiology, and kinetics of mineral precipitation.

1 Introduction

1.1 Scope of the thesis

The four major aims of this Ph.D. thesis are *i)* to refine a preliminary calibration of clumped isotope *vs.* temperature (Δ_{47}-1/T²) for (bio)apatite and widen its applicable temperature range, *ii)* apply the refined Δ_{47}-1/T² calibration to fossil samples for reconstructing mineral formation temperatures and oxygen isotopic compositions of fluids, *iii)* support the development of dual clumped isotope (Δ_{47} and Δ_{48}) analyses at the Joint Goethe University – Senckenberg BiK-F Stable Isotope Facility (Frankfurt Main, Germany)[*], and *iv)* decipher the continental temperature variability of the Southern European Middle Miocene Climatic Transition by applying established Δ_{47} thermometry techniques. The tasks during the Ph.D. studies therefore included optimizing and evaluating analytical procedures, fieldwork and sample preparation, organizing and conducting laboratory work, evaluating and discussing data, as well as presenting and publishing research results with a high international visibility.

[*)] The Joint Goethe University – Senckenberg BiK-F Stable Isotope Facility is the first laboratory worldwide that successfully installed a precise and accurate dual (Δ_{47} and Δ_{48}) clumped isotope setup (*chapter 4*).

1.2 Clumped isotope thermometry

1.2.1 Principles of clumped isotope thermometry

Clumped isotope thermometry is a geochemical technique that emerged in the early 2000s (Wang *et al.*, 2004; Eiler & Schauble, 2004 Ghosh *et al.*, 2006; Eiler, 2007) wherein the term "clumping" refers to the grouping of naturally-occurring multiply-substituted isotopologues with two or more heavy (and rare) isotopes. Clumped isotope analysis on carbonates (*e.g.* Ghosh *et al.*, 2006; Dennis & Schrag, 2010; Zaarur *et al.*, 2013 Wacker *et al.*, 2014; Defliese *et al.*, 2015; Methner *et al.*, 2016; Kelson *et al.*, 2017; Bajnai *et al.*, 2018) or carbonate-bearing minerals (*e.g.* Eagle *et al.*, 2010, 2011; Suarez & Passey, 2014; Bradbury *et al.*, 2015; Stolper & Eiler, 2016; Bergmann *et al.*, 2018) focus on the $^{13}C^{18}O^{16}O$ isotopologue (47 u) which has the highest relative abundance (45 ppm) within the group of doubly-substituted CO_2 isotopologues (Ghosh *et al.*, 2006). However, recent advances have facilitated successful measurements of $^{12}C^{18}O^{18}O$ (48 u) whose natural abundance (4.1 ppm; Ghosh *et al.*, 2006) is one magnitude lower when compared to $^{13}C^{18}O^{16}O$. The cardinal masses 47 u and 48 u also include the less abundant isotopologues $^{12}C^{18}O^{17}O$, $^{13}C^{17}O^{17}O$ (47 u) and $^{13}C^{18}O^{17}O$ (48 u) whose contribution to the overall signals is

comparable small due to their very low natural abundances (1.5 ppm to 1.5 ppb; Ghosh *et al.*, 2006). Heavy isotopes dampen the oscillation within a isotopologue and modify its zero-point energy, which reduces the potential energy of the latter (Hoefs, 2009). This results in a stability decrease of multiply substituted isotopologues if temperature is increased – an effect that intensifies proportionally to the number of heavy isotopes within an isotopologue. This consequently affects the natural abundance of multiply substituted isotopologues such as $^{13}C^{18}O^{16}O$ or $^{12}C^{18}O^{18}O$ (Schauble *et al.*, 2006; Eiler, 2007) which form from singly substituted isotopologues by a homogenous isotopic exchange reaction (*equation 1.1. a* and *b*, respectively). Clumped isotope analysis can therefore offer insights into crystallization temperatures of carbonates and carbonate-bearing minerals, independent of the oxygen isotopic composition of the parental fluid; provided that equilibrium has been attained.

(*equation 1.1*) *a*) $^{12}C^{18}O^{16}O + {}^{13}C^{16}O^{16}O \leftrightarrow {}^{13}C^{18}O^{16}O + {}^{12}C^{16}O^{16}O$

b) $^{12}C^{18}O^{16}O + {}^{12}C^{18}O^{16}O \leftrightarrow {}^{12}C^{18}O^{18}O + {}^{12}C^{16}O^{16}O$

For mass spectrometer analysis, CO_2 analyte gas is derived from solid sample materials by digestion in heated (*e.g.* 25 to 110 °C) and hyper saturated (*ca.* 105 to 107 %) orthophosphoric acid which translates the pristine clumping of the carbonate or carbonate group isotopologue (*e.g.* $^{13}C^{18}O^{16}O_2^{-2}$) with a constant oxygen fractionation between CO_3^{-2} and CO_2 (Guo *et al.*, 2009) into the gaseous CO_2 phase. This CO_2 analyte gas can be measured with a gas source mass spectrometer (IRMS) for its *m/z* ratios of 44 to 49. Differences in the isotopic composition of the analyte gas compared to a theoretical statistic distribution of CO_2 (*e.g.* Petersen *et al.*, 2019) define the Δ_{47} and Δ_{48} variables by the deviation of measured (R^{45}, R^{46}, R^{47}, R^{48}) from stochastic ratios (R^{45*}, R^{46*}, R^{47*}, R^{48*}) according to *equation 1.2.* (Eiler & Schauble, 2004) for Δ_{47} and *equation 4.1* (page 83) for Δ_{48}. Both, Δ_{47} and Δ_{48} are thereby inversely proportional to temperature.

(*equation 1.2*) $\Delta_{47} = [(R_{47}/ R_{47}^{*} - 1) - (R_{46}/ R_{46}^{*} - 1) - (R_{45}^{*}/ R_{45}^{*} - 1)] \times 1{,}000$

(in ‰; $R_i = i/44$)

1.2.2 Recent advances in clumped isotope thermometry

Clumped isotope thermometry has become a growing field of research that quickly allowed for deciphering formation temperatures of carbonate (Ghosh *et al.*, 2006; Eiler, 2011), eggshell carbonate (Eagle *et al.*, 2015), carbonated apatite (Eagle *et al.*, 2010; 2011), and other carbonate-bearing minerals, such as dolomite, magnesite, siderite, and vaterite (*e.g.* Fernandez *et al.*, 2014; Kluge *et al.*, 2015; García del Real *et al.*, 2016; Winkelstern *et al.*, 2016). The principles of clumped isotope thermometry have furthermore been applied to other isotopologue systems such as methane (CH_4) with the most abundant doubly heavy substituted isotopologue being $^{13}CH_3D$ and $^{12}CH_2D_2$ with a *m/z* of 18 (Stolper *et. al.* 2014).

Over the course of more than ten years, a variety of Δ_{47}-temperature (Δ_{47}-$1/T^2$) calibration studies were conducted that, even though data was normalized to an absolute reference frame since 2011 (Dennis *et al.*, 2011), resulted in distinct Δ_{47}-$1/T^2$ relationships (*e.g.* Zaarur *et al.*, 2013 *vs.* Wacker *et al.*, 2014). The steep slope of the initial Δ_{47}-$1/T^2$ calibrations from 2006 to 2011 (Ghosh *et al.*, 2006; Tripati *et al.*, 2010; Thiagarajan *et al.*, 2011) could not be confirmed by most of the Δ_{47}-$1/T^2$ calibrations of subsequent studies, that tend to plot rather closely to the theoretical calibration line of Guo *et al.* (2009). In 2016, a preliminary Δ_{47}-$1/T^2$ calibration for carbonate-bearing apatite was published (Wacker *et al.*, 2016) that advocated the use of a high acid digestion temperature of 110 °C and underlined the importance of renouncing chemical pretreatment.

Since 2016, clumped isotope raw values are progressively calculated with the IUPAC isotopic paramteters for ^{17}O correction (Daëron *et al.*, 2016; Kelson *et al.*, 2017) resulting in a better interlaboratory agreement of the Δ_{47}-$1/T^2$ calibrations (Petersen *et al.*, 2019). Also, initial indications for kinetic effects on Δ_{47} (Grauel *et al.*, 2013) were confirmed for corals (Spooner *et. al.* 2016; Kimball *et. al.* 2016) and, in 2018, for brachiopods (Bajnai *et al.*, 2018). It has therefore become increasingly important to establish a Δ_{47}-based approach to determine the state of equilibrium during the precipitation of a sample. This would theoretically be feasible if Δ_{47} and Δ_{48} are simoultaneously measured and projected to a Δ_{47} *vs.* Δ_{48}-equilibrium line that can be derived from thermodynamical compution (*e.g.* Guo & Zhou, 2019a) which was recently done by Bajnai *et al.* (2020). Due to the relatively low natural abundance of $^{12}C^{18}O^{18}O$ (4.1 ppm; Ghosh *et al.*, 2006), measuring pristine Δ_{48} signals requires a very high analytical precision and an effective sample gas preparation and purification. The latter has to be constructed in such a way that both, reequilibration of CO_2 with traces of water and the introducton of iosbaric

contaminants can be excluded. This became possible by recent technical advances (*e.g.chapter 4*; Thermo Scientific™ MAT 253 Plus™, and HAL) resulting in an overall higher precision when compared to previously used analytical instruments and setups (*e.g.* Thermo Scientific MAT 253™ or Elementar™ Isoprime 100™, manual acid digestion and gas purification). In addtion to improved IRMS, recent developments of optical analytical systems for Δ_{47} analysis of CO_2, such as the tunable laser direct absorption spectroscopy (TLDAS; Prokhorov *et al.*, 2019) are further diversifying the field of clumped isotope thermometry. An increased analytical precision thereby not only allows for measuring Δ_{48} (with high-precision IRMS; *e.g.* Bajnai *et al.*, 2020), but is also benefitial for established techniques and applications, for example for temperature reconstruction on paleosoil carbonates which very recently has been performed to decipher the evolution of the continental thermal history of the Middle Miocene Climatic Optimum in the Central European Northern Atlantic Foreland Basin (NAFB; Methner *et al.*, 2020).

1.3 Laboratory work and sample materials

1.3.1 Laboratories

Research was carried out at the Climate and Tectonics working group at the Senckenberg Biodiversity and Climate Research Centre (S-BiK-F), Senckenberganlage 25, 60325 Frankfurt (Main), Germany. Δ_{47}, $\delta^{18}O$, and $\delta^{13}C$ analyses of carbonates and (bio)apatites were done at the "Labor für die leichten stabilen Isotope (Gasmassenspektrometrie)" (Laboratory for Light and Stable Isotopes (gas mass spectrometry)). Stable hydrogen (δD) and oxygen ($\delta^{18}O$) isotope analysis of water was conducted at the S-BiK-F Biomarker Laboratory. Both laboratories are part of a joint venture of the Institute of Geoscience (Goethe University, Altenhoeferallee 1, 60438 Frankfurt (Main), Germany) and the S-BiK-F.

Other laboratories that have been used to measure data for the studies of this Ph.D. thesis (*e.g.* by the co-authors) are situated at the Leibniz Institute for Baltic Sea Research (Seestrasse 15, 18119 Warnemuende, Germany), the Johannes Gutenberg University Mainz (Johann-Joachim-Becher Weg 21, 55128 Mainz, Germany), and the Georg-August-University Goettingen (Wilhelmsplatz 1, 37077 Goettingen, Germany).

1.3.2 Origin of samples

Samples analyzed for the studies of this Ph.D. thesis are *i*) pedogenic carbonates, *ii*) abiogenic carbonated hydroxylapatites (CHAP), *iii*) biogenic carbonated apatite (teeth of

Somniosus microcephalus, *Carcharias taurus*, *Carcharodon megalodon*, *Loxodonta africana*, and *Tyrannosaurus rex*), and *iv*) calcite reference materials. The origins of these samples are summarized in the following:

i) Pedogenic carbonates were collected close in the Spanish Province of Zaragoza. The two study areas Armantes (*chapter 5*) (near Calatayud, Spain, 41.38989 °N 1.72073 °W) and Aragon (*chapter 6*; near Villafeliche, Spain, 41.18931 °N 1.48436 °W) are proximate to each other (30 km NW-SE). The alluvial sediments of both sections were deposited in the Calatayud-Daroca Basin (CDB) during the Middle Miocene (Krijgsman *et al.*, 1994).

ii) Abiogenic CHAPs (*chapter 2*) were synthesized at the Leibniz Institute for Baltic Sea Research by U. Wacker and A. C. Conrad in the laboratories of the Geochemistry and Isotope Biogeochemistry Group (Seestraße 15, 18119 Warnemuende, Germany) under the supervision of M. E. Böttcher.

iii) Greenland shark (*Somniosus microcephalus*) jaws with several intact rows of teeth (*figure 1.1*) were kindly donated by the Bjarnarhöfn Shark Museum (Bjarnarhöfn, Iceland). The sharks are typically caught off the coast of Iceland and dried for food supply. The museum is located next to the road 54 at a junction with road 577 close to the northeast rim of the Bjarnarhafnarfjal.

Figure 1.1: Dried parts of the upper (left) and lower (right) jaw of *Somniosus microcephalus* illustrating the two different shapes of the teeth (pointy, left *vs.* wide and curved, right) and the various states of dental evolution ranging from young (lower rows) to mature (upper rows). Scale bar: 5 cm.

Several individual sand tiger shark (*Carcharias taurus*) teeth (*figure 1.2*) were kindly donated by the Two Oceans Aquarium (Dock Rd, V. & A. Waterfront, Cape Town, 8002, South Africa). The mature teeth were collected from the basin floor during the regular cleaning procedures of the aquarium.

Figure. 1.2: Dried individual sand tiger shark teeth (*Carcharias taurus*). The anterior teeth are pointy and awl shaped while the lateral teeth are shaped blade like (*e.g.* upper right and lower left).

A complete tooth of the mega tooth shark *C. megalodon* (*figure 2.1*; page 43) was originally bought in a rock shop in Oklahoma (U.S.A.) without further reference and donated to T. Tütken, who provided the tooth for the joint study of *chapter 2*. Its strontium isotope based age is 5.75 ± 0.06 Ma (*chapter 2.6.5*).

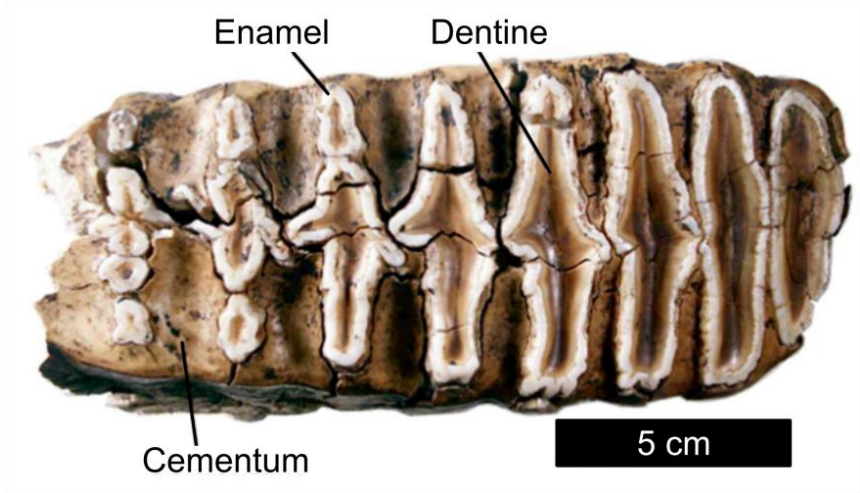

Figure. 1.3: Left side molar tooth of the African elephant (*Loxodonta africana*) that was sampled by A. Gehler (AG-LOX) who provided separated tooth enamel and dentine from this tooth. Note that enamel, dentine, and cementum have distinct colors and macro-structures.. Photo: A. Gehler, modified.

African elephant (*Loxodonta africana*) materials originate from an upper left molar (*figure* 1.3) that was originally provided by F. Mayer (Berlin, Germany). This tooth that has previously been separated into homogenized powder of tooth dentine and enamel (Gehler *et al.*,

2012). The samples were kindly provided by A. Gehler (Georg-August-University Goettingen Wilhelmsplatz 1, 37077 Goettingen, Germany).

Several *Tyrannosaurus rex* tooth fragments (37; *figure 3.2*; page 74) were provided by A. Schulp (Naturalis Biodiversity Center in Leiden, Darwinweg 2, 2333 CR Leiden, The Netherlands). The samples were found *in situ* on a ranch fifty kilometers south of Jordan (Montana, U.S.A.) in stream channel sediments of the Upper Maastrichtian Hell Creek Formation (Schulp *et al.*, 2015; Reims *et al.*, 2016) next to the skull of a well-preserved *T. rex* skeleton (*ca.* 66.5 Ma old). The *T. rex* was excavated under the lead of the Naturalis Biodiversity Center in Leiden (address: *see above*), in cooperation with the Black Hills Institute (117 Main Street, Hill City, SD, 57745 U.S.A.) (Schulp *et al.*, 2015).

iv) Pure calcite reference materials used for the study of dual Δ_{47} and Δ_{48} analyses (*chapter 4*) are pure marble from Carrara (Italy), and four international ETH reference materials (ETH 1, ETH 2, ETH 3, ETH 4, ETH 4) that were provided by S. Bernasconi (ETH Zurich, Geological Institute, Sonneggstr. 5, 8092 Zurich, Switzerland).

1.3.3 Biogenic and abiotic apatite – general information

Biogenic apatite forms vertebrate hard parts as for example scales, bones, and teeth (Zapanta LeGeros, 1981). Its crystal lattice allows for replacement of extraneous ions which results in the generalized chemical formula (*equation 1.3*) of:

(*equation 1.3*) $Ca_{10-a}(Na,K,NH_4)_{2a}(PO_4)_{6-y}[(CO_3)_{2x+(3/2)y}(F,OH)_{2-2x}]$

(modified after Fleet *et al.*, 2004)

Teeth are the hardest tissues in vertebrates (Dorozhkin & Epple, 2002; Enax *et al.*, 2012) and consist of osteodentine, orthodentine, and enamel(oid) (Grady, 1970; Fincham *et al.*, 1999; Whitenack *et al.*, 2010) with enamel(oid) being the hardest and most resistant tissue. Enamel and enameloid (collectively referred to as enamel(oid)) are homologous but not identical tissues of mammals and reptiles or sharks, respectively (*e.g.* Poole, 1967; Grady, 1970; Herold *et al.*, 1980; Kemp, 1984). Enamel(oid) is characterized by a reduced carbonate and organic content (Enax *et al.*, 2012) and a smaller porosity (Zabler *et al.*, 2007) when compared to dentine resulting in an overall lower susceptibility for diagenetic alteration (Enax *et al.*, 2012). Contrary to mammal teeth, which are formed out of hydroxylapatite, amphibians and fish teeth mainly consist of

fluorapatite and reach hardness comparable to mammal teeth (Møller *et al.*, 1975; Enax *et al.*, 2012). Thus, fresh Greenland shark teeth are not completely rigid but slightly pliable (K. Hildibrandsson, personal communication, June 23, 2020).

Aside from the biotic genesis, apatite can also precipitate under abiotic conditions and, for example, result in the formation of phosphorite (*e.g.* Filippelli, 2002; Ruttenberg, 2003; Keenan & Engel, 2017) typically containing carbonated hydroxyapatite (CHAP), which forms a gapless mixing series with chloro and fluoroapatite (Pasteris *et al.*, 2008). Marine genesis of carbonated apatite frequently takes place in coastal upwelling zones (*e.g.* Burnett, 1977; Compton & Bergh, 2016) and can be observed in hydrocarbon seep environments (*e.g.* Liu *et al.*, 2018; Zwicker *et al.*, 2020). Provided that both the formation temperature and the temperature dependent oxygen isotopic fractionation between the parental fluid and structurally bound carbonate are known, $\delta^{18}O$ values of the fluid from which a biogenic or abiotic carbonated apatite precipitated can be derived (*e.g.* body fluid for teeth and sea water for CHAP).

1.3.4 Pedogenic carbonate – general information

Soils that form under arid/semi-arid to sub-humid or monsoonal climates with seasonal precipitation (Breecker *et al.*, 2009) can show calcareous features that are bound to distinct soil horizons. These features can be identified as authigenic precipitates if clastic compounds of the surrounding sediment are cased by a micritic carbonate matrix that expands during the growth and thus forms pedogenic carbonate. The mineralogy and shape of pedogenic carbonates can vary dependent on the surrounding geology, sedimentary structure, and the mechanism that lead to the carbonate precipitation. Gile *et al.* (1966) for example describe different shapes of pedogenic carbonates such as nodules, continuous horizons, root casts, filaments and undercoatings of clasts. The precipitating fluid mainly originates from local rainfall (Cerling, 1984). Therefore, reconstruction of soil water $\delta^{18}O$ is feasible if oxygen isotope equilibrium between soil water and soil carbonate is assumed and if the temperature dependent $\delta^{18}O$ fractionation (*e.g.* Kim & O'Neil, 1997; Coplen, 2007) is taken into account. This requires knowledge of both the soil temperature during the carbonate formation and the pedogenic carbonate $\delta^{18}O$ value (*e.g.* by Δ_{47} analysis). Δ_{47} soil temperatures derived from pedogenic carbonates most likely represent warm month mean temperatures (WMMT; Passey *et al.*, 2010; Hough *et al.*, 2014) but can be biased when the season of carbonate formation is shifted to months with distinct temperatures (*e.g.* Methner *et al.*, 2020). While the $\delta^{18}O$ of pedogenic carbonate mainly reflects rainfall and

temperature, $\delta^{13}C$ is controlled by soil CO_2 which is composed out of atmospheric and biotic sources, such as respiration of plants and (micro)organisms (*e.g.* Cerling, 1984; Cerling *et al.*, 1991; Quade *et al.*, 2007). The relative contribution of respirated CO_2 is thereby proportional to the depth of the soil profile and dominates below approximately 50 cm in depth (Quade *et al.*, 2007). The recorded $\delta^{13}C$ can therefore be used as an indicator of the vegetation as the respirated CO_2 reflects the photosynthetic pathway (C3, C4, CAM), the respiration rate, and the plant cover (*e.g.* Cerling, 1984; Quade *et al.*, 2007; Davidson, 1995; Kohn, 2010; Cerling *et al.*, 1991; Cerling & Quade, 1993). Provided that these controlling factors remain constant, pedogenic carbonate $\delta^{13}C$ values would be a measure for atmospheric CO_2.

1.4 Structure of the Ph.D. thesis

This thesis presents calibrations of new and highly precise analytical techniques for oxygen ($\delta^{18}O$) and clumped (Δ_{47}) isotope analyses of carbonated (bio)apatite, and dual clumped isotope analyses (Δ_{47} and Δ_{48}) of pure carbonate. Experimentally determined $\delta^{18}O$ and Δ_{47} (bio)apatite calibrations are tested on *C. megalodon* tooth enameloid (*chapter 2*) and applied to an adult *T. rex* specimen (RGM 792.000) to measure its body temperature and the $\delta^{18}O$ of its body fluid (*chapter 3*). Results of dual Δ_{47} and Δ_{48} analyses of carbonates (*chapter 4*) demonstrate the high precision of a new analytical IRMS setup (Thermo Fischer™ MAT 253 Plus™ with HAL digestion device) and the potential to resolve kinetics and/or diagenesis in carbonates. Measurements of Δ_{47} on pedogenic carbonates from Southern European Middle Miocene paleosoils (*chapter 5*) reveal the continental thermal evolution during the Middle Miocene Climatic Transition in Spain which is complemented by results from an additional Middle Miocene section that are provided in *chapter 6*. A brief overview of all ten scientific studies the author contributed to during his Ph.D. studies (*chapter 7*) is followed by the English summary and outlook (*chapter 8*) and the German summary and conclusions “Zusammenfassung und Schlussfolgerungen” (*chapter 9*). The reference section (*chapter 10*; for all chapters) marks the end of this Ph.D. thesis and is followed by the *curriculum vitae* of Niklas M. Löffler, appendices to the chapters 1 to 6, and a digital annex (CD-ROM). The titles and contents of the individual chapters are summarized below.

1.4.0 Chapter 1

The chapter **Introduction** describes the context, focus and aims of this Ph.D. thesis including information on basic principles of the method used, places of work, origin of the samples, general sample properties, and the structure of the thesis.

1.4.1 Chapter 2

The study **Refining the temperature dependence of the oxygen and clumped isotopic compositions of structurally bound carbonate in apatite** by Niklas Löffler, Jens Fiebig, Andreas Mulch, Burkhard C. Schmidt, David Bajnai, Anika C. Conrad, Ulrike Wacker, and Michael E. Böttcher is published in Geochimica et Cosmochimica Acta (2019), 253, 19-38, *https://doi.org/10.1016/j.gca.2019.03.002* and currently listed as a key publication of the Goethe University-Senckenberg BiK-F Joint Stable Isotope Facility in Frankfurt (Main), Germany. Abiogenic and biogenic carbonated apatites are measured for its clumped, oxygen and carbon isotopic composition (Δ_{47}, $\delta^{18}O$, and $\delta^{13}C$, respectively) after phosphoric acid digestion at 110 °C. The data covers a temperature range of 1 °C to 80 °C and refines the Δ_{47}-$1/T^2$ calibration of Wacker *et al.* (2016). Furthermore, the temperature dependent $\delta^{18}O$ fractionation between structural carbonate from synthetic carbonated hydroxylapatites (CHAP) and water is calculated for a range of 7 °C to 80 °C. Both calibrations are applied to shark tooth enameloid of *Somniosus microcephalus* and *Carcharodon megalodon* to reconstruct Δ_{47}-based habitat temperatures and $\delta^{18}O$ of seawater.

1.4.2 Chapter 3

The chapter **Application of the refined clumped isotope temperature calibration on *Tyrannosaurus rex* teeth of the adult specimen "Trix" (RGM 792.000)** written by Niklas Löffler contains unpublished work that was conducted in close cooperation with Anne S. Schulp, Jens Fiebig, Thomas Tütken, David Bajnai, and Andreas Mulch. Preliminary data of this study was presented in 2017 at the 6th International Clumped Isotopes Workshop, the Goldschmidt conference, and the GEOBremen (References within the chapter). This study includes the application of the Δ_{47}-$1/T^2$ and $1{,}000\ln(\alpha_{CHAP\text{-}water})$ calibrations to *Tyrannosaurus rex* tooth enamel of the adult specimen "Trix" (RGM 792.000). A body temperature of 38 ± 3 °C and a body water $\delta^{18}O$ of -8.4 ± 0.1 $‰_{VSMOW}$ is obtained which is in agreement with currently debated thermophysiological concepts of large Theropods (endothermy *vs.* gigantothermy)

and - combined with the measured tooth enamel $\delta^{13}C$ - is in line with previously reported $\delta^{18}O$ and $\delta^{13}C$ of hadrosaurian and ceratopsian dinosaurs from the same (Hell Creek) formation.

1.4.3 Chapter 4

The study **Combined high-precision Δ_{47} and Δ_{48} analysis of carbonates** by Jens Fiebig, David Bajnai, Niklas Löffler, Katharina Methner, Emilija Krsnik, Andreas Mulch, and Sven Hofmann is published in Chemical Geology (2019), 522, 186-191, https://doi.org/10.1016/j.chemgeo.2019.05.019 and currently listed as a key publication of the Goethe University-Senckenberg BiK-F Joint Stable Isotope Facility in Frankfurt (Main), Germany. The chapter comprises the description of the first precise and accurate analyses of CO_2 isotopologues with *m/z* 48 (Δ_{48}) that evolved from varying carbonate reference materials after phosphoric acid digestion. This has been made possible by both recent advances that include the installation of a Thermo Fisher™ 253 Plus™ IRMS containing high ohmic amplifiers and a *m/z* 47.5 Faraday cup, as well as recent methodological innovations that increased the overall analytical precision. Measuring pristine Δ_{48} signals (along with Δ_{47}) was thus far not feasible due to the low abundance of ^{18}O in natural samples. Due to the agreement of the experimental data with theoretical computations, dual Δ_{48} and Δ_{47} analysis has a high potential for verifying the presence of kinetic processes and their contribution to measured Δ_{47} formation temperatures of (bio)minerals. This is exemplified by the application of dual Δ_{48} and Δ_{47} analysis to an Upper Cretaceous carbonate reference material from Northern Germany (ETH-3) yielding a mineral precipitation temperature of 15 ± 2 °C.

1.4.4 Chapter 5

The study **Southern European Middle Miocene Temperature Dynamics** by Niklas Löffler, Andreas Mulch, Wout Krijgsman, Iuliana Vasiliev, Emilija Krsnik, Katharina Methner, and Jens Fiebig is submitted for publication at Nature Geoscience (NGS-2020-08-01948). Pedogenic carbonated from the Middle Miocene Climatic Transition (MMCT) in Southern Europe (Spain) are measured for their Δ_{47}, $\delta^{13}C$, and $\delta^{18}O$ values. The resulting well-dated terrestrial temperature record ranges from 15.33 to 12.98 Ma and hence covers the end of the Middle Miocene Climatic Optimum (MCO) and the complete MMCT. A close match of the pedogenic carbonate $\delta^{13}C$ values with the marine $\delta^{13}C$ record points to a common driver of carbon dynamics at the late MCO. It is shown that the continental MMCT is characterized by strongly varying soil temperatures that define cooling events and trends that agree with the

marine record (*e.g.* Mi3a and Mi3b). Combined pedogenic carbonate Δ_{47} and $\delta^{18}O$ data further reveal that changes in rainfall seasonality, which coincide with changes in Earth's orbital configuration, affected the recorded temperature signal. The Southern European continental cooling across the whole span of the MMCT is 12 °C.

1.4.5 Chapter 6

The chapter **Complementary data to the Southern European Middle Miocene Temperature Dynamics** written by Niklas Löffler contains unpublished work that was conducted in close cooperation with Andreas Mulch, Wout Krijgsman, Iuliana Vasiliev, Emilija Krsnik, Katharina Methner, and Jens Fiebig. Preliminary data of this study was presented in 2019 at the 9th International Clumped Isotopes Workshop, and the AGU conference (references within the chapter). The presented $\Delta_{47,}$ and $\delta^{18}O$ data extends the soil temperature dataset of *chapter 5* by three additional well-dated soil temperatures from the Middle Miocene Aragon section (14.64 to 13.36 Ma) that is situated 30 km southeast of the Armantes section (Spain). The Armantes and Aragon soil temperatures and reconstructed $\delta^{18}O$ of the soil water of pedogenic carbonates are in agreement with each other and collectively underline the strong climatic dynamic of the Southern European Middle Miocene Climatic Transition which can also be identified in the mammal fossil record of Central Spain. Additionally, present-day regional climate information of the study area is compared to modeled and measured Middle Miocene climate data.

1.4.6 Chapter 7

The chapter **scientific work as a (co-) author,** gives an overview of all scientific studies Niklas M. Löffler contributed to during his Ph.D. studies which includes seven studies and manuscripts that are not contained in this thesis.

1.4.7 Chapter 8

The chapter **Summary and conclusions** provides a synopsis of the main findings of this Ph.D. study. A summary of the general outcome is followed by subchapters that further focus on the results and conclusions for (bio)apatites and carbonates. The outlook is structured into four subchapters that relate to thermophysiology of extinct vertebrates, highly precise dual Δ_{47} and Δ_{48} thermometry on carbonates, the continental Middle Miocene temperature record for Europe, and science outreach. The latter includes the image of a prepared poster that will be displayed at the Bjarnarhöfn Shark Museum in Iceland

1.4.8 Chapter 9

This chapter provides the German summary and conclusions "**Zusammenfassung und Schlussfolgerungen**" which comprises a general outcome and results and conclusions for both (bio)apatites and carbonates.

1.4.9 Chapter 10

The **References** chapter includes the bibliography of this thesis whereas citations follow the guidelines of the American Psychological Association (2019) (7th edition).

2 Refining the temperature dependence of the oxygen and clumped isotopic compositions of structurally bound carbonate in apatite

N. Löffler[a, b]*, J. Fiebig[a, b], A. Mulch[a, b], T. Tütken[c], B. C. Schmidt[d], D. Bajnai[b,1], A. C. Conrad[e, 2], U. Wacker[b, 3], M. E. Böttcher[e]

[a] *Senckenberg Biodiversity and Climate Research Center, Senckenberganlage 25, 60325 Frankfurt (Main), Germany*

[b] *Institute of Geosciences, Goethe University Frankfurt, Altenhoeferallee 1, 60438 Frankfurt (Main), Germany*

[c] *Institute of Geosciences, Johannes Gutenberg University, Johann-Joachim-Becher-Weg 21, 55128 Mainz, Germany*

[d] *Experimental and Applied Mineralogy, Georg-August-University Goettingen, 37077 Goettingen, Germany*

[e] *Leibniz Institute for Baltic Sea Research (IOW), Geochemistry & Isotope Biogeochemistry Group, Seestrasse 15, 18119 Warnemuende, Germany*

[1] *Present address: Institute of Geology and Mineralogy, University of Cologne, Zuelpicher Strasse 49a, 50674 Cologne, Germany*

[2] *Present address: Technical University Berlin, Strasse des 17. Juni 135, 10623 Berlin, Germany*

[3] *Present address: Thermo Fisher Scientific GmbH, Hanna-Kunath-Strasse 11, 28199 Bremen, Germany*

**Correspondence: niklas.loeffler@senckenberg.de*

Published in Geochimica et Cosmochimica Acta (2019), 253, 19-38.

https://doi.org/10.1016/j.gca.2019.03.002

Received 22 June 2018; accepted in revised form 2 March 2019; Available online 11 March 2019

2.0 Abstract

Clumped isotope data from carbonated apatite from *in vivo* and *in vitro* samples are presented to refine the relationship between mineral growth temperature and carbonate clumped isotopic composition (Δ_{47}). Δ_{47}, $\delta^{18}O$ and $\delta^{13}C$ data were obtained from phosphoric acid digestion (T = 110 °C) of chemically untreated teeth from an African elephant, Greenland sharks, sand tiger sharks and synthetic apatites. These data cover a temperature range between 1 °C and 80 °C and enlarge the calibration dataset presented in Wacker *et al.* (2016) by a factor of five. Taxon-specific analyses of tooth enamel(oid) and dentine reveal that both tissues show identical Δ_{47} values even though the content of organic matter differs by an order of magnitude. The following Δ_{47} temperature calibration for (bio)apatite is derived (R^2 = 0.9924, *p*-value < 0.0001, n = 122; 8 samples):

$$\Delta_{47\ CDES\ 110} = 0.0325\ (\pm\ 0.0012) \times 10^6/\ T^2 + 0.2137\ (\pm\ 0.0124)\ \text{(with T in K and } \Delta_{47} \text{ in ‰)}$$

This calibration becomes indistinguishable from a reprocessed empirical calibration of calcite made in the same laboratory if a difference of the acid fractionation factors (AFF) of 0.110 ‰ between 25 °C and 110 °C is considered. The measured AFF for bioapatite matches the one that is extrapolated from experimental data on calcite and aragonite. The oxygen isotope fractionation between structural carbonate in the synthesized carbonated hydroxylapatites (CHAP) and water between 7 °C and 80 °C closely follows the temperature dependence for the calcite-water system. It is described by the following (CHAP-water) equation (R^2 = 0.997, *p*-value < 0.04 n = 17, 3 samples):

$$1{,}000\ln(\alpha_{CHAP\text{-}water}) = 17.23\ (\pm\ 0.59) \times 10^3 \times T^{-1} - 27.28\ (\pm\ 1.73)\ \text{(with T in K)}$$

Both calibrations are applied to shark teeth from a modern Greenland shark and a fossil megatooth shark (*Carcharodon megalodon*) specimen to reconstruct the apparent Δ_{47}-based habitat temperature of *C. megalodon* (19 ± 4 °C) and the oxygen isotopic compositions of seawater.

Keywords: Clumped isotopes, carbonated apatite, temperature calibration, oxygen isotope fractionation, paleoenvironmental reconstruction, *C. megalodon*

2.1 Introduction

Biogenic apatite (bioapatite) is a major constituent of vertebrate hard parts such as scales, bones and teeth Zapanta LeGeros (1981). Extraneous cations and anions can replace Ca, PO_4 and OH in the crystal lattice (Fleet *et al.*, 2004; Fleet, 2015, and references therein), thereby leading to the formation of solids with the generalized composition $Ca_{10-a}(Na,K,NH_4)_{2a}(PO_4)_{6-y}[(CO_3)_{2x+(3/2)y}(F,OH)_{2-2x}]$ (modified after *e.g.*, Fleet *et al.*, 2004; Fleet, 2015). Carbonated apatites represent excellent archives for the reconstruction of environmental conditions that prevailed during their growth (Tütken & Vennemann, 2011; Fleet, 2015). This is especially true for tooth enamel which is among the hardest and most resistant tissues in mammals and sharks (Dorozhkin & Epple, 2002; Enax *et al.*, 2012). Moreover, phosphate rocks (phosphorites) are formed under different environmental conditions (Filippelli, 2002, Ruttenberg, 2003). The major mineral in important phosphate deposits is carbonated hydroxylapatite (CHAP). CHAP can be formed via the replacement of marine carbonates by phosphate-bearing solutions. Furthermore, abiogenic

apatite forms during diagenetic recrystallization of former bioapatite (*e.g.*, Keenan & Engel, 2017, and references therein).

Bulk analyses of stable isotopes of oxygen ($^{18}O/^{16}O$) and carbon ($^{13}C/^{12}C$) in bioapatite are widely used for paleoenvironmental and paleobiological studies that, for example, address research questions related to dietary behavior (*e.g.*, Longinelli, 1984; Lee-Thorp & Sponheimer, 2003; Widga *et al.*, 2010; Zazzo *et al.*, 2010; Lüdecke, 2016), ecological niches (*e.g.*, Feranec & MacFadden, 2000), seasonal variability of environmental conditions (*e.g.*, Tütken *et al.*, 2004; Stevens *et al.*, 2011), migration (*e.g.*, Hoppe & Koch, 2007), hunting strategies (*e.g.*, Hoppe, 2004), paleoclimate (*e.g.*, Levin *et al.*, 2006;Tütken *et al.*, 2007) and the adaptation to it (*e.g.*, Koch, 2004) as well as diagenesis (Stolper & Eiler, 2016). Aside from these well-established bulk isotopic analyses, clumped isotope analysis has become an effective tool to decipher formation temperatures of carbonates (Ghosh *et al.*, 2006; Eiler, 2011). Previous studies suggested that this homogeneous phase thermometer may also be applied to carbonated apatites to deduce body temperatures of extinct vertebrates, albeit discrepant Δ_{47}-$1/T^2$ relationships were obtained (Eagle *et al.*, 2011; Wacker *et al.*, 2016). So far, various (bio)apatites such as teeth (Eagle *et al.*, 2010, 2011), bone (Suarez & Passey, 2014), phosphatic marine brachiopods (Bergmann *et al.*, 2018), apatite from carbonatites (Stolper & Eiler, 2015), as well as phosphatic hardgrounds, phosphorites and nodules (Bradbury *et al.*, 2015; Stolper & Eiler, 2016; Bergmann *et al.*, 2018) have been studied. Initially the clumped isotope composition of carbonated bioapatites was shown to follow the Ghosh *et al.*, 2006 calcite Δ_{47}-$1/T^2$ calibration (Eagle *et al.*, 2010); a result that could not be confirmed in a follow-up study (Wacker *et al.*, 2016). In this respect, it must be noted that both the calibration regression lines of Ghosh *et al.* (2006) for calcite Wacker *et al.* (2016) for (bio)apatite show considerable uncertainties in their 95 % confidence intervals (CI). This limits applications that require precise temperature estimates, as for instance deciphering the evolution of endothermy (*e.g.*, Grellet-Tinner, 2006; Blatteis, 2014; Bernard *et al.*, 2010), which is one of the most fundamental physiological advancements in the evolution of vertebrates (Hayes & Garland, 1995). A well-defined and precise clumped isotope paleothermometer for bioapatite could potentially allow body temperature reconstruction of extinct animals with a resolution of a few degrees centigrade, independent from the oxygen isotopic composition ($\delta^{18}O$) of vertebrate body fluid. In addition to body temperature, information about the $\delta^{18}O$ of ingested water and the influence of diagenesis on the sample material could be assessed.

The preliminary temperature calibration for (bio)apatite (Wacker *et al.*, 2016) was calculated from three samples with approximately eight replicate measurements per sample using the [*Gonfiantini*] isotopic parameters (Daëron *et al.*, 2016) for ^{17}O correction exclusively. The consistency of clumped isotope data has since shown to improve if the [*Brand*] isotopic parameters are used for raw data processing instead (Daëron *et al.*, 2016;Kelson *et al.*, 2017). Furthermore, the accuracy of calibration studies is thought to increase with the number of samples, number of replicate measurements per sample and the temperature range (Fernandez *et al.*, 2017). For the refinement of the Δ_{47}-$1/T^2$ relationship presented in this study, the numbers of samples and replicates per sample have therefore been increased fivefold relative to Wacker *et al.* (2016) and the temperature range has been extended by 20 °C from 1 °C to 80 °C. In addition, all data (including the Wacker *et al.*, 2016 data) were (re)processed using the [*Brand*] isotopic parameters. The enlarged dataset confirms the preliminary temperature dependence of Δ_{47} of carbonated apatite provided by Wacker *et al.* (2016). The refined (bio)apatite calibration of this study is furthermore indistinguishable from the [*Brand*] reprocessed calcite calibration of Wacker *et al.* (2014) if acid fractionation is taken into account.

2.2 Materials

2.2.1 Biogenic apatite

Two identical batches of the original African elephant enamel and dentine samples from Wacker *et al.* (2016) were used for this study. Additionally, Greenland and sand tiger shark teeth from different specimens were acquired (*table 2.1*). The African elephant (*Loxodonta africana*) materials originate from an upper left molar that formed at an actively regulated (Weissenböck *et al.*, 2010) body temperature of 37 ± 1 °C (Elder & Rodgers, 1975; Kinahan *et al.*, 2007). Teeth are generally composed of enamel(oid) and dentine whereas enameloid is not homologous to enamel of mammals and reptiles and generally refers to the highly mineralized outer layer of amphibian and fish teeth (*e.g.* Poole, 1967; Grady, 1970; Davit-Béal *et al.*, 2007; Sasagawa *et al.*, 2009). Enamel consists of densely arranged bioapatite crystals and has a low content of organic matter and water (< 1 wt.% and < 3 wt.%, respectively; Kohn & Cerling T. E., 2002; Boskey, 2007). Dentine differs in its structure, which is porous due to µm-sized tubuli (Zabler *et al.*, 2007). In contrast to enamel, the content of organic matter and water in dentine is generally higher (Zapanta LeGeros, 1981; Pasteris *et al.*, 2008). Its nm-sized apatite crystals have a plate-like habitus and higher surface area when compared to the larger apatite crystals in enamel. The

total inorganic carbonate contents (TIC) of the African elephant enamel and dentine are 8.2 and 7.8 wt.%, respectively (*table 2.1*). The total organic carbon contents (TOC) for enamel and dentine are 0.2 and 9.7 wt.%, respectively (Wacker *et al.*, 2016). Tooth enamel and dentine were separated with a drill, a hammer and a chisel. Fragments of both tissues were pulverized and homogenized using an agate vibratory disc mill and dried at 50 °C for two days. The molar was kindly provided by A. Gehler (Georg-August-University, Goettingen) and the enamel represents an aliquot of the standard AG-LOX (Gehler *et al.*, 2012).

The Greenland shark (*Somniosus microcephalus*) tooth samples measured in this study are from the lower jaws of two different specimens with a body length of approximately > 3 m that were kindly supplied by the Bjarnarhöfn Shark Museum (Iceland). The cold water sharks are typically found in the North Atlantic Ocean, proximate to the coasts of Canada, Greenland and Iceland at depths of 0 to 2200 m (Herdendorf & Berra, 1995). The water depth of the shark's habitat is assumed to be chosen actively and dependent on the ambient water temperature (Stokesbury *et al.*, 2005). According to measurements from data loggers that were attached to Greenland sharks (Watanabe *et al.*, 2015), specimens longer than 2.5 m prefer water temperatures between -1.2 and 3.4 °C, which correspond to water depths < 270 m. Dietary studies based on stable isotopes, ubiquitous pollutants and stomach contents imply that the Greenland shark feeds at a high trophic level which can vary with size (Fisk *et al.*, 2002). The shark focuses on pelagic and benthic resources (Fisk *et al.*, 2002; McMeans *et al.*, 2010) and occasionally feeds on terrestrial animals such as polar bears (McMeans *et al.*, 2010). Following the concept of aerobic red muscle (RM) endothermy (Watanabe *et al.*, 2015), the Greenland shark's slow cruising speed (Watanabe *et al.*, 2012; their figure 3) suggests a low heat production. Teeth from ectothermic sharks are interpreted to reflect the ambient water temperature because of their permanent exposure to seawater during growth. According to the size of the investigated specimen and logger data (Watanabe *et al.*, 2012) the temperature of mineral precipitation is considered to be 1 ± 2 °C.

To cover an intermediate temperature range, shark teeth from different specimens of the lamniform sand tiger shark (*Carcharias taurus*) were sampled. Sand tiger sharks occur in tropical to warm temperate habitats in inshore to offshore settings at various depths up to possibly 1600 m (Compagno, 2001). The sampled specimen lived under controlled temperatures at 20 ± 1 °C in an aquarium (Two Oceans Aquarium, Cape Town, South Africa). The large (1 to 2.5 cm height) and pointy anterior and lateral teeth are shaped awl and blade like, respectively. Only naturally

erupted mature teeth were sampled. Shark teeth generally consist of fluorapatite with traces of hydroxylapatite (Møller *et al.*, 1975; Enax *et al.*, 2012). They are constantly formed and replaced row by row within days to weeks (Berkovitz, 2000; Botella *et al.*, 2009). Due to the thin (<< 0.5 mm) enameloid layer and its small carbonate content (~2 wt.%), it was not feasible to sample enough enameloid powder to produce a sufficient number of Δ_{47} replicate measurements. Sampling was consequently focused on tooth dentine (TIC = 5 wt.%, *table 2.1*). Carbon isotope measurements of complete teeth ($\delta^{13}C$ = -2.3 ± 0.1 ‰, n = 3), enameloid ($\delta^{13}C$ = 7.4 ± 0.4 ‰, n = 2) and dentine ($\delta^{13}C$ = -4.0 ± 0.1 ‰, n = 13) imply that the bulk sand tiger shark teeth contain approximately 15 wt.% enameloid. Complete sand tiger shark teeth were further excluded from the calibration study to avoid systematic uncertainties that could arise from nonlinear mixing effects of Δ_{47} (Defliese & Lohmann, 2015) because enameloid and dentine differ in their bulk isotopic composition.

Table 2.1: Overview on growth temperatures (Tgrowth), total inorganic carbon (TIC) and total organic carbon (TOC) values and sample size (required per replicate) of the materials used for this study. The TOC values of the African elephant and Greenland shark are compiled from (Wacker *et al.*, 2016). The TIC values are calculated from the ratio of the partial pressures of CO_2 that evolved during acid digestion of the respective sample and pure carbonate. TOC was inferred from the difference between the total carbon and TIC.

Sample material	T_{growth} (°C)	TIC (wt.%)	TOC (wt.%)	Sample size (mg)
Elephant tooth enamel	37 ± 1	8.2	0.2	60-120
Elephant tooth dentine	37 ± 1	7.8	9.7	70-120
Greenland shark tooth enameloid	1 ± 2	2.9	7.6	180-240
Greenland shark tooth dentine	1 ± 2	3.3 - 6.2	17.8	90-220
Sand tiger shark tooth dentine	20 ± 1	5.0	n.d.	105-150
Megatooth shark tooth enameloid	n.d.	3.6	0.3	100-120
Synthetic apatite	7 ± 1	6.2	0	80
Synthetic apatite	59 ± 0.5	6.0	0	100-110
Synthetic apatite	80 ± 0.5	8.7	0	65-80

A tooth from the megatooth shark with unknown origin is used for applying the temperature calibration of this study to fossil material. The genus of the shark is debated and, for example, has been stated to be *Carcharodon* (Agassiz, 1833; Pimiento & Clements, 2014 and 2016), *Carcharocles* (Renz, 2002; Nyberg *et al.*, 2006; Pimiento *et al.*, 2010), *Procarcharodon* (Klimley, 1996) and *Otodus* (Cappetta H., 1987; Ferrón, 2017). The shark is further referred to as *Carcharodon megalodon*, being aware of the taxonomical uncertainty. *C. megalodon* was one of

the most powerful and largest predators ever known in Earth's vertebrate history (Wroe *et al.*, 2008) and may have approached a maximum length of 16 to 20 m (Cappetta *et al.*, 2012; Wroe *et al.*, 2008; Klimley, 1996). The cosmopolitan shark may have looked similar to an enlarged great white shark (*Carcharodon carcharias*) and had a preference for warm waters (Klimley, 1996). It occurred from the late Oligocene and became extinct during the Pliocene to Pleistocene (Pimiento & Clements, 2015). Its triangular and serrated teeth have a similar morphology to the teeth of the great white shark (Klimley, 1996), which is interpreted as its modern analogue (Pimiento *et al.*, 2010). The sampled tooth is 12 cm high and 10 cm wide (*figure 2.1*). The $CaCO_3$ content of the *C. megalodon* tooth enameloid is 3.6 wt.%. (TIC, *table 1*). The respective TOC value is 0.3 wt.%.

Figure 2.1.: Photograph of the labial (left) and lingual (right) side of the sampled Carcharodon Megalodon tooth (12 cm height, 10 cm width) showing the typical robust root and wide bourlette. The sampling areas for Δ_{47}, $\delta^{13}C$, $\delta^{18}O_{CO3}$ (polygons), serial $\delta^{18}O_{PO4}$ (circles) and $^{87}Sr/^{86}Sr$ (cross) measurements are highlighted in the picture. Scale bar: 5 cm.

2.2.2 Abiogenic apatite

Abiogenic carbonated hydroxylapatites (CHAPs) were synthesized at the Leibniz Institute for Baltic Sea Research (IOW) at temperatures of 7 °C, 59 °C and 80 °C using two different experimental approaches. First attempts via transformation of metastable brushite (Lécuyer *et al.*, 2010) yielded CHAP with a CO_3 concentration below the current limit of clumped isotope analysis. Therefore, CHAPs with higher CO_3-contents were prepared by conversion of metastable

to more stable solids in well-designed experiments (*e.g.*, Matthews & Katz, 1977; Lécuyer *et al.*, 2010; Kasioptas *et al.*, 2011; Zheng & Böttcher, 2016; Böttcher *et al.*, 2018; Bötcher, 2000).

2.3 Methods

2.3.1 Synthesizing abiogenic apatite

Synthetic CHAP formed from an aqueous 0.9 M solution of di-potassium or di-ammonium hydrogenphosphate that was initially 0.01 M in sodium (hydrogen) carbonate (prepared from p.a. quality chemicals, Merck). Before synthetic calcite was added (p.a. grade quality, Merck; only in one experiment at 7 °C, a calcite powder delivered by Applichem was used), the dissolved inorganic carbon species (DIC) were equilibrated with the water of the mother solution for at least 48 h, a duration that is sufficient to allow for the establishment of the isotope exchange equilibrium between DIC and water (Zeebe & Wolf-Gladrow, 2001; Beck *et al.*, 2005; Lécuyer *et al.*, 2010). To further confirm this, test experiments with $NaHCO_3$ solutions were carried out at 7 °C, 21 °C and 60 °C. After specific reaction times, DIC was quantitatively precipitated as $BaCO_3$, filtered, washed, dried and isotopically measured at IOW using a Gasbench III coupled to a MAT 253 gas source mass spectrometer (Thermo Fisher Scientific, Bremen, Germany), as described earlier (Böttcher *et al.*, 2018). This approach is simlar to the one used by (Beck *et al.*, 2005) to study oxygen isotope fractionation between DIC and water. It became obvious that at all run temperatures, the isotope exchange equilibrium between DIC (essentially HCO_3^-) and water was reached within less than 24 h. Synthesis of CHAP at 7 °C and 59 °C were performed using closed PTFE-lined autoclaves (Heinrichs *et al.*, 1986). After DIC equilibration, 300 mg of fine-grained $CaCO_3$ powder was added and the aqueous solution was allowed to react in a drying oven or a refrigerator with manual agitation in regular time intervals. At 80 °C, 15 g synthetic calcite powder was transformed under permanent agitation using a magnetic stirrer in a 1500 ccm double-walled glass reactor that was kept at run temperature by flushing a heated solution through the outer wall. At the end of the run (13,030 h at 7 °C, 214 to 242 h at 59 °C; 141 h at 80 °C), pH was measured using an ion-selective Schott BlueLine 23 electrode and a Schott HandyLab 11 pH meter. The $\delta^{18}O$ of the water was measured by means of cavity ring-down laser absorption spectroscopy (Picarro L2140-I). The synthesis product was separated from the aqueous solution by membrane filtration (0.45 µm membrane filter), washed with deionized water and ethanol and dried at 60 °C in a drying oven. For the characterization of the mineralogy and composition of the synthetic CHAP, different techniques such as X-ray

powder diffraction (including Rietveld refinement for selected samples; Siemens X-ray diffractometer), FTIR spectroscopy, SEM-EDX (MERLIN VP compact, Carl Zeiss) with AztecEnergy (Oxford Instruments), elemental analysis and micro-Raman spectroscopy (Horiba Jobin Yvon LabRam HR-800UV) were applied. The TIC content of synthetic CHAPs was analyzed with a Eurovector elemental analyzer using p.a. grade acetanilide and sulfanilamide for calibration.

2.3.2 Sample pretreatment, acid digestion and purification

Prior to the preparation of sample powder, individual teeth were disarticulated mechanically and cleaned of surrounding tissue and debris. Areas that showed irregular features (*e.g.*, fissures or color) were removed. The labial and lingual sides of the teeth were sampled with a hand drill that was equipped with a dental diamond tip to create bulk samples for each specimen. To avoid mixing with incompletely mineralized tooth material, unerupted teeth older than approximately six months were not sampled (*e.g.*, last three to four rows of teeth of the Greenland sharks). To assess diagenetic recrystallization of the *C. megalodon* tooth enameloid, the area used for clumped isotope analysis was additionally sampled with a 5 mm spaced axial $\delta^{18}O_{PO4}$ profile.

Bleaching of samples can induce alteration of bulk and clumped isotopic compositions of the carbonate fraction inside (bio)apatites (Wacker *et al.*, 2016; Pellegrini & Snoeck, 2016). Therefore (and to uphold the methodological comparability with the preexisting data of Wacker *et al.* (2016), no chemical pretreatment was performed.

All Δ_{47} analyses were carried out at the Goethe University-Senckenberg BiK-F stable isotope facility (Frankfurt Main). Samples were digested in a fully automated device that was directly connected to a MAT 253 gas source mass spectrometer (IRMS; Thermo Fisher Scientific, Bremen, Germany). The acid digestion device was built according to the conceptual design of Passey *et al.* (2010) and contains a rotating autosampler (Zero Blank autosampler; Costech, Valencia, CA, USA), a stirred and heated common acid bath (d= 9 cm), H_2O and CO_2 traps for cryogenic purification and a GC (1.2 m x 2.15 mm stainless steel column, packed with Porapak Q 80/120). The H_2O and CO_2 traps were held at -80 °C (using ethanol cooled with liquid nitrogen) and -196 °C (liquid nitrogen), respectively. Traps and acid bath were pumped individually by two turbo pumps (Pfeiffer, Asslar, Germany).

Prior to digestion, samples were loaded into silver capsules (IVA Analysentechnik e.K., Meerbusch, Germany) and stored for 30 min at 30 °C within vacuum (25 mbar). This compacts the sample and limits the risk of sample powder blowout that can be caused by expanding air while evacuating the loaded autosampler, especially for large samples (> 50 mg). After loading the autosampler, it was evacuated for 8 to 12 hours. The pressure within the autosampler and the acid bath was typically below 5 x 10^{-3} mbar. As soon as the first cryogenic CO_2 trap behind the acid bath reached -196 °C, the sample capsules were dropped into the common acid bath which contained 105 to 107 % orthophosphoric acid (≥ 99.9 %, Merck; hyper saturated with ≥ 99 % phosphorous pentoxide, Carl Roth) that was stirred constantly at 110 ± 0.1 °C. This procedure enables that the CO_2 evolving from phosphoric acid digestion is immediately removed from the acid bath which is constantly connected to the first cryogenic CO_2 trap during the overall reaction time of 60 min. After a reaction time of 30 min within closed vacuum, the acid bath was pumped through the first CO_2 trap for an additional 30 min to ensure a fast and complete fixation of the evolved analyte gas. The trapped gas was defrosted at -80 °C and then refrozen at -196 °C into a second CO_2 trap that was placed in front of the GC. Afterwards, the second CO_2 trap was heated to -80 °C, the CO_2 entrained into a He 6.0 (Linde AG, Pullach, Germany; purity ≥ 99.9999 %) carrier gas flow and purged through two additional water traps (-80 °C) and a GC column packed with Porapak Q 80/120 (-15 °C). After passing the GC, the CO_2 was frozen out in a third cold trap at -196 °C. Helium was pumped off, the third CO_2 trap heated to -80 °C and the CO_2 was finally transferred into a small cold finger (-196 °C) located directly in front of the dual inlet system of the MAT 253 IRMS. For isotopic measurement, the CO_2 gas was expanded into the sample bellow after heating the small cold finger to -80 °C. The gas pressure before and after the GC was compared within an identical volume to ensure quantitative recovery of the analyte gas. Vacuum and temperatures of the automated digestion device including various traps, GC and acid bath were monitored during all steps. No indication for gas loss was detected. The gas yield produced by reactions of Carrara marble at 110 °C (60 min. reaction incl. 30 min pumping) of 4.00 ± 0.23 mbar/mg (n = 26) is indistinguishable from the value reported for 90 °C reactions (30 min reaction time w/o pumping) of Wacker *et al.* (2016) of 4.10 ± 0.14 mbar/mg (n = 9).

2.3.3 Mass spectrometric analysis

All samples, with the exception of those reported in (Wacker *et al.*, 2016), were measured between February 2016 and October 2017 (supplementary data *S.2.III).* Each dual inlet

measurement included 10 acquisitions of 10 cycles each with an ion integration time of 20 s. Peak center, pressure adjustments of the reference and sample gas bellows as well as background determinations without and with analyte gas in the ion source were made at the start of each acquisition. A second background detection with analyte gas in the ion source was performed at the end of each acquisition (Fiebig *et al.*, 2016). For isotopic measurements, the signal intensities on *m/z* 44 were adjusted to 16,000 ± 150 mV for both, sample and reference gas. The *m/z* ratios 44 to 49 are measured simultaneously on six Faraday-cups with distinct amplification (*m/z* 44: 3 x 10^8 Ω, *m/z* 45: 3 x 10^{10} Ω, *m/z* 46: 10^{11} Ω, *m/z* 47 to 49: 10^{12} Ω). The slit widths for the *m/z* 44 to 47, 48 and 49 are 1.5, 3.5 and 4.5 mm, respectively. The CO_2 reference gas used (Air Liquide Deutschland GmbH, Düsseldorf, Germany) has an isotopic composition of $\delta^{18}O$ = 25.16 ‰$_{VSMOW}$ and $\delta^{13}C$ = -4.30 ‰$_{VPDB}$.

2.3.4 Micro-Raman spectroscopy

Raman spectra were measured at the University of Goettingen (Mineralogy at GZG) using a confocal Horiba Jobin Yvon LabRam HR800 UV Raman system with attached Olympus BX 41 microscope and 488 nm laser excitation. The laser power was set to 50 mW at the laser exit, corresponding to approximately 4 mW at the sample surface. The Stokes-Raman scattered light was dispersed by a grating of 600 grooves/mm on a Peltier cooled CCD detector (Andor™) with 1024 × 256 pixels, yielding a spectral dispersion of about 2 cm^{-1} per pixel. A 100× objective (N.A. = 0.9) and a confocal hole of 100 µm was used for the measurements, yielding an axial resolution of < 3.5 µm and a lateral resolution of < 1.5 µm. Raman spectra were collected in a single spectral window in the range 100 to 2200 cm^{-1} with acquisition times of 2 × 30 s to 8 × 30 s. Spectra were referenced using the main peak of a silicon wafer at 520.4 cm^{-1}. The overall wavenumber uncertainty of the setup used is ± 2 cm^{-1}.

2.4 Clumped isotope data

2.4.1 Data processing

Measured *m/z* 47 intensities were corrected for the contribution of secondary electrons by scaling the negative background intensities on *m/z* 47 to the peak intensity of *m/z* 49 (Fiebig *et al.*, 2016; Wacker *et al.*, 2016). The quality of this background correction method was monitored by analyzing CO_2 equilibrated at 1,000 °C (HG) and 25 °C (25G), along with the samples. The 25Gs and HGs were measured continuously two and three times per week, respectively. The

equilibrated HGs and 25Gs were passed through the same capillaries, traps and pathways as the sample gas (excl. common acid bath). A plot of δ^{47} *vs.* Δ_{47} of the HGs and 25Gs revealed slopes < 0.001. A residual slope correction of background corrected Δ_{47} values was performed if these slopes were - within error - distinguishable from zero. In these cases, the residual slope for additional correction was determined from the merged HG and 25G data (supplementary data *S.2.I*). Afterwards Δ_{47} values were corrected for scale compression and reported on the Carbon Dioxide Equilibrium Scale (CDES) as recommended by Dennis *et al.* (2011), where the CDES is exclusively based on data from equilibrated gases (HG and 25G). Bulk and clumped isotopic compositions were processed with the [*Gonfiantini*] and [*Brand*] isotopic parameters (Daëron *et al.*, 2016). Sample gases were monitored for contaminant gases by plotting the *m/z* 47 background *vs. m/z* 49 peak intensities both for the sample and reference gas (Fiebig *et al.*, 2016; Wacker *et al.*, 2016). No indication for contamination was found.

The $\Delta_{47\ CDES\ 110}$ values of (bio)apatites digested at 110 °C are not projected to the 25 °C reference frame ($\Delta_{47\ CDES\ 25}$; Dennis *et al.*, 2011) because reacting carbonated apatite at 25 °C is not feasible within reasonable amounts of time. This notwithstanding, the acid fractionation factors of Defliese *et al.* (2015) of +0.062 (25 °C *vs.* 70 °C reaction), +0.082 (25 °C *vs.* 90 °C reaction) and +0.100 ‰ (25 °C *vs.* 110 °C reaction) are applied to the $\Delta_{47CDES\ 110}$ data of carbonate and apatite standard materials of this study in order to compare them with previously published $\Delta_{47\ CDES\ 25}$ data (Dennis *et al.*, 2011; Henkes *et al.*, 2013; Meckler *et al.*, 2014; Wacker *et al.*, 2014; and 2016; Kele *et al.*, 2015; Daëron *et al.*, 2016; Stolper & Eiler, 2015). The absolute temperature used in this study is 273.2 K. The oxygen isotope phosphoric acid fractionation factors for calcite and aragonite at 110 °C are 1.00761 and 1.00805, respectively (extrapolated after Kim *et al.*, 2007). The former is also applied to the CO_2 evolved at 110 °C from (bio)apatites. Passey *et al.* (2007) demonstrated that the oxygen isotope acid fractionation factor of modern enamel at 90 °C is identical within 0.2 % to the Kim *et al.* (2007)value for calcite. All bulk isotopic compositions are given in VPDB notation and the precision of the isotopic data is reported as 1σ standard error (1 se), unless stated otherwise.

2.4.2 Data quality assurance

Six internal standard materials (Carrara marble, *Arctica islandica*, ETH 1, ETH 2, ETH 3 and NIST SRM 120c) were measured regularly during the analytical period of this study. For comparison with published values, it is further referred to the [*Gonfiantini*] $\Delta_{47\ CDES\ 25}$ values as

the majority of the data published thus far was calculated with these isotopic parameters (*table 2.2*). Four out of these six standards (Carrara marble, *Arctica islandica*, ETH 2, ETH 3) were also digested at 90 °C to screen for possible effects of reequilibration at reaction temperatures of 110 °C. The isotopic compositions of the standard materials mentioned below do not differ significantly between the individual analytical periods. The corresponding data are given in the supplementary data (*S.2.II*). The mean values for the internal standards of this study are (av ± 1σ sd):

i) Pure Carrara marble: $\Delta_{47\ CDES\ 25}$ = 0.399 ± 0.024 ‰ (110 °C, n = 26) and 0.396 ± 0.019 ‰ (90 °C, n = 32). Both values are identical to results (90 °C) obtained by Dennis *et al.* (2011), Fiebig *et al.* (2016) and Bonifacie *et al.* (2017), who reported $\Delta_{47\ CDES\ 25}$ values of 0.395 ± 0.008 (n = 115), 0.392 ± 0.016 ‰ (n =15) and 0.393 ± 0.014 ‰ (n = 24), respectively.

ii) *Arctica islandica* (MuStd), an aragonitic cold water bivalve. The specimen was collected alive near Langanas (NE Iceland, August 2006) at a water depth of approximately 30 m (Wacker *et al.*, 2013): $\Delta_{47\ CDES\ 25}$ = 0.753 ± 0.021 ‰ (110°C, n = 29) and 0.750 ± 0.019 ‰ (90 °C, n = 20). Kele *et al.* (2015) measured this standard with $\Delta_{47\ CDES\ 25}$ = 0.757 ± 0.025 ‰ (70 °C; n = 40). Previously reported Δ_{47} values of *Arctica islandica* are $\Delta_{47\ CDES\ 25}$ = 0.737 ± 0.018 ‰ (90 °C, n = 28; Wacker *et al.*, 2013) and 0.738 ± 0.012 ‰ (90 °C, n = 11; Wacker *et al.*, 2016).

iii) ETH 1 (Iso A), which is Carrara marble heated at 600 °C and 155 MPa for 10 h (Meckler *et al.*, 2014): $\Delta_{47\ CDES\ 25}$ = 0.300 ± 0.020 ‰ (110 °C, n = 12). (Daëron *et al.*, 2016) measured this standard with $\Delta_{47\ CDES\ 25}$ = 0.310 ± 0.024 ‰ (90 °C, n = 18).

iv) ETH 2 (Iso B), a fine-grained commercial carbonate that was treated identically to ETH 1: $\Delta_{47\ CDES\ 25}$ = 0.298 ± 0.008 ‰ (110 °C, n = 8) and $_{\Delta 47}$ = 0.292 ± 0.022 ‰ (90 °C, n = 4). (Daëron *et al.*, 2016) reported $\Delta_{47\ CDES\ 25}$ = 0.289 ± 0.025 ‰ (90 °C, n = 13). It is noteworthy that the measured clumped isotopic compositions of ETH 1 and ETH 2 of this study are identical for both, [*Gonfiantini*] and [*Brand*] processed data (110 °C data, supplementary data *S.2.II*) because both materials were heated at identical conditions. It can be observed that the ETH 1 and ETH 2 $\Delta_{47\ CDES\ 25}$ values of this study are 30 ppm more positive when compared to Meckler *et al.* (2014) who reacted at 70 °C using a Kiel IV device. Further interlaboratory comparisons are required in order to define globally accepted values for ETH 1 and ETH 2.

v) ETH 3 (Iso C), a Cretaceous chalk from northern Germany: $\Delta_{47\ CDES\ 25}$ = 0.714 ± 0.016 ‰ (110 °C, n = 41) and 0.709 ± 0.018 ‰ (90 °C, n = 11) are identical with the reported $\Delta_{47\ CDES}$

$_{25}$ value of 0.703 ± 0.015 ‰ (70 °C, n = 12, Meckler *et al.*, 2014). All ETH standards were kindly provided by S. M. Bernasconi (ETH Zürich).

vi) NIST SRM 120c, a natural Miocene phosphorite from Florida (U.S.A.). It contains different forms of authigenic and biogenic phosphate, siliciclastic material, carbonate and organic matter (LaPorte *et al.*, 2009): $\Delta_{47\ CDES\ 25}$ = 0.679 ± 0.014 ‰ (110 °C, n = 35). The $\Delta_{47\ CDES\ 25}$ value of a different batch was measured by (Wacker *et al.*, 2016) with 0.670 ± 0.012 ‰ (n = 9) at 90 °C. Stolper and Eiler (2016), who bleached their material with H_2O_2 prior to isotopic analysis, reported $\Delta_{47\ CDES\ 25}$ of 0.710 ± 0.018 ‰ (90 °C, n = 10).

The relatively high acid digestion temperature of 110 °C chosen for this study could potentially foster reequilibration of CO_2 with traces of water within the common acid bath because the acid temperature is directly correlated to the partial pressure of water vapor which derives from phosphoric acid polymerization (Defliese *et al.*, 2015). If apparent, such a reequilibration would bias the measured temperature dependency of the clumped isotopic compositions. Four standards with distinct clumped isotopic compositions (Carrara, *A. islandica*, ETH 2 and ETH 3) were reacted at 90 °C and 110 °C. However, independent of the clumped isotopic composition of the standard materials, $\Delta_{47\ CDES\ 25}$ values resulting from reactions at 90 °C were - within the range of uncertainties reflected by the corresponding standard errors - reproduced at 110 °C, after considering the corresponding acid fractionation factors (AFF) of Defliese *et al.* (2015) (*table 2.2*). The observed differences in (non-acid fractionation corrected) Δ_{47} values between 90 °C and 110 °C reactions are, therefore, in agreement with the 90-110 °C acid fractionation factor that can be extrapolated from the dataset of Defliese *et al.* (2015). Hence, no indication for a significant occurrence of reequilibration of sample CO_2 with traces of water at 110 °C can be found.

Comparison of the [*Brand*] processed Δ_{47} standard values of this study (supplementary data *S.2.II*) is currently limited by the small number of studies that have applied the [*Brand*] isotopic parameters so far (supplementary data *S.2.IV*). Briefly, the [*Brand*] processed values of ETH 1, ETH 2 and ETH 3 of this study are indistinguishable from the [*Gonfiantini*] processed values: ETH 1: $\Delta_{47\ CDES\ 25}$ = 0.304 ± 0.021 ‰ (110 °C reaction), ETH 2: $\Delta_{47\ CDES\ 25}$ = 0.290 ± 0.008 ‰ (110 °C reaction) and $\Delta_{47\ CDES\ 25}$ = 0.290 ± 0.022 ‰ (90 °C reaction), ETH 3: $\Delta_{47\ CDES\ 25}$ = 0.711 ± 0.019 ‰ (110 °C reaction) and $\Delta_{47\ CDES\ 25}$ = 0.704 ± 0.017 ‰ (90 °C). Considering the standard deviations, these values are in agreement with the $\Delta_{47\ CDES\ 25}$ reported by Daëron *et al.* (2016) and Schauer *et al.* (2016).

Table 2.2: Overview on the isotopic compositions of the standard materials measured for this study and published reference values. All isotopic compositions (in ‰) are calculated with the [*Gonfiantini*] isotopic parameters. For a direct comparison of the data, Δ_{47} values are normalized to a 25 °C reaction temperature ($\Delta_{47\ CDES\ 25}$) by applying acid fractionation factors of +0.062 ‰, +0.082 ‰ and +0.100 ‰ (Defliese *et al.*, 2015, extrapolated for 70 °C, 90 °C and 110 °C, respectively). The $\Delta_{47\ CDES\ 25}$ values of CO_2 evolved from digestions at 90 °C and 110 °C of four standard materials (this study) are identical within the standard errors.

Standard	Study	$T_{Digestion}$	$\delta^{13}C$	sd	$\delta^{18}O$	sd	$\Delta_{47\ CDES\ 25}$	sd	se	n
Carrara marble	*this study*	110	1.97	0.08	-1.67	0.15	0.399	0.024	0.005	26
	this study	90	1.97	0.02	-1.68	0.14	0.396	0.019	0.003	32
	Fiebig *et. al.* (2016)	90	1.86	0.05	-1.50	0.08	0.392	0.016	0.004	15
	Bonifacie *et. al.* (2017)	90	n.n.	n.n.	n.n.	n.n.	0.393	0.014	0.003	24
	Dennis *et. al.* (2011)	n.d.	n.n.	n.n.	n.n.	n.n.	0.395	0.008	0.001	115
	Henkes *et. al.* (2013)	90	2.05	0.03	-1.85	0.03	0.392	0.015	0.002	93
Arctica islandica	*this study*	110	1.47	0.11	3.07	0.21	0.753	0.021	0.004	29
	this study	90	1.54	0.03	3.22	0.17	0.750	0.019	0.004	20
	Kele *et. al.* (2015)	70	1.67	n.n.	3.48	n.n.	0.757	0.025	0.005	30
	Wacker *et. al.* (2014)	90	1.64	0.06	3.37	0.24	0.737	0.018	0.003	28
	Wacker *et. al.* (2016)	90	1.47	0.06	3.20	0.09	0.738	0.012	0.004	11
	Wacker *et. al.* (2016)	110	1.52	0.04	3.40	0.12	0.736	0.019	0.005	13
ETH 1	*this study*	110	1.94	0.12	-2.15	0.16	0.300	0.020	0.006	12
	Daeron *et. al.* (2016)	90	n.n.	n.n.	n.n.	n.n.	0.310	0.024	0.006	18
	Meckler *et al* (2014)	70	2.14	0.03	-2.18	0.06	0.265	0.012	0.003	23
ETH 2	*this study*	110	-10.19	0.07	-18.68	0.16	0.298	0.008	0.003	8
	this study	90	-10.20	0.04	-18.57	0.37	0.292	0.022	0.011	4
	Daeron *et. al.* (2016)	90	n.n.	n.n.	n.n.	n.n.	0.289	0.025	0.007	13
	Meckler *et al* (2014)	70	-10.10	0.03	-18.76	0.09	0.267	0.011	0.002	24
ETH 3	*this study*	110	1.62	0.09	-1.84	0.17	0.714	0.016	0.002	41
	this study	90	1.66	0.02	-1.82	0.09	0.709	0.018	0.005	11
	Meckler *et al* (2014)	70	1.81	0.03	-1.77	0.06	0.703	0.015	0.004	12
	Kele *et. al.* (2015)	70	1.83	0.03	-1.75	0.06	0.703	0.016	0.003	22
NIST SRM 120c	*this study*	110	-6.41	0.10	-1.35	0.16	0.679	0.014	0.002	35
	Wacker *et. al.* (2016)	90	-6.20	0.26	-0.98	0.23	0.670	0.012	0.004	9
	Wacker *et. al.* (2016)	110	-6.42	0.07	-1.24	0.14	0.655	0.017	0.004	16
	Stolper and Eiler (2016)	90	-6.29	0.05	-1.48	0.10	0.710	0.018	0.006	10

2.4.3 Comparison with previously measured 110 °C data

Wacker *et al.* (2016) presented a preliminary $\Delta_{47\ CDES\ 110}$ temperature calibration for (bio)apatites reacted at 110 °C. Their data was processed using the [*Gonfiantini*] set of isotopic parameters for ^{17}O correction and the background correction scheme described in Fiebig *et al.* (2016). The latter correction did not consider that not only the measured *m/z* 47 intensity, but also

the measured *m/z* 49 intensity needs to be corrected for the corresponding background, which is determined in the absence of analyte gas in the ion source and that is automatically subtracted by the Isodat software. The Wacker *et al.* (2016) data was therefore reevaluated using an improved background correction scheme and applying both the [*Gonfiantini*] and [*Brand*] sets of isotopic parameters (Daëron *et al.*, 2016). The average difference between the published (Wacker *et al.*, 2016; their table 4) and the reprocessed [*Gonfiantini*] $\delta^{18}O$, $\delta^{13}C$ and $\Delta_{47\ \mathrm{CDES\ 110}}$ values of Wacker *et al.* (2016) (supplementary data *S.2.III*) are 14, 2 and 8 ppm, respectively (n = 58) and therefore within analytical uncertainty of clumped isotope analysis. This is due to the fact that the *m/z* 49 background without any gas in the source was always negligibly small compared to the *m/z* 49 intensities of sample and reference gases.

Wacker *et al.* (2016) measured African elephant tooth enamel and dentine, the *Arctica islandica* and NIST SRM 120c between March 2014 and May 2015 (110 °C data). For this study, identical batches of those materials were measured between February 2016 and October 2017. The differences of the [*Brand*] bulk and clumped isotopic compositions measured during the two time intervals are, again, within or below the analytical error ($\Delta\delta^{18}O$ = 10 ppm, $\Delta\delta^{13}C$ = 29 ppm and $\Delta\Delta_{47}$ = 8ppm; n = 159; *figure 2.2*). The same is observed for the Wacker *et al.* (2016) [*Gonfiantini*] reprocessed data and the [*Gonfiantini*] processed new data ($\Delta\delta^{18}O$ = 3 ppm, $\Delta\delta^{13}C$ = 29 ppm and $\Delta\Delta_{47}$ = 10 ppm). It can be concluded that the analytical setups for clumped isotope measurements produced consistent values in the entire period from 2014 to 2017. The [*Gonfiantini*] reprocessed dataset of Wacker *et al.* (2016) and the new [*Gonfiantini*] processed dataset are therefore merged into a single integrated dataset. The same is done with the corresponding [*Brand*] processed datasets (supplementary data *S.2.III*).

2.4.4 Impact of different sets of isotopic parameters on complete (bio)apatite Δ_{47} dataset

No systematic difference between the [*Gonfiantini*] and [*Brand*] processed bulk and clumped isotopic compositions can be observed in the overall (bio)apatite dataset (*table 2.3*, n = 122, with $\delta^{13}C$ ranging from -12.2 to 1.4 ‰ and $\delta^{18}O$ from -13.0 to 2.9 ‰).

For individual replicate measurements, the differences between the [*Gonfiantini*] and [*Brand*] processed values ($\Delta(\Delta_{47})$) range from -7 to +12 ppm (supplementary data *S.2.III*), which is roughly 50 % lower when compared to the measured range of $\Delta(\Delta_{47})$ reported by (Daëron *et al.*, 2016). This implies that the different isotopic parameters have a minor effect on the reported values with the difference being comparable to the analytical error. This observation can be

ascribed to the circumstance that the reference gas used in this study has a bulk isotopic composition bracketed by the total range of $\delta^{13}C$ and $\delta^{18}O$ values of equilibrated gases and samples.

2.5 Results

The $\Delta_{47\ CDES\ 110}$, bulk $\delta^{18}O$ and $\delta^{13}C$ values of the biotic and abiotic apatite calibration samples (all processed using [*Brand*] parameters) are listed in *table 2.3*. The results of the Δ_{47} analysis (± 1 se) are: *i*) African elephant: $\Delta_{47\ CDES\ 110}$ = 0.550 ± 0.003 ‰ (enamel, n = 49) and $\Delta_{47\ CDES\ 110}$ = 0.555 ± 0.004 ‰ (dentine, n = 16), *ii*) Greenland sharks: $\Delta_{47\ CDES\ 110}$ = 0.636 ± 0.004 ‰ (enameloid, n = 10) and $\Delta_{47\ CDES\ 110}$ = 0.647 ± 0.008 ‰ (dentine, n = 17), *iii*) sand tiger sharks: $\Delta_{47\ CDES\ 110}$ = 0.596 ± 0.008 ‰ (dentine, n = 13), *iv*) CHAP 7 °C: $\Delta_{47\ CDES\ 110}$ = 0.631 ± 0.006 ‰ (n = 4), *v*) CHAP 59 °C: $\Delta_{47\ CDES\ 110}$ = 0.495 ± 0.008 ‰ (n = 7) and *vi*) CHAP 80 °C: $\Delta_{47\ CDES\ 110}$ = 0.475 ± 0.004 ‰ (n = 6). The fossil *C. megalodon* yielded $\Delta_{47\ CDES\ 110}$ = 0.593 ± 0.005 ‰ (n = 4).

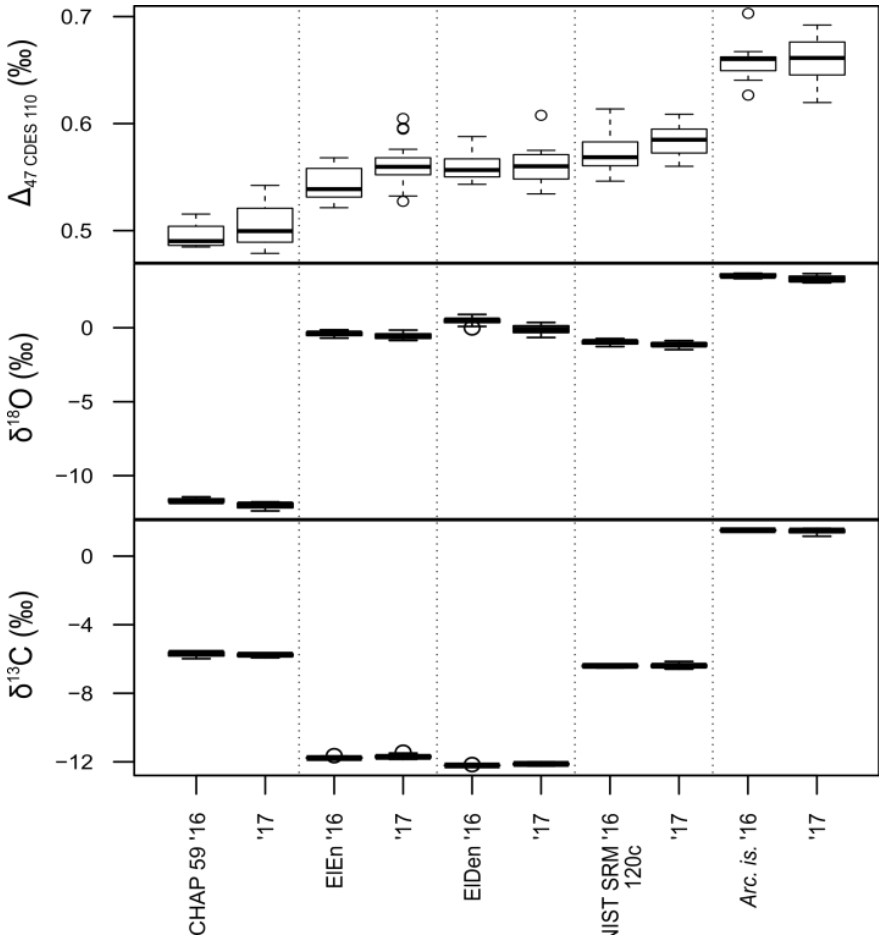

Figure. 2.2.: Boxplot for comparing pairs of $\Delta_{47\ CDES\ 110}$ datasets from five identical or comparable (TE-60) materials that were measured before 2016 (’16) and between 2016 and 2017 (’17). Each pair is divided by dotted lines. All isotopic compositions are calculated with the [*Brand*] isotopic parameters. The bulk and clumped isotopic compositions of all

Comprehensive information on all measurements including δ^{47} and raw Δ_{47} values is given in the supplementary data (*S.2.III*). Using micro-Raman spectroscopy, all synthetic samples were found to consist of CHAP (*figure* 2.3) with dominating substitution of the CO_3^{2-} group for the phosphate group (B-type), but a small Raman shift band close to 1107 cm^{-1} was always found indicating minor carbonate substitution on the hydroxyl position (A-type; Nelson & Williamson, 1982; Penel *et al.*, 1998).

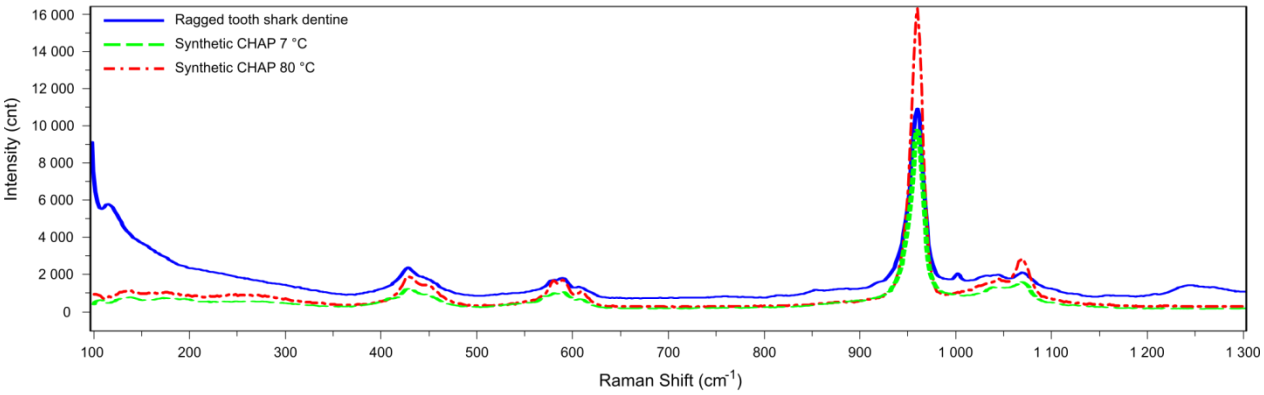

Figure 2.3: Comparison of micro-Raman spectra for biogenic sand tiger shark dentine (blue solid line) and abiotic carbonated hydroxylapatites (CHAPs) synthetized at 7 °C (green dashed line) and 80 °C (red dashed and dotted line). All spectra were frequency corrected using the mean Raman band of silicon. Changes in the background and the rise at the low end of the spectrum and above 1200 cm-1 in dentine samples is caused by organic compounds (*e.g.*, Awonusi *et al.*, 2007). All samples show the characteristic Raman band for the PO_4^{3-} and CO_3^{2-} groups (Nelson & Williamson, 1982; Penel *et al.*, 1998; Antonakos *et al.*, 2007; Awonusi *et al.*, 2007).

2.6 Discussion

2.6.1 Comparison of enamel(oid) and dentine isotopic data

Tooth enamel(oid) and dentine from identical specimens of both mammals (African Elephant) and sharks (Greenland sharks) were analyzed. This allows for comparison of clumped isotopic compositions of samples dominated by hydroxylapatite (African elephant) and fluorapatite (Greenland shark) all having distinct TIC and TOC contents (*table 2.1*) as well as bulk isotopic compositions (*table 2.3*). No differences in the carbonate clumped isotopic compositions of the tooth enamel(oid) and dentine can be detected. If existing, the impact of differences in the chemical compositions between tooth enamel(oid) and dentine on the pristine

clumping of isotopologues in the carbonate group ($^{13}C^{18}O^{16}O_2^{2-}$) of bioapatites ($\Delta_{63}$, Guo *et al.*, 2009) must be below the current limit of resolution. While the clumped isotopic compositions of tooth enamel(oid) and dentine from a given species are identical within errors, the mean oxygen and carbon isotopic compositions differ by 0.8 ± 0.1 and 0.4 ± 0.3 ‰, respectively (African elephant) and 2.0 ± 0.3 and 4.4 ± 1.2 ‰, respectively (Greenland sharks) (*table 2.3*). The relatively large variations in $\delta^{13}C$ and $\delta^{18}O$ between shark tooth enameloid and dentine could point to variations in *i*) the relative contributions of dietary carbon and seawater DIC to DIC of the body fluid (Vennemann *et al.*, 2001), *ii*) the oxygen isotopic composition of seawater and/or body fluid, *iii*) temperature and/or iv) to the importance of kinetic effects. The consistent $\Delta_{47\ CDES\ 110}$ data for enameloid and dentine suggest that thermodynamic equilibrium of Δ_{63} may have been attained in both substances while the carbonate groups of tooth enameloid and/or dentine were in bulk oxygen isotope disequilibrium with the DIC of the body fluid. Alternatively, the $\delta^{18}O$ value of the body fluid might differ from that of seawater. The $\delta^{18}O$ value of tooth enameloid should record the respective $\delta^{18}O$ value of surrounding seawater more directly when compared to dentine because the latter is successively shielded by enameloid from seawater during tooth mineralization (Grady, 1970). Moreover, differences in the Greenland shark tooth $\delta^{18}O$ values from individual specimens could be biased by the exposition to different Arctic water masses with varying fresh water content (*e.g.*, Bédard *et al.*, 1981). The depth-dependent $\delta^{18}O$ of the Arctic water masses can thereby differ by approximately 4 ‰ (van Donk & Mathieu, 1969):

The simplest explanation for the $\delta^{13}C$ variation of the Greenland shark samples is the dietary intake of varying food sources over time (MacNeil *et al.*, 2012) at constant seawater DIC input. The $\delta^{13}C$ values of the Greenland shark diet range from -15.2 to -19.3 ‰ (Teleostei and invertebrates, n = 100; McMeans *et al.*, 2010). This variation of ~4 ‰ also occurs in the muscle tissue ($\delta^{13}C$ = -15.7 to -20.6 ‰, n = 32; Fisk *et al.*, 2002; McMeans *et al.*, 2010), whereas McMeans *et al.* (2010) measured an average value of -17.8 ± 0.3 ‰. In contrast to the low diet-bulk muscle tissue discrimination of sharks (≤1 ‰, Hussey *et. al.*, 2010), the apparent $\Delta\delta^{13}C$ between Greenland shark soft tissue (-17.8 ± 0.3 ‰, McMeans *et al.*, 2010) and tooth enameloid (*table 2.3*) averages at a higher value of 19.2 ± 0.7 ‰.

2.6.2 Temperature dependence of clumped isotopic composition of (bio)apatites

As a first step, the relationships between $\Delta_{47\ CDES\ 110}$ values and $1/T^2$ were investigated for enamel(oid), dentine and synthetic apatite samples separately using both ([*Gonfiantini*] and [*Brand*] processed) datasets (*table 2.3*). For each dataset, fitted least squares linear regressions were calculated according to the statistical concept of York *et al.* (2004) and Wacker *et al.* (2014) by using the computing software R (R Core Team, 2013). While the materials vary in their composition (TOC, TIC, $\delta^{13}C$ and $\delta^{18}O$), the respective regressions are - within errors - indistinguishable from each other (*table 2.4*). The choice of isotopic parameters does not significantly affect the slope and intercept of the equations either. The use of the [*Brand*] parameters leads to a slight improvement of the correlation coefficients (R^2) and the *p*-values of the dentine and CHAP datasets. These slight improvements are in agreement with previous findings of (Daëron *et al.*, 2016).

The overall consistency of the (bio)apatite clumped isotope data for enamel(oid), dentine and synthetic apatites implies that for a given temperature the Δ_{63} value of the carbonate group in the *in vivo*

Table 2.3: Mean $\Delta_{47\ CDES\ 110}$, bulk $\delta^{18}O_{CO3}$ and $\delta^{13}C_{\ CO3}$ values (in ‰; incl. 1σ se) as well as $10^6/T^2$ (in $1/K^2$, incl. error), number of replicates (n) measured per sample, and weights (in %) of the biotic and abiotic apatite samples that are used for the Δ_{47}-$/T^2$ calibration. Data are calculated with the [*Gonfiantini*] and [*Brand*] isotopic parameters (Daëron *et al.*, 2016). The abiotic carbonated hydroxylapatite (CHAP) at 7 °C formed from two carbonates with distinct $\delta^{18}O$ and $\delta^{13}C$. Comprehensive data is listed in the supplementary data (*S.2.III.*). The elevated standard errors (se) of the Greenland shark and CHAP 7 °C sample are caused by the sample heterogeneity because the values average individual specimens and experiments that represent identical temperatures of mineral precipitation.

	[*Gonfiantini*]			[*Brand*]					
Sample	$\Delta_{47\ CDES\ 110}$ ± se	$\delta^{13}C_{CO3}$ ± se	$\delta^{18}O_{CO3}$ ± se	$\Delta_{47\ CDES\ 110}$ ± se	$\delta^{13}C_{CO3}$ ± se	$\delta^{18}O_{CO3}$ ± se	$10^6/T^2$ ± error	n	weight
African elephant tooth enamel	0.547 ± 0.003	-11.73 ± 0.01	-0.71 ± 0.03	0.550 ± 0.003	-11.71 ± 0.01	-0.70 ± 0.03	10.39 ± 0.07	49	32
African elephant tooth dentine	0.551 ± 0.004	-12.18 ± 0.25	0.04 ± 0.07	0.555 ± 0.004	-12.15 ± 0.26	0.05 ± 0.07	10.39 ± 0.07	17	17
Greenland shark tooth enameloid	0.636 ± 0.004	1.38 ± 0.41	2.89 ± 0.43	0.636 ± 0.004	1.38 ± 0.41	2.90 ± 0.43	13.30 ± 0.20	10	7
Greenland shark tooth dentine	0.646 ± 0.008	-3.03 ± 0.09	0.91 ± 0.20	0.647 ± 0.008	-3.02 ± 0.79	0.91 ± 0.20	13.30 ± 0.20	16	3
Sand tiger shark tooth dentine	0.595 ± 0.008	-3.97 ± 0.04	1.25 ± 0.12	0.596 ± 0.008	-3.96 ± 0.03	1.26 ± 0.10	11.63 ± 0.08	13	6
CHAP 7 °C	0.635 ± 0.006	-2.05 ± 1.44	-2.46 ± 0.32	0.631 ± 0.006	-2.05 ± 1.44	-2.45 ± 0.32	12.74 ± 0.09	4	9
CHAP 59 °C	0.501 ± 0.009	-5.74 ± 0.06	-12.03 ± 0.11	0.495 ± 0.008	-5.74 ± 0.06	-12.03 ± 0.11	9.01 ± 0.03	7	5
CHAP 80 °C	0.486 ± 0.004	-5.69 ± 0.02	-12.98 ± 0.13	0.475 ± 0.004	-5.68 ± 0.02	-12.97 ± 0.13	8.02 ± 0.02	6	21

samples (enamel(oid) and dentine) represents an identical state of thermal equilibrium when compared to the *in vitro* CHAP samples (synthetic). In a second step, data from CHAPs, tooth dentine and enamel(oid) are consequently integrated into a global dataset (*figure 2.4*) for calculating an error considering regression line (R^2= 0.9924, *p*-value= 1.36 x 10^{-7}, n = 122, 8 samples, [*Brand*] processed):

(*equation 2.1*) $\Delta_{47\ CDES\ 110} = 0.0325\ (\pm\ 0.0012) \times 10^6/\ T^2 + 0.2137\ (\pm\ 0.0124)$
(with T in K and Δ_{47} in ‰)

The use of the [*Gonfiantini*] isotopic parameters gives an indistinguishable equation if the respective errors are considered (R^2 = 0.9855, *p*-value = 9.58 x 10^{-7}):

(*equation 2.2*) $\Delta_{47\ CDES\ 110} = 0.0305\ (\pm\ 0.0012) \times 10^6/\ T^2 + 0.2352\ (\pm\ 0.0123)$
(with T in K and Δ_{47} in ‰)

The choice of the [*Brand*] isotopic parameters improves the R^2 and *p*-value of the calculated linear regression line (*equation 1*) when compared to the one calculated with the data that was processed with the [*Gonfiantini*] isotopic parameters (*equation 2.2*). Again, this observation agrees with Daëron *et al.* (2016) and Kelson *et al.* (2017). It is therefore recommended to process (bio)apatite Δ_{47} data using the [*Brand*] isotopic parameters and to apply *Equation 1* for temperature reconstruction. No significant change in the 95% CI, slope or intercept occurs if t-value corrected errors are used (Fernandez *et al.*, 2017).

The absolute difference in Δ_{47} between the empirical calibration for calcite done in the same laboratory (Wacker *et al.* (2014) but reprocessed with [*Brand*] isotopic parameters, 25 °C reference frame) and (bio)apatite (*equation 2.1*) between 10 °C and 40 °C is 110 ± 3 ppm. This agrees with the difference of fractionation factors accompanied with acid digestion of calcite, aragonite and dolomite at temperatures of 25 °C and 110 °C, which is 100 ± 6 ppm (extrapolated from the experimental dataset presented by Defliese *et al.* (2015). It can be concluded that the Δ_{47} temperature dependencies of calcite and carbonated apatite are indistinguishable from each other if the AFF of Defliese *et al.* (2015) are considered. This finding is in agreement with Stolper and Eiler (2015), who noted identical Δ_{47} values on optical calcites and apatites from carbonatites after scrambling the isotopologue abundances of both materials at 700 °C.

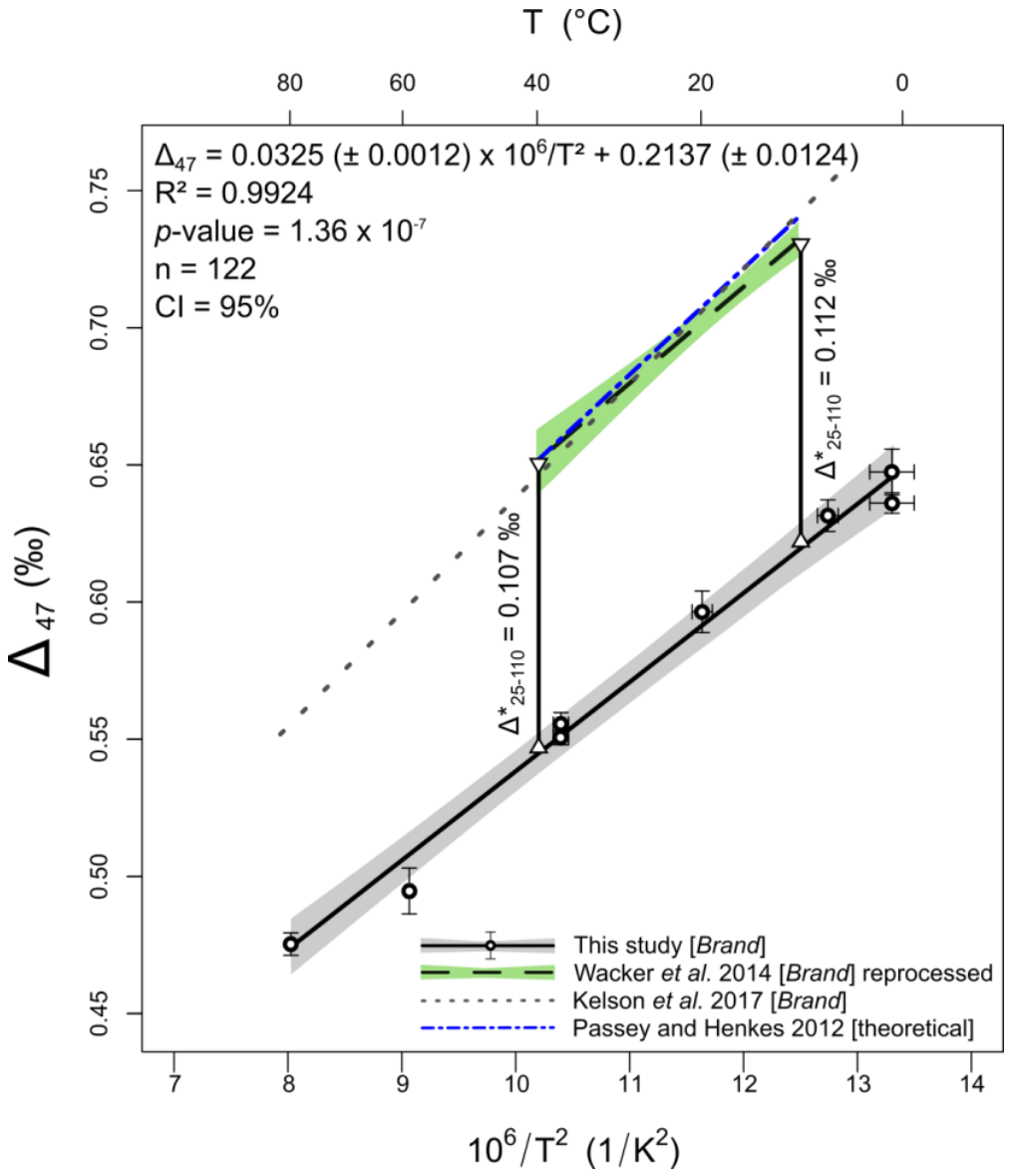

Figure 2.4: Refined temperature calibration of $\Delta_{47\ CDES\ 110}$ on (bio)apatites (black solid line, white dots) and its 95% confidence interval (CI, grey shade). The error-considering regression line is integrating data from synthetic apatites, tooth enamel(oid) and tooth dentine of this study and Wacker *et al.* (2016), whereas all data are (re)calculated with the [*Brand*] isotopic parameters. The error bars indicate 1 SE. The theoretical temperature calibration for carbonate of Passey and Henkes (2012) (blue dashed and dotted line), the [*Brand*] processed empirical calibration of Kelson *et al.* (2017), (their equation. 1, grey dotted line), and the [*Brand*] reprocessed empirical calcite calibration of (Wacker *et al.*, 2014) along with the CI (black dashed line, green shade, $\Delta_{47\ CDES\ 25}$= 0.0348 (± 0.0027) × 10^6 / T^2 + 0.2969 (± 0.0319) with T in K and Δ_{47} in ‰) are displayed for comparison. All calcite calibration data is normalized to a reaction temperature of 25 °C with the temperature dependence of the acid fractionation factor determined by Defliese *et al.* (2015). The difference in Δ_{47} between the empirical calcite calibration of Wacker *et al.* (2014) and the (bio)apatite calibration (*equation 2.1*) matches to the experimentally determined difference ($\Delta^*_{25\text{-}110}$) between the corresponding acid fractionations at 25 and 110 °C ($\Delta^*_{25\text{-}110}$ = 0.100 ± 0.006 ‰; Defliese *et al.*, 2015). The absolute $\Delta^*_{25\text{-}110}$ is illustrated with vertical bars.

Table 2.4: Parameters of the error considering regression lines of $\Delta_{47\ CDES\ 110}$ *vs.* $10^6/T^2$ calculated for the different apatite materials (see t*able 2.3*). Note that even though the distinct materials vary in their amount of hydroxylapatite, fluorapatite and TOC, the respective regression lines are identical within errors.

				Linear regressions of $\Delta_{47\ CDES\ 110}$ *vs.* $10^6/T^2$			
Material	n	Datasets	Isotopic parameters	Slope	Intercept	R^2	*p*-value
Synthetic CHAP	17	3	[*Gonfiantini*]	0.0318 ± 0.0017	0.2285 ± 0.0159	0.9907	0.0614
			[*Brand*]	0.0333 ± 0.0016	0.2060 ± 0.0156	0.9934	0.0516
Enamel(oid)	59	2	[*Gonfiantini*]	0.0306 ± 0.0027	0.2293 ± 0.0296	1	N/A
			[*Brand*]	0.0294 ± 0.0026	0.2447 ± 0.0287	1	N/A
Dentine	46	3	[*Gonfiantini*]	0.0331 ± 0.0038	0.2073 ± 0.0426	0.9981	0.0277
			[*Brand*]	0.0318 ± 0.0038	0.2247 ± 0.0416	0.9995	0.0138

2.6.3 Temperature dependence of oxygen isotope fractionation between CHAP carbonate and water

The average bulk oxygen isotopic compositions of the synthetic CHAP samples and their respective mineralizing fluids (*table 2.5*) are used to determine the temperature dependence of $1{,}000\ln(\alpha_{CHAP\text{-}water})$ between 7 °C and 80 °C (R^2 = 0.997, *p*-value = 0.033 n = 17, 3 samples; *figure 2.5*):

(*equation 2.3*) $1{,}000\ln(\alpha_{CHAP\text{-}water}) = 17.23\ (\pm\ 0.59) \times 10^3 \times T^{-1} - 27.28\ (\pm\ 1.73)$ (with T in K)

The errors provided in *equation 2.3* consider the standard errors of the $1{,}000\ln(\alpha_{CHAP\text{-}water})$ datasets and the temperature uncertainties.

The calculated temperature-dependent slope $d(\alpha_{CHAP\text{-}water})/dT$ of -0.00023 ± 0.00001 K^{-1} is slightly lower when compared to experiments between 10 and 37 °C (Lécuyer *et al.*, 2010) but close to the commonly accepted $d(\alpha_{calcite\text{-}water})/dT$ of -0.00020 K^{-1} (Epstein *et al.*, 1953; Kim & O'Neil, 1997) (*figure 2.5*). The slope of the calibration regression line (*equation 2.3*) also roughly agrees with those computed for structural carbonate in A-type carbonated apatite and B-type carbonated hydroxyl and fluorapatite (Aufort *et al.*, 2017). It plots intermediately between the latter two calibration lines if a positive offset of 6.5 ‰ is added to the $1{,}000\ln(\alpha)$ values provided by (Aufort *et al.*, 2017) for the A-type apatite-liquid water and B-type hydroxyl/fluorapatite-liquid water system (*figure 2.5*). This offset was chosen by (Aufort *et al.*, 2017) to match their theoretical $1{,}000\ln(\alpha)$ values for the system calcite-$H_2O_{(l)}$ to those experimentally determined by Kim and O'Neil (1997). B-type substitution dominates over A-type in biogenic CHAPs and

abiogenic synthesis products below about 100 °C, with an estimated relation of about 9 to 1 (Penel *et al.*, 1998; Antonakos *et al.*, 2007). The presence of A and B-type carbonate in the biogenic apatites and synthetic CHAPs is evident from Raman spectroscopic measurements (*figure 2.3*) and Rietveld powder X-ray diffraction refinements, albeit they do not allow for an absolute quantification of A *vs.* B-type substitution The incorporation of CO_3^{2-} leads to changes of the CHAP lattice parameters along the a-axis (Zapanta-LeGeros, 1965; Shimoda *et al.*, 1990). According to the approach given by Shimoda *et al.* (1990), the powder X-ray diffraction results for the synthetic CHAP prepared at 7 °C would be consistent with about 80 % substitution on the B position. However, incorporation of foreign anions and cations may further modify the unit cell parameters to an extent that is difficult to quantify (Shimoda *et al.*, 1990).

Sample	$\delta^{18}O_{CO3}$	$\delta^{13}C_{CO3}$	$\delta^{18}O_{H2O}$	1,000ln(α)
CHAP 7 ± 1 °C	-3.0	-4.6	-5.9	
	-2.9	-4.5	-5.9	
	-2.2	0.4	-6.0	
	-1.7	0.4	-6.0	34.0 ± 0.4
CHAP 59 ± 0.5 °C	-11.9	-5.7	-6.1	
	-11.6	-5.6	-6.1	
	-12.0	-6.0	-7.0	
	-12.0	-5.6	-7.0	
	-12.1	-5.6	-6.1	
	-12.6	-5.8	-6.2	
	-12.0	-5.9	-7.0	24.9 ± 0.2
CHAP 80 ± 0.5 °C	-12.6	-5.7	-4.0	
	-12.6	-5.7	-4.0	
	-12.9	-5.6	-4.0	
	-13.2	-5.7	-4.0	
	-13.2	-5.7	-4.0	21.4 ±0.1

Table 2.5: $\delta^{18}O_{CO3}$ and $\delta^{13}C_{CO3}$ values of the synthetic carbonated hydroxylapatites (CHAP) and the $\delta^{18}O_{H2O}$ values of the respective parental fluids (in ‰). The oxygen isotope fractionation factors between CHAP and water (1,000ln(α)) and the formation temperatures (in K^{-1}) of the synthetic CHAP samples (incl. se) are derived from the average values at 7 °C, 59 °C and 80 °C. $\delta^{18}O_{H2O}$ is expressed relative to VSMOW, $\delta^{18}O_{CO3}$ relative to VPDB.

It should be noticed that the theoretical computations made by (Aufort *et al.*, 2017) need to be corrected by an empirical offset (see above) to match experimental results. In addition, theoretical computations depend on a number of model assumptions that sometimes lead to very different results. According to (Aufort *et al.*, 2017), A-type carbonated hydroxylapatite and B-type substituted fluorapatite should not have any substantial oxygen isotope fractionation in the temperature range between 0 °C and 50 °C, whereas a difference of up to 15 ‰ between these two phases was derived by the model approach of Zheng (2016). These observed discrepancies

imply that relatively large uncertainties are associated with the determination of the corresponding equilibrium fractionation factors by means of theoretical computations. The actual impact of the crystal chemical position of the carbonate group in the CHAP lattice on β-factors and oxygen isotope equilibrium fractionation factors therefore remains disputable. Notably, the regression line (*equation 2.3*) only shows small offsets to the calcite-water oxygen isotope fractionation obtained by Coplen (2007) (their equation 3) for very slowly-precipitated cave carbonate and to the experimentally determined fractionation of Beck *et al.* (2005) for the system HCO_3-water (*figure 2.5*).

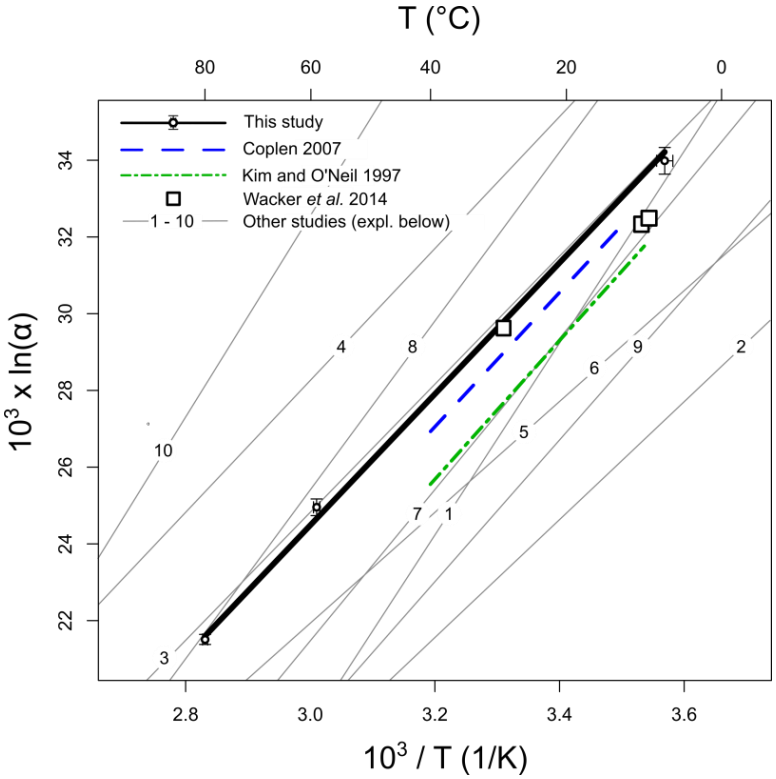

Figure 2.5: Plot of the regression line for the CHAP-H_2O oxygen isotope fractionation (e*quation 3*; solid black line, white dots incl. SE), which is compared to the corresponding temperature dependencies estimated for natural carbonate and water of Coplen (2007) (dashed blue line) and synthetic carbonate and water of Kim and O'Neil (1997) (dashed and dotted green line). The white squares indicate the 1,000ln($\alpha_{Carbonate\text{-}water}$) values of three slope determining calibration points of Wacker *et al.* (2014) (*Spondylus* sp., *Dyscolia wyvillei* and cold seep carbonate). Additional oxygen fractionation equations for different mineral chemistries of carbonate-bearing apatites and dissolved carbonates (1 to 10) are displayed for comparison. Note that the oxygen isotopic fractionation regression line of this study plots close to the respective temperature dependency of the system of HCO^{3-} and water of (Beck *et al.*, 2005) (line 3) and between the predictions for fluorapatite and carbonate-apatite of Aufort *et al.* (2017) (lines 4 to 6) and Zheng (2016) (lines 7 to 10). 1: Lécuyer *et al.* (2010), 2 and 3: Beck *et al.* (2005) CO_3^{2-} and HCO_3^- respectively, 4, 5 and 6: Aufort *et al.* (2017) A-type HAP, B-type HAP and B-type FAP, respectively, 7, 8, 9 and 10: Zheng (2016) BSC1, BSC2, ASC and F, respectively.

Coplen (2007), who was accommodated by Watkins *et al.* (2013), suggested that overall equilibrium in the system calcite-water might be represented by the equation of Kim and O'Neil (1997) after adding 1.5 ‰. For three of the four calcite samples that determine the slope of the Wacker *et al.* (2014) calibration (*Spondylus* sp., *Dyscolia wyvillei*, cold seep carbonate, see their chapter 3.3), $\delta^{18}O$ values of the seawater are available (Wacker *et al.*, 2014; their table 5). The corresponding apparent oxygen isotope fractionations for these samples also plot close to the oxygen isotope regression line for synthetic apatite and to that for calcite provided by Coplen (2007) (*figure 2.5*). Close concordance of oxygen isotope equilibria for calcite-water and (bio)apatite-water might help to explain why the obtained Δ_{47}/T^2 relationship for (bio)apatites is indistinguishable from the [*Brand*] reprocessed empirical calcite calibration of Wacker *et al.* (2014).

2.6.4 pH of tooth mineralization

Kinetics (vital effects) were shown to affect the clumped and oxygen isotopic compositions of certain marine biogenic carbonates (*e.g.*, Thiagarajan *et al.*, 2011; Saenger *et al.*, 2012; Bajnai *et al.*, 2018). For example, brachiopod calcite exhibits offsets from oxygen and clumped isotope equilibrium that correlate with each other (Bajnai *et al.*, 2018). These paired offsets point to the importance of solution kinetics in governing the oxygen and clumped isotopic compositions which have to be addressed in the case of the *in vivo* samples (African elephant, Greenland sharks, sand tiger sharks and *C. megalodon*).

During biomineralization of dental tissues (*e.g.*, biogenic apatite), the physical and chemical properties of the body fluid are efficiently regulated in ion concentration, temperature and pH; not only by biochemical regulation (Krieg *et al.*, 2014) of a rather large body reservoir but also by behavioral adaption, such as migration according to the preferred habitat (*e.g.*, Stokesbury *et al.*, 2005), actively regulated thermal windows (*e.g.*, Phillips, P., K. & Heath, 1992; Erdsack *et al.*, 2012), sweating, and body covering (*e.g.*, Gagge *et al.*, 1938; Chevalier-Skolnikoff & Liska, 1993). The mineralization of mammal teeth takes place from a body fluid with a pH close to 7.4 Ahne (2000), which is buffered by a bicarbonate system (Krieg *et al.*, 2014). The general variation of the pH of elasmobranch blood is 6.8 to 7.7 (Urist, 1961; Bushnell *et al.*, 1982; Chin Lai *et al.*, 1990; Gallagher *et al.*, 2010) and the pH of Greenland shark meat was reported to be 6.8 (Davidson, 1983). This is up to 1.5 log units lower when compared to the pH of seawater. A relatively low pH during tooth formation would lead to a higher abundance of $CO_{2(aq)}$

in the DIC pool and therefore enhance oxygen isotope exchange between the corresponding DIC pool and water (McConnaughey, 1989) as it is the availability of $CO_{2(aq)}$ that limits the rate of this isotopic exchange reaction (Usdowski, 1982; Beck *et al.*, 2005; Zeebe & Wolf-Gladrow, 2001). When compared to marine invertebrate carbonates, attainment of full equilibrium in structural carbonate of bioapatite might therefore be more likely.

2.6.5 Application on modern and fossil tooth enameloid

To assess the state of preservation of fossil *C. megalodon* tooth enameloid (*figure 2.1*), its phosphate ($\delta^{18}O_{PO4}$) and carbonate ($\delta^{18}O_{CO3}$) oxygen isotopic composition is evaluated prior to applying the clumped and oxygen isotopic calibrations. Additional analysis of $\delta^{18}O_{PO4}$ as a supplement for carbonate $\delta^{18}O_{CO3}$ can provide insight into diagenesis because $\delta^{18}O_{CO3}$-$\delta^{18}O_{PO4}$ values ($\Delta\delta^{18}O_{CO3\text{-}PO4}$) of well-preserved skeletal tissue should have a consistent offset (Iacumin *et al.*, 1996; Tütken & Vennemann, 2011). The $\delta^{18}O_{CO3}$ and $\delta^{18}O_{PO4}$ values of bioapatite from modern vertebrates are positively correlated with an offset of $\Delta\delta^{18}O_{CO3\text{-}PO4}$ = 8.4 to 9.0 ‰ (Bryant *et al.*, 1996; Pellegrini *et al.*, 2011). A comparable offset ($\Delta\delta^{18}O_{CO3\text{-}PO4}$= 9.1 ±0.2 ‰) was obtained for numerous shark teeth from different species (Vennemann *et al.*, 2001). The $\delta^{18}O_{PO4}$ of the shark teeth is measured on Ag_3PO_4 which was formed from enameloid using the rapid precipitation protocol (Tütken *et al.*, 2006). Each sample is analyzed with two to three replicates using a Finnigan TC-EA resulting in an average precision of 0.1 ‰.

Table 2.6: Overview on the [*Brand*] processed stable and clumped isotopic compositions from the fossil *C. megalodon* tooth enameloid (in ‰). $\delta^{13}C_{CO3}$ and $\delta^{18}O_{CO3}$ are expressed relative to VPDB, $\delta^{18}O_{PO4}$ relative to VSMOW.

C. megalodon	Date	$\Delta_{47\ CDES\ 110}$	$\delta^{13}C_{CO3}$	$\delta^{18}O_{CO3}$	$\delta^{18}O_{PO4}$
Enameloid	5/20/2014	0.599	5.33	-0.10	22.05
	5/22/2014	0.582	4.81	-0.20	21.42
	5/22/2014	0.602	4.35	-0.21	22.11
	5/22/2014	0.589	3.47	0.16	21.78
	av	0.593	4.49	-0.09	21.84
	sd	0.009			
	se	0.005			

The $\delta^{18}O_{PO4}$ values of the Greenland shark (s*pecimen 1*) average 25.5 ± 0.2 $‰_{VSMOW}$ (n = 6). Serial $\delta^{18}O_{PO4}$ measurements of *C. megalodon* tooth enameloid studied here range from 21.0 to 21.9 $‰_{VSMOW}$ with no substantial variation along the sampled tooth length of 10 cm (20 profile

points, axial; n = 58, supplementary data *S.2.III)*. Additional $\delta^{18}O_{PO4}$ analyses were performed for each *C. megalodon* sample batch that was also analyzed for Δ_{47} (t*able 2.6*). Because the average $\Delta\delta^{18}O_{CO3\text{-}PO4}$ for *C. megalodon* of 9.2 ± 0.2 ‰ is close to the average $\delta^{18}O_{CO3\text{-}PO4}$ of Greenland shark tooth enameloid ($\Delta\delta^{18}O_{CO3\text{-}PO4}$= 8.8 ± 0.7 ‰) and both values, in turn, are consistent with the range of $\Delta\delta^{18}O_{CO3\text{-}PO4}$ from modern vertebrates, it is likely that $\delta^{18}O_{CO3}$ of the *C. megalodon* tooth sample was not affected by diagenesis.

Table 2.7: Oxygen isotopic composition of the fluids from which tooth enameloid from the fossil *C. megalodon* and modern *S. microcephalus* precipitated as reconstructed with (Δ_{47}-based) temperatures and oxygen isotopic fractionation equations of Pucéat *et al.* (2010) (their equation 3, with an adopted value of $\delta^{18}O_{NBS120c}$ = 21.7) and this study. The errors are the geometric mean calculated from the respective standard errors (in ‰). $\delta^{18}O_{H2O}$ is expressed relative to VSMOW.

	C. megalodon enameloid	*S. microcephalus* enameloid
Calibration	$\delta^{18}O_{H2O}$	$\delta^{18}O_{H2O}$
Pucéat *et. al.* (2010)	-0.87 ± 0.84	-1.25 ± 0.78
this study (*equation 2.3*)	-1.32 ± 0.96	-2.01 ± 1.31

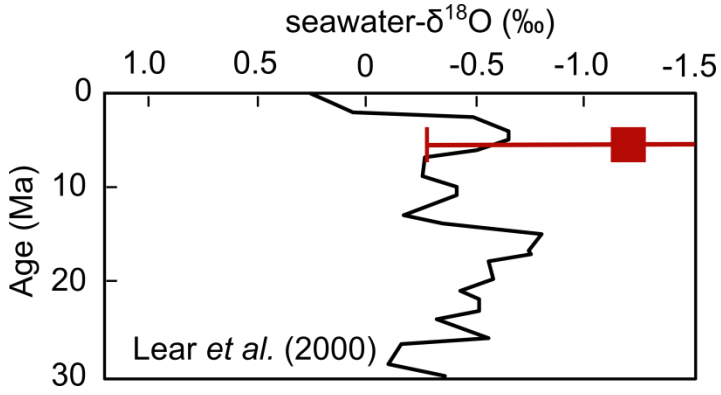

Figure 2.6: Reconstructed $\delta^{18}O_{H2O}$ (VSMOW) value of the *C. megalodon* body fluid as calculated with the *equations 1* and *3* (-1.2 ± 0.9 ‰, red square), plotted on the seawater-$\delta^{18}O$ curve of Lear *et al.* (2000) from the late Oligocene to Plio-Pleistocene (curved line) at the measured $^{87}Sr/^{86}Sr$ age of 5.75 ± 0.06 Ma. The graphic is adapted from Lear *et al.* (2000) who calculated $\delta^{18}O$ of seawater from Mg temperatures and benthic foraminiferal $\delta^{18}O$ data.

By applying the Δ_{47}-$1/T^2$ relationship (*equation 2.1*), the apparent Δ_{47}-based temperature of the otodontid *C. megalodon* tooth is 19 ± 4 °C ($\Delta_{47\ CDES\ 110}$ = 0.593 ‰, sd = 9 ppm, n = 4) which is within the preferred habitat temperature range of the lamniform great white shark (*Carcharodon carcharias*) of 16 to 22 °C (Dewar *et al.*, 2004) and the *C. megalodon* habitat temperatures of 12 to 27 °C determined by Pimiento *et al.* (2016). Otodontids are often regarded

as lamnids (Gottfried *et al.*, 1996; Purdy, 1996) or as closely related (Cappetta *et al.*, 2012; Dana Joseph Ehret, 2010) and might have been mesotherm (Ferrón, 2017). Even though modern lamniform sharks have core body temperatures that are higher than the surrounding water temperatures, peripheral body parts approach sea water temperatures (Bernal *et al.*, 2003). The hypothesis is therefore that the Δ_{47}-based temperature from *C. megalodon* reflects the ambient water temperature.

It is feasible to determine the $\delta^{18}O$ values of the corresponding fluid from which the *C. megalodon* and Greenland shark teeth precipitated by using the Δ_{47}-based temperature (or known habitat temperature), $\delta^{18}O_{PO4}$ and the temperature dependence of oxygen isotope fractionation between phosphate and water (Longinelli & Nuti, 1973; Pucéat *et al.*, 2010). The same applies if the Δ_{47}-based temperature, $\delta^{18}O_{CO3}$ and the experimentally determined temperature dependence of oxygen isotope fractionation between structural carbonate in apatite and water are used. To avoid circular reasoning when calculating the $\delta^{18}O_{H2O}$ from the Greenland shark sample (that is also used for calibrating the Δ_{47}-$1/T^2$ relationship), the habitat temperature (1 ± 2 °C) is used rather than the Δ_{47}-based temperature. The $\delta^{18}O_{H2O}$ values of -1.3 ± 1.0 ‰-and -2.0 ± 1.3 ‰ computed from $\delta^{18}O_{CO3}$ and *equation 2.1* for *C. megalodon* and Greenland shark (*specimen 1*), respectively, occur close to the respective $\delta^{18}O_{H2O}$ values derived from the corresponding $\delta^{18}O_{PO4}$ and the calibration of Pucéat *et al.* (2010) (*table 2.7*). Using the Δ_{47}-based temperature of the Greenland shark enameloid (4 ± 3 °C, *specimen 1*) rather than the habitat temperature gives a $\delta^{18}O_{H2O}$ value of -1.4 ± 1.2 ‰ which is indistinguishable from the one stated above (-2.0 ± 1.3 ‰). The $\delta^{18}O_{H2O}$ of the Greenland shark matches the $\delta^{18}O$ of seawater at depths of approximately 0 to 200 m (Arctic Ocean) with water temperatures of 0 °C to -1 °C (van Donk & Mathieu, 1969). Moreover, this depth range corresponds to the mean depth recorded from six different Greenland shark specimens (86 m, Watanabe *et al.*, 2012).

The low $\delta^{18}O_{H2O}$ value of *C. megalodon* sample (-1.3 ± 0.9 ‰) is consistent with oceanic $\delta^{18}O$ values in a world with only small ice shields (Miller *et al.*, 2005; their figure 1; Lear *et al.*, 2000; their figure 1E). It is apparent that the reconstructed $\delta^{18}O_{H2O}$ and Δ_{47}-based temperature fit to the respective models from partly cosmopolitan marine vertebrates of Amiot *et al.* (2008) during the late Miocene. Strontium isotopes analysis of *C. megalodon* tooth enameloid yields an age of 5.75 ± 0.06 Ma ($^{87}Sr/^{86}Sr$ = 0.709006 ± 0.000013; McArthur *et al.*, 2001). Within errors, the reconstructed $\delta^{18}O_{H2O}$ agrees with the oxygen isotopic composition of the seawater calculated by Lear *et al.* (2000) from Mg temperatures and benthic foraminiferal $\delta^{18}O$ data (*figure 2.6*).

The fact that consistent and reasonable temperatures and $\delta^{18}O_{H2O}$ values can be reconstructed on modern and fossil shark tooth enameloid corroborates the hypothesis that the oxygen and clumped isotope calibrations presented in this study are closely representative of equilibrium and largely independent of the chemical composition of (bio)apatite.

2.7. Conclusions

A comprehensive clumped isotope (Δ_{47}) dataset integrating over 122 replicate analyses is provided to establish the temperature dependence of Δ_{47} for (bio)apatites of different chemical and isotopic composition from 1 °C to 80 °C. Structural carbonate yields a Δ_{47}-$1/T^2$ relationship that is indistinguishable from calcite if the difference of the acid fractionation factors between 25 °C and 110 °C reactions for calcite (Defliese *et al.*, 2015) is taken into account. Both calcite and synthetic apatite closely follow the temperature dependence of oxygen isotope equilibrium fractionation between calcite and water as presented by Coplen (2007).

When applied to modern and fossil tooth enameloid, reconstructed Δ_{47}-based temperatures and $\delta^{18}O$ values of mineralizing fluids agree well with published data. Furthermore, $\delta^{18}O_{H2O}$ values computed from (Δ_{47}-based) temperatures, $\delta^{18}O_{CO3}$ and the $1{,}000\ln(\alpha_{CHAP\text{-}H2O})$ temperature relationship (*equation 2.3*) consistently plot close to the respective values that are independently reconstructed from (Δ_{47}-based) temperatures, $\delta^{18}O_{PO4}$ and the $1{,}000\ln(\alpha_{CHAP\text{-}H2O})$ temperature relationship of Pucéat *et al.* (2010). Collectively, it can be concluded that the (bio)apatite $\delta^{18}O$ and Δ_{47} values presented in this study closely reflect isotopic equilibrium and that the chemical and/or mineralogical composition (*e.g.*, hydroxylapatite *vs.* fluorapatite, enamel(oid) *vs.* dentine) of (bio)apatite does not significantly affect the clumped isotopic composition and the associated oxygen isotope fractionation.

2.8 Acknowledgements

We greatly acknowledge S. Hofmann and C. Schreiber (J. W. Goethe-University) for their excellent assistance during the clumped isotope analyses and I. Schmiedinger (Leibniz IOW) for invaluable support during the synthesis experiments. We sincerely thank A. Gehler (University of Goettingen), who kindly supplied a large aliquot of the AG-LOX elephant enamel standard and elephant dentine and Martin Rosner (Federal Institute for Materials Research and Testing (BAM), Berlin) for the strontium isotopes analysis of the *C. megalodon* tooth. We greatly acknowledge the Bjarnarhöfn Shark Museum (Bjarnarhöfn, Iceland) for providing jaws from two Greenland shark specimens and the Two Oceans Aquarium (Cape Town, South Africa) who supplied us

with individual sand tiger shark teeth. We would kindly like to thank the three anonymous reviewers for providing constructive comments that helped to improve the validity of this study as well as C. Chislett for editing support.

2.9 Funding

This research was supported by German Science Foundation (DFG) to M.E.B. and J.F. (BO 1548/8 and FI 948/7) within EXCALIBOR project and Leibniz IOW.

2.10 Author contribution

N. L., J. F., M. E. B., and A. M. designed the study and wrote the manuscript. M. E. B. and A. C. C. synthesized the abiogenic apatite samples. T. T. carried out the phosphate oxygen isotope analysis. B. C. S. measured the micro-Raman spectra. N. L, U. W., and D. B. performed the clumped isotope analyses between 2014 and 2017. All authors discussed the results, read the manuscript, contributed to writing the manuscript guided by N.L., and agreed to the submission.

3 Application of the refined clumped isotope temperature calibration on *Tyrannosaurus rex* teeth from the adult specimen "Trix" (RGM 792.000)

N. Löffler[a, c*]

In close cooperation with:

A. S. Schulp [b], J. Fiebig[a, c], T. Tütken[d], D. Bajnai[c1] A. Mulch[a, c]

[a] *Senckenberg Biodiversity and Climate Research Center, Senckenberganlage 25, 60325 Frankfurt (Main), Germany*

[b] *Naturalis Biodiversity Center in Leiden, Darwinweg 2, 2333 CR Leiden, The Netherlands*

[c] *Institute of Geosciences, Goethe University Frankfurt, Altenhoeferallee 1, 60438 Frankfurt (Main), Germany*

[d] *Institute of Geosciences, Johannes Gutenberg University, Johann-Joachim-Becher-Weg 21, 55128 Mainz, Germany*

[1] *Present address: Institute of Geology and Mineralogy, University of Cologne, Zuelpicher Strasse 49a, 50674 Cologne, Germany*

**Correspondence: niklas.loeffler@senckenberg.de*

Preliminary data of this study was presented 2017 at the following conferences and workshops:

6th International Clumped Isotopes Workshop, Paris (France)

Goldschmidt conference, Paris (France)

GEOBremen, Bremen (Germany)

3.0 Abstract

Studying the thermophysiology of extinct vertebrates is challenging and strongly limited by quantitative information on metabolism, migration, growth rates, and feeding strategies. Established approaches used for thermophysiological studies of dinosaurs, such as oxygen isotope based analyses or bone histology, typically lack the necessary precision to pinpoint exact body temperatures. Clearly distinguishing between different types of thermoregulation (*e.g.* ecto, meso, and endothermy) remains challenging. In this study, the recently refined clumped isotope thermometer for (bio)apatite is applied to tooth enamel from an adult *Tyrannosaurus rex* to decipher the body temperature of a fully grown specimen. This increases the understanding of the thermophysiology of large Theropods by revealing a *T. rex* body temperature of 38 ± 3 °C. This temperature is within the body temperature range of birds and mammals and, together with previous findings, is in well agreement with aspects of endothermy. However, distinguishing between inertial homeothermy (gigantothermy) and endothermy will only be feasible once the results of this study can be complemented by measured body temperatures of a juvenile *T. rex*.

Keywords

Tyrannosaurus rex, clumped isotopes, body temperature, dinosaurs, thermophysiology

3.1 Introduction

3.1.1 Determining the thermophysiology of dinosaurs

Reconstructing the thermophysiology of dinosaurs has been a persistent challenge over the past two centuries since their first scientific description (Owen, 1841). It is still debated, if, when, and to which extent endothermy developed in dinosaurs (*e.g.* Grellet-Tinner, 2006; Bernard *et al.*, 2010). This is also due to the fact that established approaches for studying dinosaur thermophysiology such as bone histology (*e.g.* Tütken *et al.*, 2004; Sander & Klein, 2005), modeling (*e.g.* Gillooly *et al.*, 2006; Griebeler, 2013), and stable oxygen isotope analyses ($\delta^{18}O$; *e.g.* Tütken *et al.*, 2004; Amiot *et al.*, 2006), do not result in direct temperature measurements due to remaining unknowns (*e.g.* $\delta^{18}O$ of the body fluid). Additionally, alternative thermophysiological concepts emerged (*e.g.* Grady *et al.*, 2014), which made high precision paleothermometry mandatory for independently constraining dinosaur body temperatures.

Since 2010, clumped isotope (Δ_{47}) thermometry, which bases on the temperature dependent abundance of ^{13}C-^{18}O bonds, has repeatedly been used to measure precipitation temperatures of carbonate-bearing biotic minerals such as modern and fossil tooth enamel and eggshell carbonate (*e.g.* Eagle *et al.*, 2010, 2011, 2015; Wacker *et al.*, 2016; Löffler *et al.*, 2019; Dawson *et al.*, 2020). Thus far, Δ_{47} thermometry has been applied to reconstruct body temperatures of birds (*e.g.* Dawson *et al.*, 2020), mammals (*e.g.* Eagle *et al.*, 2010), sharks (*e.g.* Löffler *et al.*, 2019), Archosauria (Alligators) and Dinosauria (Ornithischia, and Saurischia, incl. Sauropoda and Theropoda) (*e.g.* Eagle *et al.*, 2010, 2015; Dawson *et al.*, 2020). However, only a very limited number of dinosaur species and specimen have been measured for their Δ_{47}-based body temperatures. Analyzing the mineral growth temperature of tooth enamel from an adult *T. rex* could therefore contribute to the discussion of dinosaur thermophysiology and the evolution of endothermy and would further verify the applicability of the Δ_{47}-temperature (Δ_{47}-$1/T^2$) calibration for (bio)apatite of *chapter 2* (Löffler *et al.*, 2019). Grady *et al.* (2014) stated that the thermophysiology of dinosaurs might have been more complex than previously thought. They suggested the thermophysiological concept of mesothermy that is characterized by a varying metabolic control as an alternative concept to endo and ectothermy, which for example applies to leatherback turtles, tuna, and furred echidnas (Grady *et al.*, 2014). Barrick and Showers (1994)

showed that at least for *T. rex*, homeothermy could be assumed because of only small interskeletal $\delta^{18}O_{PO4}$ variations. Though no actual body temperatures were reported due to unknown $\delta^{18}O$ of the parental body fluid ($\delta^{18}O_{H2O}$), which – in combination with temperature – determines the skeletal $\delta^{18}O_{PO4}$. The first direct measurements of dinosaur body temperatures were performed by Eagle *et al.* (2011) and Dawson *et al.* (2020) and partly agree with previous growth size models of Gillooly *et al.* (2006). Until now, Theropod and Sauropod tooth enamel and eggshell carbonate of Theropod, Ornithischian, and Sauropod dinosaurs were reported with Δ_{47}-based body temperatures that range from 27 to 44 °C. The variation of body temperatures thereby reduces at higher (>1,000 kg) body masses (*e.g.* Eagle *et al.*, 2011; Dawson *et al.*, 2020).

3.1.2 General information on T. rex

T. rex is a publicly well known (Brochu, 2003; Sanz, 2003) bipedal Theropod that existed during the upper Maastrichtian (68 to 66 Ma). It became extinct at the Cretaceous-Paleogene (K-Pg) boundary (Pearson *et al.*, 2001; Renne *et al.*, 2013) making it one of the latest non-avian dinosaurs in Earth history. Its carnivorous feeding strategy and large body mass made it an apex predator (Schaeffer, 2016) possibly hunting smaller prey such as Hadrosaurs, Edmontosaurus (Rothschild & Depalma, 2013; DePalma *et al.*, 2013; Carpenter, 1998), and other *T. rex* (Longrich *et al.*, 2010). A puncture-pull feeding strategy is suggested by its cranial mechanics (Rayfield, 2004). The largest and heaviest *T. rex* found to date is “Scotty” (RSM P2523.8) with a body mass of approximately 9,000 kg (Persons *et al.*, 2020). Other adult specimen have been reported with lower body masses of 5,400 to 6,800 kg (Farlow *et al.*, 1995; Seebacher, 2001; Erickson *et al.*, 2004; Christiansen & Fariña, 2004). Juvenile *T. rex* are rare and it is debated if *Nanotyrannus* contains juvenile *T. rex* specimens. (Woodward *et al.*, 2020; Yun, 2015). The availability of juvenile *T. rex* fossils for thermophysiological studies is crucial because the sheer body mass and related heat production of adult specimens could cause inertial homeothermy resulting in body temperatures comparable to those of endotherm species (*e.g.* Paladino *et al.*, 1990). This effect could potentially be verified by applying clumped isotope thermometry to tooth enamel of *T. rex* younger than approximately 20 years, which is the age after which skeletal maturity was reached (Erickson *et al.*, 2004).

3.1.3 Geological setting and sample preservation

The 13 m long *T. rex* specimen (also referred to as “Trix”; RGM 792.000) was found during the summer of 2013 on a Ranch 50 kilometers SW of Jordan (Montana, U.S.A.) in stream

channel sediments of the Upper Maastrichtian Hell Creek Formation (HCF; Schulp *et al.*, 2015; Reims *et al.*, 2016) after identifying individual pieces of a *T. rex* skull on the surface of a hill (Schulp, 2014).

The predominantly fluviatile HCF extends over the three U.S.A. states Montana, North Dakota, and South Dakota and has been first described by Brown (1907). According to Hicks *et. al.* (2002), sedimentation took place during the subchrons C29n, C29r, and C30n with an estimated duration of 1.36 Ma. While the youngest age is marked by the well constrained Creteaceous-Paleogene (K-Pg) boundary at 65.51 Ma (Hicks *et. al.*, 2002), the basal age is still in discussion. However, the beginning of the HCF sedimentation must be at least younger as the last underlying ammonite (*Baculites grandis*) which is dated with an age of 70.15 Ma (Johnson *et al.*, 2002). Paleobotanical evidence indicates an increase of local mean annual temperatures from 10 to 23 °C during the whole depositional phase of the HCF (Johnson, 1997). The paleofauna is characterized by a dense vegetation of angiosperms (*e.g.* palms and conifers) that grew on floodplains with meandering rivers (Johnson, 1997; Murphy *et al.*, 2002). Intermitted connection to the Western Interior Seaway led to the formation of two marine members in North Dakota (Johnson *et al.*, 2002).

The HCF is known for its well-preserved fossils. Previous finds include a *T. rex* specimen with soft tissue (MOR 1125; Schweitzer *et al.*, 2005) from which intact peptides were sequenced (Asara *et al.*, 2007). While the HCF overall contains a high abundance of Cretaceous dinosaur fossils with 23 known species (Russell & Manabe, 2002), its top three meters bear no dinosaurs at all because the sedimentation of the HCF continued after the K-Pg boundary (Lyson *et al.*, 2011). The sampled *T. rex* was excavated after a LIDAR-laser scan (deVries, 2016) under the lead of the Naturalis Biodiversity Center in Leiden (Darwinweg 2, 2333 CR Leiden, The Netherlands) and in cooperation with the Black Hills Institute (117 Main Street, Hill City, SD, 57745 U.S.A.) (Schulp *et al.*, 2015). According to its bone histology, the specimen died at an age of ≥30 years which is currently the oldest age of all known *T. rex* specimens. The bones and teeth are extraordinarily well-preserved due to a rapid burial below 3.25 m of fine to medium grained unconsolidated and well-sorted carbonate rich sand (Schulp *et al.*, 2015) which buffered dissolution of the fossil bioapatite by acids with its high content of $CaCO_3$ (Kaskes, 2016). Magnetostratigraphic data suggest a deposition during the C30n chron (approx. 66 to 67.5 Ma), which is equivalent to the lower to middle part of the HCF (Schulp *et al.*, 2015). Considering the extinction of *T. rex* at the K-Pg boundary (Pearson *et al.*, 2001; Renne *et al.*, 2013), the sample age is estimated to be *ca.*

66.5 Ma old. Trix represents a robust *T. rex* morphotype. Its excavated skeleton consists of the pelvis, large parts of the rib cage and vertebral column (incl. approx. half of the tail), right leg, left scapula and coracoid, the furcular, and a nearly complete and articulated skull of approximately 1.5 m length (Schulp *et al.*, 2015) with several intact teeth. Additional tooth fragments were found in close proximity (cm to dm) to the skull. The overall mass of the presumably female specimen was analyzed to be approximately 5,000 kg (A. S. Schulp, personal communication, 2018). The $^{44}Ca/^{42}Ca$ values have been previously reported to vary between -0.669‰ and -0.817‰ which has been interpreted as an indicator for a high level of bone consumption (Schaeffer, 2016). Varying $^{87}Sr/^{86}Sr$ ratios suggest seasonal migration of the specimen, its prey, or a combination of both (Schaeffer, 2016).

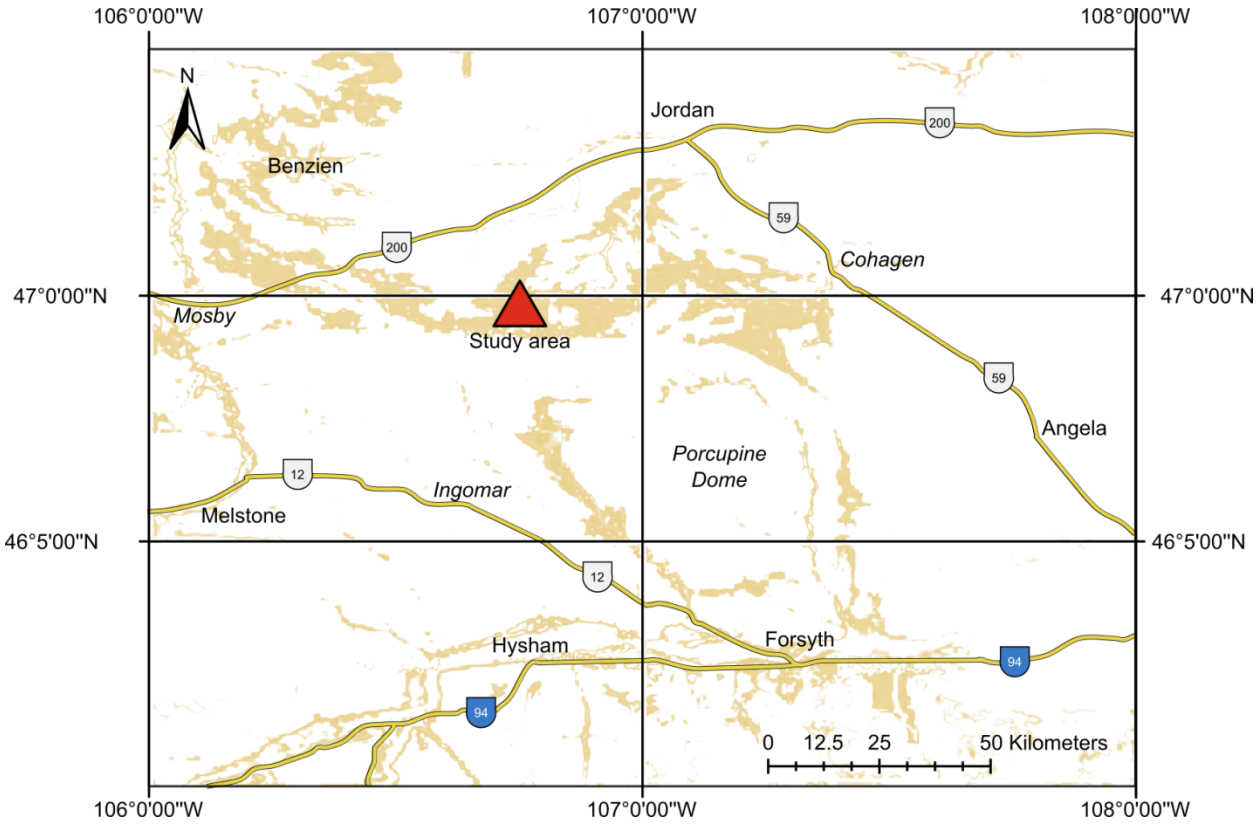

Figure. 3.1: Overview on the study area (red triangle) where the fossil remains of the *T. rex* "Trix" were found and excavated in 2013 by the Naturalis Biodiversity Center (Leiden, The Netherlands) and the Black Hills Institute (Hill City, SD, U.S.A). The outcropping Hell Creek Formation (HCF) is highlighted in beige.

3.2 Material and methods

3.2.1 Sampled T. rex tooth fragments

Dr. A. S. Schulp (Naturalis Biodiversity Center Leiden, The Netherlands) provided 38 incisiform tooth fragments for Δ_{47} analysis. The D-shaped tooth fragments were found in direct proximity to the skull and measure 0.3 x 0.7 cm to 1.7 x 4.1 cm (width and height respectively). Thirteen fragments are serrated (*figure* 3.2). For comparison, a photo of an intact tooth is shown in the appendix (supplementary data *S.3.I*, page 183).

Figure 3.2: 38 *T. rex* tooth fragments of the sampled specimen "Trix" (RGM 792.000). The largest fragment (bottom right) has not been sampled for Δ_{47} analyses and is currently analyzed for its microstructure in collaboration with T. Tütken, J.G. University Mainz.

The enamel surfaces of all tooth fragments show traces from plant root growth. The tooth surfaces show a consistent coloring under ultraviolet light. This notwithstanding, all areas with traces of root growth were mechanically removed to limit the potential impact of chemical alteration on the sample batch used for Δ_{47} analysis. Due to the limited thickness of the enamel of approximately 0.2 mm, the enamel of all fragments was pooled to one bulk sample with a dental diamond tipped handheld drill and homogenized using a mortar and pestle. The same procedure was performed for tooth dentine to uphold the comparability of the results of both tooth

substances. As in *chapter 2*, no chemical pretreatment was performed to guarantee comparability and consistency with the calibration study. Additional measurements of the oxygen isotope composition of the phosphate group are in preparation to further address the impact of diagenesis (in cooperation with T. Tütken, J.G. University, Mainz).

3.2.2 Clumped isotope analyses

The clumped isotope analyses were performed at the joint Goethe University – Senckenberg BiK-F Stable Isotope Facility using a fully automated acid digestion device (HAL; Fiebig *et. al.*, 2019) connected to a to a Thermo Scientific™ MAT 253™ gas source mass spectrometer (IRMS; Thermo Fisher Scientific, Bremen, Germany). The automated digestion device follows the design of Passey *et. al.* (2010) and is described in *chapter 2.3.2*. *Chapter 2* also includes all specifications and information of the analytical protocol and the acid digestion at 110 °C (*chapter 2.3.2* and *2.3.3*). Screening for hydrocarbon contaminants in the sample gas was done by plotting the *m/z* 47 background *vs.* the *m/z* 49 peak intensities of the analyte and reference gases (Wacker *et al.*, 2016; Fiebig *et al.*, 2016). No contaminants were detected.

Unless stated otherwise, all oxygen ($\delta^{18}O$) and carbon ($\delta^{13}C$) isotopic compositions are given in VPDB notation and the precision of the analyses is stated as 1σ standard error (1 se). All Δ_{47} data are given in the 110 °C reference frame (*chapter 2*) The measurements of the *T. rex* tooth enamel and dentine were performed between 11/2016 and 10/2017 and within the analytical period of Löffler *et al.* (2019) (*chapter 2.3.3*; 02/2016 to 10/2017), who determined the clumped isotope temperature calibration that is applied to the *T. rex* data.

3.3 Results

T. rex dentine was measured with Δ_{47} = 0.562 ± 0.007 ‰, $\delta^{18}O$ = -10.31 ± 0.10 ‰, and = $\delta^{13}C$ = -6.53 ± 0.01 ‰ (n = 8). *T. rex* enamel was measured with Δ_{47} = 0.549 ± 0.006 ‰, $\delta^{18}O$ = -10.49 ± 0.11 ‰, and $\delta^{13}C$ = -9.28 ± 0.04 ‰ (n = 8). Based on a student t-test, the difference between the Δ_{47} of both datasets is statistically insignificant. Applying the Δ_{47}-$1/T^2$ (bio)apatite calibration of *chapter 2* (*equation 2.1*) to the *T. rex* tooth enamel and dentine gives temperatures of 38 ± 3 °C and 32 ± 3 °C, respectively. The $CaCO_3$ contents estimated by comparing their CO_2 gas yields with the gas yield of pure carbonate is 11.4 wt.% (enamel) and 10.9 wt.% (dentine).

Table. 3.1.: Overview on the results of the Δ_{47} analyses of the *T. rex* tooth enamel (TrixEn) and dentine (TrixDen). The TrixEn $\delta^{18}O_{H2O}$ value is calculated with the equations 1 and 3 of Löffler *et al.* (2019).

Identifier	Age ±error [Ma]	Δ_{47} ±se [‰]	T (Δ_{47}) ± se [‰]	$\delta^{13}C$ ± sd [‰]	$\delta^{18}O$ ± sd [‰]	n	$\delta^{18}O_{H2O}$ [‰]
TrixEn	*ca.* 66.5	0.549 ± 0.006	38 ± 3	-9.28 ± 0.04	-10.69 ± 0.11	8	-8.35
TrixDen		0.562 ± 0.007	32 ± 3	-6.53 ± 0.01	-10.51 ± 0.10	8	n.a.

3.4 Discussion

3.4.1 Preservation of the tooth enamel

Aside from the well preserved overall state of the skeleton (Schulp *et al.*, 2015; Schaeffer, 2016), previously measured $^{44}Ca/^{42}Ca$ and $^{87}Sr/^{86}Sr$ ratios reflected variations that can be interpreted as primary signals of diet and migration (Schaeffer, 2016). As a working hypothesis, it is assumed that the bulk oxygen and clumped isotopic composition of the *T. rex* tooth are well-preserved because the $^{44}Ca/^{42}Ca$ and $^{87}Sr/^{86}Sr$ ratios, which should be more susceptible for diagenetic alteration, seemingly reflect pristine values. A final assessment of the preservation of the sample materials will be done as soon as the $\delta^{18}O_{PO4}$ results are present. If the sample is indeed well-preserved, the $\delta^{18}O_{PO4}$-$\delta^{18}O_{CO3}$ difference should be around 8 to 9 ‰; provided that *T. rex* tooth enamel precipitates with the same oxygen fractionation when compared to modern mammals (Iacumin *et al.*, 1996), which was previously reported to be true for Jurassic sauropods (Tütken *et al.*, 2004). Furthermore, recently developed dual (Δ_{47} and Δ_{48}) clumped isotope analyses (Fiebig *et al.*, 2019) could offer valuable insights into diagenesis and/or potential kinetics of the precipitation of the *T. rex* tooth enamel, provided that the required sample mass for dual Δ_{47} and Δ_{48} analyses can be reduced in near future (*e.g.* by implementation of a modified Kiel IV Carbonate Device). To minimize the potential impact of diagenesis on the outcome of this study, the further discussion relies on the results from tooth enamel exclusively. It is overall less prone to diagenetic alteration when compared to dentine because of its smaller specific surface area, reduced macroporosity and enhanced hardness (*e.g.* Elliott, 1994; Enax *et al.*, 2012.; Tütken & Vennemann, 2011).

3.4.2 Thermophysiology

The Δ_{47}-based *T. rex* body temperature (38 ± 3 °C) is comparable to previously reported temperatures of large Theropods and Sauropods (Eagle *et al.*, 2011, 2015; Dawson *et al.*, 2020) and the growth size model of Gillooly *et al.* (2006). It furthermore falls in the middle of the temperature range of birds and mammals (Clarke & Rothery, 2008; *figure 3.3*) and is above the

environmental temperatures of the HCF during the C30n chron of approximately 23 °C (Johnson, 1997). The presented *T. rex* body temperature is though in agreement with both endothermy and gigantothermy (inertial homeothermy). For endothermy, the metabolic rate of an animal has to be high and variable within a sufficient range to actively regulate the thermal state of the body (32 to 40 °C) whereas the body mass is rather redundant. In contrast, gigantothermy requires *i)* a body size large enough to buffer any changes in environmental temperatures, *ii)* low metabolic rates, and *iii)* insulation by peripheral tissues (Paladino *et al.*, 1990). According to Seymour (2013), large ectotherm vertebrates have a lower endurance and muscular power when compared to endotherm vertebrates. Ectothermic metabolism would therefore contradict the high trophic position, behavioral features, and feeding strategies of *T. rex*, as for example, active hunting of large prey or potential migration (Carpenter, 1998; Rothschild & Depalma, 2013; DePalma *et al.*, 2013; Schaeffer, 2016).

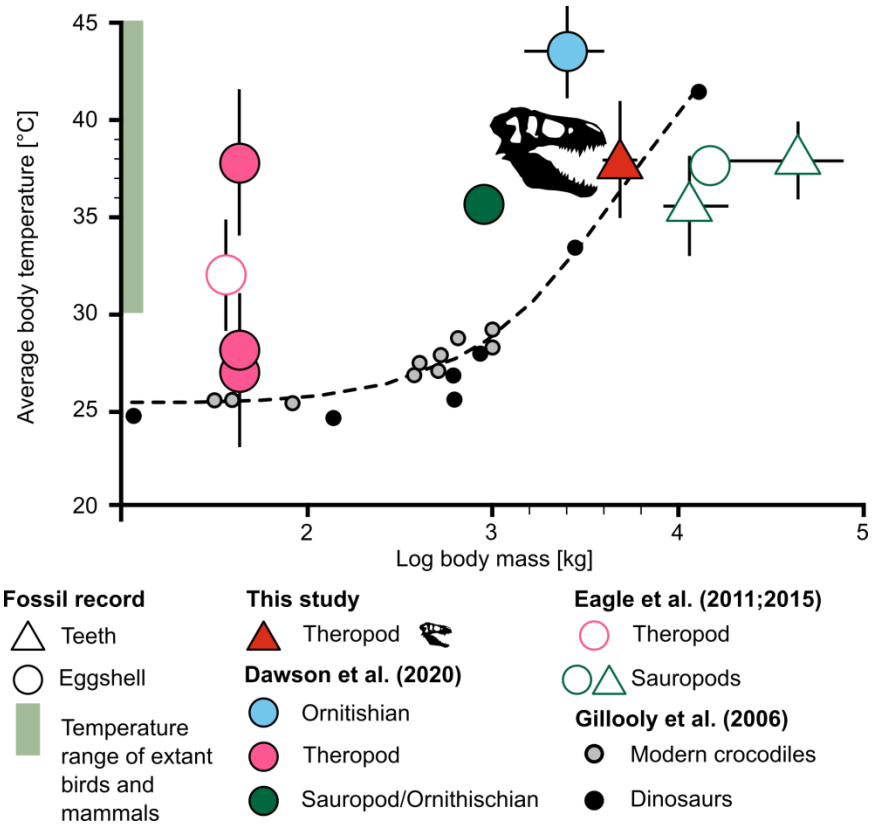

Figure 3.3: Body temperature *vs.* log body mass plot of data from Ornischtians, Sauropods, and Theropod tooth enamel and eggshell carbonate (Eagle *et al.*, 2011, 2015; Dawson *et al.*, 2020; this study). The data is plotted along with results from growth rate analyses of modern crocodiles and dinosaurs (grey and white dots) and the temperature-body size model of Gillooly *et al.* (2006) (dashed line).

Barrick and Showers (1994) used $\delta^{18}O_{PO4}$ analyses to measure intrabone temperature variation of skeletal materials from a well-preserved *T. rex* (MOR 555; Horner & Lessem, 1993). The resulting $\delta^{18}O_{PO4}$ showed only little variation implying homeothermy (Bligh & Johnson, 1973) with a temperature variation as low as 4 °C. Furthermore, the lack of high intrabone variations in $\delta^{18}O_{PO4}$, especially in the limbs and tail, suggest an endothermic metabolism (Barrick & Showers, 1994) if a diagenetical homogenization of $\delta^{18}O_{PO4}$ is excluded. When combined with the findings of this study, mammal-like endothermy with body temperatures of 38 ± 3 °C would be plausible. However, this would be only valid for (adult) *T. rex* and it cannot be excluded that other Mesozoic Theropods had varying concepts of thermophysiology (*e.g.* <30 °C Theropods of Dawson *et al.*, 2020). Clearly distinguishing between endothermy and gigantothermy will be feasible as soon as tooth enamel from a juvenile *T. rex* with a significant lower body mass (*e.g.* 1,000 kg) is measured for its Δ_{47}; ideally from the HCF to exclude a potential bias by varying local climatic conditions.

3.4.3 Oxygen and carbon isotopic compositions

Fricke and Pearson (2008) measured dental bioapatite $\delta^{18}O$ and $\delta^{13}C$ values from hadrosaurian and ceratopsian dinosaurs from the HCF. It is apparent that their $\delta^{18}O_{VSMOW}$ and $\delta^{13}C$ values (15 to 25 ‰ and -10 to -1 ‰, respectively) cover the measured *T. rex* values of $\delta^{18}O_{VSMOW}$ = 20.1 ‰ and $\delta^{13}C$ = -9.3 ‰ (*figure 3.4*). This indicates that *T. rex* had a direct predator-prey relationship with hadrosaurians and ceratopsians and/or that these dinosaurs shared a common water source. It is noteworthy that the tooth dentine samples of Fricke and Pearson (2008) (their figure 2), which are more susceptible for diagenetic alteration, have consistently elevated carbon *vs.* oxygen ratios when compared to their tooth enamel samples.

The $\delta^{18}O$ and $\delta^{13}C$ isotopic compositions of the structurally bound carbonate in tooth bioapatite generally reflect the isotopic composition of the body fluid (Kolodny *et al.*, 1983; Longinelli, 1984) which is, in turn, dependent on the isotopic compositions of ingested food and water, metabolism, and physiology (*e.g.* Bryant & Froelich, 1995; Kohn *et al.*, 1996). Because the temperature dependent oxygen fractionation between bioapatite and the precipitating fluid is constant for homoeothermic vertebrates, it is feasible to calculate the $\delta^{18}O$ of the body water which ultimately reflects the $\delta^{18}O$ of ingested water. This requires knowledge of the temperature of tooth formation and the oxygen fractionation between the mineralizing fluid and tooth enamel.

Integrating the measured *T. rex* $\delta^{18}O_{CO3}$ value (-10.69 ± 0.11 ‰) and its body temperature (38 ± 3 °C) with the temperature dependent 1,000ln($\alpha_{CHAP\text{-}H2O}$) and Δ_{47} calibrations of *chapter 2.6* (*equations 2.1* and *2.3*) results in a $\delta^{18}O_{H2O\ VSMOW}$ of -8.35 ‰. This generally agrees with mean surface water $\delta^{18}O_{H2O}$ values of Fricke *et al.* (2010) calculated from North American Foreland Basin sediments (-17.2 to -7.6 ‰). More specifically, the reconstructed $\delta^{18}O_{H2O\ VSMOW}$ of *T. rex* is indistinguishable from the $\delta^{18}O_{CO3}$ of a bivalve cluster (-9.6 ± 0.3 ‰) that is reported from the HCF (Dettman & Lohmann, 2000). The comparable high $\delta^{18}O$ values thereby suggest inland precipitation as a possible water source for the Maastrichtian catchment area of the HCF (Fricke *et al.*, 2010). Collectively, it can be concluded that the *T. rex* tooth enamel $\delta^{18}O$ and $\delta^{13}C$ values are in close agreement with the $\delta^{18}O_{H2O}$ of (potentially ingested) surface water and prey.

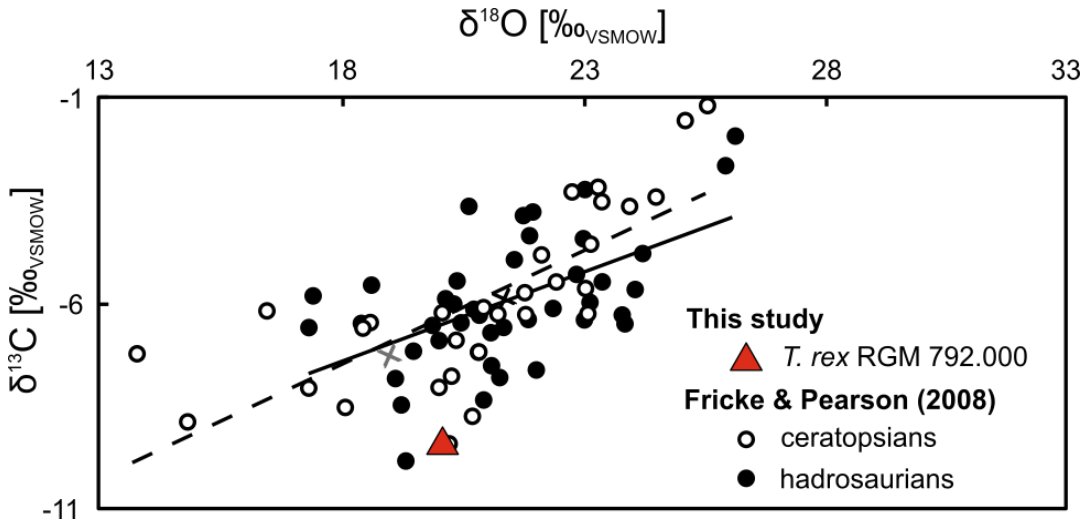

Figure 3.4: $\delta^{18}O$ *vs.* $\delta^{13}C$ plot of structurally bound carbonate in tooth enamel from *T. rex* (RGM 792.000; red triangle), ceratopsians (white circles, dashed line, grey "x") and hadrosaurians (black dots, solid line, black "x") (Fricke & Pearson, 2008) from the Hell Creek Formation. Average values of the ceratopsians and hadrosaurians are indicated by Xs. Note that the *T. rex* data falls well within the data of Fricke and Pearson (2008) and plots at low $\delta^{18}O$ *vs.* $\delta^{13}C$ ratios. This indicates a good preservation as the measured *T. rex* $\delta^{18}O$ and $\delta^{13}C$ are in agreement with primary signals (*e.g.* ingested food and water).

3.5 Conclusions

The body temperature of the well-preserved adult *T. rex* "Trix" (RGM 792.000) has been determined to be 38 ± 3 °C by analyzing the Δ_{47} of its tooth enamel and by applying the recently published $\delta^{18}O_{CO3}$ and Δ_{47} temperature calibrations for (bio)apatite of *chapter 2*. The body temperature falls within the range of modern endothermic vertebrates of 34 to 44 °C (*e.g.*

mammals and birds; Clarke & Rothery, 2008). Together with evidence from $\delta^{18}O_{PO4}$ of the adult specimen MOR 555 (Barrick & Showers, 1994), it can be concluded that adult *T. rex* were probably homeotherm at a mammal to bird-like body temperature. Nonetheless, solving the research question of endothermy in *T. rex* requires future Δ_{47} analyses of juvenile *T. rex* specimens because it cannot be distinguished between endothermy and gigantothermy based on a single body temperature of a specimen with such a high body mass (5,000 kg). The reconstructed *T. rex* body fluid $\delta^{18}O_{H2O}$ value agrees well with previously reported North American surface waters $\delta^{18}O_{H2O}$ values and $\delta^{18}O_{CO3}$ values of bivalves from the HCF. In $\delta^{18}O$ *vs.* $\delta^{13}C$ space, the *T. rex* tooth enamel plots within the cloud of the respective data from herbivore dinosaurs suggesting a potential local predator-prey relationship with hadrosaurian and ceratopsian dinosaurs. These consistent results collectively underline the good quality of sample preservation, the validity of the clumped isotope analyses, and the applicability of the $\delta^{18}O_{CO3}$ and Δ_{47} temperature calibrations for (bio)apatite of *chapter 2* (Löffler *et al.*, 2019).

3.6 Comments and acknowledgements

This chapter is a spinoff of the Löffler *et al.* (2019) study (*chapter 2*). There are no defined co-authorships yet because the format of a possible peer-reviewed publication of the results of this chapter has not been fully decided upon. It was therefore decided to write this chapter in order to document the research in this Ph.D. thesis. However, it should be stressed that this study would not have been possible without the great support and contribution of the research partners A.S. Schulp, J. Fiebig, T. Tütken, D. Bajnai, and A. Mulch. A.S. provided the sample material. T.T. established the contact between A.S. and N.L. N.L. performed the clumped isotope analyses. D.B. prepared and measured HG and 25G. A.S., J.F., T.T., and A.M. discussed the results and supported the presentation of the preliminary results in 2017.

4 Combined high-precision Δ_{47} and Δ_{48} analysis of carbonates

J. Fiebig[a, b*], D. Bajnai[b, 1], N. Löffler[a, b], K. Methner[a], E. Krsnik[a, b], A. Mulch[a, b], S. Hofmann[a]

[a] *Institute of Geosciences, Goethe University Frankfurt, Altenhoeferallee 1, 60438 Frankfurt (Main), Germany*

[b] *Senckenberg Biodiversity and Climate Research Center, Senckenberganlage 25, 60325 Frankfurt (Main), Germany*

[1] *Present address: Institute of Geology and Mineralogy, University of Cologne, Zülpicher Str. 49a 50674 Cologne, Germany*

**Correspondence: Jens.Fiebig@em.uni-frankfurt.de*

Published in Chemical Geology (2019), 522, 186-191.

https://doi.org/10.1016/j.chemgeo.2019.05.019

Received 11 February 2019; accepted in revised form 14 May 2019; Available online 25 May 2019

4.0 Abstract

High-precision analysis of the excess abundance (relative to the stochastic distribution) of mass 48 isotopologues in CO_2 evolved from acid digestion of carbonates (Δ_{48}) has not been possible until recently due to the relatively low natural abundance of ^{18}O. Here we show that the 253 Plus™ gas source mass spectrometer equipped with Faraday cups and 1013 Ω resistors can perform combined Δ_{47} and Δ_{48} analyses on carbonates with external reproducibilities (1SD) of 0.010 ‰ and 0.030 ‰, respectively.

~10 mg aliquots of five carbonate reference materials (ETH 1, ETH 2, ETH 3, ETH 4, and Carrara) are digested with phosphoric acid at 90 °C using a common acid bath. The evolved CO_2 is purified using an automated gas preparation system (including cryotraps and a GC) and analyzed for its Δ_{47} and Δ_{48} compositions using the dual inlet system of a 253 Plus™ gas source mass spectrometer. Raw Δ_{47} and Δ_{48} values are finally normalized to the Carbon Dioxide Equilibrium Scale (CDES).

In $\Delta_{47, \text{CDES } 90°C}$ *vs.* $\Delta_{48, \text{CDES } 90°C}$ space, calcite reference materials Carrara, ETH 3 and ETH 4 agree with the equilibrium curve for calcite after adding semi-empirically determined 90 °C acid fractionation factors of 0.196 ‰ (for Δ_{47}) and 0.136 ‰ (for Δ_{48}) to theoretical Δ_{63} and Δ_{64} data. Agreement between measured and theoretically expected $\Delta_{48, \text{CDES } 90°C}$ highlights the accuracy of our high-precision clumped isotope analytical setup. Combined analysis of the abundances of mass 47 and mass 48 isotopologues in CO_2 evolved from acid digestion of natural carbonates has excellent potential for the determination of accurate and highly precise paleotemperatures as well as for the identification of rate-limiting kinetic processes involved in

biomineralization. A formation temperature of 15(±2) °C is obtained on the 95 % confidence level for the Upper Cretaceous chalk sample ETH 3.

Keywords: Clumped isotopes, Carbonates, Δ_{47}, Δ_{48}, Paleotemperatures, Biomineralization

4.1 Introduction

Clumped isotope analysis of the sum of $^{13}C^{18}O^{16}O$ and $^{12}C^{18}O^{17}O$ isotopologues (Δ_{47}) in CO_2 evolved from phosphoric acid digestion of carbonates (Ghosh *et al.*, 2006) has become a now increasingly utilized (paleo)thermometer (Eiler, 2011) to determine marine (*e.g.*, Wierzbowski *et al.*, 2018) and terrestrial (*e.g.* Methner *et al.*, 2016) paleotemperatures, body temperatures of extinct vertebrates (*e.g.*, Eagle *et al.*, 2011), diagenetic (*e.g.*, Huntington *et al.*, 2011) and hydrothermal temperatures (*e.g.*, Bristow *et al.*, 2011) as well as closure temperatures of metamorphic rocks (*e.g.*, Passey & Henkes, 2012). Since this type of thermometer is based on the internal fractionation of isotopes amongst carbonate isotopologues, it is independent on the isotopic composition of the water from which the carbonate-bearing phase precipitated. Nonetheless, discrepant Δ_{47}–temperature calibrations have been obtained in different laboratories (Dennis & Schrag, 2010; Ghosh *et al.*, 2006; Fernandez *et al.*, 2017; Petersen *et al.*, 2019). Accuracy of Δ_{47} calibration data has been shown to be sensitive to the choice of parameters used for the correction of (1) contributions deriving from ^{17}O-bearing CO_2 (Daëron *et al.*, 2016; Schauer *et al.*, 2016), (2) pressure baseline effect (Bernasconi *et al.*, 2013; Fiebig *et al.*, 2016; He *et al.*, 2012), (3) scale compression (Dennis *et al.*, 2011; Huntington *et al.*, 2009), and (4) acid fractionation (Petersen *et al.*, 2019). Also, calibration regression lines can be biased if the number of samples and replicates per sample, as well as the investigated temperature range, is relatively low (Fernandez *et al.*, 2017). The observed discrepancy in Δ_{47}-T calibrations is slightly reduced if calibration data from eight experimental and six empirical studies are processed with the IUPAC ^{17}O parameters, recommended by (Daëron *et al.*, 2016), and with a unique temperature dependence of the acid fractionation factor (Petersen *et al.*, 2019). However, even for these reprocessed calibrations the absolute spread in Δ_{47} at a given temperature remains as large as 0.08 ‰, with slopes ranging from 0.033 to 0.042 in Δ_{47} *vs.* $1/T^2$ space (Petersen *et al.*, 2019). Most recent investigations suggest that much of the observed scatter could be due to kinetics occurring in the solution prior to carbonate precipitation and at the solution-carbonate interface (Bajnai *et*

al., 2018; Daëron *et al.*, 2019). If relevant, kinetic departures from equilibrium would limit the accuracy of the clumped isotope Δ_{47} paleothermometer.

The second most abundant carbonate isotopologue containing two heavy isotopes is $^{12}C^{18}O^{18}O^{16}O$. CO_2 derived from acid digestion of carbonate contains on average 4.1 ppm of $^{12}C^{18}O^{18}O$ (mass 48), which is an order of magnitude lower than its $^{13}C^{18}O^{16}O$ (mass 47) content (Ghosh *et al.*, 2006). Another mass 48 isotopologue is $^{13}C^{18}O^{17}O$ that has an average natural abundance of 16.7 ppb only. The weighted sum of the excess abundances of mass 48 isotopologues (relative to their stochastic distributions) is reflected by the Δ_{48} value:

(*equation 4.1*) $\Delta_{48} = [(R_{48}/R_{48}^{*}-1)-2 \times (R_{46}/R_{46}^{*}-1) \times 1{,}000$

where Ri and Ri* represent the measured and stochastic* i/44 isotopologue ratios.

Like Δ_{47}, the carbonate Δ_{48} composition does not depend on the oxygen isotopic composition of the water from which the carbonate crystallized. The position of a given carbonate sample in Δ_{47} *vs.* Δ_{48} space is, therefore, determined by its formation temperature and, if kinetics prevailed during formation, by the extent of kinetic departure from equilibrium. Since kinetically induced departures from equilibrium follow for given rate-limiting exchange mechanisms characteristic trajectories in Δ_{47} *vs.* Δ_{48} space, it should be possible to determine accurate carbonate formation temperatures based on measured Δ_{47} and Δ_{48} compositions even if these were affected by kinetics (Guo & Zhou, 2019b).

So far, the precision of Δ_{48} measurements with common gas source mass spectrometers equipped with $\leq 10^{12}$ Ω amplifiers has been inadequate to permit temperature estimates based on Δ_{48}. Instead, laboratories that analyze Δ_{48} use its magnitude for data quality assurance of Δ_{47} data, *e.g.*, as an indicator of potential isobaric interferences on *m/z* 47 (Huntington *et al.*, 2009). Here we demonstrate that high-precision Δ_{47} and Δ_{48} analyses of carbonates are possible using a common acid bath and the dual inlet of a Thermo Scientific™ 253 Plus™ gas source mass spectrometer. The external reproducibilities for these measurements are close to the predicted shot noise limits. Our results imply that internal isotopic equilibrium is closely attained in calcite reference materials ETH 1, ETH 2, ETH 3, ETH 4, and Carrara.

4.2 Experiments

4.2.1 Samples

Calcite reference materials analyzed for this study were an in-house Carrara and the internationally distributed ETH 1, ETH 2, ETH 3, and ETH 4 standards (Bernasconi *et al.*, 2018). ETH 1 (Carrara marble) and ETH 2 (synthetic high-purity calcite) were internally equilibrated at 600 °C. ETH 3 represents Upper Cretaceous chalk from the Isle of Rügen, Germany, whereas ETH 4 is the synthetic high-purity calcite that was also used for the preparation of ETH 2. The formation temperatures of ETH 3 and ETH 4 calcites are unknown (Meckler *et al.*, 2014; Bernasconi *et al.*, 2018). Bernasconi *et al.* (2018) reported $\Delta_{47,\ \mathrm{CDES\ 25\ °C}}$ for ETH 1, ETH 2, ETH 3 and ETH 4 that were assigned using the dual inlet system for equilibrated gas measurements and a Thermo Scientific™ KIEL IV Carbonate Device for carbonate-derived CO_2 measurements.

4.2.2 Carbonate reaction and gas purification

The setup of the self-constructed automated carbonate acid digestion and gas purification system (Hofmann's Auto Line, HAL) used for sample preparation is displayed in *figure 4.1*. It consists of a Zero Blank Autosampler (Costech Analytical Technologies, USA), a common acid bath, several cryotraps and a gas chromatograph (GC; 2.0 m of 1/8 ″ stainless steel tube packed with Porapak™ Q 80–100 mesh, Merck, Germany) and two turbopumps (HiCube 80 Eco, Pfeiffer Vacuum, Germany) with cryogenic water traps upstream of the turbo pumps. One pumps the part of the extraction line in front of the GC, including the autosampler and the common acid bath, the other provides the high vacuum for the two cryotraps in front of and behind the GC. Per replicate, ~10 mg of calcite is loaded into silver capsules (IVA Analysentechnik, Germany). These are then placed into the autosampler, located on top of the common acid bath. Once loading is completed, the autosampler and the common acid bath are turbo-pumped for at least 5 h. Slight rotation of the autosampler forces a sample-bearing silver capsule to drop down into the phosphoric acid (>105 wt%). Carbonate samples are routinely reacted for 30 min, and the evolving CO_2 is continuously removed at -196 °C in trap 2. Trap 1 is kept at -80 °C to remove water. During the reaction, the pressure is continuously monitored at trap 2. After the reaction is complete, traps 2, 3 and 4 are set to -80 °C, while trap 5 is cooled to -196 °C. Helium (purity >5.0; Alphagaz™ He, Air Liquide, France, gas led through a Supelco® 27600-U, Merck, Germany, helium purifier) enters trap 2 at a flow rate of 15 ml/min and purges the CO_2 through trap 3, the GC column (kept at -15 °C) and trap 4, before it is frozen out again in trap 5. After

45 min, the GC column is purged with He in the reverse flow, heated to 150 °C and kept at this temperature until the next sample is being prepared. Helium is pumped away from trap 5. Afterwards, trap 5 is warmed up to -80 °C and trap 6 cooled down to -196 °C. The yield of CO_2 is determined in the volume of trap 5 and the CO_2 then frozen out in trap 6. Once freezing is complete, trap 6 is isolated from trap 5, warmed up to -80 °C and the pure CO_2 introduced into the sample bellow of the mass spectrometer through expansion. HAL is controlled with the software LabVIEW (National Instruments, USA).

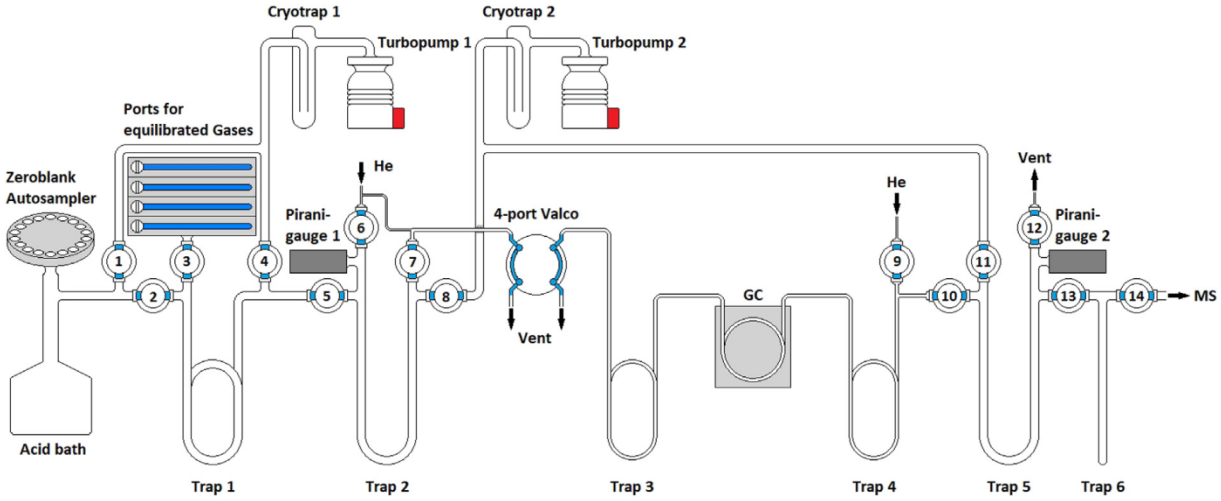

Figure 4.1: Schematic setup of Hofmann's Auto Line (HAL). For more detailed explanation see text.

4.2.3 Equilibrated gases and purification

CO_2, equilibrated at 1,000 °C for at least 2 h in a quartz break seal tube (GM Associates, USA), is taken off the muffle furnace and quenched to room temperature within 2 min. The break seal tube is mounted on a tube cracker that is connected to a high vacuum (water trap upstream the turbopump), manually operated gas extraction line. Within <5 min after having left the muffle furnace, the break seal tube is cracked, and the CO_2 is passed twice over a water trap kept at -80 °C. The CO_2 is finally quantitatively transferred into a quartz glass with a pneumatic diaphragm valve (Swagelok, USA) at its top ("autofinger"). The same high vacuum line is used to clean CO_2 equilibrated at 25 °C and to transfer it to the autofinger. However, before CO_2 equilibrated at 25 °C is allowed to enter the manually operated high-vacuum gas purification line, liquid water is stripped off on a separate, rotary vane-pumped gas extraction line by passing the CO_2 five times over a cryogenic water trap kept at -80 °C. This way we can avoid that any significant amounts of water enter the high-vacuum gas preparation line.

The autofinger is finally connected to HAL in front of trap 2 (*figure 4.1*). There, equilibrated gases follow the same preparation pathway as carbonate-derived CO_2 with the exception that they enter HAL isolated from the common acid bath. Equilibrated gases are prepared in amounts equivalent to the CO_2 derived from carbonates (between 80 and 100 µmol).

4.2.4 Mass spectrometric measurements

Isotopic analyses are carried out on a Thermo Scientific™ 253 Plus™ (Thermo Fisher Scientific, Germany) gas source mass spectrometer using its dual inlet system. The 253 Plus™ at the Goethe University has Faraday cups for *m/z* 44, 45, 46, 47, 47.5, 48 and 49. Cups for *m/z* 44-46 have 3×10^8 Ω, 3×10^{10} Ω, and 10^{11} Ω resistors, respectively, while *m/z* 47-49 cups are amplified by 10^{13} Ω resistors. The *m/z* 47.5 cup is used to continuously read in the pressure baseline next to *m/z* 47.

After the sample bellow has been loaded with CO_2, an equivalent amount (80–100 µmol) of reference gas CO_2 (ISO-TOP, Air Liquide; $\delta^{18}O_{VSMOW}$ = 25.26 ‰, $\delta^{13}C_{VPDB}$ = -4.20 ‰) is introduced into the reference gas bellow. Reference and sample gas enter the ion source of the 253 Plus™ gas source mass spectrometer through stainless steel capillaries whose inner surface is coated with inert fused silica (Thermo Fisher Scientific; bre 00014684). Reference and sample gas intensity are automatically adjusted to an intensity of 16,000 (± 100) mV on *m/z* 44. Sample and reference gas are measured in 10 acquisitions, consisting of 10 cycles each. Each cycle considers an integration time of 20 s both for the reference and the sample gas, yielding a total integration time of 2,000 s per replicate. Idle time is set to 16 s.

4.2.5 Data processing

The common background correction with no gas in the source is not applied. The negative background that is read in on *m/z* 47.5 is directly added to the raw intensities obtained for *m/z* 47, *m/z* 48 and *m/z* 49 in Isodat using a scaling factor of -1. Acquisition files are then exported to Easotope (release 20190125) (John & Bowen, 2016) which performs the calculation of $\delta^{13}C_{VPDB}$, $\delta^{18}O_{VSMOW}$, δ_{47}, δ_{48}, $\Delta_{47,\,raw}$ and $\Delta_{48,\,raw}$ using the IUPAC parameters (Daëron *et al.*, 2016)

4.3 Results

A total of 76 carbonate reference samples and 38 equilibrated gases were run within a period of 8 weeks in January and February 2019. $\delta^{13}C_{VPDB}$, $\delta^{18}O_{VSMOW}$, δ_{47}, δ_{48}, $\Delta_{47,\,raw}$ and $\Delta_{48,\,raw}$ of equilibrated gases and carbonate reference materials are listed in the supplementary data (*S.4.I*

and *II*). For the carbonate reference materials, we also present a summary table in which measured $\Delta_{47,\ raw}$ and $\Delta_{48,\ raw}$ values were finally projected onto the carbon dioxide equilibrium scale (CDES) (*table 4.1*).

Table 4.1: $\Delta_{47,\ CDES\ 90°C}$ and $\Delta_{48,\ CDES\ 90°C}$ of carbonate reference materials analyzed in this study. All values are processed using the IUPAC parameters recommended by Daëron *et al.* (2016) and are reported in ‰-deviation relative to the stochastic distribution. 1 sd and 2 se denote the 1 σ standard deviation and the 2 σ standard error, respectively. The shot noise limit represents the best analytical precision that can be obtained. It was calculated from equation 15 of Merritt and Hayes (1994), considering the total integration time represented by the total number of replicates (2,000 s × number of replicates).

	Carrara		ETH 4		ETH 3		ETH 3		ETH 1	
	0.312	0.173	0.462	0.263	0.623	0.305	0.226	0.171	0.220	0.093
	0.318	0.123	0.469	0.196	0.630	0.242	0.212	0.136	0.222	0.132
	0.312	0.103	0.464	0.167	0.611	0.285	0.213	0.123	0.216	0.158
	0.319	0.172	0.456	0.227	0.615	0.296	0.214	0.151	0.203	0.159
	0.317	0.127	0.437	0.205	0.629	0.255	0.200	0.119	0.193	0.138
	0.307	0.144	0.447	0.218	0.628	0.212	0.223	0.195	0.201	0.181
	0.307	0.125	0.455	0.240	0.602	0.289	0.203	0.129	0.213	0.106
	0.303	0.111	0.455	0.249	0.627	0.260	0.207	0.135	0.218	0.115
	0.316	0.126	0.462	0.238	0.630	0.208	0.202	0.167	0.211	0.107
	0.314	0.141	0.458	0.258	0.614	0.252	0.205	0.089	0.208	0.094
	0.310	0.106	0.457	0.194	0.616	0.277	0.206	0.168	0.200	0.143
	0.335	0.229			0.609	0.285	0.212	0.147	0.215	0.116
					0.613	0.286	0.210	0.138	0.228	0.134
					0.630	0.304	0.235	0.121	0.216	0.129
					0.623	0.237	0.222	0.137	0.223	0.133
					0.611	0.321	0.227	0.125	0.220	0.121
							0.230	0.082	0.215	0.220
							0.221	0.156	0.224	0.174
									0.222	0.175
Average	0.314	0.140	0.457	0.223	0.619	0.270	0.215	0.138	0.214	0.138
1 sd	0.008	0.036	0.009	0.030	0.009	0.033	0.011	0.028	0.009	0.033
2 se	0.005	0.023	0.006	0.020	0.005	0.018	0.005	0.014	0.005	0.016
Shot noise limit	0.002	0.008	0.002	0.008	0.002	0.007	0.002	0.006	0.002	0.006

4.4 Discussion

4.4.1 Background correction

Figure 4.2 displays the correlation between δ_{47} and $\Delta_{47,\ raw}$ for CO_2 equilibrated at 1,000 °C and 25 °C, respectively, as well as for ETH 1 and ETH 2. The slopes of the corresponding regression lines are almost zero, demonstrating that the *m/z* 47.5 cup accurately reads in the negative background below *m/z* 47. However, since there is a slight residual slope for

the heated gases that is distinguishable from zero, an additional slope correction of $\Delta_{47,\ raw}$ data needs to be applied (Huntington *et al.*, 2009). To determine this slope, 1,000 °C and 25 °C gas data are merged, adding the average difference between the two corresponding regression lines to the heated gas $\Delta_{47,\ raw}$ values. This way, a residual slope of 0.00012 (±0.00008) is obtained that exactly matches the residual slope displayed by ETH 1 and ETH 2 raw data (*figure 4.2*). Slope corrected $\Delta_{47,\ sc}$ values are calculated according to *equation 4.2*:

(*equation 4.2*) $\Delta_{47,sc} = \Delta_{47,raw} = (m_{47} \times \delta_{47})$

where m_{47} is the residual slope, in our case 0.00012.

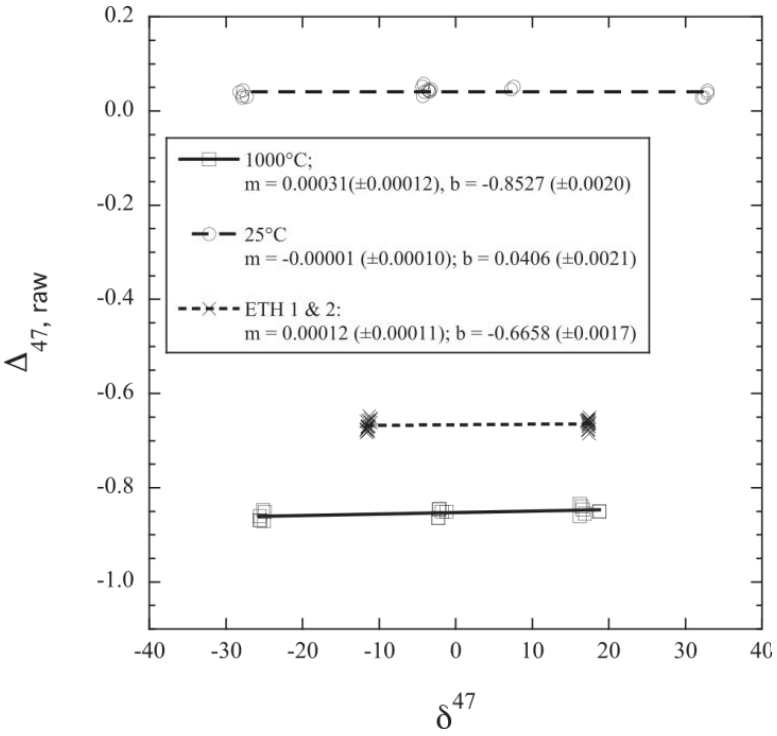

Figure 4.2: Plot of $\Delta_{47,\ raw}$ *vs.* δ_{47} for CO_2 equilibrated at 1,000 °C and 25 °C, respectively, as well as for carbonate reference materials ETH 1 and ETH 2. $\Delta_{47,\ raw}$ and δ_{47} values are relative to the working gas composition. Slopes (m) and intercepts (b) of the corresponding regression lines, as well as their errors, are provided for further information.

Correlation plots of δ_{48} *vs.* $\Delta_{48,\ raw}$, however, yield significant steeper residual negative slopes (*figure 3*). In addition, the slopes vary slightly between -0.01435 (± 0.00036) for 25 °C gases, -0.01474 (± 0.00030) for ETH 1 and ETH 2 and -0.01560 (± 0.00048) for heated gases. These residual slopes result from an overcorrection of the negative background occurring below *m/z* 48 when using the intensity monitored by the *m/z* 47.5 cup. The merged data set of equilibrated gases is characterized by a slope of -0.01479 (± 0.00027), which is indistinguishable from the slope displayed by ETH 1 and ETH 2 data. As was done for slope correction of $\Delta_{47,\ raw}$

data, we, therefore, use the slope obtained from the ETH 1 and ETH 2 data (*figure 4.3*) to correct all sample $\Delta_{48,\,raw}$ data for the overcorrection induced by the *m/z* 47.5 intensities.

(*equation 4.3*) $\Delta_{48,sc} = \Delta_{48,raw} = (m_{47} \times \delta_{47})$

where m_{48} is the residual slope, in this study -0.01474.

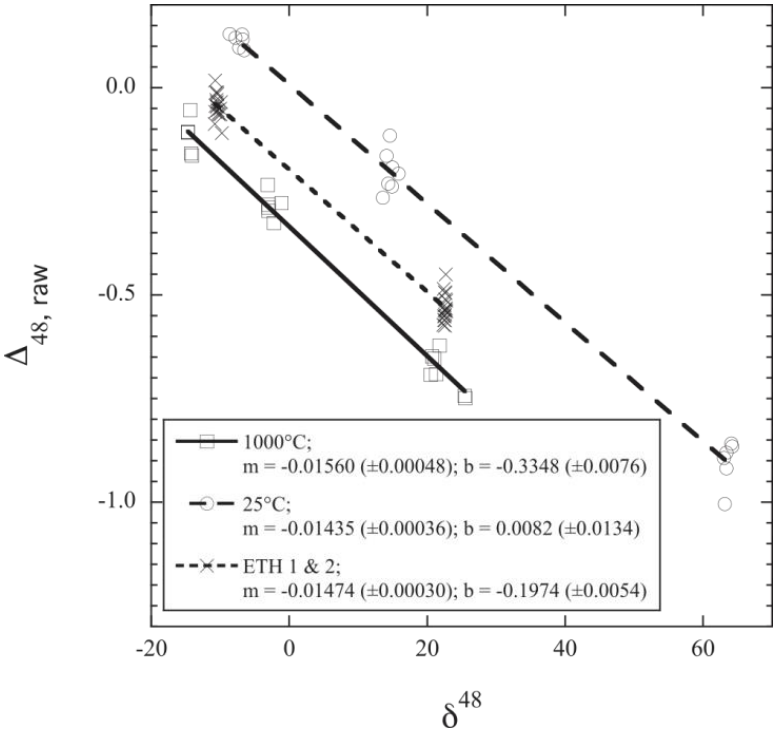

Figure 4.3: Plot of $\Delta_{48,\,raw}$ *vs.* δ_{48} for CO_2 equilibrated at 1,000 °C and 25 °C, respectively, as well as for carbonate reference materials ETH 1 and ETH 2. $\Delta_{48,\,raw}$ and δ_{48} values are relative to the working gas composition. Slopes (m) and intercepts (b) of the corresponding linear regression lines, as well as their errors, are provided for further information.

4.4.2 Projecting $\Delta_{47,\,sc}$ and $\Delta_{48,\,sc}$ sample values to the carbon dioxide equilibrium scale

Empirical transfer functions for the projection of $\Delta_{47,\,sc}$ and $\Delta_{48,\,sc}$ sample values onto the CDES can be derived following the principles outlined in Dennis *et al.* (2011), by plotting $\Delta_{47,\,sc}$ and $\Delta_{48,\,sc}$ values of equilibrated gases against their corresponding theoretical values. $\Delta_{47,\,sc}$ and $\Delta_{48,\,sc}$ values of equilibrated gases are reflected by the intercepts of equilibrated gas data regression lines in $\Delta_{47,\,raw}$ *vs.* δ_{47} space (*figure 4.2*) and $\Delta_{48,\,raw}$ *vs.* δ_{48} space (*figure 4.3*), respectively. Theoretical $\Delta_{48,\,1000°C}$ and $\Delta_{48,\,25°C}$ values are not directly available but can be computed from the data provided by Wang *et al.* (2004), who calculated the temperature dependence of $\Delta_{12C18O18O}$ and $\Delta_{13C18O17O}$ as a function of temperature. Considering that $^{12}C^{18}O^{18}O$ contributes 99.6 % and $^{13}C^{18}O^{17}O$ 0.4 % to *m/z* 48, theoretical Δ_{48} values at any temperature can be computed according to:

(*equation 4.4*) $\Delta_{48,CO2} = 0.996 \times \Delta_{12C18O16O} + 0.004 \times \Delta_{13C18O17O}$

After processing the data of Wang *et al.* (2004) (their table 4(I)) through Eq. (4), a best fit polynomial regression yields:

(*equation 4.5*) $\Delta_{48,CO2} = -1.0345 \times 10^{-4} \times (10^6/T^2) + 4.22629 \times 10^{-3} \times (10^6/T^2) - 3.76112 \times 10^{-3} \times (10^6/T^2)$

According to *equation 4.5*, the theoretical Δ_{48} should be 0.345 ‰ and 0.000 ‰ for CO_2 at temperatures of 25 °C and 1,000 °C, respectively. At these temperatures, the corresponding theoretical Δ_{47} values are 0.9252 ‰ and 0.0266 ‰, respectively (Dennis *et al.*, 2011).

In $\Delta_{47,\,raw}$ *vs.* δ_{47} space, the difference in intercepts between 1,000 °C (-0.8527 (± 0.0020)) ‰ and 25 °C CO_2 (0.0406 (± 0.0021)) ‰ matches the theoretical difference of 0.90 ‰ (*figure 4.2*). This observation strongly implies that the 253 Plus™ installed at the joint Goethe University – Senckenberg BIK-F Stable Isotope Facility is devoid of any significant scale compression for Δ_{47}, contrary to the MAT 253™ that was run in the same laboratory using electropolished nickel capillaries (Fiebig *et al.*, 2016). For the determination of $\Delta_{47,\,CDES\ 90°C}$ the following empirical transfer function is obtained:

(*equation 4.6*) $\Delta_{47,\,CDES\ 90°C} = 1.0060 \times \Delta_{47,sc} + 0.8843$

In $\Delta_{48,\,raw}$ *vs.* δ_{48} space, intercepts of -0.3348 (± 0.0076) ‰ and 0.0082 (± 0.0134) ‰ are obtained for CO_2 equilibrated at 1,000 °C and 25 °C, respectively (*figure 4.3*). Again, the difference between the two intercepts is in perfect agreement with the theoretically expected value of 0.345‰. The hypothesis that the 253 Plus™ installed in our laboratory is not affected by any significant scale compression is, therefore, confirmed by Δ_{48} data of equilibrated gases. It follows:

(*equation 4.7*) $\Delta_{48,\,CDES\ 90°C} = 1.0056 \times \Delta_{48,sc} + 0.3367$

$\Delta_{47,\,CDES\ 90°C}$ and $\Delta_{48,\,CDES\ 90°C}$ computed for carbonate reference materials ETH 1, ETH 2, ETH 3, ETH 4 and Carrara are listed in *table 4.1*. For these, it becomes obvious that $\Delta_{48,\,CDES\ 90°C}$ increases with $\Delta_{47,\,CDES\ 90°C}$. Such behavior is expected if both compositions are largely controlled by temperature. External reproducibilities (expressed as 1 σ standard deviation, 1 sd) range from ± 0.008 ‰ to ± 0.011 ‰ for $\Delta_{47,\,CDES\ 90°C}$ and from ± 0.028 to ± 0.036 ‰ for $\Delta_{48,\,CDES\ 90°C}$ (*table 4.1*). These values are only slightly higher than the predicted shot noise limits of 0.008 ‰ and

0.027 ‰, respectively, which represent the best attainable precision for the chosen analytical conditions of 2000 s integration time per replicate (Merritt & Hayes, 1994). Compared to the MAT 253™ (1SD of 11–16 ppm, see Fiebig *et al.*, 2016), the external reproducibility for dual inlet-based Δ_{47} measurements with the high-ohmic 253 Plus™ is improved by a factor of 1.5.

4.4.3 $\Delta_{47,\ CDES\ 25\ °C}$ values of ETH carbonate reference materials

Addition of a 25–90 °C acid fractionation factor of 0.088 ‰ (Petersen *et al.*, 2019) to the $\Delta_{47,\ CDES\ 90°C}$ values reported in *table 4.1* yields $\Delta_{47,\ CDES\ 25°C}$ values (± 1 SD) of 0.302 (± 0.009) ‰ for ETH 1, 0.303 (± 0.011) ‰ for ETH 2, 0.707 (± 0.009) ‰ for ETH 3, and 0.545 (± 0.009) ‰ for ETH 4. These values are significantly different from those reported in (Bernasconi *et al.*, 2018), even if 0.004 ‰ are added to the latter data to account for the unique temperature dependence of the acid fractionation factor (note that (Bernasconi *et al.*, 2018) reacted at 70 °C and that a 25–70 °C acid fractionation of 0.062 ‰ was applied to their data, which slightly deviates from the 0.066 ‰ reported in Petersen *et al.*, 2019). We speculate that the observed differences may arise from the circumstance that in the analytical setup used by Meckler *et al.* (2014) and Bernasconi *et al.* (2018), CO_2 gas derived from the ETH standards did not enter the ion source of the gas source mass spectrometer through the same stainless steel capillary as the equilibrated gases. If small amounts of water were adsorbed at the inner surface of the sample gas capillary, partial re-equilibration of CO_2 at ambient temperature may happen while the CO_2 passes through the capillary, finally introducing a compression of the Δ_{47}-scale. Partial re-equilibration may attain a steady state as long as the water content and the gas flux through the capillary are constant. Under such conditions, sample-derived CO_2 can still be accurately projected onto the CDES if the equilibrated gases enter the ion source through the same capillary as the sample gases. However, the same correction procedure may deliver inaccurate results if two different capillaries with distinct water contents and fluxes are used, as already stated by (Bernasconi *et al.*, 2018)

4.5 Comparing measured $\Delta_{47,\ CDES\ 90°C}$ and $\Delta_{48,\ CDES\ 90°C}$ with predicted equilibrium values

According to Hill *et al.* (2014), the B3LYP (6-311++G(2d,2p)) supramolecular cluster model describes the temperature dependence of equilibrium clumping in calcite most reliably. To make measured $\Delta_{47,\ CDES\ 90°C}$ and $\Delta_{48,\ CDES\ 90°C}$ comparable with equilibrium Δ_{63} and Δ_{64} values, the acid fractionation factors $\Delta^*_{47–63}$ and $\Delta^*_{48–64}$, characteristic for a reaction at 90 °C, have to be added to the Δ_{63} and Δ_{64} values, respectively. These can be constrained from measured and

theoretical data. For ETH 1 and ETH 2, we obtain mean $\Delta_{47,\ CDES\ 90°C}$ and $\Delta_{48,\ CDES\ 90°C}$ values of 0.214 (± 0.010) ‰ and 0.138 (± 0.030) ‰, respectively (*table 4.1*). According to Hill *et al.* (2014), a Δ_{63} value of 0.018 ‰ and a Δ_{64} value of 0.002 ‰ is predicted for calcite at 600 °C, *e.g.*, the temperature at which ETH 1 and ETH 2 were prepared. Subtracting these values from the mean $\Delta_{47,\ CDES\ 90°C}$ and $\Delta_{48,\ CDES\ 90°C}$ values obtained for ETH 1 and ETH 2 yields Δ^*_{47-63} and Δ^*_{48-64} acid fractionation factors of 0.196 ‰ and 0.136 ‰, respectively. Theoretically expected $\Delta_{47,\ CDES\ 90°C}$ and $\Delta_{48,\ CDES\ 90°C}$ values for CO_2 derived from acid digestion of equilibrated calcite may now be computed adding Δ^*_{47-63} and Δ^*_{48-64} to the theoretical Δ_{63} and Δ_{64} values of Hill *et al.* (2014) at any temperature.

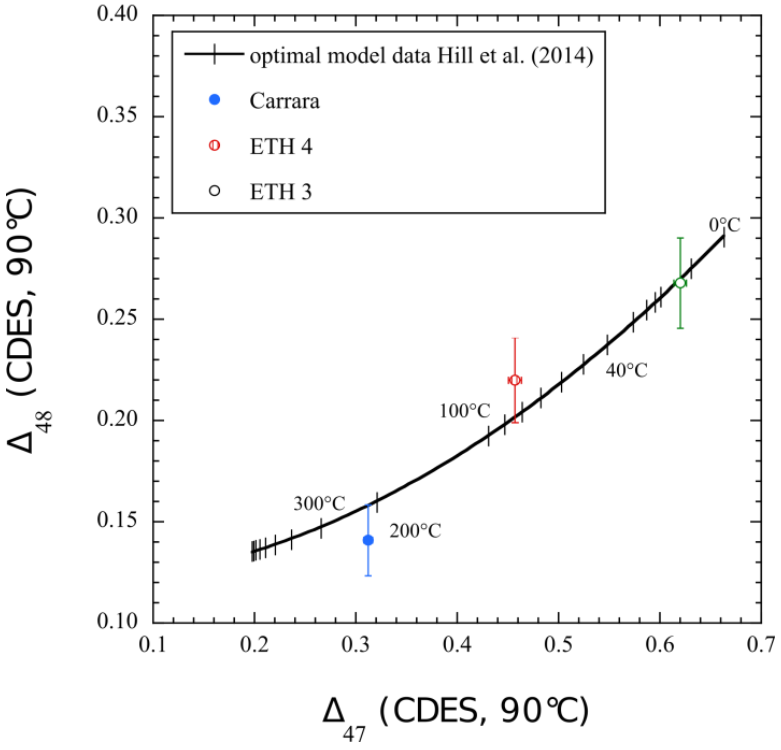

Figure 4.4: Plot of $\Delta_{48,\ CDES\ 90°C}$ *vs.* $\Delta_{47,\ CDES\ 90°C}$ for ETH 3, ETH 4 and Carrara. Within errors (2 SE, 95 % confidence level), all data points agree with the theoretical equilibrium curve after adding the experimentally determined phosphoric acid fractionation factors of 0.136 ‰ and 0.196 ‰, respectively, to the theoretical Δ_{64} and Δ_{63} values for calcite (Hill *et al.*, 2014).

Figure 4.4 provides a comparison of theoretical equilibrium with measured values in $\Delta_{47,\ CDES\ 90°C}$ *vs.* $\Delta_{48,\ CDES\ 90°C}$ space. Generally, measured $\Delta_{48,\ CDES\ 90°C}$ for ETH 3, ETH 4 and Carrara confirm measured $\Delta_{47,\ CDES\ 90°C}$ values in that $\Delta_{48,\ CDES\ 90°C}$ increases with $\Delta_{47,\ CDES\ 90°C}$. This is expected if both $\Delta_{48,\ CDES\ 90°C}$ and $\Delta_{47,\ CDES\ 90°C}$ are primarily controlled by temperature. Moreover, within errors (2 se, 95 % confidence level), measured $\Delta_{47,\ CDES\ 90°C}$ and $\Delta_{48,\ CDES\ 90°C}$ values agree with theoretical equilibrium implying that internal isotopic equilibrium may have been attained in all investigated carbonates. We would not expect such a systematic correlation

between $\Delta_{47, \text{CDES 90°C}}$ and $\Delta_{48, \text{CDES 90°C}}$ for these three carbonates if isobaric interferences on *m/z* 47 and *m/z* 48 were of importance.

Should equilibrium really have been attained in ETH 3, ETH 4 and Carrara, it would have been established at temperatures of 15 (± 2) °C, 86 (± 4) °C, and 210 (± 7) °C, respectively, as reflected from measured $\Delta_{47, \text{CDES 90°C}}$ values (*figure 4.4*). However, considering the error in $\Delta_{48, \text{CDES 90°C}}$, we alternatively cannot rule out that the true $\Delta_{47, \text{CDES 90°C}}$ and $\Delta_{48, \text{CDES 90°C}}$ compositions of Carrara and ETH 4 plot slightly below or above the equilibrium line, respectively (*figure 4*). Generally, departures from equilibrium would be introduced by rate-limiting kinetic effects. It has recently been shown that the most prominent rate-limiting processes involved in carbonate precipitation, CO_2 absorption and CO_2 degassing, follow specific trajectories in $\Delta_{47, \text{CDES 90°C}}$ *vs.* $\Delta_{48, \text{CDES 90°C}}$ space (Guo & Zhou, 2019b). Hence, even if kinetics were of any importance during carbonate mineralization, it should be possible to determine accurate formation temperatures, along with the rate-limiting step governing isotopic exchange, solely based on the position of measured data in $\Delta_{47, \text{CDES 90°C}}$ *vs.* $\Delta_{48, \text{CDES 90°C}}$ space (Guo & Zhou, 2019b).

4.6 Conclusions

We describe an analytical setup that allows accurate and precise determination of Δ_{48} along with Δ_{47} in CO_2 evolved from phosphoric acid digestion of carbonates. External reproducibilities for Δ_{48} and Δ_{47} analyses occur close to the corresponding shot-noise limits. There is no indication that the chosen setup introduces any significant artificial biases in the measured abundances of mass 47 and mass 48 CO_2 isotopologues.

4.7 Acknowledgments

We would like to thank Stefano Bernasconi for reviewing this paper. This work became possible through DFG grant INST 161/871-1.

4.8 Author contribution

J.F. designed the study. S.H. programmed the software and improved the hardware of the analytical setup. A.M. supported the infrastructure of the laboratory. N.L., D.B., K.M. and E.K. performed the clumped isotope analysis. All authors discussed the results, read the manuscript, contributed to writing the manuscript guided by J.F., and agreed to the submission.

5 Southern European Middle Miocene Temperature Dynamics

Niklas Löffler[1,2*], Andreas Mulch[1,2], Wout Krijgsman[3], Iuliana Vasiliev[1], Emilija Krsnik[1,2], Katharina Methner[a, #], and Jens Fiebig[1,2]

[1] Senckenberg Biodiversity and Climate Research Centre, Senckenberganlage 25, 60325 Frankfurt (Main), Germany

[2] Institute of Geosciences, Goethe University, Altenhoeferallee 1, 60438 Frankfurt (Main), Germany

[3] Paleomagnetic Laboratory "Fort Hoofddijk", Utrecht University, Budapestlaan 17, 3584 CD Utrecht, The Netherlands

[#]present address: Geological and Environmental Sciences. Stanford University, 450 Serra Mall, Stanford, CA 94305 U.S.A.

**Correspondence: niklas.loeffler@senckenberg.de*

Submitted to Nature Geoscience (NGS-2020-08-01948)

Received 16 August 2020

5.0 Introductory paragraph

Between 14.5 and 12.9 Ma, Earth's warm climate with a low latitudinal temperature gradient changed during the Middle Miocene Climatic Transition (MMCT) to a colder phase with accelerated Antarctic ice sheet formation. Terrestrial temperature records, however, still lack the necessary resolution to constrain the magnitude and rate of continental climate change during this transition. Here we present a well-dated terrestrial clumped isotope (Δ_{47}) paleosoil carbonate record from Southern Europe (Spain) that covers the time interval from 15.33 to 12.98 Ma and hence includes the end of the Middle Miocene Climatic optimum (MCO) and the complete MMCT. Δ_{47}-based soil temperatures (T(Δ_{47})) reveal a prominent temperature decline centered at 13.94 Ma and define continental cooling in Southern Europe by *ca.* 12 °C. Our data document that the MMCT was highly dynamic and that the transition into the post-MCO world was characterized by ample fluctuations in temperature that contrast relatively stable warm conditions during extended parts of the MCO.

Keywords: Middle Miocene, climatic transition, clumped isotopes, temperature, Southern Europe, Spain

5.1 Introduction

Global warming during the Middle Miocene Climatic Optimum (MCO; *ca.* 16.9 to 14.7 Ma; Mudelsee *et al.*, 2014; Holbourn *et al.*, 2015) represents an important transition in Earth's climate system with a protracted interruption of long-term Cenozoic cooling. Modeling studies point to global mean annual temperatures (MAT) 3 ± 1 °C higher than today (You *et al.*, 2009; Goldner *et al.*, 2014) and hence approximate the temperature limits that currently guide future climate projections (Bates *et al.*, 2008; Maclean, 2020). Compared to the present day, the MCO was characterized by a weak latitudinal temperature gradient in the Northern Hemisphere (Bruch *et al.*, 2007; You *et al.*, 2009), drastically reduced extension of ice sheets St. John, 2008 and considerably warmer sea surface temperatures (SST) at mid and high latitudes (Holbourn *et al.*, 2014, 2015; Super *et al.*, 2018, 2020). Despite an overall global warm period, available Middle Miocene climate records (Holbourn *et al.*, 2014; Super *et al.*, 2018) point to increasingly variably temperature conditions as apparent from $\delta^{18}O$ excursions (*e.g.* Mi2 & Mi3; Abels *et al.*, 2005) and the Middle Miocene Climate Transition (MMCT; Flower & Kennett, 1994) – that is directly related to oceanic cooling (Shevenell *et al.*, 2004; Super *et al.*, 2020). Whereas the dynamics of Middle Miocene ocean temperatures (Super *et al.*, 2018, 2020; Sosdian *et al.*, 2018), ocean chemistry Pearson & Palmer, 1999, varying pCO_2 (Pagani *et al.*, 1999; Sosdian *et al.*, 2018), and faunal assemblages (van der Meulen & Daams, 1992; Böhme, 2003) have been studied with high temporal resolution, continental temperature records during the MCO and MMCT (Mosbrugger *et al.*, 2005; Domingo *et al.*, 2009; Methner *et al.*, 2020) are currently still elusive. This particularly applies to the precise magnitude and rate of continental temperature change at the end of the MCO and during the subsequent MMCT (*ca.* 14.2 to 13.8 Ma; Mudelsee *et al.*, 2014; Shevenell *et al.*, 2004). For southern Europe, previous studies report valuable estimates of mean annual temperatures (Hernández Fernández *et al.*, 2006), precipitation (Böhme *et al.*, 2011), and faunal adaptation (van der Meulen *et al.*, 2005). A mean annual temperature decline during the MMCT has previously been estimated to be approximately 5 to 10 °C (Böhme, 2003; Domingo *et al.*, 2009); a magnitude that is comparable to Pleistocene glacial-interglacial oscillations (Fauquette *et al.*, 1998) and is supported by oxygen isotope ($\delta^{18}O$) analyses of tooth enamel and pedogenic carbonates (Hernández Fernández *et al.*, 2006). Understanding the dynamics of temperature change is a prerequisite to evaluate and forecast the natural dynamics of the Mediterranean climate system, in an area vulnerable to projected future climate change with large

associated natural and socioeconomic hazards (Piñol *et al.*, 1998; Pérez Pérez & Barreiro-Hurlé, 2009).

Here we present a precisely dated terrestrial pedogenic carbonate clumped isotope (Δ_{47}) temperature ($T(\Delta_{47})$) record of the MCO and MMCT from the Calatayud-Daroca Basin (CDB; Spain) that relates continental environmental change, marine carbon ($\delta^{13}C$) and oxygen ($\delta^{18}O$) isotope records (Holbourn *et al.*, 2007), the radiation and turnover of species (Janis *et al.*, 2002; van Dam *et al.*, 2006), and prominent changes in faunal assemblages (Böhme, 2003; van der Meulen *et al.*, 2005). Collectively, our Δ_{47}, $\delta^{13}C$, and $\delta^{18}O$ data show that the continental climate during the southern European MMCT was strongly in line with ocean $\delta^{18}O$ and $\delta^{13}C$ dynamics and was characterized by large-magnitude cooling and warming intervals.

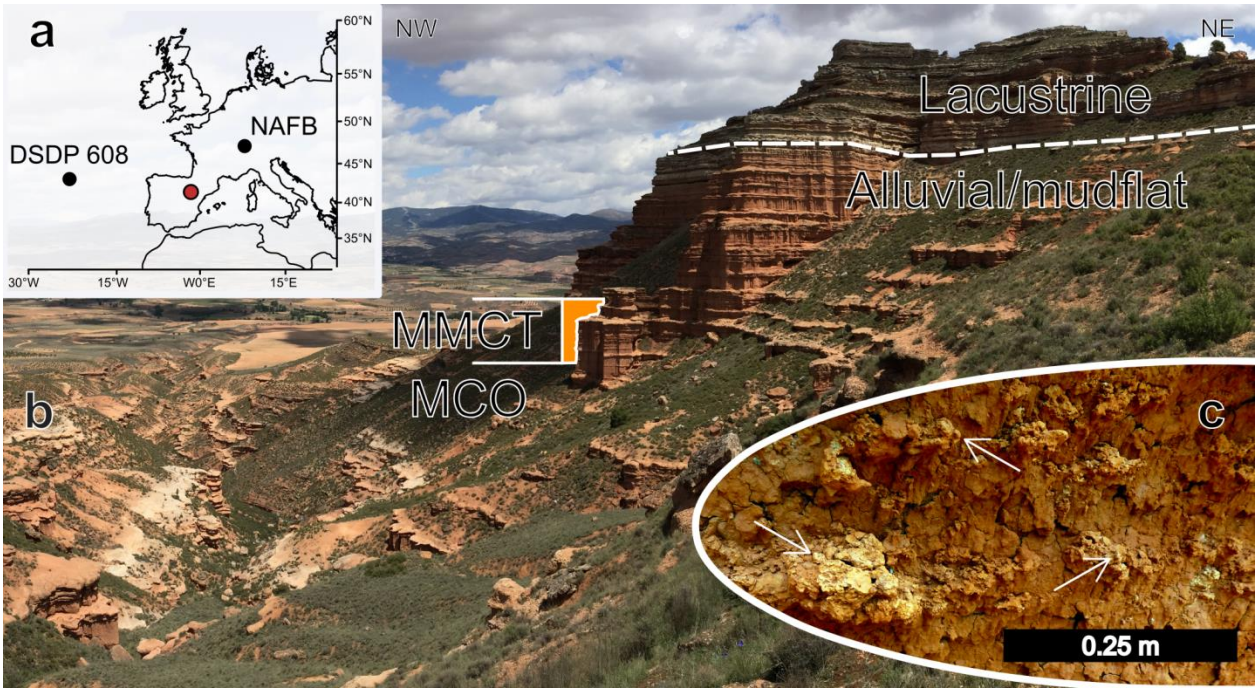

Figure 5.1: a) Map indicating the location of Calatayud-Daroca Basin (CDB; red dot), DSDP 608, and Northern Alpine Foreland Basin (NAFB) records. **b)** Armantes section (CDB, Spain) that has been sampled for stable and clumped isotope analyses. At the top, deposition transitions rapidly from alluvial/mudflat sediments, with a rhythmic alternation of reddish soil horizons and greyish caliche, to grey and more resistant lacustrine carbonates (dashed line). The position of the MMCT based on the Δ_{47} record is highlighted in orange ('MMCT'). **c)** Detail of nodular carbonate formation within a reddish paleosoil.

5.2 Geology

The Middle Miocene Armantes section Bruijn, 1965 (CDB, Northern Spain; *figure 5.1*) represents a *ca.* 280 m-thick continental section with numerous well-preserved paleosoil horizons that have been dated using high-resolution magnetostratigraphy (Krijgsman *et al.*, 1994, 1997). Paleobiological studies on the Spanish/Aragonian faunal assemblages suggest a warm climate that progressively cooled from 15 to 13 Ma (van der Meulen & Daams, 1992) and local variation in humidity connected to fundamental shifts of the climatic belts (Wolfe, 1985; van der Meulen & Daams, 1992; Luis & Hernando, 2000). Palynological data indicate arid, subtropical conditions during the Langhian to Serravallian (15.97 to 13.65 Ma; Jiménez-Moreno & Suc, 2007). Pronounced marine deposition of aeolian dust off the NW coast of Africa (Sarnthein *et al.*, 1982) completes the image of intense continental aridity on the Middle Miocene Iberian Peninsula.

The Armantes section in the NW-SE-oriented extensional CDB contains proximal to distal alluvial fan-floodplain and shallow palustrine/lacustrine sediments deposited as part of an alluvial fan system [34] under seasonally arid conditions (Jiménez-Moreno & Suc, 2007; Cuevas González, 2005). Here we focus on the basal 240 m that are characterized by red carbonate-rich silts and sands with a rhythmic alternation of red clays that contain numerous pedogenic carbonate nodules and pinkish-white caliche layers (Krijgsman *et al.*, 1994). Most of the section lacks distinct fine-scale sedimentary structures, likely due to the strong pedogenic overprint, documented by *i)* intense reddish-yellow to greyish-yellow mottling, *ii)* numerous carbonate soil nodules that may aggregate to caliche-like horizons, and *iii)* calcified root casts. Individual layers of sand and conglomerate indicate the presence of a gentle paleorelief, governing the (alluvial) sediment transport.

5.3 The Middle Climatic Optimum and the Middle Miocene Climatic Transition

Δ_{47} thermometry on pedogenic carbonate has been documented to reliably record soil temperatures (Passey *et al.*, 2010; Tobin *et al.*, 2014; Page *et al.*, 2019; Methner *et al.*, 2020) as well as $\delta^{18}O$ of soil water and ultimately precipitation (Suarez *et al.*, 2011; Hudson *et al.*, 2017; Methner *et al.*, 2020). Recently refined ages date the onset of the MCO at 16.9 to 16.8 Ma Holbourn *et al.*, 2015. The MCO is terminated by the onset of the MMCT at 14.2 to 13.8 Ma Shevenell *et al.*, 2004 and the onset and end of the MMCT vary with latitude (Mudelsee *et al.*, 2014). We refer to the reported MCO and MMCT durations of DSDP site 608 (Mudelsee *et al.*,

2014) (North Atlantic Ocean) as the most proximate DSDP/IODP site to the Armantes section (*table 5.1*).

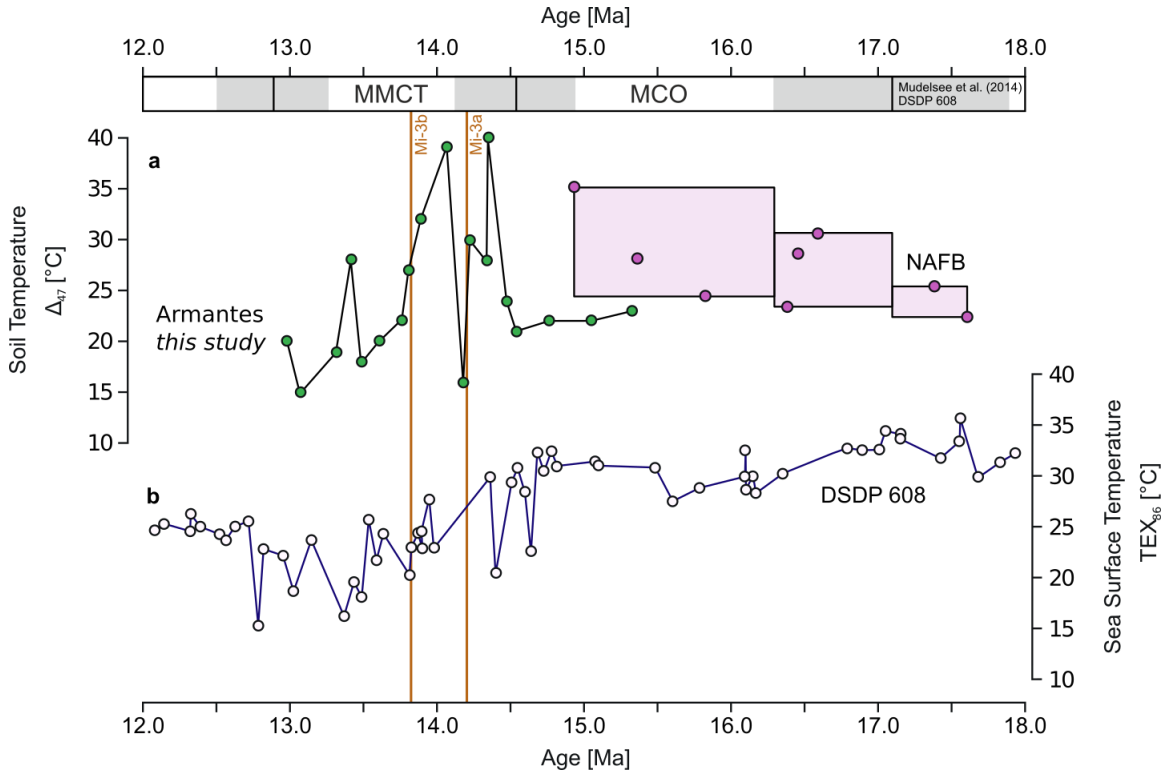

Figure 5.2: Comparison of **a)** the terrestrial soil temperatures of this study (green dots, solid line, Armantes, Spain) and the MCO (Methner *et al.*, 2020; purple boxes and dots, North Alpine Foreland Basin (NAFB)/Fontannen section, Switzerland), and **b)** North Atlantic SSTs (white dots, DSDP Site 608; Super *et al.*, 2020) for the MCO and MMCT interval. The duration of the MCO and MMCT of DSDP 608 (Mudelsee *et al.*, 2014) are indicated at top of the figure. The Mi3a and Mi3b events (Abels *et al.*, 2005) are marked with vertical lines.

During the end of the MCO at 14.53 Ma (Mudelsee *et al.*, 2014), Δ_{47} soil temperatures range from 21 to 23 °C, with an average of 22 ± 1 °C (15.33 to 14.54 Ma; *figure 5.2a*). At the beginning of the MMCT, Δ_{47} soil temperatures increase by 3 °C from 21 ± 2 °C (at 14.54 Ma) to 24 ± 4 °C (at 14.48 Ma) and subsequently rise to temperatures of 40 ± 3 °C (at 14.35 Ma) before rapidly cooling to 16 ± 3 °C (at 14.18 Ma) at the Mi3a event (Abels *et al.*, 2005). Mi3a cooling is followed by a second high temperature peak of 36 ± 5 °C (at 14.07 Ma) and progressive cooling to 20 ± 3 °C (at 13.61 Ma) over the Mi3b event at 13.82 ± 0.03 Ma (Abels *et al.*, 2005). Subsequently, Δ_{47} soil temperatures remain at 15 to 19 °C until 12.98 Ma with a distinct high temperature peak of 28 ± 5 °C at 13.42 Ma.

Table 5.1: Overview on the results of the Δ_{47} analyses of the Armantes paleosoil carbonate nodules including the respective ages, measured $\delta^{13}C$ and $\delta^{18}O$ of the carbonate, calculated $\delta^{18}O_{H2O}$ of the soilwater (Coplen, 2007), number of replicate analyses (n), start and end point of the MMCT as determined for DSDP 608 (Mudelsee *et al.*, 2014), and ages of the Mi3a and Mi3b events (Abels *et al.*, 2005).

						Soil water
Identifier	Age ±error [Ma]	T (Δ_{47}) ± se [°C]	$\delta^{13}C$ ± sd [‰]	$\delta^{18}O$ ± sd [‰]	n	$\delta^{18}O_{H2O}$ ± error[‰]
MMCT DSDP 608 end	*12.88 ± 0.38*					
2017-AM-011	12.98 ± 0.02	20 ± 1	-8.03 ± 0.02	23.34 ± 0.06	5	-7.64 ± 0.26
2017-AM-013	13.08 ± 0.02	15 ± 3	-7.71 ± 0.04	23.87 ± 0.09	6	-8.15 ± 0.71
2017-AM-016	13.32 ± 0.03	19 ± 3	-6.90 ± 0.08	23.80 ± 0.01	6	-7.40 ± 0.62
2017-AM-018	13.42 ± 0.03	28 ± 5	-7.27 ± 0.02	22.83 ± 0.05	6	-6.57 ± 1.00
2017-AM-019	13.49 ± 0.02	18 ± 3	-7.15 ± 0.02	23.54 ± 0.04	5	-7.85 ± 0.65
2017-AM-020	13.61 ± 0.02	20 ± 3	-6.61 ± 0.03	23.95 ± 0.21	6	-7.05 ± 0.79
2017-AM-022	13.76 ± 0.02	22 ± 2	-6.92 ± 0.02	23.34 ± 0.05	5	-7.24 ± 0.44
2018-AM-114	13.81 ± 0.02	27 ± 2	-6.88 ± 0.05	23.35 ± 0.06	5	-6.26 ± 0.25
Mi3b	*13.82 ± 0.03*					
2018-AM-110	13.89 ± 0.02	32 ± 2	-7.44 ± 0.03	23.33 ± 0.06	5	-5.34 ± 0.43
2017-AM-024	14.07 ± 0.01	36 ± 5	-6.47 ± 0.14	23.89 ± 0.08	7	-4.05 ± 0.98
2018-AM-092a	14.18 ± 0.01	16 ± 3	-7.06 ± 0.05	23.21 ± 0.05	6	-8.58 ± 0.67
Mi3a	*14.2*					
2017-AM-025	14.23 ± 0.01	30 ± 4	-6.43 ± 0.08	23.70 ± 0.04	6	-5.35 ± 0.79
2018-AM-075a	14.34 ± 0.02	28 ± 2	-6.67 ± 0.02	23.68 ± 0.08	5	-5.75 ± 0.65
2017-AM-026	14.35 ± 0.02	40 ± 3	-6.08 ± 0.02	23.82 ± 0.05	5	-3.41 ± 0.58
2017-AM-028	14.48 ± 0.02	24 ± 3	-7.22 ± 0.02	23.17 ± 0.08	6	-7.02 ± 0.86
MMCT DSDP 608 start	*14.53 ± 0.41*					
2017-AM-029	14.54 ± 0.02	21 ± 2	-7.02 ± 0.01	23.46 ± 0.07	5	-7.33 ± 0.47
2018-AM-065a	14.76 ± 0.02	22 ± 3	-6.34 ± 0.04	23.67 ± 0.05	5	-6.92 ± 0.45
2018-AM-057	15.06 ± 0.02	22 ± 2	-6.22 ± 0.02	23.82 ± 0.22	5	-6.78 ± 0.61
2018-AM-037II	15.33 ± 0.02	23 ± 1	-6.46 ± 0.00	23.41 ± 0.04	4	-6.98 ± 0.24

Figure 5.3 (next page): Comparison of data from this study and climate proxy data of previously published climate studies. **a)** Measured soil temperatures of Armantes section/Mediterranean (green dots, solid line, this study). **b)** $\delta^{13}C_{terrestrial}$ data of this study (white dots, caliche) superimposed on the $\delta^{13}C_{bentic}$ (blue) data (Holbourn *et al.*, 2014). **c)** $\delta^{18}O_{benthic}$ (orange) (Holbourn *et al.*, 2014). **d)** $\delta^{18}O_{C.\ mundulus}$, interpreted as an ice volume proxy (Shevenell *et al.*, 2004), (grey). **e)** Southern Ocean SST (Sosdian *et al.*, 2020) (orange). The position of the MMCT and MCO of DSDP 608 (Mudelsee *et al.*, 2014) is indicated in the top box including their uncertainty in age (grey). The position of Mi3a and Mi3b (Abels *et al.*, 2005) are indicated with vertical brown lines. Dominant rhythms of the wavelet periods of the $\delta^{13}C$ from the Pacific (Holbourn *et al.*, 2014) (top), indicate defining changes in orbital frequencies before and after the variability of the terrestrial temperatures increases. A late spike in terrestrial temperatures at *ca.* 13.4 Ma **(a)** is highlighted with a dashed line.

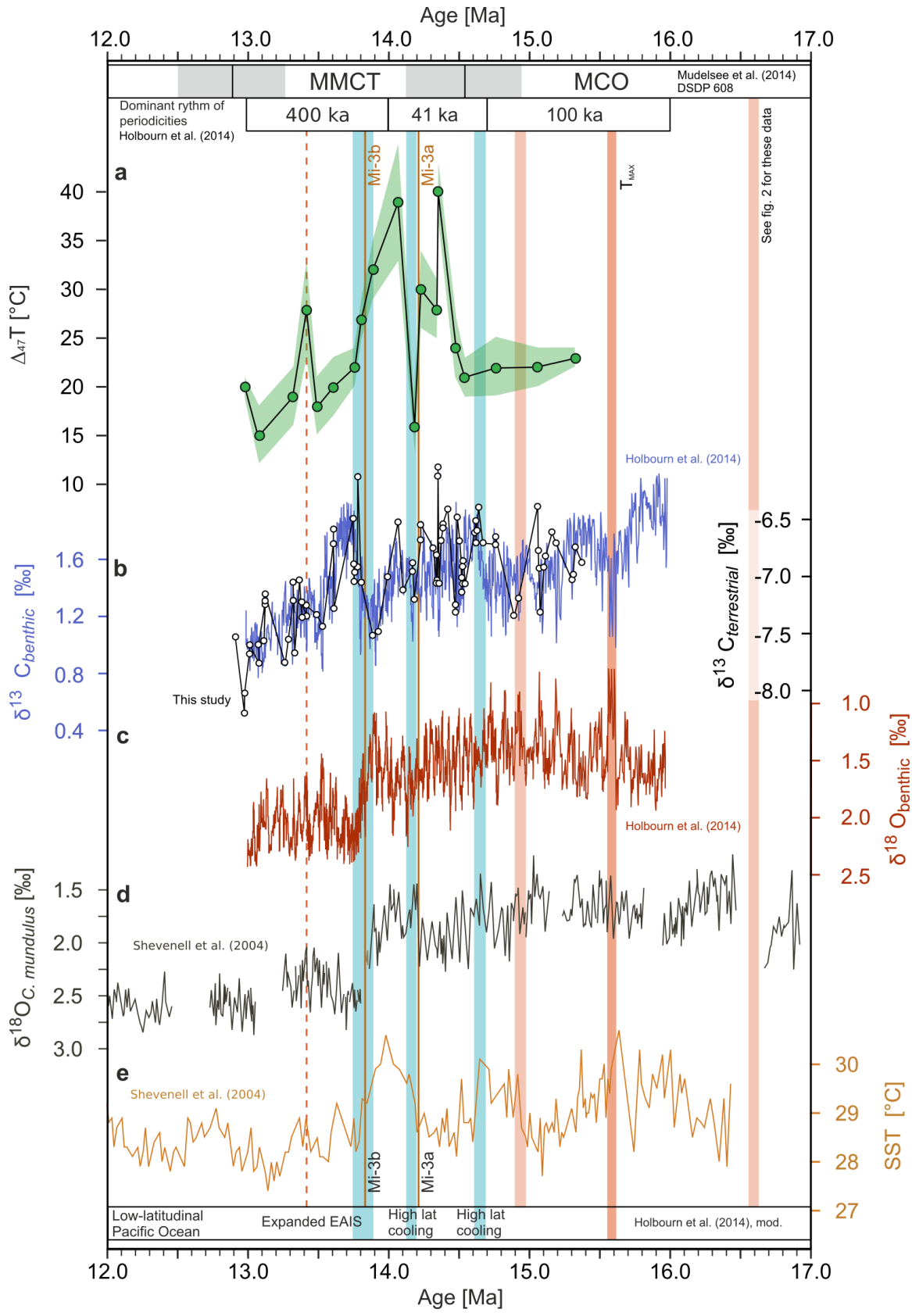
Age [Ma]
12.0
13.0
14.0
15.0
16.0
17.0
MMCT
MCO
Mudelsee et al. (2014)
DSDP 608
Dominant rythm of periodicities Holbourn et al. (2014)
400 ka
41 ka
100 ka
Mi-3b
Mi-3a
T_MAX
See fig. 2 for these data
a
Δ47T [°C]
40
35
30
25
20
15
10
Holbourn et al. (2014)
b
δ13 Cbenthic [‰]
1.6
1.2
0.8
0.4
This study
δ13 Cterrestrial [‰]
-6.5
-7.0
-7.5
-8.0
c
1.0
1.5
2.0
2.5
δ18 Obenthic [‰]
Holbourn et al. (2014)
d
δ18OC. mundulus [‰]
1.5
2.0
2.5
3.0
Shevenell et al. (2004)
e
Shevenell et al. (2004)
30
29
28
27
SST [°C]
Low-latitudinal Pacific Ocean
Expanded EAIS
High lat cooling
High lat cooling
Holbourn et al. (2014), mod.
Age [Ma]

Even though the Δ_{47} soil temperatures show a large temperature variability, the caliche $\delta^{18}O$ and $\delta^{13}C$ values exhibit an overall small absolute spread over the entire record of only 3 ‰ and 2 ‰, respectively (supplementary data *S. 5.VI.*). Pedogenic carbonate $\delta^{13}C$ values include an interval of high variability at the beginning of the MMCT (14.7 to 14.3 Ma) that starts with comparably high $\delta^{13}C$ values and includes a prolonged positive $\delta^{13}C$ excursion between 13.6 and 13.9 Ma (*figure 5.3b*). The end of the MMCT is characterized by declining $\delta^{13}C$ values (12.9 to 13.5 Ma). Both, overall trend and internal variability, show high similarity to the marine $\delta^{13}C$ record Holbourn *et al.*; *figure 5.3b*). Due to the low overall variation of carbonate $\delta^{18}O$ values, we consider that the soil water $\delta^{18}O$ values ($\delta^{18}O_{H2O}$) are primarily modulated by temperature. $\delta^{18}O_{H2O}$ values calculated from the Armantes Δ_{47} and $\delta^{18}O$ values of carbonate nodules range from -3.4 ± 0.6 $‰_{VMSOW}$ to -8.2 ± 0.7 $‰_{VMSOW}$ (*table 5.1*).

The large soil temperature variability prior to the prominent temperature decline between 14.07 and 13.76 Ma (*ca.* Mi3b; *table 5.1*, *figure 5.3a*), the positive $\delta^{13}C$ excursion at the end of the MMCT (*figure 5.3*), and the range of the reconstructed soil water $\delta^{18}O_{H2O}$ values (*table 5.1, figure 5.4*) point to the importance of recurring changes in environmental conditions (*e.g.* aridity and pCO_2). This underlines that the MMCT was not a continuous cooling event but rather an interval of severe climatic disturbance characterized by alternating warm and cold pulses and shifts in seasonality 2020. This hypothesis is supported by the marine record of DSDP 608 (*figure 5.2b*) which shows high MCO temperatures that are rather invariant when compared to the overall declining MMCT temperature swings (Super *et al.*, 2020). As suggested for the Mi3a event, altered circulation patterns in the Mediterranean – possibly induced by an increased meridional temperature gradient – could be a driver for climatic changes (Flower & Kennett, 1994) with the potential of recurrently altering seasonality and/or soil temperatures on the Iberian Peninsula.

5.4 Paleontological implications compared to local climate proxy data

Between 14.3 and 13.3 Ma, Miocene rodent communities from the CDB transition from open country dwellers to rodents associated with open woodlands and permanent water bodies (van der Meulen *et al.*, 2005). Based on the habitat preferences of the rodent taxa, CDB paleofloral reconstructions include shrubs, trees, and occasionally forest during the middle Aragonian (MN5), whereas the abundance of rodent taxa associated with trees increased towards the Late Aragonian (>14.1 Ma) although, rodents related to open habitats remain dominant (van der Meulen *et al.*, 2005). Major short-term (<Ma) climate variations between 16.0 and 14.8 Ma

(Flower & Kennett, 1994) are in agreement with variable MMCT soil temperatures presented here. During the prominent terrestrial cooling centered at 13.9 Ma (*figure 5.3*; *ca.* Mi3b), Central Spain mammal turnover rates noticeably increase and subsequently transit to lower rates (van Dam *et al.*, 2006) as cooler soil temperatures establish at 13.6 Ma.

The last occurrence of the thermophilic Chamaeleonidae (also inhabiting the Iberian Peninsula) at ca. 13.7 Ma in the Swiss Molasse Basin (Böhme, 2003) is in agreement with the prominent soil temperature decline centered at 13.9 Ma. After the MMCT, the thermophilic crocodile *Dyplocynodon* still persists on the Iberian Peninsula until 9.1 to 11.1 Ma (Antunes, 1994) consistent with cooling towards the end of the MMCT as crocodiles are tolerant to lower winter temperatures when compared to Chamaelonidae (Haller-Probst, 1997). Collectively, the disappearance of the Chamaeleonidae and the persistence of *Dyplocynodon* across the MMCT suggest that MAT could have decreased by up to 13 °C. This amplitude is in line with rapid temperature decline from 27 to 16 °C across the late MN5 (*ca.* 14 to 13.8 Ma) estimated from $\delta^{18}O_{PO4}$ (Hernández Fernández *et al.*, 2006).

Assuming that our Middle Miocene soil temperature Δ_{47} record reflects both temperature change and changes in carbonate formation seasonality (Methner *et al.*, 2020), a transition from relatively wet to increasingly dry summer conditions would be a possible mechanism for shifting soil carbonate formation towards the (dry) warm season and *vice versa*, consequently amplifying or dampening the amplitude of soil temperature variations over time. Mean annual precipitation (MAP) values from the paleontological record range from 130 mm to 880 mm (13.8 to 13.4 Ma; Böhme *et al.*; the strongest MAP decline and highest MAP correlate with the prominent cooling (centered at 13.9 Ma) and the late warm peak (at 13.4 Ma) detected here. Soil water $\delta^{18}O_{H2O}$ values derived from pedogenic carbonate (calculated from $\delta^{18}O_{CO3}$ and $T(\Delta_{47})$) are compared to both, $\delta^{18}O_{H2O}$ values derived from *Gomphotherium angustidens* teeth $\delta^{18}O_{PO4}$ (MN5, 14.1 to 13.7 Ma Domingo *et al.*, 2009; Proboscideans Ayliffe *et al.*, 1992; T = 37 °C), and modern $\delta^{18}O_{H2O}$ of local precipitation (Rodríguez-Arévalo *et al.*, 2011; *figure 5.4*). *G. angustidens* teeth give an average $\delta^{18}O_{H2O}$ of -7.1 ± 1.5 ‰ (range: -4.1 to -10.1 ‰) that agrees with the reconstructed soil water $\delta^{18}O_{H2O}$ of the Armantes soil carbonate of -6.6 ± 1.4 ‰ and is slightly below the modern local precipitation $\delta^{18}O_{H2O}$ of -6.3 ± 3.2 ‰ (with a seasonal DJF-JJA variation of 5.3 ‰). Individual samples of this study with particularly high or low $\delta^{18}O_{H2O}$ may reflect carbonate formation that has been shifted towards mean warmest or coldest month temperatures, respectively. In contrary, constant (or close to average ± sd) $\delta^{18}O_{H2O}$ values would indicate a soil

carbonate formation during comparable seasons. Consequently, changes in the seasonality of carbonate formation at the Armantes section are most likely to have occurred at 14.35 Ma, 14.18 (Mi3a), 14.07 Ma, and 13.08 Ma (*table 5.1, figure 5.4*).

5.5 Varying continental temperatures in pace with oceanic records

The Armantes soil temperatures extend Δ_{47}-based paleotemperature reconstructions for Central Europe (Methner *et al.*, 2020). Despite lower temporal coverage of the MMCT, Central European temperatures fall in a comparable range (13 ± 1 °C to 30 ± 3 °C) as the Southern European/Armantes soil temperatures (*figure 5.2a*) underlining the strong climate dynamics of the MMCT. Using marine events Mi3a and Mi3b, the Δ_{47} soil temperatures of Armantes can be structured in three intervals with distinct long *vs.* short term temperature changes: *i)* the end of the MCO, *ii)* the beginning of the MMCT until Mi3b (as defined in DSDP 608), and *iii)* the Mi3b until the end of the MMCT (as defined in DSDP 608). These intervals are characterized by *i)* constant warm temperatures of 21 ± 1 °C (15.33 to 14.54 Ma), *ii)* hot to cold swings and changes in seasonality contributing collectively to soil carbonate formation temperatures averaging 29 ± 8°C (at 14.07 and 14.35 Ma), and *iii)* overall declining temperatures finally reaching 20 ± 1 °C. The last interval (*iii*) further includes a warm temperature spike at 13.42 Ma also known from the Southern Ocean (Shevenell *et al.*, 2004). Focusing on the MMCT exclusively, an overall cooling trend across the MMCT from 30 °C at 14.53 Ma to 19 °C at 12.88 Ma can be derived from an (error considering) linear regression (R Core Team, 2013). The most obvious T(Δ_{47}) decline occurs between 14.1 Ma to 13.5 Ma during which the recorded soil temperatures decrease by 21 °C.

Interestingly, our terrestrial paleosoil record and the marine SST, $\delta^{13}C$, and $\delta^{18}O$ values (Shevenell *et al.*, 2004; Holbourn *et al.*, 2014; Super *et al.*, 2020 show similar trends and events (*e.g. figures 5.2, 5.3a, e*). The timing of the prominent terrestrial temperature decline that is centered at 13.9 Ma (*figure 5.3a*; *ca.* Mi3b) matches well to both marine $\delta^{18}O$ data (Shevenell *et al.*, 2004; Holbourn *et al.*, 2014; *figures 3a, c, d*) and Middle Miocene SSTs that cover a range of 13 to 32 °C at different latitudes (Shevenell *et al.*, 2004; Super *et al.*, 2018; 2020; Sosdian *et al.*, 2020). The ice volume proxy that is based on the positive correlation of the $\delta^{18}O$ of *Cibicidoides mundulus* with global ice volume (Shevenell *et al.*, 2004; *e.g.* at 13.5 Ma; *figure 3d*) correlates to the terrestrial temperatures (*e.g.* Mi3a to the end of the MMCT). The mechanism behind this positive correlation could involve an increased moisture transport from hot to cool climate zones

during warm (and wet; Böhme *et al.*, 2011) intervals, facilitating the precipitation of snow and the accumulation of ice at high latitudes.

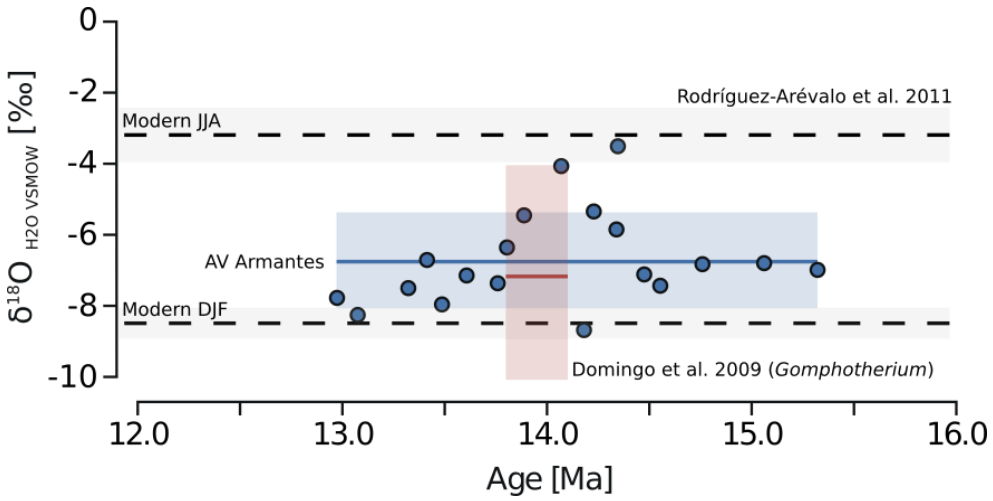

Figure 5.4: $\delta^{18}O_{H2O}$ soil water values reconstructed for the pedogenic carbonate nodules from Armantes (based on measured Δ_{47} and $\delta^{18}O_{CO3;}$ blue dots) with the average value indicated by a solid blue line (SD: blue shaded area). The values are compared to precipitation $\delta^{18}O_{H2O}$ values calculated from 20 Middle Miocene *Gomphotherium angustidens* teeth from Somosaguas (MN5, $\delta^{18}O_{PO4}$; Domingo *et al.*, 2009; Ayliffe *et al.*, 1992; AV: red solid line, range: red shaded area) and modern data of local GNIP stations for JJA and DJF(Rodríguez-Arévalo *et al.*, 2011) (AV: dashed black lines, sd: grey shaded area). Note that the range of modern and Middle Miocene $\delta^{18}O_{H2O}$ of 5 to 6 ‰ and the *Gomphotherium* $\delta^{18}O_{H2O}$ value (Domingo *et al.*, 2009) are in agreement with this study.

Based on frequency analysis of $\delta^{13}C$ data, dominant rhythms of periodicities are known from the global oceans Holbourn *et al.*, 2014. These rhythms change from 100 ka to 41 ka cycles during the onset of the MMCT at *ca.* 14.7 Ma and switch to 400 ka at *ca.* 14.0 Ma, which coincides with the onset of the prominent soil temperature decline at the Armantes section at *ca.* 14.1 Ma (*figure 5.3a, f*). The close match of equatorial Pacific (Holbourn *et al.*, 2014) and continental Southern European $\delta^{13}C$ values (*figure 5.3b*) points to a relay of $\delta^{13}C$ signals *via* atmospheric CO_2 suggesting that changes in paleo pCO_2 (Sosdian *et al.*, 2020) contributed to the high temperature variability that characterizes the MMCT.

5.6 Conclusions

The Δ_{47}-based soil temperatures from the Middle Miocene Armantes section in Southern Europe (Spain) reveal a substantial climatic change centered at 13.9 Ma which is in agreement with oceanic (Holbourn *et al.*, 2014; Super *et al.*, 2020) and paleontological data (Böhme, 2003;

Hernández Fernández *et al.*, 2006). MMCT soil temperatures from Southern Europe are in strong agreement with recently published MMCT soil temperatures from Central Europe (Methner *et al.*, 2020) indicating a contemporary climatic change. The internal thermal structure of the MMCT is characterized by short-termed (0.1 Ma) cooling pulses of several °C that coincide with the oceanic Mi3a and Mi3b events and increased mammal turnover rates in Central Spain (van Dam *et al.*, 2006). The variability of calculated soil water $\delta^{18}O_{H2O}$ thereby implies a varying seasonality of carbonate formation during the MMCT with an amplitude that is comparable to the range of $\delta^{18}O_{H2O}$ derived from modern precipitation (JJA-DJF; Rodríguez-Arévalo *et al.*, 2011) and Middle Miocene mammal $\delta^{18}O_{PO4}$ (Domingo *et al.*, 2009). The profound difference in the soil temperature variability during the MMCT when compared to the late MCO is synchronous with changing dominant orbital frequencies (Holbourn *et al.*, 2014) indicating an orbitally paced change of climate variability. Considering all MMCT soil temperatures of Armantes and unavoidable uncertainties in ages and temperature, the statistical long-term (1.5 Ma) cooling across the Mediterranean MMCT is 12 °C.5.7

5.7 Methods

Sampling for stable isotope geochemistry closely followed Krijgsman *et al.* (1997). 19 pedogenic carbonate nodules were collected for analyses of Δ_{47}, $\delta^{18}O$, and $\delta^{13}C$. 49 pedogenic caliche horizons where sampled for $\delta^{18}O$ and $\delta^{13}C$ exclusively. Δ_{47} analyses were done at the Joint Goethe University – Senckenberg BiK-F stable isotope facility (Frankfurt Main), Germany) between 01/06/2017 and 05/16/2019. Δ_{47} analyses, sample digestion and gas purification were performed by a fully automated gas extraction and purification line (Fiebig *et al.*, 2019). Measurements were conducted on Thermo Scientific™ MAT 253™ and MAT 253 Plus™ gas source mass spectrometers (IRMS). Methodological details are provided in the supplementary.

5.8 Acknowledgements

As part of LOEWE VeWa, clumped isotope work in the Joint Goethe University-Senckenberg BiK-F Stable isotope facility is supported through the LOEWE program (Landes-Offensive zur Entwicklung Wissenschaftlich ökonomischer Exzellenz) of the German State of Hesse Ministry of Higher Education, Research, and the Arts. We acknowledge funding through the Feodor-Lynen-Fellowship of the Alexander von Humboldt Foundation (K.M.).

5.9 Author contributions

N.L., A.M., W.K., and I.V. designed the study. N.L. conducted the analyses. A.M., W.K, I.V., E.K. participated at collecting and documenting the samples in the field. E.K., J.F. and K.M. supported the clumped isotope analyses. N.L., A.M., J.F., W.K., I.V., K.M., and E.K. discussed the results. All authors contributed to writing the manuscript guided by N.L. and agreed to the submission.

6 Complementary data to the Southern European Middle Miocene Temperature Dynamics

N. Löffler[a, b]*

In close cooperation with:

Andreas Mulch[a, b], Wout Krijgsman[c], Iuliana Vasiliev[a], Emilija Krsnik[a, b], Katharina Methner[a, #], and Jens Fiebig[a, b]

[a] *Senckenberg Biodiversity and Climate Research Centre, Senckenberganlage 25, 60325 Frankfurt (Main), Germany*

b Institute of Geosciences, Goethe University, Altenhoeferallee 1, 60438 Frankfurt (Main), Germany

[c] *Paleomagnetic Laboratory "Fort Hoofddijk", Utrecht University, Budapestlaan 17, 3584 CD Utrecht, The Netherlands*

[#]*present address: Geological and Environmental Sciences. Stanford University, 450 Serra Mall, Stanford, CA 94305 U.S.A.*

**Correspondence: niklas.loeffler@senckenberg.de*

Preliminary data of this study was presented 2019 at the following conferences and workshops:

AGU Fall meeting, San Francisco (U.S.A.)

7th International Clumped Isotope Workshop, Los Angeles (U.S.A.)

6.0 Abstract

The terrestrial sediments of the Middle Miocene Calatayud-Daroca Basin (Spain) yield invaluable insights into the climatic dynamics of the Middle Miocene Climatic Transition in Southern Europe. This study focuses on the Aragon section (14.64 to 13.36 Ma) which is situated 30 km southeast to the Armantes section where soil temperatures of the South European Middle Miocene have been previously reconstructed (*chapter 5*). This study refines the current continental dataset of the Middle Miocene Climatic Transition by additional stable oxygen, carbon, and clumped isotope analyses and illustrates the interconnection of the Middle Miocene Climatic Transition in Southern Europe with local faunal changes. Present-day regional climate information from the study area is provided for comparison.

Keywords: Middle Miocene, climatic transition, clumped isotopes, temperature, Southern Europe, Spain

6.1 Introduction

The South European continental Middle Miocene Climatic Transition (MMCT; *ca.* 14.53 to 12.88 Ma at DSDP 608; Mudelsee *et al.*, 2014) is characterized by highly dynamic changes in soil temperatures which transit to lower temperatures when compared to the Middle Miocene Climatic Optimum (MCO; *ca.* 16.9 to 14.7 Ma; *e.g.* Mudelsee *et al.*, 2014; Holbourn *et al.*, 2015, for details, see *e.g. chapter 5*). It has also been shown that the MMCT South and Central European soil temperatures (*chapter 5* and Methner *et al.*, 2020) agree with each other and the North Atlantic sea surface temperatures (SST) of DSDP 608 (Super *et al.*, 2020). For improving the understanding of local spatial variation in soil temperatures (*e.g.* induced by varying plant cover or microclimates) and to further increase the resolution of the Southern European soil temperature record, results from the Armantes section are complemented by data from the Aragon section, which is situated proximate (30 km SE) to the Armantes section (*figure 6.1*).

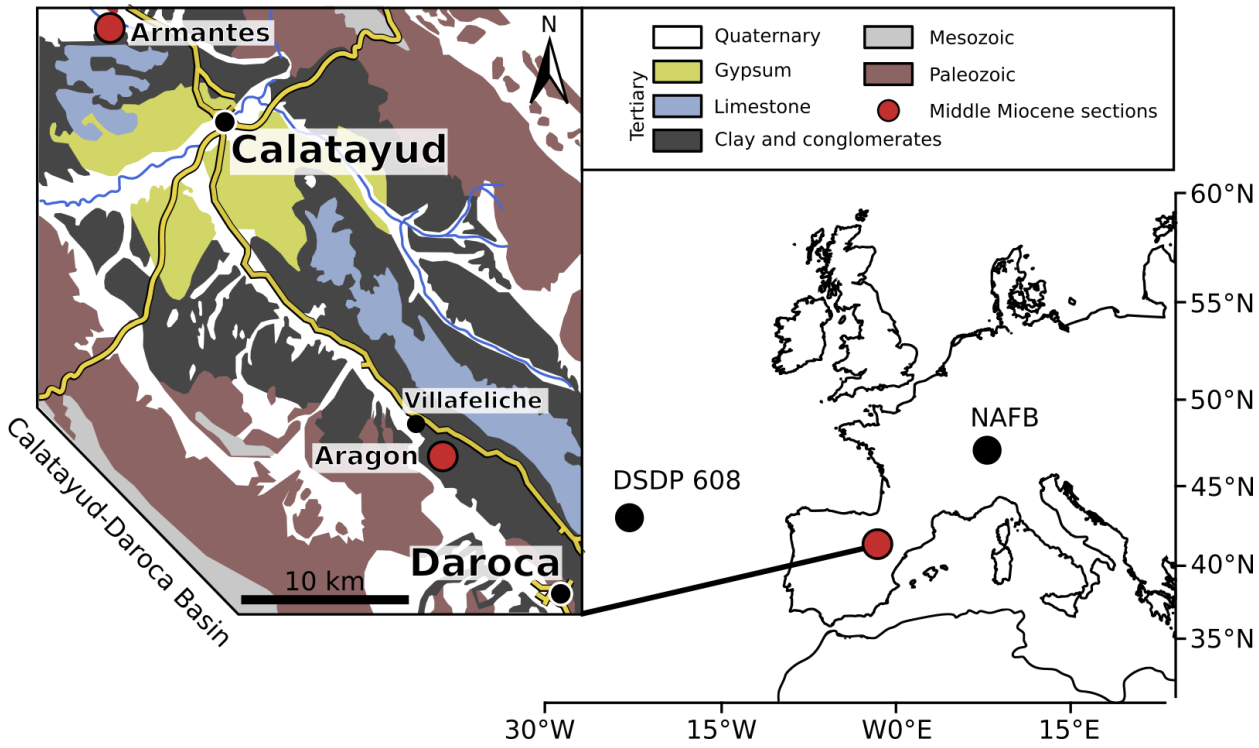

Figure. 6.1.: Map indicating the location of Calatayud-Daroca Basin (CDB; right; red dot), DSDP 608, and Northern Alpine Foreland Basin (NAFB) records. The positions of the Armantes and Aragon sections and the geology of the CDB are shown on the left.

Both sections are part of the Calatayud-Daroca Basin (CDB) (Bruijn, 1965) and consist of the same geology which includes well-preserved paleosoil horizons with a high abundance of

pedogenic carbonates (*chapter 5.2*). This study provides well dated terrestrial Δ_{47} temperatures ($T(\Delta_{47})$) that are measured on pedogenic carbonate nodules from Southern Europe (Spain) and extend the $T(\Delta_{47})$ record of *chapter 5* by 15 %. Reconstructed oxygen isotopic compositions of soil water ($\delta^{18}O_{H2O}$) are related to the paleontological record (van Dam *et al.*, 2006; Domingo *et al.*, 2009) to verify the relation of climate (temperature) change and faunal turnover rates. The age model of the 170 m thick Aragon section is derived from Krijgsman *et al.* (1994) – updated to the geological time scale (Gradstein, 2012) – which allows for combining the Aragon soil temperatures with the Armantes data of *chapter 5*.

6.2 Aragon section

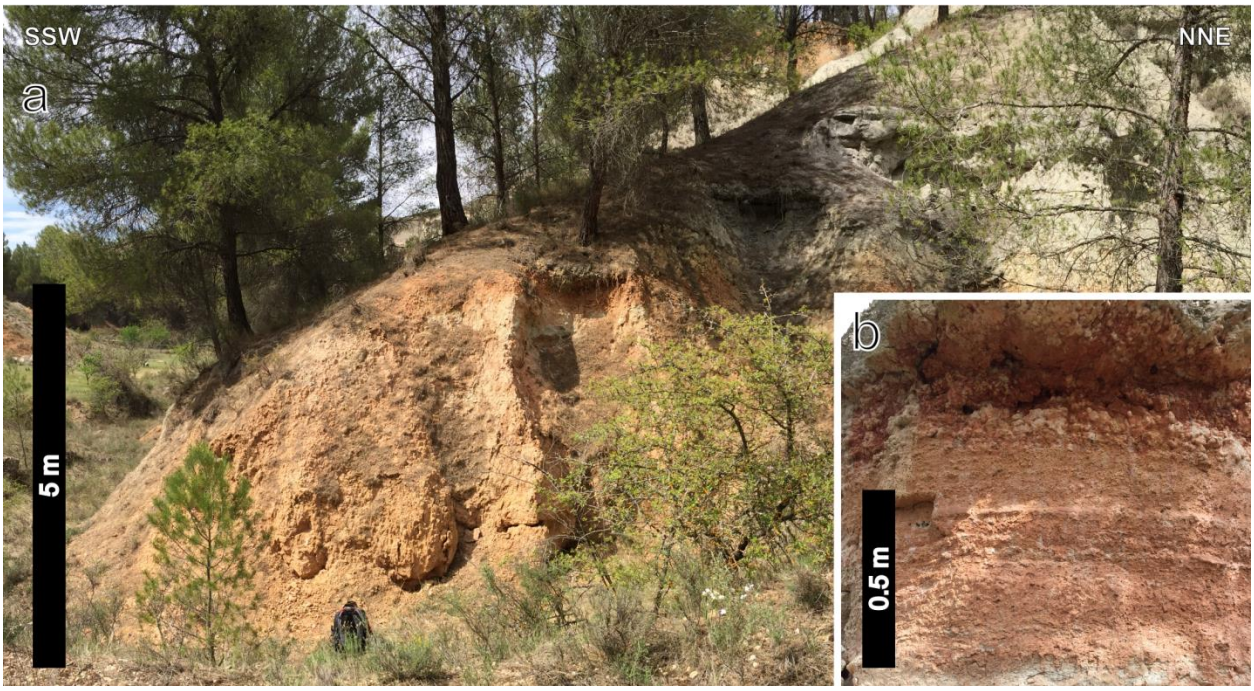

Figure. 6.2.: a) Overview on the lower part of the sampled Aragon section with the characteristic alternation of reddish paleosoils (bottom) and grey caliche horizons (top). **b**) Detail view of a paleosoil profile containing a particularly large numbers of pedogenic carbonate nodules, topped by a thick caliche band.

The Aragon section is situated one km SE of Villafeliche (Spain; 41.18931 °N 1.48436 °W) in the NW-SE-oriented CDB (*figure 6.1*) that is enclosed by the Western and Eastern Iberian Chains. The 170 m thick Armantes section (Krijgsman *et. al.* 1994) consists of proximal to distal alluvial fan-floodplain sediments of the intermediate unit (Rubio, 1999; Alonso-Zarza *et al.*, 2014) with pedogenically overprinted red silts and clays, individual conglomerates, at least one thin (dm) black organic rich layer, and shallow palustrine/lacustrine limestone. These Miocene

sediments were deposited on the underlying Cambrian basement (Krijgsman *et. al.* 1994) which can be found at a small (dm to m wide) fluvial incision at the NE end of the section. The red silts contain numerous carbonate nodules and individual root casts and clays and are characterized by reddish-green to yellow mottling and the lack of primary sediment structures (*figure 6.2*).

6.3 Material and methods

Sampling was done across the original Aragon profile of Krijgsman *et. al.* (1994). Three pedogenic carbonate nodules were collected at 38 ± 6 m spacing for analyses of their compositions of clumped (Δ_{47}), oxygen ($\delta^{18}O$), and carbon ($\delta^{13}C$) isotopic compositions. Additionally, 63 pedogenic carbonate nodules and caliche horizons were sampled for $\delta^{18}O$ and $\delta^{13}C$ exclusively. $\delta^{18}O$ and $\delta^{13}C$ analyses of all 66 samples as well as the Δ_{47} analyses of the three pedogenic carbonate nodules were done during the analytical period of *chapter 5* using identical analytical protocols whereas Δ_{47} was measured on a Thermo Fisher™ MAT 253™ gas source mass spectrometer (IRMS) exclusively (between 08/05/2018 and 9/17/2018). For information on the $\delta^{18}O$, $\delta^{13}C$, and Δ_{47} sample preparation and analyses, it is therefore referred to *chapter 5.7* and the supplementary of *chapter 5*. $\delta^{18}O$ and $\delta^{13}C$ results are given in VSMOW and VPDB, respectively with errors being 1δ standard deviation (sd). The errors of the Δ_{47} data are given as 1δ standard error (se).

A groundwater well situated at the bottom of the valley of the Armantes section at 610 m a.s.l. (41.39878 N, 1.69246 W) was sampled on the fifth May 2017 by collecting 30 ml of unfiltered water in a high-density polyethylene (PE) bottle. The PE bottle was carefully filled to the top without leaving a headspace of air. The sample was sun-shielded and kept at room temperature until being stored within a laboratory refrigerator. A sample aliquot of one ml was analyzed for its stable hydrogen (δD) and oxygen ($\delta^{18}O$) isotopic compositions using a liquid water isotope analyzer (LWIA-24d; Los Gatos Research; CRD Laser Spectroscopy). The measured δD and $\delta^{18}O$ values were corrected by using internal standard waters that are calibrated against VSMOW. The analytical precision is 1 ‰ and 0.3 ‰ for δD and $\delta^{18}O$, respectively.

6.4 Results and discussion

Prior to the end of the MCO at DSDP 608 (14.53 Ma; Mudelsee *et al.*, 2014), a Δ_{47} soil temperature of 24 ± 3 °C is measured (at 14.64 Ma). This temperature is identical to the average soil temperature of Armantes during this interval (22 ± 1 °C; 15.33 to 14.54 Ma). At the beginning of the MMCT and between Mi3a and Mi3b (Abels *et al.*, 2005), the Aragon Δ_{47} soil

temperature is 23 ± 3 °C (at 14.54 Ma). After Mi3b and the end of the MMCT at DSDP 608 (12.88 Ma; Mudelsee *et al.*, 2014), the Δ_{47} soil temperature decreases to 14 ± 1 °C (at 13.74 Ma). The results of the Δ_{47} analyses are summarized in *table 6.1*. and displayed in *figure 6.3*.

Table 6.1: Overview on the results of the Δ_{47} analyses of the Aragon paleosoil carbonate nodules including the respective ages, calculated $\delta^{18}O_{H2O}$ of the soilwater (Coplen, 2007), start and end point of the MMCT as determined for DSDP 608 (Mudelsee *et al.*, 2014), and ages of the Mi3a and Mi3b events (Abels *et al.*, 2005).

Identifier	Age ±error [Ma]	T (Δ_{47}) ± se [°C]	$\delta^{13}C$ ± sd [‰]	$\delta^{18}O$ ± sd [‰]	n	$\delta^{18}O_{H2O}$ ± error [‰]
MMCT DSDP 608 End	*12.88 ± 0.38*					
2017-AR-037	13.74 ± 0.01	14 ± 1	-7.17 ± 0.01	23.81 ± 0.02	4	-8.42 ± 0.23
Mi3b	*13.82 ± 0.03*					
2017-AR-014	14.10 ± 0.01	23 ± 3	-6.54 ± 0.02	24.42 ± 0.06	5	-6.00 ± 0.65
Mi3a	*14.2*					
MMCT DSDP 608 Start	*14.53 ± 0.41*					
2017-AR-001	14.64 ± 0.01	24 ± 3	-6.81 ± 0.01	23.50 ± 0.04	5	-6.70 ± 0.63
MCO DSDP 608 Start	*17.09 ± 0.8*					

The $\delta^{18}O$ and $\delta^{13}C$ values of the caliches range from 22.4 ‰ to 24.7 ‰ and -8.2 ‰ to -6.3 ‰, respectively, whereas the latter peak at 14.26 Ma (supplementary data *S.6.VI.*).

Soil water $\delta^{18}O_{H2O}$ values are calculated from measured pedogenic carbonate nodule $\delta^{18}O$ and Δ_{47} that average to $\delta^{18}O_{H2O}$ = -7.04 ± 1.25‰ (14.6 to 13.7 Ma; *table 6.1*). The individual $\delta^{18}O_{H2O}$ show a 2 ‰ decline across Mi3a (*table 6.1*). The results of the modern water sample (2017-AM-005) are: $\delta^{18}O$ = -9.3 ± 0.1‰ and δD = -64 ± 0.5‰. The reconstructed MMCT $\delta^{18}O_{H2O}$ is indistinguishable from the $\delta^{18}O_{H2O}$ reported in *chapter 5* for soil water (-6.6 ± 1.3 ‰) and for fossil tooth data (-7.1 ± 1.5 ‰; Domingo *et al.*, 2009) (*figure 6.4*)

Identical to the Armantes soil temperatures (*chapter 5*), the Aragon data shows a cooling centered at 13.9 Ma although the amplitude is lower (9 °C) when compared to Armantes. This could be due to the less detailed temporal resolution of the Aragon Δ_{47} record or a generally cooler and/or more stable MMCT microclimate at Aragon. However, the late MCO (14.64 Ma) and early MMCT (14.10 Ma) soil temperatures of Aragon compare well to the temperatures of the Armantes section and the marine SST of Super *et al.* (2020) (*figure 6.3*)

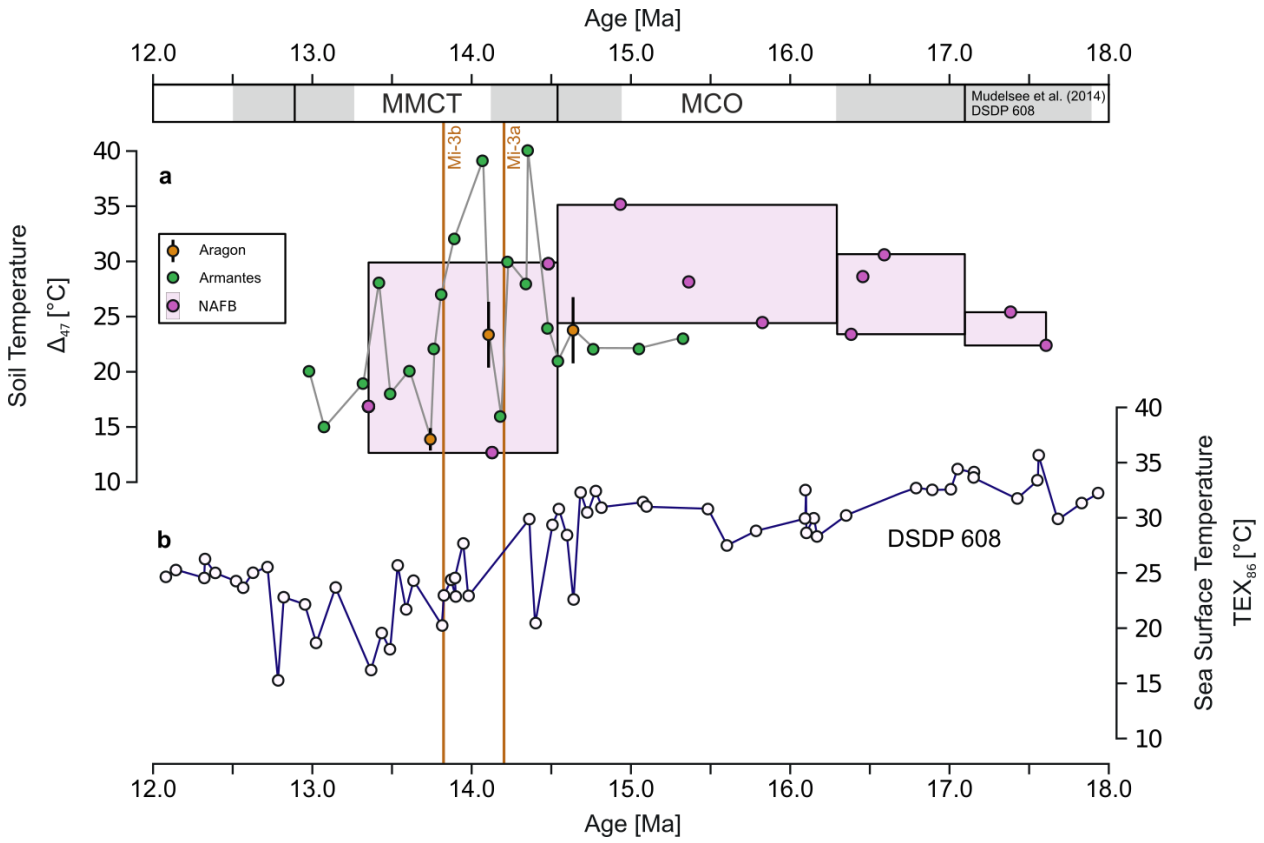

Figure. 6.3: a) Terrestrial soil temperatures of Southern Europe (orange dots, vertical error bars, Aragon, Spain; green dots, grey shaded line, Armantes, Spain) and the Northern Alpine Foreland Basin (NAFB; purple dots, pink boxes, Methner *et al.*, 2020). **b)** Sea surface temperatures of Super *et al.* (2020) (DSDP Site 608) for the MCO and MMCT. The duration of the MCO and MMCT of DSDP 608 (Mudelsee *et al.*, 2014) are indicated at the top. The Mi3a and Mi3b (Abels *et al.*, 2005) are marked with vertical lines.

From 14.07 to 13.81 Ma, sedimentation rates, soil temperatures, and $\delta^{18}O_{H2O}$ decrease simultaneously as indicated by *figure 6.4* (vertical green bar). During this interval, taxon turnover rates are relatively high – especially when compared to the outgoing MMCT (<13.5 Ma; van Dam *et al.*, 2006) where low turnover rates are established. This finding is in agreement with van Dam *et al.* (2006) who showed that pulses of faunal turnover coincide with minima in eccentricity and nodes of obliquity which are Milankovitch oscillations (Laskar *et al.*, 2004) that in turn can affect cooling (Zachos *et al.*, 2001) and precipitation (van Dam *et al.*, 2006). In combination with the measured enhanced climate variability during the MMCT (*chapter 5*), it is hypothesized that varying climate conditions (*e.g.* temperature and precipitation) played an important role in the reorganization of MMCT faunal assemblages; especially between 14.07 to 13.81 Ma where the data of this study and *chapter 5* define substantial cooling and decreasing moisture availability.

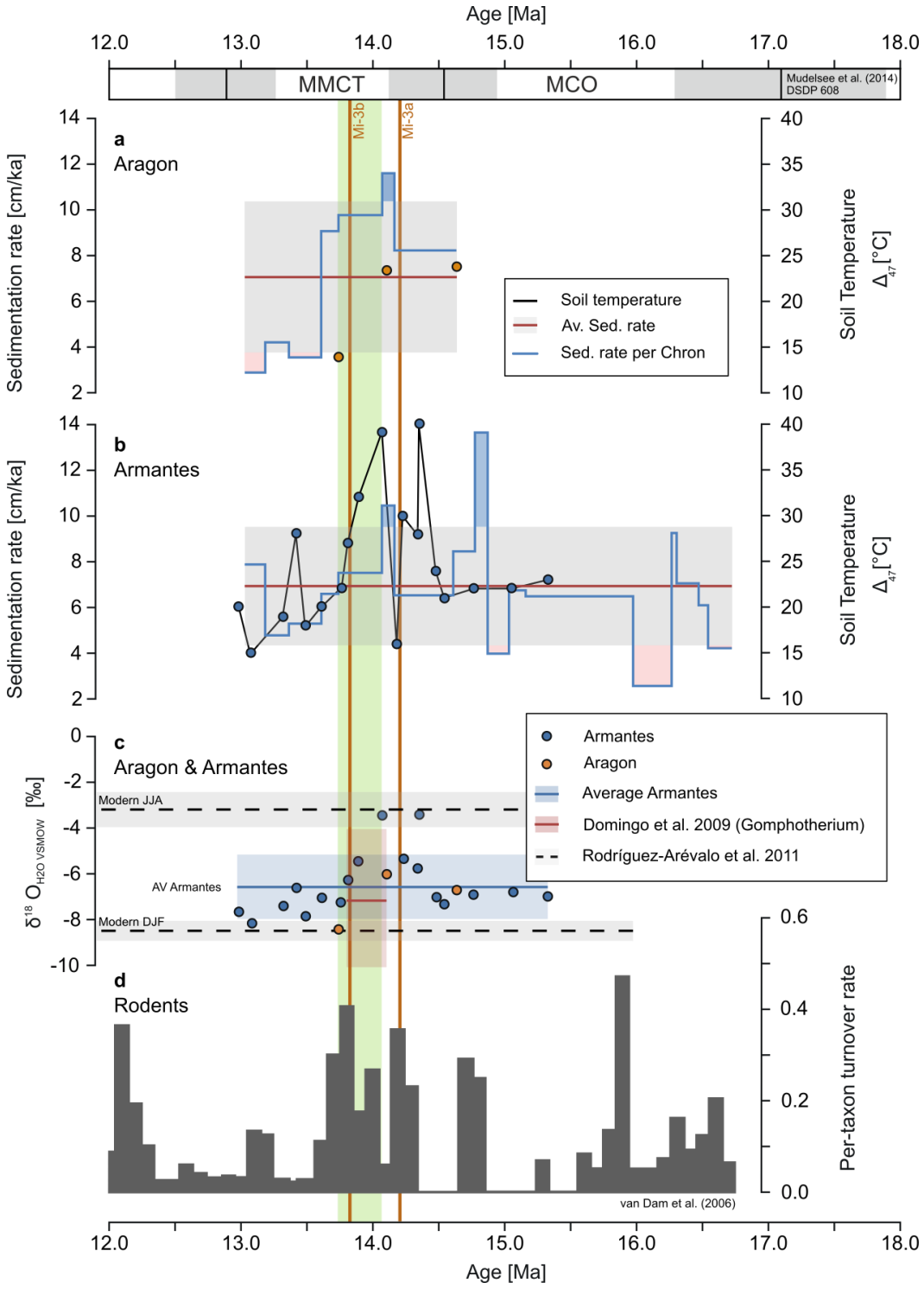

Figure. 6.4: Δ_{47} soil temperatures and sedimentation rates per Chron of (**a**) Aragon (Spain) and (**b**) Armantes (Spain; *chapter 5*). **c:** $\delta^{18}O_{H2O}$ values of the sections Armantes (blue dots; Average ± sd: blue line and shaded area), Aragon (orange dots, this study), Somosaguas (Spain; *Gomphotherium* $\delta^{18}O_{PO4}$; Domingo *et. al.* 2009), and modern $\delta^{18}O_{H2O}$ values of the JJA and DJF precipitation in the Calatayud area (Rodríguez-Arévalo *et. al.* 2011). **d:** Rodent per-taxon turnover rates for Central Spain (van Dam *et. al.* 2006). The vertical green bar indicates an interval where soil temperatures, sedimentation rates, and $\delta^{18}O_{H2O}$ synchronously decline.

6.5 Modern *vs.* Middle Miocene climate

The modern climate of the study areas Armantes (41.38989 °N 1.72073 °W) and Aragon (41.18931 °N 1.48436 °W) is currently characterized by a temperate oceanic to warm summer Mediterranean Koeppen climate (Cfb and Csb, respectively; Mitchell & Jones, 2005) and west winds with < 3 m/s in average (NCEP/NCAR Reanalysis at 1,000 mbar isosurface). The monthly climatological air surface temperatures range from approximately 4 to 28 °C (University of East Anglia Climatic Research Unit (CRU) Global 0.5° Monthly Time Series, Version 2.1 (CRU TS 2.1)) whereas the average MMP varies between 15 and 40 mm/month (CPC CAMS-OPI v0208 monthly gridded precipitation data set) (Kalnay *et al.*, 1996). These mean monthly temperature (MMT) and mean monthly precipitation (MMP) data are confirmed by local measurements (6.4 to 24.9 °C, *figure 6.4*; 18 to 44 mm/month, *figure 6.5*) at the three nearest GNIP stations referred to in *chapter 5* (Noguera de Albarracin /D.G.A., Zaragoza Aeropuerto, and Soria; Rodríguez-Arévalo *et al.*, 2011; 2000 to 2015 data), whereas peak values reach 28 °C and 142 mm. All derived mean annual values of these GNIP stations average to $\delta^{18}O$ = -6.2 ± 2.3‰, δD = -42.9 ± 15.8‰, 15.9 ± 9.7 °C, and 31.7 ± 9.1 mm/month (Rodríguez-Arévalo *et al.*, 2011).

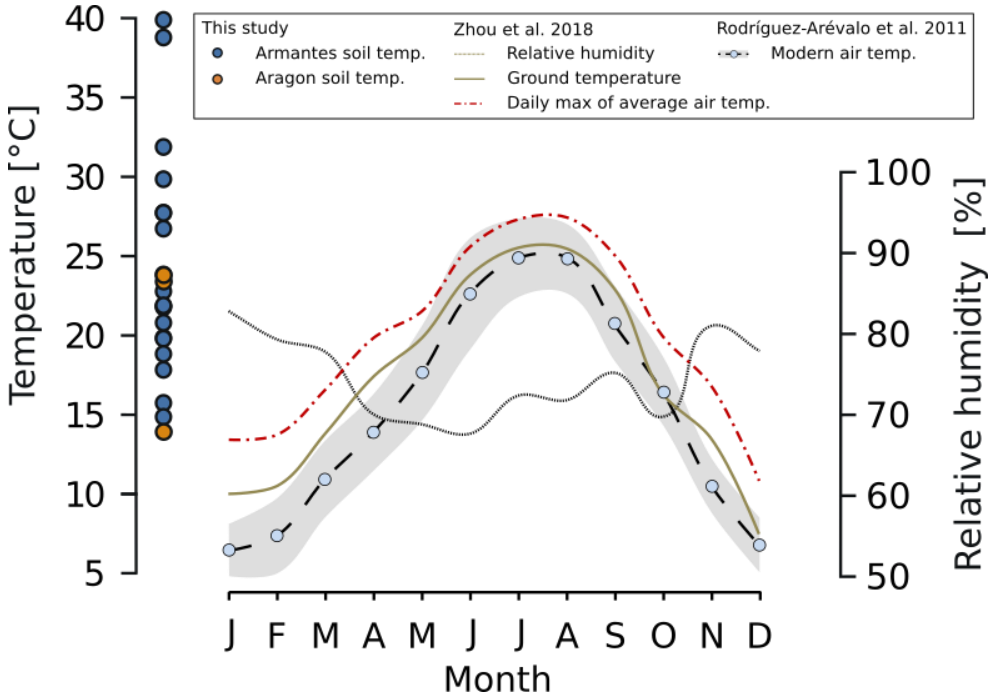

Figure. 6.5: Δ_{47} soil temperatures from Armantes (blue dots, *chapter 5*) and Aragon (orange dots, this study) along with model data of (Zhou *et al.*, 2018) of Middle Miocene (14 Ma) relative humidity (grey hatched line), ground temperature (olive solid line), and daily max. of 2m average air temperature (red dashed and dotted line). Modern local air temperatures (cyan dots, black dashed line; Rodríguez-Arévalo *et al.*, 2011) are shown for comparison.

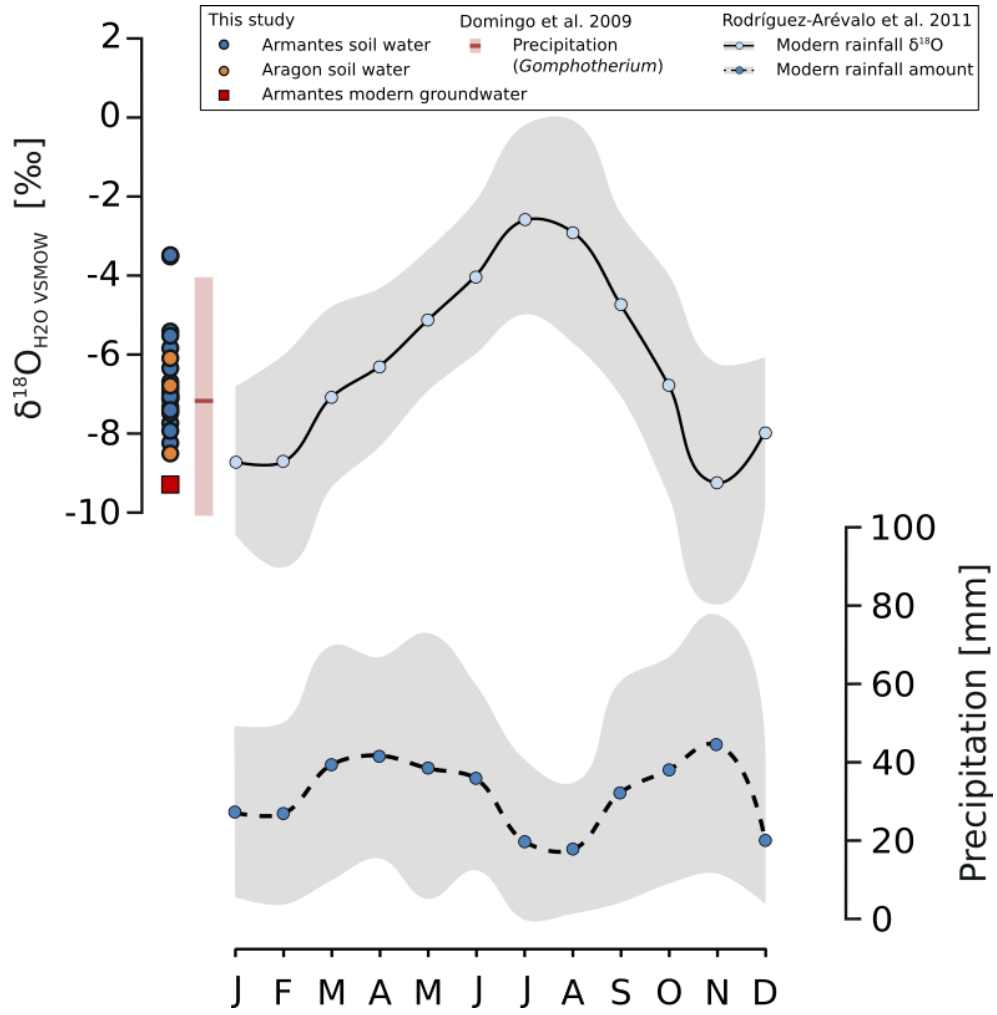

Figure. 6.6: Modern ground water $\delta^{18}O_{H2O}$ from Armantes, Middle Miocene soil water $\delta^{18}O_{H2O}$ of Armantes and Aragon (this study), and calculated Middle Miocene $\delta^{18}O_{H2O}$ of precipitation (Domingo *et. al.*, 2009) compared to present-day rainfall $\delta^{18}O_{H2O}$ (top, solid line) and MMP (bottom, dashed line) (Rodríguez-Arévalo *et. al.*, 2011).

The present-day MMT are compared to the measured soil temperatures of Armantes and Aragon, as well as to modeled Middle Miocene (14 Ma) ground temperatures, daily maxima of average air temperatures, and relative humidity (Zhou *et al.*, 2018) (*figure 6.5*). When compared to the Middle Miocene model data, present-day cold month mean temperatures (CMMT; DJF) are approximately 5 °C colder while the respective warm month mean temperatures (WMMT; JJA) are generally comparable. The amplitude of modeled Middle Miocene seasonal temperature variation is as large as 17 to 18 °C (Zhou *et al.*, 2018) and could therefore explain the short term soil temperature changes observed during the MMCT that were previously linked to potential changes in seasonality (*chapter 5*). Comparing the modeled Middle Miocene temperatures to the measured soil temperatures of Armantes further shows that local soil temperatures are

underestimated by the model of Zhou *et al.* (2018) by up to 12 °C. In contrary, the Aragon soil temperatures agree well with the modeled seasonal temperature range. Considering the modeled relative humidity curve of Zhou *et al.* (2018), warm JJA temperatures generally coincided with reduced moisture availability. Though, this correlation cannot be further resolved across the MMCT.

Modern ground water $\delta^{18}O_{H2O}$ from Armantes, the reconstructed Middle Miocene soil water $\delta^{18}O_{H2O}$ of Armantes and Aragon (this study), and calculated Middle Miocene $\delta^{18}O_{H2O}$ of precipitation (Domingo *et al.*, 2009) are compared to present-day rainfall $\delta^{18}O_{H2O}$ and MMP (Rodríguez-Arévalo *et al.*, 2011) (*figure 6.6*). The results of the modern groundwater sample 2017-AM-005 ($\delta^{18}O$ = -9.3 ± 0.1‰ and δD = -64 ± 0.5‰) are equivalent to the present-day November precipitation (δD = -64.1 ± 23.2‰ and δD = -9.3 ± 3.1‰; 2000 to 2015; Rodríguez-Arévalo *et al.*, 2011) suggesting a local soil-/groundwater residence time of approximately 6 months (*figure 6.4*). Alternatively, δD and $\delta^{18}O$ of modern groundwater might be dominated by the respective isotopic compositions of the local November precipitation because November is currently the month with the highest MMP (44 ± 33 mm; calculated from Rodríguez-Arévalo *et al.*, 2011). As in *chapter 5*, Middle Miocene soilwater $\delta^{18}O_{H2O}$ reconstructed from pedogenic carbonate nodules (Aragon) agree with the $\delta^{18}O_{H2O}$ *Gomphotherium angustidens* teeth data (Domingo *et al.*, 2009) and average to a $\delta^{18}O_{H2O}$ value that is approximately 1 ‰ lower when compared to the modern annual mean $\delta^{18}O_{H2O}$ of local precipitation.

6.6 Conclusions

The Δ_{47}-based soil temperatures from the Middle Miocene Aragon section in Southern Europe (Spain) support the timing of the substantial climate change reported in *chapter 5* (centered at 13.9 Ma). Between 14.07 and 13.81 Ma, synchronously declining soil temperatures, soil water $\delta^{18}O_{H2O}$, and sedimentation rates imply cooling and drying which coincides with high per-taxa turnover rates (van Dam *et al.*, 2006). This suggests that increased climate dynamics of the MMCT where an important driver for the reorganization of faunal assemblages. Southern Europa (Armantes) soil temperatures partly show higher temperatures (up to 12 °C) when compared to model data of Middle Miocene air and ground temperatures (Zhou *et al.*, 2018). Modern rainfall $\delta^{18}O_{H2O}$ and air temperatures illustrate that the range of measured MMCT $\delta^{18}O_{H2O}$ and soil temperatures generally could be explained by seasonal variations which

underlines the importance to resolve seasonal biases in pedogenic carbonate formation in future studies.

6.7 Comments and acknowledgements

This chapter is included in this Ph.D. thesis because it extends the results of *chapter 5* with additional data from the Middle Miocene that are related to model data and present-day climate information. This study was facilitated by the support and contribution of A. Mulch, W. Krijgsman, I. Vasiliev, E. Krsnik, K. Methner, and J. Fiebig. N.L., A.M., W.K., and I.V. designed the study. N.L. conducted the analyses and wrote the manuscript. A.M., W.K, I.V., and E.K. participated at collecting and documenting the samples in the field. E.K., J.F. and K.M. supported the clumped isotope analyses. A.M., I.V., K.M., and E.K. discussed the results.

7 Scientific work as a (co-) author

In addition to the studies presented in the chapters 2 to 6, five additional peer reviewed studies were published during the author's Ph.D. studies from 2016 to 2020. Furthermore, three studies are in the process of being published at the time of this thesis (in prep./subm./in revision).

The author's contributions to these studies include fieldwork and sample preparation, laboratory work (*e.g.* Δ_{47}, Δ_{48}, $\delta^{18}O$, and $\delta^{18}C$ analyses), data evaluation and discussion, writing and revisions, as well as submitting and presenting as illustrated by *table 7.1*.

Table 7.1: Matrix illustrating the author contribution to the (peer-reviewed) studies that were published and prepared for publishing during the Ph.D. studies of Niklas M. Löffler (2016 to 2020). #) The Methner *et. al.* (2020) study was presented at the AGU Fall meeting 2019 in San Francisco (U.S.A.) by Niklas M. Löffler as a representative of the lead author, Katharina Methner. *) Studies included in this Ph. D. thesis are marked with an asterisk.

Contribution in %	Fieldwork and Sample preparation	Laboratory work	Data evaluation and discussion	Writing and reivision	Submitting and presenting	AV Contribution
Löffler *et. al.* (subm.)*	70	80	90	90	100	86
Methner *et. al.* (in rev.)	0	20	10	10	0	8
Krsnik *et. al.* (in prep.)	20	30	30	10	0	18
Bajnai *et. al.* (2020)	0	30	20	10	0	12
Methner *et. al.* (2020)	0	50	10	10	10#	16
Fiebig *et. al.* (2019)*	0	70	30	10	0	22
Löffler *et. al.* (2019)*	80	80	90	80	100	86
Bajnai *et. al.* (2018)	0	30	30	10	0	14
Wacker *et. al.* (2016)	50	50	30	20	0	30
Fiebig *et. al.* (2016)	30	20	10	0	0	12

The full references for the additional studies are:

Methner, K., Mulch, A., Fiebig, J., Krsnik, E., **Löffler, N.**, Bajnai, D., Chamberlain, P. (in revision) Warm high-elevation mid-latitudes during the Miocene Climatic Optimum: Paleosol clumped isotope temperatures from the Northern Rocky Mountains, USA. *Paleoceanography and Paleoclimatology*. Paper #2020PA003991.

Krsnik, E., Methner, K., Campani, M., Kempf, O., **Löffler, N.**, Fiebig, J., Mulch, A. (in prep.) Stable isotope records from the NAFB continental sediments reveal higher paleoelevations for the Miocene Central Alps than previously assumed.

Bajnai, D., Guo, W., Spötl, C., Coplen, T. B., Methner, K., **Löffler, N**, Krsnik, E., Gischler, E., Hansen, M., Henkel, D., Price, G. D., Raddatz, J., Scholz, D., Fiebig J. (2020) Dual clumped isotope thermometry resolves kinetic biases in carbonate formation temperatures. *Nature Communication 11*, 4005. https://doi.org/10.1038/s41467-020-17501-0

Methner, K., Campani, M., Fiebig, J. **Löffler, N.**, Kempf, O. Mulch, A. (2020) Middle Miocene long-term continental temperature change in and out of pace with marine climate records. *Scientific Rep*orts *10*(1), 1-10. https://doi.org/10.1038/s41598-020-64743-5

Bajnai, D., Fiebig, J., Tomašových, A., Milner Garcia, S., Rollion-Bard, C., Raddatz, J., **Löffler, N.**, Primo-Ramos, C., & Brand, U. (2018). Assessing kinetic fractionation in brachiopod calcite using clumped isotopes. *Scientific Reports*, *8*(1), 533. https://doi.org/10.1038/s41598-017-17353-7

Wacker, U., Rutz, T., **Löffler, N.**, Conrad, A. C., Tütken, T., Böttcher, M. E., & Fiebig, J. (2016). Clumped isotope thermometry of carbonate-bearing apatite: Revised sample pre-treatment, acid digestion, and temperature calibration. *Chemical Geology*, *443*, 97–110. https://doi.org/10.1016/j.chemgeo.2016.09.009

Fiebig, J., Hofmann, S., **Löffler, N.**, Lüdecke, T., Methner, K., & Wacker, U. (2016). Slight pressure imbalances can affect accuracy and precision of dual inlet-based clumped isotope analysis. *Isotopes in Environmental and Health Studies*, *52*(1-2), 12–28. https://doi.org/10.1080/10256016.2015.1010531

8 Summary and conclusions

8.1 General outcome

This Ph.D. thesis demonstrates *i*) the highly precise performance of refined and new analytical setups for clumped isotope analysis (Δ_{47} and Δ_{48}) at the Joint Goethe University – Senckenberg BiK-F Stable Isotope Facility in Frankfurt Main, Germany, and *ii*) the applicability of clumped isotope analyses to biogenic and abiogenic carbonated apatite (Δ_{47}) and abiogenic carbonates (Δ_{47} and Δ_{48}) for research related to paleothermophysiology and paleoclimatology, whereas the overall analytical precision has been increased. Currently achieved typical standard deviations (sd) of individual measurements of the carbonate setup (Thermo Fischer™ MAT 253 Plus™ with HAL. digestion device; Fiebig *et al.*, 2019) are: sd Δ_{47} = 25 ppm, sd Δ_{48} = 90 ppm, sd $\delta^{13}C$ < 10 ppm, and sd $\delta^{18}O \leq 10$ ppm (based on equilibrated gas data of *chapter 4*). The individual results of the studies on the ***Clumped Isotope Thermometry Techniques and their Application to Fossil Teeth and Pedogenic Carbonates*** are summarized in the following. *Figure 8.1* illustrates that "temperature" represents the predominant subject of this thesis.

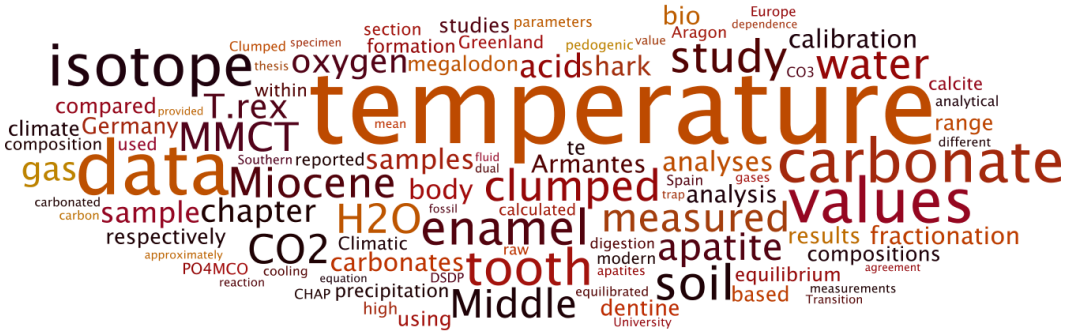

Figure 8.1: Word art that summarizes the 100 most common words used in this thesis. Words frequently used are shown larger when compared to words with a lower word count.

8.2 Δ_{47}, $\delta^{18}O$, and $\delta^{13}C$ measured on (bio)apatites – results and conclusions

A comprehensive Δ_{47} dataset with 122 replicate analyses is provided from which the temperature dependence of Δ_{47} for (bio)apatite (Δ_{47}-$1/T^2$) is calculated. The samples vary in their chemical and isotopic compositions and cover a temperature range of 1 °C to 80 °C. The Δ_{47}-$1/T^2$ of structural carbonate is indistinguishable from calcite if the acid fractionation between 25 °C

and 110 °C reactions for calcite (Defliese *et al.*, 2015) is considered. When compared to the only previous (bio)apatite Δ_{47}-$1/T^2$ calibration of Wacker *et al.* (2016), the refined calibration increases the temperature range by 36 % (from 58 °C to 79 °C), the number of datasets by 170 % (from 3 to 8), and the number of total replicate analyses by 430 % (from 23 to 122). Furthermore, all data is reprocessed using the state of the art [*Brand*]/IUPAC parameters (Daëron *et al.*, 2016; Kelson *et al.*, 2017) which improves the applicability and intercomparability of the calibration; especially for other laboratories and end users.

The temperature dependence of oxygen isotope equilibrium fractionation between carbonated synthetic apatite and water ($1{,}000\ln(\alpha_{CHAP\text{-}H2O})$) is experimentally determined from analyses of synthesized carbonated hydroxyapatites (CHAP). This allows for the calculation of the $\delta^{18}O$ of the mineralizing fluid ($\delta^{18}O_{H2O}$) if the formation temperature of a (bio)apatite is known – as for example by the aforementioned Δ_{47} analyses. It can be shown that the $1{,}000\ln(\alpha_{CHAP\text{-}H2O})$ is comparable to the respective fractionation between calcite and water (Coplen, 2007).

When applied to tooth enameloid from a modern Greenland shark (*Somniosus microcephalus*), a Late Miocene megatooth shark (*Carcharodon megalodon*), and an Upper Cretaceous *Tyrannosaurus rex*, reconstructed Δ_{47}-based temperatures and $\delta^{18}O_{H2O}$ are in line with previously published data. For the modern Greenland shark tooth enameloid, $\delta^{18}O_{H2O}$ values computed from Δ_{47}-based temperatures (*equation 2.1*), $\delta^{18}O_{CO3}$ and the $1{,}000\ln(\alpha_{CHAP\text{-}H2O})$ temperature relationship (*equation 2.3*) agree with the $\delta^{18}O_{H2O}$ that is independently reconstructed by using measured $\delta^{18}O_{PO4}$ (Pucéat *et al.*, 2010; their equation 3) instead of $\delta^{18}O_{CO3}$.

The reconstructed *C. megalodon* habitat temperature (19 ± 4 °C) is identical to both, the respective temperature of its modern analogue – the great white shark (*Carcharodon carcharias*) – that ranges from 16 to 22 °C (Dewar *et al.*, 2004) and previous estimates of Pimiento *et al.* (2016) who reported a habitat temperature range of 12 to 27 °C.

The reconstructed *T. rex* body temperature of the adult specimen “Trix” (RGM 792.000) of 38 ± 3 °C falls within the range of modern Endotherms such as mammals and birds (34 to 44 °C; Clarke & Rothery, 2008) and is furthermore approximately 15 °C above the local paleoenvironmental temperature of the Hell Creek Formation (23 °C; Johnson, 1997). Though, it cannot be distinguished between endothermy and gigantothermy because the body mass of “Trix” (5,000 kg) is too large to exclude gigantothermy. The reconstructed *T. rex* body fluid $\delta^{18}O$ agrees with published local $\delta^{18}O_{H2O}$ of (paleo)surface waters and $\delta^{18}O_{CO3}$ of bivalves, whereas the *T. rex*

data is conform with previously reported $\delta^{18}O$ and $\delta^{13}C$ of tooth enamel from herbivore hadrosaurian and ceratopsian dinosaurs which are potential prey.

Due to the close agreement with previously published data (*e.g. C. megalodon* habitat temperature), other proxies (*e.g.* $\delta^{18}O_{PO4}$), and the strong similarities when compared to results from pure carbonates (*e.g.* $1{,}000\ln(\alpha_{CHAP\text{-}H2O})$ and Δ_{47}-$1/T^2$), it is concluded that the (bio)apatite $\delta^{18}O$ and Δ_{47} values presented in this thesis closely reflect isotopic equilibrium and that the chemical composition (*e.g.*, hydroxylapatite *vs.* fluorapatite) of (bio)apatite does not alter the clumped isotopic composition and the associated temperature dependent fractionation of $\delta^{18}O$. The consistent results of $\delta^{18}O$, $\delta^{13}C$, and Δ_{47} from *T. rex* tooth enamel further underline the applicability of the $\delta^{18}O_{CO3}$ and Δ_{47} temperature calibrations for (bio)apatite (*equations 2.1 and 2.3*) to fossil vertebrates.

8.3 Δ_{47}, Δ_{48}, $\delta^{18}O$, and $\delta^{13}C$ measured on carbonates – results and conclusions

An analytical setup for highly precise clumped isotope analysis is described that allows for the simultaneous measurement of Δ_{47} and Δ_{48} in CO_2 (incl. $\delta^{18}O$ and $\delta^{13}C$) with external reproducibilities close to the respective shot-noise limits. The analyte gases originate from pure carbonates that were digested in hypersaturated orthophosphoric acid and purified using a fully automated device. The measured Δ_{47} and Δ_{48} values of the Upper Cretaceous ETH-3 carbonate plot on the theoretical Δ_{47} *vs.* Δ_{48} equilibrium line which allows for the accurate determination of its formation temperature of 15 ± 2 °C. The corresponding formation temperatures of Carrara marble and ETH-4 are 210 ± 7°C and 86 ± 4 °C, whereas – based on their Δ_{48} errors – rate-limiting kinetic effects cannot be ruled out for these samples. No indication for artificial biases of the measured Δ_{47} and Δ_{48} of the analyte CO_2 gases can be found. It should therefore be feasible to resolve rate-limiting effects on measured Δ_{47} and determine precise temperatures of carbonate formation by projecting measured Δ_{47} to the equilibrium position in Δ_{47} *vs.* Δ_{48} space, provided that the exact directions of kinetic vectors of *e.g.* CO_2 degassing and CO_2 absorption are sufficiently known (*e.g.* Guo, 2020; Bajnai *et al.*, 2020). Kinetic deviations from the isotopic equilibrium can generally arise from slow reactions of dehydration/dehydroxylation (*equation 8.1.a*) and hydration/hydroxylation (*equation 8.2.b*) (McConnaughey, 1989) that convert dissolved CO_2 ($CO_{2(aq)}$) into the bicarbonate ion (HCO_3^-) and *vice versa*, as well as from the incorporation of dissolved inorganic carbon (DIC) into the crystal lattice (Watson, 2004; DePaolo, 2011).

(*equation 8.1*) *a*) $CO_{2\,(aq)} + H_2O \leftrightarrow H^+ + HCO_3^-$

b) $CO_{2\,(aq)} + OH^- \leftrightarrow HCO_3^-$

Two Δ_{47} data sets with 117 replicate analyses in total on 22 pedogenic carbonate nodules from the spanish Middle Miocene sections Armantes (*chapter 5*) and Aragon (*chapter 6*) reveal the continental Southern European thermal structure during the end of the Middle Miocene Climatic Optimum (MCO) and the complete Middle Miocene Climatic Transition (MMCT; from 15.33 to 12.98 Ma). The data is in agreement with oceanic sea surface temperatures (*e.g.* Shevenell *et al.*, 2004; Super *et al.*, 2020), $\delta^{13}C$ and $\delta^{18}O$ isotope records (*e.g.* Holbourn *et al.*, 2014), and paleontological studies (*e.g.* Böhme, 2003; Hernández Fernández *et al.*, 2006; van Dam *et al.*, 2006). It is shown that the continental climate during the MMCT was characterized by substantial fluctuations in temperature. The Southern European MMCT is marked by a short-termed cooling pulse at 14.18 Ma (to 16 ± 3 °C; *ca.* Mi3a) and a recovery to warm soil temperatures (39 ± 6 °C at 14.07 Ma). Between 14.07 and 13.49 Ma, soil temperatures cool continuously from 39 to 18 °C (midpoint: 13.94; *ca.* Mi3b). The data shows a statistical 12 °C cooling across the MMCT whereas a last warm spike in soil temperatures (28 ± 5 °C) is recorded at 13.42 Ma – an event that coincides with increased global ice volume (Shevenell *et al.*, 2004).

As a result of the agreement of the Southern European data with both recently published MMCT soil temperatures from the Northern Alpine Foreland Basin (Methner *et al.*, 2020) and the marine temperature record of the the proximate DSDP 608 (Super *et al.*, 2020), a contemporary climatic change can be assumed for Southern Europe, Central Europe, and the North Atlantic (at the current temporal resolution of the data). Between 14.07 and 13.81 Ma, simultaneously declining sedimentation rates, temperatures, and $\delta^{18}O_{H2O}$ imply cooling and drying. Notably, the Southern European cooling events (at *ca.* Mi3a and Mi3b) coincide with increased mammal turnover rates in Central Spain (van Dam *et al.*, 2006). It can therefore be concluded that an increased climate dynamics during the MMCT affected the reorganization of faunal assemblages. The variability of calculated soil water $\delta^{18}O_{H2O}$ and temperatures furthermore documents variation in seasonality of carbonate formation during the MMCT with an amplitude that is comparable to the modern range of annual temperatures and precipitation $\delta^{18}O_{H2O}$ (JJA-DJF) as well as Middle Miocene mammal $\delta^{18}O_{PO4}$ (Rodríguez-Arévalo *et al.*, 2011; Domingo *et al.*, 2009, respectively).

Due to the partly increased Armantes soil temperatures, when compared to model data of Middle Miocene air and ground temperatures (Zhou *et al.*, 2018), aiming on resolving a possible seasonal bias in pedogenic carbonate formation could be the focus of future studies. Modern rainfall $\delta^{18}O_{H2O}$ and air temperatures illustrate that the range of measured MMCT $\delta^{18}O_{H2O}$ and soil temperatures potentially could be explained by seasonal variations. Collectively it can be concluded that the climate of the MMCT was highly dynamic when compared to the predominantly stable and warm conditions of the MCO.

8.4 Outlook

8.4.1 Thermophysiology of extinct vertebrates

The refined (bio)apatite temperature calibration of Δ_{47} and the experimentally determined temperature dependence of $1{,}000\ln(\alpha_{CHAP\text{-}H2O})$ build a foundation for future thermophysiological and paleoenvironmental studies on extinct vertebrates. Because it has been demonstrated that reliable results can be obtained from fossil shark (*C. megalodon)* and dinosaur (*T. rex*) tooth enamel(oid), future studies can now focus on additional taxa and/or specimens. Possible research questions could relate to the investigation of the thermophysiology of reptiles and dinosaurs, as for example the marine Upper Cretaceous Mosasauridae and Tyrannosauridae. It would therefore be important to sample specimens with relatively large and small body masses to verify inertial homeothermy (gigantothermy) within one taxa (*e.g. T. rex*). Aside from the availability of sample material, which is *e.g.* limited for juvenile *T. rex*, it will become increasingly important to reduce the amount of sample material per analysis. Analytical techniques therefore have to be refined and adapted further, for example by installing a Thermo Scientific™ Kiel IV Device and adapting the default sample digestion and gas purification according to the presented (bio)apatite method (*chapter 2.3.2*). This will require a redesign of the heating, insulation, and gas purification, to allow for a higher acid digestion temperature (*e.g.* 110 °C) and effective removal of possible contaminants such as hydrocarbons. Aiming to extend the dual Δ_{47} and Δ_{48} analysis of carbonates to carbonated apatite (*e.g.* by connecting a Thermo Scientific™ Kiel IV Device to a Thermo Scientific™ MAT 253 Plus™) could be the next step. This would allow for verification of the presence of kinetic effects in biotic apatite (*e.g.* teeth and bone) and possibly enable temperature reconstruction on altered sample materials.

8.4.2 Highly precise dual Δ_{47} and Δ_{48} thermometry on carbonates

The new dual Δ_{47} and Δ_{48} methodology offers the potential to constrain rate-limiting kinetic effects on the CO_3^{-2} bond abundances during the formation of a sample. Because kinetic effects are already known for certain taxa (*e.g.* corals and brachiopods), it would be beneficial to systematically verify the presence and extent of kinetic biases in biotic carbonates. This could ultimately allow for a back-calculation of virtual equilibrium temperatures once the kinetic vectors in Δ_{47} *vs.* Δ_{48} are constrained (*e.g.* Bajnai *et al.*, 2020). This would require both thermodynamical modelling and experimental data on (dis)equilibrium precipitation of carbonate. This principle could also be applied to abiotic carbonates such as cave carbonates and pedogenic carbonates; preferably covering a wide range of temperatures (*e.g.* high latitudinal/cryogenic and low latitudinal/MMCO).

8.4.3 Continental Middle Miocene temperature record for Europe

The presented Middle Miocene soil temperature dataset from Southern Europe (*chapter 5* and *6*) is complemented by the Central European dataset of Methner *et al.* (2020). If additional soil temperatures from varying sites and latitudes would be reported by future studies, one could improve the understanding of the internal climate variability during the MCO and MMCT. One could also better constrain potential leads/lags with the marine record and verify latitudinal differences in the onsets and durations of the MCO and MMCT; which have been previously identified for the marine record (Mudelsee *et al.*, 2014). The reconstruction of the Middle Miocene paleoclimate and the identification of possible drivers of temperature and seasonality could further be supported by triple oxygen isotope analysis ($\Delta^{17}O$) of tooth enamel from small and abundant mammals (*e.g.* rodents), once the atmospheric partial pressure of CO_2 is reliably calibrated *vs.* $\Delta^{17}O$ (*e.g.* Gehler *et al.*, 2016 for the PETM).

8.4.4 Science outreach

To increase the accessibility and visibility of the results of this Ph.D. thesis, it is planned to present individual studies to the public and professionals (in addition to already performed presentations at scientific conferences). This particularly applies to the outcome of the (bio)apatite studies (*chapter 2* and *3*) because of the established link to European museums (Bjarnarhöfn Shark Museum and Naturalis Biodiversity Center), which provided sample materials that were essential to the respective studies. As a result, a poster that illustrates the interconnection between the Greenland sharks from Iceland and the body temperature of *T. rex*

has been prepared (*figure* 8.2) and will be displayed to the visitors of the Bjarnarhöfn Shark Museum in Iceland.

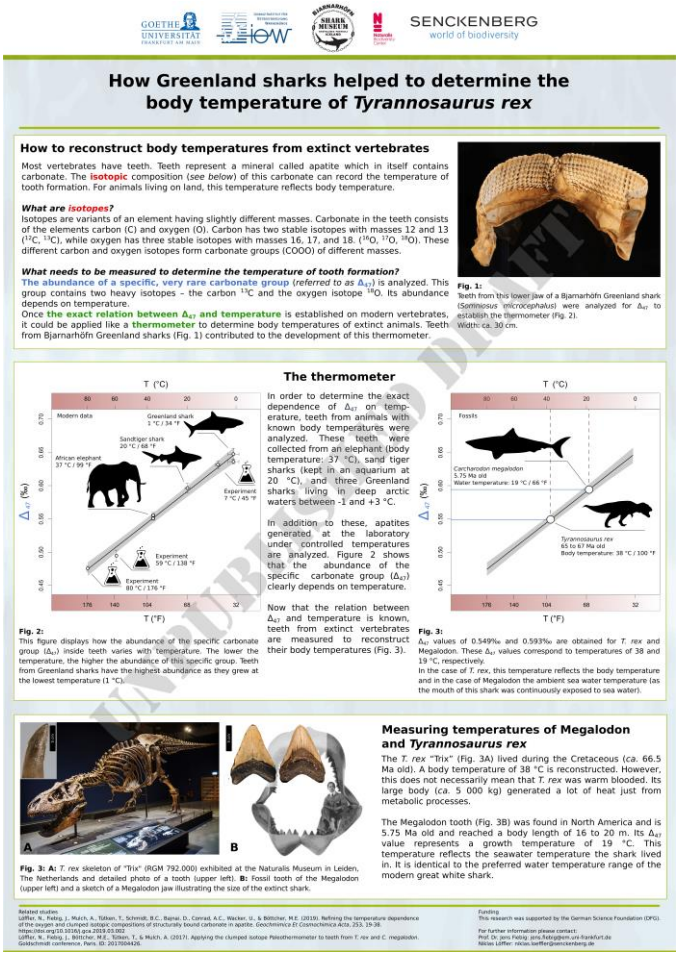

Figure 8.2: Draft of a poster that will be exhibited at the Bjarnarhöfn Shark Museum (Bjarnarhöfn, Iceland).
The museum provided numerous Greenland shark teeth for the calibration study in *chapter 2.*

Additionally, the results of the Δ_{47}-1/T² (bio)apatite calibration and its application to *C. megalodon* and *T. rex* will be presented at the 2020 annual Meeting of the Society of Vertebrate Paleontology (SVP) in Cincinnati (OH, U.S.A.)* by the author as an invited speaker during the podium symposium "New geochemical and dental wear approaches to reconstruct the diet, ecology, and physiology of fossil vertebrates". The outcome of the studies on the Middle Miocene Climatic Transition (*chapter 5* and *6*) will be presented as invited talk at the annual meeting of the Geological Society of America (GSA) in Montréal (QC, Canada)* at the session "The Co-Evolution of Phanerozoic Climate, Landscapes, and Terrestrial Ecosystems" (T62).

*) Due to the 2020 SARS-CoV-2 pandemy, the SVP and GSA meetings were rescheduled as online meetings.

9 Zusammenfassung und Schlussfolgerungen

9.1 Allgemeines Ergebnis

Diese Dissertation belegt *i*) die hochpräzise Performance von verfeinerten und neuen analytischen Verfahren für „clumped isotope"-Analysen (Δ_{47} und Δ_{48}) im Labor für die leichten stabilen Isotope (Gasmassenspektrometrie), das eine gemeinschaftliche Einrichtung des Senckenberg Biodiversität und Klima – Forschungszentrums (S-BiK-F) und dem Institut für Geowissenschaften der Goethe Universität ist (Altenhöferallee 1, 60438 Frankfurt am Main, Deutschland), und *ii*) die Anwendbarkeit von „clumped isotope"-Analysen an biogenem und abiogenem Karbonatapatit (Δ_{47}) sowie abiogenem Karbonat (Δ_{47} und Δ_{48}) für Forschungsfragen der Paläothermophysiologie und Paläoklimatologie, wobei die insgesamte analytische Präzision erhöht wurde. Die derzeit erreichten typischen Standardabweichungen (sd) von Einzelmessungen der Karbonat-Anlage (Thermo Fischer™ MAT 253 Plus™ mit HAL Probenaufbereitung; Fiebig *et al.*, 2019) sind: sd Δ_{47} = 25 ppm, sd Δ_{48} = 90 ppm, sd $\delta^{13}C$ < 10 ppm und sd $\delta^{18}O \leq 10$ ppm (basierend auf den Daten von equilibrierten Gasen aus *Kapitel 4*). Die jeweiligen Ergebnisse der einzelnen Studien zu „clumped isotope"-Thermometrie-Verfahren und deren Anwendung an fossilen Zähnen und pedogenen Karbonaten ***(„Clumped Isotope Thermometry Techniques and their Application to Fossil Teeth and Pedogenic Carbonates"***) sind im Folgenden zusammengefasst.

9.2 Δ_{47}-, $\delta^{18}O$-, und $\delta^{13}C$-Messungen an (Bio)Apatit – Ergebnisse und Schlussfolgerungen

Es wird ein umfassender Δ_{47}-Datensatz mit 122 Replikatanalysen präsentiert, aus dem die Temperaturabhängigkeit von Δ_{47} für (Bio)Apatit (Δ_{47}-$1/T^2$) berechnet wird. Die Proben variieren in ihrer chemischen und isotopischen Zusammensetzung und decken einen Temperaturbereich von 1 °C bis 80 °C ab. Die Δ_{47}-$1/T^2$ von strukturellem Karbonat in (Bio-)Apatit ist ununterscheidbar von Karbonat, wenn die Säurefraktionierung zwischen den Reaktionstemperaturen von 25 °C und 110 °C (Defliese *et al.*, 2015) berücksichtigt wird. Im Vergleich zur bisher einzigen (Bio-)Apatit-Δ_{47}-$1/T^2$-Kalibrierung von Wacker *et al.* (2016) vergrößert die verfeinerte Kalibrierung den Temperaturbereich um 36 % (von 58 auf 79 °C), die Anzahl der Datensätze um 170 % (von 3 auf 8) und die Anzahl der gesamten Replikatanalysen um 430 % (von 23 auf 122). Darüber hinaus sind alle Daten mit den aktuellen [*Brand*]/IUPAC

Parametern (Daëron *et al.*, 2016; Kelson *et al.*, 2017) ausgewertet, was die Anwendbarkeit und Vergleichbarkeit der Kalibrierung erhöht; vor allem für weitere Labore und Endnutzer.

Die Temperaturabhängigkeit der Gleichgewichtsfraktionierung von Sauerstoffisotopen zwischen synthetischem Karbonatapatit und Wasser ($1000\ln(\alpha_{CHAP\text{-}H2O})$) wurde mittels Analysen von synthetischen Karbonat-Hydroxylapatiten (CHAP) experimentell bestimmt. Dies ermöglicht die Berechnung des $\delta^{18}O$ des mineralisierenden Fluid ($\delta^{18}O_{H2O}$), sofern die Bildungstemperatur des (Bio-)Apatits bekannt ist. Letztere kann durch die zuvor genannte Δ_{47}-Methodik bestimmt werden.

Es kann belegt werden, dass $1000\ln(\alpha_{CHAP\text{-}H2O})$ gut mit der entsprechenden Fraktionierung zwischen Kalzit und Wasser (Coplen, 2007) vergleichbar ist. Durch die Anwendung der oben genannten Methoden an Zahnschmelz des modernen Grönlandhais (*Somniosus microcephalus*), dem spätmiozänen Megazahnhai (*Carcharodon megalodon*), und einem oberkreidezeitlichen *Tyrannosaurus rex*, werden Δ_{47}-basierte Temperaturen und $\delta^{18}O_{H2O}$ rekonstruiert, die mit zuvor publizierten Daten übereinstimmen. Im Falle des modernen Grönlandhai-Zahnschmelzes entspricht der aus den gemessenen Δ_{47}-basierten Temperaturen (*Gleichung 2.1*) $\delta^{18}O_{CO3}$ und der aus der $1000\ln(\alpha_{CHAP\text{-}H2O})$- Temperaturbeziehung (*Gleichung 2.3*) berechnete $\delta^{18}O_{H2O}$ dem Wert, der am gleichen Material mittels des Phosphatsauerstoffs berechnet wurde ($\delta^{18}O_{PO4}$; Pucéat *et al.*, 2010; deren Gleichung 3). Die rekonstruierte Habitattemperatur des *C. megalodon* (19 ± 4 °C) ist identisch mit der Habitattemperatur seines modernen Analogs, dem Weißen Hai (*Carcharodon carcharias*), die von 16 bis 22 °C reicht (Dewar *et al.*, 2004). Weiterhin liegt sie im durch Pimiento *et al.* (2016) publizierten *C. megalodon* Temperaturbereich von 12 bis 27 °C. Die Körpertemperatur des adulten *T. rex* „Trix“ (RGM 792.000) von 38 ± 3 °C liegt im Körpertemperaturbereich endothermer Wirbeltiere (z.B. Säugetiere & Vögel; 34 bis 44 °C; Clarke & Rothery, 2008) und darüber hinaus etwa 15 °C über der lokalen Paläoumgebungstemperatur der Hell Creek Formation (23 °C; Johnson, 1997). Obschon die rekonstruierte Körpertemperatur über der Umgebungstemperatur liegt, kann nicht zwischen Endothermie und Gigantothermie unterschieden werden, da die Körpermasse von „Trix“ (*ca.* 5.000 kg) zu hoch ist um Gigantothermie auszuschließen. Der rekonstruierte $\delta^{18}O_{H2O}$ des *T. rex*-Körperfluid stimmt mit bereits publizierten lokalen Werten von (Paläo-)Niederschlag und Karbonat von Muscheln überein. Zusätzlich fallen die *T. rex*-$\delta^{18}O$ und -$\delta^{13}C$-Werte in einen Bereich, der für Hadrosaurian und Ceratopsidae berichtet wurde, die beide potentielle Beute des *T. rex* sind.

Aufgrund der engen Übereinstimmung der Ergebnisse mit zuvor publizierten Studienergebnissen (z.B. *C. megalodon* Habitattemperatur), weiteren Proxies (z.B. $\delta^{18}O_{PO4}$), und den auffallenden Ähnlichkeiten mit Ergebnissen aus Messungen von reinen Karbonaten (z.B. $1000\ln(\alpha_{CHAP\text{-}H2O})$ und Δ_{47}-$1/T^2$), kann geschlussfolgert werden, dass $\delta^{18}O$ und Δ_{47} Werte von (Bio-)Apatit der in dieser Studie präsentierten Proben isotopische Gleichgewichtsbedingungen widerspiegeln und die unterschiedlichen chemischen Zusammensetzungen (z.B. Hydroxylapatit *vs.* Fluorapatite) von (Bio-)Apatit gemessene „clumped isotopes"-Werte und die assoziierte temperaturabhängige Fraktionierung von $\delta^{18}O$ nicht beeinflussen.

Die konsistenten Ergebnisse von $\delta^{18}O$, $\delta^{13}C$ und Δ_{47} des *T. rex*-Zahnschmelzes unterstreichen zusätzlich die Anwendbarkeit der $\delta^{18}O_{CO3}$- und Δ_{47}-Temperaturkalibrierungen für (Bio-)Apatit (*Gleichungen 2.1* und *2.3*) an fossilen Wirbeltieren. Zukünftige Studien können mit weiterer thermophysiologischen Forschung an fossilen Reptilien und Dinosauriern, wie zum Beispiel den oberkreidezeitlichen Mosasauridae und Tyrannosauridae, auf den bisherigen Ergebnissen aufbauen – unter anderem mit dem Ziel, die Entwicklung der Homeothermie besser nachzuvollziehen. Dabei wird es entscheidend sein, die Probenmenge pro Analyse durch die Methodenentwicklung an neuer Messtechnik weiter zu verringern (z.B: Thermo Scientific™ Kiel IV Device und Thermo Scientific™ MAT 253 Plus™).

9.3 Δ_{47}-, $\delta^{18}O$-, und $\delta^{13}C$-Messungen an Karbonat – Ergebnisse und Schlussfolgerungen

Es wird ein analytisches Verfahren für hochpräzise „clumped isotope"-Analysen beschrieben, das eine gleichzeitige Messung von Δ_{47} und Δ_{48} in CO_2 ermöglicht (inkl. $\delta^{18}O$ und $\delta^{13}C$) und dabei externe Reproduzierbarkeiten erreicht, die nahe der Detektionsgrenzen („shot-noise limit") liegen. Die Analytgase stammen von reinen Karbonaten, die in übersättigter orthophosphorischer Säure aufgelöst und mittels einer vollautomatisierten Anlage gereinigt wurden. Gemessene Δ_{47} und Δ_{48} des oberkreidezeitlichen ETH-3-Karbonats liegen auf der theoretischen Linie des Δ_{47}-*vs.*-Δ_{48} Equilibriums, was eine hochpräzise Bestimmung der Bildungstemperatur von 15 ± 2 °C ermöglicht. Die entsprechenden Bildungstemperaturen von Carrara Marmor und ETH-4 sind 210 ± 7°C und 86 ± 4 °C, wobei – auf deren Δ_{48}-Fehlern basierend – limitierende kinetische Effekte für diese Proben nicht ausgeschlossen werden können. Es wurden keine Indikation für einen Bias der gemessenen Δ_{47}- und Δ_{48}-Werte der CO_2-Analytgase nachgewiesen. Künftig wird es daher durchführbar sein, limitierende kinetische Effekte auf gemessene Δ_{47} Werte und äußerst präzise Temperaturen der Karbonatbildung zu

bestimmen. Ermöglicht wird dies dadurch, dass gemessene Δ_{47} -Werte auf die Position des Δ_{47}-*vs.*-Δ_{48}-Equilibrium projiziert werden können. Dies setzt voraus, dass die exakten Richtungen der kinetischen Vektoren von z.B. CO_2-Entgasung und CO_2-Absorption hinreichend bekannt sind (*e.g.* Guo, 2020; Bajnai *et al.,* 2020). Kinetische Abweichungen vom isotopischen Equilibrium können grundsätzlich durch langsam ablaufende Reaktionen der Dehydratation/Dehydroxylierung ($CO_{2\,(aq)} + H_2O \leftrightarrow H^+ + HCO_3^-$) und Hydratation/Hydroxylierung ($CO_{2\,(aq)} + OH^- \leftrightarrow HCO_3^-$) hervorgerufen werden (McConnaughey, 1989). Diese Reaktionen translatieren gelöstes CO_2 ($CO_{2(aq)}$) in das Bikarbonat-Ion (HCO_3^-). Zusätzlich können Abweichungen durch die Inkorporation von gelöstem inorganischem Kohlenstoff (DIC) in das Kristallgitter verursacht werden (Watson, 2004; DePaolo, 2011). Da kinetische Effekte bereits für verschiedene Taxa bekannt sind (z.B. Korallen und Brachiopoden), wäre es für weitere Studien sinnvoll, die Anwesenheit von kinetischen Biases in biotischen Karbonaten systematisch zu untersuchen. Für die Berechnung virtueller pristiner Karbonatbildungstemperaturen mittels der dualen Δ_{47}-*vs.*-Δ_{48}Methodik sind weitere thermodynamische Modellierungen und Experimente notwendig.

Zwei Δ_{47}-Datensätze mit insgesamt 117 Replikatanalysen an 22 pedogenen Karbonatknollen der mittelmiozänen spanischen Aufschlüsse Armantes (*Kapitel 5*) und Aragon (*Kapitel 6*) offenbaren die thermale Struktur während des endenden mittelmiozänen Klimaoptimums („Middle Miocene Climatic Optimum“; MCO) und des kompletten mittelmiozänen Klimawechsels („Middle Miocene Climatic Transition“; MMCT; 15,33 bis 12,98 Ma) im südlichen Kontinentaleuropa. Die Ergebnisse sind konsistent mit den Studienergebnissen zu marinen Meeresoberflächentemperaturen (*z.B.* Super *et al.*, 2020), marinen $\delta^{13}C$-und $\delta^{18}O$-Isotopenwerten (*z.B.* Holbourn *et al.*, 2014), und paläontologischen Studien (*z.B.* Böhme, 2003; Hernández Fernández *et al.*, 2006; van Dam *et al.*, 2006). Es wird gezeigt, dass das kontinentale Klima während der MMCT durch deutliche Temperaturfluktuationen charakterisiert war. Die südeuropäische MMCT zeichnete sich durch folgende Merkmale aus: *i*) Ein kurzfristiger Abkühlungsimpuls bei 14,18 Ma (auf 16 ± 3 °C; *ca.* Mi3a; Abels *et al.*, 2005), gefolgt von *ii*) einem Zurückschwingen der Temperaturen zu warmen Werten (39 ± 6 °C bei 14,07 Ma), *iii*) eine kontinuierliche Abkühlung zwischen 14,07 und 13,49 Ma von 39 zu 18 °C (Mittelpunkt: 13,94; *ca.* Mi3b; Abels *et al.*, 2005), und *iv*) einen letzten warmen Ausschlag von 28 ± 5 °C bei 13,42 Ma – ein Ereignis, das zeitgleich mit erhöhtem globalem Eisvolumen auftritt (Shevenell *et al.*, 2004). Die Daten ergeben insgesamt eine statistische Abkühlung von 12 °C über die komplette MMCT (14,53 ± 0,41 bis 12,88 ± 0.38; Mudelsee *et al.*, 2014; DSDP 608).

Als Ergebnis der Übereinstimmung der südeuropäischen Daten mit kürzlich veröffentlichten MMCT-Bodentemperaturen aus dem Nordalpinen Vorlandbecken (Methner *et al.*, 2020) und dem marinen Temperaturarchiv des proximalen DSDP 608 (Super *et al.*, 2020) kann unter Berücksichtigung der derzeitigen zeitlichen Auflösung der Proben festgehalten werden, dass der Klimawechsel im Mittleren Miozän (MMCT) in Südeuropa, Zentraleuropa und dem Nordatlantik synchron erfolgte. Gleichzeitig abnehmende südeuropäische Sedimentationsraten, Bodentemperaturen, und Bodenwasser-$\delta^{18}O_{H2O}$ (Armantes und Aragon) implizieren eine kontinentale Abkühlung und Zunahme der Aridität zwischen 14,07 und 13,81 Ma. Auffälliger Weise korrelieren die südeuropäischen Abkühlungsereignisse (bei *ca.* Mi3a und Mi3b) mit erhöhten Fluktuationen der zentralspanischen Vergesellschaftung von Säugetieren (van Dam *et al.*, 2006). Daher kann geschlussfolgert werden, dass eine erhöhte Klimadynamik während des MMCT die Reorganisation von Faunenvergesellschaftungen begünstigte. Die Variabilität der berechneten Bodenwasser-δO_{H2O} und Bodentemperaturen dokumentiert zusätzlich eine mögliche Variation der Saisonalität der pedogenen Karbonatbildung während des MMCT. Die Amplitude dieser Änderungen ist vergleichbar mit der modernen Spannbreite von jährlichen Umgebungstemperaturen und Niederschlags-$\delta^{18}O_{H2O}$ (JJA-DJF; Rodríguez-Arévalo *et al.*, 2011), sowie mit mittelmiozänen Säugetier-$\delta^{18}O_{PO4}$ (Domingo *et al.*, 2009).

Aufgrund der im Vergleich zu Modelldaten von mittelmiozänen Luft- und Bodentemperaturen (Zhou *et al.*, 2018) teilweise erhöhten Bodentemperaturen (Armantes), könnte die genauere Untersuchung eines möglichen saisonalen Bias der in den pedogenen Karbonaten dokumentierten Bodentemperaturen ein erstrebenswertes Forschungsziel für weitere wissenschaftliche Studien sein. Moderne Niederschlags-$\delta^{18}O_{H2O}$-Werte und -Umgebungstemperaturen veranschaulichen, dass die Spannbreite der gemessenen MMCT-$\delta^{18}O_{H2O}$ und -Bodentemperaturen potentiell durch saisonale Variabilität erklärt werden könnten. Abschließend kann festgestellt werden, dass das Klima während des MMCT hochdynamisch war – vor allem im Vergleich mit den überwiegend stabilen und warmen Bedingungen des MCO.

10 References

Abels, H. A., Hilgen, F. J., Krijgsman, W., Kruk, R. W., Raffi, I., Turco, E., & Zachariasse, W. J. (2005). Long-period orbital control on middle Miocene global cooling: Integrated stratigraphy and astronomical tuning of the Blue Clay Formation on Malta. *Paleoceanography*, *20*(4). https://doi.org/10.1029/2004pa001129

Agassiz, L. (1833). *Recherches sur les poissons fossiles.* Petitpierre. https://doi.org/10.5962/bhl.title.4275

Ahne, W. (2000). *Zoologie: Lehrbuch für Studierende der Veterinärmedizin und Agrarwissenschaften*. Schattauer.

Alonso-Zarza, A. M., Genise, J. F., & Verde, M. (2014). Paleoenvironments and ichnotaxonomy of insect trace fossils in continental mudflat deposits of the Miocene Calatayud–Daroca Basin, Zaragoza, Spain. *Palaeogeography, Palaeoclimatology, Palaeoecology*, *414*, 342–351. https://doi.org/10.1016/j.palaeo.2014.09.012

American Psychological Association. (2019). *Publication Manual of the American Psychological Association, Seventh Edition* (Seventh edition). American Psychological Association.

Amiot, R., Göhlich, U. B., Lécuyer, C., Muizon, C. de, Cappetta, H., Fourel, F., Héran, M. ‐A., & Martineau, F. (2008). Oxygen isotope compositions of phosphate from Middle Miocene–Early Pliocene marine vertebrates of Peru. *Palaeogeography, Palaeoclimatology, Palaeoecology*, *264*(1-2), 85–92. https://doi.org/10.1016/j.palaeo.2008.04.001

Amiot, R., Lécuyer, C., Buffetaut, E., Escarguel, G., Fluteau, F., & Martineau, F. (2006). Oxygen isotopes from biogenic apatites suggest widespread endothermy in Cretaceous dinosaurs. *Earth and Planetary Science Letters*, *246*(1-2), 41–54. https://doi.org/10.1016/j.epsl.2006.04.018

Antonakos, A., Liarokapis, E., & Leventouri, T. (2007). Micro-Raman and FTIR studies of synthetic and natural apatites. *Biomaterials*, *28*(19), 3043–3054. https://doi.org/10.1016/j.biomaterials.2007.02.028

Antunes, M. T. (1994). On Western Europe Miocene gavials (Crocodylia) their paleogeography, migrations and climatic significance. *Comun. Inst. Geol. E Mineiro*, *80*, 57–69.

Asara, J. M., Schweitzer, M. H., Freimark, L. M., Phillips, M., & Cantley, L. C. (2007). Protein sequences from mastodon and *Tyrannosaurus rex* revealed by mass spectrometry. *Science*, *316*(5822), 280–285. https://doi.org/10.1126/science.1137614

Aufort, J., Ségalen, L., Gervais, C., Paulatto, L., Blanchard, M., & Balan, E. (2017). Site-specific equilibrium isotopic fractionation of oxygen, carbon and calcium in apatite. *Geochimica Et Cosmochimica Acta*, *219*, 57–73. https://doi.org/10.1016/j.gca.2017.09.020

Awonusi, A., Morris, M. D., & Tecklenburg, M. M. J. (2007). Carbonate assignment and calibration in the Raman spectrum of apatite. *Calcified Tissue International*, *81*(1), 46–52. https://doi.org/10.1007/s00223-007-9034-0

Ayliffe, L. K., Lister, A. M., & Chivas, A. R. (1992). The preservation of glacial-interglacial climatic signatures in the oxygen isotopes of elephant skeletal phosphate. *Palaeogeography, Palaeoclimatology, Palaeoecology*, *99*(3-4), 179–191. https://doi.org/10.1016/0031-0182(92)90014-V

Bajnai, D., Fiebig, J., Tomašových, A., Milner Garcia, S., Rollion-Bard, C., Raddatz, J., Löffler, N., Primo-Ramos, C., & Brand, U. (2018). Assessing kinetic fractionation in brachiopod calcite using clumped isotopes. *Scientific Reports*, *8*(1), 533. https://doi.org/10.1038/s41598-017-17353-7

Bajnai, D., Guo, W., Spötl, C., Coplen, T. B., Methner, K., Löffler, N., Krsnik, E., Gischler, E., Hansen, M., Henkel, D., Price, G. D., Raddatz, J., Scholz, D., & Fiebig, J. (2020). Dual clumped isotope thermometry resolves kinetic biases in carbonate formation temperatures. *Nature Communications*, *11*(1). https://doi.org/10.1038/s41467-020-17501-0

Barrick, R. E., & Showers, W. J. (1994). Thermophysiology of *Tyrannosaurus rex*: Evidence from Oxygen Isotopes. *Science (New York, N.Y.)*, *265*(5169), 222–224. https://doi.org/10.1126/science.265.5169.222

Bates, B., Kundzewicz, Z., & Wu, S. (2008). *Climate change and water* ([DesLibris e-book]). *IPCC technical paper: VI*. Intergovernmental Panel on Climate Change; Canadian Electronic Library. http://www.taccire.suanet.ac.tz:8080/xmlui/handle/123456789/552

Beck, W. C., Grossman, E. L., & Morse, J. W. (2005). Experimental studies of oxygen isotope fractionation in the carbonic acid system at 15°, 25°, and 40°C. *Geochimica Et Cosmochimica Acta*, *69*(14), 3493–3503. https://doi.org/10.1016/j.gca.2005.02.003

Bédard, P., Hillaire-Marcel, C., & Pagé, P. (1981). ^{18}O modelling of freshwater inputs in Baffin Bay and Canadian Arctic coastal waters. *Nature*, *293*(5830), 287–289. https://doi.org/10.1038/293287a0

Bergmann, K. D., Finnegan, S., Creel, R., Eiler, J. M., Hughes, N. C., Popov, L. E., & Fischer, W. W. (2018). A paired apatite and calcite clumped isotope thermometry approach to estimating Cambro-Ordovician seawater temperatures and isotopic composition. *Geochimica Et Cosmochimica Acta*, *224*, 18–41. https://doi.org/10.1016/j.gca.2017.11.015

Berkovitz, B. K. (2000). Tooth replacement patterns in non-mammalian vertebrates. In M. F. Teaford, M. M. Smith, & M. W. J. Ferguson (Eds.), *Development, function, and evolution of teeth* (pp. 186–200). Cambridge University Press. https://doi.org/10.1017/CBO9780511542626.013

Bernal, D., Smith, D., Lopez, G., Weitz, D., Grimminger, T., Dickson, K., & Graham, J. B. (2003). Comparative studies of high performance swimming in sharks II. Metabolic biochemistry of locomotor and myocardial muscle in endothermic and ectothermic sharks. *The Journal of Experimental Biology*, *206*(16), 2845–2857. https://doi.org/10.1242/jeb.00504

Bernard, A., Lécuyer, C., Vincent, P., Amiot, R., Bardet, N., Buffetaut, E., Cuny, G., Fourel, F., Martineau, F., Mazin, J.‐M., & Prieur, A. (2010). Regulation of body temperature by some Mesozoic marine reptiles. *Science*, *328*(5984), 1379–1382. https://doi.org/10.1126/science.1187443

Bernasconi, S. M., Hu, B., Wacker, U., Fiebig, J., Breitenbach, S. F. M., & Rutz, T. (2013). Background effects on Faraday collectors in gas-source mass spectrometry and implications for clumped isotope measurements. *Rapid Communications in Mass Spectrometry: RCM*, *27*(5), 603–612. https://doi.org/10.1002/rcm.6490

Bernasconi, S. M., Müller, I. A., Bergmann, K. D., Breitenbach, S. F. M., Fernandez, A. B., Hodell, D. A., Jaggi, M., Meckler, A. N., Millan, I. M., & Ziegler, M. (2018). Reducing Uncertainties in Carbonate Clumped Isotope Analysis Through Consistent Carbonate-Based Standardization. *Geochemistry, Geophysics, Geosystems*, *19*(9), 2895–2914. https://doi.org/10.1029/2017gc007385

Blatteis, C. M. (2014). A first-hand account by the international participants of the past 75 years' advancements in thermophysiology is forthcoming. *Temperature*, *1*(1), 30–31. https://doi.org/10.4161/temp.29598

Bligh, J., & Johnson, K. G. (1973). Glossary of terms for thermal physiology. *Journal of Applied Physiology*, *35*(6), 941–961. https://doi.org/10.1152/jappl.1973.35.6.941

Böhme, M. (2003). The Miocene Climatic Optimum: Evidence from ectothermic vertebrates of Central Europe. *Palaeogeography, Palaeoclimatology, Palaeoecology*, *195*(3-4), 389–401. https://doi.org/10.1016/s0031-0182(03)00367-5

Böhme, M., Winklhofer, M., & Ilg, A. (2011). Miocene precipitation in Europe: Temporal trends and spatial gradients. *Palaeogeography, Palaeoclimatology, Palaeoecology*, *304*(3-4), 212–218. https://doi.org/10.1016/j.palaeo.2010.09.028

Bonifacie, M., Calmels, D., Eiler, J. M., Horita, J., Chaduteau, C., Vasconcelos, C., Agrinier, P., Katz, A., Passey, B. H., Ferry, J. M., & Bourrand, J.‐J. (2017). Calibration of the dolomite clumped isotope thermometer from 25 to 350 °C, and implications for a universal calibration for all (Ca, Mg, Fe)CO_3 carbonates. *Geochimica Et Cosmochimica Acta*, *200*, 255–279. https://doi.org/10.1016/j.gca.2016.11.028

Boskey, A. L. (2007). Mineralization of Bones and Teeth. *Elements*, *3*(6), 385–391. https://doi.org/10.2113/GSELEMENTS.3.6.385

Bötcher, M. E. (2000). Stable Isotope Fractionation during Experimental Formation of Norsethite ($BaMg[CO_3]_2$): A Mineral Analogue of Dolomite. *Aquatic Geochemistry*, *6*(2), 201–212. https://doi.org/10.1023/A:1009646805933

Botella, H., Donoghue, P. C. J., & Martínez-Pérez, C. (2009). Enameloid microstructure in the oldest known chondrichthyan teeth. *Acta Zoologica*, *90*(3A), 103–108. https://doi.org/10.1111/j.1463-6395.2008.00337.x

Böttcher, M. E, Neubert, N., Allmen, K. von, Samankassou, E., & Nägler, T. F. (2018). Barium isotope fractionation during the experimental transformation of aragonite to witherite and of gypsum to barite, and the effect of ion (de)solvation. *Isotopes in Environmental and Health Studies*, *54*(3), 324–335. https://doi.org/10.1080/10256016.2018.1430692.

Bradbury, H. J., Vandeginste, V., & John, C. M. (2015). Diagenesis of phosphatic hardgrounds in the Monterey Formation: A perspective from bulk and clumped isotope geochemistry. *Geological Society of America Bulletin*, *127*(9-10), 1453–1463. https://doi.org/10.1130/B31160.1

Breecker, D. O., Sharp, Z. D., & McFadden, L. D. (2009). Seasonal bias in the formation and stable isotopic composition of pedogenic carbonate in modern soils from central New Mexico, USA.

Geological Society of America Bulletin, *121*(3-4), 630–640. https://doi.org/10.1130/b26413.1

Bristow, T. F., Bonifacie, M., Derkowski, A., Eiler, J. M., & Grotzinger, J. P. (2011). A hydrothermal origin for isotopically anomalous cap dolostone cements from south China. *Nature*, *474*(7349), 68–71. https://doi.org/10.1038/nature10096

Brochu, C. A. (2003). Osteology of *Tyrannosaurus rex*: Insights from a nearly complete Skeleton and High-Resolution Computed Tomographic Analysis of the Skull. *Journal of Vertebrate Paleontology*, *22*(sup4), 1–138. https://doi.org/10.1080/02724634.2003.10010947

Bruch, A. A., Uhl, D., & Mosbrugger, V. (2007). Miocene climate in Europe — Patterns and evolution. *Palaeogeography, Palaeoclimatology, Palaeoecology*, *253*(1-2), 1–7. https://doi.org/10.1016/j.palaeo.2007.03.030

Bruijn, H. de. (1965). *Miocene Gliridae, Sciuridae and Eomydae (Rodentia, Mammalia from the Calatayud area, prov Zaragoza, Spain) and their bearing on the biostratigraphy* [Ph.D.]. Utrecht University, Utrecht, the Netherlands.

Bryant, D. J., & Froelich, P. N. (1995). A model of oxygen isotope fractionation in body water of large mammals. *Geochimica Et Cosmochimica Acta*, *59*(21), 4523–4537. https://doi.org/10.1016/0016-7037(95)00250-4

Bryant, D. J., Koch, P. L., Froelich, P. N., Showers, W. J., & Genna, B. J. (1996). Oxygen isotope partitioning between phosphate and carbonate in mammalian apatite. *Geochimica Et Cosmochimica Acta*, *60*(24), 5145–5148. https://doi.org/10.1016/s0016-7037(96)00308-0

Burnett, W. C. (1977). Geochemistry and origin of phosphorite deposits from off Peru and Chile. *Geological Society of America Bulletin*, *88*(6), 813. https://doi.org/10.1130/0016-7606(1977)88<813:GAOOPD>2.0.CO;2

Bushnell, P. G., Lutz, P. L., Steffensen, J. F., Oikari, A., & Gruber, S. H. (1982). Increases in arterial blood oxygen during exercise in the lemon shark (*Negaprion brevirostris*). *Journal of Comparative Physiology*, *147*(1), 41–47. https://doi.org/10.1007/BF00689288

Cappetta, H., Schultze, H.‐P., & Kuhn, O. (2012). *Mesozoic and cenozoic elasmobranchii: Teeth*. *Handbook of paleoichthyology Chondrichthyes: Vol. 5*. Pfeil. http://pfeil-verlag.de/07pala/d4_48d.php

Cappetta H. (1987). *Handbook of Paleoichthyology. Chondrichthys II: Mesozoic and Cenozoic Elasmobranchii.*

Carpenter, K. (1998). Evidence of predatory behavior by carnivorous dinosaurs. *Gaia*, *15*, 135.

Cerling, T. E. (1984). The stable isotopic composition of modern soil carbonate and its relationship to climate. *Earth and Planetary Science Letters*, *71*(2), 229–240. https://doi.org/10.1016/0012-821X(84)90089-X

Cerling, T. E., & Quade, J. (1993). Stable Carbon and Oxygen Isotopes in Soil Carbonates. In P. K. Swart (Ed.), *Geophysical monograph: Vol. 78. Climate change in continental isotopic records* (pp. 217–231). American Geophysical Union. https://doi.org/10.1029/gm078p0217

Cerling, T. E., Solomon, D.K., Quade, J., & Bowman, J. R. (1991). On the isotopic composition of carbon in soil carbon dioxide. *Geochimica Et Cosmochimica Acta*, *55*(11), 3403–3405. https://doi.org/10.1016/0016-7037(91)90498-T

Chevalier-Skolnikoff, S., & Liska, J. (1993). Tool use by wild and captive elephants. *Animal Behaviour*, *46*(2), 209–219. https://doi.org/10.1006/anbe.1993.1183

Chin Lai, N., Graham J. B., & Burnett, L. (1990). Blood Respiratory Properties and the Effect of Swimming on Blood Gas Transport in the Leopard Shark *Triakis semifasciata*. *Journal of Experimental Biology*, *151*(1), 161–173. https://jeb.biologists.org/content/151/1/161.short

Christiansen, P., & Fariña, R. A. (2004). Mass Prediction in Theropod Dinosaurs. *Historical Biology*, *16*(2-4), 85–92. https://doi.org/10.1080/08912960412331284313

Clarke, A., & Rothery, P. (2008). Scaling of body temperature in mammals and birds. *Funct. Ecol.*, *22*, 58–67. doi:10.1111/j.1365-2435.2007.01341.x

Compagno, L. J. V. (2001). *Bullhead, mackerel and carpet sharks: (heterodontiformes, lamniformes and orectolobiformes)*. *FAO species catalogue for fishery purposes: Vol. 1*. Food and Agriculture Organization of the United Nations.

Compton, J. S., & Bergh, E. W. (2016). Phosphorite deposits on the Namibian shelf. *Marine Geology*, *380*, 290–314. https://doi.org/10.1016/j.margeo.2016.04.006

Coplen, T. B. (2007). Calibration of the calcite–water oxygen-isotope geothermometer at Devils Hole, Nevada, a natural laboratory. *Geochimica Et Cosmochimica Acta*, *71*(16), 3948–3957. https://doi.org/10.1016/j.gca.2007.05.028

Cuevas González, J. (2005). Estado actual de los conocimientos paleontológicos y estratigráficos de los yacimientos aragonienses de Somosaguas (Pozuelo de Alarcón, Madrid). *Coloquios De*

Paleontología, *55*, 103–123. https://revistas.ucm.es/index.php/copa/article/download/copa0505110103a/29052

Daëron, M., Blamart, D., Peral, M., & Affek, H. P. (2016). Absolute isotopic abundance ratios and the accuracy of Δ_{47} measurements. *Chemical Geology*, *442*, 83–96. https://doi.org/10.1016/j.chemgeo.2016.08.014

Daëron, M., Drysdale, R. N., Peral, M., Huyghe, D., Blamart, D., Coplen, T. B., Lartaud, F., & Zanchetta, G. (2019). Most Earth-surface calcites precipitate out of isotopic equilibrium. *Nature Communications*, *10*(1), 429. https://doi.org/10.1038/s41467-019-08336-5

Dana Joseph Ehret. (2010). *Paleobiology and taxonomy of extinct lamnid and otodontid sharks (Chondrichthyes, Elasmobranchii, Lamniformes): A dissertation presented to the graduate school of the University of Florida in partial fulfillment of the requirements for the degree of doctor of philosophy* [Ph.D. thesis], University of Florida.

Davidson, A. (1983). *Food in motion: The migration of foodstuffs and cookery techniques: proceedings : Oxford symposium 1983*. Prospect Books.

Davidson, G. R. (1995). The stable isotopic composition and measurement of carbon in soil CO_2. *Geochimica Et Cosmochimica Acta*, *59*(12), 2485–2489. https://doi.org/10.1016/0016-7037(95)00143-3

Davit-Béal, T., Chisaka, H., Delgado, S., & Sire, J.-Y. (2007). Amphibian teeth: Current knowledge, unanswered questions, and some directions for future research. *Biological Reviews of the Cambridge Philosophical Society*, *82*(1), 49–81. https://doi.org/10.1111/j.1469-185X.2006.00003.x

Dawson, R. R., Field, D. J., Hull, P. M., Zelenitsky, D. K., Therrien, F., & Affek, H. P. (2020). Eggshell geochemistry reveals ancestral metabolic thermoregulation in Dinosauria. *Science Advances*, *6*(7), eaax9361. https://doi.org/10.1126/sciadv.aax9361

Defliese, W. F., Hren, M. T., & Lohmann, K. C. (2015). Compositional and temperature effects of phosphoric acid fractionation on Δ_{47} analysis and implications for discrepant calibrations. *Chemical Geology*, *396*, 51–60. https://doi.org/10.1016/j.chemgeo.2014.12.018

Defliese, W. F., & Lohmann, K. C. (2015). Non-linear mixing effects on mass-47 CO_2 clumped isotope thermometry: Patterns and implications. *Rapid Communications in Mass Spectrometry : RCM*, *29*(9), 901–909. https://doi.org/10.1002/rcm.7175

Dennis, K. J., Affek, H. P., Passey, B. H., Schrag, D. P., & Eiler, J. M. (2011). Defining an absolute reference frame for 'clumped' isotope studies of CO_2. *Geochimica Et Cosmochimica Acta*, *75*(22), 7117–7131. https://doi.org/10.1016/j.gca.2011.09.025

Dennis, K. J., & Schrag, D. P. (2010). Clumped isotope thermometry of carbonatites as an indicator of diagenetic alteration. *Geochimica Et Cosmochimica Acta*, *74*(14), 4110–4122. https://doi.org/10.1016/j.gca.2010.04.005

DePalma, R. A., Burnham, D. A., Martin, L. D., Rothschild, B. M., & Larson, P. L. (2013). Physical evidence of predatory behavior in *Tyrannosaurus rex*. *Proceedings of the National Academy of Sciences*, *110*(31), 12560–12564. https://doi.org/10.1073/pnas.1216534110

DePaolo, D. J. (2011). Surface kinetic model for isotopic and trace element fractionation during precipitation of calcite from aqueous solutions. *Geochimica Et Cosmochimica Acta*, *75*(4), 1039–1056. https://doi.org/10.1016/j.gca.2010.11.020

Dettman, D. L., & Lohmann, K. C. (2000). Oxygen isotope evidence for high-altitude snow in the Laramide Rocky Mountains of North America during the Late Cretaceous and Paleogene. *Geology*, *28*(3), 243. https://doi.org/10.1130/0091-7613(2000)28<243:OIEFHS>2.0.CO;2

deVries, D. R. (2016). *T.rex Trix in Naturalis*. Naturalis; Leopold.

Dewar, H., Domeier, M., & Nasby-Lucas, N. (2004). Insights into Young of the Year White Shark, Carcharodon carcharias, Behavior in the Southern California Bight. *Environmental Biology of Fishes*, *70*(2), 133–143. https://doi.org/10.1023/B:EBFI.0000029343.54027.6a

Domingo, L., Cuevas-González, J., Grimes, S. T., Hernández Fernández, M., & López-Martínez, N. (2009). Multiproxy reconstruction of the palaeoclimate and palaeoenvironment of the Middle Miocene Somosaguas site (Madrid, Spain) using herbivore dental enamel. *Palaeogeography, Palaeoclimatology, Palaeoecology*, *272*(1-2), 53–68. https://doi.org/10.1016/j.palaeo.2008.11.006

Dorozhkin, S. V., & Epple, M. (2002). Biological and Medical Significance of Calcium Phosphates. *Angewandte Chemie International Edition*, *41*(17), 3130–3146. https://doi.org/10.1002/1521-3773(20020902)41:17<3130::AID-ANIE3130>3.0.CO;2-1

Eagle, R. A., Enriquez, M., Grellet-Tinner, G., Pérez-Huerta, A., Hu, D., Tütken, T., Montanari, S., Loyd, S. J., Ramirez, P., Tripati, A. K., Kohn, M. J., Cerling, T. E., Chiappe, L. M., & Eiler, J. M. (2015). Isotopic ordering in eggshells

reflects body temperatures and suggests differing thermophysiology in two Cretaceous dinosaurs. *Nature Communications*, *6*(1), 8296. https://doi.org/10.1038/ncomms9296

Eagle, R. A., Schauble, E. A., Tripati, A. K., Tütken, T., Hulbert, R. C., & Eiler, J. M. (2010). Body temperatures of modern and extinct vertebrates from ^{13}C-^{18}O bond abundances in bioapatite. *Proceedings of the National Academy of Sciences of the United States of America*, *107*(23), 10377–10382. https://doi.org/10.1073/pnas.0911115107

Eagle, R. A., Tütken, T., Martin, T. S., Tripati, A. K., Fricke, H. C., Connely, M., Cifelli, R. L., & Eiler, J. M. (2011). Dinosaur body temperatures determined from isotopic (^{13}C-^{18}O) ordering in fossil biominerals. *Science (New York, N.Y.)*, *333*(6041), 443–445. https://doi.org/10.1126/science.1206196

Eiler, J. M. (2007). "Clumped-isotope" geochemistry—The study of naturally-occurring, multiply-substituted isotopologues. *Earth and Planetary Science Letters*, *262*(3-4), 309–327. https://doi.org/10.1016/j.epsl.2007.08.020

Eiler, J. M. (2011). Paleoclimate reconstruction using carbonate clumped isotope thermometry. *Quaternary Science Reviews*, *30*(25-26), 3575–3588. https://doi.org/10.1016/j.quascirev.2011.09.001

Eiler, J. M., & Schauble, E. (2004). 18o13c16o in Earth's atmosphere. *Geochimica Et Cosmochimica Acta*, *68*(23), 4767–4777. https://doi.org/10.1016/j.gca.2004.05.035

Elder, W. H., & Rodgers, D. H. (1975). Body temperature in the African elephant as related to ambient temperature. *Mammalia*, *39*(3). https://doi.org/10.1515/mamm.1975.39.3.395

Elliott, J. C. (Ed.). (1994). *Structure and chemistry of the apatites and other calcium orthophosphates*. Elsevier.

Enax, J., Prymak, O., Raabe, D., & Epple, M. (2012). Structure, composition, and mechanical properties of shark teeth. *Journal of Structural Biology*, *178*(3), 290–299. https://doi.org/10.1016/j.jsb.2012.03.012

Epstein, S., Buchsbaum, R., Lowenstam, H. A., & Urey, H. C. (1953). Revised carbonate-water isotopic temperature scale. *Geological Society of America Bulletin*, *64*(11), 1315. https://doi.org/10.1130/0016-7606(1953)64[1315:RCITS]2.0.CO;2

Erdsack, N., Hanke, F. D., Dehnhardt, G., & Hanke, W. (2012). Control and amount of heat dissipation through thermal windows in harbor seals (*Phoca vitulina*). *Journal of Thermal Biology*, *37*(7), 537–544. https://doi.org/10.1016/j.jtherbio.2012.06.002

Erickson, G. M., Makovicky, P. J., Currie, P. J., Norell, M. A., Yerby, S. A., & Brochu, C. A. (2004). Gigantism and comparative life-history parameters of tyrannosaurid dinosaurs. *Nature*, *430*(7001), 772–775. https://doi.org/10.1038/nature02699

Farlow, J. O., Dodson, P., & Chinsamy, A. (1995). Dinosaur Biology. *Annual Review of Ecology and Systematics*, *26*(1), 445–471. https://doi.org/10.1146/annurev.es.26.110195.002305

Fauquette, S., Guiot, J., & Suc, J.‐P. (1998). A method for climatic reconstruction of the Mediterranean Pliocene using pollen data. *Palaeogeography, Palaeoclimatology, Palaeoecology*, *144*(1-2), 183–201. https://doi.org/10.1016/s0031-0182(98)00083-2

Feranec, R. S., & MacFadden, B. J. (2000). Evolution of the grazing niche in Pleistocene mammals from Florida: evidence from stable isotopes. *Palaeogeography, Palaeoclimatology, Palaeoecology*, *162*(1-2), 155–169. https://doi.org/10.1016/S0031-0182(00)00110-3

Fernandez, A. B., Müller, I. A., Rodríguez-Sanz, L., van Dijk, J., Looser, N., & Bernasconi, S. M. (2017). A Reassessment of the Precision of Carbonate Clumped Isotope Measurements: Implications for Calibrations and Paleoclimate Reconstructions. *Geochemistry, Geophysics, Geosystems*, *18*(12), 4375–4386. https://doi.org/10.1002/2017gc007106

Fernandez, A. B., Tang, J., & Rosenheim, B. E. (2014). Siderite 'clumped' isotope thermometry: A new paleoclimate proxy for humid continental environments. *Geochimica Et Cosmochimica Acta*, *126*, 411–421. https://doi.org/10.1016/j.gca.2013.11.006

Ferrón, H. G. (2017). Regional endothermy as a trigger for gigantism in some extinct macropredatory sharks. *PloS One*, *12*(9), e0185185. https://doi.org/10.1371/journal.pone.0185185

Fiebig, J., Bajnai, D., Löffler, N., Methner, K., Krsnik, E., Mulch, A., & Hofmann, S. (2019). Combined high-precision Δ_{48} and Δ_{47} analysis of carbonates. *Chemical Geology*, *522*, 186–191. https://doi.org/10.1016/j.chemgeo.2019.05.019

Fiebig, J., Hofmann, S., Löffler, N., Lüdecke, T., Methner, K., & Wacker, U. (2016). Slight pressure imbalances can affect accuracy and precision of dual inlet-based clumped isotope analysis. *Isotopes in Environmental and Health*

Studies, *52*(1-2), 12–28. https://doi.org/10.1080/10256016.2015.1010531

Filippelli, G. M. (2002). The Global Phosphorus Cycle. *Reviews in Mineralogy and Geochemistry*, *48*(1), 391–425. https://doi.org/10.2138/rmg.2002.48.10

Fincham, A. G., Moradian-Oldak, J., & Simmer, J. P. (1999). The structural biology of the developing dental enamel matrix. *Journal of Structural Biology*, *126*(3), 270–299. https://doi.org/10.1006/jsbi.1999.4130

Fisk, A. T., Tittlermier, S. A., Pranschke J. L., & Norstrom R. J (2002). Using anthropogenic contaminants and stable isotopes to assess the feeding ecology of Greenland shark. *Ecology*, *83*, 2162–2172. http://www.jstor.org/stable/3072048

Fleet, M. E. (2015). *Carbonated hydroxyapatite: Materials, synthetis, and applications*. Pan Stanford Publishing.

Fleet, M. E., Liu, X., & King, P. L. (2004). Accommodation of the carbonate ion in apatite: An FTIR and X-ray structure study of crystals synthesized at 2–4 GPa. *American Mineralogist*, *89*(10), 1422–1432. https://doi.org/10.2138/am-2004-1009

Flower, B. P., & Kennett, J. P. (1994). The middle Miocene climatic transition: East Antarctic ice sheet development, deep ocean circulation and global carbon cycling. *Palaeogeography, Palaeoclimatology, Palaeoecology*, *108*(3-4), 537–555. https://doi.org/10.1016/0031-0182(94)90251-8

Fricke, H. C., Foreman, B. Z., & Sewall, J. O. (2010). Integrated climate model-oxygen isotope evidence for a North American monsoon during the Late Cretaceous. *Earth and Planetary Science Letters*, *289*(1-2), 11–21. https://doi.org/10.1016/j.epsl.2009.10.018

Fricke, H. C., & Pearson, D. A. (2008). Stable isotope evidence for changes in dietary niche partitioning among hadrosaurian and ceratopsian dinosaurs of the Hell Creek Formation, North Dakota. *Paleobiology*, *34*(4), 534–552. https://doi.org/10.1666/08020.1

Gagge, A. P., Winslow, C.‐E. A., & Herrington, L. P. (1938). The influence of clothing on the physiological reactions of the human body to varying environmental temperatures. *American Journal of Physiology-Legacy Content*, *124*(1), 30–50. https://doi.org/10.1152/ajplegacy.1938.124.1.30

Gallagher, A. J., Frick, L. H., Bushnell, P. G., Brill, R. W., & Mandelman, J. W. (2010). Blood gas, oxygen saturation, pH, and lactate values in elasmobranch blood measured with a commercially available portable clinical analyzer and standard laboratory instruments. *Journal of Aquatic Animal Health*, *22*(4), 229–234. https://doi.org/10.1577/H10-012.1

García del Real, P., Kluge, T., Bird, D. K., Brown, G. E., & John, C. M. (2016). Clumped-isotope thermometry of magnesium carbonates in ultramafic rocks. *Geochimica Et Cosmochimica Acta*, *193*, 222–250. https://doi.org/10.1016/j.gca.2016.08.003

Gehler, A., Gingerich, P. D., & Pack, A. (2016). Temperature and atmospheric CO_2 concentration estimates through the PETM using triple oxygen isotope analysis of mammalian bioapatite. *Proceedings of the National Academy of Sciences*, *113*(28), 7739–7744. https://doi.org/10.1073/pnas.1518116113

Gehler, A., Tütken, T., & Pack, A. (2012). Oxygen and carbon isotope variations in a modern rodent community - implications for palaeoenvironmental reconstructions. *PloS One*, *7*(11), e49531. https://doi.org/10.1371/journal.pone.0049531

Ghosh, P., Adkins, J., Affek, H. P., Balta, B., Guo, W., Schauble, E. A., Schrag, D. P., & Eiler, J. M. (2006). $^{13}C–^{18}O$ bonds in carbonate minerals: A new kind of paleothermometer. *Geochimica Et Cosmochimica Acta*, *70*(6), 1439–1456. https://doi.org/10.1016/j.gca.2005.11.014

Gile, L. H., Peterson, F. F., & Grossman, R. B. (1966). Morphological and genetic sequences of carbonate accumulation in desert soils. *Soil Science*, *101*(5), 347. https://journals.lww.com/soilsci/citation/1966/05000/morphological_and_genetic_sequences_of_carbonate.1.aspx

Gillooly, J. F., Allen, A. P., & Charnov, E. L. (2006). Dinosaur fossils predict body temperatures. *PLoS Biology*, *4*(8), e248. https://doi.org/10.1371/journal.pbio.0040248

Goldner, A., Herold, N., & Huber, M. (2014). The challenge of simulating the warmth of the mid-Miocene climatic optimum in CESM1. *Climate of the Past*, *10*(2), 523–536. https://doi.org/10.5194/cp-10-523-2014

Gottfried, M. D., Compagno, L. J. V., & Bowman, S. C. (1996). *Size and Skeletal Anatomy of the Giant "Megatooth" Shark Carcharodon megalodon* (Great White Sharks). Elsevier. http://dx.doi.org/10.1016/B978-012415031-7/50008-2

Gradstein, F. M. (2012). *The geologic time scale 2012. Volume 2* (The Geologic Time Scale). Elsevier.

Grady, J. E. (1970). Tooth development in sharks. *Archives of Oral Biology*, *15*(7), 613-IN23. https://doi.org/10.1016/0003-9969(70)90130-5

Grady, J. M., Enquist, B. J., Dettweiler-Robinson, E., Wright Natalie A., & Smith, F. A. (2014). Dinosaur physiology. Evidence for mesothermy in dinosaurs. *Science*, *344*(6189), 1268–1272. https://doi.org/10.1126/science.1253143

Grauel, A.‐L., Schmid, T. W., Hu, B., Bergami, C., Capotondi, L., Zhou, L., & Bernasconi, S. M. (2013). Calibration and application of the 'clumped isotope' thermometer to foraminifera for high-resolution climate reconstructions. *Geochimica Et Cosmochimica Acta*, *108*, 125–140. https://doi.org/10.1016/j.gca.2012.12.049

Grellet-Tinner, G. (2006). Oology and the evolution of thermophysiology in saurischian dinosaurs: homeotherm and endotherm deinonychosaurians? *Papéis Avulsos De Zoologia (São Paulo)*, *46*(1). https://doi.org/10.1590/S0031-10492006000100001

Griebeler, E. M. (2013). Body temperatures in dinosaurs: What can growth curves tell us? *PloS One*, *8*(10), e74317. https://doi.org/10.1371/journal.pone.0074317

Guo, W. (2020). Kinetic clumped isotope fractionation in the DIC-H_2O-CO_2 system: Patterns, controls, and implications. *Geochimica Et Cosmochimica Acta*, *268*, 230–257. https://doi.org/10.1016/j.gca.2019.07.055

Guo, W., Mosenfelder, J. L., Goddard, W. A., & Eiler, J. M. (2009). Isotopic fractionations associated with phosphoric acid digestion of carbonate minerals: Insights from first-principles theoretical modeling and clumped isotope measurements. *Geochimica Et Cosmochimica Acta*, *73*(24), 7203–7225. https://doi.org/10.1016/j.gca.2009.05.071

Guo, W., & Zhou, C. (2019a). Patterns and controls of disequilibrium isotope effects in speleothems: Insights from an isotope-enabled diffusion-reaction model and implications for quantitative thermometry. *Geochimica Et Cosmochimica Acta*, *267*, 196–226. https://doi.org/10.1016/j.gca.2019.07.028

Guo, W., & Zhou, C. (2019b). *Δ48 fractionation in carbonates and its implications for clumped isotope thermometry.* 7th International Clumped Isotope workshop, Queen Mary, Long Beach, CA, U.S.A.

Haller-Probst, M. (1997). Die Verbreitung der Reptilia in den Klimazonen der Erde, *Cour. Forsch.instit. Senckenberg*(203), 1–67.

Hayes, J. P., & Garland, T. (1995). The evolution of endothermy: Testing the aerobic capacity model. *Evolution; International Journal of Organic Evolution*, *49*(5), 836–847. https://doi.org/10.1111/j.1558-5646.1995.tb02320.x

He, B., Olack, G. A., & Colman, A. S. (2012). Pressure baseline correction and high-precision CO2 clumped-isotope (Δ_{47}) measurements in bellows and micro-volume modes. *Rapid Communications in Mass Spectrometry : RCM*, *26*(24), 2837–2853. https://doi.org/10.1002/rcm.6436

Heinrichs, H., Brumsack, H.‐J., Loftfield, N., & König, N. (1986). Verbessertes Druckaufschlußsystem für biologische und anorganische Materialien. *Zeitschrift Für Pflanzenernährung Und Bodenkunde*, *149*(3), 350–353. https://doi.org/10.1002/jpln.19861490313

Henkes, G. A., Passey, B. H., Wanamaker, A. D., Grossman, E. L., Ambrose, W. G., & Carroll, M. L. (2013). Carbonate clumped isotope compositions of modern marine mollusk and brachiopod shells. *Geochimica Et Cosmochimica Acta*, *106*, 307–325. https://doi.org/10.1016/j.gca.2012.12.020

Herdendorf, C. E., & Berra, T. M. (1995). A Greenland Shark from the Wreck of the SS Central America at 2,200 Meters. *Transactions of the American Fisheries Society*, *124*(6), 950–953. https://doi.org/10.1577/1548-8659(1995)124<0950:AGSFTW>2.3.CO;2

Hernández Fernández, M., Cárdaba, J. A., Cuevas-González, J., Fesharaki, O., Salesa, M. J., Corrales, B., Domingo, L., Elez, J., López Guerrero, P., Sala-Burgos, N., Morales, J., & López Martínez, N. (2006). Los yacimientos de vertebrados del Mioceno medio de Somosaguas (Pozuelo de Alarcón, Madrid): implicaciones paleoambientales y paleoclimáticas. *1988-3250*.

Herold, R. C., Graver, H. T., & Christner, P. (1980). Immunohistochemical localization of amelogenins in enameloid of lower vertebrate teeth. *Science*, *207*(4437), 1357–1358. https://doi.org/10.1126/science.6986656

Hill, P. S., Tripati, A. K., & Schauble, E. A. (2014). Theoretical constraints on the effects of pH, salinity, and temperature on clumped isotope signatures of dissolved inorganic carbon species and precipitating carbonate minerals. *Geochimica Et Cosmochimica Acta*, *125*, 610–652. https://doi.org/10.1016/j.gca.2013.06.018

Hoefs, J. (2009). *Stable isotope geochemistry* (6. ed.). Springer. http://swbplus.bsz-bw.de/bsz284675652cov.htm

Holbourn, A. E. L., Kuhnt, W., Kochhann, K. G.D., Andersen, N., & Sebastian Meier, K. J. (2015). Global perturbation of the carbon cycle at the onset of the Miocene Climatic Optimum. *Geology*, *43*(2), 123–126. https://doi.org/10.1130/G36317.1

Holbourn, A. E. L., Kuhnt, W., Lyle, M., Schneider, L., Romero, O., & Andersen, N. (2014). Middle Miocene climate cooling linked to intensification of eastern equatorial Pacific upwelling. *Geology*, *42*(1), 19–22. https://doi.org/10.1130/G34890.1

Holbourn, A. E. L., Kuhnt, W., Schulz, M., Flores, J.‐A., & Andersen, N. (2007). Orbitally-paced climate evolution during the middle Miocene "Monterey" carbon-isotope excursion. *Earth and Planetary Science Letters*, *261*(3-4), 534–550. https://doi.org/10.1016/j.epsl.2007.07.026

Hoppe, K. A. (2004). Late Pleistocene mammoth herd structure, migration patterns, and Clovis hunting strategies inferred from isotopic analyses of multiple death assemblages. *Paleobiology*, *30*(1), 129–145. https://doi.org/10.1666/0094-8373(2004)030<0129:LPMHSM>2.0.CO;2

Hoppe, K. A., & Koch, P. L. (2007). Reconstructing the migration patterns of late Pleistocene mammals from northern Florida, USA. *Quaternary Research*, *68*(3), 347–352. https://doi.org/10.1016/j.yqres.2007.08.001

Horner, J. R., & Lessem, D. (1993). *The Complete T. rex*. Simon and Schuster.

Hough, B. G., Fan, M., & Passey, B. H. (2014). Calibration of the clumped isotope geothermometer in soil carbonate in Wyoming and Nebraska, USA: Implications for paleoelevation and paleoclimate reconstruction. *Earth and Planetary Science Letters*, *391*, 110–120. https://doi.org/10.1016/j.epsl.2014.01.008

Hudson, A. M., Quade, J., Ali, G., Boyle, D., Bassett, S., Huntington, K. W., los Santos, M. G. de, Cohen, A. S., Lin, K., & Wang, X. (2017). Stable C, O and clumped isotope systematics and ^{14}C geochronology of carbonates from the Quaternary Chewaucan closed-basin lake system, Great Basin, USA: Implications for paleoenvironmental reconstructions using carbonates. *Geochimica Et Cosmochimica Acta*, *212*, 274–302. https://doi.org/10.1016/j.gca.2017.06.024

Huntington, K. W., Budd, D. A., Wernicke, B. P., & Eiler, J. M. (2011). Use of Clumped-Isotope Thermometry To Constrain the Crystallization Temperature of Diagenetic Calcite. *Journal of Sedimentary Research*, *81*(9), 656–669. https://doi.org/10.2110/jsr.2011.51

Huntington, K. W., Eiler, J. M., Affek, H. P., Guo, W., Bonifacie, M., Yeung, L. Y., Thiagarajan, N., Passey, B. H., Tripati, A. K., Daëron, M., & Came, R. (2009). Methods and limitations of 'clumped' CO_2 isotope (Delta47) analysis by gas-source isotope ratio mass spectrometry. *Journal of Mass Spectrometry*, *44*(9), 1318–1329. https://doi.org/10.1002/jms.1614

Iacumin, P., Bocherens, H., Mariotti, A., & Longinelli, A. (1996). Oxygen isotope analyses of co-existing carbonate and phosphate in biogenic apatite: a way to monitor diagenetic alteration of bone phosphate? *Earth and Planetary Science Letters*, *142*(1-2), 1–6. https://doi.org/10.1016/0012-821X(96)00093-3

Janis, C. M., Damuth, J., & Theodor, J. M. (2002). The origins and evolution of the North American grassland biome: The story from the hoofed mammals. *Palaeogeography, Palaeoclimatology, Palaeoecology*, *177*(1-2), 183–198. https://doi.org/10.1016/s0031-0182(01)00359-5

Jiménez-Moreno, G., & Suc, J.‐P. (2007). Middle Miocene latitudinal climatic gradient in Western Europe: Evidence from pollen records. *Palaeogeography, Palaeoclimatology, Palaeoecology*, *253*(1-2), 208–225. https://doi.org/10.1016/j.palaeo.2007.03.040

John, C. M., & Bowen, D. (2016). Community software for challenging isotope analysis: First applications of 'Easotope' to clumped isotopes. *Rapid Communications in Mass Spectrometry : RCM*, *30*(21), 2285–2300. https://doi.org/10.1002/rcm.7720

Johnson, K. R. (1997). *Hell Creek Flora*. *The Encyclopedia of Dinosaurs.*

Johnson, K. R., Nichols, D. J., & Hartman, J. H. (2002). Hell Creek Formation: A 2001 synthesis. In *The Hell Creek Formation and the Cretaceous-Tertiary boundary in the northern Great Plains: An Integrated continental record of the end of the Cretaceous.* Geological Society of America. https://doi.org/10.1130/0-8137-2361-2.503

Kalnay, E., Kanamitsu, M., Kistler, R., Collins, W., Deaven, D., Gandin, L., Iredell, M., Saha, S., White, G., Woollen, J., Zhu, Y., Leetmaa, A., Reynolds, R., Chelliah, M., Ebisuzaki, W., Higgins, W., Janowiak, J., Mo, K. C., Ropelewski, C., . . . Joseph, D. (1996). The NCEP/NCAR 40-Year Reanalysis Project. *Bulletin of the American Meteorological Society*, *77*(3), 437–471. https://doi.org/10.1175/1520-0477(1996)077<0437:TNYRP>2.0.CO;2

Kasioptas, A., Geisler, T., Perdikouri, C., Trepmann, C., Gussone, N., & Putnis, A. (2011).

Polycrystalline apatite synthesized by hydrothermal replacement of calcium carbonates. *Geochimica Et Cosmochimica Acta*, *75*(12), 3486–3500. https://doi.org/10.1016/j.gca.2011.03.027

Kaskes, P. (2016). *Unearthing the background of the Naturalis Tyrannosaurus rex: taphonomy, stratigraphy and paleoenvironment* [Master Thesis]. Vrije Universiteit Amsterdam.

Keenan, S. W., & Engel, A. S. (2017). Early diagenesis and recrystallization of bone. *Geochimica Et Cosmochimica Acta*, *196*, 209–223. https://doi.org/10.1016/j.gca.2016.09.033

Kele, S., Breitenbach, S. F. M., Capezzuoli, E., Meckler, A. N., Ziegler, M., Millan, I. M., Kluge, T., Deák, J., Hanselmann, K., John, C. M., Yan, H., Liu, Z., & Bernasconi, S. M. (2015). Temperature dependence of oxygen- and clumped isotope fractionation in carbonates: A study of travertines and tufas in the 6–95°C temperature range. *Geochimica Et Cosmochimica Acta*, *168*, 172–192. https://doi.org/10.1016/j.gca.2015.06.032

Kelson, J. R., Huntington, K. W., Schauer, A. J., Saenger, C., & Lechler, A. R. (2017). Toward a universal carbonate clumped isotope calibration: Diverse synthesis and preparatory methods suggest a single temperature relationship. *Geochimica Et Cosmochimica Acta*, *197*, 104–131. https://doi.org/10.1016/j.gca.2016.10.010

Kemp, N. E. (1984). Organic Matrices and Mineral Crystallites in Vertebrate Scales, Teeth and Skeletons. *American Zoologist*, *24*(4), 965–976. https://doi.org/10.1093/icb/24.4.965

Kim, S.‐T., Mucci, A., & Taylor, B. E. (2007). Phosphoric acid fractionation factors for calcite and aragonite between 25 and 75 °C: Revisited. *Chemical Geology*, *246*(3-4), 135–146. https://doi.org/10.1016/j.chemgeo.2007.08.005

Kim, S.‐T., & O'Neil, J. R. (1997). Equilibrium and nonequilibrium oxygen isotope effects in synthetic carbonates. *Geochimica Et Cosmochimica Acta*, *61*(16), 3461–3475. https://doi.org/10.1016/S0016-7037(97)00169-5

Kinahan, A. A., Inge-moller, R., Bateman, P. W., Kotze, A., & Scantlebury, M. (2007). Body temperature daily rhythm adaptations in African savanna elephants (*Loxodonta africana*). *Physiology & Behavior*, *92*(4), 560–565. https://doi.org/10.1016/j.physbeh.2007.05.001

Klimley, A. P. (Ed.). (1996). *Great white sharks: The biology of Carcharodon carcharias*. Acad. Press.

Kluge, T., John, C. M., Jourdan, A.‐L., Davis, S., & Crawshaw, J. (2015). Laboratory calibration of the calcium carbonate clumped isotope thermometer in the 25 - 250° C temperature range. *Geochimica Et Cosmochimica Acta*, *157*, 213–227. https://doi.org/10.1016/j.gca.2015.02.028 [In Citavi anzeigen]

Koch, P. L. (2004). The effects of late Quaternary climate and pCO_2 change on C4 plant abundance in the south-central United States. *Palaeogeography, Palaeoclimatology, Palaeoecology*, *207*(3-4), 331–357. https://doi.org/10.1016/j.palaeo.2003.09.034

Kohn, M. J. (2010). Carbon isotope compositions of terrestrial C3 plants as indicators of (paleo)ecology and (paleo)climate. *Proceedings of the National Academy of Sciences*, *107*(46), 19691–19695. https://doi.org/10.1073/pnas.1004933107

Kohn, M. J., & Cerling T. E. (2002). Stable Isotope Compositions of Biological Apatite. *Reviews in Mineralogy and Geochemistry*, *48*(1), 455–488. https://doi.org/10.2138/rmg.2002.48.12

Kohn, M. J., Schoeninger, M. J., & Valley, J. W. (1996). Herbivore tooth oxygen isotope compositions: Effects of diet and physiology. *Geochimica Et Cosmochimica Acta*, *60*(20), 3889–3896. https://doi.org/10.1016/0016-7037(96)00248-7

Kolodny, Y., Luz, B., & Navon, O. (1983). Oxygen isotope variations in phosphate of biogenic apatites, I. Fish bone apatite—rechecking the rules of the game. *Earth and Planetary Science Letters*, *64*(3), 398-404.

Krieg, B. J., Taghavi, S. M., Amidon, G. L., & Amidon, G. E. (2014). In vivo predictive dissolution: Transport analysis of the CO_2 bicarbonate in vivo buffer system. *Journal of Pharmaceutical Sciences*, *103*(11), 3473–3490. https://doi.org/10.1002/jps.24108

Krijgsman, W., Delahaije, W., Langereis, C. G., & Boer, P. L. de (1997). Cyclicity and NRM acquisition in the armantes section (Miocene, Spain): Potential for an astronomical polarity time scale for the continental record. *Geophysical Research Letters*, *24*(9), 1027–1030. https://doi.org/10.1029/97GL00944

Krijgsman, W., Langereis, C. G., Daams, R., & van der Meulen, A. J. (1994). Magnetostratigraphic dating of the middle Miocene climate change in the continental deposits of the Aragonian type area in the Calatayud-Teruel basin (Central Spain). *Earth and Planetary Science Letters*, *128*, 513–526.

LaPorte, D. F., Holmden, C., Patterson, W. P., Prokopiuk, T., & Eglington, B. M. (2009). Oxygen isotope analysis of phosphate: Improved

precision using TC/EA CF-IRMS. *Journal of Mass Spectrometry*, *44*(6), 879–890. https://doi.org/10.1002/jms.1549

Laskar, J., Robutel, P., Joutel, F., Gastineau, M., Correia, A. C. M., & Levrard, B. (2004). A long-term numerical solution for the insolation quantities of the Earth. *Astronomy & Astrophysics*, *428*(1), 261–285. https://doi.org/10.1051/0004-6361:20041335

Lear, C. H., Elderfield, & Wilson (2000). Cenozoic deep-Sea temperatures and global ice volumes from Mg/Ca in benthic foraminiferal calcite. *Science (New York, N.Y.)*, *287*(5451), 269–272. https://doi.org/10.1126/science.287.5451.269

Lécuyer, C., Balter, V., Martineau, F., Fourel, F., Bernard, A., Amiot, R., Gardien, V., Otero, O., Legendre, S., Panczer, G., Simon, L., & Martini, R. (2010). Oxygen isotope fractionation between apatite-bound carbonate and water determined from controlled experiments with synthetic apatites precipitated at 10–37°C. *Geochimica Et Cosmochimica Acta*, *74*(7), 2072–2081. https://doi.org/10.1016/j.gca.2009.12.024

Lee-Thorp, J., & Sponheimer, M. (2003). Three case studies used to reassess the reliability of fossil bone and enamel isotope signals for paleodietary studies. *Journal of Anthropological Archaeology*, *22*(3), 208–216. https://doi.org/10.1016/S0278-4165(03)00035-7

Levin, N. E., Cerling, T. E., Passey, B. H., Harris, J. M., & Ehleringer, J. R. (2006). A stable isotope aridity index for terrestrial environments. *Proceedings of the National Academy of Sciences of the United States of America*, *103*(30), 11201–11205. https://doi.org/10.1073/pnas.0604719103

Liu, J., Izon, G., Wang, J, Antler, G., Wang, Z, Zhao, J., & Egger, M. (2018). Vivianite formation in methane-rich deep-sea sediments from the South China Sea. *Biogeosciences*, *15*(20), 6329–6348. https://doi.org/10.5194/bg-15-6329-2018

Löffler, N., Fiebig, J., Mulch, A., Tütken, T., Schmidt, B. C., Bajnai, D., Conrad, A. C., Wacker, U., & Böttcher, M. E (2019). Refining the temperature dependence of the oxygen and clumped isotopic compositions of structurally bound carbonate in apatite. *Geochimica Et Cosmochimica Acta*, *253*, 19–38. https://doi.org/10.1016/j.gca.2019.03.002

Longinelli, A. (1984). Oxygen isotopes in mammal bone phosphate: A new tool for paleohydrological and paleoclimatological research? *Geochimica Et Cosmochimica Acta*, *48*(2), 385–390. https://doi.org/10.1016/0016-7037(84)90259-X

Longinelli, A., & Nuti, S. (1973). Revised phosphate-water isotopic temperature scale. *Earth and Planetary Science Letters*, *19*(3), 373–376. https://doi.org/10.1016/0012-821X(73)90088-5

Longrich, N. R., Horner, J. R., Erickson, G. M., & Currie, P. J. (2010). Cannibalism in *Tyrannosaurus rex*. *PLOS ONE*, *5*(10), e13419. https://doi.org/10.1371/journal.pone.0013419

Lüdecke, T. (2016). *Stable isotope-based paleoenvironmental reconstructions of Neogene terrestrial archives* [Dissertation, Universitätsbibliothek Johann Christian Senckenberg, Frankfurt am Main]. Deutsche Nationalbibliothek.

Luis, A., & Hernando, J. M. (2000). Los microvertebrados del Mioceno Medio de Somosaguas Sur (Pozuelo de Alarcón, Madrid, España). *Coloquios de Paleontología*(51), 87–136. https://dialnet.unirioja.es/servlet/articulo?codigo=169722

Lyson, T. R., Bercovici, A., Chester, S. G. B., Sargis, E. J., Pearson, D. A., & Joyce, W. G. (2011). Dinosaur extinction: Closing the '3 m gap'. *Biology Letters*, *7*(6), 925–928. https://doi.org/10.1098/rsbl.2011.0470

Maclean, I. M. D. (2020). Predicting future climate at high spatial and temporal resolution. *Global Change Biology*, *26*(2), 1003–1011. https://doi.org/10.1111/gcb.14876

MacNeil, M. A., McMeans, B. C., Hussey, N. E., Vecsei, P., Svavarsson, J., Kovacs, K. M., Lydersen, C., Treble, M. A., Skomal, G. B., Ramsey, M., & Fisk, A. T. (2012). Biology of the Greenland shark *Somniosus microcephalus*. *Journal of Fish Biology*, *80*(5), 991–1018. https://doi.org/10.1111/j.1095-8649.2012.03257.x

Matthews, A., & Katz, A. (1977). Oxygen isotope fractionation during the dolomitization of calcium carbonate. *Geochimica Et Cosmochimica Acta*, *41*(10), 1431–1438. https://doi.org/10.1016/0016-7037(77)90249-6

McArthur, J. M., Howarth, R. J., & Bailey, T. R. (2001). Strontium Isotope Stratigraphy: LOWESS Version 3: Best Fit to the Marine Sr-Isotope Curve for 0–509 Ma and Accompanying Look-up Table for Deriving Numerical Age. *The Journal of Geology*, *109*(2), 155–170. https://doi.org/10.1086/319243

McConnaughey, T. (1989). 13C and 18O isotopic disequilibrium in biological carbonates: II. In vitro simulation of kinetic isotope effects. *Geochimica Et Cosmochimica Acta*, *53*(1), 163–171. https://doi.org/10.1016/0016-7037(89)90283-4

McMeans, B. C., Svavarsson, J., Dennard, S., & Fisk, A. T. (2010). Diet and resource use among Greenland sharks (*Somniosus microcephalus*) and

teleosts sampled in Icelandic waters, using $\delta^{13}C$, $\delta^{15}N$, and mercury. *Canadian Journal of Fisheries and Aquatic Sciences*, *67*(9), 1428–1438. https://doi.org/10.1139/F10-072

Meckler, A. N., Ziegler, M., Millan, I. M., Breitenbach, S. F. M., & Bernasconi, S. M. (2014). Long-term performance of the Kiel carbonate device with a new correction scheme for clumped isotope measurements. *Rapid Communications in Mass Spectrometry : RCM*, *28*(15), 1705–1715. https://doi.org/10.1002/rcm.6949

Merritt, D. A., & Hayes, J. M. (1994). Factors controlling precision and accuracy in isotope-ratio-monitoring mass spectrometry. *Analytical Chemistry*, *66*(14), 2336–2347. https://doi.org/10.1021/ac00086a020

Methner, K., Campani, M., Fiebig, J., Löffler, N., Kempf, O., & Mulch, A. (2020). Middle Miocene long-term continental temperature change in and out of pace with marine climate records. *Scientific Reports*, *10*(1), 1–10. https://doi.org/10.1038/s41598-020-64743-5

Methner, K., Mulch, A., Fiebig, J., Wacker, U., Gerdes, A., Graham, S. A., & Chamberlain, C. P. (2016). Rapid Middle Eocene temperature change in western North America. *Earth and Planetary Science Letters*, *450*, 132–139. https://doi.org/10.1016/j.epsl.2016.05.053

Miller, K. G., Wright, J. D., & Browning, J. V. (2005). Visions of ice sheets in a greenhouse world. *Marine Geology*, *217*(3-4), 215–231. https://doi.org/10.1016/j.margeo.2005.02.007

Mitchell, T. D., & Jones, P. D. (2005). An improved method of constructing a database of monthly climate observations and associated high-resolution grids. *International Journal of Climatology*, *25*(6), 693–712. https://doi.org/10.1002/joc.1181

Møller, I. J., Melsen, B., Jensen, S. J., & Kirkegaard, E. (1975). A histological, chemical and X-ray diffraction study on contemporary (*Carcharias glaucus*) and fossilized (*Macrota odontaspis*) shark teeth. *Archives of Oral Biology*, *20*(12), 797-IN10. https://doi.org/10.1016/0003-9969(75)90056-4

Montes, M., Beamud, B., Garcés, M., & Calvo Sorando, J. P. (2006). Magnetoestratigrafía de las unidades inferior e intermedia del Mioceno de la Cuenca de Madrid. *Revista de la Sociedad Geológica de España*, *19*(3-4), 281–298. https://eprints.ucm.es/27154/

Mosbrugger, V., Utescher, T., & Dilcher, D. L. (2005). Cenozoic continental climatic evolution of Central Europe. *Proceedings of the National Academy of Sciences of the United States of America*, *102*(42), 14964–14969. https://doi.org/10.1073/pnas.0505267102

Mudelsee, M., Bickert, T., Lear, C. H., & Lohmann, G. (2014). Cenozoic climate changes: A review based on time series analysis of marine benthic $\delta^{18}O$ records. *Reviews of Geophysics*, *52*(3), 333–374. https://doi.org/10.1002/2013RG000440

Murphy, E. C., Hoganson, J. W., & Johnson, K. R. (2002). Lithostratigraphy of the Hell Creek Formation in North Dakota. *Geological Society of America*, *361*, 9–34.

Nelson, D. G.A., & Williamson, B. E. (1982). Low-temperature laser Raman spectroscopy of synthetic carbonated apatites and dental enamel. *Australian Journal of Chemistry*, *35*(4), 715. https://doi.org/10.1071/CH9820715

Nyberg, K. G., Ciampaglio, C. N., & Wray, G. A. (2006). Tracing the ancestry of the great white shark, *Carcharodon carcharias*, using morphometric analyses of fossil teeth. *Journal of Vertebrate Paleontology*, *26*(4), 806–814. https://doi.org/10.1671/0272-4634(2006)26[806:TTAOTG]2.0.CO;2

Owen (1841). Report on British fossil reptiles. *Rep. Brit. Assn. Adv. Sci.*, *11*, 60.

Pagani, M., Arthur, M. A., & Freeman, K. H. (1999). Miocene evolution of atmospheric carbon dioxide. *Paleoceanography*, *14*(3), 273–292. https://doi.org/10.1029/1999PA900006

Page, M., Licht, A., Dupont-Nivet, G., Meijer, N., Barbolini, N., Hoorn, C., Schauer, A. J., Huntington, K. W., Bajnai, D., Fiebig, J., Mulch, A., & Guo, Z. (2019). Synchronous cooling and decline in monsoonal rainfall in northeastern Tibet during the fall into the Oligocene icehouse. *Geology*, *47*(3), 203–206. https://doi.org/10.1130/G45480.1

Paladino, F. V., O'Connor, M. P., & Spotila, J. R. (1990). Metabolism of leatherback turtles, gigantothermy, and thermoregulation of dinosaurs. *Nature*, *344*(6269), 858–860. https://doi.org/10.1038/344858a0

Passey, B. H., Cerling, T. E., & Levin, N. E. (2007). Temperature dependence of oxygen isotope acid fractionation for modern and fossil tooth enamels. *Rapid Communications in Mass Spectrometry : RCM*, *21*(17), 2853–2859. https://doi.org/10.1002/rcm.3149

Passey, B. H., & Henkes, G. A. (2012). Carbonate clumped isotope bond reordering and geospeedometry. *Earth and Planetary Science Letters*, *351-352*, 223–236. https://doi.org/10.1016/j.epsl.2012.07.021

Passey, B. H., Levin, N. E., Cerling, T. E., Brown, F. H., & Eiler, J. M. (2010). High-temperature environments of human evolution in East Africa based on bond ordering in paleosol carbonates. *Proceedings of the National Academy of Sciences of the United States of America*, *107*(25), 11245–11249. https://doi.org/10.1073/pnas.1001824107

Pasteris, J. D., Wopenka, B., & Valsami-Jones, E. (2008). Bone and Tooth Mineralization: Why Apatite? *Elements*, *4*(2), 97–104. https://doi.org/10.2113/GSELEMENTS.4.2.97

Pearson, & Palmer (1999). Middle eocene seawater pH and atmospheric carbon dioxide concentrations. *Science*, *284*(5421), 1824–1826. https://doi.org/10.1126/science.284.5421.1824

Pearson, D. A., Schaefer , Terry, Johnson, K. R., & Nichols, D. J. (2001). Palynologically calibrated vertebrate record from North Dakota consistent with abrupt dinosaur extinction at the Cretaceous-Tertiary boundary. *Geology*, *29*(1), 39. https://doi.org/10.1130/0091-7613(2001)029<0039:PCVRFN>2.0.CO;2

Pellegrini, M., Lee-Thorp, J. A., & Donahue, R. E. (2011). Exploring the variation of the δ18Op and δ18Oc relationship in enamel increments. *Palaeogeography, Palaeoclimatology, Palaeoecology*, *310*(1-2), 71–83. https://doi.org/10.1016/j.palaeo.2011.02.023

Pellegrini, M., & Snoeck, C. (2016). Comparing bioapatite carbonate pre-treatments for isotopic measurements: Part 2 — Impact on carbon and oxygen isotope compositions. *Chemical Geology*, *420*, 88–96. https://doi.org/10.1016/j.chemgeo.2015.10.038

Penel, G., Leroy, G., Rey, C., & Bres, E. (1998). Microraman spectral study of the PO_4 and CO_3 vibrational modes in synthetic and biological apatites. *Calcified Tissue International*, *63*(6), 475–481. https://doi.org/10.1007/s002239900561

Pérez Pérez, L., & Barreiro-Hurlé, J. (2009). Assessing the socio-economic impacts of drought in the Ebro river basin. *Spanish Journal of Agricultural Research*(2), 269–280. https://dialnet.unirioja.es/servlet/articulo?codigo=2995490

Persons, W. S., Currie, P. J., & Erickson, G. M. (2020). An Older and Exceptionally Large Adult Specimen of *Tyrannosaurus rex*. *Anatomical Record (Hoboken, N.J. : 2007)*, *303*(4), 656–672. https://doi.org/10.1002/ar.24118

Petersen, S. V., Defliese, W. F., Saenger, C., Daëron, M., Huntington, K. W., John, C. M., Kelson, J. R., Bernasconi, S. M., Colman, A. S., Kluge, T., Olack, G. A., Schauer, A. J., Bajnai, D., Bonifacie, M., Breitenbach, S. F. M., Fiebig, J., Fernandez, A. B., Henkes, G. A., Hodell, D. A., . . . Winkelstern, I. Z. (2019). Effects of Improved ^{17}O Correction on Interlaboratory Agreement in Clumped Isotope Calibrations, Estimates of Mineral-Specific Offsets, and Temperature Dependence of Acid Digestion Fractionation. *Geochemistry, Geophysics, Geosystems*, *6016*(19), 1. https://doi.org/10.1029/2018GC008127

Phillips, P., K., & Heath, J. E. (1992). Heat exchange by the pinna of the african elephant (Loxodonta africana). *Comparative Biochemistry and Physiology Part a: Physiology*, *101*(4), 693–699. https://doi.org/10.1016/0300-9629(92)90345-Q

Pimiento, C., & Clements, C. F. (2014). When did *Carcharocles megalodon* become extinct? A new analysis of the fossil record. *PloS One*, *9*(10), e111086. https://doi.org/10.1371/journal.pone.0111086

Pimiento, C., & Clements, C. F. (2015). Correction: When Did *Carcharocles megalodon* Become Extinct? A New Analysis of the Fossil Record. *PloS One*, *10*(1), e0117877. https://doi.org/10.1371/journal.pone.0117877

Pimiento, C., Ehret, D. J., MacFadden, B. J., & Hubbel, G. (2010). Ancient nursery area for the extinct giant shark megalodon from the Miocene of Panama. *PloS One*, *5*(5), e10552. https://doi.org/10.1371/journal.pone.0010552

Pimiento, C., MacFadden, B. J., Clements, C. F., Varela, S., Jaramillo, C., Velez-Juarbe, J., & Silliman, B. R. (2016). Geographical distribution patterns of *Carcharocles megalodon* over time reveal clues about extinction mechanisms. *Journal of Biogeography*, *43*(8), 1645–1655. https://doi.org/10.1111/jbi.12754

Piñol, J., Terradas, J., & Loret, F. (1998). Climate warming, wildfire hazard, and wildfire occurrence in coastal eastern Spain. *Climatic Change*, *38*(3), 345–357. https://doi.org/10.1023/A:1005316632105

Poole, D. F.G. (1967). Phylogeny of tooth tissues : enameloid and enamel in recent vertebrates with a note on the history of cementum. *Structural and Chemical Organization of Teeth*. https://ci.nii.ac.jp/naid/10021998037/

Prokhorov, I., Kluge, T., & Janssen, C. (2019). Optical clumped isotope thermometry of carbon dioxide. *Scientific Reports*, *9*(1), 4765. https://doi.org/10.1038/s41598-019-40750-z

Pucéat, E., Joachimski, M. M., Bouilloux, A., Monna, F., Bonin, A., Motreuil, S., Morinière, P., Hénard, S., Mourin, J., & Dera, G. (2010). Revised phosphate–water fractionation equation

reassessing paleotemperatures derived from biogenic apatite. *Earth and Planetary Science Letters*, *298*(1-2), 135–142. https://doi.org/10.1016/j.epsl.2010.07.034

Purdy, R. W. (1996). *Paleoecology of Fossil White Sharks* (Great White Sharks). Elsevier. http://dx.doi.org/10.1016/B978-012415031-7/50009-4

Quade, J., Garzione, C., & Eiler, J. M. (2007). Paleoelevation Reconstruction using Pedogenic Carbonates. *Reviews in Mineralogy and Geochemistry*, *66*(1), 53–87. https://doi.org/10.2138/rmg.2007.66.3

R Core Team. (2013). *R: A language and environment for statistical computing*. https://repo.bppt.go.id/cran/web/packages/dplr/vignettes/intro-dplr.pdf

Rayfield, E. J. (2004). Cranial mechanics and feeding in Tyrannosaurus rex. *Proceedings. Biological Sciences*, *271*(1547), 1451–1459. https://doi.org/10.1098/rspb.2004.2755

Reims, N., Schulp, A. S., Böhnel, M., & Larson, P. (2016). *An XXL-CT-scan of an XXL Tyrannosaurus rex skull*. 19th World Conference on Non-Destructive Testing (WCNDT 2016), Munich, Germany. https://pdfs.semanticscholar.org/9180/0299120404b1d00e4aeaa54c0861f8550545.pdf

Renne, P. R., Deino, A. L., Hilgen, F. J., Kuiper, K. F., Mark, D. F., Mitchell, W. S., Morgan, L. E., Mundil, R., & Smit, J. (2013). Time scales of critical events around the Cretaceous-Paleogene boundary. *Science*, *339*(6120), 684–687. https://doi.org/10.1126/science.1230492

Renz, M. (2002). *Megalodon: Hunting the Hunter*. PaleoPress.

Rodríguez-Arévalo, J., Díaz-Teijeiro, M. F., & Castaño, S. (2011). Modelling and mapping oxygen-18 isotope composition of precipitation in Spain for hydrologic and climatic applications, *Isotopes in Hydrology, Marine Ecosystems and Climate Change Studies Proceedings of an International Symposium*(1), 171–177. http://www.cedex.es/edex/lang_castellano/organismo/centylab/ceta/lineas/07_revip.htm

Rothschild, B. M., & Depalma, R. (2013). Skin pathology in the Cretaceous: Evidence for probable failed predation in a dinosaur. *Cretaceous Research*, *42*, 44–47. https://doi.org/10.1016/j.cretres.2013.01.005

Rubio, E. S. (1999). *Análisis de los sistemas deposicionales carbonáticos y evaporíticos del Neógeno de la Cuenca de Calatayud (provincia de Zaragoza)* [University of Madrid, Madrid]. RIS. https://core.ac.uk/download/pdf/19706601.pdf

Russell, D. A., & Manabe, M. (2002). Synopsis of the Hell Creek (uppermost Cretaceous) dinosaur assemblage. The Hell Creek Formation and the Cretaceous-Tertiary boundary in the northern Great Plains: An integrated continental record of the end of the Cretaceous. *Special Paper - Geological Society of America*, *361*, 169–176.

Ruttenberg, K. C. (2003). The Global Phosphorus Cycle. In H. D. Holland (Ed.), *Treatise on geochemistry* (pp. 585–643). Elsevier. https://doi.org/10.1016/B0-08-043751-6/08153-6

Saenger, C., Affek, H. P., Felis, T., Thiagarajan, N., Lough, J. M., & Holcomb, M. (2012). Carbonate clumped isotope variability in shallow water corals: Temperature dependence and growth-related vital effects. *Geochimica Et Cosmochimica Acta*, *99*, 224–242. https://doi.org/10.1016/j.gca.2012.09.035

Sander, P. M., & Klein, N. (2005). Developmental plasticity in the life history of a prosauropod dinosaur. *Science*, *310*(5755), 1800–1802. https://doi.org/10.1126/science.1120125

Sanz, J. L. (2003). *Starring T. rex!: Dinosaur mythology and popular culture / José Luis Sanz*. Indiana University Press; Chesham : Combined Academic.

Sarnthein, M., Thiede, J., Pflaumann, U., Erlenkeuser, H., Fütterer Dieter, Koopmann, B., Lange, H., & Seibold, E. (1982). Atmospheric and Oceanic Circulation Patterns off Northwest Africa During the Past 25 Million Years. In *Geology of the Northwest African Continental Margin* (pp. 545–604). Springer, Berlin, Heidelberg. https://doi.org/10.1007/978-3-642-68409-8_24

Sasagawa, I., Ishiyama, M., Yokosuka, H., Mikami, M., & Uchida, T. (2009). Tooth enamel and enameloid in actinopterygian fish. *Frontiers of Materials Science in China*, *3*(2), 174–182. https://doi.org/10.1007/s11706-009-0030-3

Schaeffer, J. (2016). *Feeding habits and migratory behaviour of Tyrannosaurus rex: Using stable calcium and strontium isotopes* [B.Sc.]. VU University Amsterdam, De Boelelaan 1105, 1081 HV Amsterdam, Netherlands.

Schauble, E. A., Ghosh, P., & Eiler, J. M. (2006). Preferential formation of ^{13}C–^{18}O bonds in carbonate minerals, estimated using first-principles lattice dynamics. *Geochimica Et Cosmochimica Acta*, *70*(10), 2510–2529. https://doi.org/10.1016/j.gca.2006.02.011

Schauer, A. J., Kelson, J. R., Saenger, C., & Huntington, K. W. (2016). Choice of ^{17}O correction affects clumped isotope (Δ_{47}) values of

CO2 measured with mass spectrometry. *Rapid Communications in Mass Spectrometry : RCM*, *30*(24), 2607–2616. https://doi.org/10.1002/rcm.7743

Schulp, A. S. (2014). Een *Tyrannosaurus* voor Naturalis. *Gea*, *4*, 97–99.

Schulp, A. S., Bastiaans, D., Kaskes, P., Manning, P., & Larson, P. L. (2015). *A New, Mature and Pathologic specimen of Tyrannosaurus rex*. Society of Vertebrate Paleontology, Dallas, TX, U.S.A.

Schweitzer, M. H., Wittmeyer, J. L., Horner, J. R., & Toporski, J. K. (2005). Soft-tissue vessels and cellular preservation in *Tyrannosaurus rex*. *Science*, *307*(5717), 1952–1955. https://doi.org/10.1126/science.1108397

Seebacher, F. (2001). A new method to calculate allometric length-mass relationships of dinosaurs. *Journal of Vertebrate Paleontology*, *21*(1), 51–60. https://doi.org/10.1671/0272-4634(2001)021[0051:ANMTCA]2.0.CO;2

Seymour, R. S. (2013). Maximal aerobic and anaerobic power generation in large crocodiles versus mammals: Implications for dinosaur gigantothermy. *PLOS ONE*, *8*(7), e69361. https://doi.org/10.1371/journal.pone.0069361

Shevenell, A. E., Kennett, J. P., & Lea, D. W. (2004). Middle Miocene Southern Ocean cooling and Antarctic cryosphere expansion. *Science*, *305*(5691), 1766–1770. https://doi.org/10.1126/science.1100061

Shimoda, S., Aoba, T., Moreno, E. C., & Miake, Y. (1990). Effect of solution composition on morphological and structural features of carbonated calcium apatites. *Journal of Dental Research*, *69*(11), 1731–1740. https://doi.org/10.1177/00220345900690110501

Sosdian, S. M., Babila, T. L., Greenop, R., Foster, G. L., & Lear, C. H. (2020). Ocean Carbon Storage across the middle Miocene: A new interpretation for the Monterey Event. *Nature Communications*, *11*(1), 134. https://doi.org/10.1038/s41467-019-13792-0

Sosdian, S. M., Greenop, R., Hain, M. P., Foster, G. L., Pearson, P. N., & Lear, C. H. (2018). Constraining the evolution of Neogene ocean carbonate chemistry using the boron isotope pH proxy. *Earth and Planetary Science Letters*, *498*, 362–376. https://doi.org/10.1016/j.epsl.2018.06.017

Spötl, C., & Vennemann, T. W. (2003). Continuous-flow isotope ratio mass spectrometric analysis of carbonate minerals. *Rapid Communications in Mass Spectrometry : RCM*, *17*(9), 1004–1006. https://doi.org/10.1002/rcm.1010

St. John, K. (2008). Cenozoic ice-rafting history of the central Arctic Ocean: Terrigenous sands on the Lomonosov Ridge. *Paleoceanography*, *23*(1), n/a-n/a. https://doi.org/10.1029/2007PA001483

Stevens, R. E., Balasse, M., & O'Connell, T. C. (2011). Intra-tooth oxygen isotope variation in a known population of red deer: Implications for past climate and seasonality reconstructions. *Palaeogeography, Palaeoclimatology, Palaeoecology*, *301*(1-4), 64–74. https://doi.org/10.1016/j.palaeo.2010.12.021

Stokesbury, M. J. W., Harvey-Clark, C., Gallant, J., Block, B. A., & Myers, R. A. (2005). Movement and environmental preferences of Greenland sharks (*Somniosus microcephalus*) electronically tagged in the St. Lawrence Estuary, Canada. *Marine Biology*, *148*(1), 159–165. https://doi.org/10.1007/s00227-005-0061-y

Stolper, D. A., & Eiler, J. M. (2015). The kinetics of solid-state isotope-exchange reactions for clumped isotopes: A study of inorganic calcites and apatites from natural and experimental samples. *American Journal of Science*, *315*(5), 363–411. https://doi.org/10.2475/05.2015.01

Stolper, D. A., & Eiler, J. M. (2016). Constraints on the formation and diagenesis of phosphorites using carbonate clumped isotopes. *Geochimica Et Cosmochimica Acta*, *181*, 238–259. https://doi.org/10.1016/j.gca.2016.02.030

Suarez, M. B., & Passey, B. H. (2014). Assessment of the clumped isotope composition of fossil bone carbonate as a recorder of subsurface temperatures. *Geochimica Et Cosmochimica Acta*, *140*, 142–159. https://doi.org/10.1016/j.gca.2014.05.026

Suarez, M. B., Passey, B. H., & Kaakinen, A. (2011). Paleosol carbonate multiple isotopologue signature of active East Asian summer monsoons during the late Miocene and Pliocene. *Geology*, *39*(12), 1151–1154. https://doi.org/10.1130/G32350.1

Super, J. R., Thomas, E., Pagani, M., Huber, M., O'Brien, C., & Hull, P. M. (2018). North Atlantic temperature and pCO_2 coupling in the early-middle Miocene. *Geology*, *46*(6), 519–522. https://doi.org/10.1130/G40228.1

Super, J. R., Thomas, E., Pagani, M., Huber, M., O'Brien, C. L., & Hull, P. M. (2020). Miocene Evolution of North Atlantic Sea Surface Temperature. *Paleoceanography and Paleoclimatology*, *35*(5). https://doi.org/10.1029/2019PA003748

Thiagarajan, N., Adkins, J., & Eiler, J. M. (2011). Carbonate clumped isotope thermometry of deep-sea corals and implications for vital effects.

Geochimica Et Cosmochimica Acta, *75*(16), 4416–4425. https://doi.org/10.1016/j.gca.2011.05.004

Tobin, T. S., Wilson, G. P., Eiler, J. M., & Hartmann, J. H. (2014). Environmental change across a terrestrial Cretaceous-Paleogene boundary section in eastern Montana, USA, constrained by carbonate clumped isotope paleothermometry. *Geology*, *42*(4), 351–354. https://doi.org/10.1130/G35262.1

Tripati, A. K., Eagle, R. A., Thiagarajan, N., Gagnon, A. C., Bauch, H., Halloran, P. R., & Eiler, J. M. (2010). ^{13}C–^{18}O isotope signatures and 'clumped isotope' thermometry in foraminifera and coccoliths. *Geochimica Et Cosmochimica Acta*, *74*(20), 5697–5717. https://doi.org/10.1016/j.gca.2010.07.006

Tütken, T., Furrer, H., & Vennemann, T. W. (2007). Stable isotope compositions of mammoth teeth from Niederweningen, Switzerland: Implications for the Late Pleistocene climate, environment, and diet. *Quaternary International*, *164-165*, 139–150. https://doi.org/10.1016/j.quaint.2006.09.004

Tütken, T., Pfretzschner, H.‐U., Vennemann, T. W., Sun, G., & Wang, Y. D. (2004). Paleobiology and skeletochronology of Jurassic dinosaurs: implications from the histology and oxygen isotope compositions of bones. *Palaeogeography, Palaeoclimatology, Palaeoecology*, *206*(3-4), 217–238. https://doi.org/10.1016/j.palaeo.2004.01.005

Tütken, T., & Vennemann, T. W. (2011). Fossil bones and teeth: Preservation or alteration of biogenic compositions? *Palaeogeography, Palaeoclimatology, Palaeoecology*, *310*(1-2), 1–8. https://doi.org/10.1016/j.palaeo.2011.06.020

Tütken, T., Vennemann, T. W., Janz, H., & Heizmann, E.P.J. (2006). Palaeoenvironment and palaeoclimate of the Middle Miocene lake in the Steinheim basin, SW Germany: A reconstruction from C, O, and Sr isotopes of fossil remains. *Palaeogeography, Palaeoclimatology, Palaeoecology*, *241*(3-4), 457–491. https://doi.org/10.1016/j.palaeo.2006.04.007

Urist, M. R. (1961). Calcium and phosphorus in the blood and skeleton of the Elasmobranchii. *Endocrinology*, *69*, 778–801. https://doi.org/10.1210/endo-69-4-778

Usdowski, E. (1982). Reactions and Equilibria in the Systems CO2-H2O and $CaCO_3$—Co_2—H_2O (0°-50 °C) - A Review. *Neues Jahrbuch Für Mineralogie - Abhandlungen*, 148–171. https://doi.org/10.1127/njma/144/1982/148

van Dam, J. A., Abdul Aziz, H., Alvarez Sierra, M. A., Hilgen, F. J., van den Hoek Ostende, L. W., Lourens, L. J., Mein, P., van der Meulen, A. J., & Pelaez-Campomanes, P. (2006). Long-period astronomical forcing of mammal turnover. *Nature*, *443*(7112), 687–691. https://doi.org/10.1038/nature05163

van der Meulen, A. J., & Daams, R. (1992). Evolution of early-middle miocene rodent faunas in relation to long-term palaeoenvironmental changes. *Palaeogeography, Palaeoclimatology, Palaeoecology*, *93*(3-4), 227–253. https://doi.org/10.1016/0031-0182(92)90099-q

van der Meulen, A. J., Peláez-Campomanes, P., & Levin, S. A. (2005). Age structure, residents, and transients of Miocene rodent communities. *The American Naturalist*, *165*(4), E108-25. https://doi.org/10.1086/428683

van Donk, J., & Mathieu, G. (1969). Oxygen isotope compositions of foraminifera and water samples from the Arctic Ocean. *Journal of Geophysical Research*, *74*(13), 3396–3407. https://doi.org/10.1029/JC074i013p03396

Vennemann, T. W., Hegner, E., Cliff, G., & Benz, G.W. (2001). Isotopic composition of recent shark teeth as a proxy for environmental conditions. *Geochimica Et Cosmochimica Acta*, *65*(10), 1583–1599. https://doi.org/10.1016/S0016-7037(00)00629-3

Wacker, U., Bahr, A., & Friedrich, O. (2014). *Empirical calibration of the clumped isotope paleothermometer using calcites of various origins.*

Wacker, U., Fiebig, J., & Schoene, B. R. (2013). Clumped isotope analysis of carbonates: Comparison of two different acid digestion techniques. *Rapid Communications in Mass Spectrometry*, *27*(14), 1631–1642. https://doi.org/10.1002/rcm.6609

Wacker, U., Rutz, T., Löffler, N., Conrad, A. C., Tütken, T., Böttcher, M. E, & Fiebig, J. (2016). Clumped isotope thermometry of carbonate-bearing apatite: Revised sample pre-treatment, acid digestion, and temperature calibration. *Chemical Geology*, *443*, 97–110. https://doi.org/10.1016/j.chemgeo.2016.09.009

Wang, Z, Schauble, E. A., & Eiler, J. M. (2004). Equilibrium thermodynamics of multiply substituted isotopologues of molecular gases. *Geochimica Et Cosmochimica Acta*, *68*(23), 4779–4797. https://doi.org/10.1016/j.gca.2004.05.039

Watanabe, Y. Y., Goldman, K. J., Caselle, J. E., Chapman, D. D., & Papastamatiou, Y. P. (2015). Comparative analyses of animal-tracking data reveal ecological significance of endothermy in fishes. *Proceedings of the National Academy of*

Sciences of the United States of America, *112*(19), 6104–6109. https://doi.org/10.1073/pnas.1500316112

Watanabe, Y. Y., Lydersen, C., Fisk, A. T., & Kovacs, K. M. (2012). The slowest fish: Swim speed and tail-beat frequency of Greenland sharks. *Journal of Experimental Marine Biology and Ecology*, *426-427*, 5–11. https://doi.org/10.1016/j.jembe.2012.04.021

Watkins, J. M., Nielsen, L. C., Ryerson, F. J., & DePaolo, D. J. (2013). The influence of kinetics on the oxygen isotope composition of calcium carbonate. *Earth and Planetary Science Letters*, *375*, 349–360. https://doi.org/10.1016/j.epsl.2013.05.054

Watson, E.B. (2004). A conceptual model for near-surface kinetic controls on the trace-element and stable isotope composition of abiogenic calcite crystals. Associate editor: R.H. Byrne. *Geochimica Et Cosmochimica Acta*, *68*(7), 1473–1488. https://doi.org/10.1016/j.gca.2003.10.003

Weissenböck, N. M., Weiss, C. M., Schwammer, H. M., & Kratochvil, H. (2010). Thermal windows on the body surface of African elephants (*Loxodonta africana*) studied by infrared thermography. *Journal of Thermal Biology*, *35*(4), 182–188. https://doi.org/10.1016/j.jtherbio.2010.03.002

Whitenack, L. B., Simkins, D. C., Motta, P. J., Hirai, M., & Kumar, A. (2010). Young's modulus and hardness of shark tooth biomaterials. *Archives of Oral Biology*, *55*(3), 203–209. https://doi.org/10.1016/j.archoralbio.2010.01.001

Widga, C., Walker, J. D., & Stockli, L. D. (2010). Middle Holocene Bison diet and mobility in the eastern Great Plains (USA) based on $\delta^{13}C$, $\delta^{18}O$, and $^{87}Sr/^{86}Sr$ analyses of tooth enamel carbonate. *Quaternary Research*, *73*(3), 449–463. https://doi.org/10.1016/j.yqres.2009.12.001

Wierzbowski, H., Bajnai, D., Wacker, U., Rogov, M. A., Fiebig, J., & Tesakova, E. M. (2018). Clumped isotope record of salinity variations in the Subboreal Province at the Middle–Late Jurassic transition. *Global and Planetary Change*, *167*, 172–189. https://doi.org/10.1016/j.gloplacha.2018.05.014

Winkelstern, I. Z., Kaczmarek, S. E., Lohmann, K. C., & Humphrey, J. D. (2016). Calibration of dolomite clumped isotope thermometry. *Chemical Geology*, *433*, 32–38. https://doi.org/10.1016/j.chemgeo.2016.09.021

Wolfe, J. A. (1985). Distribution of Major Vegetational Types During the Tertiary. In E. T. Sundquist & W. S. Broecker (Eds.), *Geophysical monograph series: Vol. 32. The Carbon Cycle and Atmospheric CO_2: Natural Variations Archean to Present The Carbon Cycle and Atmospheric CO_2: Natural Variations Archean to Present* (pp. 357–375).

Woodward, H. N., Tremaine, K., Williams, S. A., Zanno, L. E., Horner, J. R., & Myhrvold, N. (2020). Growing up *Tyrannosaurus rex*: Osteohistology refutes the pygmy "*Nanotyrannus*" and supports ontogenetic niche partitioning in juvenile *Tyrannosaurus*. *Science Advances*, *6*(1), eaax6250. https://doi.org/10.1126/sciadv.aax6250

Wroe, S., Huber, D. R., Lowry, M., McHenry, C., Moreno, K., Clausen, P., Ferrara, T. L., Cunningham, E., Dean, M. N., & Summers, A. P. (2008). Three-dimensional computer analysis of white shark jaw mechanics: how hard can a great white bite? *Journal of Zoology*, *276*(4), 336–342. https://doi.org/10.1111/j.1469-7998.2008.00494.x

York, D., Evensen, N. M., Martínez, M. L., & Basabe, D. J. de (2004). Unified equations for the slope, intercept, and standard errors of the best straight line. *American Journal of Physics*, *72*(3), 367. https://doi.org/10.1119/1.1632486

You, Y., Huber, M., Müller, R. D., Poulsen, C. J., & Ribbe, J. (2009). Simulation of the Middle Miocene Climate Optimum. *Geophysical Research Letters*, *36*(4), 289. https://doi.org/10.1029/2008GL036571

Yun, C.‐g. (2015). *Evidence points out that " Nanotyrannus" is a juvenile Tyrannosaurus rex.* https://doi.org/10.7287/peerj.preprints.852v1

Zaarur, S., Affek, H. P., & Brandon, M. T. (2013). A revised calibration of the clumped isotope thermometer. *Earth and Planetary Science Letters*, *382*, 47–57. https://doi.org/10.1016/j.epsl.2013.07.026

Zabler, S., Cloetens, P., & Zaslansky, P. (2007). Fresnel-propagated submicrometer x-ray imaging of water-immersed tooth dentin. *Optics Letters*, *32*(20), 2987–2989. https://doi.org/10.1364/ol.32.002987

Zachos, J., Pagani, M., Sloan, L., Thomas, E., & Billups, K. (2001). Trends, rhythms, and aberrations in global climate 65 Ma to present. *Science (New York, N.Y.)*, *292*(5517), 686–693. https://doi.org/10.1126/science.1059412

Zapanta LeGeros, R. (1981). Apatites in biological systems. *Progress in Crystal Growth and Characterization*, *4*(1-2), 1–45. https://doi.org/10.1016/0146-3535(81)90046-0

Zapanta-LeGeros, R. (1965). Effect of carbonate on the lattice parameters of apatite. *Nature*, *206*(982), 403–404. https://doi.org/10.1038/206403a0

Zazzo, A., Balasse, M., Passey, B. H., Moloney, A. P., Monahan, F. J., & Schmidt, O. (2010). The isotope record of short- and long-term dietary changes in sheep tooth enamel: Implications for quantitative reconstruction of paleodiets. *Geochimica Et Cosmochimica Acta*, *74*(12), 3571–3586. https://doi.org/10.1016/j.gca.2010.03.017

Zeebe, R. E., & Wolf-Gladrow, D. (2001). *CO_2 in Seawater: Equilibrium, Kinetics, Isotopes*. Gulf Professional Publishing.

Zheng, Y.‐F. (2016). Oxygen isotope fractionation in phosphates: The role of dissolved complex anions in isotope exchange. *Isotopes in Environmental and Health Studies*, *52*(1-2), 47–60. https://doi.org/10.1080/10256016.2014.999678

Zheng, Y.‐F., & Böttcher, M. E (2016). Oxygen isotope fractionation in double carbonates. *Isotopes in Environmental and Health Studies*, *52*(1-2), 29–46. https://doi.org/10.1080/10256016.2014.977278

Zhou, H., Helliker, B. R., Huber, M., Dicks, A., & Akçay, E. (2018). C4 photosynthesis and climate through the lens of optimality. *Proceedings of the National Academy of Sciences*, *115*(47), 12057–12062. https://doi.org/10.1073/pnas.1718988115

Zwicker, J., Smrzka, D., Steindl, F., Böttcher, M. E, Libowitzky, E., Kiel, S., & Peckmann, J. (2020). Mineral authigenesis within chemosynthetic microbial mats: Coated grain formation and phosphogenesis at a Cretaceous hydrocarbon seep, New Zealand. *The Depositional Record.* Advance online publication. https://doi.org/10.1002/dep2.123

Curriculum Vitae

Personal data

Name	Niklas Maximilian Löffler
Birth	August 20, 1988 in Mechernich, Germany
Address	Herderstraße 33, 60316 Frankfurt (Main), Germany
Email	niklas.loeffler@stadt-frankfurt.de
ITU Callsigns	DK1DE, DN1DOG
ORCID	0000-0002-3026-8126
Scopus	55907159600

Profession

09/2020 to 08/2023	Research scientist at the Johann Wolfgang Goethe-University (JGU) Frankfurt (Main), Germany (VeWa B3)
09/2020 to 08/2023	Guest scientist at the Senckenberg Biodiversity and Climate Research Centre, Frankfurt (Main), Germany in the Tectonic and Climate working group of Prof. Dr. Andreas Mulch.
05/2020 to 08/2020	Scholarship holder at the Senckenberg Biodiversity and Climate Research Centre, Frankfurt (Main), Germany
06/2019 (ongoing)	Head of the search and rescue dog special unit, Fire department Frankfurt (Main), Germany
05/2016 to 05/2020	Research scientist at the Senckenberg Biodiversity and Climate Research Centre, Frankfurt (Main), Germany in the Tectonic and Climate working group of Prof. Dr. Andreas Mulch.
01/2015 to 12/2015	Guest scientist at the Senckenberg Biodiversity and Climate Research Centre, Frankfurt (Main), Germany in the Tectonic and Climate working group of Prof. Dr. Andreas Mulch.

Teaching

2018 and 2019	Tutorials and supervision of exams for the M.Sc. class “tectonic and climate” at the Johann Wolfgang Goethe-University (JGU) Frankfurt (Main), Germany with Prof. Dr. Andreas Mulch
2012 and 2015	Supervision of a geological mapping excursion in the Saargau area (Germany) with Prof. Dr. Peter Prinz-Grimm.

Education

06/2017 to 2020	Studies in Geosciences Geology/Paleontology (Ph.D.) at the Johann Wolfgang Goethe-University (JGU) Frankfurt (Main), Germany under supervision of Prof. Dr. Andreas Mulch and Prof. Dr. Jens Fiebig.
10/2012 to 12/2015	Studies in Geosciences Geology/Paleontology (M.Sc.) at the Johann Wolfgang Goethe-University (JGU) Frankfurt (Main), Germany under supervision of Prof. Dr. Jens Fiebig and Prof. Dr. Thomas Tütken (1.2). M.Sc. Thesis: A refinement of the clumped isotope paleothermometer for biogenic apatite (1.3)
06/2012 to 07/2012	Internship at CDM Consult GmbH, engineering office (contaminated sites), Alsbach-Haehnlein, Germany
08/2009 to 02/2013	Studies in Geosciences (B.Sc.) at the Johann Wolfgang Goethe-University (JGU)-Frankfurt (Main), Germany under supervision of Prof. Dr. Peter Prinz-Grimm and Dr. Joachim Blau (1.9) B.Sc. Thesis: Quantitative Analyse von Wirbeltierfragmenten aus dem Muschelkalk-Keuper-Grenzbonebed bei Palzem / Mosel (1.0)

Scientific work

First author publications

Journals

Löffler, N., Mulch, A., Krijgsman, W., Krsnik, E., Methner, K., Fiebig, J. (submitted). Southern European Middle Miocene Temperature Dynamics *Nature Geoscience*, NGS-2020-08-01948. Received 16 August 2020.

Löffler, N., Fiebig, J., Mulch, A., Tütken, T., Schmidt, B. C., Bajnai, D., Conrad, A. C., Wacker, U., & Böttcher, M. E. (2019). Refining the temperature dependence of the oxygen and clumped isotopic compositions of structurally bound carbonate in apatite. *Geochimica Et Cosmochimica Acta*, *253*, 19-38. https://doi.org/10.1016/j.gca.2019.03.002

Löffler N., Prinz-Grimm P. (2013) Quantitative Analyse von Wirbeltierfragmenten aus einem Muschelkalk-Keuper-Bonebed bei Palzem (Mosel). *Mainzer geowiss. Mitt. 41*, 37-50.

Conference abstracts

Löffler, N., Mulch, A., Krijgsman, W., Krsnik, E., Methner, K., Fiebig, J. (2020). Temperature Dynamics of the Middle Miocene Climatic Transition in Southern Europe as recorded in pedogenic carbonates. *GSA Annual Meeting 2020, 26-30.10.2020, Online*.ID: 357137, invited talk.

Löffler, N., Fiebig, J., Mulch, A., Tütken, T., Schmidt, B. C., Conrad, A., Wacker, U., Schulp, A. S., Böttcher, M. E. (2020) Applying refined Clumped and Oxygen Isotope Temperature Calibrations to Teeth from *T. rex* and *C. megalodon* (invited*). Society of Vertebrate Paleontology Annual Meeting, 14.10.-17.10., Online.* ID: 3439304, invited talk

Löffler, N., Mulch, A., Krijgsman, W., Krsnik, E., Fiebig, J. (2020). The continental Middle Miocene Climatic Transition in Southern Europe as derived from clumped isotope analyses. *EGU General Assembly 2020, 04-08.05.2020, Online*. https://doi.org/10.5194/egusphere-egu2020-10864, talk.

Löffler, N., Mulch, A., Krijgsman, W., Fiebig, J. (2019). The Magnitude of Continental Temperature Change during the Middle Miocene Climatic Transition in Southern Europe. *AGU Fall meeting 2019*, 25.-28.01.2019, Moscone Centre, San Francisco, CA 2019. #PP14A-08, talk.

Löffler, N., Mulch, A., Krijgsman, W., Fiebig, J. (2019). Clumped isotope-based characterization of the continental Middle Miocene Climatic Transition in Southern Europe.*7th International Clumped Isotope Workshop*, Queen Mary, Los Angeles, CA 2019, talk.

Löffler N., Böttcher M.E., Fiebig J., Tütken T., Mulch A. (2017c). Improving the accuracy of the Δ_{47}-$1/T^2$ relationship for (bio)apatites to facilitate temperature reconstruction on teeth from dinosaurs and sharks. *GEOBremen 2017*, Marum Research Center, University Bremen 2017, talk.

Löffler N., Fiebig J., Böttcher M.E., Tütken T., Mulch A. (2017b). Applying the Clumped Isotope Paleothermometer to Teeth from *T. rex* and *C. megalodon*. Goldschmidt conference, Paris 2017. ID: 2017004426, poster.

Löffler N., Fiebig J., Böttcher M.E., Tütken T., Mulch A. (2017a). Clumped isotope analysis of tooth enamel(oid) and dentine: Improving the accuracy of the Δ_{47}-$1/T^2$ relationship for (bio)apatites. *6th International Clumped Isotopes Workshop*, Institute de physique du globe de Paris 2017, poster.

Löffler N., Rutz T., Wacker U., Tütken T., Conrad A., Böttcher M. E., Fiebig J. (2014). A preliminary refinement of the clumped isotope paleothermometer for biogenic apatite and an experimental approach for abiotic apatite. *35th annual meeting of the Arbeitsgemeinschaft stabile Isotope e.V.*, Helmholtz Center Munich, Munich 2014, poster.

Co-author publications

Journals

Bajnai, D., Guo, W., Spötl, C., Coplen, T. B., Methner, K., **Löffler, N**, Krsnik, E., Gischler, E., Hansen, M., Henkel, D., Price, G. D., Raddatz, J., Scholz, D., Fiebig J. (2020) Dual clumped isotope thermometry resolves kinetic biases in carbonate formation temperatures. *Nature comm. 11*, 4005. https://doi.org/10.1038/s41467-020-17501-0

Methner, K., Campani, M., Fiebig, J. **Löffler, N.**, Kempf, O. Mulch, A. (2020) Middle Miocene long-term continental temperature change in and out of pace with marine climate records. *Scientific Rep*orts *10*(1), 1-10. https://doi.org/10.1038/s41598-020-64743-5

Fiebig, J., Bajnai, D., **Löffler, N.**, Methner, K., Krsnik, E., Mulch, A., & Hofmann, S. (2019). Combined high-precision Δ_{48} and Δ_{47} analysis of carbonates. *Chemical Geology*, *522*, 186-191. https://doi.org/10.1016/j.chemgeo.2019.05.019

Wacker, U., Rutz, T., **Löffler, N.**, Conrad, A. C., Tütken, T., Böttcher, M. E., & Fiebig, J. (2016). Clumped isotope thermometry of carbonate-bearing apatite: Revised sample pre-treatment, acid digestion, and temperature calibration. *Chemical Geology*, *443*, 97-110. https://doi.org/10.1016/j.chemgeo.2016.09.009

Fiebig, J., Hofmann, S., **Löffler, N.**, Lüdecke, T., Methner, K., & Wacker, U. (2016). Slight pressure imbalances can affect accuracy and precision of dual inlet-based clumped isotope analysis. *Isotopes in Environmental and Health Studies*, *52*(1-2), 12-28. https://doi.org/10.1080/10256016.2015.1010531

Conference abstracts

Methner, K., Chamberlain, P. C., Badgley, C., Bajnai, D., Fiebig, J., Krsnik, E., **Löffler, N.**, Loughney, K. M., Mulch, A. (2020) Middle Miocene continental temperature and precipitation changes recorded in paleosol carbonates (a transatlantic approach) (Invited). *AGU Fall Meeting 2020, 07.-11.12.2020, Online*. ID# 771821

Krsnik, E., Methner, K., **Löffler, N.**, Kempf, O., Fiebig, J., Mulch, A. (2020). New paleoelevation constraints on the Mid-Miocene Central Alps. *EGU General Assembly 2020, 04-08.05.2020, Online*. https://doi.org/10.5194/egusphere-egu2020-10060

Bajnai, D., Guo, W., **Löffler, N.**, Methner, K., Krsnik, E., Coplen, T. B., Gischler, E., Hansen, M., Henkel, D., Price, G. D., Raddatz, J., Scholz, D., & Fiebig, J. (2020) Combined clumped isotope measurements resolve kinetic biases in carbonate formation temperatures. *EGU General Assembly 2020, 04-08.05.2020, Online*. https://doi.org/10.5194/egusphere-egu2020-3051

Fiebig, J., Bajnai, D., **Löffler, N.**, Methner, K., Krsnik, E., & Guo, W. (2019). CombinedΔ_{48} and Δ_{47} Measurements Reveal the Importance of Kinetics in Carbonate (Bio) Mineralization. *AGU Fall Meeting 2019*, 25.-28.01.2019, Moscone Centre, San Francisco, CA 2019#V14B-06

Fiebig, J., Bajnai, D., **Löffler, N.**, Methner, K., Krsnik, E., Mulch, A., Prud'homme, C. & Guo, W. (2019). High-Precision Analysis of Δ_{48} and Δ_{47}: Resolving Temperature from the Kinetic Information Recorded in Carbonates. *Goldschmidt Abstracts*, 988. ID: 2019004432

Bajnai, D., Fiebig, J., **Löffler, N.**, Methner, K., Krsnik, E., Prud'homme, C. & Hofmann, S. (2019). Long-Term Precision and Accuracy of Clumped Isotope Measurements. *Goldschmidt Abstracts*, 168. ID: 2019004315

Methner, K., Chamberlain, P., C., Bajnai, D., Campani, M., Fiebig, J., Kempf, O., Krsnik, E., **Löffler, N.**, Mulch, A. (2019). Terrestrial temperature response to middle Miocene northern hemisphere climate change: Case studies from Central European and continental North American paleosols. *21st EGU General Assembly, EGU2019*, Proceedings from the conference held 7-12 April, 2019 in Vienna, Austria, id.7910. 2019EGUGA..21.7910M

Methner K., Fiebig J., Krsnik E., **Löffler N.**, & Mulch A. (2018). Stable ($\delta^{18}O$) and clumped (Δ_{47}) isotope geochemistry reveal Central European temperature and rainfall seasonality across the Middle Miocene Climate Transition. *20th EGU General Assembly, EGU2018*, Proceedings from the conference held 4-13 April, 2018 in Vienna, Austria, p.12574. 2018EGUGA..2012574M

Bajnai, D., Fiebig, J., Tomašových, A., Milner Garcia, S., Rollion-Bard, C., Raddatz, J., **Löffler, N.**, Primo-Ramos, C., & Brand, U. (2018). Assessing kinetic fractionation in brachiopod calcite using clumped isotopes. *20th EGU General Assembly, EGU2018*, Proceedings from the conference held 4-13 April, 2018 in Vienna, Austria, p.7079. 2018EGUGA..20.7079B

Bajnai, D., Fiebig, J., Tomašových, A., Milner Garcia, S., Rollion-Bard, C., Raddatz, J., **Löffler, N.**, Primo-Ramos, C., & Brand, U. (2018). Assessing kinetic fractionation in brachiopod calcite using clumped isotopes. *Scientific Reports*, *8*(1), 533. https://doi.org/10.1038/s41598-017-17353-7

Wacker, U., **Löffler, N.**, Rutz, T., Tütken, T., Conrad, A.C., Schmiedinger, I., Böttcher, M. E., Fiebig, J. (2016). Clumped isotope thermometry of carbonate-bearing apatites: Digestion techniques and calibrations. *36th annual meeting of the Arbeitsgemeinschaft stabile Isotope e.V.*, Heidelberg University, Heidelberg 2015

Wacker, U., **Löffler, N.**, Rutz, T., Conrad, A.C., Tütken, T., Böttcher, M.E. & Fiebig, J. (2015). Clumped isotope thermometry of carbonate-bearing apatites: Digestion techniques and calibrations. *Goldschmidt Abstracts*, 3295. ID: 2015003579

Reviews

Heliyon (Elsevier), clumped isotope based study of dinosaur eggshell carbonate (2020)

Research project affiliations

EXCALIBOR (DFG)	*e.g.* Löffler *et al.* (2019)*;* Wacker *et al.* (2016)
4D-MB (DFG)	*e.g.* Methner *et al.* (2020)
BASE-LiNE Earth (EU)	*e.g.* Bajnai *et al.* (2018)
VeWa (LOEWE)	*e.g.* Löffler *et. al.* (submitted)

Appendices

Due to the limited durability and readability of digital storage media, supplementary data for the chapters 1 to 6 are printed on the following pages. The figures shown and data referred to in this chapter are also provided as digital annex (CD-ROM) which is enclosed at the end of the printed version of this thesis (page 275).

Appendix to chapter 1

none

Appendix to chapter 2

Compilation of all measured and calculated data from equilibrated gases and empirical transfer functions (*S.2.I.*), standard (*S.2.II.*) and sample (*S.2.III.*) measurements including δ^{47} and raw Δ_{47} values. Comparison of [*Brand*] processed Δ_{47} values of ETH 1, ETH 2, and ETH 3 with Δ_{47} values from prior studies (*S.2.IV*).

The data of the original Supplementary S1 table is shown on the following pages and can also be found online at https://doi.org/10.1016/j.gca.2019.03.002

Equilibrated gas data and transfer functions – S.2.I

I. Equilibrated gas data (continued)

Heated gases		[*Gonfiantini*] in ‰		[*Brand*] in ‰	
date	δ^{47}	Δ_{47raw}	se	Δ_{47raw}	se
2/19/2014	16.885	-0.848	0.011	-0.844	0.011
2/25/2014	-26.966	-0.851	0.010	-0.848	0.010
2/27/2014	-1.885	-0.840	0.006	-0.841	0.006
3/3/2014	14.111	-0.858	0.006	-0.855	0.006
3/11/2014	-1.408	-0.856	0.008	-0.857	0.008
3/14/2014	14.520	-0.890	0.007	-0.887	0.007
3/19/2014	-26.704	-0.859	0.008	-0.857	0.008
3/21/2014	-1.852	-0.826	0.006	-0.827	0.006
3/24/2014	16.324	-0.862	0.006	-0.857	0.006
3/28/2014	-26.751	-0.824	0.009	-0.822	0.009
4/1/2014	-1.404	-0.886	0.008	-0.887	0.008
4/10/2014	-27.780	-0.886	0.004	-0.883	0.004
4/10/2014	14.149	-0.869	0.008	-0.866	0.008
4/14/2014	-1.498	-0.859	0.008	-0.860	0.008
4/16/2014	14.968	-0.884	0.009	-0.880	0.009
4/22/2014	-24.355	-0.850	0.009	-0.848	0.009

25 °C equilibrated gases		[*Gonfiantini*] in ‰		[*Brand*] in ‰	
date	δ^{47}	Δ_{47raw}	se	Δ_{47raw}	se
2/19/2014	-26.986	-0.045	0.008	-0.024	0.008
2/21/2014	-27.597	-0.037	0.005	-0.017	0.005
2/28/2014	8.274	-0.049	0.006	-0.045	0.006
2/28/2014	-27.916	-0.029	0.019	-0.008	0.019
3/4/2014	-27.643	-0.049	0.008	-0.028	0.008
3/17/2014	-27.323	-0.037	0.009	-0.016	0.009
3/17/2014	-26.896	-0.040	0.008	-0.019	0.008
3/24/2014	-27.824	-0.036	0.007	-0.016	0.007
3/24/2014	-27.493	-0.022	0.005	-0.001	0.005
3/31/2014	8.884	-0.024	0.007	-0.019	0.007
4/9/2014	-27.466	-0.031	0.008	-0.010	0.008
4/10/2014	9.240	-0.021	0.006	-0.016	0.006
4/14/2014	-27.304	-0.046	0.007	-0.025	0.007
4/22/2014	-27.567	-0.026	0.007	-0.005	0.007
4/28/2014	19.055	-0.050	0.003	-0.039	0.003
4/28/2014	18.836	-0.060	0.006	-0.049	0.006

4/25/2014	-1.651	-0.878	0.010	-0.880	0.010
4/29/2014	16.501	-0.872	0.007	-0.868	0.007
5/2/2014	-26.646	-0.852	0.007	-0.850	0.007
5/6/2014	-1.914	-0.907	0.006	-0.865	0.006
5/9/2014	16.476	-0.883	0.007	-0.879	0.007
5/14/2014	-26.514	-0.859	0.007	-0.856	0.007
5/16/2014	-0.971	-0.888	0.003	-0.889	0.003
5/20/2014	18.258	-0.891	0.007	-0.885	0.007
5/23/2014	-26.681	-0.877	0.009	-0.874	0.009
5/27/2014	-1.240	-0.907	0.008	-0.862	0.008
6/5/2014	-1.914	-0.864	0.006	-0.865	0.006
1/8/2015	-2.998	-0.881	0.008	-0.883	0.008
1/8/2015	-24.457	-0.888	0.011	-0.887	0.011
1/12/2015	18.568	-0.841	0.010	-0.836	0.010
1/13/2015	-2.732	-0.871	0.007	-0.873	0.007
1/15/2015	-25.003	-0.841	0.009	-0.839	0.009
1/19/2015	15.705	-0.823	0.009	-0.830	0.009
1/21/2015	-2.653	-0.867	0.009	-0.869	0.009
1/22/2015	-23.622	-0.859	0.007	-0.857	0.007
1/26/2015	18.783	-0.869	0.008	-0.864	0.008
1/30/2015	-23.942	-0.850	0.006	-0.859	0.006
2/2/2015	11.799	-0.827	0.011	-0.836	0.011
2/4/2015	-2.920	-0.852	0.010	-0.865	0.010
2/6/2015	-24.291	-0.881	0.004	-0.890	0.004
2/9/2015	15.585	-0.834	0.007	-0.841	0.007
2/10/2015	-2.612	-0.851	0.005	-0.863	0.005
2/13/2015	-24.038	-0.847	0.012	-0.856	0.012
2/16/2015	17.288	-0.829	0.006	-0.824	0.006
2/23/2015	-3.723	-0.871	0.007	-0.873	0.007
2/25/2015	-24.694	-0.839	0.005	-0.847	0.005
2/27/2015	13.150	-0.861	0.006	-0.859	0.006
3/2/2015	-1.311	-0.877	0.006	-0.878	0.006
3/4/2015	-24.813	-0.856	0.009	-0.865	0.009
3/7/2015	13.103	-0.886	0.010	-0.894	0.010
3/9/2015	-1.821	-0.913	0.007	-0.915	0.007
3/10/2015	-24.764	-0.895	0.006	-0.904	0.006
3/12/2015	-24.844	-0.897	0.012	-0.895	0.012
3/16/2015	17.417	-0.847	0.011	-0.842	0.011
3/17/2015	-3.742	-0.897	0.006	-0.899	0.006
3/19/2015	-24.909	-0.877	0.004	-0.876	0.004
3/23/2015	16.806	-0.903	0.005	-0.899	0.005
3/25/2015	-3.730	-0.905	0.008	-0.908	0.008
4/8/2015	16.568	-0.887	0.007	-0.883	0.007
4/9/2015	-3.870	-0.875	0.009	-0.888	0.009
4/10/2015	-24.901	-0.875	0.012	-0.873	0.012
4/17/2015	-3.349	-0.879	0.007	-0.882	0.007

5/7/2014	9.068	-0.039	0.006	-0.034	0.006
5/12/2014	14.855	-0.055	0.011	-0.046	0.011
5/22/2014	-26.710	-0.042	0.005	-0.020	0.005
5/30/2014	9.565	-0.046	0.009	-0.051	0.009
6/5/2014	-27.187	-0.042	0.007	-0.020	0.007
1/8/2015	15.558	-0.055	0.006	-0.056	0.006
1/14/2015	-23.935	-0.038	0.010	-0.015	0.010
1/15/2015	-21.048	-0.036	0.006	-0.012	0.006
1/17/2015	-21.119	-0.059	0.007	-0.034	0.007
1/21/2015	15.527	-0.069	0.008	-0.060	0.008
1/21/2015	15.619	-0.072	0.005	-0.063	0.005
1/22/2015	-24.106	-0.058	0.006	-0.035	0.006
1/22/2015	-24.022	-0.053	0.008	-0.030	0.008
1/28/2015	14.933	-0.074	0.007	-0.066	0.007
1/28/2015	14.961	-0.055	0.007	-0.047	0.007
1/29/2015	13.088	-0.057	0.011	-0.060	0.011
1/29/2015	13.006	-0.071	0.004	-0.074	0.004
2/5/2015	-21.365	-0.074	0.007	-0.060	0.007
2/6/2015	-23.628	-0.064	0.008	-0.051	0.008
2/11/2015	13.232	-0.061	0.009	-0.064	0.009
2/13/2015	14.990	-0.103	0.007	-0.094	0.007
2/19/2015	-21.023	-0.020	0.007	0.005	0.007
2/20/2015	-21.062	-0.038	0.006	-0.013	0.006
2/24/2015	-23.331	-0.048	0.007	-0.024	0.007
3/6/2015	15.010	-0.069	0.004	-0.060	0.004
3/7/2015	-20.266	-0.085	0.008	-0.059	0.008
3/10/2015	13.465	-0.101	0.006	-0.093	0.006
3/13/2015	-22.688	-0.103	0.009	-0.090	0.009
3/19/2015	-19.569	-0.076	0.006	-0.051	0.006
3/21/2015	15.764	-0.081	0.009	-0.072	0.009
4/9/2015	16.723	-0.088	0.004	-0.078	0.004
4/17/2015	-22.272	-0.082	0.011	-0.058	0.011
4/22/2015	13.874	-0.093	0.010	-0.085	0.010
4/24/2015	-19.748	-0.082	0.008	-0.057	0.008
4/29/2015	16.755	-0.093	0.003	-0.083	0.003
5/6/2015	14.424	-0.090	0.005	-0.082	0.005
5/13/2015	-19.951	-0.061	0.011	-0.036	0.011
1/22/2016	7.862	-0.093	0.009	-0.089	0.009
1/22/2016	16.674	-0.060	0.007	-0.051	0.007
1/25/2016	16.457	-0.082	0.005	-0.072	0.005
1/25/2016	-29.168	-0.067	0.004	-0.048	0.004
1/26/2016	-19.939	-0.098	0.007	-0.072	0.007
1/28/2016	7.925	-0.072	0.003	-0.068	0.003
2/1/2016	7.633	-0.053	0.005	-0.049	0.005
2/9/2016	-28.555	-0.076	0.009	-0.056	0.009
2/15/2016	7.627	-0.107	0.008	-0.103	0.008

4/20/2015	-23.915	-0.889	0.004	-0.887	0.004
4/21/2015	12.094	-0.878	0.007	-0.887	0.007
4/23/2015	-3.766	-0.893	0.006	-0.906	0.006
4/27/2015	-24.222	-0.874	0.006	-0.871	0.006
4/28/2015	12.017	-0.881	0.010	-0.880	0.010
5/5/2015	11.774	-0.896	0.005	-0.895	0.005
5/7/2015	-2.574	-0.888	0.007	-0.889	0.007
5/11/2015	-23.531	-0.864	0.010	-0.861	0.010
5/15/2015	17.235	-0.893	0.009	-0.888	0.009
5/18/2015	-1.334	-0.900	0.007	-0.901	0.007
5/19/2015	-23.679	-0.889	0.007	-0.887	0.007
1/19/2016	-2.905	-0.889	0.007	-0.891	0.007
1/19/2016	-24.612	-0.870	0.012	-0.868	0.012
1/21/2016	-1.497	-0.894	0.007	-0.895	0.007
1/21/2016	-24.217	-0.909	0.007	-0.906	0.007
1/22/2016	12.196	-0.879	0.004	-0.876	0.004
1/26/2016	-2.167	-0.923	0.009	-0.924	0.009
1/27/2016	-24.388	-0.907	0.008	-0.905	0.008
1/29/2016	13.284	-0.931	0.007	-0.929	0.007
2/1/2016	-24.051	-0.876	0.005	-0.874	0.005
2/3/2016	-1.352	-0.938	0.007	-0.939	0.007
2/5/2016	18.352	-0.914	0.007	-0.908	0.007
2/8/2016	-24.346	-0.924	0.008	-0.921	0.008
2/10/2016	-1.727	-0.904	0.005	-0.906	0.005
2/11/2016	-24.153	-0.929	0.010	-0.927	0.010
2/16/2016	-2.253	-0.892	0.002	-0.893	0.002
2/18/2016	-2.708	-0.909	0.008	-0.911	0.008
2/25/2016	-24.834	-0.863	0.004	-0.862	0.004
2/26/2016	-1.626	-0.868	0.009	-0.869	0.009
2/26/2016	16.453	-0.891	0.006	-0.887	0.006
3/1/2016	-25.241	-0.868	0.008	-0.866	0.008
3/8/2016	-1.727	-0.880	0.006	-0.881	0.006
3/10/2016	18.420	-0.896	0.010	-0.890	0.010
3/15/2016	-3.049	-0.893	0.008	-0.895	0.008
3/17/2016	14.550	-0.897	0.011	-0.894	0.011
3/18/2016	-1.927	-0.898	0.008	-0.899	0.008
3/18/2016	-24.074	-0.886	0.008	-0.883	0.008
3/22/2016	17.817	-0.917	0.013	-0.912	0.013
3/24/2016	-1.373	-0.895	0.005	-0.896	0.005
3/25/2016	13.323	-0.888	0.006	-0.886	0.006
3/31/2016	-24.282	-0.875	0.008	-0.873	0.008
4/1/2016	-1.850	-0.878	0.006	-0.879	0.006
4/5/2016	-2.670	-0.895	0.008	-0.897	0.008
4/7/2016	9.923	-0.902	0.010	-0.901	0.010
4/8/2016	-24.059	-0.923	0.008	-0.920	0.008
4/11/2016	-1.964	-0.888	0.004	-0.890	0.004
2/22/2016	-28.641	-0.079	0.008	-0.059	0.008
2/23/2016	-20.266	-0.091	0.006	-0.066	0.006
2/27/2016	16.311	-0.096	0.009	-0.087	0.009
3/2/2016	-28.812	-0.083	0.008	-0.064	0.008
3/3/2016	-20.257	-0.093	0.009	-0.067	0.009
3/8/2016	7.278	-0.079	0.004	-0.075	0.004
3/10/2016	15.310	-0.094	0.006	-0.084	0.006
3/15/2016	-28.342	-0.082	0.006	-0.062	0.006
3/21/2016	14.832	-0.085	0.009	-0.075	0.009
3/22/2016	-20.168	-0.103	0.012	-0.078	0.012
3/30/2016	7.717	-0.079	0.004	-0.075	0.004
4/1/2016	-28.825	-0.096	0.007	-0.077	0.007
4/5/2016	14.629	-0.083	0.009	-0.073	0.009
4/8/2016	-20.357	-0.102	0.008	-0.077	0.008
4/11/2016	7.733	-0.090	0.008	-0.086	0.008
4/14/2016	-28.370	-0.095	0.006	-0.076	0.006
4/20/2016	-19.625	-0.127	0.007	-0.102	0.007
4/21/2016	-20.600	-0.101	0.007	-0.076	0.007
4/22/2016	7.817	-0.105	0.008	-0.101	0.008
4/29/2016	-28.238	-0.071	0.010	-0.051	0.010
5/3/2016	16.920	-0.041	0.006	-0.041	0.006
5/9/2016	-18.661	-0.058	0.007	-0.032	0.007
5/10/2016	7.323	-0.032	0.008	-0.029	0.008
5/10/2016	-28.328	-0.049	0.007	-0.029	0.007
5/13/2016	16.511	-0.035	0.009	-0.026	0.009
5/18/2016	-19.056	-0.068	0.006	-0.043	0.006
5/19/2016	7.958	-0.041	0.005	-0.036	0.005
5/23/2016	-28.613	-0.060	0.005	-0.040	0.005
5/25/2016	17.054	-0.061	0.006	-0.051	0.006
5/30/2016	8.213	-0.060	0.006	-0.055	0.006
6/1/2016	-28.522	-0.006	0.008	0.014	0.008
6/4/2016	17.276	-0.056	0.007	-0.046	0.007
6/6/2016	-20.211	-0.033	0.004	-0.008	0.004
6/10/2016	8.895	-0.063	0.005	-0.058	0.005
6/13/2016	-28.416	-0.028	0.008	-0.008	0.008
6/17/2016	17.274	-0.053	0.007	-0.043	0.007
6/22/2016	-19.432	-0.074	0.007	-0.048	0.007
6/23/2016	8.760	-0.057	0.006	-0.052	0.006
6/28/2016	-28.047	-0.043	0.005	-0.023	0.005
6/30/2016	17.434	-0.051	0.006	-0.041	0.006
7/4/2016	-19.779	-0.037	0.006	-0.011	0.006
7/8/2016	7.987	-0.044	0.007	-0.040	0.007
7/8/2016	-27.504	-0.013	0.005	0.008	0.005
7/13/2016	7.982	-0.037	0.011	-0.033	0.011
7/18/2016	-19.629	-0.050	0.010	-0.024	0.010
7/19/2016	16.838	-0.035	0.006	-0.026	0.006

4/13/2016	-24.099	-0.923	0.009	-0.921	0.009
4/15/2016	-2.305	-0.907	0.007	-0.909	0.007
4/19/2016	-24.616	-0.902	0.007	-0.900	0.007
4/21/2016	15.142	-0.909	0.008	-0.905	0.008
4/22/2016	-4.195	-0.903	0.006	-0.905	0.006
4/25/2016	-24.985	-0.879	0.007	-0.877	0.007
4/28/2016	9.372	-0.915	0.008	-0.915	0.008
5/3/2016	-1.224	-0.868	0.007	-0.880	0.007
5/3/2016	-24.570	-0.849	0.009	-0.857	0.009
5/9/2016	-2.723	-0.845	0.009	-0.847	0.009
5/10/2016	14.420	-0.839	0.012	-0.836	0.012
5/12/2016	13.001	-0.872	0.006	-0.870	0.006
5/12/2016	-25.270	-0.845	0.007	-0.843	0.007
5/17/2016	12.369	-0.840	0.010	-0.838	0.010
5/18/2016	-1.662	-0.860	0.006	-0.861	0.006
5/19/2016	-25.511	-0.846	0.007	-0.845	0.007
5/25/2016	-1.424	-0.862	0.007	-0.863	0.007
5/27/2016	-2.418	-0.829	0.007	-0.830	0.007
5/30/2016	-24.307	-0.851	0.010	-0.849	0.010
6/1/2016	-25.194	-0.839	0.006	-0.837	0.006
6/4/2016	-23.878	-0.857	0.005	-0.854	0.005
6/6/2016	-1.347	-0.866	0.012	-0.867	0.012
6/8/2016	-3.178	-0.844	0.009	-0.846	0.009
6/9/2016	17.106	-0.845	0.005	-0.840	0.005
6/13/2016	-24.872	-0.822	0.007	-0.820	0.007
6/16/2016	-1.589	-0.874	0.007	-0.875	0.007
6/20/2016	15.935	-0.866	0.009	-0.862	0.009
6/23/2016	-1.876	-0.845	0.008	-0.846	0.008
6/24/2016	-24.188	-0.855	0.006	-0.852	0.006
6/28/2016	17.985	-0.880	0.004	-0.875	0.004
6/29/2016	-4.079	-0.841	0.004	-0.843	0.004
7/1/2016	-24.997	-0.828	0.005	-0.825	0.005
7/6/2016	-3.741	-0.840	0.003	-0.843	0.003
7/7/2016	-30.359	-0.893	0.009	-0.890	0.009
7/7/2016	12.757	-0.899	0.009	-0.896	0.009
7/7/2016	12.788	-0.887	0.014	-0.885	0.014
7/12/2016	-30.396	-0.831	0.004	-0.828	0.004
7/14/2016	-30.197	-0.889	0.008	-0.885	0.008
7/14/2016	16.598	-0.899	0.009	-0.894	0.009
7/21/2016	-2.501	-0.868	0.006	-0.870	0.006
7/25/2016	17.694	-0.890	0.004	-0.885	0.004
7/27/2016	-25.285	-0.887	0.007	-0.885	0.007
7/29/2016	-2.685	-0.874	0.005	-0.876	0.005
8/3/2016	15.034	-0.863	0.012	-0.860	0.012
8/11/2016	-3.736	-0.880	0.007	-0.883	0.007
8/16/2016	17.020	-0.894	0.004	-0.890	0.004
7/21/2016	16.969	-0.038	0.007	-0.028	0.007
7/22/2016	-28.668	-0.044	0.004	-0.024	0.004
7/26/2016	8.147	-0.037	0.006	-0.033	0.006
7/28/2016	-19.743	-0.028	0.007	-0.002	0.007
8/3/2016	-28.826	-0.013	0.009	0.007	0.009
8/9/2016	30.729	-0.052	0.007	-0.034	0.007
8/12/2016	-28.660	-0.010	0.006	0.010	0.006
8/16/2016	17.043	-0.048	0.009	-0.038	0.009
8/18/2016	-19.437	-0.032	0.006	-0.006	0.006
8/23/2016	7.860	-0.036	0.009	-0.032	0.009
8/25/2016	8.119	-0.022	0.009	-0.018	0.009
8/30/2016	-28.643	-0.030	0.007	-0.010	0.007
9/2/2016	30.811	-0.038	0.007	-0.020	0.007
9/14/2016	-7.293	-0.040	0.010	-0.006	0.010
9/16/2016	-29.120	-0.016	0.005	0.004	0.005
9/20/2016	31.160	-0.062	0.007	-0.043	0.007
9/22/2016	-6.843	-0.068	0.007	-0.033	0.007
9/27/2016	7.866	-0.037	0.006	-0.032	0.006
10/6/2016	8.275	-0.055	0.004	-0.051	0.004
10/12/2016	-28.811	-0.065	0.009	-0.045	0.009
10/14/2016	30.874	-0.050	0.004	-0.031	0.004
10/17/2016	-6.673	-0.064	0.007	-0.029	0.007
10/25/2016	30.776	-0.052	0.007	-0.034	0.007
10/31/2016	-6.553	-0.058	0.009	-0.023	0.009
11/3/2016	-28.654	-0.025	0.009	-0.005	0.009
11/7/2016	8.019	-0.034	0.004	-0.029	0.004
11/12/2016	30.522	-0.080	0.006	-0.062	0.006
11/15/2016	-6.612	-0.076	0.006	-0.041	0.006
11/17/2016	-28.506	-0.036	0.006	-0.015	0.006
11/23/2016	7.434	-0.044	0.006	-0.040	0.006
11/25/2016	30.776	-0.045	0.003	-0.027	0.003
11/30/2016	-6.394	-0.063	0.004	-0.028	0.004
12/2/2016	-28.640	-0.026	0.009	-0.006	0.009
12/7/2016	7.892	-0.042	0.009	-0.038	0.009
12/13/2016	30.619	-0.036	0.007	-0.018	0.007
12/15/2016	-6.500	-0.059	0.005	-0.025	0.005
12/20/2016	-28.508	-0.040	0.005	-0.020	0.005
12/22/2016	8.065	-0.036	0.010	-0.032	0.010
1/7/2017	-6.306	-0.064	0.005	-0.029	0.005
1/7/2017	30.765	-0.043	0.003	-0.024	0.003
1/11/2017	8.032	-0.048	0.005	-0.043	0.005
1/13/2017	-28.077	-0.053	0.006	-0.032	0.006
1/17/2017	-28.527	-0.048	0.006	-0.027	0.006
1/24/2017	30.627	-0.059	0.007	-0.040	0.007
1/26/2017	-6.463	-0.052	0.007	-0.017	0.007
1/30/2017	7.934	-0.038	0.006	-0.033	0.006

8/19/2016	-30.107	-0.891	0.007	-0.888	0.007
8/20/2016	-1.423	-0.884	0.004	-0.885	0.004
8/22/2016	16.356	-0.870	0.006	-0.865	0.006
8/23/2016	-30.353	-0.879	0.008	-0.875	0.008
8/25/2016	-2.500	-0.865	0.005	-0.866	0.005
8/30/2016	17.178	-0.862	0.005	-0.857	0.005
8/31/2016	-30.392	-0.879	0.010	-0.875	0.010
9/1/2016	-1.466	-0.873	0.006	-0.874	0.006
9/6/2016	-25.459	-0.858	0.005	-0.856	0.005
9/7/2016	-2.111	-0.872	0.006	-0.873	0.006
9/7/2016	13.790	-0.855	0.006	-0.853	0.006
9/13/2016	-2.940	-0.865	0.007	-0.866	0.007
9/15/2016	16.371	-0.873	0.007	-0.869	0.007
9/19/2016	-2.656	-0.846	0.007	-0.847	0.007
9/21/2016	12.267	-0.882	0.005	-0.880	0.005
9/23/2016	-3.327	-0.849	0.005	-0.851	0.005
9/27/2016	-30.189	-0.896	0.005	-0.892	0.005
9/30/2016	11.873	-0.882	0.006	-0.881	0.006
10/1/2016	-2.161	-0.863	0.006	-0.865	0.006
10/3/2016	-25.627	-0.861	0.004	-0.859	0.004
10/5/2016	-3.550	-0.856	0.007	-0.858	0.007
10/11/2016	-24.319	-0.860	0.005	-0.857	0.005
10/12/2016	-3.822	-0.887	0.006	-0.889	0.006
10/15/2016	16.783	-0.882	0.009	-0.878	0.009
10/18/2016	-3.695	-0.894	0.009	-0.896	0.009
10/18/2016	-24.632	-0.859	0.006	-0.857	0.006
10/19/2016	11.451	-0.874	0.005	-0.873	0.005
10/20/2016	11.619	-0.869	0.006	-0.868	0.006
10/24/2016	-25.060	-0.877	0.011	-0.874	0.011
10/25/2016	-24.779	-0.860	0.010	-0.857	0.010
10/26/2016	-3.811	-0.863	0.007	-0.866	0.007
11/1/2016	12.497	-0.887	0.008	-0.885	0.008
11/2/2016	-26.305	-0.878	0.007	-0.876	0.007
11/4/2016	-2.916	-0.852	0.006	-0.854	0.006
11/8/2016	15.318	-0.870	0.006	-0.867	0.006
11/12/2016	-5.251	-0.894	0.002	-0.897	0.002
11/14/2016	12.451	-0.871	0.006	-0.870	0.006
11/16/2016	-4.796	-0.837	0.007	-0.840	0.007
11/16/2016	-25.427	-0.857	0.005	-0.855	0.005
11/21/2016	-1.455	-0.875	0.003	-0.876	0.003
11/22/2016	-1.944	-0.856	0.007	-0.857	0.007
11/25/2016	13.659	-0.886	0.013	-0.883	0.013
12/1/2016	-5.621	-0.855	0.007	-0.859	0.007
12/2/2016	11.634	-0.899	0.010	-0.897	0.010
12/7/2016	-26.023	-0.865	0.011	-0.863	0.011
12/8/2016	-1.918	-0.848	0.007	-0.849	0.007
2/1/2017	-28.554	-0.016	0.006	0.005	0.006
2/7/2017	30.672	-0.059	0.005	-0.041	0.005
2/9/2017	-7.816	-0.070	0.005	-0.036	0.005
2/14/2017	7.355	-0.029	0.007	-0.025	0.007
2/16/2017	-29.004	-0.047	0.008	-0.027	0.008
2/22/2017	30.609	-0.073	0.008	-0.055	0.008
2/24/2017	-6.668	-0.037	0.006	-0.003	0.006
2/28/2017	7.745	-0.036	0.004	-0.031	0.004
3/4/2017	-28.597	-0.050	0.004	-0.030	0.004
3/10/2017	30.851	-0.070	0.011	-0.052	0.011
3/13/2017	-6.711	-0.048	0.010	-0.014	0.010
3/17/2017	8.121	-0.041	0.004	-0.037	0.004
3/21/2017	-28.519	-0.059	0.005	-0.039	0.005
3/24/2017	30.596	-0.051	0.008	-0.032	0.008
3/29/2017	-6.437	-0.040	0.013	-0.005	0.013
3/31/2017	8.035	-0.044	0.005	-0.040	0.005
4/3/2017	-28.490	-0.036	0.011	-0.015	0.011
4/11/2017	30.974	-0.018	0.009	0.001	0.009
4/20/2017	7.848	-0.026	0.007	-0.021	0.007
4/26/2017	30.909	-0.036	0.005	-0.018	0.005
4/28/2017	-6.627	-0.059	0.006	-0.024	0.006
5/3/2017	-28.444	-0.007	0.006	0.014	0.006
5/9/2017	-6.291	-0.031	0.004	0.004	0.004
5/24/2017	-6.369	-0.016	0.009	0.019	0.009
6/7/2017	-28.469	-0.020	0.008	0.000	0.008
6/13/2017	31.179	-0.028	0.005	-0.009	0.005
6/21/2017	-28.459	-0.041	0.005	-0.021	0.005
6/22/2017	-7.511	-0.047	0.005	-0.013	0.005
6/27/2017	30.786	-0.034	0.006	-0.016	0.006
6/29/2017	-30.083	-0.074	0.008	-0.055	0.008
7/4/2017	30.853	-0.043	0.009	-0.025	0.009
7/6/2017	-28.558	-0.038	0.006	-0.017	0.006
7/19/2017	7.523	-0.042	0.006	-0.038	0.006
7/20/2017	-6.829	-0.024	0.008	0.011	0.008
7/27/2017	-28.701	-0.022	0.005	-0.002	0.005
7/28/2017	8.349	-0.036	0.005	-0.031	0.005
7/31/2017	-27.935	-0.051	0.006	-0.031	0.006
8/1/2017	30.552	-0.045	0.007	-0.026	0.007
8/29/2017	-28.665	-0.019	0.004	0.002	0.004
8/29/2017	30.457	-0.001	0.009	0.018	0.009
8/30/2017	-7.209	0.002	0.009	0.036	0.009
8/31/2017	31.014	-0.002	0.004	0.017	0.004
9/1/2017	-28.658	-0.028	0.007	-0.008	0.007
9/5/2017	8.457	-0.020	0.003	-0.016	0.003
9/8/2017	-6.911	-0.059	0.006	-0.025	0.006
9/12/2017	8.306	-0.046	0.009	-0.041	0.009

12/9/2016	10.457	-0.883	0.002	-0.882	0.002
12/13/2016	-1.861	-0.869	0.006	-0.871	0.006
12/14/2016	17.184	-0.894	0.007	-0.889	0.007
12/16/2016	-24.994	-0.846	0.006	-0.844	0.006
12/20/2016	14.817	-0.870	0.008	-0.867	0.008
12/22/2016	-1.591	-0.876	0.010	-0.877	0.010
1/6/2017	-2.694	-0.824	0.007	-0.825	0.007
1/9/2017	-1.860	-0.868	0.005	-0.869	0.005
1/10/2017	-25.059	-0.844	0.009	-0.841	0.009
1/10/2017	16.859	-0.876	0.007	-0.871	0.007
1/11/2017	-4.622	-0.858	0.005	-0.861	0.005
1/12/2017	13.144	-0.881	0.007	-0.879	0.007
1/12/2017	-3.925	-0.872	0.009	-0.874	0.009
1/17/2017	-25.646	-0.874	0.006	-0.872	0.006
1/17/2017	14.088	-0.878	0.008	-0.875	0.008
1/20/2017	-25.255	-0.850	0.007	-0.847	0.007
1/23/2017	17.699	-0.876	0.007	-0.871	0.007
1/25/2017	-25.841	-0.848	0.007	-0.846	0.007
1/26/2017	-3.978	-0.859	0.011	-0.862	0.011
1/30/2017	17.741	-0.866	0.008	-0.861	0.008
1/31/2017	-25.670	-0.886	0.007	-0.884	0.007
2/1/2017	-1.864	-0.857	0.005	-0.858	0.005
2/7/2017	16.862	-0.877	0.010	-0.873	0.010
2/7/2017	-25.647	-0.866	0.004	-0.864	0.004
2/7/2017	-1.545	-0.856	0.007	-0.857	0.007
2/14/2017	-25.035	-0.870	0.008	-0.867	0.008
2/21/2017	-2.140	-0.866	0.006	-0.867	0.006
2/22/2017	16.928	-0.883	0.007	-0.878	0.007
2/24/2017	-25.144	-0.867	0.010	-0.864	0.010
2/27/2017	-2.738	-0.852	0.005	-0.853	0.005
2/28/2017	13.340	-0.869	0.007	-0.866	0.007
3/3/2017	-26.037	-0.871	0.007	-0.868	0.007
3/7/2017	-4.233	-0.862	0.006	-0.865	0.006
3/9/2017	11.599	-0.884	0.005	-0.883	0.005
3/13/2017	-2.595	-0.875	0.009	-0.877	0.009
3/15/2017	-25.015	-0.847	0.007	-0.844	0.007
3/16/2017	17.391	-0.863	0.003	-0.858	0.003
3/17/2017	-4.587	-0.855	0.007	-0.858	0.007
3/21/2017	-25.344	-0.866	0.004	-0.863	0.004
3/24/2017	17.849	-0.866	0.009	-0.861	0.009
3/24/2017	-1.637	-0.855	0.006	-0.856	0.006
3/27/2017	16.853	-0.861	0.004	-0.856	0.004
3/29/2017	-25.076	-0.848	0.011	-0.846	0.011
3/30/2017	-1.248	-0.879	0.006	-0.880	0.006
4/4/2017	-2.664	-0.859	0.007	-0.861	0.007
4/4/2017	-25.090	-0.835	0.007	-0.832	0.007
9/14/2017	-29.040	-0.040	0.008	-0.020	0.008
9/19/2017	-6.011	-0.071	0.008	-0.036	0.008
9/20/2017	7.965	-0.039	0.006	-0.035	0.006
9/26/2017	31.097	-0.031	0.006	-0.012	0.006
9/27/2017	-27.945	-0.032	0.007	-0.011	0.007
10/4/2017	-5.921	-0.049	0.008	-0.014	0.008
10/9/2017	8.514	-0.025	0.009	-0.021	0.009
10/11/2017	31.112	-0.026	0.006	-0.007	0.006
10/18/2017	-6.325	-0.059	0.007	-0.025	0.007
10/20/2017	8.251	-0.043	0.007	-0.038	0.007
10/23/2017	-28.843	-0.044	0.005	-0.024	0.005
10/26/2017	-6.405	-0.070	0.004	-0.035	0.004
10/30/2017	31.512	-0.051	0.007	-0.032	0.007
11/1/2017	8.073	-0.030	0.007	-0.026	0.007
				av	0.007
				sd	0.002

4/5/2017	12.515	-0.866	0.005	-0.865	0.005
4/7/2017	-25.914	-0.838	0.007	-0.836	0.007
4/10/2017	-1.876	-0.844	0.008	-0.845	0.008
4/19/2017	12.420	-0.872	0.007	-0.870	0.007
4/19/2017	-2.566	-0.845	0.007	-0.847	0.007
4/25/2017	-1.862	-0.842	0.006	-0.843	0.006
4/25/2017	-25.049	-0.851	0.009	-0.848	0.009
4/27/2017	-1.506	-0.852	0.005	-0.853	0.005
5/5/2017	13.438	-0.842	0.004	-0.840	0.004
5/8/2017	-4.713	-0.852	0.004	-0.855	0.004
5/10/2017	-2.961	-0.856	0.006	-0.858	0.006
5/25/2017	-1.473	-0.857	0.006	-0.858	0.006
5/30/2017	-26.748	-0.834	0.007	-0.832	0.007
6/6/2017	-25.313	-0.858	0.012	-0.856	0.012
6/12/2017	16.374	-0.838	0.007	-0.834	0.007
6/13/2017	17.225	-0.866	0.008	-0.861	0.008
6/23/2017	17.225	-0.866	0.008	-0.861	0.008
6/26/2017	-25.365	-0.838	0.006	-0.835	0.006
6/28/2017	17.453	-0.878	0.007	-0.873	0.007
6/30/2017	-0.940	-0.874	0.009	-0.874	0.009
7/3/2017	-0.597	-0.880	0.007	-0.880	0.007
7/5/2017	-25.669	-0.849	0.009	-0.846	0.009
7/7/2017	17.302	-0.862	0.007	-0.857	0.007
7/10/2017	-1.060	-0.848	0.012	-0.849	0.012
7/14/2017	15.653	-0.903	0.008	-0.899	0.008
7/17/2017	-0.532	-0.906	0.006	-0.906	0.006
7/19/2017	-26.782	-0.873	0.006	-0.871	0.006
7/21/2017	17.168	-0.870	0.006	-0.865	0.006
7/26/2017	-24.691	-0.884	0.013	-0.881	0.013
7/29/2017	16.906	-0.882	0.009	-0.878	0.009
7/31/2017	-1.115	-0.884	0.008	-0.885	0.008
8/29/2017	-24.231	-0.828	0.009	-0.825	0.009
8/30/2017	-0.880	-0.852	0.006	-0.852	0.006
8/31/2017	12.067	-0.873	0.010	-0.871	0.010
9/1/2017	18.480	-0.845	0.006	-0.840	0.006
9/4/2017	19.150	-0.874	0.005	-0.868	0.005
9/6/2017	-26.284	-0.881	0.005	-0.878	0.005
9/8/2017	-0.700	-0.870	0.006	-0.871	0.006
9/11/2017	18.852	-0.877	0.007	-0.871	0.007
9/13/2017	-26.547	-0.877	0.010	-0.874	0.010
9/15/2017	-0.595	-0.871	0.007	-0.872	0.007
9/19/2017	-23.803	-0.891	0.008	-0.889	0.008
9/21/2017	16.911	-0.874	0.008	-0.870	0.008
9/22/2017	-1.922	-0.872	0.005	-0.872	0.005
9/26/2017	-23.801	-0.861	0.010	-0.858	0.010
9/28/2017	15.770	-0.884	0.007	-0.880	0.007

9/29/2017	-1.034	-0.882	0.007	-0.883	0.007
10/5/2017	-24.818	-0.884	0.011	-0.881	0.011
10/6/2017	17.623	-0.892	0.005	-0.887	0.005
10/10/2017	-3.699	-0.902	0.007	-0.904	0.007
10/12/2017	-23.882	-0.891	0.006	-0.889	0.006
10/17/2017	-24.556	-0.844	0.009	-0.841	0.009
10/19/2017	16.702	-0.871	0.005	-0.866	0.005
10/24/2017	-0.994	-0.880	0.004	-0.881	0.004
10/25/2017	-25.763	-0.877	0.005	-0.874	0.005
10/27/2017	14.963	-0.865	0.006	-0.861	0.006
10/31/2017	-25.454	-0.895	0.009	-0.892	0.009
11/2/2017	15.333	-0.854	0.007	-0.850	0.007
11/3/2017	-1.398	-0.886	0.007	-0.887	0.007
				av	0.007
				sd	0.002

Data correction		[*Gonfiantini*]			[*Brand*]		
			ETF			ETF	
Time interval HG/25G		residual slope*	slope	intercept	residual slope*	slope	intercept
2/19/2014	6/5/2014	-0.0003	1.0863	0.9703	-0.0005	1.0791	0.9586
1/8/2015	5/19/2015	-0.0003	1.1226	1.0044	-0.0005	1.1025	0.9892
1/19/2016	4/29/2016	0.0000	1.1050	1.0213	-0.0003	1.0904	1.0071
5/3/2016	7/4/2016	-0.0003	1.1172	0.9796	-0.0005	1.1007	0.9650
7/6/2016	12/22/2016	-0.0002	1.0823	0.9712	-0.0003	1.0611	0.9514
1/6/2017	7/10/2017	-0.0002	1.0983	0.9727	-0.0002	1.0672	0.9506
7/14/2016	11/3/2017	0.0000	1.0697	0.9636	-0.0003	1.0492	0.9429

* the residual slope is derived from the 25G and HG data. This correction step was performed even though the HGL slopes are below 0.001. This assures a precise data correction, especially for samples with extreme δ^{47} values.

Standard data – S.2.II

II. Standard data (continued)

Reference materials

NIST SRM 120c

		[*Gonfiantini*] in ‰					[*Brand*] in ‰				
Date	δ^{47}	Δ_{47raw}	$\Delta_{47\ CDES\ 110}$	se	$\delta^{13}C_{V\text{-}PDB}$	$\delta^{18}O_{V\text{-}PDB}$	Δ_{47raw}	$\Delta_{47\ CDES\ 110}$	se	$\delta^{13}C_{V\text{-}PDB}$	$\delta^{18}O_{V\text{-}PDB}$
3/10/2014	9.405	-0.367	0.575	0.024	-6.53	-1.47	-0.359	0.576	0.024	-6.52	-1.67
4/4/2014	10.103	-0.374	0.567	0.016	-6.37	-0.93	-0.365	0.570	0.016	-6.36	-1.13
4/8/2014	9.778	-0.357	0.585	0.030	-6.52	-1.13	-0.349	0.587	0.030	-6.51	-1.33
4/9/2014	9.760	-0.389	0.551	0.018	-6.52	-1.12	-0.380	0.553	0.018	-6.50	-1.32
4/10/2014	9.801	-0.385	0.556	0.018	-6.45	-1.15	-0.376	0.558	0.018	-6.44	-1.35
4/15/2014	9.857	-0.383	0.557	0.011	-6.37	-1.17	-0.375	0.559	0.011	-6.36	-1.37
4/16/2014	9.577	-0.396	0.543	0.027	-6.47	-1.33	-0.388	0.545	0.027	-6.46	-1.53
4/17/2014	9.673	-0.364	0.578	0.028	-6.43	-1.31	-0.355	0.580	0.028	-6.42	-1.51
4/30/2014	9.546	-0.378	0.562	0.025	-6.48	-1.37	-0.370	0.564	0.025	-6.47	-1.57
5/20/2014	9.804	-0.379	0.561	0.023	-6.35	-1.24	-0.371	0.563	0.023	-6.34	-1.44
5/22/2014	10.027	-0.398	0.541	0.019	-6.30	-1.06	-0.389	0.544	0.019	-6.29	-1.26
2/24/2015	9.712	-0.419	0.537	0.023	-6.43	-1.22	-0.411	0.541	0.023	-6.42	-1.42
3/11/2015	9.914	-0.404	0.555	0.024	-6.36	-1.10	-0.395	0.559	0.024	-6.35	-1.30
4/21/2015	9.875	-0.398	0.561	0.024	-6.35	-1.15	-0.390	0.564	0.024	-6.34	-1.35
4/29/2015	10.036	-0.371	0.591	0.020	-6.39	-0.98	-0.363	0.595	0.020	-6.38	-1.18
5/5/2015	10.077	-0.358	0.606	0.029	-6.36	-0.98	-0.350	0.609	0.029	-6.35	-1.19
2/2/2016	9.758	-0.417	0.560	0.030	-6.42	-1.18	-0.409	0.564	0.030	-6.41	-1.38
2/3/2016	9.660	-0.407	0.572	0.021	-6.48	-1.23	-0.398	0.576	0.021	-6.47	-1.43
2/5/2016	9.610	-0.402	0.577	0.022	-6.52	-1.25	-0.394	0.581	0.022	-6.51	-1.45
2/10/2016	9.782	-0.398	0.582	0.026	-6.46	-1.14	-0.389	0.585	0.026	-6.45	-1.34
3/1/2016	9.516	-0.405	0.574	0.023	-6.60	-1.26	-0.397	0.577	0.023	-6.59	-1.46
3/17/2016	9.735	-0.399	0.580	0.035	-6.51	-1.14	-0.391	0.584	0.035	-6.50	-1.34
3/25/2016	9.170	-0.416	0.562	0.018	-6.60	-1.58	-0.407	0.565	0.018	-6.59	-1.78
5/18/2016	9.897	-0.363	0.577	0.024	-6.43	-1.35	-0.354	0.580	0.024	-6.41	-1.54
6/7/2016	9.776	-0.348	0.593	0.022	-6.49	-1.42	-0.340	0.596	0.022	-6.48	-1.61
6/8/2016	10.026	-0.360	0.580	0.023	-6.37	-1.28	-0.352	0.583	0.023	-6.36	-1.47
6/9/2016	9.736	-0.374	0.564	0.023	-6.52	-1.41	-0.366	0.567	0.023	-6.50	-1.60
6/30/2016	9.808	-0.352	0.589	0.019	-6.34	-1.53	-0.343	0.592	0.019	-6.33	-1.72
7/2/2016	9.702	-0.353	0.589	0.017	-6.38	-1.60	-0.344	0.591	0.017	-6.36	-1.79
7/26/2016	9.869	-0.359	0.586	0.013	-6.39	-1.42	-0.350	0.583	0.013	-6.38	-1.61
7/27/2016	9.855	-0.362	0.582	0.013	-6.30	-1.51	-0.354	0.580	0.013	-6.29	-1.70
7/29/2016	9.819	-0.351	0.594	0.012	-6.52	-1.35	-0.342	0.592	0.012	-6.51	-1.54
7/31/2016	9.421	-0.362	0.582	0.010	-6.56	-1.69	-0.354	0.579	0.010	-6.55	-1.88
8/16/2016	10.133	-0.342	0.604	0.029	-6.35	-1.21	-0.333	0.602	0.029	-6.34	-1.41
8/18/2016	10.108	-0.374	0.570	0.017	-6.41	-1.15	-0.365	0.568	0.017	-6.40	-1.34
8/22/2016	10.086	-0.350	0.595	0.018	-6.37	-1.24	-0.341	0.593	0.018	-6.36	-1.43
9/27/2016	9.802	-0.368	0.575	0.023	-6.26	-1.60	-0.360	0.573	0.023	-6.25	-1.79

9/29/2016	10.020	-0.368	0.575	0.029	-6.40	-1.25	-0.360	0.574	0.029	-6.39	-1.44
10/5/2016	9.866	-0.368	0.576	0.022	-6.51	-1.29	-0.359	0.574	0.022	-6.50	-1.48
11/2/2016	10.342	-0.354	0.591	0.022	-6.27	-1.08	-0.345	0.589	0.022	-6.26	-1.27
11/13/2016	9.852	-0.348	0.597	0.014	-6.45	-1.39	-0.340	0.595	0.014	-6.43	-1.58
11/18/2016	10.174	-0.339	0.607	0.020	-6.37	-1.16	-0.330	0.604	0.020	-6.36	-1.35
11/20/2016	9.987	-0.359	0.585	0.018	-6.39	-1.31	-0.350	0.583	0.018	-6.37	-1.50
12/19/2016	9.913	-0.381	0.561	0.009	-6.32	-1.42	-0.373	0.560	0.009	-6.31	-1.61
4/3/2017	10.020	-0.375	0.562	0.019	-6.24	-1.40	-0.367	0.562	0.019	-6.23	-1.59
9/5/2017	10.256	-0.358	0.581	0.015	-6.34	-1.09	-0.349	0.580	0.015	-6.32	-1.29
9/10/2017	10.052	-0.381	0.556	0.022	-6.15	-1.44	-0.373	0.555	0.022	-6.14	-1.64
9/17/2017	10.006	-0.376	0.562	0.015	-6.33	-1.32	-0.367	0.561	0.015	-6.32	-1.51
10/25/2017	9.806	-0.375	0.562	0.013	-6.41	-1.45	-0.367	0.561	0.013	-6.39	-1.64
10/27/2017	9.718	-0.375	0.563	0.026	-6.41	-1.53	-0.366	0.562	0.026	-6.40	-1.72
10/30/2017	9.736	-0.342	0.598	0.035	-6.42	-1.54	-0.333	0.596	0.035	-6.41	-1.73
av			0.574		-6.41	-1.29		0.575		-6.40	-1.49
se			0.002					0.002			

Arc. islandica 110°C

		[*Gonfiantini*] in ‰					[*Brand*] in ‰				
Date	δ^{47}	Δ_{47raw}	$\Delta_{47\ CDES\ 110}$	se	$\delta^{13}C_{V\text{-}PDB}$	$\delta^{18}O_{V\text{-}PDB}$	Δ_{47raw}	$\Delta_{47\ CDES\ 110}$	se	$\delta^{13}C_{V\text{-}PDB}$	$\delta^{18}O_{V\text{-}PDB}$
3/6/2014	22.555	-0.316	0.634	0.027	1.52	3.12	-0.308	0.638	0.027	1.51	3.12
3/7/2014	22.815	-0.299	0.652	0.027	1.56	3.32	-0.291	0.656	0.027	1.55	3.32
3/10/2014	22.938	-0.309	0.641	0.017	1.56	3.44	-0.301	0.645	0.017	1.56	3.44
3/11/2014	22.726	-0.299	0.652	0.025	1.49	3.29	-0.291	0.656	0.025	1.48	3.30
4/3/2014	22.938	-0.331	0.618	0.019	1.55	3.47	-0.322	0.622	0.019	1.54	3.48
4/8/2014	22.816	-0.318	0.632	0.015	1.55	3.34	-0.310	0.636	0.015	1.54	3.35
4/9/2014	22.856	-0.304	0.646	0.023	1.49	3.42	-0.296	0.650	0.023	1.48	3.43
4/15/2014	22.613	-0.299	0.652	0.036	1.52	3.16	-0.291	0.656	0.036	1.51	3.16
4/16/2014	22.634	-0.297	0.654	0.029	1.46	3.23	-0.289	0.658	0.029	1.45	3.24
4/17/2014	22.576	-0.297	0.654	0.025	1.47	3.17	-0.289	0.658	0.025	1.47	3.17
5/9/2014	22.966	-0.294	0.658	0.047	1.56	3.45	-0.286	0.661	0.047	1.56	3.46
5/20/2014	22.782	-0.292	0.660	0.022	1.55	3.29	-0.284	0.663	0.022	1.54	3.29
5/22/2014	22.759	-0.259	0.696	0.028	1.51	3.27	-0.251	0.699	0.028	1.50	3.27
2/2/2016	22.801	-0.347	0.638	0.035	1.52	3.39	-0.339	0.644	0.035	1.51	3.39
2/2/2016	22.836	-0.317	0.671	0.021	1.55	3.36	-0.309	0.677	0.021	1.54	3.37
2/3/2016	22.805	-0.370	0.613	0.013	1.50	3.44	-0.362	0.619	0.013	1.49	3.44
2/4/2016	22.716	-0.374	0.608	0.014	1.39	3.45	-0.366	0.615	0.014	1.38	3.46
3/23/2016	22.287	-0.356	0.628	0.019	1.50	2.92	-0.349	0.633	0.019	1.50	2.92
3/30/2016	22.382	-0.319	0.669	0.030	1.35	3.12	-0.311	0.674	0.030	1.34	3.12
5/18/2016	22.241	-0.302	0.648	0.020	1.17	2.88	-0.294	0.653	0.020	1.16	2.89
6/10/2016	22.734	-0.316	0.634	0.018	1.49	3.06	-0.307	0.639	0.018	1.48	3.08
6/12/2016	22.607	-0.298	0.653	0.017	1.37	3.04	-0.289	0.658	0.017	1.36	3.05
6/22/2016	22.713	-0.284	0.670	0.019	1.57	2.94	-0.275	0.674	0.019	1.56	2.95
6/24/2016	22.307	-0.270	0.684	0.008	1.24	2.84	-0.262	0.688	0.008	1.24	2.85

7/25/2016	23.088	-0.288	0.666	0.015	1.60	3.27	-0.279	0.664	0.015	1.59	3.28
7/27/2016	23.117	-0.276	0.679	0.019	1.59	3.29	-0.267	0.676	0.019	1.58	3.31
7/28/2016	22.926	-0.295	0.658	0.020	1.56	3.16	-0.287	0.655	0.020	1.56	3.17
7/30/2016	22.770	-0.281	0.673	0.020	1.51	3.04	-0.273	0.670	0.020	1.50	3.06
8/11/2016	23.124	-0.295	0.658	0.017	1.58	3.33	-0.286	0.656	0.017	1.57	3.35
8/12/2016	22.670	-0.305	0.647	0.014	1.52	2.96	-0.297	0.645	0.014	1.52	2.97
8/20/2016	22.978	-0.269	0.686	0.020	1.55	3.19	-0.261	0.683	0.020	1.54	3.20
10/2/2016	22.400	-0.290	0.663	0.020	1.32	2.88	-0.282	0.660	0.020	1.31	2.89
10/9/2016	22.469	-0.290	0.663	0.016	1.39	2.88	-0.282	0.660	0.016	1.38	2.89
11/14/2016	22.491	-0.308	0.644	0.014	1.36	2.95	-0.299	0.642	0.014	1.35	2.96
12/23/2016	22.599	-0.301	0.647	0.019	1.49	2.92	-0.292	0.645	0.019	1.48	2.93
4/1/2017	22.695	-0.305	0.643	0.022	1.47	3.03	-0.296	0.640	0.022	1.47	3.04
9/2/2017	22.694	-0.263	0.682	0.011	1.62	2.84	-0.255	0.683	0.011	1.62	2.86
9/12/2017	22.736	-0.285	0.658	0.018	1.54	2.98	-0.277	0.659	0.018	1.53	3.00
9/15/2017	22.599	-0.317	0.625	0.017	1.49	2.93	-0.309	0.626	0.017	1.48	2.95
9/18/2017	22.846	-0.287	0.657	0.014	1.56	3.07	-0.278	0.658	0.014	1.55	3.09
10/27/2017	22.322	-0.313	0.629	0.021	1.31	2.83	-0.305	0.630	0.021	1.31	2.84
10/31/2017	22.562	-0.301	0.641	0.016	1.45	2.92	-0.293	0.643	0.016	1.44	2.93
av			0.652		1.48	3.14		0.654		1.48	3.15
se			0.003					0.003			

Arc. islandica	90°C	[*Gonfiantini*] in ‰					[*Brand*] in ‰				
Date	δ^{47}	Δ_{47raw}	Δ_{47}	se	$\delta^{13}C_{V\text{-}PDB}$	$\delta^{18}O_{V\text{-}PDB}$	Δ_{47raw}	Δ_{47}	se	$\delta^{13}C_{V\text{-}PDB}$	$\delta^{18}O_{V\text{-}PDB}$
2/2/2017	23.040	-0.312	0.634	0.016	1.51	3.55	-0.304	0.633	0.016	1.51	3.16
3/18/2017	23.055	-0.283	0.667	0.029	1.52	3.13	-0.274	0.664	0.029	1.51	3.14
3/22/2017	23.114	-0.302	0.645	0.023	1.51	3.21	-0.294	0.643	0.023	1.50	3.22
3/25/2017	23.752	-0.267	0.684	0.019	1.52	3.78	-0.258	0.681	0.019	1.52	3.79
3/27/2017	23.114	-0.295	0.654	0.020	1.48	3.23	-0.286	0.651	0.020	1.47	3.24
3/30/2017	23.085	-0.244	0.710	0.021	1.53	3.10	-0.235	0.706	0.021	1.52	3.11
4/4/2017	23.149	-0.281	0.669	0.012	1.54	3.19	-0.272	0.666	0.012	1.53	3.20
4/26/2017	23.206	-0.273	0.677	0.018	1.57	3.21	-0.264	0.674	0.018	1.56	3.22
6/8/2017	23.147	-0.270	0.681	0.021	1.54	3.18	-0.261	0.678	0.021	1.53	3.19
7/4/2017	23.077	-0.271	0.680	0.023	1.56	3.10	-0.262	0.677	0.023	1.55	3.11
7/5/2017	23.144	-0.262	0.689	0.015	1.57	3.14	-0.254	0.686	0.015	1.56	3.15
7/7/2017	23.081	-0.273	0.677	0.034	1.54	3.12	-0.265	0.674	0.034	1.54	3.13
7/10/2017	23.200	-0.296	0.647	0.018	1.55	3.24	-0.287	0.649	0.018	1.55	3.25
7/15/2017	23.169	-0.265	0.680	0.020	1.57	3.17	-0.257	0.681	0.020	1.57	3.18
7/16/2017	23.241	-0.267	0.678	0.019	1.58	3.23	-0.258	0.679	0.019	1.58	3.24
7/18/2017	23.060	-0.280	0.664	0.025	1.51	3.14	-0.272	0.665	0.025	1.50	3.15
7/20/2017	22.933	-0.268	0.677	0.011	1.46	3.05	-0.259	0.678	0.011	1.45	3.06
7/28/2017	23.096	-0.295	0.647	0.018	1.53	3.17	-0.287	0.649	0.018	1.52	3.18
7/29/2017	23.140	-0.291	0.653	0.027	1.54	3.19	-0.282	0.654	0.027	1.54	3.20
7/30/2017	23.226	-0.304	0.638	0.023	1.58	3.25	-0.296	0.640	0.023	1.57	3.26
av			0.668		0.67	0.67		0.666		1.53	3.21
se			0.004					0.004			

Carrara marble 110 °C		[*Gonfiantini*] in ‰					[*Brand*] in ‰				
Date	δ^{47}	Δ_{47raw}	$\Delta_{47\ CDES\ 110}$	se	$\delta^{13}C_{V\text{-}PDB}$	$\delta^{18}O_{V\text{-}PDB}$	Δ_{47raw}	$\Delta_{47\ CDES\ 110}$	se	$\delta^{13}C_{V\text{-}PDB}$	$\delta^{18}O_{V\text{-}PDB}$
3/24/2016	17.222	-0.679	0.271	0.021	1.83	-1.52	-0.674	0.277	0.021	1.97	-1.52
3/29/2016	17.264	-0.626	0.330	0.019	1.86	-1.55	-0.621	0.334	0.019	2.00	-1.55
6/1/2016	17.561	-0.643	0.266	0.018	2.08	-1.71	-0.638	0.271	0.018	2.07	-1.70
6/3/2016	17.469	-0.641	0.269	0.019	2.04	-1.76	-0.636	0.274	0.019	2.03	-1.76
6/8/2016	17.332	-0.617	0.296	0.035	1.91	-1.80	-0.612	0.300	0.035	1.90	-1.79
6/9/2016	17.334	-0.600	0.314	0.013	1.85	-1.75	-0.595	0.319	0.013	1.84	-1.74
6/22/2016	17.856	-0.640	0.270	0.020	2.14	-1.49	-0.635	0.275	0.020	2.13	-1.48
6/29/2016	17.479	-0.599	0.316	0.023	1.95	-1.71	-0.594	0.320	0.023	1.94	-1.70
7/28/2016	17.592	-0.625	0.300	0.016	2.02	-1.64	-0.620	0.300	0.016	2.01	-1.63
7/30/2016	17.434	-0.605	0.321	0.017	1.88	-1.68	-0.600	0.321	0.017	1.87	-1.68
8/11/2016	17.819	-0.613	0.312	0.021	2.05	-1.46	-0.608	0.312	0.021	2.03	-1.45
8/20/2016	17.903	-0.601	0.325	0.023	2.03	-1.37	-0.596	0.325	0.023	2.02	-1.36
10/1/2016	17.872	-0.599	0.328	0.019	2.01	-1.39	-0.594	0.328	0.019	2.00	-1.38
10/8/2016	17.831	-0.587	0.341	0.021	2.04	-1.47	-0.582	0.341	0.021	2.03	-1.46
10/31/2016	17.615	-0.627	0.297	0.016	2.04	-1.63	-0.622	0.298	0.016	2.03	-1.62
11/4/2016	17.630	-0.597	0.330	0.024	2.03	-1.65	-0.592	0.330	0.024	2.02	-1.64
11/11/2016	17.427	-0.619	0.306	0.016	1.95	-1.74	-0.614	0.307	0.016	1.94	-1.73
2/8/2017	17.357	-0.642	0.271	0.023	2.00	-1.83	-0.637	0.275	0.023	1.99	-1.82
2/12/2017	17.353	-0.655	0.257	0.022	1.97	-1.80	-0.650	0.261	0.022	1.96	-1.79
4/2/2017	17.282	-0.625	0.289	0.026	1.94	-1.87	-0.620	0.293	0.026	1.93	-1.86
9/1/2017	17.496	-0.601	0.321	0.015	2.00	-1.74	-0.596	0.323	0.015	1.99	-1.73
9/2/2017	17.332	-0.637	0.282	0.021	1.97	-1.84	-0.632	0.285	0.021	1.96	-1.83
9/3/2017	17.302	-0.641	0.278	0.012	1.95	-1.84	-0.636	0.281	0.012	1.94	-1.84
9/10/2017	17.515	-0.619	0.301	0.008	1.96	-1.67	-0.614	0.304	0.008	1.95	-1.66
10/24/2017	17.460	-0.609	0.312	0.017	1.91	-1.68	-0.604	0.315	0.017	1.90	-1.67
10/28/2017	17.221	-0.638	0.281	0.008	1.88	-1.86	-0.633	0.284	0.008	1.87	-1.85
av			0.299		1.97	-1.67		0.302		1.97	-1.66
se			0.005					0.004			

Carrara marble 90 °C		[*Gonfiantini*] in ‰					[*Brand*] in ‰				
Date	δ^{47}	Δ_{47raw}	$\Delta_{47\ CDES\ 110}$	se	$\delta^{13}C_{V\text{-}PDB}$	$\delta^{18}O_{V\text{-}PDB}$	Δ_{47raw}	$\Delta_{47\ CDES\ 110}$	se	$\delta^{13}C_{V\text{-}PDB}$	$\delta^{18}O_{V\text{-}PDB}$
12/15/2016	18.103	-0.586	0.342	0.020	1.99	-1.37	-0.581	0.342	0.020	1.98	-1.36
12/18/2016	17.447	-0.632	0.292	0.019	1.98	-1.95	-0.627	0.293	0.019	1.97	-1.94
12/20/2016	17.309	-0.634	0.290	0.015	1.98	-2.08	-0.629	0.290	0.015	1.97	-2.07
12/21/2016	17.347	-0.637	0.287	0.029	1.96	-2.02	-0.632	0.287	0.029	1.94	-2.01
1/30/2017	17.690	-0.618	0.297	0.024	1.97	-1.72	-0.613	0.301	0.024	1.96	-1.71
2/6/2017	17.739	-0.567	0.354	0.025	1.95	-1.71	-0.562	0.356	0.025	1.94	-1.70
2/16/2017	17.744	-0.623	0.292	0.024	1.96	-1.66	-0.618	0.296	0.024	1.95	-1.65
3/23/2017	17.702	-0.604	0.313	0.021	1.94	-1.70	-0.599	0.316	0.021	1.93	-1.69
3/25/2017	18.020	-0.582	0.337	0.020	1.94	-1.42	-0.577	0.340	0.020	1.93	-1.41
3/27/2017	17.788	-0.598	0.320	0.054	1.95	-1.63	-0.593	0.323	0.054	1.94	-1.62

3/29/2017	17.677	-0.619	0.297	0.026	1.97	-1.73	-0.614	0.300	0.026	1.96	-1.72
4/26/2017	17.737	-0.592	0.326	0.025	1.96	-1.70	-0.587	0.329	0.025	1.95	-1.69
6/8/2017	17.912	-0.585	0.334	0.026	2.00	-1.57	-0.580	0.337	0.026	1.99	-1.56
6/9/2017	17.906	-0.599	0.319	0.016	1.99	-1.55	-0.594	0.322	0.016	1.98	-1.54
7/5/2017	17.716	-0.600	0.317	0.012	1.96	-1.71	-0.595	0.320	0.012	1.95	-1.70
7/6/2017	17.732	-0.599	0.318	0.020	1.97	-1.70	-0.594	0.321	0.020	1.96	-1.69
7/7/2017	17.763	-0.607	0.309	0.014	1.98	-1.68	-0.602	0.313	0.014	1.97	-1.67
7/8/2017	17.801	-0.571	0.349	0.019	1.98	-1.67	-0.566	0.352	0.019	1.97	-1.66
7/9/2017	17.730	-0.626	0.288	0.029	1.98	-1.69	-0.621	0.292	0.029	1.97	-1.68
7/11/2017	17.749	-0.607	0.315	0.023	1.99	-1.70	-0.601	0.317	0.023	1.98	-1.69
7/14/2017	17.776	-0.613	0.308	0.027	2.00	-1.68	-0.607	0.311	0.027	1.99	-1.67
7/15/2017	17.773	-0.616	0.304	0.025	1.99	-1.67	-0.611	0.307	0.025	1.98	-1.66
7/17/2017	17.744	-0.585	0.337	0.018	1.98	-1.71	-0.580	0.340	0.018	1.96	-1.70
7/19/2017	17.759	-0.591	0.332	0.029	1.96	-1.67	-0.586	0.334	0.029	1.95	-1.66
7/20/2017	17.774	-0.605	0.316	0.021	1.99	-1.67	-0.600	0.319	0.021	1.98	-1.66
7/27/2017	17.721	-0.614	0.307	0.020	1.95	-1.68	-0.609	0.309	0.020	1.94	-1.67
7/28/2017	17.692	-0.596	0.326	0.024	1.92	-1.70	-0.591	0.329	0.024	1.91	-1.69
7/29/2017	17.741	-0.620	0.300	0.019	1.93	-1.64	-0.615	0.303	0.019	1.92	-1.63
7/31/2017	17.704	-0.592	0.330	0.020	1.95	-1.71	-0.587	0.332	0.020	1.94	-1.70
10/20/2017	17.827	-0.642	0.277	0.025	2.02	-1.61	-0.637	0.280	0.025	2.00	-1.60
10/21/2017	17.774	-0.615	0.306	0.028	1.96	-1.64	-0.610	0.309	0.028	1.95	-1.63
10/23/2017	17.955	-0.615	0.306	0.014	2.03	-1.53	-0.610	0.309	0.014	2.02	-1.52
av			0.315		1.97	-1.65		0.318		1.96	-1.64
se			0.003					0.003			

ETH-1 110°C		[*Gonfiantini*] in ‰					[*Brand*] in ‰				
Date	δ^{47}	Δ_{47raw}	$\Delta_{47\ CDES\ 110}$	se	$\delta^{13}C_{V\text{-}PDB}$	$\delta^{18}O_{V\text{-}PDB}$	Δ_{47raw}	$\Delta_{47\ CDES\ 110}$	se	$\delta^{13}C_{V\text{-}PDB}$	$\delta^{18}O_{V\text{-}PDB}$
3/2/2016	16.594	-0.746	0.197	0.027	1.91	-2.13	-0.742	0.203	0.027	1.90	-2.13
6/1/2016	16.889	-0.725	0.174	0.027	2.04	-2.24	-0.721	0.180	0.027	2.03	-2.23
6/7/2016	16.758	-0.695	0.208	0.020	1.81	-2.18	-0.690	0.214	0.020	1.80	-2.17
6/22/2016	17.417	-0.689	0.215	0.030	2.21	-1.92	-0.685	0.220	0.030	2.19	-1.91
8/19/2016	16.839	-0.696	0.222	0.008	1.85	-2.14	-0.691	0.224	0.008	1.84	-2.13
9/21/2016	17.014	-0.738	0.177	0.021	2.03	-2.10	-0.733	0.179	0.021	2.02	-2.09
11/22/2016	17.150	-0.684	0.235	0.009	1.77	-1.78	-0.679	0.237	0.009	1.76	-1.77
9/3/2017	16.796	-0.714	0.200	0.014	2.00	-2.30	-0.710	0.204	0.014	1.99	-2.29
9/3/2017	16.739	-0.723	0.190	0.019	1.99	-2.34	-0.718	0.195	0.019	1.98	-2.34
9/10/2017	16.769	-0.727	0.186	0.019	1.94	-2.26	-0.723	0.190	0.019	1.93	-2.25
9/16/2017	16.904	-0.698	0.217	0.019	1.88	-2.10	-0.693	0.221	0.019	1.87	-2.09
10/30/2017	16.645	-0.737	0.175	0.014	1.86	-2.29	-0.733	0.180	0.014	1.85	-2.28
av			0.200		1.94	-2.15		0.204		1.93	-2.14
se			0.006					0.006			

ETH-2 110°C		[*Gonfiantini*] in ‰					[*Brand*] in ‰				
Date	δ^{47}	Δ_{47raw}	$\Delta_{47\ CDES\ 110}$	se	$\delta^{13}C_{V\text{-}PDB}$	$\delta^{18}O_{V\text{-}PDB}$	Δ_{47raw}	$\Delta_{47\ CDES\ 110}$	se	$\delta^{13}C_{V\text{-}PDB}$	$\delta^{18}O_{V\text{-}PDB}$
7/28/2016	-11.929	-0.705	0.205	0.010	-10.18	-18.70	-0.706	0.198	0.010	-10.17	-18.69
10/3/2016	-11.918	-0.717	0.192	0.014	-10.21	-18.65	-0.718	0.186	0.014	-10.20	-18.64
11/14/2016	-11.978	-0.715	0.194	0.013	-10.18	-18.75	-0.716	0.188	0.013	-10.16	-18.74
2/13/2017	-12.341	-0.706	0.195	0.018	-10.34	-18.96	-0.707	0.193	0.018	-10.32	-18.95
9/3/2017	-11.824	-0.700	0.214	0.019	-10.12	-18.67	-0.701	0.204	0.019	-10.10	-18.66
9/18/2017	-11.973	-0.716	0.198	0.031	-10.20	-18.72	-0.716	0.188	0.031	-10.19	-18.71
10/28/2017	-11.535	-0.725	0.188	0.017	-10.10	-18.38	-0.726	0.178	0.017	-10.09	-18.37
10/31/2017	-11.861	-0.719	0.195	0.013	-10.16	-18.64	-0.720	0.184	0.013	-10.15	-18.63
av			0.198		-10.19	-18.68		0.190		-10.17	-18.67
se			0.003					0.003			

ETH-2 90°C		[*Gonfiantini*] in ‰					[*Brand*] in ‰				
Date	δ^{47}	Δ_{47raw}	$\Delta_{47\ CDES\ 90}$	Se	$\delta^{13}C_{V\text{-}PDB}$	$\delta^{18}O_{V\text{-}PDB}$	Δ_{47raw}	$\Delta_{47\ CDES\ 90}$	se	$\delta^{13}C_{V\text{-}PDB}$	$\delta^{18}O_{V\text{-}PDB}$
2/3/2017	-11.782	-0.690	0.213	0.021	-10.21	-19.05	-0.690	0.211	0.021	-10.20	-19.04
2/7/2017	-11.821	-0.712	0.188	0.021	-10.24	-19.05	-0.713	0.186	0.021	-10.22	-19.04
3/17/2017	-11.792	-0.703	0.198	0.017	-10.20	-19.06	-0.704	0.197	0.017	-10.19	-19.05
3/21/2017	-10.928	-0.665	0.240	0.025	-10.14	-18.32	-0.666	0.237	0.025	-10.12	-18.31
av			0.210		-10.20	-18.87		0.208		-10.18	-18.86
se			0.011					0.011			

ETH-3 110°C		[*Gonfiantini*] in ‰					[*Brand*] in ‰				
Date	δ^{47}	Δ_{47raw}	$\Delta_{47\ CDES\ 110}$	Se	$\delta^{13}C_{V\text{-}PDB}$	$\delta^{18}O_{V\text{-}PDB}$	Δ_{47raw}	$\Delta_{47\ CDES\ 110}$	Se	$\delta^{13}C_{V\text{-}PDB}$	$\delta^{18}O_{V\text{-}PDB}$
2/4/2016	17.287	-0.383	0.598	0.025	1.63	-1.55	-0.378	0.600	0.025	1.62	-1.55
3/3/2016	17.292	-0.356	0.628	0.025	1.57	-1.51	-0.351	0.629	0.025	1.56	-1.51
3/31/2016	17.472	-0.382	0.558	0.031	1.75	-1.49	-0.377	0.559	0.031	1.74	-1.49
5/17/2016	17.581	-0.335	0.610	0.032	1.72	-1.65	-0.330	0.610	0.032	1.71	-1.65
6/1/2016	17.562	-0.306	0.643	0.025	1.69	-1.68	-0.301	0.642	0.025	1.68	-1.67
6/3/2016	17.334	-0.333	0.612	0.019	1.72	-1.89	-0.328	0.613	0.019	1.71	-1.88
6/10/2016	17.259	-0.336	0.609	0.014	1.62	-1.87	-0.331	0.609	0.014	1.61	-1.86
6/11/2016	17.594	-0.316	0.632	0.019	1.56	-1.51	-0.311	0.632	0.019	1.55	-1.50
6/22/2016	17.652	-0.320	0.627	0.010	1.78	-1.66	-0.315	0.627	0.010	1.77	-1.65
6/23/2016	17.294	-0.320	0.627	0.018	1.63	-1.86	-0.315	0.627	0.018	1.62	-1.85
6/28/2016	17.308	-0.314	0.634	0.015	1.64	-1.87	-0.309	0.633	0.015	1.63	-1.86
6/29/2016	17.364	-0.342	0.603	0.022	1.66	-1.80	-0.337	0.603	0.022	1.65	-1.80
7/1/2016	17.282	-0.314	0.634	0.025	1.62	-1.87	-0.309	0.634	0.025	1.61	-1.86
7/3/2016	16.906	-0.344	0.604	0.012	1.42	-2.02	-0.339	0.598	0.012	1.41	-2.01
8/1/2016	17.298	-0.325	0.624	0.016	1.53	-1.76	-0.320	0.618	0.016	1.52	-1.75
8/23/2016	16.862	-0.341	0.606	0.019	1.38	-2.02	-0.336	0.600	0.019	1.37	-2.02
9/21/2016	17.169	-0.347	0.600	0.012	1.65	-1.97	-0.342	0.595	0.012	1.64	-1.96
9/28/2016	17.150	-0.317	0.633	0.019	1.59	-1.96	-0.312	0.626	0.019	1.58	-1.95
9/30/2016	17.257	-0.316	0.634	0.015	1.58	-1.86	-0.311	0.628	0.015	1.57	-1.85

10/1/2016	17.466	-0.348	0.599	0.017	1.67	-1.71	-0.343	0.594	0.017	1.66	-1.70
10/6/2016	17.135	-0.317	0.632	0.017	1.59	-1.98	-0.312	0.626	0.017	1.58	-1.97
11/1/2016	17.240	-0.336	0.612	0.019	1.68	-1.94	-0.331	0.606	0.019	1.67	-1.93
11/3/2016	17.318	-0.349	0.598	0.026	1.71	-1.88	-0.344	0.593	0.026	1.70	-1.87
11/9/2016	16.717	-0.334	0.614	0.011	1.36	-2.15	-0.329	0.608	0.011	1.35	-2.14
11/12/2016	17.311	-0.334	0.615	0.011	1.62	-1.82	-0.329	0.609	0.011	1.61	-1.81
11/18/2016	17.551	-0.324	0.626	0.007	1.61	-1.59	-0.319	0.620	0.007	1.60	-1.58
11/21/2016	17.109	-0.344	0.603	0.024	1.57	-1.96	-0.340	0.597	0.024	1.56	-1.95
12/20/2016	17.179	-0.335	0.613	0.019	1.65	-1.97	-0.330	0.607	0.019	1.64	-1.96
2/9/2017	17.029	-0.354	0.587	0.031	1.63	-2.09	-0.349	0.582	0.031	1.62	-2.08
2/11/2017	17.172	-0.347	0.595	0.016	1.66	-1.98	-0.342	0.590	0.016	1.65	-1.97
3/16/2017	17.248	-0.314	0.631	0.014	1.69	-1.97	-0.310	0.625	0.014	1.68	-1.96
9/1/2017	17.282	-0.316	0.625	0.012	1.66	-1.90	-0.311	0.622	0.012	1.65	-1.89
9/2/2017	17.117	-0.337	0.603	0.013	1.64	-2.03	-0.332	0.600	0.013	1.63	-2.02
9/4/2017	17.130	-0.333	0.607	0.011	1.62	-2.00	-0.328	0.604	0.011	1.61	-1.99
9/6/2017	17.301	-0.329	0.611	0.019	1.64	-1.86	-0.324	0.608	0.019	1.63	-1.85
9/7/2017	17.160	-0.325	0.616	0.019	1.63	-1.98	-0.320	0.613	0.019	1.62	-1.97
9/9/2017	17.559	-0.340	0.600	0.010	1.73	-1.68	-0.335	0.597	0.010	1.72	-1.67
9/12/2017	17.399	-0.325	0.615	0.015	1.70	-1.82	-0.320	0.612	0.015	1.69	-1.81
9/17/2017	17.343	-0.325	0.616	0.021	1.70	-1.87	-0.320	0.613	0.021	1.69	-1.86
9/18/2017	17.379	-0.306	0.636	0.023	1.53	-1.70	-0.301	0.633	0.023	1.52	-1.69
10/24/2017	17.263	-0.322	0.619	0.017	1.59	-1.85	-0.317	0.616	0.017	1.58	-1.84
av			0.614		1.62	-1.84		0.611		1.61	-1.83
se			0.003					0.003			

ETH-3 90°C		[*Gonfiantini*] in ‰					[*Brand*] in ‰				
Date	δ^{47}	Δ_{47raw}	$\Delta_{47\ CDES\ 90}$	se	$\delta^{13}C_{V\text{-}PDB}$	$\delta^{18}O_{V\text{-}PDB}$	Δ_{47raw}	$\Delta_{47\ CDES\ 90}$	se	$\delta^{13}C_{V\text{-}PDB}$	$\delta^{18}O_{V\text{-}PDB}$
12/15/2016	17.549	-0.310	0.641	0.019	1.66	-2.17	-0.304	0.635	0.019	1.65	-2.16
2/1/2017	17.406	-0.304	0.643	0.020	1.63	-2.28	-0.299	0.636	0.020	1.62	-2.27
2/14/2017	17.705	-0.311	0.634	0.025	1.67	-2.02	-0.306	0.628	0.025	1.66	-2.01
2/14/2017	17.724	-0.344	0.599	0.025	1.69	-1.99	-0.338	0.594	0.025	1.68	-1.98
2/16/2017	17.669	-0.330	0.613	0.013	1.67	-2.04	-0.325	0.608	0.013	1.66	-2.03
3/26/2017	17.665	-0.305	0.642	0.027	1.68	-2.08	-0.299	0.636	0.027	1.67	-2.07
4/25/2017	17.510	-0.304	0.643	0.017	1.66	-2.21	-0.299	0.636	0.017	1.65	-2.20
4/27/2017	17.545	-0.335	0.608	0.023	1.66	-2.15	-0.330	0.603	0.023	1.65	-2.14
10/19/2017	17.557	-0.324	0.617	0.018	1.69	-2.17	-0.319	0.614	0.018	1.68	-2.16
10/21/2017	17.582	-0.333	0.607	0.025	1.64	-2.10	-0.328	0.604	0.025	1.63	-2.09
10/22/2017	17.648	-0.297	0.646	0.020	1.66	-2.08	-0.292	0.642	0.020	1.65	-2.07
av			0.627		1.66	-2.12		0.622		1.65	-2.11
se			0.005					0.005			

Sample data – S.2.III

III. Sample data (continued)

African elephant

Enamel		[*Gonfiantini*] in ‰					[*Brand*] in ‰					
Date	δ^{47}	Δ_{47raw}	$\Delta_{47\ CDES\ 110}$	se	$\delta^{13}C_{V\text{-}PDB}$	$\delta^{18}O_{V\text{-}PDB}$	Δ_{47raw}	$\Delta_{47\ CDES\ 110}$	se	$\delta^{13}C_{V\text{-}PD}$	$\delta^{18}O_{V\text{-}PDB}$	$\Delta(\Delta_{47})$ [‰]
3/7/2014	4.734	-0.418	0.518	0.021	-11.88	-0.87	-0.407	0.522	0.021	-11.85	-0.88	-0.004
4/4/2014	5.389	-0.381	0.558	0.019	-11.72	-0.42	-0.370	0.562	0.019	-11.69	-0.42	-0.004
4/4/2014	5.342	-0.408	0.528	0.024	-11.82	-0.34	-0.397	0.533	0.024	-11.80	-0.34	-0.004
4/8/2014	5.185	-0.423	0.512	0.027	-11.77	-0.53	-0.412	0.516	0.027	-11.74	-0.54	-0.004
4/9/2014	4.994	-0.413	0.523	0.026	-11.85	-0.66	-0.402	0.528	0.026	-11.82	-0.66	-0.004
4/15/2014	5.018	-0.394	0.544	0.016	-11.80	-0.69	-0.383	0.548	0.016	-11.78	-0.69	-0.004
4/17/2014	4.787	-0.386	0.552	0.026	-11.83	-0.90	-0.375	0.556	0.026	-11.80	-0.90	-0.004
1/16/2015	5.111	-0.426	0.528	0.036	-11.80	-0.58	-0.415	0.534	0.036	-11.77	-0.58	-0.006
1/16/2015	5.108	-0.422	0.533	0.031	-11.77	-0.61	-0.411	0.539	0.031	-11.74	-0.61	-0.006
1/19/2015	5.187	-0.434	0.519	0.023	-11.82	-0.47	-0.423	0.526	0.023	-11.80	-0.47	-0.007
3/6/2015	5.100	-0.437	0.515	0.023	-11.81	-0.56	-0.426	0.522	0.023	-11.79	-0.56	-0.007
3/11/2015	5.383	-0.400	0.557	0.019	-11.68	-0.44	-0.389	0.563	0.019	-11.66	-0.45	-0.006
4/22/2015	4.878	-0.431	0.523	0.029	-11.83	-0.77	-0.420	0.529	0.029	-11.80	-0.77	-0.006
4/29/2015	5.157	-0.409	0.547	0.019	-11.80	-0.54	-0.398	0.553	0.019	-11.77	-0.55	-0.006
5/5/2015	5.100	-0.411	0.545	0.016	-11.67	-0.72	-0.400	0.551	0.016	-11.64	-0.73	-0.006
2/3/2016	4.958	-0.431	0.545	0.024	-11.80	-0.72	-0.420	0.550	0.024	-11.77	-0.72	-0.005
2/4/2016	4.812	-0.434	0.542	0.016	-11.88	-0.78	-0.423	0.547	0.016	-11.85	-0.78	-0.005
2/5/2016	4.850	-0.433	0.543	0.017	-11.83	-0.79	-0.422	0.549	0.017	-11.81	-0.79	-0.005
2/9/2016	4.882	-0.428	0.549	0.022	-11.81	-0.79	-0.417	0.554	0.022	-11.78	-0.79	-0.005
2/26/2016	4.970	-0.447	0.528	0.020	-11.79	-0.70	-0.436	0.533	0.020	-11.76	-0.70	-0.006
2/29/2016	4.993	-0.421	0.556	0.023	-11.80	-0.69	-0.410	0.561	0.023	-11.78	-0.69	-0.005
3/2/2016	5.186	-0.435	0.541	0.021	-11.52	-0.76	-0.424	0.546	0.021	-11.49	-0.76	-0.005
3/3/2016	5.445	-0.432	0.544	0.022	-11.46	-0.56	-0.421	0.549	0.022	-11.44	-0.57	-0.005
3/16/2016	4.943	-0.418	0.559	0.024	-11.81	-0.73	-0.408	0.564	0.024	-11.79	-0.73	-0.005
6/7/2016	5.809	-0.372	0.566	0.026	-11.58	-0.41	-0.360	0.571	0.026	-11.56	-0.40	-0.005
7/26/2016	5.003	-0.393	0.547	0.011	-11.70	-1.06	-0.382	0.548	0.011	-11.67	-1.06	-0.001
7/29/2016	5.266	-0.376	0.566	0.014	-11.56	-0.95	-0.365	0.567	0.014	-11.54	-0.94	0.000
8/1/2016	5.055	-0.379	0.562	0.012	-11.68	-1.05	-0.368	0.563	0.012	-11.65	-1.04	-0.001
8/16/2016	5.146	-0.354	0.589	0.020	-11.74	-0.92	-0.343	0.590	0.020	-11.72	-0.91	-0.001
8/17/2016	5.304	-0.393	0.548	0.020	-11.66	-0.81	-0.382	0.549	0.020	-11.64	-0.80	-0.001
9/25/2016	5.398	-0.398	0.542	0.020	-11.76	-0.61	-0.387	0.543	0.020	-11.74	-0.60	-0.001
9/30/2016	5.230	-0.383	0.558	0.017	-11.78	-0.77	-0.372	0.559	0.017	-11.76	-0.76	-0.001
10/1/2016	5.363	-0.383	0.558	0.012	-11.80	-0.62	-0.371	0.559	0.012	-11.77	-0.62	-0.001
10/4/2016	5.216	-0.344	0.600	0.013	-11.61	-0.99	-0.333	0.600	0.013	-11.58	-0.98	0.000
11/1/2016	5.276	-0.379	0.563	0.025	-11.68	-0.83	-0.367	0.563	0.025	-11.65	-0.82	-0.001
11/12/2016	5.496	-0.384	0.558	0.014	-11.62	-0.67	-0.372	0.558	0.014	-11.59	-0.66	-0.001
11/17/2016	5.849	-0.376	0.566	0.014	-11.58	-0.36	-0.364	0.567	0.014	-11.56	-0.36	-0.001

11/21/2016	5.194	-0.395	0.545	0.018	-11.62	-0.95	-0.384	0.546	0.018	-11.59	-0.94	-0.001
12/19/2016	5.298	-0.386	0.555	0.024	-11.72	-0.76	-0.375	0.555	0.024	-11.69	-0.76	-0.001
2/9/2017	5.492	-0.414	0.519	0.017	-11.76	-0.51	-0.403	0.522	0.017	-11.73	-0.50	-0.003
2/11/2017	5.540	-0.390	0.546	0.012	-11.73	-0.51	-0.378	0.548	0.012	-11.71	-0.50	-0.003
3/16/2017	5.664	-0.387	0.549	0.021	-11.74	-0.38	-0.375	0.551	0.021	-11.72	-0.37	-0.003
3/31/2017	5.589	-0.375	0.562	0.012	-11.70	-0.51	-0.363	0.564	0.012	-11.67	-0.50	-0.002
4/2/2017	5.118	-0.379	0.557	0.014	-11.76	-0.91	-0.368	0.559	0.014	-11.74	-0.90	-0.002
9/6/2017	4.988	-0.409	0.526	0.027	-11.68	-1.08	-0.398	0.527	0.027	-11.65	-1.07	-0.001
9/16/2017	5.486	-0.348	0.591	0.018	-11.69	-0.64	-0.337	0.591	0.018	-11.67	-0.63	0.000
9/18/2017	5.141	-0.409	0.526	0.018	-11.70	-0.92	-0.398	0.527	0.018	-11.67	-0.91	-0.001
10/24/2017	5.016	-0.376	0.561	0.011	-11.79	-0.98	-0.365	0.561	0.011	-11.76	-0.97	0.000
10/29/2017	4.932	-0.391	0.545	0.015	-11.77	-1.07	-0.380	0.546	0.015	-11.74	-1.06	-0.001
av			0.547		-11.73	-0.71		0.550		-11.71	-0.71	
se			0.003		0.01	0.03		0.003		0.01	0.03	

Dentine

3/6/2014	4.424	-0.404	0.533	0.024	-12.22	-0.86	-0.393	0.537	0.024	-12.20	-0.86	-0.004
3/10/2014	4.837	-0.370	0.570	0.019	-12.19	-0.52	-0.359	0.574	0.019	-12.16	-0.52	-0.004
3/11/2014	5.060	-0.384	0.554	0.018	-12.25	-0.23	-0.373	0.559	0.018	-12.22	-0.23	-0.004
4/4/2014	5.436	-0.394	0.544	0.039	-12.27	0.16	-0.383	0.548	0.039	-12.24	0.16	-0.005
4/10/2014	5.227	-0.385	0.554	0.019	-12.25	-0.07	-0.373	0.559	0.019	-12.22	-0.07	-0.005
4/16/2014	4.827	-0.400	0.537	0.019	-12.22	-0.47	-0.389	0.542	0.019	-12.20	-0.47	-0.004
2/3/2016	5.765	-0.441	0.534	0.030	-12.14	0.41	-0.430	0.540	0.030	-12.12	0.41	-0.007
2/4/2016	5.608	-0.418	0.559	0.031	-12.22	0.31	-0.407	0.565	0.031	-12.19	0.30	-0.006
2/5/2016	6.086	-0.432	0.544	0.029	-12.13	0.71	-0.420	0.551	0.029	-12.11	0.70	-0.007
3/17/2016	5.423	-0.437	0.538	0.037	-12.25	0.17	-0.426	0.544	0.037	-12.22	0.17	-0.006
5/17/2016	6.120	-0.398	0.537	0.021	-12.03	0.34	-0.386	0.543	0.021	-12.00	0.35	-0.007
6/9/2016	5.915	-0.388	0.548	0.019	-12.27	0.36	-0.376	0.555	0.019	-12.24	0.37	-0.007
7/31/2016	5.540	-0.375	0.567	0.020	-12.16	-0.12	-0.363	0.568	0.020	-12.13	-0.11	-0.001
8/23/2016	5.972	-0.374	0.568	0.020	-12.11	0.26	-0.362	0.570	0.020	-12.09	0.27	-0.002
9/18/2017	6.130	-0.384	0.553	0.017	-12.07	0.39	-0.372	0.555	0.017	-12.05	0.39	-0.002
10/25/2017	5.441	-0.338	0.602	0.012	-12.19	-0.22	-0.326	0.603	0.012	-12.16	-0.21	-0.001
10/27/2017	5.834	-0.409	0.526	0.020	-12.10	0.14	-0.397	0.529	0.020	-12.07	0.15	-0.002
av			0.551		-12.18	0.04		0.555		-12.15	0.05	
se			0.004		0.25	0.07		0.004		0.25	0.07	

Greenland sharks

Enameloid		[*Gonfiantini*] in [‰]					[*Brand*] in [‰]					
Date	δ^{47}	Δ_{47raw}	$\Delta_{47\ CDES\ 110}$	Se	$\delta^{13}C_{V\text{-}PDB}$	$\delta^{18}O_{V\text{-}PDB}$	Δ_{47raw}	$\Delta_{47\ CDES\ 110}$	se	$\delta^{13}C_{V\text{-}PDB}$	$\delta^{18}O_{CO3V\text{-}PDB}$	$\Delta(\Delta_{47})$
Specimen 1												
4/30/2014	21.231	-0.316	0.633	0.021	1.69	2.13	-0.309	0.636	0.021	1.68	2.13*	-0.002
4/30/2014	20.113	-0.334	0.613	0.025	1.29	1.45	-0.328	0.615	0.025	1.28	1.45*	-0.002
5/2/2014	24.156	-0.303	0.648	0.024	2.46	4.20	-0.295	0.652	0.024	2.45	4.20#	-0.004
5/9/2014	25.194	-0.310	0.640	0.026	3.08	4.62	-0.303	0.645	0.026	3.07	4.62#	-0.004
								$\delta^{18}O_{PO4\ V\text{-}SMOW}$ ± se [‰] (n) =			25.32 ± 0.17 (3)*	
											25.74 ± 0.18 (3)#	
Specimen 2												
7/27/2016	25.549	-0.316	0.636	0.024	3.04	4.75	-0.307	0.635	0.024	3.03	4.75	0.002
10/6/2016	24.104	-0.316	0.635	0.012	2.14	4.21	-0.308	0.634	0.012	2.13	4.22	0.002
Specimen 3												
11/10/2016	20.193	-0.311	0.640	0.018	0.35	2.13	-0.303	0.637	0.018	0.35	2.14	0.003
11/13/2016	19.717	-0.299	0.653	0.014	0.15	1.85	-0.291	0.650	0.014	0.15	1.86	0.003
11/15/2016	19.975	-0.311	0.640	0.010	0.08	2.18	-0.303	0.637	0.010	0.07	2.19	0.003
11/18/2016	18.646	-0.327	0.622	0.019	-0.44	1.41	-0.319	0.620	0.019	-0.45	1.42	0.003
av			0.636		1.38	2.89		0.636		1.38	2.90	
se			0.004		0.41	0.43		0.004		0.41	0.56	

Dentine

Specimen 2												
3/17/2016	16.430	-0.307	0.682	0.023	-3.16	2.08	-0.298	0.687	0.023	-3.16	2.08	-0.005
3/18/2016	16.168	-0.356	0.628	0.024	-3.19	1.91	-0.347	0.633	0.024	-3.19	1.91	-0.005
3/24/2016	15.687	-0.344	0.641	0.026	-3.17	1.40	-0.336	0.646	0.026	-3.16	1.40	-0.005
3/25/2016	14.907	-0.341	0.644	0.025	-3.61	1.07	-0.333	0.649	0.025	-3.61	1.07	-0.004
3/30/2016	15.889	-0.343	0.642	0.018	-3.26	1.69	-0.334	0.647	0.018	-3.26	1.69	-0.005
6/24/2016	15.454	-0.318	0.628	0.013	-3.38	1.10	-0.309	0.632	0.013	-3.37	1.10	-0.004
7/1/2016	15.578	-0.251	0.704	0.017	-3.31	1.09	-0.242	0.707	0.017	-3.31	1.09	-0.003
7/2/2016	15.391	-0.256	0.698	0.013	-3.41	1.01	-0.247	0.701	0.013	-3.41	1.02	-0.003
7/28/2016	15.925	-0.300	0.651	0.013	-3.29	1.45	-0.290	0.649	0.013	-3.28	1.45	0.002
10/26/2017	16.397	-0.265	0.680	0.016	-3.29	1.88	-0.255	0.680	0.016	-3.29	1.88	0.000
Specimen 3												
9/29/2016	15.431	-0.296	0.655	0.012	-2.59	0.30	-0.288	0.652	0.012	-2.58	0.31	0.003
9/30/2016	15.276	-0.305	0.645	0.005	-2.57	0.14	-0.297	0.642	0.005	-2.56	0.15	0.003
10/2/2016	14.977	-0.339	0.608	0.020	-2.63	-0.05	-0.331	0.606	0.020	-2.63	-0.04	0.003
10/26/2017	15.030	-0.306	0.636	0.020	-2.51	-0.15	-0.298	0.634	0.020	-2.51	-0.14	0.002
10/28/2017	14.942	-0.350	0.589	0.013	-2.51	-0.19	-0.342	0.589	0.013	-2.51	-0.18	0.001
10/28/2017	14.965	-0.335	0.605	0.019	-2.53	-0.17	-0.327	0.604	0.019	-2.52	-0.16	0.001
av			0.646		-3.03	0.91		0.647		-3.02	0.91	
se			0.008		0.10	0.20		0.008		0.10	0.20	

Sandtiger sharks

Dentine*		[*Gonfiantini*] in ‰					[*Brand*] in ‰					
Date	δ^{47}	Δ_{47raw}	$\Delta_{47\ CDES\ 110}$	se	$\delta^{13}C_{V\text{-}PDB}$	$\delta^{18}O_{V\text{-}PDB}$	Δ_{47raw}	$\Delta_{47\ CDES\ 110}$	se	$\delta^{13}C_{V\text{-}PDB}$	$\delta^{18}O_{V\text{-}PDB}$	$\Delta(\Delta_{47})$
7/2/2016	14.442	-0.350	0.593	0.013	-3.85	0.59	-0.341	0.597	0.013	-3.84	0.60	-0.004
7/2/2016	14.442	-0.359	0.583	0.009	-3.89	0.64	-0.350	0.587	0.009	-3.88	0.65	-0.004
7/26/2016	14.720	-0.353	0.593	0.012	-3.90	0.92	-0.344	0.592	0.012	-3.90	0.93	0.001
7/27/2016	15.171	-0.315	0.634	0.025	-3.88	1.30	-0.306	0.632	0.025	-3.88	1.31	0.002
8/21/2016	15.594	-0.329	0.619	0.012	-3.80	1.64	-0.319	0.618	0.012	-3.79	1.65	0.001
9/2/2017	15.108	-0.355	0.584	0.011	-3.90	1.29	-0.346	0.585	0.011	-3.89	1.30	-0.001
9/5/2017	15.427	-0.335	0.605	0.018	-4.10	1.78	-0.325	0.606	0.018	-4.10	1.78	-0.001
9/5/2017	14.967	-0.391	0.546	0.011	-4.09	1.37	-0.381	0.548	0.011	-4.08	1.38	-0.002
9/6/2017	15.198	-0.383	0.554	0.024	-3.94	1.44	-0.373	0.556	0.024	-3.93	1.45	-0.002
9/9/2017	15.440	-0.299	0.644	0.019	-3.93	1.58	-0.289	0.644	0.019	-3.92	1.59	0.000
9/9/2017	14.796	-0.326	0.614	0.017	-4.15	1.20	-0.317	0.615	0.017	-4.14	1.21	-0.001
9/10/2017	14.659	-0.349	0.590	0.022	-4.10	1.04	-0.340	0.591	0.022	-4.10	1.05	-0.001
9/12/2017	15.157	-0.358	0.581	0.014	-4.04	1.47	-0.349	0.582	0.014	-4.03	1.48	-0.001
av			0.595		-3.97	1.25		0.596		-3.96	1.26	
se			0.008		0.04	0.12		0.008		0.04	0.12	

*) Three different sample batches from an identical pool of teeth are divided from each other by horizontal lines.

Synthetic CHAP

7°C*		[*Gonfiantini*] in ‰					[*Brand*] in ‰						
Date	δ^{47}	Δ_{47raw}	$\Delta_{47\ CDES\ 110}$	se	$\delta^{13}C_{V\text{-}PDB}$	$\delta^{18}O_{V\text{-}PDB}$	Δ_{47raw}	$\Delta_{47\ CDES\ 110}$	se	$\delta^{13}C_{V\text{-}PDB}$	$\delta^{18}O_{V\text{-}PDB}$	$\delta^{18}O_{\ H2O\ V\text{-}SMOW}$	$\Delta(\Delta_{47})$
9/7/2017	9.987	-0.319	0.623	0.015	-4.59	-3.04	-0.312	0.619	0.015	-4.59	-3.04	-5.9	0.004
9/8/2017	10.242	-0.294	0.649	0.013	-4.50	-2.91	-0.287	0.644	0.013	-4.49	-2.90	-5.9	0.004
9/7/2017	15.780	-0.301	0.641	0.011	0.45	-2.22	-0.296	0.637	0.011	0.44	-2.21	-6.0	0.004
9/8/2017	16.364	-0.313	0.628	0.013	0.45	-1.66	-0.308	0.625	0.013	0.45	-1.65	-6.0	0.003
av			0.635					0.631				-6.0	
se			0.006					0.006				0.03	
59°C*													
3/13/2015	-0.600	-0.464	0.483	0.018	-5.65	-11.91	-0.463	0.479	0.018	-5.65	-11.91	-6.1	0.005
7/30/2016	-0.567	-0.452	0.482	0.022	-5.65	-12.15	-0.451	0.473	0.022	-5.65	-12.14	-6.1	0.009
3/13/2015	-0.200	-0.457	0.492	0.028	-5.56	-11.62	-0.455	0.487	0.028	-5.56	-11.62	-6.2	0.005
8/2/2016	-1.068	-0.392	0.547	0.019	-5.76	-12.59	-0.391	0.537	0.019	-5.75	-12.58	-6.2	0.010
3/19/2015	-1.025	-0.460	0.487	0.018	-5.99	-12.01	-0.459	0.482	0.018	-5.98	-12.02	-6.5	0.005
8/17/2016	-0.646	-0.433	0.503	0.021	-5.93	-11.98	-0.431	0.494	0.021	-5.93	-11.97	-7.0	0.009
3/19/2015	-0.596	-0.435	0.516	0.019	-5.63	-11.96	-0.434	0.510	0.019	-5.63	-11.96	-6.5	0.005
av			0.501		-5.74	-12.03		0.495		-5.74	-12.03	-6.4	
se			0.009		0.06	0.11		0.008		0.06	0.11	0.12	

80°C

9/15/2017	-1.074	-0.454	0.477	0.009	-5.69	-12.60	-0.453	0.467	0.009	-5.69	-12.59	-4.0	0.010
9/15/2017	-1.064	-0.443	0.490	0.023	-5.69	-12.61	-0.442	0.479	0.023	-5.68	-12.60	-4.0	0.011
9/17/2017	-1.358	-0.455	0.477	0.017	-5.63	-12.94	-0.454	0.467	0.017	-5.63	-12.93	-4.0	0.011
9/17/2017	-1.704	-0.454	0.478	0.020	-5.66	-13.25	-0.453	0.467	0.020	-5.65	-13.24	-4.0	0.011
10/24/2017	-1.718	-0.431	0.502	0.010	-5.69	-13.25	-0.431	0.490	0.010	-5.69	-13.24	-4.0	0.012
10/25/2017	-1.819	-0.440	0.493	0.015	-5.77	-13.26	-0.439	0.482	0.015	-5.77	-13.25	-4.0	0.011
av			0.486		-5.69	-12.98		0.475		-5.68	-12.97	-4.0	
se			0.004		0.02	0.13		0.004		0.02	0.13	0.00	

*) Individual experiments at identical temperatures are divided from each other by horizontal lines.

The errors for the δ18OH2O values are <0.07 ‰ (7 and 59°C) and <0.05 ‰ (80 °C).

C. megalodon

Enameloid		[*Gonfiantini*] in ‰					[*Brand*] in ‰						
Date	δ^{47}	Δ_{47raw}	$\Delta_{47\ CDES\ 110}$	se	$\delta^{13}C_{V\text{-}PDB}$	$\delta^{18}O_{V\text{-}PDB}$	Δ_{47raw}	$\Delta_{47\ CDES\ 110}$	se	$\delta^{13}C_{V\text{-}PDB}$	$\delta^{18}O_{V\text{-}PDB}$	$\delta^{18}O_{PO4\ V\text{-}SMOW}$ ± SE	$\Delta(\Delta_{47})$
5/20/2014	22.476	-0.347	0.600	0.022	5.35	-0.10	-0.343	0.599	0.022	5.33	-0.10	22.05 ± 0.02 (2)	0.001
5/22/2014	21.841	-0.363	0.582	0.012	4.83	-0.20	-0.359	0.582	0.012	4.81	-0.20	21.42 ± 0.03 (3)	0.000
5/22/2014	21.394	-0.345	0.602	0.021	4.37	-0.21	-0.340	0.602	0.021	4.35	-0.21	22.11 ± 0.10 (2)	0.000
5/22/2014	20.904	-0.358	0.588	0.022	3.48	0.16	-0.353	0.589	0.022	3.47	0.16	21.78 ± 0.09 (3)	-0.001
av			0.593		0.59	0.59		0.593		4.49	-0.09	21.84	
se			0.005					0.005					

Serial $\delta^{18}O_{PO4}$ profile of the *C. megalodon* tooth (axial)

Sample name	$\delta^{18}O_{PO4\ VSMOW}$ [‰]	sd [‰]	n	Distance from tooth tip [cm]
Z Hai M R1	21.25	0.24	3	10.0
Z Hai M R2	21.62	0.20	2	9.5
Z Hai M R3	21.53	0.05	3	9.0
Z Hai M R4	21.38	0.05	3	8.5
Z Hai M R5	21.54	0.09	3	8.0
Z Hai M R6	21.32	0.02	3	7.5
Z Hai M R 7	21.51	0.20	3	7.0
Z Hai M R8	21.69	0.05	3	6.5
Z Hai M R9	21.78	0.20	3	6.0
Z Hai M R10	21.60	0.11	3	5.5
Z Hai M R11	21.48	0.14	3	5.0
Z Hai M R12	21.28	0.18	3	4.5
Z Hai M R13	21.43	0.15	3	4.0
Z Hai M R14	21.51	0.30	3	3.5
Z Hai M R15	21.02	0.25	3	3.0
Z Hai M R16	21.58	0.17	3	2.5
Z Hai M R17	21.70	0.07	2	2.0
Z Hai M R18	21.36	0.04	3	1.5
Z Hai M R 19	21.92	0.19	3	1.0
Z Hai M R20	21.21	0.20	3	0.5
av	21.49			
se	0.05			

Comparison of [Brand] processed Δ_{47} values of ETH 1, ETH 2, and ETH 3 – S.2.IV

IV. Comparison of ETH Δ_{47} [Brand] calculated standard values

Standard	Study	$\Delta_{47\ CDES\ 25}$ ± sd (n) [‰]
ETH-1	*this study*	0.304 ± 0.021 (12)
	Daeron *et. al.* (2016)	0.311 ± 0.024 (18)
	Bernasconi *et. al.* (2018)	0.256 ± 0.027 (82)
	Schauer *et. al.* (2016)	0.286 ± 0.017 (8)
ETH-2	*this study, 110 °C reaction*	0.290 ± 0.008 (8)
	this study, 90 °C reaction	0.290 ± 0.022 (4)
	Daeron *et. al.* (2016)	0.306 ± 0.022 (13)
	Bernasconi *et. al.* (2018)	0.254 ± 0.036 (83)
	Schauer *et. al.* (2016)	0.282 ± 0.017 (12)
ETH-3	*this study, 110 °C reaction*	0.711 ± 0.019 (41)
	this study, 90 °C reaction	0.704 ± 0.017 (11)
	Bernasconi *et. al.* (2018)	0.689 ± 0.034 (73)
	Schauer *et. al.* (2016)	0.695 ± 0.022 (6)

All $\Delta_{47\ CDES\ 25}$ values are normalized to the 25 °C reference frame by applying the temperature dependence of the acid fractionation factor of Daeron *et. al.* (2015)

Appendix to chapter 3

Photograph of an intact *Tyrannosaurus rex* tooth of the sampled specimen (*S.3.I*). Compilation of all measured and calculated data from equilibrated gases and empirical transfer functions (*S.3.II*), standard (*S.3.III*) and sample (*S.3.IV*) measurements including δ^{47} and raw Δ_{47} values.

Photograph of an intact T. rex tooth – S.3.I

Supplementary figure 3.I: Photo of an intact *T. rex* tooth from "Trix" (RGM 792.000) for comparison with the sampled tooth fragments of *figure 3.2* (page 74). Photo: Anne Schulp, modified.

Equilibrated gas data and transfer functions – S.3.II

I. Equilibrated gas data (continued)

Heated gases		[*Brand*] in ‰	
date	δ^{47}	Δ_{47raw}	se
7/6/2016	-3.741	-0.843	0.003
7/7/2016	-30.359	-0.890	0.009
7/7/2016	12.757	-0.896	0.009
7/7/2016	12.788	-0.885	0.014
7/12/2016	-30.396	-0.828	0.004
7/14/2016	-30.197	-0.885	0.008
7/14/2016	16.598	-0.894	0.009
7/21/2016	-2.501	-0.870	0.006

25 °C equilibrated gases		[*Brand*] in ‰	
date	δ^{47}	Δ_{47raw}	se
7/8/2016	7.987	-0.040	0.007
7/8/2016	-27.504	0.008	0.005
7/13/2016	7.982	-0.033	0.011
7/18/2016	-19.629	-0.024	0.010
7/19/2016	16.838	-0.026	0.006
7/21/2016	16.969	-0.028	0.007
7/22/2016	-28.668	-0.024	0.004
7/26/2016	8.147	-0.033	0.006

7/25/2016	17.694	-0.885	0.004
7/27/2016	-25.285	-0.885	0.007
7/29/2016	-2.685	-0.876	0.005
8/3/2016	15.034	-0.860	0.012
8/11/2016	-3.736	-0.883	0.007
8/16/2016	17.020	-0.890	0.004
8/19/2016	-30.107	-0.888	0.007
8/20/2016	-1.423	-0.885	0.004
8/22/2016	16.356	-0.865	0.006
8/23/2016	-30.353	-0.875	0.008
8/25/2016	-2.500	-0.866	0.005
8/30/2016	17.178	-0.857	0.005
8/31/2016	-30.392	-0.875	0.010
9/1/2016	-1.466	-0.874	0.006
9/6/2016	-25.459	-0.856	0.005
9/7/2016	-2.111	-0.873	0.006
9/7/2016	13.790	-0.853	0.006
9/13/2016	-2.940	-0.866	0.007
9/15/2016	16.371	-0.869	0.007
9/19/2016	-2.656	-0.847	0.007
9/21/2016	12.267	-0.880	0.005
9/23/2016	-3.327	-0.851	0.005
9/27/2016	-30.189	-0.892	0.005
9/30/2016	11.873	-0.881	0.006
10/1/2016	-2.161	-0.865	0.006
10/3/2016	-25.627	-0.859	0.004
10/5/2016	-3.550	-0.858	0.007
10/11/2016	-24.319	-0.857	0.005
10/12/2016	-3.822	-0.889	0.006
10/15/2016	16.783	-0.878	0.009
10/18/2016	-3.695	-0.896	0.009
10/18/2016	-24.632	-0.857	0.006
10/19/2016	11.451	-0.873	0.005
10/20/2016	11.619	-0.868	0.006
10/24/2016	-25.060	-0.874	0.011
10/25/2016	-24.779	-0.857	0.010
10/26/2016	-3.811	-0.866	0.007
11/1/2016	12.497	-0.885	0.008
11/2/2016	-26.305	-0.876	0.007
11/4/2016	-2.916	-0.854	0.006
11/8/2016	15.318	-0.867	0.006
11/12/2016	-5.251	-0.897	0.002
11/14/2016	12.451	-0.870	0.006
11/16/2016	-4.796	-0.840	0.007
11/16/2016	-25.427	-0.855	0.005
11/21/2016	-1.455	-0.876	0.003
7/28/2016	-19.743	-0.002	0.007
8/3/2016	-28.826	0.007	0.009
8/9/2016	30.729	-0.034	0.007
8/12/2016	-28.660	0.010	0.006
8/16/2016	17.043	-0.038	0.009
8/18/2016	-19.437	-0.006	0.006
8/23/2016	7.860	-0.032	0.009
8/25/2016	8.119	-0.018	0.009
8/30/2016	-28.643	-0.010	0.007
9/2/2016	30.811	-0.020	0.007
9/14/2016	-7.293	-0.006	0.010
9/16/2016	-29.120	0.004	0.005
9/20/2016	31.160	-0.043	0.007
9/22/2016	-6.843	-0.033	0.007
9/27/2016	7.866	-0.032	0.006
10/6/2016	8.275	-0.051	0.004
10/12/2016	-28.811	-0.045	0.009
10/14/2016	30.874	-0.031	0.004
10/17/2016	-6.673	-0.029	0.007
10/25/2016	30.776	-0.034	0.007
10/31/2016	-6.553	-0.023	0.009
11/3/2016	-28.654	-0.005	0.009
11/7/2016	8.019	-0.029	0.004
11/12/2016	30.522	-0.062	0.006
11/15/2016	-6.612	-0.041	0.006
11/17/2016	-28.506	-0.015	0.006
11/23/2016	7.434	-0.040	0.006
11/25/2016	30.776	-0.027	0.003
11/30/2016	-6.394	-0.028	0.004
12/2/2016	-28.640	-0.006	0.009
12/7/2016	7.892	-0.038	0.009
12/13/2016	30.619	-0.018	0.007
12/15/2016	-6.500	-0.025	0.005
12/20/2016	-28.508	-0.020	0.005
12/22/2016	8.065	-0.032	0.010
1/7/2017	-6.306	-0.029	0.005
1/7/2017	30.765	-0.024	0.003
1/11/2017	8.032	-0.043	0.005
1/13/2017	-28.077	-0.032	0.006
1/17/2017	-28.527	-0.027	0.006
1/24/2017	30.627	-0.040	0.007
1/26/2017	-6.463	-0.017	0.007
1/30/2017	7.934	-0.033	0.006
2/1/2017	-28.554	0.005	0.006
2/7/2017	30.672	-0.041	0.005
2/9/2017	-7.816	-0.036	0.005

11/22/2016	-1.944	-0.857	0.007
11/25/2016	13.659	-0.883	0.013
12/1/2016	-5.621	-0.859	0.007
12/2/2016	11.634	-0.897	0.010
12/7/2016	-26.023	-0.863	0.011
12/8/2016	-1.918	-0.849	0.007
12/9/2016	10.457	-0.882	0.002
12/13/2016	-1.861	-0.871	0.006
12/14/2016	17.184	-0.889	0.007
12/16/2016	-24.994	-0.844	0.006
12/20/2016	14.817	-0.867	0.008
12/22/2016	-1.591	-0.877	0.010
1/6/2017	-2.694	-0.825	0.007
1/9/2017	-1.860	-0.869	0.005
1/10/2017	-25.059	-0.841	0.009
1/10/2017	16.859	-0.871	0.007
1/11/2017	-4.622	-0.861	0.005
1/12/2017	13.144	-0.879	0.007
1/12/2017	-3.925	-0.874	0.009
1/17/2017	-25.646	-0.872	0.006
1/17/2017	14.088	-0.875	0.008
1/20/2017	-25.255	-0.847	0.007
1/23/2017	17.699	-0.871	0.007
1/25/2017	-25.841	-0.846	0.007
1/26/2017	-3.978	-0.862	0.011
1/30/2017	17.741	-0.861	0.008
1/31/2017	-25.670	-0.884	0.007
2/1/2017	-1.864	-0.858	0.005
2/7/2017	16.862	-0.873	0.010
2/7/2017	-25.647	-0.864	0.004
2/7/2017	-1.545	-0.857	0.007
2/14/2017	-25.035	-0.867	0.008
2/21/2017	-2.140	-0.867	0.006
2/22/2017	16.928	-0.878	0.007
2/24/2017	-25.144	-0.864	0.010
2/27/2017	-2.738	-0.853	0.005
2/28/2017	13.340	-0.866	0.007
3/3/2017	-26.037	-0.868	0.007
3/7/2017	-4.233	-0.865	0.006
3/9/2017	11.599	-0.883	0.005
3/13/2017	-2.595	-0.877	0.009
3/15/2017	-25.015	-0.844	0.007
3/16/2017	17.391	-0.858	0.003
3/17/2017	-4.587	-0.858	0.007
3/21/2017	-25.344	-0.863	0.004
3/24/2017	17.849	-0.861	0.009
2/14/2017	7.355	-0.025	0.007
2/16/2017	-29.004	-0.027	0.008
2/22/2017	30.609	-0.055	0.008
2/24/2017	-6.668	-0.003	0.006
2/28/2017	7.745	-0.031	0.004
3/4/2017	-28.597	-0.030	0.004
3/10/2017	30.851	-0.052	0.011
3/13/2017	-6.711	-0.014	0.010
3/17/2017	8.121	-0.037	0.004
3/21/2017	-28.519	-0.039	0.005
3/24/2017	30.596	-0.032	0.008
3/29/2017	-6.437	-0.005	0.013
3/31/2017	8.035	-0.040	0.005
4/3/2017	-28.490	-0.015	0.011
4/11/2017	30.974	0.001	0.009
4/20/2017	7.848	-0.021	0.007
4/26/2017	30.909	-0.018	0.005
4/28/2017	-6.627	-0.024	0.006
5/3/2017	-28.444	0.014	0.006
5/9/2017	-6.291	0.004	0.004
5/24/2017	-6.369	0.019	0.009
6/7/2017	-28.469	0.000	0.008
6/13/2017	31.179	-0.009	0.005
6/21/2017	-28.459	-0.021	0.005
6/22/2017	-7.511	-0.013	0.005
6/27/2017	30.786	-0.016	0.006
6/29/2017	-30.083	-0.055	0.008
7/4/2017	30.853	-0.025	0.009
7/6/2017	-28.558	-0.017	0.006
7/19/2017	7.523	-0.038	0.006
7/20/2017	-6.829	0.011	0.008
7/27/2017	-28.701	-0.002	0.005
7/28/2017	8.349	-0.031	0.005
7/31/2017	-27.935	-0.031	0.006
8/1/2017	30.552	-0.026	0.007
8/29/2017	-28.665	0.002	0.004
8/29/2017	30.457	0.018	0.009
8/30/2017	-7.209	0.036	0.009
8/31/2017	31.014	0.017	0.004
9/1/2017	-28.658	-0.008	0.007
9/5/2017	8.457	-0.016	0.003
9/8/2017	-6.911	-0.025	0.006
9/12/2017	8.306	-0.041	0.009
9/14/2017	-29.040	-0.020	0.008
9/19/2017	-6.011	-0.036	0.008
9/20/2017	7.965	-0.035	0.006

3/24/2017	-1.637	-0.856	0.006
3/27/2017	16.853	-0.856	0.004
3/29/2017	-25.076	-0.846	0.011
3/30/2017	-1.248	-0.880	0.006
4/4/2017	-2.664	-0.861	0.007
4/4/2017	-25.090	-0.832	0.007
4/5/2017	12.515	-0.865	0.005
4/7/2017	-25.914	-0.836	0.007
4/10/2017	-1.876	-0.845	0.008
4/19/2017	12.420	-0.870	0.007
4/19/2017	-2.566	-0.847	0.007
4/25/2017	-1.862	-0.843	0.006
4/25/2017	-25.049	-0.848	0.009
4/27/2017	-1.506	-0.853	0.005
5/5/2017	13.438	-0.840	0.004
5/8/2017	-4.713	-0.855	0.004
5/10/2017	-2.961	-0.858	0.006
5/25/2017	-1.473	-0.858	0.006
5/30/2017	-26.748	-0.832	0.007
6/6/2017	-25.313	-0.856	0.012
6/12/2017	16.374	-0.834	0.007
6/13/2017	17.225	-0.861	0.008
6/23/2017	17.225	-0.861	0.008
6/26/2017	-25.365	-0.835	0.006
6/28/2017	17.453	-0.873	0.007
6/30/2017	-0.940	-0.874	0.009
7/3/2017	-0.597	-0.880	0.007
7/5/2017	-25.669	-0.846	0.009
7/7/2017	17.302	-0.857	0.007
7/10/2017	-1.060	-0.849	0.012
7/14/2017	15.653	-0.899	0.008
7/17/2017	-0.532	-0.906	0.006
7/19/2017	-26.782	-0.871	0.006
7/21/2017	17.168	-0.865	0.006
7/26/2017	-24.691	-0.881	0.013
7/29/2017	16.906	-0.878	0.009
7/31/2017	-1.115	-0.885	0.008
8/29/2017	-24.231	-0.825	0.009
8/30/2017	-0.880	-0.852	0.006
8/31/2017	12.067	-0.871	0.010
9/1/2017	18.480	-0.840	0.006
9/4/2017	19.150	-0.868	0.005
9/6/2017	-26.284	-0.878	0.005
9/8/2017	-0.700	-0.871	0.006
9/11/2017	18.852	-0.871	0.007
9/13/2017	-26.547	-0.874	0.010
9/26/2017	31.097	-0.012	0.006
9/27/2017	-27.945	-0.011	0.007
10/4/2017	-5.921	-0.014	0.008
10/9/2017	8.514	-0.021	0.009
10/11/2017	31.112	-0.007	0.006
10/18/2017	-6.325	-0.025	0.007
10/20/2017	8.251	-0.038	0.007
10/23/2017	-28.843	-0.024	0.005
10/26/2017	-6.405	-0.035	0.004
10/30/2017	31.512	-0.032	0.007
11/1/2017	8.073	-0.026	0.007
		AV	0.007
		SD	0.002

9/15/2017	-0.595	-0.872	0.007
9/19/2017	-23.803	-0.889	0.008
9/21/2017	16.911	-0.870	0.008
9/22/2017	-1.922	-0.872	0.005
9/26/2017	-23.801	-0.858	0.010
9/28/2017	15.770	-0.880	0.007
9/29/2017	-1.034	-0.883	0.007
10/5/2017	-24.818	-0.881	0.011
10/6/2017	17.623	-0.887	0.005
10/10/2017	-3.699	-0.904	0.007
10/12/2017	-23.882	-0.889	0.006
10/17/2017	-24.556	-0.841	0.009
10/19/2017	16.702	-0.866	0.005
10/24/2017	-0.994	-0.881	0.004
10/25/2017	-25.763	-0.874	0.005
10/27/2017	14.963	-0.861	0.006
10/31/2017	-25.454	-0.892	0.009
11/2/2017	15.333	-0.850	0.007
11/3/2017	-1.398	-0.887	0.007
		AV	0.007
		SD	0.002

Data correction [*Brand*]

ETF

Time interval HG/25G		residual slope*	slope	intercept
7/6/2016	12/22/2016	-0.0003	1.0611	0.9514
1/6/2017	7/10/2017	-0.0002	1.0672	0.9506
7/14/2016	11/3/2017	-0.0003	1.0492	0.9429

* the residual slope is derived from the 25G and HG data. This correction step was performed even though the HGL slopes are below 0.001. This assures a precise data correction, especially for samples with extreme δ^{47} values.

Standard data – S.3.III

II. Standard data (continued)

NIST SRM 120c [*Brand*] in ‰

Date	δ^{47}	Δ_{47raw}	Δ_{47}	se	$\delta^{13}C_{V\text{-}PDB}$	$\delta^{18}O_{V\text{-}PDB}$
7/26/2016	9.869	-0.350	0.583	0.013	-6.38	-1.61
7/27/2016	9.855	-0.354	0.580	0.013	-6.29	-1.70
7/29/2016	9.819	-0.342	0.592	0.012	-6.51	-1.54
7/31/2016	9.421	-0.354	0.579	0.010	-6.55	-1.88

8/16/2016	10.133	-0.333	0.602	0.029	-6.34	-1.41
8/18/2016	10.108	-0.365	0.568	0.017	-6.40	-1.34
8/22/2016	10.086	-0.341	0.593	0.018	-6.36	-1.43
9/27/2016	9.802	-0.360	0.573	0.023	-6.25	-1.79
9/29/2016	10.020	-0.360	0.574	0.029	-6.39	-1.44
10/5/2016	9.866	-0.359	0.574	0.022	-6.50	-1.48
11/2/2016	10.342	-0.345	0.589	0.022	-6.26	-1.27
11/13/2016	9.852	-0.340	0.595	0.014	-6.43	-1.58
11/18/2016	10.174	-0.330	0.604	0.020	-6.36	-1.35
11/20/2016	9.987	-0.350	0.583	0.018	-6.37	-1.50
12/19/2016	9.913	-0.373	0.560	0.009	-6.31	-1.61
4/3/2017	10.020	-0.367	0.562	0.019	-6.23	-1.59
9/5/2017	10.256	-0.349	0.580	0.015	-6.32	-1.29
9/10/2017	10.052	-0.373	0.555	0.022	-6.14	-1.64
9/17/2017	10.006	-0.367	0.561	0.015	-6.32	-1.51
10/25/2017	9.806	-0.367	0.561	0.013	-6.39	-1.64
10/27/2017	9.718	-0.366	0.562	0.026	-6.40	-1.72
10/30/2017	9.736	-0.333	0.596	0.035	-6.41	-1.73

Carrara marble

[*Brand*] in ‰

Date	δ^{47}	Δ_{47raw}	Δ_{47}	se	$\delta^{13}C_{V\text{-}PDB}$	$\delta^{18}O_{V\text{-}PDB}$
7/28/2016	17.592	-0.620	0.300	0.016	2.01	-1.63
7/30/2016	17.434	-0.600	0.321	0.017	1.87	-1.68
8/11/2016	17.819	-0.608	0.312	0.021	2.03	-1.45
8/20/2016	17.903	-0.596	0.325	0.023	2.02	-1.36
10/1/2016	17.872	-0.594	0.328	0.019	2.00	-1.38
10/8/2016	17.831	-0.582	0.341	0.021	2.03	-1.46
10/31/2016	17.615	-0.622	0.298	0.016	2.03	-1.62
11/4/2016	17.630	-0.592	0.330	0.024	2.02	-1.64
11/11/2016	17.427	-0.614	0.307	0.016	1.94	-1.73
2/8/2017	17.357	-0.637	0.275	0.023	1.99	-1.82
2/12/2017	17.353	-0.650	0.261	0.022	1.96	-1.79
4/2/2017	17.282	-0.620	0.293	0.026	1.93	-1.86
9/1/2017	17.496	-0.596	0.323	0.015	1.99	-1.73
9/2/2017	17.332	-0.632	0.285	0.021	1.96	-1.83
9/3/2017	17.302	-0.636	0.281	0.012	1.94	-1.84
9/10/2017	17.515	-0.614	0.304	0.008	1.95	-1.66
10/24/2017	17.460	-0.604	0.315	0.017	1.90	-1.67
10/28/2017	17.221	-0.633	0.284	0.008	1.87	-1.85

Arc. islandica

[*Brand*] in ‰

Date	δ^{47}	Δ_{47raw}	Δ_{47}	se	$\delta^{13}C_{V\text{-}PDB}$	$\delta^{18}O_{V\text{-}PDB}$
7/25/2016	23.088	-0.279	0.664	0.015	1.59	3.28
7/27/2016	23.117	-0.267	0.676	0.019	1.58	3.31

7/28/2016	22.926	-0.287	0.655	0.020	1.56	3.17
7/30/2016	22.770	-0.273	0.670	0.020	1.50	3.06
8/11/2016	23.124	-0.286	0.656	0.017	1.57	3.35
8/12/2016	22.670	-0.297	0.645	0.014	1.52	2.97
8/20/2016	22.978	-0.261	0.683	0.020	1.54	3.20
10/2/2016	22.400	-0.282	0.660	0.020	1.31	2.89
10/9/2016	22.469	-0.282	0.660	0.016	1.38	2.89
11/14/2016	22.491	-0.299	0.642	0.014	1.35	2.96
12/23/2016	22.599	-0.292	0.645	0.019	1.48	2.93
4/1/2017	22.695	-0.296	0.640	0.022	1.47	3.04
9/2/2017	22.694	-0.255	0.683	0.011	1.62	2.86
9/12/2017	22.736	-0.277	0.659	0.018	1.53	3.00
9/15/2017	22.599	-0.309	0.626	0.017	1.48	2.95
9/18/2017	22.846	-0.278	0.658	0.014	1.55	3.09
10/27/2017	22.322	-0.305	0.630	0.021	1.31	2.84
10/31/2017	22.562	-0.293	0.643	0.016	1.44	2.93

ETH-3

					[*Brand*] in ‰	
Date	δ^{47}	Δ_{47raw}	Δ_{47}	se	$\delta^{13}C_{V\text{-}PDB}$	$\delta^{18}O_{V\text{-}PDB}$
8/1/2016	17.298	-0.320	0.618	0.016	1.52	-1.75
8/23/2016	16.862	-0.336	0.600	0.019	1.37	-2.02
9/21/2016	17.169	-0.342	0.595	0.012	1.64	-1.96
9/28/2016	17.150	-0.312	0.626	0.019	1.58	-1.95
9/30/2016	17.257	-0.311	0.628	0.015	1.57	-1.85
10/1/2016	17.466	-0.343	0.594	0.017	1.66	-1.70
10/6/2016	17.135	-0.312	0.626	0.017	1.58	-1.97
11/1/2016	17.240	-0.331	0.606	0.019	1.67	-1.93
11/3/2016	17.318	-0.344	0.593	0.026	1.70	-1.87
11/9/2016	16.717	-0.329	0.608	0.011	1.35	-2.14
11/12/2016	17.311	-0.329	0.609	0.011	1.61	-1.81
11/18/2016	17.551	-0.319	0.620	0.007	1.60	-1.58
11/21/2016	17.109	-0.340	0.597	0.024	1.56	-1.95
12/20/2016	17.179	-0.330	0.607	0.019	1.64	-1.96
2/9/2017	17.029	-0.349	0.582	0.031	1.62	-2.08
2/11/2017	17.172	-0.342	0.590	0.016	1.65	-1.97
3/16/2017	17.248	-0.310	0.625	0.014	1.68	-1.96
9/1/2017	17.282	-0.311	0.622	0.012	1.65	-1.89
9/2/2017	17.117	-0.332	0.600	0.013	1.63	-2.02
9/4/2017	17.130	-0.328	0.604	0.011	1.61	-1.99
9/6/2017	17.301	-0.324	0.608	0.019	1.63	-1.85
9/7/2017	17.160	-0.320	0.613	0.019	1.62	-1.97
9/9/2017	17.559	-0.335	0.597	0.010	1.72	-1.67
9/12/2017	17.399	-0.320	0.612	0.015	1.69	-1.81
9/17/2017	17.343	-0.320	0.613	0.021	1.69	-1.86
9/18/2017	17.379	-0.301	0.633	0.023	1.52	-1.69

	10/24/2017	17.263	-0.317	0.616	0.017	1.58	-1.84

ETH-1

		[*Brand*] in ‰				
Date	δ^{47}	Δ_{47raw}	Δ_{47}	se	$\delta^{13}C_{V\text{-}PDB}$	$\delta^{18}O_{V\text{-}PDB}$
8/19/2016	16.839	-0.691	0.224	0.008	1.84	-2.13
9/21/2016	17.014	-0.733	0.179	0.021	2.02	-2.09
11/22/2016	17.15	-0.679	0.237	0.009	1.76	-1.77
9/3/2017	16.796	-0.710	0.204	0.014	1.99	-2.29
9/3/2017	16.739	-0.718	0.195	0.019	1.98	-2.34
9/10/2017	16.769	-0.723	0.190	0.019	1.93	-2.25
9/16/2017	16.904	-0.693	0.221	0.019	1.87	-2.09
10/30/2017	16.645	-0.733	0.180	0.014	1.85	-2.28

ETH-2

		[*Brand*] in ‰				
Date	δ^{47}	Δ_{47raw}	Δ_{47}	se	$\delta^{13}C_{V\text{-}PDB}$	$\delta^{18}O_{V\text{-}PDB}$
7/28/2016	-11.93	-0.706	0.198	0.010	-10.17	-18.69
10/3/2016	-11.92	-0.718	0.186	0.014	-10.20	-18.64
11/14/2016	-11.98	-0.716	0.188	0.013	-10.16	-18.74
2/13/2017	-12.34	-0.707	0.193	0.018	-10.32	-18.95
9/3/2017	-11.82	-0.701	0.204	0.019	-10.10	-18.66
9/18/2017	-11.97	-0.716	0.188	0.031	-10.19	-18.71
10/28/2017	-11.53	-0.726	0.178	0.017	-10.09	-18.37
10/31/2017	-11.86	-0.720	0.184	0.013	-10.15	-18.63

Sample data – S.3.IV

III. Sample data

Date	Sample	δ47 (raw) (‰)	Δ47 (raw) (‰)	SD Δ47 (raw) (‰)	δ47 (bgcorr) (‰)	Δ47 (bgcorr) (‰)	SD Δ47 (bgcorr) (‰)	δ13C CO2 (‰ VPDB)	δ18O CO2 (‰ VSMOW)	Diff Bellow (mV)	Weight (g)	Pressure Bellow (mBar)	ETF period
2016/11/09	TrixDen	0.987	-0.245	0.032	0.901	-0.330	0.017	-6.570	28.418	-194.4	32.3	13.6	2016.07.06-2016.12.22
2016/11/11	TrixDen	0.393	-0.394	0.031	0.411	-0.375	0.015	-6.490	27.890	162.2	61.7	26.6	2016.07.06-2016.12.22
2016/11/13	TrixEn	-2.654	-0.397	0.023	-2.650	-0.393	0.015	-9.277	27.546	-14.5	57.8	25.4	2016.07.06-2016.12.22
2016/11/13	TrixDen	0.381	-0.357	0.025	0.381	-0.357	0.021	-6.555	27.905	99.8	49.5	20.0	2016.07.06-2016.12.22
2016/11/14	TrixDen	0.412	-0.334	0.021	0.365	-0.381	0.020	-6.566	27.923	-95.6	47.2	19.1	2016.07.06-2016.12.22
2016/11/15	TrixEn	-2.052	-0.373	0.030	-2.062	-0.382	0.021	-9.261	28.114	-72.8	52.2	22.6	2016.07.06-2016.12.22
2016/11/18	TrixEn	-3.099	-0.398	0.017	-3.080	-0.379	0.011	-9.435	27.252	-28.3	51.4	21.9	2016.07.06-2016.12.22
2016/11/20	TrixEn	-2.177	-0.383	0.030	-2.145	-0.350	0.016	-9.408	28.142	98.9	54.4	22.8	2016.07.06-2016.12.22
2016/11/21	TrixDen	0.313	-0.352	0.026	0.280	-0.385	0.014	-6.504	27.781	-21.8	55.1	23.1	2016.07.06-2016.12.22
2017/02/09	TrixEn	-2.272	-0.364	0.026	-2.278	-0.370	0.021	-9.286	27.908	-54.6	56.3	22.2	2017.01.06-2017.07.10
2017/02/11	TrixEn	-2.169	-0.378	0.031	-2.190	-0.398	0.022	-9.314	28.053	-31.8	55.9	23.4	2017.01.06-2017.07.10
2017/02/12	TrixDen	1.020	-0.345	0.028	0.993	-0.372	0.020	-6.516	28.500	16.3	59.3	25.8	2017.01.06-2017.07.10
2017/03/28	TrixDen	0.666	-0.345	0.024	0.662	-0.349	0.023	-6.591	28.216	13.5	53.2	22.6	2017.01.06-2017.07.10
2017/04/02	TrixEn	-2.232	-0.374	0.029	-2.238	-0.379	0.023	-9.277	27.949	-25.4	53.7	23.1	2017.01.06-2017.07.10
2017/09/05	TrixEn	-1.928	-0.373	0.038	-1.921	-0.366	0.019	-9.064	28.047	-5.8	51.5	22.4	2017.07.14-2017.11.03
2017/10/28	TrixDen	0.363	-0.337	0.030	0.319	-0.381	0.017	-6.512	27.824	-36.8	50.5	21.1	2017.07.14-2017.11.03

Appendix to chapter 4

Supplementary data

Clumped isotope raw data of gases (HG: *S.4.Ia* and 25G: *S.4.Ib*) and carbonates (Carrara, ETH-1, ETH-2, ETH-3, ETH-4; *S.4.IIa* to *b*). The data is shown on the following pages and can also be found online at https://doi.org/10.1016/j.chemgeo.2019.05.019

Clumped isotope raw data of HG – S.4.Ia

ID	Sample	δ45	δ45 SD	δ46	δ46 SD	δ47	δ47 SD	δ48	δ48 SD	δ49	δ49 SD	Δ47 raw	Δ47, raw SD	Δ48, raw	Δ48, raw SD	Δ49, raw	Δ49, raw SD	δ13C, VPDB	δ13C SD	δ18O, VSMOW	δ18O SD
2019-01-09 18:55 CET	HG	6.405	0.003	10.935	0.003	16.569	0.027	21.284	0.117	-32.069	2.117	-0.846	0.027	-0.691	0.115	-58.961	2.060	2.22	0.00	36.47	0.00
2019-01-10 22:43 CET	HG	-0.029	0.002	-1.355	0.003	-2.208	0.022	-3.004	0.103	-4.172	2.302	-0.846	0.021	-0.297	0.104	-1.483	2.309	-4.18	0.00	23.87	0.00
2019-01-12 01:06 CET	HG	-16.788	0.002	-7.051	0.003	-24.959	0.020	-14.207	0.119	22.843	4.108	-0.851	0.020	-0.158	0.119	56.052	4.244	-21.83	0.00	18.06	0.00
2019-01-14 18:29 CET	HG	6.479	0.004	13.048	0.005	18.732	0.030	25.498	0.111	-36.393	2.572	-0.849	0.028	-0.749	0.108	-67.073	2.499	2.22	0.00	38.64	0.00
2019-01-15 16:07 CET	HG	0.068	0.002	-1.383	0.004	-2.132	0.025	-3.045	0.140	0.567	0.975	-0.844	0.026	-0.282	0.142	3.219	0.977	-4.08	0.00	23.84	0.00
2019-01-17 20:22 CET	HG	6.350	0.003	10.608	0.004	16.201	0.033	20.667	0.075	11.123	1.632	-0.834	0.035	-0.648	0.070	-16.286	1.583	2.18	0.00	36.13	0.00
2019-01-18 04:55 CET	HG	0.040	0.002	-0.450	0.004	-1.250	0.026	-1.178	0.065	1.235	1.585	-0.850	0.024	-0.278	0.066	2.078	1.590	-4.14	0.00	24.80	0.00
2019-01-21 19:56 CET	HG	6.477	0.003	11.142	0.004	16.840	0.020	21.772	0.102	11.818	1.071	-0.855	0.017	-0.622	0.104	-16.763	1.042	2.29	0.00	36.68	0.00
2019-01-23 14:54 CET	HG	-17.157	0.003	-7.327	0.005	-25.621	0.022	-14.704	0.100	-11.493	0.798	-0.868	0.023	-0.106	0.105	21.569	0.824	-22.21	0.00	17.78	0.01
2019-01-25 16:22 CET	HG	-0.057	0.002	-1.381	0.004	-2.280	0.023	-3.048	0.072	-0.093	0.983	-0.864	0.027	-0.289	0.073	2.687	0.985	-4.21	0.00	23.84	0.00
2019-01-29 21:58 CET	HG	6.436	0.002	10.537	0.003	16.194	0.016	20.479	0.053	9.504	0.712	-0.860	0.016	-0.692	0.049	-17.816	0.692	2.27	0.00	36.06	0.00
2019-01-30 18:53 CET	HG	-17.041	0.001	-7.336	0.004	-25.511	0.027	-14.722	0.119	-9.538	1.270	-0.868	0.026	-0.107	0.117	23.480	1.315	-22.09	0.00	17.77	0.00
2019-02-01 20:39 CET	HG	-0.025	0.002	-1.430	0.005	-2.294	0.020	-3.092	0.073	-0.360	1.392	-0.863	0.021	-0.234	0.067	2.482	1.389	-4.17	0.00	23.79	0.00
2019-02-04 19:54 CET	HG	6.526	0.001	13.016	0.004	18.748	0.029	25.439	0.108	11.045	2.041	-0.850	0.028	-0.743	0.110	-21.134	1.980	2.28	0.00	38.60	0.00
2019-02-05 16:36 CET	HG	-16.779	0.003	-7.160	0.004	-25.075	0.030	-14.322	0.084	-9.139	1.485	-0.870	0.029	-0.054	0.086	23.243	1.540	-21.82	0.00	17.95	0.00
2019-02-12 13:57 CET	HG	-0.023	0.003	-0.956	0.004	-1.813	0.026	-2.237	0.055	0.025	1.542	-0.850	0.029	-0.326	0.058	1.932	1.541	-4.19	0.00	24.28	0.00
2019-02-13 15:37 CET	HG	-17.144	0.003	-7.333	0.005	-25.606	0.035	-14.718	0.065	-10.895	1.029	-0.860	0.030	-0.108	0.066	22.186	1.065	-22.20	0.00	17.77	0.01
2019-02-15 20:14 CET	HG	6.405	0.003	10.776	0.004	16.419	0.041	21.002	0.090	10.802	1.638	-0.839	0.039	-0.653	0.092	-16.977	1.596	2.23	0.00	36.31	0.00
2019-02-18 19:06 CET	HG	-17.041	0.002	-7.012	0.004	-25.178	0.027	-14.136	0.114	-10.796	0.770	-0.847	0.028	-0.163	0.115	21.526	0.791	-22.10	0.00	18.10	0.00

In the replicates marked blue, the Δ49, raw values were not corrected for the negative background measured on the *m/z* 47.5 cup.

Clumped isotope raw data of 25G – S.4.Ib

ID	Sample	δ45	δ45 SD	δ46	δ46 SD	δ47	δ47 SD	δ48	δ48 SD	δ49	δ49 SD	Δ47 raw	Δ47, raw SD	Δ48, raw	Δ48, raw SD	Δ49, raw	Δ49, raw SD	δ13C, VPDB	δ13C SD	δ18O, VSMOW	δ18O SD
2019-01-09 23:09 CET	25G	-33.082	0.001	31.647	0.002	-4.071	0.031	63.319	0.136	-31.465	3.257	0.041	0.032	-0.918	0.127	-55.640	3.176	-40.61	0.00	57.82	0.00
2019-01-11 03:06 CET	25G	0.324	0.002	7.308	0.002	7.573	0.020	14.553	0.112	-21.907	2.973	0.052	0.019	-0.115	0.110	-36.135	2.930	-4.12	0.00	32.76	0.00
2019-01-11 20:51 CET	25G	-33.071	0.002	31.474	0.004	-4.205	0.014	62.989	0.108	-37.172	2.675	0.058	0.014	-0.893	0.104	-60.907	2.613	-40.59	0.00	57.64	0.00
2019-01-14 22:46 CET	25G	-33.887	0.002	7.522	0.003	-27.787	0.020	14.859	0.087	14.097	2.136	0.044	0.020	-0.238	0.086	36.726	2.184	-40.59	0.00	33.06	0.00
2019-01-16 18:10 CET	25G	1.178	0.004	31.658	0.006	32.396	0.024	63.381	0.049	24.939	1.518	0.029	0.023	-0.880	0.047	-37.151	1.418	-4.10	0.00	57.75	0.01
2019-01-18 00:38 CET	25G	-33.963	0.003	7.113	0.004	-28.257	0.025	14.110	0.138	-5.181	1.123	0.041	0.023	-0.164	0.135	17.916	1.147	-40.65	0.00	32.64	0.00
2019-01-18 22:07 CET	25G	1.231	0.003	32.031	0.005	32.833	0.023	64.166	0.069	25.285	0.881	0.043	0.024	-0.865	0.071	-37.564	0.828	-4.06	0.00	58.13	0.00
2019-01-22 17:18 CET	25G	-0.026	0.001	-3.510	0.004	-3.435	0.022	-6.880	0.076	-1.246	1.451	0.043	0.023	0.129	0.075	5.709	1.459	-4.10	0.00	21.66	0.00
2019-01-23 21:02 CET	25G	-0.029	0.002	-3.327	0.003	-3.254	0.025	-6.552	0.060	0.371	1.157	0.047	0.027	0.091	0.060	6.975	1.161	-4.11	0.00	21.85	0.00
2019-01-24 17:57 CET	25G	-33.907	0.001	7.537	0.004	-27.805	0.018	14.936	0.090	-5.462	1.733	0.033	0.018	-0.192	0.087	16.724	1.777	-40.61	0.00	33.07	0.00
2019-01-25 20:31 CET	25G	-0.008	0.002	-4.395	0.005	-4.298	0.024	-8.642	0.056	-2.056	1.067	0.032	0.024	0.130	0.055	6.628	1.072	-4.05	0.00	20.75	0.00
2019-01-28 19:48 CET	25G	0.354	0.002	6.896	0.004	7.193	0.019	13.570	0.074	5.821	1.476	0.046	0.021	-0.265	0.077	-8.045	1.457	-4.08	0.00	32.34	0.00
2019-01-31 19:45 CET	25G	-0.030	0.004	-3.448	0.006	-3.380	0.022	-6.768	0.121	-1.402	1.217	0.042	0.026	0.117	0.120	5.432	1.229	-4.11	0.00	21.72	0.01
2019-02-05 00:04 CET	25G	-33.743	0.002	7.250	0.005	-27.911	0.039	14.318	0.077	-6.593	1.622	0.028	0.038	-0.231	0.072	15.951	1.659	-40.42	0.00	32.78	0.01
2019-02-05 20:45 CET	25G	0.984	0.002	31.590	0.004	32.123	0.036	63.110	0.098	21.002	1.246	0.028	0.033	-1.004	0.094	-40.529	1.176	-4.31	0.00	57.68	0.00
2019-02-09 00:24 CET	25G	-0.029	0.002	-3.684	0.004	-3.608	0.024	-7.259	0.065	-0.029	1.816	0.045	0.024	0.097	0.066	7.282	1.834	-4.10	0.00	21.48	0.00
2019-02-11 17:02 CET	25G	-33.804	0.003	7.974	0.004	-27.287	0.022	15.802	0.088	-5.139	2.359	0.030	0.021	-0.207	0.087	16.073	2.416	-40.52	0.00	33.52	0.00
2019-02-13 19:47 CET	25G	1.283	0.001	31.985	0.004	32.840	0.020	64.080	0.104	23.737	1.725	0.038	0.017	-0.858	0.098	-38.988	1.619	-4.00	0.00	58.09	0.00
2019-02-20 16:06 CET	25G	-0.492	0.002	-3.968	0.005	-4.356	0.024	-7.800	0.077	-0.608	1.777	0.052	0.024	0.121	0.075	7.759	1.787	-4.58	0.00	21.19	0.00

In the replicates marked blue, the Δ49, raw values were not corrected for the negative background measured on the *m/z* 47.5 cup.

Clumped isotope raw data of Carrara – S.4.IIa

ID	Sample	Weight (mg)	δ45	δ45 SD	δ46	δ46 SD	δ47	δ47 SD	δ48	δ48 SD	δ49	δ49 SD	Δ47 raw	Δ47, raw SD	Δ48, raw	Δ48, raw SD	Δ49, raw	Δ49, raw SD	δ13C, VPDB	δ13C SD	δ18O, VSMOW	δ18O SD
2019-01-10 03:23 CET	Carrara	9.8	6.383	0.002	11.924	0.005	17.808	0.033	23.468	0.073	-33.855	3.275	-0.567	0.036	-0.509	0.076	-62.478	3.182	2.16	0.00	37.48	0.00
2019-01-15 03:03 CET	Carrara	9.5	6.436	0.002	12.059	0.002	18.003	0.032	23.689	0.056	-35.827	3.379	-0.561	0.029	-0.562	0.057	-64.690	3.280	2.22	0.00	37.62	0.00
2019-01-19 19:43 CET	Carrara	9.8	6.500	0.002	12.119	0.003	18.123	0.032	23.787	0.091	12.768	1.559	-0.567	0.030	-0.583	0.091	-17.730	1.509	2.28	0.00	37.68	0.00
2019-01-19 23:59 CET	Carrara	9.7	6.427	0.003	12.034	0.004	17.970	0.025	23.688	0.070	12.261	1.086	-0.560	0.024	-0.513	0.066	-17.984	1.052	2.21	0.00	37.60	0.00
2019-01-27 01:34 CET	Carrara	10.1	6.445	0.003	11.965	0.003	17.918	0.027	23.505	0.102	11.534	1.636	-0.562	0.025	-0.555	0.100	-18.577	1.583	2.23	0.00	37.53	0.00
2019-01-30 06:18 CET	Carrara	9.8	6.443	0.002	12.021	0.002	17.961	0.041	23.634	0.099	10.849	1.377	-0.572	0.041	-0.540	0.097	-19.346	1.337	2.22	0.00	37.58	0.00
2019-02-04 02:46 CET	Carrara	10.6	6.443	0.003	11.975	0.004	17.916	0.016	23.524	0.067	11.194	1.575	-0.572	0.017	-0.557	0.062	-18.924	1.532	2.23	0.00	37.54	0.00
2019-02-04 06:55 CET	Carrara	9.9	6.453	0.002	11.990	0.002	17.937	0.036	23.539	0.125	10.885	1.369	-0.576	0.034	-0.571	0.120	-19.262	1.325	2.24	0.00	37.55	0.00
2019-02-04 11:27 CET	Carrara	9.9	6.451	0.001	12.006	0.003	17.964	0.022	23.586	0.041	11.963	1.894	-0.563	0.022	-0.557	0.042	-18.245	1.839	2.23	0.00	37.57	0.00
2019-02-06 00:54 CET	Carrara	9.6	6.468	0.002	12.013	0.005	17.987	0.028	23.614	0.093	10.891	0.865	-0.565	0.027	-0.543	0.095	-19.315	0.844	2.25	0.00	37.57	0.00
2019-02-07 14:59 CET	Carrara	9.9	6.453	0.003	12.018	0.006	17.972	0.022	23.590	0.089	11.033	2.281	-0.569	0.021	-0.577	0.086	-19.172	2.221	2.23	0.00	37.58	0.01
2019-02-15 09:15 CET	Carrara	9.4	6.438	0.004	12.034	0.004	17.997	0.019	23.744	0.107	13.530	1.542	-0.544	0.019	-0.457	0.106	-16.764	1.492	2.22	0.00	37.60	0.00

In the replicates marked blue, the Δ49, raw values were not corrected for the negative background measured on the *m/z* 47.5 cup.

Clumped isotope raw data of ETH-1 – S.4.IIb

ID	Sample	Weight (mg)	δ45	δ45 SD	δ46	δ46 SD	δ47	δ47 SD	δ48	δ48 SD	δ49	δ49 SD	Δ47 raw	Δ47, raw SD	Δ48, raw	Δ48, raw SD	Δ49, raw	Δ49, raw SD	δ13C, VPDB	δ13C SD	δ18O, VSMOW	δ18O SD
2019-01-10 07:39 CET	ETH-1	9.4	6.286	0.003	11.394	0.002	17.090	0.025	22.333	0.088	-33.226	2.897	-0.658	0.024	-0.572	0.087	-60.805	2.816	2.08	0.00	36.94	0.00
2019-01-10 11:55 CET	ETH-1	9.6	6.414	0.002	11.575	0.003	17.405	0.018	22.733	0.082	-34.629	2.573	-0.656	0.016	-0.539	0.078	-62.625	2.501	2.21	0.00	37.13	0.00
2019-01-20 08:38 CET	ETH-1	10.1	6.449	0.002	11.557	0.004	17.417	0.027	22.722	0.058	12.276	1.535	-0.662	0.023	-0.513	0.055	-17.081	1.489	2.25	0.00	37.11	0.00
2019-01-22 13:01 CET	ETH-1	9.8	6.449	0.002	11.510	0.003	17.357	0.012	22.630	0.065	13.151	1.202	-0.675	0.012	-0.510	0.063	-16.143	1.165	2.25	0.00	37.06	0.00
2019-01-22 21:35 CET	ETH-1	9.7	6.458	0.003	11.553	0.004	17.398	0.028	22.696	0.094	11.788	1.551	-0.685	0.025	-0.532	0.092	-17.558	1.509	2.26	0.00	37.10	0.00
2019-01-26 13:08 CET	ETH-1	10.4	6.438	0.001	11.381	0.004	17.217	0.024	22.396	0.095	11.296	1.292	-0.677	0.025	-0.485	0.092	-17.686	1.256	2.24	0.00	36.93	0.00
2019-01-26 17:17 CET	ETH-1	10.0	6.420	0.003	11.431	0.003	17.258	0.022	22.420	0.107	11.385	0.801	-0.665	0.021	-0.560	0.107	-17.676	0.775	2.22	0.00	36.98	0.00
2019-01-29 17:57 CET	ETH-1	10.0	6.357	0.002	11.441	0.003	17.208	0.018	22.449	0.099	11.503	1.878	-0.660	0.016	-0.551	0.094	-17.515	1.826	2.15	0.00	36.99	0.00
2019-01-31 23:55 CET	ETH-1	10.4	6.429	0.002	11.486	0.004	17.320	0.021	22.529	0.145	11.233	1.355	-0.667	0.023	-0.561	0.138	-17.937	1.312	2.23	0.00	37.03	0.00
2019-02-02 21:38 CET	ETH-1	10.0	6.451	0.003	11.503	0.005	17.358	0.026	22.552	0.099	9,48	3.040	-0.670	0.024	-0.574	0.100	-19.697	2.960	2.25	0.00	37.05	0.00
2019-02-03 01:47 CET	ETH-1	10.5	6.447	0.002	11.463	0.004	17.305	0.028	22.521	0.088	10.360	1.615	-0.678	0.030	-0.525	0.089	-18.761	1.569	2.25	0.00	37.01	0.00
2019-02-03 05:56 CET	ETH-1	10.7	6.452	0.003	11.472	0.004	17.336	0.021	22.512	0.079	10.473	2.015	-0.663	0.020	-0.551	0.078	-18.675	1.963	2.25	0.00	37.02	0.00
2019-02-07 02:11 CET	ETH-1	10.4	6.451	0.002	11.551	0.006	17.425	0.031	22.686	0.073	10.872	1.929	-0.650	0.027	-0.536	0.064	-18.435	1.874	2.25	0.00	37.10	0.01
2019-02-09 04:33 CET	ETH-1	10.9	6.541	0.002	11.455	0.004	17.318	0.027	22.491	0.104	10.652	1.698	-0.662	0.026	-0.538	0.102	-18.467	1.649	2.25	0.00	37.00	0.00
2019-02-10 17:52 CET	ETH-1	10.1	6.299	0.003	11.482	0.006	17.193	0.034	22.547	0.067	10.258	1.250	-0.655	0.034	-0.535	0.066	-18.741	1.214	2.09	0.00	37.03	0.01
2019-02-12 09:40 CET	ETH-1	10.1	6.426	0.002	11.499	0.005	17.339	0.035	22.570	0.072	11.108	1.270	-0.658	0.036	-0.547	0.072	-18.081	1.233	2.22	0.00	37.05	0.01
2019-02-14 20:37 CET	ETH-1	11.0	6.446	0.003	11.494	0.004	17.350	0.024	22.660	0.042	12.161	1.375	-0.663	0.021	-0.450	0.044	-17.070	1.334	2.25	0.00	37.04	0.00
2019-02-17 17:53 CET	ETH-1	10.1	6.413	0.003	11.489	0.003	17.320	0.025	22.603	0.063	12.881	1.559	-0.654	0.023	-0.495	0.061	-16.327	1.517	2.21	0.00	37.04	0.00
2019-02-20 20:15 CET	ETH-1	10.6	6.445	0.003	11.467	0.004	17.329	0.021	22.560	0.096	12.823	1.136	-0.656	0.020	-0.493	0.095	-16.374	1.103	2.25	0.00	37.01	0.00

In the replicates marked blue, the Δ49, raw values were not corrected for the negative background measured on the *m/z* 47.5 cup.

Clumped isotope raw data of ETH-2 – S.4.IIc

ID	Sample	Weight (mg)	δ45	δ45 SD	δ46	δ46 SD	δ47	δ47 SD	δ48	δ48 SD	δ49	δ49 SD	Δ47 raw	Δ47, raw SD	Δ48, raw	Δ48, raw SD	Δ49, raw	Δ49, raw SD	δ13C, VPDB	δ13C SD	δ18O, VSMOW	δ18O SD
2019-01-09 01:13 CET	ETH-2	10.0	-5.508	0.002	-5.225	0.004	-11.439	0.013	-10.433	0.043	7.051	2.726	-0.656	0.014	-0.011	0.045	23.478	2.773	-9.88	0.00	19.91	0.00
2019-01-09 05:27 CET	ETH-2	10.7	-5.567	0.002	-5.242	0.004	-11.531	0.021	-10.502	0.080	8.910	2.603	-0.670	0.020	-0.045	0.082	25.468	2.648	-9.94	0.00	19.89	0.00
2019-01-11 07:19 CET	ETH-2	12.8	-5.493	0.003	-5.113	0.003	-11.327	0.025	-10.261	0.093	9.959	2.578	-0.669	0.025	-0.061	0.094	26.191	2.621	-9.87	0.00	20.02	0.00
2019-01-11 11:32 CET	ETH-2	10.7	-5.519	0.002	-5.289	0.004	-11.525	0.014	-10.579	0.070	9.977	3.577	-0.668	0.015	-0.029	0.066	26.595	3.638	-9.89	0.00	19.84	0.00
2019-01-17 02:47 CET	ETH-2	9.7	-5.565	0.003	-5.353	0.003	-11.647	0.018	-10.734	0.076	-3.655	1.152	-0.682	0.021	-0.058	0.074	12.914	1.170	-9.93	0.00	19.78	0.00
2019-01-17 15:45 CET	ETH-2	9.7	-5.569	0.003	-5.409	0.004	-11.684	0.034	-10.770	0.061	-3.875	1.477	-0.659	0.034	0.018	0.061	12.807	1.504	-9.93	0.00	19.72	0.00
2019-01-20 17:19 CET	ETH-2	10.9	-5.521	0.002	-5.177	0.004	-11.428	0.019	-10.381	0.071	-4.745	1.303	-0.679	0.016	-0.054	0.069	11.409	1.321	-9.89	0.00	19.96	0.00
2019-01-26 00:41 CET	ETH-2	10.3	-5.567	0.001	-5.334	0.004	-11.624	0.029	-10.681	0.086	-4.797	1.424	-0.675	0.028	-0.043	0.083	11.717	1.444	-9.94	0.00	19.80	0.00
2019-01-30 10:28 CET	ETH-2	9.9	-5.566	0.002	-5.234	0.005	-11.531	0.043	-10.455	0.095	-3.394	3.201	-0.680	0.044	-0.015	0.099	12.944	3.260	-9.94	0.00	19.90	0.01
2019-02-02 13:20 CET	ETH-2	9.8	-5.581	0.001	-5.379	0.004	-11.686	0.034	-10.815	0.107	-4.966	0.721	-0.677	0.034	-0.087	0.105	11.652	0.733	-9.95	0.00	19.75	0.00
2019-02-02 17:29 CET	ETH-2	9.9	-5.580	0.002	-5.336	0.002	-11.642	0.023	-10.655	0.069	-4.544	1.355	-0.676	0.024	-0.011	0.068	11.995	1.376	-9.95	0.00	19.80	0.00
2019-02-06 13:20 CET	ETH-2	10.8	-5.575	0.002	-5.244	0.004	-11.540	0.038	-10.494	0.070	-3.899	2.189	-0.670	0.035	-0.034	0.074	12.461	2.226	-9.95	0.00	19.89	0.00
2019-02-09 17:00 CET	ETH-2	10.1	-5.552	0.003	-5.215	0.005	-11.491	0.033	-10.447	0.116	-5.379	2.112	-0.672	0.030	-0.044	0.114	10.874	2.151	-9.92	0.00	19.92	0.00
2019-02-11 02:10 CET	ETH-2	10.4	-5.528	0.004	-5.083	0.005	-11.312	0.031	-10.202	0.079	-5.428	1.723	-0.647	0.030	-0.064	0.079	10.533	1.750	-9.90	0.00	20.06	0.00
2019-02-13 11:28 CET	ETH-2	9.9	-5.548	0.002	-5.015	0.005	-11.279	0.029	-10.054	0.075	-5.494	1.139	-0.660	0.027	-0.050	0.077	10.352	1.151	-9.93	0.00	20.13	0.00
2019-02-17 05:26 CET	ETH-2	9.9	-5.479	0.003	-4.954	0.004	-11.162	0.024	-9.947	0.075	-4.556	1.540	-0.655	0.026	-0.064	0.072	11.129	1.567	-9.88	0.00	20.19	0.00
2019-02-18 06:20 CET	ETH-2	10.0	-5.476	0.004	-4.854	0.006	-11.040	0.029	-9.792	0.101	-5.588	1.452	-0.652	0.026	-0.109	0.099	9.859	1.474	-9.86	0.00	20.29	0.01
2019-02-21 00:24 CET	ETH-2	10.9	-5.403	0.002	-4.943	0.007	-11.061	0.017	-9.896	0.105	-4.907	1.462	-0.661	0.014	-0.034	0.107	10.649	1.480	-9.77	0.00	20.20	0.01

In the replicates marked blue, the Δ49, raw values were not corrected for the negative background measured on the *m/z* 47.5 cup.

Clumped isotope raw data of ETH-3 – S.4.IId

CarbonatesID	Sample	Weight (mg)	δ45	δ45 SD	δ46	δ46 SD	δ47	δ47 SD	δ48	δ48 SD	δ49	δ49 SD	Δ47 raw	Δ47, raw SD	Δ48, raw	Δ48, raw SD	Δ49, raw	Δ49, raw SD	δ13C, VPDB	δ13C SD	δ18O, VSMOW	δ18O SD
2019-01-14 04:59 CET	ETH-3	9.0	6.004	0.002	11.685	0.003	17.490	0.028	23.125	0.109	-37.017	4.167	-0.258	0.028	-0.372	0.105	-64.737	4.049	1.77	0.00	37.24	0.00
2019-01-18 09:12 CET	ETH-3	9.7	6.139	0.003	11.799	0.005	17.751	0.028	23.289	0.094	12.701	1.827	-0.251	0.030	-0.437	0.092	-16.808	1.768	1.91	0.00	37.36	0.00
2019-01-21 06:19 CET	ETH-3	9.5	6.155	0.002	11.834	0.004	17.783	0.024	23.402	0.064	12.655	1.472	-0.270	0.024	-0.396	0.064	-16.937	1.427	1.92	0.00	37.39	0.00
2019-01-23 06:11 CET	ETH-3	9.5	6.163	0.002	11.927	0.003	17.887	0.026	23.599	0.111	12.488	1.316	-0.266	0.026	-0.388	0.107	-17.284	1.278	1.93	0.00	37.49	0.00
2019-01-30 23:01 CET	ETH-3	9.9	6.143	0.002	11.855	0.005	17.810	0.024	23.415	0.122	11.247	1.681	-0.252	0.027	-0.426	0.120	-18.332	1.628	1.91	0.00	37.41	0.01
2019-02-02 00:49 CET	ETH-3	10.0	6.145	0.003	11.826	0.004	17.783	0.024	23.314	0.051	10.918	1.100	-0.253	0.025	-0.468	0.050	-18.598	1.065	1.91	0.00	37.38	0.00
2019-02-02 04:58 CET	ETH-3	10.8	6.150	0.003	11.855	0.003	17.789	0.041	23.447	0.069	11.520	0.962	-0.279	0.038	-0.393	0.071	-18.072	0.932	1.92	0.00	37.41	0.00
2019-02-04 15:36 CET	ETH-3	10.1	6.158	0.001	11.884	0.004	17.852	0.027	23.478	0.061	11.339	1.478	-0.254	0.025	-0.422	0.058	-18.314	1.440	1.93	0.00	37.44	0.00
2019-02-05 04:14 CET	ETH-3	9.7	6.151	0.002	11.849	0.004	17.813	0.030	23.356	0.118	10.812	1.805	-0.251	0.030	-0.472	0.117	-18.751	1.752	1.92	0.00	37.41	0.00
2019-02-05 08:25 CET	ETH-3	10.4	6.134	0.005	11.827	0.011	17.758	0.029	23.356	0.093	9.820	2.903	-0.267	0.019	-0.429	0.092	-19.655	2.839	1.90	0.01	37.38	0.01
2019-02-05 12:35 CET	ETH-3	9.9	6.147	0.002	11.809	0.004	17.756	0.026	23.345	0.082	11.857	2.772	-0.265	0.024	-0.403	0.084	-17.656	2.694	1.92	0.00	37.37	0.00
2019-02-08 03:34 CET	ETH-3	9.9	6.162	0.002	11.904	0.003	17.858	0.023	23.542	0.078	12.212	1.581	-0.272	0.023	-0.398	0.077	-17.509	1.534	1.93	0.00	37.46	0.00
2019-02-10 05:27 CET	ETH-3	9.8	6.070	0.003	11.833	0.003	17.696	0.022	23.402	0.071	12.309	1.357	-0.268	0.021	-0.395	0.067	-17.183	1.318	1.83	0.00	37.39	0.00
2019-02-11 21:11 CET	ETH-3	9.9	6.129	0.003	11.873	0.005	17.814	0.022	23.498	0.061	12.839	1.323	-0.251	0.025	-0.379	0.058	-16.805	1.288	1.89	0.00	37.43	0.00
2019-02-12 23:02 CET	ETH-3	10.9	6.148	0.003	11.885	0.005	17.839	0.033	23.455	0.072	11.566	1.817	-0.258	0.034	-0.445	0.066	-18.030	1.766	1.91	0.00	37.44	0.00
2019-02-16 04:32 CET	ETH-3	10.7	6.139	0.002	11.836	0.005	17.768	0.026	23.442	0.091	11.768	1.709	-0.270	0.024	-0.361	0.087	-17.785	1.666	1.91	0.00	37.39	0.01

In the replicates marked blue, the Δ49, raw values were not corrected for the negative background measured on the *m/z* 47.5 cup.

Clumped isotope raw data of ETH-4 – S.4.IIe

ID	Sample	Weight (mg)	δ45	δ45 SD	δ46	δ46 SD	δ47	δ47 SD	δ48	δ48 SD	δ49	δ49 SD	Δ47 raw	Δ47, raw SD	Δ48, raw	Δ48, raw SD	Δ49, raw	Δ49, raw SD	δ13C, VPDB	δ13C SD	δ18O, VSMOW	δ18O SD
2019-01-09 09:44 CET	ETH-4	11.0	-5.593	0.003	-5.277	0.005	-11.344	0.018	-10.445	0.080	6.520	2.699	-0.421	0.022	0.081	0.077	23.136	2.749	-9.96	0.00	19.86	0.01
2019-01-09 14:20 CET	ETH-4	9.7	-5.610	0.002	-5.474	0.002	-11.548	0.024	-10.897	0.073	3.750	2.253	-0.414	0.025	0.021	0.073	20.737	2.291	-9.98	0.00	19.65	0.00
2019-01-14 09:17 CET	ETH-4	9.7	-5.545	0.003	-5.317	0.003	-11.332	0.022	-10.617	0.112	6.196	3.589	-0.419	0.021	-0.012	0.110	22.836	3.656	-9.91	0.00	19.82	0.00
2019-01-18 13:30 CET	ETH-4	9.5	-5.613	0.002	-5.435	0.004	-11.526	0.028	-10.792	0.078	-3.368	1.233	-0.427	0.028	0.050	0.079	13.424	1.254	-9.98	0.00	19.69	0.00
2019-01-19 06:45 CET	ETH-4	9.5	-5.578	0.002	-5.311	0.004	-11.387	0.023	-10.569	0.067	-4.666	1.593	-0.446	0.022	0.025	0.070	11.818	1.620	-9.95	0.00	19.82	0.00
2019-01-21 15:30 CET	ETH-4	9.6	-5.685	0.002	-5.492	0.003	-11.663	0.034	-10.910	0.093	-5.072	1.349	-0.436	0.033	0.043	0.094	11.883	1.370	-10.06	0.00	19.64	0.00
2019-01-24 05:40 CET	ETH-4	9.7	-5.604	0.003	-5.237	0.004	-11.323	0.026	-10.391	0.075	-4.027	1.367	-0.428	0.029	0.057	0.074	12.349	1.392	-9.98	0.00	19.90	0.00
2019-01-29 08:19 CET	ETH-4	9.5	-5.599	0.002	-5.377	0.003	-11.455	0.022	-10.656	0.082	-3.614	1.362	-0.428	0.021	0.070	0.081	13.043	1.385	-9.97	0.00	19.75	0.00
2019-02-03 14:14 CET	ETH-4	10.6	-5.610	0.002	-5.352	0.004	-11.435	0.028	-10.617	0.115	-3.816	2.432	-0.421	0.027	0.058	0.121	12.798	2.479	-9.98	0.00	19.78	0.00
2019-02-03 18:25 CET	ETH-4	10.5	-5.591	0.002	-5.013	0.002	-11.089	0.013	-9.933	0.057	-3.478	1.228	-0.425	0.012	0.068	0.061	12.444	1.249	-9.97	0.00	20.13	0.00
2019-02-14 08:14 CET	ETH-4	9.3	-5.586	0.003	-5.217	0.006	-11.283	0.031	-10.395	0.066	-5.515	1.311	-0.426	0.031	0.011	0.070	10.776	1.337	-9.96	0.00	19.92	0.01

In the replicates marked blue, the Δ49, raw values were not corrected for the negative background measured on the *m/z* 47.5 cup.

Appendix to chapter 5

The data of the original supplementary is shown on the following pages and can also be found as online supplementary once the manuscript is published with a DOI.

Methods – S.5.I

All sample materials were dried at room temperature for one week after being collected in the field. After drying, the surface of the samples was mechanically cleaned by abrasion of the upper 2 to 4 mm using a handheld micro drill equipped with a diamond milling cutter at 5,000 rpm and by applying minimum pressure on the tool. 100 to 200 mg of sample powder was prepared from each sample using the same technique. No chemical pretreatment was conducted to avoid alteration of bulk and clumped isotopic compositions which has been identified for chemically pretreated carbonate bearing minerals in previous studies (Wacker *et al.*, 2016; Pellegrini & Snoeck, 2016).

Samples were measured with four to seven replicates each consisting of ten acquisitions of ten cycles and a total ion integration time of 200 s. The acquisitions included peak centering, pressure adjustments of the reference and sample gas bellows, and background determinations. When using the MAT 253™, the negative background below *m/z* 47 was scaled to the intensity of the *m/z* 49 ion beam before and after each acquisition both for the sample and the reference gas. Raw $_{m/z}$ 47 intensities of the respective cycles of sample and reference gas measurements were then corrected for non-linearity using a previously described approach (Fiebig *et al.*, 2016). When using MAT 253 plus™, the negative background was continuously monitored on the *m/z* 47.5 half cup. The sample and reference gas *m/z* 44 signal intensities were adjusted to 16,000 ± 150 mV for isotopic measurements. For each cycle of reference and sample gas measurement, the corresponding intensity was then subtracted from the measured *m/z* 47 intensities using a scaling factor of -1 (Fiebig *et al.*, 2019). Samples were typically measured with a routine that brackets two unknowns with two carbonate standards (ETH 1 to 4, Carrara marble, *Arctica islandica*). Sample masses of 6.6 to 40.1 mg were loaded into silver capsules (IVA Analysentechnik e.K., Meerbusch, Germany) and stored for 30 min at 30 °C within vacuum (25 mbar). Digestion took place in 105 to 107 % orthophosphoric acid (H_3PO_4, ≥99.9%, Merck; hyper saturated with ≥99% phosphorous pentoxide, Carl Roth) that was stirred constantly in an common acid bath (d= 9cm) heated to 90 ± 0.1 °C after loading the autosampler (Zero Blank autosampler; Costech, Valencia, CA, USA) and evacuating the line for 8 to 12 hours. The acid bath was directly connected to H_2O

and CO_2 traps for cryogenic purification and a GC (1.2 m x 2.15 mm stainless steel column, packed with Porapak Q 80/120). The H_2O and CO_2 traps were held at -80 °C (ethanol cooled with liquid N_2) and -196 °C (liquid N_2). Traps and acid bath were pumped individually by two turbo pumps (Pfeiffer, Asslar, Germany).

CO_2 gases equilibrated at 1,000 °C (HG) and 25 °C (25G) were measured continuously two and three times per week, respectively. The HGs and 25Gs were passed through the same capillaries and gas purification system as the sample gases (*excl.* common acid bath). In δ_{47} vs. Δ_{47} plots, the slopes displayed by the non-linearity corrected raw values of HGs and 25Gs were constantly below 0.001. If these slopes were distinguishable from zero within error, a residual slope correction was performed. The former were calculated from the merged HG and 25G data sets (s*upplementary data II*). Δ_{47} values were subsequently corrected for scale compression and reported on the Carbon Dioxide Equilibrium Scale (CDES; Dennis *et al.*, 2011). The bulk and clumped isotopic compositions were processed with the [*Brand*]/IUPAC isotopic parameters (Daëron *et al.*, 2016) and the Δ_{47} values are projected to the 25 °C reference frame (Dennis *et al.*, 2011) by applying the 90 °C acid fractionation factor of +0.088 ± 0.006 ‰ (Petersen *et al.*, 2019). The $\delta^{18}O$ phosphoric acid fractionation factors for calcite and aragonite at 90 °C are 1.00813 and 1.00854, respectively (Kim *et al.*, 2007). The precision of the Δ_{47} data is reported as 1σ standard error (se). Further details on the HAL system, the IRMS setup, and data processing can be found in the literature (Löffler *et al.*, 2019; Fiebig *et al.*, 2019). Temperatures were calculated with the synthetic carbonate Δ_{47}–$1/T^2$ calibration(2019). This calibration was chosen over the [*Brand*]/IUPAC recalculated in-house calibration (Wacker *et al.*, 2014) because it grounds on a larger data set of eight individual calibration studies from 2012 to 2017, potentially increasing the accuracy of the calibration.

For $\delta^{18}O$ and $\delta^{13}C$ analyses, the samples were digested in 99% orthophosphoric acid and analyzed as CO_2 using the continuous flow mode of a Thermo Scientific™ MAT 253™ gas source isotope ratio mass spectrometer which was directly connected to a Thermo Scientific GasBench II™. Measurements were conducted between 08/2017 and 04/2019. The analytical procedure follows Spötl and Vennemann (2003) whereas raw isotopic ratios were normalized with an internal Carrara marble standard. Additional analyses of the carbonate standards NBS18 and Merck (100 µg) were used for a secondary correction (decompression) of the calculated $\delta^{13}C$ and $\delta^{18}O$ values. All oxygen and carbon isotopic compositions are given in V-SMOW and V-PDB notation, respectively. The precision of the bulk isotopic data is reported as 1σ standard deviation (sd).

Carbonate contents were calculated from the ratios between the *m/z* 44 peak areas of Carrara marble (25 to 130 µg; pure $CaCO_3$) and samples. The average carbonate contents of the pedogenic carbonate nodules and caliche samples yield identical values of 60 wt.% (60 ± 16 wt.% and 60 ± 17 wt.%, respectively). The long-term values of the reference materials are $\delta^{18}O$ =13.28 ± 0.11 ‰, $\delta^{13}C$ = -35.34 ± 0.17 ‰ (Merck) and $\delta^{18}O$ =7.03 ± 0.10 ‰, $\delta^{13}C$ = -5.01 ± 0.06 ‰ (NBS 18). The in-house standard Carrara marble was measured with $\delta^{18}O$ = 29.19 ± 0.25 ‰ and $\delta^{13}C$ =2.00 ± 0.03 ‰.

No correlation between the size of the nodules and soil temperatures can be found, whereas the size was approximated by the area calculated from major and minor axis measurements assuming an ellipsoidal geometry of carbonate nodules[58].

The position of every sample within the Armantes profile was calculated by combined GPS data and point-to-point measurements. Individual sample locations were tied to the original sampling points of the paleomagnetic profile (Krijgsman *et al.*, 1997) whereas the ages of the originally assigned magnetic chrons were updated to the geological time scale (Gradstein, 2012). The average sedimentation rate derived from the age model and field measurements is 6.9 ± 2.6 cm/ka (2.6 to 13.6 cm/ka) and comparable to the typical sedimentation rate for the intermediate unit in the Madrid basin (4.0 to 4.7 cm/ka; Montes *et al.*, 2006). The sample ages within one magnetic chron were referenced to the marine record (Holbourn *et al.*, 2014) by peak-matching the $\delta^{13}C$ data measured on the caliche samples, further resulting in an average adjustment of 42 ± 32 kyr for all 68 samples.

Measured Δ_{47} and $\delta^{18}O$ values of the pedogenic carbonate nodules were used for calculating $\delta^{18}O_{H2O}$ of the soil water (Coplen, 2007). Present day $\delta^{18}O_{H2O}$ values for the Armantes section were derived from three GNIP stations (Zaragoza aeropuerto, Noguera de Albarracin./D.G.A., Soria) from the projects GNIP/M/ES/01 GNIP/M/ES/02 (Rodríguez-Arévalo *et al.*, 2011) that define a triangle with an area of 8,422 km² with the geographical center 11 km south of the Armantes section. Their $\delta^{18}O_{H2O}$ measurements from 2000 to 2015 average to -3.2 ± 0.8 ‰ (JJA) and -8.5 ± 0.4 ‰ (DJF) with an annual mean $\delta^{18}O_{H2O}$ of -6.3 ± 3.2 ‰.

Supplementary data –S.5.II to S.5.VI

Measured and calculated data from equilibrated gases (HG: *S.5.IIa*, 25G: *S.5.IIb*) and empirical transfer functions (*S.5.II.c*), standard materials (*S.5.III*) and samples (*S.5.IV*) including δ_{47} and raw Δ_{47} values. Overview on the Δ_{47} soil temperature datasets (*S.5.V*) and $\delta^{18}O$ and $\delta^{13}C$ of pedogenic carbonates (*S.5.VI*).

Equilibrated gases and empirical transfer functions – S.5.IIa to 5.IIc

Date	Sample	δ47 (raw) (‰)	Δ47 (raw) (‰)	SD Δ47 (raw) (‰)	δ47 (bgcorr) (‰)	Δ47 (bgcorr) (‰)	SD Δ47 (bgcorr) (‰)	δ13C CO2 (‰ VPDB)	δ18O CO2 (‰ [illegible]	Diff Bellow (mV)	ETF period
1/6/2017	HG	-2.694	-0.826	0.029	-2.694	-0.825	0.016	-3.592	22.590	-21.6	2017.01.06–2017.07.10
1/9/2017	HG	-1.872	-0.881	0.045	-1.860	-0.869	0.029	-3.673	23.553	42.7	2017.01.06–2017.07.10
1/10/2017	HG	-25.391	-1.182	0.031	-25.059	-0.841	0.021	-21.633	17.515	75.4	2017.01.06–2017.07.10
1/10/2017	HG	17.057	-0.676	0.019	16.859	-0.871	0.017	2.038	36.777	167.2	2017.01.06–2017.07.10
1/11/2017	HG	-4.690	-0.928	0.033	-4.622	-0.861	0.021	-3.467	20.563	124.8	2017.01.06–2017.07.10
1/12/2017	HG	13.335	-0.690	0.030	13.144	-0.879	0.028	2.102	33.004	-13.5	2017.01.06–2017.07.10
1/12/2017	HG	-3.955	-0.904	0.040	-3.925	-0.874	0.020	-3.539	21.349	-36.1	2017.01.06–2017.07.10
1/17/2017	HG	-25.962	-1.195	0.033	-25.646	-0.872	0.024	-21.517	16.831	38.6	2017.01.06–2017.07.10
1/17/2017	HG	14.263	-0.702	0.018	14.088	-0.875	0.021	2.040	34.005	72.1	2017.01.06–2017.07.10
1/20/2017	HG	-25.571	-1.171	0.027	-25.255	-0.847	0.021	-21.524	17.213	20.9	2017.01.06–2017.07.10
1/23/2017	HG	17.960	-0.614	0.018	17.699	-0.871	0.021	2.229	37.431	9.6	2017.01.06–2017.07.10
1/25/2017	HG	-26.162	-1.176	0.043	-25.841	-0.846	0.036	-21.471	16.561	15.8	2017.01.06–2017.07.10
1/26/2017	HG	-4.018	-0.902	0.022	-3.978	-0.862	0.024	-3.524	21.267	20.5	2017.01.06–2017.07.10
1/30/2017	HG	17.968	-0.638	0.035	17.741	-0.861	0.022	2.055	37.634	32.0	2017.01.06–2017.07.10
1/31/2017	HG	-25.945	-1.165	0.024	-25.670	-0.884	0.015	-21.509	16.810	-67.7	2017.01.06–2017.07.10
2/1/2017	HG	-1.862	-0.856	0.024	-1.864	-0.858	0.031	-3.665	23.529	-9.0	2017.01.06–2017.07.10
2/7/2017	HG	17.102	-0.636	0.029	16.862	-0.873	0.012	2.070	36.751	-1.8	2017.01.06–2017.07.10
2/7/2017	HG	-25.955	-1.180	0.029	-25.647	-0.864	0.023	-21.522	16.827	5.6	2017.01.06–2017.07.10
2/7/2017	HG	-1.561	-0.873	0.041	-1.545	-0.857	0.021	-3.681	23.864	55.5	2017.01.06–2017.07.10
2/14/2017	HG	-25.320	-1.160	0.029	-25.035	-0.867	0.025	-21.614	17.548	-63.5	2017.01.06–2017.07.10
2/21/2017	HG	-2.168	-0.895	0.031	-2.140	-0.867	0.019	-3.687	23.281	67.8	2017.01.06–2017.07.10
2/22/2017	HG	17.137	-0.673	0.035	16.928	-0.878	0.023	2.029	36.862	80.3	2017.01.06–2017.07.10
2/24/2017	HG	-25.439	-1.166	0.022	-25.144	-0.864	0.031	-21.858	17.672	-12.3	2017.01.06–2017.07.10
2/27/2017	HG	-2.749	-0.865	0.024	-2.738	-0.853	0.017	-3.576	22.558	-44.6	2017.01.06–2017.07.10
2/28/2017	HG	13.486	-0.723	0.038	13.340	-0.866	0.023	1.996	33.290	119.3	2017.01.06–2017.07.10
3/3/2017	HG	-26.345	-1.185	0.032	-26.037	-0.868	0.022	-21.791	16.697	-6.9	2017.01.06–2017.07.10
3/7/2017	HG	-4.244	-0.875	0.034	-4.233	-0.865	0.018	-3.502	20.992	-66.3	2017.01.06–2017.07.10
3/9/2017	HG	11.721	-0.762	0.032	11.599	-0.883	0.017	1.958	31.601	124.5	2017.01.06–2017.07.10
3/13/2017	HG	-2.578	-0.861	0.027	-2.595	-0.877	0.029	-3.732	22.878	-58.4	2017.01.06–2017.07.10
3/15/2017	HG	-25.290	-1.125	0.035	-25.015	-0.844	0.021	-21.797	17.724	-74.2	2017.01.06–2017.07.10
3/16/2017	HG	17.612	-0.641	0.018	17.391	-0.858	0.011	1.937	37.396	14.6	2017.01.06–2017.07.10
3/17/2017	HG	-4.642	-0.912	0.059	-4.587	-0.858	0.023	-3.525	20.651	13.8	2017.01.06–2017.07.10
3/21/2017	HG	-25.631	-1.157	0.044	-25.344	-0.863	0.014	-21.813	17.422	15.8	2017.01.06–2017.07.10

3/24/2017	HG	18.039	-0.674	0.029	17.849	-0.861	0.029	2.092	37.706	96.1	2017.01.06–2017.07.10
3/24/2017	HG	-1.629	-0.848	0.026	-1.637	-0.856	0.020	-3.666	23.757	-48.0	2017.01.06–2017.07.10
3/27/2017	HG	17.027	-0.686	0.025	16.853	-0.856	0.011	2.078	36.717	115.5	2017.01.06–2017.07.10
3/29/2017	HG	-25.341	-1.118	0.036	-25.076	-0.846	0.034	-21.792	17.660	-80.8	2017.01.06–2017.07.10
3/30/2017	HG	-1.229	-0.860	0.031	-1.248	-0.880	0.020	-3.661	24.167	-2.9	2017.01.06–2017.07.10
4/4/2017	HG	-2.641	-0.838	0.021	-2.664	-0.861	0.022	-3.658	22.721	-85.7	2017.01.06–2017.07.10
4/4/2017	HG	-25.372	-1.121	0.036	-25.090	-0.832	0.024	-21.702	17.542	13.5	2017.01.06–2017.07.10
4/5/2017	HG	12.666	-0.716	0.032	12.515	-0.865	0.016	2.183	32.281	39.0	2017.01.06–2017.07.10
4/7/2017	HG	-26.207	-1.136	0.019	-25.914	-0.836	0.021	-21.647	16.648	-31.2	2017.01.06–2017.07.10
4/10/2017	HG	-1.878	-0.847	0.024	-1.876	-0.845	0.024	-3.674	23.513	-11.7	2017.01.06–2017.07.10
4/19/2017	HG	12.601	-0.691	0.032	12.420	-0.870	0.023	2.179	32.195	-12.9	2017.01.06–2017.07.10
4/19/2017	HG	-2.571	-0.851	0.046	-2.566	-0.847	0.022	-3.656	22.801	-10.9	2017.01.06–2017.07.10
4/25/2017	HG	-1.850	-0.831	0.047	-1.862	-0.843	0.020	-3.696	23.546	-54.2	2017.01.06–2017.07.10
4/25/2017	HG	-25.330	-1.136	0.024	-25.049	-0.848	0.029	-21.835	17.732	-12.2	2017.01.06–2017.07.10
4/27/2017	HG	-1.510	-0.856	0.036	-1.506	-0.853	0.015	-3.634	23.854	-11.4	2017.01.06–2017.07.10
5/5/2017	HG	13.620	-0.660	0.017	13.438	-0.840	0.012	2.149	33.213	5.3	2017.01.06–2017.07.10
5/8/2017	HG	-4.747	-0.890	0.043	-4.713	-0.855	0.013	-3.543	20.540	1.9	2017.01.06–2017.07.10
5/10/2017	HG	-3.024	-0.921	0.051	-2.961	-0.858	0.020	-3.618	22.379	96.6	2017.01.06–2017.07.10
5/25/2017	HG	-1.482	-0.866	0.020	-1.473	-0.858	0.019	-3.668	23.925	69.8	2017.01.06–2017.07.10
5/30/2017	HG	-27.031	-1.123	0.029	-26.748	-0.832	0.021	-21.681	15.824	-52.1	2017.01.06–2017.07.10
6/6/2017	HG	-25.609	-1.159	0.056	-25.313	-0.856	0.037	-22.003	17.633	25.2	2017.01.06–2017.07.10
6/12/2017	HG	16.598	-0.613	0.026	16.374	-0.834	0.021	2.135	36.158	-8.9	2017.01.06–2017.07.10
6/13/2017	HG	17.445	-0.644	0.035	17.225	-0.861	0.024	2.076	37.096	25.5	2017.01.06–2017.07.10
6/26/2017	HG	-25.669	-1.146	0.050	-25.365	-0.835	0.019	-21.866	17.425	61.6	2017.01.06–2017.07.10
6/28/2017	HG	17.664	-0.666	0.025	17.453	-0.873	0.021	2.019	37.393	79.8	2017.01.06–2017.07.10
6/30/2017	HG	-0.946	-0.880	0.028	-0.940	-0.874	0.028	-3.765	24.572	62.4	2017.01.06–2017.07.10
7/3/2017	HG	-0.592	-0.875	0.038	-0.597	-0.880	0.022	-3.646	24.808	22.2	2017.01.06–2017.07.10
7/5/2017	HG	-25.958	-1.142	0.045	-25.669	-0.846	0.028	-22.456	17.704	-16.0	2017.01.06–2017.07.10
7/7/2017	HG	17.507	-0.656	0.040	17.302	-0.857	0.021	2.079	37.166	7.3	2017.01.06–2017.07.10
7/10/2017	HG	-1.071	-0.860	0.035	-1.060	-0.849	0.039	-3.666	24.330	21.5	2017.01.06–2017.07.10
7/14/2017	HG	15.899	-0.657	0.025	15.653	-0.899	0.025	1.806	35.826	23.9	2017.07.14–2017.11.13
7/17/2017	HG	-0.507	-0.881	0.033	-0.532	-0.906	0.019	-3.464	24.723	-6.2	2017.07.14–2017.11.13
7/19/2017	HG	-27.097	-1.194	0.027	-26.782	-0.871	0.020	-22.681	16.809	-59.7	2017.07.14–2017.11.13
7/21/2017	HG	17.441	-0.598	0.045	17.168	-0.865	0.019	2.217	36.906	-49.6	2017.07.14–2017.11.13
7/26/2017	HG	-25.044	-1.241	0.062	-24.691	-0.881	0.042	-21.614	17.913	53.6	2017.07.14–2017.11.13
7/29/2017	HG	17.126	-0.662	0.043	16.906	-0.878	0.028	2.169	36.703	73.5	2017.07.14–2017.11.13
7/31/2017	HG	-1.154	-0.923	0.034	-1.115	-0.885	0.025	-3.899	24.537	66.1	2017.07.14–2017.11.13
8/30/2017	HG	-0.907	-0.880	0.048	-0.880	-0.852	0.018	-3.679	24.528	94.4	2017.07.14–2017.11.13
8/31/2017	HG	12.185	-0.755	0.060	12.067	-0.871	0.031	2.140	31.881	136.1	2017.07.14–2017.11.13
9/1/2017	HG	18.744	-0.581	0.042	18.480	-0.840	0.018	2.151	38.257	-41.4	2017.07.14–2017.11.13
9/4/2017	HG	19.399	-0.625	0.041	19.150	-0.868	0.015	2.301	38.810	37.2	2017.07.14–2017.11.13
9/6/2017	HG	-26.643	-1.247	0.036	-26.284	-0.878	0.017	-23.026	17.667	148.9	2017.07.14–2017.11.13
9/8/2017	HG	-0.718	-0.889	0.067	-0.700	-0.871	0.020	-3.539	24.591	50.3	2017.07.14–2017.11.13
9/11/2017	HG	19.077	-0.650	0.048	18.852	-0.871	0.023	1.875	38.932	44.6	2017.07.14–2017.11.13

9/13/2017	HG	-26.906	-1.242	0.036	-26.547	-0.874	0.031	-23.085	17.451	127.3	2017.07.14–2017.11.13
9/15/2017	HG	-0.613	-0.889	0.041	-0.595	-0.872	0.022	-3.560	24.719	55.0	2017.07.14–2017.11.13
9/19/2017	HG	-24.131	-1.223	0.038	-23.803	-0.889	0.025	-21.043	18.269	129.9	2017.07.14–2017.11.13
9/21/2017	HG	17.125	-0.660	0.033	16.911	-0.870	0.025	1.834	37.028	19.4	2017.07.14–2017.11.13
9/22/2017	HG	-1.953	-0.903	0.039	-1.922	-0.872	0.014	-4.077	23.885	47.7	2017.07.14–2017.11.13
9/26/2017	HG	-24.077	-1.140	0.040	-23.801	-0.858	0.031	-21.019	18.218	3.7	2017.07.14–2017.11.13
9/28/2017	HG	15.974	-0.680	0.033	15.770	-0.880	0.022	2.050	35.685	32.3	2017.07.14–2017.11.13
9/29/2017	HG	-1.077	-0.926	0.054	-1.034	-0.883	0.021	-3.730	24.454	115.1	2017.07.14–2017.11.13
10/5/2017	HG	-25.114	-1.185	0.033	-24.818	-0.881	0.036	-21.823	17.989	27.5	2017.07.14–2017.11.13
10/6/2017	HG	17.878	-0.637	0.039	17.623	-0.887	0.015	2.104	37.494	-48.8	2017.07.14–2017.11.13
10/10/2017	HG	-3.737	-0.943	0.038	-3.699	-0.904	0.023	-3.520	21.587	32.7	2017.07.14–2017.11.13
10/12/2017	HG	-24.199	-1.213	0.039	-23.882	-0.889	0.018	-20.952	18.099	95.0	2017.07.14–2017.11.13
10/17/2017	HG	-24.826	-1.117	0.030	-24.556	-0.841	0.028	-21.697	18.093	24.0	2017.07.14–2017.11.13
10/19/2017	HG	16.924	-0.647	0.032	16.702	-0.866	0.017	2.108	36.547	6.5	2017.07.14–2017.11.13
10/24/2017	HG	-0.995	-0.882	0.026	-0.994	-0.881	0.014	-3.704	24.466	14.1	2017.07.14–2017.11.13
10/25/2017	HG	-26.091	-1.210	0.019	-25.763	-0.874	0.017	-22.393	17.574	74.6	2017.07.14–2017.11.13
10/27/2017	HG	15.167	-0.660	0.041	14.963	-0.861	0.018	1.783	35.118	-19.2	2017.07.14–2017.11.13
10/31/2017	HG	-25.754	-1.200	0.075	-25.454	-0.892	0.030	-22.217	17.737	-11.7	2017.07.14–2017.11.13
11/2/2017	HG	15.634	-0.554	0.064	15.333	-0.850	0.021	1.887	35.376	-26.3	2017.07.14–2017.11.13
11/3/2017	HG	-1.422	-0.911	0.072	-1.398	-0.887	0.022	-3.843	24.200	33.2	2017.07.14–2017.11.13
11/7/2017	HG	-0.936	-0.862	0.035	-0.951	-0.876	0.013	-3.600	24.404	-9.6	2017.07.14–2017.11.13
11/8/2017	HG	-25.131	-1.301	0.045	-24.715	-0.875	0.027	-21.967	18.230	5.9	2017.07.14–2017.11.13
11/13/2017	HG	-25.937	-1.300	0.046	-25.522	-0.874	0.029	-22.378	17.807	-21.0	2017.07.14–2017.11.13
3/13/2018	HG	19.349	-0.402	0.029	18.925	-0.818	0.019	2.167	38.665	8.4	2018.03.07–2018.04.27
3/14/2018	HG	-25.331	-1.246	0.032	-24.849	-0.752	0.024	-22.111	18.112	18.5	2018.03.07–2018.04.27
3/15/2018	HG	-1.466	-0.743	0.035	-1.467	-0.744	0.029	-3.663	23.812	-81.1	2018.03.07–2018.04.27
3/16/2018	HG	-24.324	-1.251	0.020	-23.851	-0.765	0.025	-21.284	18.335	11.1	2018.03.07–2018.04.27
3/16/2018	HG	-1.376	-0.790	0.038	-1.369	-0.782	0.034	-3.574	23.863	-10.6	2018.03.07–2018.04.27
3/17/2018	HG	-25.215	-1.284	0.026	-24.731	-0.789	0.019	-21.601	17.768	41.8	2018.03.07–2018.04.27
3/19/2018	HG	17.233	-0.466	0.015	16.857	-0.835	0.015	2.081	36.698	9.7	2018.03.07–2018.04.27
3/21/2018	HG	-1.077	-0.818	0.030	-1.085	-0.827	0.025	-4.341	24.940	39.8	2018.03.07–2018.04.27
3/22/2018	HG	-24.931	-1.315	0.051	-24.417	-0.788	0.060	-21.491	17.981	-6.2	2018.03.07–2018.04.27
3/26/2018	HG	-23.582	-1.266	0.029	-23.127	-0.800	0.020	-21.125	18.954	-33.0	2018.03.07–2018.04.27
3/27/2018	HG	18.436	-0.399	0.013	18.019	-0.809	0.011	1.972	37.940	-137.4	2018.03.07–2018.04.27
3/28/2018	HG	-1.399	-0.801	0.040	-1.407	-0.809	0.042	-4.112	24.374	-53.0	2018.03.07–2018.04.27
3/29/2018	HG	17.961	-0.423	0.051	17.555	-0.822	0.049	2.277	37.189	-76.9	2018.03.07–2018.04.27
4/10/2018	HG	-24.653	-1.455	0.033	-23.973	-0.759	0.035	-21.055	17.978	29.0	2018.03.07–2018.04.27
4/11/2018	HG	-1.590	-0.806	0.022	-1.553	-0.769	0.028	-4.180	24.254	10.5	2018.03.07–2018.04.27
4/12/2018	HG	19.968	-0.247	0.025	19.355	-0.847	0.029	2.118	39.173	-23.5	2018.03.07–2018.04.27
4/16/2018	HG	-1.413	-0.839	0.024	-1.376	-0.801	0.029	-4.245	24.528	55.1	2018.03.07–2018.04.27
4/17/2018	HG	18.088	-0.378	0.055	17.646	-0.812	0.038	2.222	37.324	5.0	2018.03.07–2018.04.27
4/20/2018	HG	-1.671	-0.879	0.048	-1.583	-0.790	0.092	-4.157	24.223	40.1	2018.03.07–2018.04.27
4/24/2018	HG	-24.502	-1.300	0.047	-23.988	-0.773	0.058	-21.416	18.332	70.3	2018.03.07–2018.04.27
4/26/2018	HG	19.924	-0.383	0.030	19.480	-0.819	0.034	2.361	39.031	-45.0	2018.03.07–2018.04.27

7/11/2018	HG	-24.719	-1.425	0.027	-24.119	-0.811	0.019	-21.468	18.287	30.8	2018.07.10–2018.10.19
7/12/2018	HG	-26.397	-1.451	0.025	-25.775	-0.814	0.025	-22.895	17.996	128.5	2018.07.10–2018.10.19
7/13/2018	HG	-1.553	-0.800	0.023	-1.559	-0.805	0.023	-4.197	24.301	141.3	2018.07.10–2018.10.19
7/14/2018	HG	19.746	-0.303	0.024	19.225	-0.813	0.015	2.359	38.773	71.7	2018.07.10–2018.10.19
7/18/2018	HG	19.777	-0.319	0.022	19.244	-0.842	0.027	2.239	38.938	70.3	2018.07.10–2018.10.19
7/19/2018	HG	-23.678	-1.372	0.022	-23.121	-0.802	0.012	-20.525	18.372	95.1	2018.07.10–2018.10.19
7/23/2018	HG	-1.308	-0.849	0.026	-1.296	-0.838	0.024	-4.373	24.768	22.2	2018.07.10–2018.10.19
7/25/2018	HG	19.441	-0.305	0.038	18.882	-0.853	0.023	2.161	38.663	68.3	2018.07.10–2018.10.19
7/26/2018	HG	-26.936	-1.505	0.039	-26.269	-0.821	0.035	-23.059	17.657	37.2	2018.07.10–2018.10.19
7/31/2018	HG	-1.308	-0.818	0.029	-2.149	-0.823	0.023	-4.424	23.945	157.6	2018.07.10–2018.10.19
8/1/2018	HG	18.060	-0.335	0.062	17.547	-0.839	0.032	2.288	37.188	40.6	2018.07.10–2018.10.19
8/2/2018	HG	-24.150	-1.426	0.036	-23.543	-0.806	0.029	-20.714	18.129	62.0	2018.07.10–2018.10.19
8/6/2018	HG	-1.959	-0.807	0.024	-1.953	-0.801	0.023	-4.505	24.198	114.7	2018.07.10–2018.10.19
8/10/2018	HG	-23.387	-1.442	0.037	-22.765	-0.805	0.024	-20.580	18.794	18.1	2018.07.10–2018.10.19
8/13/2018	HG	19.599	-0.309	0.033	19.083	-0.815	0.015	2.369	38.622	-50.5	2018.07.10–2018.10.19
8/15/2018	HG	-1.180	-0.811	0.033	-1.186	-0.817	0.021	-3.957	24.454	81.1	2018.07.10–2018.10.19
8/16/2018	HG	-23.114	-1.399	0.050	-22.529	-0.801	0.029	-20.435	18.888	125.6	2018.07.10–2018.10.19
8/21/2018	HG	17.830	-0.300	0.046	17.289	-0.831	0.024	2.296	36.916	37.1	2018.07.10–2018.10.19
8/22/2018	HG	-1.140	-0.836	0.029	-1.139	-0.835	0.018	-4.014	24.575	34.5	2018.07.10–2018.10.19
8/23/2018	HG	-26.939	-1.523	0.033	-26.247	-0.813	0.029	-22.964	17.579	139.5	2018.07.10–2018.10.19
8/27/2018	HG	18.898	-0.213	0.054	18.286	-0.814	0.027	1.950	38.234	157.4	2018.07.10–2018.10.19
8/29/2018	HG	-27.787	-1.588	0.028	-27.016	-0.795	0.029	-23.252	17.056	61.8	2018.07.10–2018.10.19
9/3/2018	HG	-24.389	-1.359	0.048	-23.868	-0.826	0.041	-21.315	18.407	163.5	2018.07.10–2018.10.19
9/5/2018	HG	18.034	-0.345	0.032	17.561	-0.810	0.012	2.085	37.372	-2.6	2018.07.10–2018.10.19
9/10/2018	HG	-27.420	-1.556	0.043	-26.669	-0.786	0.035	-23.227	17.377	-32.5	2018.07.10–2018.10.19
9/12/2018	HG	-1.367	-0.820	0.036	-1.367	-0.819	0.031	-4.120	24.434	60.6	2018.07.10–2018.10.19
9/14/2018	HG	17.492	-0.316	0.071	16.961	-0.838	0.038	2.228	36.660	62.6	2018.07.10–2018.10.19
9/18/2018	HG	-1.145	-0.822	0.021	-1.167	-0.843	0.024	-4.050	24.591	78.0	2018.07.10–2018.10.19
9/19/2018	HG	-25.161	-1.452	0.046	-24.515	-0.790	0.033	-21.469	17.860	91.2	2018.07.10–2018.10.19
9/22/2018	HG	17.642	-0.271	0.052	17.077	-0.826	0.026	2.172	36.819	87.5	2018.07.10–2018.10.19
9/27/2018	HG	-1.453	-0.810	0.042	-1.476	-0.833	0.022	-4.410	24.619	82.3	2018.07.10–2018.10.19
9/28/2018	HG	17.385	-0.300	0.038	16.876	-0.800	0.011	1.920	36.838	25.4	2018.07.10–2018.10.19
10/1/2018	HG	-26.402	-1.535	0.064	-25.680	-0.794	0.010	-22.507	17.692	24.6	2018.07.10–2018.10.19
10/5/2018	HG	-0.842	-0.806	0.049	-0.870	-0.834	0.015	-4.030	24.861	61.9	2018.07.10–2018.10.19
10/9/2018	HG	18.102	-0.291	0.042	17.572	-0.811	0.020	2.256	37.217	-10.9	2018.07.10–2018.10.19
10/10/2018	HG	-25.852	-1.538	0.031	-25.133	-0.801	0.020	-22.149	17.907	50.4	2018.07.10–2018.10.19
10/10/2018	HG	-1.317	-0.819	0.030	-1.324	-0.827	0.025	-4.274	24.634	50.8	2018.07.10–2018.10.19
10/15/2018	HG	-1.463	-0.815	0.035	-1.484	-0.837	0.020	-4.190	24.401	88.5	2018.07.10–2018.10.19
10/17/2018	HG	-27.173	-1.549	0.048	-26.439	-0.796	0.028	-22.890	17.292	103.6	2018.07.10–2018.10.19
10/18/2018	HG	17.236	-0.237	0.051	16.597	-0.865	0.024	2.213	36.339	223.0	2018.07.10–2018.10.19

ID	Sample	Weight (mg)	δ45	δ45 SD	δ46	δ46 SD	δ47	δ47 SD	δ48	δ48 SD	δ49	δ49 SD
2019-01-09 18:55 CET	HG	6.4	0.0	10.9	0.0	16.569	0.0270	21.284	0.1170	-32.069	2.1	-0.846
2019-01-10 22:43 CET	HG	0.0	0.0	-1.4	0.0	-2.208	0.0220	-3.004	0.1030	-4.172	2.3	-0.846
2019-01-12 01:06 CET	HG	-16.8	0.0	-7.1	0.0	-24.959	0.0200	-14.207	0.1190	22.843	4.1	-0.851
2019-01-14 18:29 CET	HG	6.5	0.0	13.0	0.0	18.732	0.0300	25.498	0.1110	-36.393	2.6	-0.849
2019-01-15 16:07 CET	HG	0.1	0.0	-1.4	0.0	-2.132	0.0250	-3.045	0.1400	0.567	1.0	-0.844
2019-01-17 20:22 CET	HG	6.4	0.0	10.6	0.0	16.201	0.0330	20.667	0.0750	11.123	1.6	-0.834
2019-01-18 04:55 CET	HG	0.0	0.0	-0.5	0.0	-1.250	0.0260	-1.178	0.0650	1.235	1.6	-0.850
2019-01-21 19:56 CET	HG	6.5	0.0	11.1	0.0	16.840	0.0200	21.772	0.1020	11.818	1.1	-0.855
2019-01-23 14:54 CET	HG	-17.2	0.0	-7.3	0.0	-25.621	0.0220	-14.704	0.1000	-11.493	0.8	-0.868
2019-01-25 16:22 CET	HG	-0.1	0.0	-1.4	0.0	-2.280	0.0230	-3.048	0.0720	-0.093	1.0	-0.864
2019-01-29 21:58 CET	HG	6.4	0.0	10.5	0.0	16.194	0.0160	20.479	0.0530	9.504	0.7	-0.860
2019-01-30 18:53 CET	HG	-17.0	0.0	-7.3	0.0	-25.511	0.0270	-14.722	0.1190	-9.538	1.3	-0.868
2019-02-01 20:39 CET	HG	0.0	0.0	-1.4	0.0	-2.294	0.0200	-3.092	0.0730	-0.360	1.4	-0.863
2019-02-04 19:54 CET	HG	6.5	0.0	13.0	0.0	18.748	0.0290	25.439	0.1080	11.045	2.0	-0.850
2019-02-05 16:36 CET	HG	-16.8	0.0	-7.2	0.0	-25.075	0.0300	-14.322	0.0840	-9.139	1.5	-0.870
2019-02-12 13:57 CET	HG	0.0	0.0	-1.0	0.0	-1.813	0.0260	-2.237	0.0550	0.025	1.5	-0.850
2019-02-13 15:37 CET	HG	-17.1	0.0	-7.3	0.0	-25.606	0.0350	-14.718	0.0650	-10.895	1.0	-0.860
2019-02-15 20:14 CET	HG	6.4	0.0	10.8	0.0	16.419	0.0410	21.002	0.0900	10.802	1.6	-0.839
2019-02-18 19:06 CET	HG	-17.0	0.0	-7.0	0.0	-25.178	0.0270	-14.136	0.1140	-10.796	0.8	-0.847
2019-03-01 01:13 CET	HG	6.3	0.0	9.5	0.0	15.136	0.0200	18.261	0.1000	12.102	1.5	-0.806
2019-03-01 17:50 CET	HG	0.0	0.0	-1.2	0.0	-1.996	0.0190	-2.588	0.0600	1.237	1.2	-0.844
2019-03-04 18:30 CET	HG	6.4	0.0	12.6	0.0	18.303	0.0360	25.104	0.0600	13.484	1.6	-0.836
2019-03-05 15:18 CET	HG	0.0	0.0	-1.1	0.0	-1.939	0.0320	-2.480	0.1000	-0.468	1.6	-0.849
2019-03-06 17:55 CET	HG	6.3	0.0	11.1	0.0	16.619	0.0240	21.902	0.0840	12.272	1.8	-0.850
2019-03-06 22:07 CET	HG	-17.1	0.0	-7.3	0.0	-25.520	0.0270	-14.967	0.0470	-12.632	1.2	-0.848
2019-03-07 18:55 CET	HG	0.0	0.0	-1.2	0.0	-2.040	0.0200	-2.742	0.0790	-0.363	1.1	-0.850
2019-03-07 23:02 CET	HG	-17.1	0.0	-7.4	0.0	-25.580	0.0150	-15.070	0.0680	-12.330	0.7	-0.855
2019-03-11 18:41 CET	HG	0.0	0.0	-0.6	0.0	-1.410	0.0210	-1.496	0.0720	-0.735	1.3	-0.858
2019-03-12 17:34 CET	HG	6.4	0.0	11.6	0.0	17.205	0.0250	23.154	0.0940	12.730	1.6	-0.852
2019-03-13 20:57 CET	HG	-16.8	0.0	-7.1	0.0	-25.097	0.0260	-14.603	0.0830	-11.524	1.9	-0.845
2019-03-14 17:41 CET	HG	6.5	0.0	11.5	0.0	17.186	0.0290	22.944	0.0720	12.154	1.6	-0.862
2019-03-15 21:24 CET	HG	0.0	0.0	-1.3	0.0	-2.118	0.0310	-2.801	0.1010	0.217	1.4	-0.861
2019-03-18 19:58 CET	HG	6.5	0.0	12.9	0.0	18.624	0.0270	25.327	0.1000	14.453	1.8	-0.848
2019-03-19 00:08 CET	HG	-16.9	0.0	-7.3	0.0	-25.321	0.0210	-14.634	0.0740	-14.441	1.4	-0.871
2019-03-20 17:42 CET	HG	0.0	0.0	-1.1	0.0	-1.971	0.0290	-2.598	0.1230	-0.919	2.0	-0.853
2019-03-22 00:05 CET	HG	6.5	0.0	12.6	0.0	18.320	0.0270	24.914	0.0950	14.738	1.3	-0.870
2019-03-22 17:22 CET	HG	-17.4	0.0	-7.4	0.0	-25.966	0.0250	-14.989	0.0690	-13.229	1.8	-0.847
2019-03-25 20:04 CET	HG	0.0	0.0	-0.7	0.0	-1.585	0.0240	-1.843	0.1150	-0.420	1.8	-0.855

2019-03-28 16:53 CET	HG	-17.4	0.0	-7.4	0.0	-25.974	0.0280	-15.028	0.0930	-14.580	1.7	-0.855
2019-03-29 18:39 CET	HG	0.0	0.0	-1.0	0.0	-1.898	0.0220	-2.385	0.0970	-0.767	1.9	-0.864
2019-04-01 22:28 CEST	HG	6.4	0.0	12.6	0.0	18.171	0.0240	24.926	0.0810	14.319	1.8	-0.858
2019-04-02 15:06 CEST	HG	-18.1	0.0	-7.7	0.0	-27.023	0.0250	-15.682	0.0870	-15.803	2.8	-0.865
2019-04-03 20:12 CEST	HG	0.0	0.0	-1.1	0.0	-1.933	0.0260	-2.462	0.0810	-1.070	1.3	-0.866
2019-04-04 17:02 CEST	HG	6.4	0.0	11.5	0.0	17.101	0.0250	22.674	0.0560	12.363	1.6	-0.861
2019-04-05 17:59 CEST	HG	-17.4	0.0	-7.5	0.0	-26.015	0.0230	-15.089	0.1220	-14.125	1.9	-0.855
2019-04-08 21:02 CEST	HG	0.0	0.0	-0.8	0.0	-1.672	0.0220	-1.911	0.0800	-1.132	1.7	-0.861
2019-04-09 17:47 CEST	HG	6.4	0.0	11.4	0.0	17.019	0.0240	22.417	0.1340	12.687	1.6	-0.853
2019-04-10 18:50 CEST	HG	-16.8	0.0	-7.1	0.0	-25.064	0.0200	-14.476	0.0800	-14.872	1.8	-0.870
2019-04-12 13:37 CEST	HG	-0.1	0.0	-1.5	0.0	-2.426	0.0240	-3.292	0.0930	-0.775	2.2	-0.854
2019-04-15 17:48 CEST	HG	6.4	0.0	13.1	0.0	18.789	0.0200	26.008	0.1240	14.958	1.2	-0.847
2019-04-16 18:58 CEST	HG	-18.0	0.0	-7.7	0.0	-26.807	0.0310	-15.466	0.1080	-15.681	2.0	-0.861
2019-04-17 19:48 CEST	HG	0.0	0.0	-0.5	0.0	-1.359	0.0190	-1.333	0.1120	-0.190	1.5	-0.856
2019-04-23 18:32 CEST	HG	6.5	0.0	12.8	0.0	18.480	0.0150	25.247	0.0590	13.180	1.1	-0.856
2019-04-24 19:39 CEST	HG	-17.3	0.0	-7.3	0.0	-25.758	0.0250	-14.839	0.0860	-14.269	1.7	-0.847
2019-04-25 16:25 CEST	HG	0.0	0.0	-1.1	0.0	-1.973	0.0120	-2.544	0.0830	-1.133	1.6	-0.864
2019-04-26 19:32 CEST	HG	6.4	0.0	11.4	0.0	17.053	0.0250	22.460	0.0800	13.410	1.9	-0.869
2019-04-29 19:15 CEST	HG	-14.3	0.0	-6.2	0.0	-21.659	0.0230	-12.577	0.0980	-12.165	1.3	-0.880
2019-04-30 20:33 CEST	HG	0.1	0.0	-0.4	0.0	-1.209	0.0270	-1.152	0.0730	0.382	1.4	-0.868
2019-05-02 19:23 CEST	HG	6.4	0.0	13.1	0.0	18.775	0.0230	26.012	0.0620	13.920	1.6	-0.863
2019-05-03 18:06 CEST	HG	-14.1	0.0	-6.4	0.0	-21.592	0.0270	-13.110	0.1090	-11.295	1.7	-0.837
2019-05-06 19:51 CEST	HG	0.0	0.0	-0.5	0.0	-1.413	0.0200	-1.480	0.1200	-1.243	1.4	-0.862
2019-05-08 19:57 CEST	HG	6.5	0.0	13.3	0.0	18.971	0.0180	26.215	0.1010	14.759	2.1	-0.854
2019-05-10 15:49 CEST	HG	-14.3	0.0	-6.3	0.0	-21.707	0.0200	-12.921	0.0930	-11.813	1.9	-0.879
2019-05-14 15:25 CEST	HG	-0.1	0.0	-1.1	0.0	-2.025	0.0200	-2.500	0.0860	-0.153	1.5	-0.878
2019-05-15 20:10 CEST	HG	6.3	0.0	11.8	0.0	17.251	0.0280	23.231	0.0810	15.391	2.1	-0.893
2019-05-16 19:16 CEST	HG	-17.1	0.0	-7.2	0.0	-25.426	0.0300	-14.588	0.0890	-14.191	1.3	-0.867

ID	Δ47 raw	Δ47, raw SD	Δ48, raw	Δ48, raw SD	Δ49, raw	Δ49, raw SD	δ13C, VPDB	δ13C SD	δ18O, VSMOW	δ18O SD	ETF period
2019-01-09 18:55 CET	0.027	-0.6910	0.1150	-59.0	2.06	2.220	0.000	36.470	0.0	10	2019.01.09–2019.03.34
2019-01-10 22:43 CET	0.021	-0.2970	0.1040	-1.5	2.309	-4.180	0.000	23.870	0.0	10	2019.01.09–2019.03.35
2019-01-12 01:06 CET	0.020	-0.1580	0.1190	56.1	4.244	-21.830	0.000	18.060	0.0	10	2019.01.09–2019.03.36
2019-01-14 18:29 CET	0.028	-0.7490	0.1080	-67.1	2.499	2.220	0.000	38.640	0.0	10	2019.01.09–2019.03.37
2019-01-15 16:07 CET	0.026	-0.2820	0.1420	3.2	0.977	-4.080	0.000	23.840	0.0	10	2019.01.09–2019.03.38
2019-01-17 20:22 CET	0.035	-0.6480	0.0700	-16.3	1.583	2.180	0.000	36.130	0.0	10	2019.01.09–2019.03.39
2019-01-18 04:55 CET	0.024	-0.2780	0.0660	2.1	1.59	-4.140	0.000	24.800	0.0	10	2019.01.09–2019.03.40
2019-01-21 19:56 CET	0.017	-0.6220	0.1040	-16.8	1.042	2.290	0.000	36.680	0.0	10	2019.01.09–2019.03.41
2019-01-23 14:54 CET	0.023	-0.1060	0.1050	21.6	0.824	-22.210	0.000	17.780	0.0	10	2019.01.09–2019.03.42
2019-01-25 16:22 CET	0.027	-0.2890	0.0730	2.7	0.985	-4.210	0.000	23.840	0.0		2019.01.09–2019.03.43

2019-01-29 21:58 CET	0.016	-0.6920	0.0490	-17.8	0.692	2.270	0.000	36.060	0.0	10	2019.01.09–2019.03.44
2019-01-30 18:53 CET	0.026	-0.1070	0.1170	23.5	1.315	-22.090	0.000	17.770	0.0	10	2019.01.09–2019.03.45
2019-02-01 20:39 CET	0.021	-0.2340	0.0670	2.5	1.389	-4.170	0.000	23.790	0.0	10	2019.01.09–2019.03.46
2019-02-04 19:54 CET	0.028	-0.7430	0.1100	-21.1	1.98	2.280	0.000	38.600	0.0	10	2019.01.09–2019.03.47
2019-02-05 16:36 CET	0.029	-0.0540	0.0860	23.2	1.54	-21.820	0.000	17.950	0.0	10	2019.01.09–2019.03.48
2019-02-12 13:57 CET	0.029	-0.3260	0.0580	1.9	1.541	-4.190	0.000	24.280	0.0	10	2019.01.09–2019.03.49
2019-02-13 15:37 CET	0.030	-0.1080	0.0660	22.2	1.065	-22.200	0.000	17.770	0.0	10	2019.01.09–2019.03.50
2019-02-15 20:14 CET	0.039	-0.6530	0.0920	-17.0	1.596	2.230	0.000	36.310	0.0	10	2019.01.09–2019.03.51
2019-02-18 19:06 CET	0.028	-0.1630	0.1150	21.5	0.791	-22.100	0.000	18.100	0.0	10	2019.01.09–2019.03.52
2019-03-01 01:13 CET	0.020	-0.8710	0.0980	-13.2	1.506	2.190	0.000	35.030	0.0	10	2019.01.09–2019.03.53
2019-03-01 17:50 CET	0.019	-0.2780	0.0620	3.5	1.237	-4.170	0.000	24.070	0.0	10	2019.01.09–2019.03.54
2019-03-04 18:30 CET	0.034	-0.3310	0.0570	-18.0	1.533	2.200	0.000	38.220	0.0	10	2019.01.09–2019.03.55
2019-03-05 15:18 CET	0.031	-0.3100	0.1040	1.7	1.57	-4.180	0.000	24.150	0.0	10	2019.01.09–2019.03.56
2019-03-06 17:55 CET	0.028	-0.3140	0.0830	-16.0	1.726	2.160	0.000	36.590	0.0	10	2019.01.09–2019.03.57
2019-03-06 22:07 CET	0.024	-0.3740	0.0500	20.3	1.259	-22.130	0.000	17.780	0.0	10	2019.01.09–2019.03.58
2019-03-07 18:55 CET	0.017	-0.3800	0.0850	2.0	1.061	-4.190	0.000	24.050	0.0	10	2019.01.09–2019.03.59
2019-03-07 23:02 CET	0.015	-0.3650	0.0660	20.7	0.721	-22.120	0.000	17.720	0.0	10	2019.01.09–2019.03.60
2019-03-11 18:41 CET	0.022	-0.3610	0.0770	0.4	1.269	-4.170	0.000	24.680	0.0	10	2019.01.09–2019.03.61
2019-03-12 17:34 CET	0.026	-0.1830	0.0920	-16.7	1.531	2.180	0.000	37.150	0.0	10	2019.01.09–2019.03.62
2019-03-13 20:57 CET	0.028	-0.3770	0.0860	20.8	1.986	-21.880	0.000	17.970	0.0	10	2019.01.09–2019.03.63
2019-03-14 17:41 CET	0.027	-0.1630	0.0700	-17.1	1.553	2.290	0.000	37.040	0.0	10	2019.01.09–2019.03.63
2019-03-15 21:24 CET	0.030	-0.2690	0.1000	2.7	1.37	-4.170	0.000	23.960	0.0	10	2019.03.15–2019.05.16
2019-03-18 19:58 CET	0.026	-0.5960	0.1000	-17.6	1.709	2.280	0.000	38.470	0.0	10	2019.03.15–2019.05.16
2019-03-19 00:08 CET	0.023	-0.1820	0.0750	18.1	1.48	-21.970	0.000	17.850	0.0	10	2019.03.15–2019.05.16
2019-03-20 17:42 CET	0.031	-0.3700	0.1220	1.3	2.011	-4.180	0.000	24.120	0.0	10	2019.03.15–2019.05.16
2019-03-22 00:05 CET	0.026	-0.5160	0.0920	-16.8	1.251	2.250	0.000	38.220	0.0	10	2019.03.15–2019.05.16
2019-03-22 17:22 CET	0.025	-0.1840	0.0690	20.3	1.856	-22.480	0.000	17.670	0.0	10	2019.03.15–2019.05.16
2019-03-25 20:04 CET	0.023	-0.3810	0.1180	1.0	1.814	-4.180	0.000	24.510	0.0	10	2019.03.15–2019.05.16
2019-03-28 16:53 CET	0.028	-0.2470	0.0950	18.9	1.787	-22.500	0.000	17.680	0.0	10	2019.03.15–2019.05.16
2019-03-29 18:39 CET	0.020	-0.3340	0.0980	1.3	1.901	-4.190	0.000	24.210	0.0	10	2019.03.15–2019.05.16
2019-04-01 22:28 CEST	0.023	-0.4550	0.0820	-17.0	1.712	2.110	0.000	38.190	0.0	10	2019.03.15–2019.05.16
2019-04-02 15:06 CEST	0.026	-0.2570	0.0890	19.0	2.895	-23.240	0.000	17.350	0.0	10	2019.03.15–2019.05.16
2019-04-03 20:12 CEST	0.026	-0.3170	0.0830	1.1	1.254	-4.170	0.000	24.160	0.0	10	2019.03.15–2019.05.16
2019-04-04 17:02 CEST	0.025	-0.4800	0.0490	-16.8	1.601	2.170	0.000	37.070	0.0	10	2019.03.15–2019.05.16
2019-04-05 17:59 CEST	0.022	-0.2370	0.1260	19.4	1.91	-22.500	0.000	17.650	0.0	10	2019.03.15–2019.05.16
2019-04-08 21:02 CEST	0.023	-0.2930	0.0790	0.5	1.696	-4.190	0.000	24.430	0.0	10	2019.03.15–2019.05.16
2019-04-09 17:47 CEST	0.023	-0.4500	0.1310	-16.3	1.534	2.230	0.000	36.920	0.0	10	2019.03.15–2019.05.16
2019-04-10 18:50 CEST	0.023	-0.2590	0.0820	17.3	1.838	-21.830	0.000	17.970	0.0	10	2019.03.15–2019.05.16
2019-04-12 13:37 CEST	0.026	-0.3090	0.0920	2.3	2.192	-4.250	0.000	23.730	0.0	10	2019.03.15–2019.05.16
2019-04-15 17:48 CEST	0.016	-0.4420	0.1260	-17.5	1.196	2.180	0.000	38.740	0.0	10	2019.03.15–2019.05.16
2019-04-16 18:58 CEST	0.031	-0.2200	0.1070	18.8	2.106	-23.110	0.000	17.450	0.0	10	2019.03.15–2019.05.16
2019-04-17 19:48 CEST	0.020	-0.3390	0.1160	0.8	1.545	-4.200	0.000	24.750	0.0	10	2019.03.15–2019.05.16
2019-04-23 18:32 CEST	0.017	-0.4750	0.0570	-18.6	1.071	2.250	0.000	38.370	0.0	10	2019.03.15–2019.05.16
2019-04-24 19:39 CEST	0.028	-0.2740	0.0860	18.9	1.716	-22.390	0.000	17.800	0.0	10	2019.03.15–2019.05.16

2019-04-25 16:25 CEST	0.009	-0.3560	0.0840	1.1	1.652	-4.190	0.000	24.140	0.0	10	2019.03.15–2019.05.16
2019-04-26 19:32 CEST	0.028	-0.4650	0.0820	-15.7	1.866	2.250	0.000	36.950	0.0	10	2019.03.15–2019.05.16
2019-04-29 19:15 CEST	0.024	-0.2350	0.0990	15.5	1.375	-19.260	0.000	18.940	0.0	10	2019.03.15–2019.05.16
2019-04-30 20:33 CEST	0.028	-0.3120	0.0740	1.1	1.398	-4.110	0.000	24.830	0.0	10	2019.03.15–2019.05.16
2019-05-02 19:23 CEST	0.024	-0.4280	0.0600	-18.5	1.57	2.190	0.000	38.730	0.0	10	2019.03.15–2019.05.16
2019-05-03 18:06 CEST	0.027	-0.2710	0.1120	16.6	1.776	-18.970	0.000	18.680	0.0	10	2019.03.15–2019.05.16
2019-05-06 19:51 CEST	0.018	-0.3970	0.1200	-0.2	1.399	-4.200	0.000	24.700	0.0	10	2019.03.15–2019.05.16
2019-05-08 19:57 CEST	0.020	-0.4970	0.0980	-18.0	2.026	2.240	0.000	38.870	0.0	10	2019.03.15–2019.05.16
2019-05-10 15:49 CEST	0.020	-0.3160	0.0960	16.0	1.937	-19.170	0.000	18.800	0.0	10	2019.03.15–2019.05.16
2019-05-14 15:25 CEST	0.021	-0.3050	0.0850	2.1	1.469	-4.230	0.000	24.130	0.0	10	2019.03.15–2019.05.16
2019-05-15 20:10 CEST	0.027	-0.4060	0.0800	-14.3	2.046	2.110	0.000	37.310	0.0	10	2019.03.15–2019.05.16
2019-05-16 19:16 CEST	0.029	-0.2760	0.0920	18.4	1.391	-22.160	0.000	17.930	0.0	10	2019.03.15–2019.05.16

In the replicates marked blue, the Δ49, raw values were not corrected for the negative background measured on the *m/z* 47.5 cup.

Date	Sample	δ47 (raw) (‰)	Δ47 (raw) (‰)	SD Δ47 (raw) (‰)	δ47 (bgcorr) (‰)	Δ47 (bgcorr) (‰)	SD Δ47 (bgcorr) (‰)	δ13C CO2 (‰ VPDB)	δ18O CO2 (‰ VSMOW)	Diff Bellow (mV)	ETF period
1/7/2017	25G	-6.367	-0.090	0.023	-6.3062	-0.029	0.017	-40.763	55.497	25.8	2017.01.06–2017.07.10
1/7/2017	25G	31.165	0.364	0.014	30.7651	-0.024	0.010	-3.587	55.437	45.0	2017.01.06–2017.07.10
1/11/2017	25G	8.149	0.072	0.032	8.0319	-0.043	0.015	-3.572	32.575	60.2	2017.01.06–2017.07.10
1/13/2017	25G	-28.404	-0.369	0.019	-28.0770	-0.032	0.018	-40.825	32.862	-43.9	2017.01.06–2017.07.10
1/17/2017	25G	-28.892	-0.403	0.029	-28.5267	-0.027	0.020	-40.813	32.377	69.9	2017.01.06–2017.07.10
1/24/2017	25G	31.043	0.363	0.032	30.6273	-0.040	0.023	-3.763	55.491	25.8	2017.01.06–2017.07.10
1/26/2017	25G	-6.552	-0.108	0.029	-6.4626	-0.017	0.021	-40.752	55.310	73.0	2017.01.06–2017.07.10
1/30/2017	25G	8.022	0.054	0.030	7.9338	-0.033	0.018	-3.624	32.517	74.1	2017.01.06–2017.07.10
2/1/2017	25G	-28.901	-0.353	0.026	-28.5541	0.005	0.020	-40.777	32.279	8.2	2017.01.06–2017.07.10
2/7/2017	25G	31.083	0.357	0.019	30.6717	-0.041	0.014	-3.587	55.360	-2.3	2017.01.06–2017.07.10
2/9/2017	25G	-7.888	-0.109	0.019	-7.8157	-0.036	0.015	-40.796	53.965	14.6	2017.01.06–2017.07.10
2/16/2017	25G	-29.355	-0.388	0.029	-29.0043	-0.027	0.026	-40.753	31.816	-13.0	2017.01.06–2017.07.10
2/22/2017	25G	30.993	0.317	0.031	30.6093	-0.055	0.025	-3.602	55.326	73.5	2017.01.06–2017.07.10
2/24/2017	25G	-6.754	-0.089	0.032	-6.6683	-0.003	0.019	-40.786	55.116	39.2	2017.01.06–2017.07.10
2/28/2017	25G	7.848	0.070	0.023	7.7455	-0.031	0.014	-3.570	32.272	49.2	2017.01.06–2017.07.10
3/4/2017	25G	-28.969	-0.413	0.022	-28.5974	-0.030	0.011	-40.822	32.315	134.5	2017.01.06–2017.07.10
3/10/2017	25G	31.255	0.340	0.033	30.8514	-0.052	0.033	-3.563	55.528	22.2	2017.01.06–2017.07.10
3/13/2017	25G	-6.791	-0.095	0.038	-6.7107	-0.014	0.033	-40.795	55.093	10.2	2017.01.06–2017.07.10
3/17/2017	25G	8.231	0.073	0.023	8.1206	-0.037	0.013	-3.564	32.650	5.1	2017.01.06–2017.07.10
3/21/2017	25G	-28.850	-0.379	0.031	-28.5194	-0.039	0.017	-40.810	32.392	-0.4	2017.01.06–2017.07.10
3/24/2017	25G	30.974	0.334	0.029	30.5964	-0.032	0.025	-3.645	55.333	66.1	2017.01.06–2017.07.10
3/29/2017	25G	-6.497	-0.065	0.031	-6.4373	-0.005	0.043	-40.772	55.345	-4.8	2017.01.06–2017.07.10
3/31/2017	25G	8.154	0.078	0.028	8.0353	-0.040	0.016	-3.613	32.615	12.1	2017.01.06–2017.07.10
4/3/2017	25G	-28.861	-0.397	0.039	-28.4903	-0.015	0.034	-40.794	32.383	71.4	2017.01.06–2017.07.10
4/11/2017	25G	31.353	0.368	0.036	30.9742	0.001	0.028	-3.611	55.645	0.2	2017.01.06–2017.07.10
4/20/2017	25G	7.947	0.076	0.023	7.8485	-0.021	0.023	-3.555	32.352	40.4	2017.01.06–2017.07.10
4/26/2017	25G	31.276	0.338	0.030	30.9089	-0.018	0.017	-3.572	55.560	74.0	2017.01.06–2017.07.10
4/28/2017	25G	-6.689	-0.087	0.032	-6.6272	-0.024	0.019	-40.805	55.201	-0.1	2017.01.06–2017.07.10

5/3/2017	25G	-28.802	-0.355	0.043	-28.4438	0.014	0.018	-40.823	32.431	38.5	2017.01.06–2017.07.10
5/9/2017	25G	-6.364	-0.070	0.025	-6.2908	0.004	0.014	-40.791	55.507	4.7	2017.01.06–2017.07.10
5/24/2017	25G	-6.418	-0.031	0.030	-6.3686	0.019	0.028	-40.761	55.380	8.7	2017.01.06–2017.07.10
6/7/2017	25G	-28.811	-0.352	0.026	-28.4693	0.000	0.026	-40.790	32.385	20.9	2017.01.06–2017.07.10
6/13/2017	25G	31.576	0.375	0.046	31.1790	-0.009	0.016	-3.576	55.826	-8.4	2017.01.06–2017.07.10
6/21/2017	25G	-28.783	-0.355	0.029	-28.4591	-0.021	0.015	-40.751	32.377	-2.8	2017.01.06–2017.07.10
6/22/2017	25G	-7.597	-0.100	0.024	-7.5110	-0.013	0.015	-40.696	54.156	36.5	2017.01.06–2017.07.10
6/27/2017	25G	31.153	0.340	0.025	30.7861	-0.016	0.020	-3.510	55.371	52.0	2017.01.06–2017.07.10
6/29/2017	25G	-30.480	-0.464	0.040	-30.0829	-0.055	0.025	-40.769	30.737	139.6	2017.01.06–2017.07.10
7/4/2017	25G	31.226	0.337	0.027	30.8530	-0.025	0.028	-3.585	55.523	-8.0	2017.01.06–2017.07.10
7/6/2017	25G	-28.893	-0.362	0.026	-28.5581	-0.017	0.019	-40.822	32.343	33.6	2017.01.06–2017.07.10
7/19/2017	25G	7.647	0.086	0.039	7.5228	-0.038	0.019	-3.719	32.202	8.2	2017.07.14–2017.11.13
7/20/2017	25G	-6.882	-0.043	0.043	-6.8289	0.011	0.025	-40.835	54.986	-35.1	2017.07.14–2017.11.13
7/27/2017	25G	-29.096	-0.409	0.017	-28.7011	-0.002	0.017	-40.819	32.174	53.6	2017.07.14–2017.11.13
7/28/2017	25G	8.477	0.095	0.033	8.3489	-0.031	0.017	-3.580	32.890	18.1	2017.07.14–2017.11.13
7/31/2017	25G	-28.310	-0.416	0.032	-27.9354	-0.031	0.020	-40.823	33.007	26.1	2017.07.14–2017.11.13
8/1/2017	25G	30.971	0.379	0.035	30.5522	-0.026	0.022	-3.548	55.185	30.8	2017.07.14–2017.11.13
9/1/2017	25G	-29.022	-0.382	0.043	-28.6584	-0.008	0.023	-40.863	32.269	104.3	2017.07.14–2017.11.13
9/5/2017	25G	8.508	0.034	0.039	8.4573	-0.016	0.009	-3.605	33.007	172.5	2017.07.14–2017.11.13
9/7/2017	25G	-7.005	-0.120	0.051	-6.9112	-0.025	0.020	-41.024	55.133	78.1	2017.07.14–2017.11.13
9/12/2017	25G	8.377	0.030	0.058	8.3062	-0.041	0.028	-3.530	32.807	125.0	2017.07.14–2017.11.13
9/14/2017	25G	-29.452	-0.445	0.035	-29.0399	-0.020	0.025	-40.997	32.020	187.4	2017.07.14–2017.11.13
9/19/2017	25G	-6.093	-0.119	0.049	-6.0105	-0.036	0.025	-40.723	55.771	51.4	2017.07.14–2017.11.13
9/20/2017	25G	8.030	0.030	0.042	7.9649	-0.035	0.019	-3.663	32.588	110.8	2017.07.14–2017.11.13
9/26/2017	25G	31.507	0.385	0.034	31.0969	-0.012	0.020	-3.641	55.812	-15.7	2017.07.14–2017.11.13
9/27/2017	25G	-28.290	-0.367	0.047	-27.9449	-0.011	0.023	-40.708	32.860	60.0	2017.07.14–2017.11.13
10/4/2017	25G	-5.925	-0.019	0.032	-5.9209	-0.014	0.025	-40.767	55.888	-96.2	2017.07.14–2017.11.13
10/9/2017	25G	8.602	0.067	0.053	8.5138	-0.021	0.027	-3.551	33.016	70.9	2017.07.14–2017.11.13
10/11/2017	25G	31.468	0.338	0.029	31.1120	-0.007	0.018	-3.615	55.795	58.8	2017.07.14–2017.11.13
10/18/2017	25G	-6.400	-0.100	0.072	-6.3245	-0.025	0.022	-40.787	55.499	56.0	2017.07.14–2017.11.13
10/20/2017	25G	8.392	0.101	0.034	8.2514	-0.038	0.021	-3.543	32.762	-17.0	2017.07.14–2017.11.13

10/23/2017	25G	-29.170	-0.360	0.038	-28.8435	-0.024	0.017	-40.935	32.166	10.0	2017.07.14–2017.11.13
10/26/2017	25G	-6.461	-0.091	0.027	-6.4053	-0.035	0.012	-40.876	55.518	23.4	2017.07.14–2017.11.13
10/30/2017	25G	31.911	0.355	0.027	31.5120	-0.032	0.023	-3.480	56.089	7.9	2017.07.14–2017.11.13
11/1/2017	25G	8.097	-0.002	0.084	8.0730	-0.026	0.023	-3.674	32.699	160.4	2017.07.14–2017.11.13
11/6/2017	25G	-7.174	-0.206	0.047	-7.0095	-0.040	0.020	-40.957	54.976	155.3	2017.07.14–2017.11.13
11/10/2017	25G	8.058	0.047	0.046	7.9650	-0.046	0.026	-3.622	32.559	138.7	2017.07.14–2017.11.13
3/7/2018	25G	32.283	0.594	0.028	31.6476	-0.023	0.020	-4.274	57.013	-40.7	2018.03.07–2018.04.27
3/8/2018	25G	-29.022	-0.499	0.018	-28.5027	0.036	0.020	-40.886	32.411	-7.2	2018.03.07–2018.04.28
3/20/2018	25G	7.660	0.177	0.016	7.4754	-0.006	0.015	-4.206	32.600	5.0	2018.03.07–2018.04.29
3/20/2018	25G	-28.589	-0.524	0.032	-28.0550	0.025	0.023	-40.548	32.545	-83.9	2018.03.07–2018.04.30
3/21/2018	25G	31.897	0.635	0.025	31.1960	-0.044	0.021	-4.172	56.478	-55.0	2018.03.07–2018.04.31
3/23/2018	25G	-5.003	-0.047	0.030	-4.9514	0.005	0.025	-40.517	56.618	-93.7	2018.03.07–2018.04.32
3/26/2018	25G	8.132	0.228	0.018	7.9132	0.011	0.014	-4.243	33.060	-156.7	2018.03.07–2018.04.33
3/27/2018	25G	-29.278	-0.601	0.049	-28.6659	0.029	0.039	-40.651	32.009	162.6	2018.03.07–2018.04.34
4/11/2018	25G	7.948	0.276	0.019	7.6888	0.019	0.021	-4.111	32.696	-113.2	2018.03.07–2018.04.35
4/12/2018	25G	7.639	0.247	0.024	7.3990	0.009	0.031	-4.257	32.559	-75.1	2018.03.07–2018.04.36
4/12/2018	25G	-5.563	-0.116	0.033	-5.4291	0.019	0.039	-40.588	56.179	-161.8	2018.03.07–2018.04.37
4/17/2018	25G	-28.977	-0.775	0.070	-28.2749	-0.053	0.069	-40.550	32.397	18.0	2018.03.07–2018.04.38
4/26/2018	25G	31.609	0.670	0.032	30.9234	0.005	0.037	-4.158	56.139	-34.9	2018.03.07–2018.04.39
4/27/2018	25G	-5.761	-0.034	0.060	-5.6896	0.038	0.043	-40.678	55.982	-206.4	2018.03.07–2018.04.40
7/10/2018	25G	30.847	0.775	0.016	30.0179	-0.030	0.015	-4.312	55.419	85.1	2018.07.10–2018.10.19
7/17/2018	25G	31.478	0.829	0.024	30.6136	-0.010	0.022	-4.306	55.991	181.4	2018.07.10–2018.10.19
7/17/2018	25G	-29.801	-0.703	0.030	-29.0815	0.038	0.025	-40.646	31.561	95.6	2018.07.10–2018.10.19
7/19/2018	25G	-29.566	-0.730	0.029	-28.8339	0.024	0.022	-40.789	31.979	-24.8	2018.07.10–2018.10.19
7/25/2018	25G	30.652	0.822	0.021	29.7692	-0.035	0.013	-4.415	55.277	203.9	2018.07.10–2018.10.19
7/27/2018	25G	32.615	0.826	0.033	31.7188	-0.042	0.021	-4.191	57.022	108.4	2018.07.10–2018.10.19
7/30/2018	25G	31.908	0.827	0.033	31.0498	-0.006	0.033	-4.154	56.274	51.9	2018.07.10–2018.10.19
8/1/2018	25G	-29.701	-0.716	0.028	-28.9874	0.020	0.027	-40.634	31.666	169.4	2018.07.10–2018.10.19
8/7/2018	25G	31.447	0.870	0.035	30.5135	-0.036	0.022	-4.351	55.963	159.4	2018.07.10–2018.10.19
8/9/2018	25G	-29.655	-0.786	0.032	-28.8505	0.042	0.030	-40.767	31.921	-38.5	2018.07.10–2018.10.19
8/14/2018	25G	32.026	0.872	0.049	31.1118	-0.014	0.013	-4.169	56.360	44.2	2018.07.10–2018.10.19

8/17/2018	25G	-28.881	-0.766	0.050	-28.0878	0.051	0.030	-40.544	32.481	0.5	2018.07.10–2018.10.19
8/20/2018	25G	31.538	0.887	0.057	30.6013	-0.021	0.034	-4.300	55.984	90.5	2018.07.10–2018.10.19
8/24/2018	25G	-29.209	-0.836	0.030	-28.3974	0.000	0.015	-40.551	32.217	-19.6	2018.07.10–2018.10.19
8/30/2018	25G	31.406	0.920	0.049	30.4402	-0.017	0.028	-4.331	55.849	84.2	2018.07.10–2018.10.19
9/6/2018	25G	-29.364	-0.679	0.029	-28.7194	-0.015	0.025	-40.645	31.991	230.5	2018.07.10–2018.10.19
9/7/2018	25G	31.779	0.833	0.032	30.8864	-0.033	0.027	-4.294	56.277	79.0	2018.07.10–2018.10.19
9/11/2018	25G	-29.258	-0.743	0.053	-28.5418	-0.006	0.036	-40.713	32.238	111.3	2018.07.10–2018.10.19
9/13/2018	25G	32.332	0.847	0.044	31.4656	0.007	0.025	-4.230	56.755	-4.6	2018.07.10–2018.10.19
9/17/2018	25G	-29.711	-0.752	0.040	-28.9966	-0.016	0.028	-40.776	31.837	180.9	2018.07.10–2018.10.19
9/20/2018	25G	32.116	0.912	0.040	31.1474	-0.028	0.040	-4.278	56.519	73.1	2018.07.10–2018.10.19
9/24/2018	25G	-29.619	-0.773	0.057	-28.8582	0.010	0.017	-40.763	31.941	99.1	2018.07.10–2018.10.19
9/26/2018	25G	31.646	0.979	0.066	30.5896	-0.046	0.027	-4.361	56.060	240.9	2018.07.10–2018.10.19
10/2/2018	25G	-28.956	-0.775	0.018	-28.2168	-0.014	0.020	-40.546	32.414	148.5	2018.07.10–2018.10.19
10/4/2018	25G	32.703	0.911	0.027	31.7456	-0.017	0.021	-4.145	56.976	-4.1	2018.07.10–2018.10.19
10/11/2018	25G	-29.063	-0.768	0.047	-28.3169	0.000	0.025	-40.586	32.336	175.8	2018.07.10–2018.10.19
10/16/2018	25G	33.096	0.982	0.028	32.0210	-0.060	0.022	-3.865	57.016	177.3	2018.07.10–2018.10.19
10/19/2018	25G	-30.424	-0.892	0.054	-29.5364	0.022	0.034	-40.732	31.190	-39.4	2018.07.10–2018.10.19

ID	Sample	d45	d45 SD	d46	d46 SD	d47	d47 SD	d48	d48 SD	d49	d49 SD
2019-01-09 23:09 CET	25G	-33.1	0.0	31.6	0.0	-4.071	0.0310	63.319	0.1360	-31.465	3.3
2019-01-11 03:06 CET	25G	0.3	0.0	7.3	0.0	7.573	0.0200	14.553	0.1120	-21.907	3.0
2019-01-11 20:51 CET	25G	-33.1	0.0	31.5	0.0	-4.205	0.0140	62.989	0.1080	-37.172	2.7
2019-01-14 22:46 CET	25G	-33.9	0.0	7.5	0.0	-27.787	0.0200	14.859	0.0870	14.097	2.1
2019-01-16 18:10 CET	25G	1.2	0.0	31.7	0.0	32.396	0.0240	63.381	0.0490	24.939	1.5
2019-01-18 00:38 CET	25G	-34.0	0.0	7.1	0.0	-28.257	0.0250	14.110	0.1380	-5.181	1.1
2019-01-18 22:07 CET	25G	1.2	0.0	32.0	0.0	32.833	0.0230	64.166	0.0690	25.285	0.9
2019-01-22 17:18 CET	25G	0.0	0.0	-3.5	0.0	-3.435	0.0220	-6.880	0.0760	-1.246	1.5
2019-01-23 21:02 CET	25G	0.0	0.0	-3.3	0.0	-3.254	0.0250	-6.552	0.0600	0.371	1.2

2019-01-24 17:57 CET	25G	-33.9	0.0	7.5	0.0	-27.805	0.0180	14.936	0.0900	-5.462	1.7
2019-01-25 20:31 CET	25G	0.0	0.0	-4.4	0.0	-4.298	0.0240	-8.642	0.0560	-2.056	1.1
2019-01-28 19:48 CET	25G	0.4	0.0	6.9	0.0	7.193	0.0190	13.570	0.0740	5.821	1.5
2019-01-31 19:45 CET	25G	0.0	0.0	-3.4	0.0	-3.380	0.0220	-6.768	0.1210	-1.402	1.2
2019-02-05 00:04 CET	25G	-33.7	0.0	7.3	0.0	-27.911	0.0390	14.318	0.0770	-6.593	1.6
2019-02-05 20:45 CET	25G	1.0	0.0	31.6	0.0	32.123	0.0360	63.110	0.0980	21.002	1.2
2019-02-09 00:24 CET	25G	0.0	0.0	-3.7	0.0	-3.608	0.0240	-7.259	0.0650	-0.029	1.8
2019-02-11 17:02 CET	25G	-33.8	0.0	8.0	0.0	-27.287	0.0220	15.802	0.0880	-5.139	2.4
2019-02-13 19:47 CET	25G	1.3	0.0	32.0	0.0	32.840	0.0200	64.080	0.1040	23.737	1.7
2019-02-20 16:06 CET	25G	-0.5	0.0	-4.0	0.0	-4.356	0.0240	-7.800	0.0770	-0.608	1.8
2019-03-01 05:23 CET	25G	0.0	0.0	-3.9	0.0	-3.821	0.0170	-7.587	0.0700	-0.103	2.0
2019-03-01 22:02 CET	25G	-32.9	0.0	32.4	0.0	-3.177	0.0210	64.174	0.0690	12.622	1.6
2019-03-04 22:39 CET	25G	1.1	0.0	32.1	0.0	32.675	0.0280	65.251	0.0890	26.926	1.4
2019-03-05 20:53 CET	25G	-33.8	0.0	7.5	0.0	-27.729	0.0170	15.056	0.0780	-7.404	1.5
2019-03-07 02:16 CET	25G	-33.8	0.0	7.9	0.0	-27.380	0.0260	15.803	0.0780	-7.070	0.9
2019-03-08 03:21 CET	25G	1.1	0.0	32.4	0.0	33.006	0.0310	66.040	0.0810	28.220	1.0
2019-03-08 15:45 CET	25G	-33.9	0.0	7.3	0.0	-28.011	0.0250	14.779	0.0930	-8.125	1.1
2019-03-08 20:00 CET	25G	-0.1	0.0	-3.5	0.0	-3.443	0.0250	-6.951	0.0880	0.038	1.5
2019-03-11 22:50 CET	25G	-0.1	0.0	-3.6	0.0	-3.559	0.0330	-7.155	0.0840	-2.811	1.9
2019-03-12 21:43 CET	25G	1.5	0.0	32.2	0.0	33.251	0.0230	65.880	0.0910	28.926	1.4
2019-03-14 05:16 CET	25G	-33.8	0.0	7.4	0.0	-27.848	0.0230	15.040	0.1100	-8.194	0.9
2019-03-14 21:51 CET	25G	0.0	0.0	-3.1	0.0	-2.977	0.0250	-6.203	0.0990	-1.075	0.9
2019-03-16 01:33 CET	25G	1.3	0.0	32.9	0.0	33.742	0.0310	66.090	0.1390	29.539	1.7
2019-03-19 16:48 CET	25G	-33.9	0.0	7.8	0.0	-27.524	0.0210	15.370	0.0740	-8.668	1.7
2019-03-20 21:53 CET	25G	-0.1	0.0	-3.5	0.0	-3.474	0.0160	-6.827	0.0800	-1.523	1.0
2019-03-21 19:54 CET	25G	1.1	0.0	32.4	0.0	33.103	0.0280	65.363	0.1040	31.473	1.3
2019-03-27 20:08 CET	25G	-0.2	0.0	-3.1	0.0	-3.268	0.0180	-6.196	0.0670	-2.750	1.0
2019-03-28 21:03 CET	25G	-33.9	0.0	6.9	0.0	-28.471	0.0260	13.712	0.0790	-9.022	1.6
2019-03-29 22:49 CET	25G	1.1	0.0	32.3	0.0	32.909	0.0280	65.088	0.0780	29.939	1.6
2019-04-01 18:17 CEST	25G	-0.1	0.0	-3.5	0.0	-3.459	0.0220	-6.914	0.0900	-2.604	1.6
2019-04-02 23:25 CEST	25G	-33.8	0.0	7.5	0.0	-27.719	0.0250	15.035	0.1170	-8.834	2.2

2019-04-04 00:20 CEST	25G	1.1	0.0	32.2	0.0	32.882	0.0170	65.081	0.0680	28.472	2.1
2019-04-04 21:11 CEST	25G	0.0	0.0	-3.6	0.0	-3.500	0.0240	-7.024	0.0810	-2.122	1.2
2019-04-05 22:07 CEST	25G	-34.0	0.0	6.8	0.0	-28.561	0.0330	13.501	0.0990	-9.440	2.3
2019-04-08 16:53 CEST	25G	-33.8	0.0	8.0	0.0	-27.242	0.0320	15.988	0.0900	-8.521	2.1
2019-04-09 21:56 CEST	25G	-33.8	0.0	7.7	0.0	-27.587	0.0270	15.372	0.1430	-9.084	1.6
2019-04-10 14:41 CEST	25G	0.0	0.0	-3.1	0.0	-2.980	0.0210	-6.151	0.0630	-2.227	1.3
2019-04-12 17:48 CEST	25G	1.2	0.0	32.7	0.0	33.518	0.0190	66.217	0.1010	31.382	1.0
2019-04-18 20:47 CEST	25G	-33.8	0.0	8.2	0.0	-27.110	0.0150	16.274	0.1280	-9.227	2.1
2019-04-23 22:41 CEST	25G	-0.2	0.0	-3.5	0.0	-3.587	0.0320	-6.996	0.1120	-1.644	1.5
2019-04-29 23:25 CEST	25G	1.1	0.0	31.6	0.0	32.276	0.0220	63.942	0.0870	28.578	1.1
2019-04-30 03:39 CEST	25G	1.2	0.0	31.9	0.0	32.669	0.0210	64.542	0.1190	29.458	2.0
2019-05-02 15:08 CEST	25G	-33.9	0.0	7.3	0.0	-28.078	0.0280	14.512	0.1000	-9.895	1.9
2019-05-07 17:11 CEST	25G	-0.1	0.0	-3.4	0.0	-3.442	0.0220	-6.825	0.1000	-3.171	1.3
2019-05-13 18:41 CEST	25G	-34.0	0.0	6.9	0.0	-28.562	0.0160	13.676	0.0950	-9.811	1.6

ID	D47 (raw)	D47 SD (raw)	D48 (raw)	D48 SD (raw)	D49 (raw)	D49 SD (raw)	d13C	d13C SD	d18O	d18O SD	Aqui	ETF period
2019-01-09 23:09 CET	0.041	0.032	-0.9180	0.1270	-55.6	3.176	-40.610	0.000	57.820	0.0	10	2019.01.09–2019.03.33
2019-01-11 03:06 CET	0.052	0.019	-0.1150	0.1100	-36.1	2.93	-4.120	0.000	32.760	0.0	10	2019.01.09–2019.03.34
2019-01-11 20:51 CET	0.058	0.014	-0.8930	0.1040	-60.9	2.613	-40.590	0.000	57.640	0.0	10	2019.01.09–2019.03.35
2019-01-14 22:46 CET	0.044	0.020	-0.2380	0.0860	36.7	2.184	-40.590	0.000	33.060	0.0	10	2019.01.09–2019.03.36
2019-01-16 18:10 CET	0.029	0.023	-0.8800	0.0470	-37.2	1.418	-4.100	0.000	57.750	0.0	10	2019.01.09–2019.03.37
2019-01-18 00:38 CET	0.041	0.023	-0.1640	0.1350	17.9	1.147	-40.650	0.000	32.640	0.0	10	2019.01.09–2019.03.38
2019-01-18 22:07 CET	0.043	0.024	-0.8650	0.0710	-37.6	0.828	-4.060	0.000	58.130	0.0	10	2019.01.09–2019.03.39
2019-01-22 17:18 CET	0.043	0.023	0.1290	0.0750	5.7	1.459	-4.100	0.000	21.660	0.0	10	2019.01.09–2019.03.40
2019-01-23 21:02 CET	0.047	0.027	0.0910	0.0600	7.0	1.161	-4.110	0.000	21.850	0.0	10	2019.01.09–2019.03.41
2019-01-24 17:57 CET	0.033	0.018	-0.1920	0.0870	16.7	1.777	-40.610	0.000	33.070	0.0	10	2019.01.09–2019.03.42
2019-01-25 20:31 CET	0.032	0.024	0.1300	0.0550	6.6	1.072	-4.050	0.000	20.750	0.0	10	2019.01.09–2019.03.43
2019-01-28 19:48 CET	0.046	0.021	-0.2650	0.0770	-8.0	1.457	-4.080	0.000	32.340	0.0	10	2019.01.09–2019.03.44

2019-01-31 19:45 CET	0.042	0.026	0.1170	0.1200	5.4	1.229	-4.110	0.000	21.720	0.0	10	2019.01.09–2019.03.45
2019-02-05 00:04 CET	0.028	0.038	-0.2310	0.0720	16.0	1.659	-40.420	0.000	32.780	0.0	10	2019.01.09–2019.03.46
2019-02-05 20:45 CET	0.028	0.033	-1.0040	0.0940	-40.5	1.176	-4.310	0.000	57.680	0.0	10	2019.01.09–2019.03.47
2019-02-09 00:24 CET	0.045	0.024	0.0970	0.0660	7.3	1.834	-4.100	0.000	21.480	0.0	10	2019.01.09–2019.03.48
2019-02-11 17:02 CET	0.030	0.021	-0.2070	0.0870	16.1	2.416	-40.520	0.000	33.520	0.0	10	2019.01.09–2019.03.49
2019-02-13 19:47 CET	0.038	0.017	-0.8580	0.0980	-39.0	1.619	-4.000	0.000	58.090	0.0	10	2019.01.09–2019.03.50
2019-02-20 16:06 CET	0.052	0.024	0.1210	0.0750	7.8	1.787	-4.580	0.000	21.190	0.0	10	2019.01.09–2019.03.51
2019-03-01 05:23 CET	0.050	0.018	0.2620	0.0670	7.7	2.016	-4.060	0.000	21.230	0.0	10	2019.01.09–2019.03.52
2019-03-01 22:02 CET	0.050	0.019	-1.6320	0.0620	-14.3	1.564	-40.500	0.000	58.620	0.0	10	2019.01.09–2019.03.53
2019-03-04 22:39 CET	0.032	0.025	0.0860	0.0850	-35.9	1.353	-4.240	0.000	58.170	0.0	10	2019.01.09–2019.03.54
2019-03-05 20:53 CET	0.039	0.018	0.0050	0.0760	14.7	1.54	-40.500	0.000	33.030	0.0	10	2019.01.09–2019.03.55
2019-03-07 02:16 CET	0.025	0.028	0.0410	0.0790	14.3	0.873	-40.480	0.000	33.400	0.0	10	2019.01.09–2019.03.56
2019-03-08 03:21 CET	0.036	0.029	0.2010	0.0740	-35.3	0.94	-4.250	0.000	58.500	0.0	10	2019.01.09–2019.03.57
2019-03-08 15:45 CET	0.036	0.025	0.0700	0.0920	14.4	1.164	-40.610	0.000	32.860	0.0	10	2019.01.09–2019.03.58
2019-03-08 20:00 CET	0.050	0.025	-0.0140	0.0920	7.0	1.487	-4.150	0.000	21.690	0.0	10	2019.01.09–2019.03.59
2019-03-11 22:50 CET	0.023	0.031	-0.0040	0.0870	4.3	1.942	-4.130	0.000	21.580	0.0	10	2019.01.09–2019.03.60
2019-03-12 21:43 CET	0.036	0.022	0.3880	0.0870	-34.7	1.277	-3.820	0.000	58.320	0.0	10	2019.01.09–2019.03.61
2019-03-14 05:16 CET	0.032	0.023	0.1510	0.1130	14.1	0.888	-40.530	0.000	32.950	0.0	10	2019.01.09–2019.03.62
2019-03-14 21:51 CET	0.048	0.026	-0.0560	0.1020	5.0	0.957	-4.090	0.000	22.100	0.0	10	2019.01.09–2019.03.63
2019-03-16 01:33 CET	0.036	0.029	-0.7410	0.1300	-35.2	1.553	-4.030	0.000	59.020	0.0	10	2019.03.15–2019.05.16
2019-03-19 16:48 CET	0.051	0.021	-0.2000	0.0730	13.0	1.724	-40.560	0.000	33.300	0.0	10	2019.03.15–2019.05.17
2019-03-20 21:53 CET	0.027	0.017	0.1200	0.0820	5.4	1.017	-4.150	0.000	21.690	0.0	10	2019.03.15–2019.05.18
2019-03-21 19:54 CET	0.031	0.027	-0.5380	0.0970	-32.4	1.256	-4.200	0.000	58.550	0.0	10	2019.03.15–2019.05.19
2019-03-27 20:08 CET	0.024	0.020	0.0430	0.0670	3.6	1.002	-4.310	0.000	22.050	0.0	10	2019.03.15–2019.05.20
2019-03-28 21:03 CET	0.034	0.026	-0.0810	0.0830	14.4	1.592	-40.620	0.000	32.390	0.0	10	2019.03.15–2019.05.21
2019-03-29 22:49 CET	0.011	0.028	-0.4510	0.0760	-33.5	1.485	-4.190	0.000	58.370	0.0	10	2019.03.15–2019.05.22
2019-04-01 18:17 CEST	0.011	0.024	0.0150	0.0960	4.3	1.633	-4.130	0.000	21.700	0.0	10	2019.03.15–2019.05.23
2019-04-02 23:25 CEST	0.024	0.027	-0.0690	0.1180	13.2	2.238	-40.500	0.000	33.060	0.0	10	2019.03.15–2019.05.24
2019-04-04 00:20 CEST	0.033	0.015	-0.3850	0.0690	-34.8	1.996	-4.200	0.000	58.330	0.0	10	2019.03.15–2019.05.25
2019-04-04 21:11 CEST	0.028	0.025	0.0820	0.0850	4.9	1.2	-4.100	0.000	21.610	0.0	10	2019.03.15–2019.05.26
2019-04-05 22:07 CEST	0.029	0.032	-0.1310	0.0990	14.2	2.328	-40.630	0.000	32.310	0.0	10	2019.03.15–2019.05.27

2019-04-08 16:53 CEST	0.023	0.032	-0.0970	0.0880	12.5	2.153	-40.500	0.000	33.560	0.0	10	2019.03.15–2019.05.28
2019-04-09 21:56 CEST	0.018	0.028	-0.0570	0.1470	12.6	1.598	-40.520	0.000	33.230	0.0	10	2019.03.15–2019.05.29
2019-04-10 14:41 CEST	0.013	0.022	0.0320	0.0630	3.8	1.311	-4.030	0.000	22.080	0.0	10	2019.03.15–2019.05.30
2019-04-12 17:48 CEST	0.031	0.019	-0.3180	0.1000	-33.1	0.934	-4.090	0.000	58.860	0.0	10	2019.03.15–2019.05.31
2019-04-18 20:47 CEST	0.005	0.016	-0.1260	0.1240	11.5	2.11	-40.510	0.000	33.720	0.0	10	2019.03.15–2019.05.32
2019-04-23 22:41 CEST	0.028	0.031	0.0310	0.1140	5.5	1.549	-4.230	0.000	21.650	0.0	10	2019.03.15–2019.05.33
2019-04-29 23:25 CEST	0.024	0.023	-0.2740	0.0860	-33.6	1.013	-4.180	0.000	57.710	0.0	10	2019.03.15–2019.05.34
2019-04-30 03:39 CEST	0.018	0.022	-0.3160	0.1140	-33.4	1.901	-4.100	0.000	58.030	0.0	10	2019.03.15–2019.05.35
2019-05-02 15:08 CEST	0.017	0.031	-0.0650	0.0980	12.7	1.904	-40.600	0.000	32.790	0.0	10	2019.03.15–2019.05.36
2019-05-07 17:11 CEST	0.018	0.023	0.0020	0.1040	3.7	1.305	-4.180	0.000	21.750	0.0	10	2019.03.15–2019.05.37
2019-05-13 18:41 CEST	0.002	0.018	-0.1030	0.0940	13.7	1.671	-40.680	0.000	32.390	0.0	10	2019.03.15–2019.05.38

In the replicates marked blue, the Δ49, raw values were not corrected for the negative background measured on the *m/z* 47.5 cup.

	Equilibrated gas lines 25G			Equilibrated gas lines HG	
	(Bold = intercept)				
2017-01-07	-0.0002	**-0.0228**	2017-01-06	-0.0003	**-0.8600**
2017-07-06	0.0001	0.0028	2017-07-10	0.0001	0.0017
	0.0566	0.0177		0.1204	0.0132
	2.2210	37		8.3524	61
	0.0007	0.0116		0.0015	0.0107
2017-07-19	-0.0002	**-0.0243**	2017-07-14	0.0001	**-0.8745**
2017-11-10	0.0001	0.0027	2017-11-13	0.0001	0.0025
	0.0476	0.0136		0.0207	0.0149
	1.1991	24		0.7411	35
	0.0002	0.0045		0.0002	0.0078
2018-03-07	-0.0006	**0.0036**	2018-03-13	-0.0011	**-0.7985**
2018-04-27	0.0003	0.0068	2018-04-26	0.0003	0.0045
	0.2019	0.0264		0.5016	0.0204
	3.2882	13		19.1251	19
	0.0023	0.0091		0.0080	0.0079
2018-07-10	-0.0006	**-0.0062**	2018-07-11	-0.0006	**-0.8205**
2018-10-19	0.0001	0.0038	2018-10-18	0.0001	0.0025
	0.4920	0.0199		0.3276	0.0152
	25.1804	26		18.5135	38
	0.0100	0.0103		0.0042	0.0087
2019-01-09	0.0000	**0.0397**	2019-01-09	0.0003	**-0.8502**
2019-03-14	0.0001	0.0017	2019-03-14	0.0001	0.0021
	0.0002	0.0092		0.1556	0.0115
	0.0070	29		5.3452	29
	0.0000	0.0024		0.0007	0.0038
3/15/2019	0.0001	**0.0234**	3/15/2019	0.0000	**-0.8614**
5/16/2019	0.0001	0.0023	5/16/2019	0.0001	0.0019
	0.0224	0.0111		0.0000	0.0113
	0.4810	21		0.0001	33
	0.0001	0.0026		0.0000	0.0042

from/until	ETF*s		Equilibrated gas line intercepts		
				Intercept	Intended
2017/01/06	**Slope:**	1.0669	HG	-0.8600	0.0266
2017/07/10	**Intercept:**	0.9441	25G	-0.0228	0.9198
	Residual slope**	-0.0002			
2017/07/14	**Slope:**	1.0507		Intercept	Intended
2017/11/13	**Intercept:**	0.9454	HG	-0.8745	0.0266
	Residual slope**	0.0000	25G	-0.0243	0.9198
2018/03/07	**Slope:**	1.1137		Intercept	Intended
2018/04/27	**Intercept:**	0.9159	HG	-0.7985	0.0266
	Residual slope**	0.0000	25G	0.0036	0.9198
2018/07/10	**Slope:**	1.0970		Intercept	Intended
2018/10/19	**Intercept:**	0.9267	HG	-0.8205	0.0266
	Residual slope**	-0.0007	25G	-0.0062	0.9198
2019/01/09	**Slope:**	1.0038		Intercept	Intended
2019/03/14	**Intercept:**	0.8800	HG	-0.8502	0.0266
	Residual slope**	0.0001	25G	0.0397	0.9198
3/15/2019	**Slope:**	1.0096		Intercept	Intended
5/16/2019	**Intercept:**	0.8962	HG	-0.8614	0.0266
	Residual slope**	0.0000	25G	0.0234	0.9198

AFF Δ47	
25–90°C	0.088

AFF δ18O (Kim *et. al.* 2007)		
	calcite	**aragonite**
90	1.008128581	1.008541256
110	1.007608497	1.008049938

*) Empirical transfer function (ETF) applied during this study with slopes (m) and intercepts (b) of the empirical transfer functions in the form of y=m*x+b.

**) the residual slope is derived from the 25G and HG data. This correction step was performed even though the HGL slopes are below 0.001. This assures a precise data correction, especially for samples with extreme δ^{47} values. A slope of 0.0000 was chosen when the residual slope, within error, indistinguishable from 0.0000.

Standard data – S.5.III

Date	Sample	δ47 (raw) (‰)	Δ47 (raw) (‰)	SD Δ47 (raw) (‰)	δ47 (bgcorr) (‰)	Δ47 (bgcorr) (‰)	SD Δ47 (bgcorr) (‰)	δ13C CO2 (‰ VPDB)	δ18O CO2 (‰ VSMOW)	Diff Bellow (mV)	Weight (g)	Pressure Bellow (mBar)	ETF period
2017/01/07	Carrara	17.898	-0.386	0.035	17.669	-0.611	0.025	1.957	37.392	95.9	6.5	22.2	2017.01.06–2017.07.10
2017/01/07	MuStd	23.489	0.094	0.023	23.129	-0.258	0.019	1.542	42.907	-112.8	4.7	16.7	2017.01.06–2017.07.10
2017/01/08	Carrara	17.963	-0.320	0.034	17.697	-0.582	0.020	1.939	37.409	-80.9	5.2	17.3	2017.01.06–2017.07.10
2017/01/08	MuStd	23.422	0.046	0.023	23.109	-0.260	0.022	1.593	42.838	-24.9	5.5	20.8	2017.01.06–2017.07.10
2017/01/09	Carrara	17.974	-0.328	0.020	17.702	-0.596	0.021	1.945	37.422	-57.5	4.9	16.3	2017.01.06–2017.07.10
2017/01/10	MuStd	23.463	0.052	0.027	23.125	-0.278	0.017	1.550	42.916	-64.8	4.8	20.2	2017.01.06–2017.07.10
2017/01/10	Carrara	18.024	-0.368	0.026	17.770	-0.618	0.019	1.962	37.495	6.3	6.3	21.5	2017.01.06–2017.07.10
2017/01/11	Carrara	18.004	-0.361	0.030	17.734	-0.626	0.030	1.992	37.439	0.2	7.7	25.8	2017.01.06–2017.07.10
2017/01/12	Carrara	17.911	-0.364	0.026	17.673	-0.598	0.037	1.926	37.413	61.2	5.0	16.7	2017.01.06–2017.07.10
2017/01/13	MuStd	23.396	0.011	0.026	23.093	-0.286	0.020	1.555	42.886	61.0	6.2	22.3	2017.01.06–2017.07.10
2017/01/13	Carrara	17.958	-0.354	0.033	17.703	-0.604	0.021	1.951	37.425	13.1	6.4	21.9	2017.01.06–2017.07.10
2017/01/14	Carrara	17.996	-0.355	0.021	17.743	-0.604	0.020	1.958	37.459	-1.4	6.9	23.2	2017.01.06–2017.07.10
2017/01/14	Carrara	17.966	-0.410	0.014	17.738	-0.634	0.017	1.946	37.496	88.4	6.9	23.6	2017.01.06–2017.07.10
2017/01/15	MuStd	23.491	0.037	0.024	23.165	-0.282	0.015	1.556	42.954	-56.6	5.7	20.0	2017.01.06–2017.07.10
2017/01/15	Carrara	17.940	-0.330	0.022	17.680	-0.585	0.018	1.923	37.411	-25.0	4.5	15.3	2017.01.06–2017.07.10
2017/01/16	Carrara	18.002	-0.325	0.029	17.724	-0.598	0.029	1.945	37.446	-81.4	5.1	17.3	2017.01.06–2017.07.10
2017/01/16	MuStd	23.402	0.003	0.020	23.085	-0.306	0.022	1.551	42.903	75.1	6.0	22.0	2017.01.06–2017.07.10
2017/01/17	Carrara	18.085	-0.330	0.023	17.816	-0.594	0.029	1.965	37.514	-57.8	6.1	20.8	2017.01.06–2017.07.10
2017/01/18	Carrara	18.034	-0.346	0.024	17.778	-0.597	0.016	1.969	37.476	-47.5	6.6	22.8	2017.01.06–2017.07.10
2017/01/18	MuStd	23.436	0.058	0.034	23.087	-0.284	0.027	1.551	42.883	-67.2	4.5	15.7	2017.01.06–2017.07.10
2017/01/19	Carrara	18.037	-0.355	0.018	17.775	-0.612	0.017	1.961	37.495	-37.4	5.9	20.2	2017.01.06–2017.07.10
2017/01/19	Carrara	18.055	-0.363	0.030	17.806	-0.607	0.018	1.966	37.517	16.5	6.5	22.0	2017.01.06–2017.07.10
2017/01/20	MuStd	23.494	0.027	0.031	23.154	-0.306	0.022	1.567	42.957	-12.9	7.0	25.6	2017.01.06–2017.07.10
2017/01/21	Carrara	17.927	-0.330	0.024	17.660	-0.592	0.020	1.904	37.416	-77.6	4.9	16.3	2017.01.06–2017.07.10
2017/01/21	Carrara	18.043	-0.335	0.018	17.776	-0.597	0.016	1.942	37.500	-76.4	5.7	19.4	2017.01.06–2017.07.10
2017/01/22	MuStd	23.392	0.038	0.032	23.044	-0.302	0.022	1.546	42.864	-46.0	5.0	17.9	2017.01.06–2017.07.10
2017/01/22	Carrara	18.021	-0.353	0.028	17.759	-0.610	0.017	1.982	37.457	-50.5	7.1	24.0	2017.01.06–2017.07.10
2017/01/23	Carrara	18.006	-0.363	0.046	17.764	-0.600	0.024	1.967	37.467	37.6	6.9	23.9	2017.01.06–2017.07.10
2017/01/24	Carrara	17.969	-0.337	0.020	17.712	-0.590	0.017	1.947	37.423	-57.9	5.8	20.0	2017.01.06–2017.07.10
2017/01/24	Carrara	17.957	-0.378	0.034	17.724	-0.607	0.017	1.957	37.443	35.4	6.5	22.0	2017.01.06–2017.07.10
2017/01/24	MuStd	23.278	-0.011	0.039	22.994	-0.289	0.019	1.540	42.806	126.2	6.8	25.3	2017.01.06–2017.07.10
2017/01/25	Carrara	18.017	-0.332	0.026	17.759	-0.585	0.018	1.968	37.445	-19.6	7.2	24.8	2017.01.06–2017.07.10
2017/01/25	Carrara	17.893	-0.392	0.021	17.678	-0.603	0.019	1.947	37.403	87.9	6.7	23.1	2017.01.06–2017.07.10
2017/01/26	MuStd	23.411	0.030	0.035	23.073	-0.300	0.022	1.547	42.889	-54.3	8.1	27.2	2017.01.06–2017.07.10
2017/01/27	Carrara	18.061	-0.344	0.021	17.800	-0.601	0.014	1.933	37.537	-46.8	8.0	27.2	2017.01.06–2017.07.10
2017/01/27	Carrara	18.018	-0.360	0.026	17.764	-0.610	0.017	1.951	37.492	-21.7	6.6	23.0	2017.01.06–2017.07.10
2017/01/28	MuStd	23.253	0.061	0.026	22.886	-0.298	0.021	1.485	42.761	-150.4	5.2	19.3	2017.01.06–2017.07.10
2017/01/29	Carrara	18.085	-0.351	0.019	17.831	-0.600	0.019	1.967	37.533	5.8	7.0	23.8	2017.01.06–2017.07.10
2017/01/29	Carrara	17.955	-0.391	0.036	17.706	-0.635	0.024	1.936	37.475	7.9	6.4	22.1	2017.01.06–2017.07.10

2017/01/30	MuStd	23.419	0.043	0.017	23.082	-0.286	0.016	1.548	42.883	-58.8	5.6	20.5	2017.01.06–2017.07.10
2017/01/30	Carrara	17.937	-0.370	0.028	17.690	-0.613	0.024	1.955	37.417	29.8	7.2	24.1	2017.01.06–2017.07.10
2017/02/01	ETH3	17.685	-0.024	0.028	17.406	-0.299	0.020	1.616	37.145	-96.7	6.4	23.4	2017.01.06–2017.07.10
2017/02/02	MuStd	23.351	0.000	0.029	23.040	-0.304	0.016	1.505	42.901	63.2	7.6	27.9	2017.01.06–2017.07.10
2017/02/03	ETH2	-11.928	-0.838	0.024	-11.782	-0.690	0.021	-10.201	19.716	17.0	6.9	25.0	2017.01.06–2017.07.10
2017/02/06	Carrara	17.978	-0.327	0.046	17.739	-0.562	0.025	1.941	37.427	9.9	6.4	20.9	2017.01.06–2017.07.10
2017/02/07	ETH2	-11.969	-0.862	0.036	-11.821	-0.713	0.021	-10.224	19.722	64.2	7.5	27.0	2017.01.06–2017.07.10
2017/02/14	ETH3	17.939	-0.076	0.037	17.705	-0.306	0.025	1.656	37.413	36.9	6.4	23.3	2017.01.06–2017.07.10
2017/02/14	ETH3	17.966	-0.101	0.028	17.724	-0.338	0.025	1.677	37.445	-0.2	7.2	26.4	2017.01.06–2017.07.10
2017/02/16	Carrara	17.992	-0.374	0.026	17.744	-0.618	0.024	1.949	37.483	-35.0	7.3	22.7	2017.01.06–2017.07.10
2017/02/16	ETH3	17.912	-0.086	0.034	17.669	-0.325	0.013	1.661	37.392	30.7	6.2	22.8	2017.01.06–2017.07.10
2017/02/16	Carrara	17.833	-0.326	0.040	17.565	-0.589	0.035	1.893	37.329	-73.4	4.5	13.6	2017.01.06–2017.07.10
2017/02/17	MuStd	23.332	-0.001	0.033	23.027	-0.299	0.026	1.507	42.881	28.2	5.2	18.5	2017.01.06–2017.07.10
2017/02/18	Carrara	17.982	-0.341	0.024	17.701	-0.617	0.019	1.925	37.462	-119.0	5.1	15.7	2017.01.06–2017.07.10
2017/02/18	Carrara	17.921	-0.360	0.038	17.682	-0.594	0.022	1.917	37.428	3.4	5.7	17.7	2017.01.06–2017.07.10
2017/02/19	MuStd	23.473	0.034	0.027	23.145	-0.287	0.021	1.540	42.955	-38.6	5.8	21.1	2017.01.06–2017.07.10
2017/02/19	Carrara	17.939	-0.357	0.013	17.696	-0.596	0.015	1.938	37.423	3.3	5.7	17.6	2017.01.06–2017.07.10
2017/02/20	MuStd	23.418	0.036	0.034	23.092	-0.283	0.020	1.530	42.907	-55.5	5.8	21.0	2017.01.06–2017.07.10
2017/02/21	Carrara	17.989	-0.311	0.043	17.709	-0.586	0.017	1.928	37.436	-111.4	4.1	14.7	2017.01.06–2017.07.10
2017/02/21	Carrara	18.136	-0.316	0.039	17.856	-0.591	0.022	1.945	37.571	-119.7	4.8	16.4	2017.01.06–2017.07.10
2017/02/21	MuStd	23.391	0.023	0.024	23.076	-0.284	0.026	1.529	42.895	-1.7	6.2	20.9	2017.01.06–2017.07.10
2017/02/22	Carrara	17.907	-0.336	0.032	17.627	-0.611	0.013	1.895	37.411	-95.4	4.4	15.8	2017.01.06–2017.07.10
2017/02/23	MuStd	23.502	0.099	0.034	23.139	-0.256	0.022	1.470	42.987	-132.2	7.5	10.2	2017.01.06–2017.07.10
2017/02/23	Carrara	17.920	-0.329	0.038	17.654	-0.590	0.023	1.923	37.390	-59.1	4.4	16.1	2017.01.06–2017.07.10
2017/02/23	Carrara	17.866	-0.368	0.043	17.631	-0.598	0.018	1.919	37.379	0.8	4.9	17.9	2017.01.06–2017.07.10
2017/02/25	MuStd	23.370	0.009	0.023	23.055	-0.298	0.016	1.517	42.899	-2.9	5.8	20.8	2017.01.06–2017.07.10
2017/02/25	Carrara	17.939	-0.317	0.040	17.667	-0.585	0.027	1.940	37.381	-101.1	5.0	18.0	2017.01.06–2017.07.10
2017/02/26	Carrara	17.926	-0.332	0.032	17.669	-0.585	0.021	1.924	37.398	-61.3	4.7	17.2	2017.01.06–2017.07.10
2017/02/26	MuStd	23.305	0.025	0.029	22.977	-0.295	0.016	1.556	42.779	-74.5	5.3	19.3	2017.01.06–2017.07.10
2017/02/27	Carrara	17.867	-0.337	0.041	17.596	-0.602	0.028	1.900	37.367	-83.7	4.3	15.5	2017.01.06–2017.07.10
2017/02/27	Carrara	17.912	-0.311	0.027	17.631	-0.587	0.035	1.925	37.361	-97.8	4.7	16.8	2017.01.06–2017.07.10
2017/02/28	MuStd	23.429	0.068	0.034	23.093	-0.260	0.028	1.533	42.883	-126.1	4.6	16.9	2017.01.06–2017.07.10
2017/03/01	Carrara	17.926	-0.358	0.030	17.683	-0.597	0.034	1.919	37.429	26.4	4.5	18.2	2017.01.06–2017.07.10
2017/03/02	Carrara	18.014	-0.354	0.020	17.758	-0.605	0.021	1.978	37.454	-7.4	7.6	27.6	2017.01.06–2017.07.10
2017/03/02	Carrara	18.008	-0.393	0.040	17.777	-0.619	0.033	1.978	37.488	3.0	8.3	30.9	2017.01.06–2017.07.10
2017/03/02	MuStd	23.418	0.015	0.025	23.095	-0.301	0.015	1.551	42.908	-9.9	7.4	26.6	2017.01.06–2017.07.10
2017/03/02	MuStd	23.267	0.021	0.032	22.968	-0.271	0.020	1.531	42.770	26.1	6.6	24.5	2017.01.06–2017.07.10
2017/03/03	Carrara	17.901	-0.334	0.030	17.636	-0.594	0.024	1.939	37.359	-66.4	4.4	16.1	2017.01.06–2017.07.10
2017/03/04	Carrara	17.932	-0.333	0.022	17.658	-0.602	0.018	1.950	37.379	-75.0	6.0	22.2	2017.01.06–2017.07.10
2017/03/04	MuStd	23.389	0.032	0.029	23.077	-0.274	0.024	1.519	42.894	-34.7	4.6	16.1	2017.01.06–2017.07.10
2017/03/05	Carrara	17.883	-0.308	0.028	17.591	-0.596	0.022	1.910	37.344	-138.0	4.6	15.9	2017.01.06–2017.07.10
2017/03/05	Carrara	18.022	-0.360	0.031	17.760	-0.617	0.016	1.945	37.501	-57.4	5.4	18.5	2017.01.06–2017.07.10
2017/03/06	MuStd	23.350	0.035	0.037	23.034	-0.274	0.017	1.489	42.881	-67.6	4.8	17.5	2017.01.06–2017.07.10
2017/03/07	Carrara	17.980	-0.322	0.026	17.710	-0.588	0.024	1.926	37.440	-80.9	4.7	17.3	2017.01.06–2017.07.10

2017/03/07	Carrara	17.903	-0.389	0.029	17.687	-0.601	0.016	1.929	37.428	103.7	5.7	20.6	2017.01.06–2017.07.10
2017/03/08	MuStd	23.365	0.024	0.023	23.067	-0.267	0.022	1.562	42.834	16.3	7.0	25.4	2017.01.06–2017.07.10
2017/03/08	Carrara	17.918	-0.367	0.031	17.692	-0.589	0.028	1.941	37.408	28.9	5.4	19.5	2017.01.06–2017.07.10
2017/03/09	Carrara	17.884	-0.355	0.035	17.635	-0.598	0.010	1.925	37.378	-50.8	5.7	21.0	2017.01.06–2017.07.10
2017/03/10	Carrara	17.923	-0.334	0.033	17.635	-0.618	0.023	1.921	37.400	-108.2	4.4	16.0	2017.01.06–2017.07.10
2017/03/10	MuStd	23.379	0.061	0.023	23.027	-0.282	0.025	1.517	42.855	-95.1	4.4	15.7	2017.01.06–2017.07.10
2017/03/10	Carrara	17.920	-0.375	0.030	17.707	-0.584	0.022	1.915	37.444	57.8	4.9	18.2	2017.01.06–2017.07.10
2017/03/11	MuStd	23.408	0.056	0.032	23.043	-0.301	0.028	1.543	42.864	-119.4	4.0	14.4	2017.01.06–2017.07.10
2017/03/12	Carrara	17.938	-0.383	0.034	17.721	-0.597	0.031	1.930	37.457	53.0	5.6	20.5	2017.01.06–2017.07.10
2017/03/12	Carrara	17.907	-0.332	0.049	17.647	-0.587	0.033	1.925	37.378	-88.5	4.2	14.9	2017.01.06–2017.07.10
2017/03/13	MuStd	23.284	0.017	0.043	22.982	-0.278	0.020	1.537	42.785	5.9	5.0	17.8	2017.01.06–2017.07.10
2017/03/16	Carrara	18.309	-0.350	0.025	18.084	-0.572	0.012	1.980	37.745	15.3	6.7	26.1	2017.01.06–2017.07.10
2017/03/17	ETH2	-11.952	-0.864	0.024	-11.792	-0.704	0.017	-10.190	19.708	86.5	6.5	23.0	2017.01.06–2017.07.10
2017/03/18	ETH3	17.723	-0.047	0.038	17.489	-0.277	0.018	1.636	37.187	-15.3	6.4	23.2	2017.01.06–2017.07.10
2017/03/18	MuStd	23.363	0.027	0.035	23.055	-0.274	0.029	1.509	42.882	-6.2	7.5	27.3	2017.01.06–2017.07.10
2017/03/19	Carrara	17.913	-0.356	0.042	17.665	-0.600	0.024	1.953	37.382	-37.2	6.2	21.9	2017.01.06–2017.07.10
2017/03/20	ETH1	17.526	-0.463	0.044	17.294	-0.691	0.008	2.041	37.016	3.9	6.4	23.7	2017.01.06–2017.07.10
2017/03/22	MuStd	23.428	0.014	0.039	23.114	-0.294	0.023	1.503	42.967	-24.6	7.6	28.2	2017.01.06–2017.07.10
2017/03/23	Carrara	17.932	-0.373	0.047	17.702	-0.599	0.021	1.930	37.440	19.8	6.3	22.3	2017.01.06–2017.07.10
2017/03/25	Carrara	18.292	-0.309	0.038	18.020	-0.577	0.020	1.935	37.730	-108.0	5.6	18.9	2017.01.06–2017.07.10
2017/03/26	ETH3	17.888	-0.080	0.042	17.665	-0.299	0.027	1.666	37.357	3.4	6.9	25.5	2017.01.06–2017.07.10
2017/03/27	MuStd	23.442	0.035	0.021	23.114	-0.286	0.020	1.472	42.990	-60.7	5.8	21.4	2017.01.06–2017.07.10
2017/03/27	Carrara	17.995	-0.389	0.028	17.788	-0.593	0.054	1.937	37.512	30.9	7.8	26.7	2017.01.06–2017.07.10
2017/03/29	Carrara	17.947	-0.348	0.025	17.677	-0.614	0.026	1.956	37.404	-71.4	5.7	19.9	2017.01.06–2017.07.10
2017/03/30	MuStd	23.327	0.001	0.049	23.085	-0.235	0.021	1.525	42.857	55.4	6.1	22.9	2017.01.06–2017.07.10
2017/04/04	MuStd	23.473	0.044	0.025	23.149	-0.272	0.012	1.532	42.951	-72.9	6.1	21.6	2017.01.06–2017.07.10
2017/04/05	Carrara	18.140	-0.298	0.028	17.846	-0.587	0.023	1.908	37.593	-168.4	6.6	12.3	2017.01.06–2017.07.10
2017/04/05	Carrara	18.158	-0.266	0.026	17.863	-0.556	0.026	1.902	37.584	-191.2	6.3	11.4	2017.01.06–2017.07.10
2017/04/05	MuStd	23.455	0.046	0.033	23.113	-0.288	0.014	1.522	42.942	-80.7	5.2	18.5	2017.01.06–2017.07.10
2017/04/06	Carrara	18.148	-0.216	0.033	17.814	-0.544	0.011	1.868	37.557	-274.0	5.1	10.5	2017.01.06–2017.07.10
2017/04/06	MuStd	23.490	0.046	0.024	23.173	-0.263	0.031	1.529	42.970	-33.9	4.7	16.8	2017.01.06–2017.07.10
2017/04/07	Carrara	18.116	-0.236	0.103	17.776	-0.570	0.030	1.858	37.555	-288.8	5.5	10.2	2017.01.06–2017.07.10
2017/04/09	MuStd	23.386	0.052	0.032	23.061	-0.265	0.017	1.522	42.867	-100.0	4.4	16.0	2017.01.06–2017.07.10
2017/04/10	Carrara	18.021	-0.316	0.030	17.748	-0.584	0.016	1.957	37.444	-112.8	4.1	19.2	2017.01.06–2017.07.10
2017/04/11	MuStd	23.138	0.012	0.035	22.850	-0.270	0.026	1.463	42.718	17.2	5.9	22.0	2017.01.06–2017.07.10
2017/04/11	Carrara	18.033	-0.323	0.029	17.752	-0.599	0.022	1.957	37.464	-84.8	5.0	17.4	2017.01.06–2017.07.10
2017/04/12	Carrara	18.030	-0.384	0.031	17.837	-0.574	0.022	1.983	37.498	74.4	8.3	30.4	2017.01.06–2017.07.10
2017/04/12	MuStd	23.298	0.040	0.042	22.987	-0.264	0.021	1.497	42.815	-44.1	5.3	19.2	2017.01.06–2017.07.10
2017/04/19	Carrara	17.886	-0.326	0.032	17.626	-0.581	0.032	1.918	37.357	-79.1	4.7	17.1	2017.01.06–2017.07.10
2017/04/19	Carrara	17.868	-0.340	0.037	17.640	-0.564	0.017	1.922	37.350	25.5	4.7	17.1	2017.01.06–2017.07.10
2017/04/19	MuStd	23.396	0.091	0.037	23.044	-0.253	0.018	1.535	42.824	-122.6	4.0	14.9	2017.01.06–2017.07.10
2017/04/21	Carrara	18.009	-0.317	0.035	17.738	-0.583	0.023	1.940	37.450	-63.2	5.4	19.3	2017.01.06–2017.07.10
2017/04/22	Carrara	17.976	-0.361	0.042	17.731	-0.603	0.026	1.954	37.448	-3.4	6.3	22.8	2017.01.06–2017.07.10
2017/04/22	Carrara	17.877	-0.340	0.033	17.612	-0.600	0.034	1.912	37.368	-72.4	4.6	16.1	2017.01.06–2017.07.10

2017/04/25	Carrara	17.953	-0.331	0.033	17.698	-0.581	0.019	1.972	37.377	-51.4	6.5	23.4	2017.01.06–2017.07.10
2017/04/25	ETH3	17.768	-0.044	0.032	17.510	-0.299	0.017	1.649	37.217	-64.7	5.7	20.6	2017.01.06–2017.07.10
2017/04/26	MuStd	23.509	0.032	0.021	23.206	-0.264	0.018	1.561	42.972	7.1	7.3	26.9	2017.01.06–2017.07.10
2017/04/26	Carrara	17.944	-0.384	0.034	17.737	-0.587	0.025	1.953	37.441	54.9	6.9	24.9	2017.01.06–2017.07.10
2017/04/27	ETH3	17.810	-0.070	0.024	17.545	-0.330	0.023	1.655	37.279	-32.6	6.6	24.2	2017.01.06–2017.07.10
2017/05/04	Carrara	17.958	-0.308	0.036	17.680	-0.581	0.012	1.921	37.408	-84.7	4.3	16.0	2017.01.06–2017.07.10
2017/05/04	Carrara	17.897	-0.306	0.022	17.640	-0.558	0.016	1.934	37.332	-48.2	6.0	15.0	2017.01.06–2017.07.10
2017/05/05	Carrara	17.863	-0.327	0.025	17.590	-0.595	0.021	1.937	37.316	-65.9	4.4	16.3	2017.01.06–2017.07.10
2017/05/06	Carrara	17.929	-0.308	0.045	17.648	-0.584	0.014	1.903	37.397	-91.4	4.4	14.4	2017.01.06–2017.07.10
2017/05/06	Carrara	17.811	-0.315	0.050	17.547	-0.575	0.023	1.930	37.260	-71.8	4.2	15.3	2017.01.06–2017.07.10
2017/05/06	MuStd	23.391	0.075	0.028	23.027	-0.281	0.019	1.539	42.832	-115.1	5.0	18.6	2017.01.06–2017.07.10
2017/05/06	Carrara	17.980	-0.285	0.041	17.673	-0.585	0.026	1.912	37.415	-150.7	4.2	13.4	2017.01.06–2017.07.10
2017/05/07	MuStd	23.358	0.048	0.031	23.057	-0.246	0.025	1.527	42.838	6.0	4.5	16.6	2017.01.06–2017.07.10
2017/05/08	Carrara	18.127	-0.257	0.032	17.825	-0.553	0.024	1.947	37.500	-144.0	5.3	17.0	2017.01.06–2017.07.10
2017/05/08	Carrara	17.972	-0.267	0.055	17.687	-0.546	0.022	1.938	37.363	-121.3	4.3	15.6	2017.01.06–2017.07.10
2017/05/09	MuStd	23.415	0.053	0.027	23.094	-0.261	0.028	1.541	42.876	-24.7	5.0	22.2	2017.01.06–2017.07.10
2017/05/09	Carrara	18.008	-0.304	0.043	17.715	-0.591	0.029	1.926	37.450	-119.1	4.9	15.8	2017.01.06–2017.07.10
2017/05/10	Carrara	17.844	-0.325	0.023	17.551	-0.612	0.017	1.931	37.301	-91.0	5.0	18.3	2017.01.06–2017.07.10
2017/05/10	Carrara	18.047	-0.304	0.034	17.747	-0.598	0.025	1.934	37.480	-125.8	5.0	16.2	2017.01.06–2017.07.10
2017/05/10	MuStd	23.360	-0.012	0.039	23.092	-0.273	0.026	1.541	42.887	42.6	6.9	25.7	2017.01.06–2017.07.10
2017/05/11	Carrara	17.996	-0.327	0.030	17.713	-0.605	0.026	1.961	37.426	-82.1	6.3	22.3	2017.01.06–2017.07.10
2017/05/11	MuStd	23.368	0.002	0.045	23.101	-0.259	0.023	1.535	42.887	63.0	8.5	31.0	2017.01.06–2017.07.10
2017/05/11	Carrara	17.833	-0.354	0.043	17.573	-0.610	0.024	1.955	37.297	-6.1	5.7	21.2	2017.01.06–2017.07.10
2017/05/16	Carrara	18.060	-0.301	0.042	17.809	-0.547	0.019	1.954	37.470	-12.0	4.7	18.2	2017.01.06–2017.07.10
2017/05/16	Carrara	18.017	-0.274	0.054	17.728	-0.558	0.017	1.986	37.368	-92.1	5.5	20.2	2017.01.06–2017.07.10
2017/05/16	MuStd	23.584	0.086	0.046	23.252	-0.239	0.022	1.574	42.979	-72.6	5.1	19.4	2017.01.06–2017.07.10
2017/05/24	Carrara	18.001	-0.346	0.019	17.778	-0.565	0.015	1.974	37.439	18.7	5.8	22.4	2017.01.06–2017.07.10
2017/05/24	Carrara	17.934	-0.335	0.047	17.718	-0.547	0.029	1.951	37.382	65.6	5.6	20.8	2017.01.06–2017.07.10
2017/05/25	Carrara	18.027	-0.346	0.046	17.798	-0.570	0.019	1.962	37.475	14.8	5.0	21.0	2017.01.06–2017.07.10
2017/05/25	Carrara	18.015	-0.386	0.029	17.799	-0.598	0.022	1.959	37.508	51.7	6.0	25.8	2017.01.06–2017.07.10
2017/05/25	Carrara	18.110	-0.341	0.033	17.858	-0.589	0.017	1.978	37.539	-17.0	6.0	23.8	2017.01.06–2017.07.10
2017/05/25	Carrara	18.126	-0.336	0.025	17.881	-0.577	0.022	1.993	37.534	-16.4	6.0	25.2	2017.01.06–2017.07.10
2017/05/25	Carrara	18.115	-0.370	0.027	17.887	-0.594	0.031	1.990	37.561	18.3	7.0	27.8	2017.01.06–2017.07.10
2017/05/26	Carrara	18.103	-0.310	0.064	17.853	-0.555	0.021	1.960	37.517	-12.9	5.4	21.5	2017.01.06–2017.07.10
2017/05/27	MuStd	23.444	0.053	0.028	23.130	-0.254	0.028	1.552	42.894	-26.9	5.6	21.4	2017.01.06–2017.07.10
2017/05/29	Carrara	18.052	-0.312	0.032	17.826	-0.534	0.022	1.961	37.467	2.7	5.5	21.8	2017.01.06–2017.07.10
2017/05/29	Carrara	17.985	-0.369	0.038	17.789	-0.561	0.021	1.962	37.457	104.0	6.5	24.5	2017.01.06–2017.07.10
2017/05/30	Carrara	18.017	-0.355	0.038	17.800	-0.568	0.018	1.966	37.470	76.4	6.5	22.0	2017.01.06–2017.07.10
2017/05/30	Carrara	18.110	-0.309	0.037	17.837	-0.578	0.023	1.990	37.494	-71.4	5.5	22.6	2017.01.06–2017.07.10
2017/05/30	Carrara	18.029	-0.357	0.032	17.816	-0.566	0.016	1.983	37.469	44.5	8.5	32.2	2017.01.06–2017.07.10
2017/05/31	Carrara	17.997	-0.385	0.033	17.800	-0.578	0.021	1.979	37.468	100.5	7.5	27.9	2017.01.06–2017.07.10
2017/05/31	Carrara	18.015	-0.352	0.039	17.783	-0.580	0.038	1.962	37.470	20.9	7.5	21.8	2017.01.06–2017.07.10
2017/05/31	Carrara	18.012	-0.382	0.035	17.809	-0.581	0.023	1.988	37.471	50.1	8.0	34.1	2017.01.06–2017.07.10
2017/05/31	MuStd	23.489	0.032	0.024	23.197	-0.253	0.021	1.554	42.959	37.1	8.1	29.9	2017.01.06–2017.07.10

2017/05/31	MuStd	23.497	0.049	0.026	23.190	-0.251	0.030	1.566	42.937	0.0	6.1	26.1	2017.01.06–2017.07.10
2017/06/01	Carrara	18.024	-0.352	0.038	17.788	-0.584	0.023	1.973	37.468	30.9	5.5	21.5	2017.01.06–2017.07.10
2017/06/01	Carrara	18.081	-0.326	0.040	17.816	-0.586	0.025	1.980	37.491	-61.0	5.5	21.7	2017.01.06–2017.07.10
2017/06/02	MuStd	23.432	0.021	0.035	23.148	-0.258	0.033	1.543	42.924	40.3	5.9	22.3	2017.01.06–2017.07.10
2017/06/02	Carrara	18.032	-0.347	0.033	17.812	-0.563	0.032	1.976	37.468	14.0	6.6	26.0	2017.01.06–2017.07.10
2017/06/03	Carrara	18.015	-0.354	0.027	17.804	-0.561	0.015	1.969	37.465	55.7	5.6	22.2	2017.01.06–2017.07.10
2017/06/03	MuStd	23.495	0.042	0.022	23.191	-0.256	0.010	1.559	42.950	-17.3	6.8	26.1	2017.01.06–2017.07.10
2017/06/04	Carrara	18.047	-0.370	0.039	17.834	-0.579	0.020	1.962	37.519	52.6	5.3	21.2	2017.01.06–2017.07.10
2017/06/04	Carrara	18.092	-0.352	0.036	17.839	-0.600	0.026	1.992	37.517	-25.9	5.8	22.9	2017.01.06–2017.07.10
2017/06/05	MuStd	23.360	-0.006	0.021	23.098	-0.261	0.024	1.552	42.869	106.1	7.7	29.0	2017.01.06–2017.07.10
2017/06/06	Carrara	18.123	-0.359	0.032	17.878	-0.599	0.026	1.988	37.560	-32.7	6.1	24.2	2017.01.06–2017.07.10
2017/06/06	Carrara	18.034	-0.373	0.039	17.816	-0.587	0.024	1.965	37.506	34.8	5.3	20.8	2017.01.06–2017.07.10
2017/06/07	ETH3	17.798	-0.070	0.034	17.577	-0.287	0.026	1.646	37.275	7.0	6.4	23.7	2017.01.06–2017.07.10
2017/06/08	Carrara	18.144	-0.352	0.028	17.912	-0.580	0.026	1.985	37.576	6.2	7.7	30.1	2017.01.06–2017.07.10
2017/06/08	MuStd	23.408	-0.007	0.030	23.147	-0.262	0.022	1.532	42.939	120.7	6.9	26.7	2017.01.06–2017.07.10
2017/06/09	Carrara	18.143	-0.360	0.028	17.906	-0.594	0.016	1.978	37.591	7.7	6.6	26.0	2017.01.06–2017.07.10
2017/06/13	Carrara	17.987	-0.364	0.033	17.770	-0.577	0.028	1.981	37.435	32.2	7.2	28.2	2017.01.06–2017.07.10
2017/06/13	Carrara	17.939	-0.351	0.021	17.713	-0.572	0.022	1.943	37.411	27.5	4.6	17.9	2017.01.06–2017.07.10
2017/06/13	MuStd	23.248	0.004	0.028	22.975	-0.262	0.020	1.522	42.777	68.7	6.5	24.7	2017.01.06–2017.07.10
2017/06/14	Carrara	18.003	-0.357	0.021	17.760	-0.595	0.024	1.974	37.450	-20.7	5.9	22.8	2017.01.06–2017.07.10
2017/06/14	MuStd	23.392	0.040	0.033	23.079	-0.266	0.020	1.531	42.876	-42.8	6.3	22.4	2017.01.06–2017.07.10
2017/06/14	Carrara	18.000	-0.354	0.039	17.776	-0.574	0.018	1.972	37.447	1.8	5.0	28.7	2017.01.06–2017.07.10
2017/06/14	Carrara	17.989	-0.347	0.032	17.779	-0.554	0.016	1.934	37.467	53.8	6.3	24.4	2017.01.06–2017.07.10
2017/06/14	Carrara	18.124	-0.324	0.041	17.890	-0.554	0.028	1.974	37.538	-6.3	6.2	24.1	2017.01.06–2017.07.10
2017/06/15	MuStd	23.279	0.030	0.022	22.971	-0.271	0.031	1.537	42.767	-6.2	5.8	21.8	2017.01.06–2017.07.10
2017/06/15	Carrara	17.961	-0.346	0.050	17.733	-0.570	0.017	1.949	37.423	15.3	4.9	19.0	2017.01.06–2017.07.10
2017/06/16	Carrara	18.017	-0.323	0.036	17.776	-0.559	0.029	1.956	37.448	-42.0	5.0	19.3	2017.01.06–2017.07.10
2017/06/17	MuStd	23.374	0.040	0.034	23.073	-0.254	0.020	1.542	42.848	-3.0	5.9	22.5	2017.01.06–2017.07.10
2017/06/17	MuStd	23.429	0.061	0.020	23.121	-0.239	0.017	1.542	42.881	-27.6	4.0	18.0	2017.01.06–2017.07.10
2017/06/17	Carrara	17.922	-0.339	0.038	17.683	-0.573	0.024	1.960	37.365	-26.2	4.0	16.0	2017.01.06–2017.07.10
2017/06/18	Carrara	17.973	-0.371	0.059	17.745	-0.595	0.020	1.956	37.453	15.2	5.5	21.4	2017.01.06–2017.07.10
2017/06/18	Carrara	17.922	-0.317	0.036	17.669	-0.565	0.022	1.946	37.356	-100.2	4.0	14.9	2017.01.06–2017.07.10
2017/06/19	MuStd	23.269	-0.007	0.041	23.013	-0.257	0.023	1.509	42.823	101.5	6.1	23.3	2017.01.06–2017.07.10
2017/06/19	Carrara	17.977	-0.353	0.036	17.730	-0.596	0.029	1.963	37.432	-16.0	5.3	20.0	2017.01.06–2017.07.10
2017/06/20	Carrara	18.036	-0.370	0.031	17.799	-0.602	0.026	1.972	37.498	5.2	8.3	32.4	2017.01.06–2017.07.10
2017/06/20	Carrara	18.057	-0.352	0.020	17.827	-0.578	0.016	1.962	37.512	-12.1	5.9	22.9	2017.01.06–2017.07.10
2017/06/21	MuStd	23.394	0.050	0.035	23.089	-0.248	0.017	1.528	42.871	-24.2	4.7	17.6	2017.01.06–2017.07.10
2017/06/21	Carrara	18.035	-0.328	0.029	17.782	-0.577	0.029	1.972	37.456	-50.4	5.9	22.6	2017.01.06–2017.07.10
2017/06/21	Carrara	18.034	-0.354	0.041	17.807	-0.577	0.024	1.959	37.494	-20.3	6.7	26.2	2017.01.06–2017.07.10
2017/06/22	MuStd	23.432	0.019	0.026	23.128	-0.278	0.016	1.532	42.937	41.4	6.1	21.9	2017.01.06–2017.07.10
2017/06/22	Carrara	18.040	-0.343	0.039	17.786	-0.593	0.020	1.968	37.480	-27.3	5.6	21.9	2017.01.06–2017.07.10
2017/06/23	Carrara	17.899	-0.379	0.023	17.685	-0.589	0.024	1.936	37.406	59.8	6.2	24.2	2017.01.06–2017.07.10
2017/06/24	MuStd	23.300	0.034	0.039	23.003	-0.255	0.029	1.505	42.815	-10.2	6.7	25.1	2017.01.06–2017.07.10
2017/06/24	Carrara	17.911	-0.365	0.033	17.692	-0.580	0.018	1.919	37.422	39.3	4.8	18.2	2017.01.06–2017.07.10

2017/06/24	Carrara	17.950	-0.347	0.052	17.717	-0.576	0.029	1.937	37.424	5.1	5.0	19.0	2017.01.06–2017.07.10
2017/06/25	MuStd	23.455	0.005	0.022	23.155	-0.287	0.022	1.553	42.953	27.0	7.7	28.9	2017.01.06–2017.07.10
2017/06/25	Carrara	17.963	-0.357	0.036	17.747	-0.570	0.023	1.946	37.439	24.6	6.6	25.5	2017.01.06–2017.07.10
2017/06/26	Carrara	18.001	-0.384	0.033	17.790	-0.591	0.035	1.976	37.474	33.3	7.8	30.3	2017.01.06–2017.07.10
2017/06/27	Carrara	17.955	-0.353	0.040	17.719	-0.585	0.033	1.947	37.426	-14.7	6.6	25.3	2017.01.06–2017.07.10
2017/06/27	Carrara	18.045	-0.333	0.017	17.793	-0.580	0.024	1.967	37.476	-76.9	4.7	18.0	2017.01.06–2017.07.10
2017/06/27	MuStd	23.333	-0.035	0.028	23.071	-0.291	0.024	1.537	42.888	91.8	8.7	32.8	2017.01.06–2017.07.10
2017/06/28	Carrara	18.003	-0.361	0.040	17.764	-0.596	0.019	1.967	37.462	-19.0	6.1	23.8	2017.01.06–2017.07.10
2017/06/28	Carrara	17.947	-0.353	0.021	17.733	-0.564	0.020	1.930	37.434	31.3	4.7	18.2	2017.01.06–2017.07.10
2017/06/29	MuStd	23.317	0.002	0.035	23.045	-0.264	0.021	1.575	42.796	29.7	6.9	26.0	2017.01.06–2017.07.10
2017/06/30	Carrara	18.021	-0.358	0.035	17.774	-0.601	0.022	1.983	37.462	-43.0	5.6	21.8	2017.01.06–2017.07.10
2017/06/30	Carrara	17.951	-0.389	0.049	17.749	-0.587	0.022	1.954	37.452	76.8	6.1	23.8	2017.01.06–2017.07.10
2017/07/01	MuStd	23.414	0.010	0.031	23.128	-0.269	0.018	1.558	42.902	13.3	8.4	30.3	2017.01.06–2017.07.10
2017/07/01	Carrara	17.958	-0.375	0.050	17.753	-0.576	0.010	1.954	37.444	52.1	5.4	20.9	2017.01.06–2017.07.10
2017/07/02	MuStd	23.429	0.018	0.048	23.126	-0.278	0.025	1.575	42.892	-20.9	6.4	23.2	2017.01.06–2017.07.10
2017/07/03	Carrara	18.009	-0.366	0.040	17.787	-0.584	0.022	1.963	37.477	4.3	4.5	17.5	2017.01.06–2017.07.10
2017/07/03	Carrara	18.014	-0.366	0.020	17.764	-0.612	0.027	1.977	37.469	-44.9	6.3	24.5	2017.01.06–2017.07.10
2017/07/04	MuStd	23.361	0.016	0.042	23.077	-0.262	0.023	1.551	42.850	10.1	6.9	25.8	2017.01.06–2017.07.10
2017/07/05	Carrara	17.933	-0.382	0.033	17.716	-0.595	0.012	1.950	37.430	32.6	6.4	24.6	2017.01.06–2017.07.10
2017/07/05	MuStd	23.425	0.020	0.018	23.144	-0.254	0.015	1.563	42.898	-18.0	7.4	27.1	2017.01.06–2017.07.10
2017/07/06	Carrara	17.931	-0.399	0.030	17.732	-0.594	0.020	1.957	37.439	38.2	6.5	24.9	2017.01.06–2017.07.10
2017/07/06	MuStd	23.344	-0.008	0.042	23.081	-0.265	0.034	1.538	42.870	55.3	7.6	29.4	2017.01.06–2017.07.10
2017/07/06	Carrara	17.976	-0.393	0.021	17.763	-0.602	0.014	1.974	37.461	29.8	7.5	29.0	2017.01.06–2017.07.10
2017/07/08	Carrara	18.030	-0.341	0.030	17.801	-0.566	0.019	1.968	37.468	-57.0	6.5	25.1	2017.01.06–2017.07.10
2017/07/09	MuStd	23.315	0.009	0.043	23.054	-0.245	0.023	1.544	42.817	94.1	5.5	21.0	2017.01.06–2017.07.10
2017/07/09	Carrara	17.952	-0.403	0.037	17.730	-0.621	0.029	1.972	37.449	19.6	7.3	28.4	2017.01.06–2017.07.10
2017/07/10	MuStd	23.493	0.000	0.038	23.200	-0.287	0.018	1.548	43.002	27.6	7.9	29.8	2017.01.06–2017.07.10
2017/07/11	Carrara	17.969	-0.385	0.023	17.749	-0.601	0.023	1.978	37.442	19.2	7.7	29.8	2017.01.06–2017.07.10
2017/07/14	Carrara	18.029	-0.359	0.013	17.776	-0.607	0.027	1.993	37.461	60.5	7.7	29.9	2017.07.14–2017.11.13
2017/07/15	MuStd	23.536	0.102	0.044	23.169	-0.257	0.020	1.567	42.921	-83.8	6.7	23.0	2017.07.14–2017.11.13
2017/07/15	Carrara	18.025	-0.364	0.023	17.773	-0.611	0.025	1.982	37.472	6.5	5.7	22.2	2017.07.14–2017.11.13
2017/07/16	MuStd	23.581	0.074	0.028	23.241	-0.258	0.019	1.576	42.986	-4.1	6.2	23.2	2017.07.14–2017.11.13
2017/07/17	Carrara	17.991	-0.338	0.032	17.744	-0.580	0.018	1.965	37.428	40.3	6.9	27.1	2017.07.14–2017.11.13
2017/07/18	MuStd	23.354	0.015	0.052	23.060	-0.272	0.025	1.503	42.891	96.6	7.3	27.9	2017.07.14–2017.11.13
2017/07/19	Carrara	17.995	-0.354	0.036	17.759	-0.586	0.029	1.949	37.465	55.4	5.9	22.8	2017.07.14–2017.11.13
2017/07/20	MuStd	23.247	0.047	0.026	22.933	-0.259	0.011	1.453	42.801	29.1	7.7	27.9	2017.07.14–2017.11.13
2017/07/20	Carrara	18.007	-0.372	0.028	17.774	-0.600	0.021	1.978	37.465	54.7	7.9	30.4	2017.07.14–2017.11.13
2017/07/27	Carrara	17.908	-0.426	0.032	17.721	-0.609	0.020	1.943	37.457	160.8	6.6	25.4	2017.07.14–2017.11.13
2017/07/28	MuStd	23.411	0.021	0.032	23.096	-0.287	0.018	1.520	42.925	84.0	6.7	25.3	2017.07.14–2017.11.13
2017/07/28	Carrara	17.936	-0.350	0.044	17.692	-0.591	0.024	1.912	37.439	7.6	6.1	22.0	2017.07.14–2017.11.13
2017/07/29	MuStd	23.476	0.046	0.036	23.140	-0.282	0.027	1.537	42.948	18.2	7.6	28.5	2017.07.14–2017.11.13
2017/07/29	Carrara	17.952	-0.407	0.028	17.741	-0.615	0.019	1.924	37.501	147.4	5.6	21.5	2017.07.14–2017.11.13
2017/07/30	MuStd	23.555	0.026	0.033	23.226	-0.296	0.023	1.574	43.012	19.3	7.6	29.0	2017.07.14–2017.11.13
2017/07/31	Carrara	17.917	-0.378	0.048	17.704	-0.587	0.020	1.936	37.424	107.5	6.0	22.4	2017.07.14–2017.11.13

2017/09/19	Carrara	18.017	-0.380	0.032	17.790	-0.603	0.010	1.970	37.492	31.2	5.3	19.8	2017.07.14–2017.11.13
2017/09/19	ETH3	17.659	-0.076	0.021	17.457	-0.274	0.027	1.636	37.153	63.3	4.4	15.6	2017.07.14–2017.11.13
2017/09/20	ETH1	17.194	-0.508	0.041	16.984	-0.714	0.026	1.971	36.799	40.2	5.2	18.0	2017.07.14–2017.11.13
2017/09/21	ETH3	17.802	-0.089	0.043	17.556	-0.330	0.017	1.645	37.300	-1.9	5.0	18.4	2017.07.14–2017.11.13
2017/09/21	ETH1	17.486	-0.460	0.042	17.258	-0.684	0.020	2.003	37.010	-9.4	4.7	15.9	2017.07.14–2017.11.13
2017/09/22	ETH3	17.755	-0.150	0.048	17.577	-0.325	0.012	1.664	37.296	116.2	6.8	25.2	2017.07.14–2017.11.13
2017/09/23	Carrara	17.943	-0.415	0.055	17.738	-0.617	0.027	1.968	37.457	72.6	4.6	17.7	2017.07.14–2017.11.13
2017/09/23	ETH3	17.831	-0.076	0.027	17.588	-0.315	0.022	1.647	37.314	-18.6	6.0	20.7	2017.07.14–2017.11.13
2017/09/24	ETH1	17.384	-0.461	0.035	17.140	-0.702	0.022	1.999	36.914	-48.6	5.3	19.4	2017.07.14–2017.11.13
2017/09/24	ETH3	17.751	-0.099	0.042	17.545	-0.302	0.023	1.634	37.270	70.1	4.8	17.3	2017.07.14–2017.11.13
2017/09/27	Carrara	17.909	-0.411	0.036	17.706	-0.611	0.017	1.976	37.410	78.2	6.8	25.9	2017.07.14–2017.11.13
2017/09/27	ETH1	17.221	-0.524	0.040	17.030	-0.712	0.021	1.979	36.834	86.5	4.3	15.6	2017.07.14–2017.11.13
2017/09/28	ETH3	17.853	-0.071	0.047	17.626	-0.294	0.021	1.652	37.326	4.6	4.3	15.7	2017.07.14–2017.11.13
2017/09/28	Carrara	18.012	-0.352	0.023	17.776	-0.583	0.016	1.945	37.484	-1.1	4.4	16.8	2017.07.14–2017.11.13
2017/09/29	ETH1	17.423	-0.479	0.021	17.194	-0.704	0.027	2.038	36.931	1.5	5.2	19.4	2017.07.14–2017.11.13
2017/09/30	ETH3	17.806	-0.050	0.055	17.542	-0.310	0.030	1.666	37.243	-54.0	4.5	16.2	2017.07.14–2017.11.13
2017/09/30	Carrara	17.890	-0.441	0.046	17.731	-0.598	0.023	1.973	37.425	174.4	6.7	25.8	2017.07.14–2017.11.13
2017/10/01	ETH1	17.345	-0.495	0.026	17.142	-0.694	0.019	1.997	36.910	42.3	4.8	17.5	2017.07.14–2017.11.13
2017/10/01	ETH3	17.772	-0.068	0.056	17.525	-0.311	0.027	1.633	37.261	-43.7	4.9	17.7	2017.07.14–2017.11.13
2017/10/02	Carrara	17.942	-0.439	0.054	17.759	-0.619	0.012	1.960	37.487	147.8	6.0	22.7	2017.07.14–2017.11.13
2017/10/04	ETH1	17.413	-0.468	0.055	17.193	-0.684	0.024	2.032	36.918	-9.9	6.4	23.1	2017.07.14–2017.11.13
2017/10/05	ETH3	17.667	-0.122	0.039	17.452	-0.333	0.023	1.624	37.219	66.6	4.9	17.6	2017.07.14–2017.11.13
2017/10/06	Carrara	18.006	-0.397	0.030	17.790	-0.608	0.021	1.996	37.473	63.4	7.9	30.1	2017.07.14–2017.11.13
2017/10/06	ETH1	17.480	-0.421	0.036	17.198	-0.698	0.028	2.035	36.932	-125.4	4.5	16.4	2017.07.14–2017.11.13
2017/10/07	ETH3	17.660	-0.128	0.035	17.474	-0.311	0.021	1.650	37.193	124.4	5.0	18.1	2017.07.14–2017.11.13
2017/10/07	Carrara	18.069	-0.372	0.032	17.823	-0.614	0.016	1.976	37.531	-3.2	5.9	22.5	2017.07.14–2017.11.13
2017/10/08	ETH1	17.379	-0.450	0.050	17.108	-0.717	0.019	2.006	36.890	-84.2	4.6	17.3	2017.07.14–2017.11.13
2017/10/08	ETH3	17.774	-0.100	0.042	17.564	-0.306	0.029	1.656	37.272	40.4	4.8	17.8	2017.07.14–2017.11.13
2017/10/09	Carrara	18.073	-0.363	0.042	17.807	-0.625	0.027	1.998	37.504	-37.7	4.8	17.4	2017.07.14–2017.11.13
2017/10/10	Carrara	18.081	-0.275	0.043	17.783	-0.567	0.017	1.893	37.525	-162.8	5.7	12.3	2017.07.14–2017.11.13
2017/10/10	Carrara	18.168	-0.393	0.024	17.940	-0.616	0.021	2.009	37.618	18.6	4.6	17.7	2017.07.14–2017.11.13
2017/10/10	ETH1	17.478	-0.530	0.077	17.282	-0.722	0.017	2.035	37.042	84.0	5.1	18.9	2017.07.14–2017.11.13
2017/10/11	ETH1	17.450	-0.490	0.041	17.246	-0.690	0.016	2.006	37.002	56.1	4.7	17.3	2017.07.14–2017.11.13
2017/10/12	ETH3	17.932	-0.048	0.037	17.652	-0.323	0.023	1.682	37.353	-89.0	4.8	16.9	2017.07.14–2017.11.13
2017/10/13	Carrara	18.155	-0.364	0.038	17.888	-0.626	0.019	2.012	37.572	-47.6	5.8	21.4	2017.07.14–2017.11.13
2017/10/18	Carrara	18.059	-0.369	0.033	17.830	-0.594	0.016	1.993	37.501	33.0	5.6	21.5	2017.07.14–2017.11.13
2017/10/18	ETH3	17.820	-0.093	0.040	17.617	-0.292	0.025	1.657	37.309	42.5	4.4	15.3	2017.07.14–2017.11.13
2017/10/18	ETH1	17.437	-0.477	0.047	17.223	-0.687	0.028	2.039	36.943	9.2	5.7	22.0	2017.07.14–2017.11.13
2017/10/19	ETH3	17.752	-0.127	0.031	17.557	-0.319	0.020	1.677	37.258	84.9	5.6	20.6	2017.07.14–2017.11.13
2017/10/20	Carrara	18.041	-0.427	0.022	17.827	-0.637	0.025	2.005	37.530	50.2	5.1	19.6	2017.07.14–2017.11.13
2017/10/20	ETH1	17.367	-0.433	0.032	17.122	-0.673	0.017	1.964	36.901	-59.0	5.7	21.1	2017.07.14–2017.11.13
2017/10/21	ETH3	17.872	-0.043	0.039	17.583	-0.327	0.025	1.630	37.338	-113.6	4.2	15.1	2017.07.14–2017.11.13
2017/10/21	Carrara	17.993	-0.394	0.062	17.774	-0.610	0.028	1.951	37.502	51.5	5.0	18.8	2017.07.14–2017.11.13
2017/10/22	ETH3	17.885	-0.059	0.013	17.644	-0.296	0.020	1.646	37.351	-24.2	5.9	21.4	2017.07.14–2017.11.13

2017/10/22	MuStd	22.886	-0.073	0.030	22.656	-0.298	0.015	1.388	42.627	151.1	7.3	28.5	2017.07.14–2017.11.13
2017/10/23	Carrara	18.183	-0.385	0.029	17.955	-0.610	0.014	2.016	37.619	10.2	6.6	25.3	2017.07.14–2017.11.13
2017/11/01	Carrara	18.202	-0.319	0.051	17.920	-0.595	0.021	1.998	37.588	-51.5	5.9	22.6	2017.07.14–2017.11.13
2017/11/01	Carrara	18.136	-0.346	0.043	17.845	-0.632	0.024	1.988	37.559	-27.2	5.6	21.2	2017.07.14–2017.11.13
2017/11/01	ETH3	17.899	-0.076	0.042	17.647	-0.323	0.024	1.666	37.363	2.7	5.8	21.2	2017.07.14–2017.11.13
2017/11/02	ETH1	17.775	-0.298	0.066	17.376	-0.690	0.034	2.022	37.116	-140.7	5.1	17.3	2017.07.14–2017.11.13
2017/11/02	Carrara	18.523	-0.045	0.041	17.960	-0.598	0.019	2.010	37.618	-234.8	4.1	15.6	2017.07.14–2017.11.13
2017/11/03	ETH3	18.233	0.190	0.131	17.714	-0.320	0.023	1.687	37.406	-151.0	6.3	22.7	2017.07.14–2017.11.13
2017/11/04	ETH1	17.695	-0.359	0.667	17.370	-0.679	0.078	2.005	37.115	-99.7	4.3	14.5	2017.07.14–2017.11.13
2017/11/04	Carrara	18.269	-0.217	0.070	17.888	-0.591	0.047	1.990	37.560	-122.1	4.2	15.4	2017.07.14–2017.11.13
2017/11/04	ETH3	18.122	0.157	0.088	17.642	-0.315	0.025	1.668	37.347	-99.2	7.1	25.6	2017.07.14–2017.11.13
2017/11/05	ETH1	17.698	-0.163	0.140	17.166	-0.686	0.023	1.994	36.929	-146.6	5.6	20.1	2017.07.14–2017.11.13
2017/11/06	Carrara	18.383	-0.047	0.149	17.814	-0.607	0.032	2.002	37.488	-200.4	6.1	22.9	2017.07.14–2017.11.13
2017/11/06	ETH3	18.010	0.003	0.087	17.669	-0.332	0.022	1.635	37.425	-11.0	4.2	14.2	2017.07.14–2017.11.13
2017/11/07	ETH1	17.634	-0.332	0.037	17.245	-0.715	0.020	1.999	37.032	-103.6	4.5	16.6	2017.07.14–2017.11.13
2017/11/08	ETH3	17.821	-0.076	0.045	17.564	-0.328	0.019	1.628	37.322	133.0	5.5	19.7	2017.07.14–2017.11.13
2017/11/08	Carrara	18.217	-0.293	0.039	17.879	-0.625	0.018	2.021	37.553	0.5	10.5	40.0	2017.07.14–2017.11.13
2017/11/09	ETH1	17.444	-0.393	0.032	17.150	-0.682	0.029	1.878	37.022	38.7	5.0	18.6	2017.07.14–2017.11.13
2017/11/09	ETH3	18.012	0.072	0.042	17.616	-0.318	0.033	1.653	37.339	-135.5	4.6	16.5	2017.07.14–2017.11.13
2017/11/10	Carrara	18.151	-0.294	0.035	17.840	-0.599	0.017	1.985	37.524	32.7	5.8	21.9	2017.07.14–2017.11.13
2017/11/11	ETH1	17.587	-0.333	0.041	17.210	-0.704	0.013	2.005	36.981	-98.5	4.7	17.0	2017.07.14–2017.11.13
2017/11/11	ETH3	17.941	0.023	0.046	17.594	-0.317	0.028	1.629	37.340	-17.4	4.4	15.7	2017.07.14–2017.11.13
2017/11/12	Carrara	18.200	-0.266	0.085	17.841	-0.619	0.023	1.979	37.550	-37.8	4.9	18.6	2017.07.14–2017.11.13
2017/11/12	ETH1	17.523	-0.343	0.050	17.143	-0.716	0.019	1.995	36.936	-104.3	4.2	15.3	2017.07.14–2017.11.13
2017/11/13	Carrara	18.133	-0.299	0.048	17.814	-0.613	0.030	1.962	37.535	27.0	4.1	15.6	2017.07.14–2017.11.13
2017/11/14	ETH1	17.649	-0.323	0.055	17.257	-0.707	0.018	1.987	37.049	-120.3	4.2	14.6	2017.07.14–2017.11.13
2017/11/14	ETH3	17.923	-0.004	0.063	17.605	-0.316	0.020	1.602	37.376	20.9	4.7	16.7	2017.07.14–2017.11.13
2018/03/17	ETH1	17.757	-0.256	0.018	17.353	-0.653	0.021	2.154	36.925	-126.2	5.3	19.7	2018.03.07–2018.03.29
2018/03/17	ETH1	17.735	-0.256	0.029	17.331	-0.654	0.024	2.147	36.910	-123.4	4.7	17.6	2018.03.07–2018.03.29
2018/03/17	ETH1	17.706	-0.270	0.027	17.317	-0.652	0.023	2.148	36.895	-82.0	4.3	15.4	2018.03.07–2018.03.29
2018/03/18	ETH1	17.669	-0.279	0.011	17.279	-0.662	0.008	2.146	36.869	-29.3	6.3	19.8	2018.03.07–2018.03.29
2018/03/18	ETH1	17.732	-0.259	0.037	17.317	-0.667	0.031	2.156	36.901	-177.0	4.3	16.5	2018.03.07–2018.03.29
2018/03/18	ETH1	17.759	-0.247	0.036	17.372	-0.627	0.030	2.148	36.924	-116.7	5.4	19.1	2018.03.07–2018.03.29
2018/03/18	ETH1	17.727	-0.240	0.035	17.320	-0.639	0.028	2.146	36.886	-200.1	3.5	12.6	2018.03.07–2018.03.29
2018/03/18	ETH2	-11.517	-0.834	0.026	-11.305	-0.620	0.022	-9.933	19.866	-70.9	4.9	16.8	2018.03.07–2018.03.29
2018/03/18	ETH2	-11.604	-0.828	0.020	-11.405	-0.627	0.015	-9.965	19.804	-29.6	4.3	15.7	2018.03.07–2018.03.29
2018/03/19	ETH2	-11.519	-0.792	0.023	-11.325	-0.597	0.017	-9.955	19.845	-164.6	4.5	16.4	2018.03.07–2018.03.29
2018/03/19	ETH2	-11.608	-0.817	0.040	-11.414	-0.622	0.033	-9.950	19.775	-132.8	7.0	22.9	2018.03.07–2018.03.29
2018/03/19	ETH2	-11.494	-0.801	0.021	-11.293	-0.598	0.018	-9.949	19.873	-164.5	5.1	18.9	2018.03.07–2018.03.29
2018/03/19	ETH2	-11.507	-0.803	0.013	-11.300	-0.593	0.013	-9.978	19.889	-107.4	4.0	15.0	2018.03.07–2018.03.29
2018/03/20	ETH2	-10.860	-0.807	0.036	-10.679	-0.624	0.028	-9.721	20.298	-129.4	5.1	19.1	2018.03.07–2018.03.29
2018/03/20	ETH2	-11.530	-0.831	0.024	-11.323	-0.622	0.024	-9.971	19.888	-110.6	5.2	18.9	2018.03.07–2018.03.29
2018/03/20	ETH1	17.694	-0.246	0.029	17.291	-0.642	0.023	2.115	36.890	-146.3	4.9	17.3	2018.03.07–2018.03.29
2018/03/20	ETH1	17.745	-0.247	0.026	17.359	-0.627	0.023	2.119	36.939	-151.8	4.2	15.0	2018.03.07–2018.03.29

2018/03/21	ETH1	17.719	-0.257	0.026	17.303	-0.666	0.019	2.147	36.895	-154.3	4.6	16.3	2018.03.07–2018.03.29
2018/03/21	ETH1	17.592	-0.248	0.017	17.193	-0.640	0.014	2.068	36.837	-176.5	4.2	15.9	2018.03.07–2018.03.29
2018/03/21	ETH1	17.684	-0.282	0.030	17.289	-0.671	0.022	2.130	36.903	-40.9	5.7	21.3	2018.03.07–2018.03.29
2018/03/22	ETH2	-10.844	-0.797	0.037	-10.658	-0.609	0.030	-9.699	20.282	-141.8	5.3	20.7	2018.03.07–2018.03.29
2018/03/22	ETH2	-11.412	-0.814	0.026	-11.197	-0.597	0.018	-9.947	19.967	-128.6	5.0	18.0	2018.03.07–2018.03.29
2018/03/22	ETH2	-11.490	-0.830	0.060	-11.283	-0.620	0.059	-9.959	19.915	-98.1	4.2	16.0	2018.03.07–2018.03.29
2018/03/22	ETH2	-11.553	-0.813	0.045	-11.345	-0.603	0.052	-9.980	19.855	-74.0	4.5	16.8	2018.03.07–2018.03.29
2018/03/23	ETH3	18.356	0.181	0.030	17.900	-0.267	0.027	1.840	37.387	-150.0	4.6	17.5	2018.03.07–2018.03.29
2018/03/23	Carrara	18.473	-0.095	0.035	17.994	-0.565	0.031	2.135	37.496	-114.2	4.1	16.1	2018.03.07–2018.03.29
2018/03/24	MuStd	23.555	0.226	0.044	23.035	-0.282	0.018	1.661	42.720	30.1	6.7	25.0	2018.03.07–2018.03.29
2018/03/24	Carrara	18.446	-0.146	0.039	18.028	-0.557	0.027	2.142	37.514	-149.3	4.9	19.3	2018.03.07–2018.03.29
2018/03/24	MuStd	23.796	0.276	0.010	23.256	-0.252	0.012	1.700	42.872	-155.9	4.8	18.6	2018.03.07–2018.03.29
2018/03/24	Carrara	18.395	-0.163	0.029	17.970	-0.579	0.022	2.134	37.487	-127.3	5.1	19.6	2018.03.07–2018.03.29
2018/03/24	MuStd	23.765	0.259	0.015	23.251	-0.243	0.011	1.693	42.865	-91.2	4.9	18.7	2018.03.07–2018.03.29
2018/03/25	ETH3	18.436	0.123	0.026	18.019	-0.286	0.021	1.889	37.478	-114.7	6.3	23.8	2018.03.07–2018.03.29
2018/03/26	ETH1	17.725	-0.263	0.026	17.337	-0.644	0.025	2.141	36.914	-9.3	5.1	18.8	2018.03.07–2018.03.29
2018/03/27	Carrara	18.442	-0.127	0.029	18.017	-0.544	0.030	2.139	37.493	-164.8	4.8	18.7	2018.03.07–2018.03.29
2018/03/28	ETH3	18.265	0.168	0.065	17.817	-0.272	0.071	1.813	37.336	-155.9	5.0	19.0	2018.03.07–2018.03.29
2018/03/29	ETH1	17.644	-0.264	0.056	17.244	-0.656	0.056	2.109	36.864	-42.1	6.3	23.2	2018.03.07–2018.03.29
2018/03/30	ETH3	18.235	0.127	0.030	17.821	-0.279	0.029	1.822	37.339	-81.3	6.4	24.1	2018.03.07–2018.03.29
2018/04/11	Carrara	18.582	0.014	0.025	18.020	-0.537	0.036	2.145	37.484	-168.4	5.7	22.5	2018.03.07–2018.03.29
2018/04/11	ETH1	17.903	-0.069	0.021	17.360	-0.602	0.024	2.152	36.883	-205.7	4.7	17.8	2018.03.07–2018.03.29
2018/04/11	ETH2	-11.859	-0.924	0.023	-11.527	-0.588	0.018	-10.038	19.713	-149.4	5.4	20.5	2018.03.07–2018.03.29
2018/04/12	ETH3	18.380	0.283	0.022	17.825	-0.262	0.020	1.823	37.325	-149.1	5.8	21.5	2018.03.07–2018.03.29
2018/04/12	MuStd	23.964	0.473	0.020	23.237	-0.238	0.024	1.707	42.831	-143.5	5.0	18.9	2018.03.07–2018.03.29
2018/04/12	Carrara	18.524	-0.019	0.023	17.961	-0.572	0.021	2.135	37.470	-33.6	5.4	20.8	2018.03.07–2018.03.29
2018/04/13	ETH3	18.421	0.268	0.023	17.847	-0.296	0.025	1.835	37.369	-138.2	6.3	23.4	2018.03.07–2018.03.29
2018/04/13	ETH2	-11.749	-0.941	0.030	-11.411	-0.600	0.028	-10.030	19.835	-120.9	6.3	20.1	2018.03.07–2018.03.29
2018/04/13	ETH1	17.729	-0.121	0.022	17.186	-0.654	0.026	2.087	36.825	-92.7	4.5	17.2	2018.03.07–2018.03.29
2018/04/17	Carrara	18.631	-0.058	0.033	18.140	-0.539	0.032	2.180	37.572	-66.4	6.8	26.4	2018.03.07–2018.03.29
2018/04/17	MuStd	23.935	0.363	0.027	23.339	-0.219	0.026	1.693	42.928	-8.5	5.1	18.8	2018.03.07–2018.03.29
2018/04/27	ETH3	18.154	0.112	0.013	17.731	-0.303	0.028	1.805	37.290	-43.5	5.6	19.1	2018.03.07–2018.03.29
2018/04/27	Carrara	18.353	-0.147	0.034	17.933	-0.559	0.033	2.124	37.440	-126.3	5.2	19.6	2018.03.07–2018.03.29
2018/04/28	MuStd	23.953	0.231	0.028	23.435	-0.276	0.028	1.765	43.011	20.0	7.2	27.1	2018.03.07–2018.03.29
2018/04/28	ETH3	18.195	0.118	0.030	17.777	-0.293	0.024	1.812	37.318	-110.5	5.6	20.6	2018.03.07–2018.03.29
2018/07/11	ETH2	-11.649	-0.893	0.030	-11.416	-0.657	0.031	-9.988	19.846	157.7	6.8	26.1	2018.07.10–2018.10.19
2018/07/11	ETH2	-11.311	-0.916	0.027	-11.056	-0.658	0.035	-9.880	20.106	45.8	7.4	27.3	2018.07.10–2018.10.19
2018/07/11	ETH1	17.708	-0.202	0.038	17.223	-0.678	0.026	2.138	36.836	92.0	7.2	26.8	2018.07.10–2018.10.19
2018/07/12	ETH1	17.770	-0.205	0.023	17.298	-0.669	0.022	2.141	36.899	62.6	7.2	26.6	2018.07.10–2018.10.19
2018/07/12	ETH2	-11.673	-0.877	0.020	-11.430	-0.631	0.019	-10.033	19.850	130.3	6.5	25.0	2018.07.10–2018.10.19
2018/07/13	ETH2	-11.660	-0.916	0.026	-11.378	-0.631	0.012	-10.035	19.904	11.7	6.3	23.2	2018.07.10–2018.10.19
2018/07/17	ETH2	-11.766	-0.903	0.035	-11.517	-0.651	0.026	-10.017	19.766	123.5	7.1	26.5	2018.07.10–2018.10.19
2018/07/18	ETH2	-11.834	-0.901	0.019	-11.574	-0.638	0.016	-10.036	19.714	130.5	7.0	25.6	2018.07.10–2018.10.19
2018/07/18	ETH1	17.672	-0.191	0.019	17.205	-0.650	0.024	2.118	36.809	60.3	7.6	28.8	2018.07.10–2018.10.19

2018/07/18	ETH1	17.784	-0.185	0.023	17.305	-0.656	0.023	2.151	36.883	97.3	6.2	23.7	2018.07.10–2018.10.19
2018/07/18	ETH2	-11.790	-0.902	0.042	-11.563	-0.672	0.026	-10.030	19.753	187.7	7.8	29.0	2018.07.10–2018.10.19
2018/07/19	ETH1	17.857	-0.183	0.033	17.350	-0.681	0.023	2.159	36.946	121.7	5.7	22.0	2018.07.10–2018.10.19
2018/07/19	ETH1	17.918	-0.217	0.034	17.473	-0.654	0.032	2.162	37.038	-45.3	6.4	24.1	2018.07.10–2018.10.19
2018/07/19	ETH1	17.831	-0.186	0.020	17.335	-0.673	0.015	2.156	36.926	105.0	5.8	21.6	2018.07.10–2018.10.19
2018/07/20	ETH1	17.836	-0.184	0.018	17.351	-0.660	0.012	2.163	36.922	78.4	5.4	20.7	2018.07.10–2018.10.19
2018/07/20	ETH2	-11.707	-0.913	0.039	-11.441	-0.645	0.027	-9.998	19.817	45.2	5.7	21.5	2018.07.10–2018.10.19
2018/07/20	ETH2	-11.701	-0.911	0.028	-11.433	-0.640	0.023	-10.035	19.858	57.0	5.9	21.1	2018.07.10–2018.10.19
2018/07/21	ETH1	17.817	-0.192	0.034	17.334	-0.666	0.017	2.157	36.917	38.4	6.2	22.3	2018.07.10–2018.10.19
2018/07/21	ETH3	18.204	0.191	0.024	17.703	-0.301	0.014	1.800	37.264	60.6	6.8	24.6	2018.07.10–2018.10.19
2018/07/22	Carrara	18.402	-0.086	0.027	17.921	-0.559	0.016	2.119	37.432	-54.9	7.2	19.8	2018.07.10–2018.10.19
2018/07/22	MuStd	23.654	0.382	0.035	22.981	-0.276	0.025	1.645	42.676	192.7	6.7	25.2	2018.07.10–2018.10.19
2018/07/23	ETH1	17.683	-0.193	0.037	17.191	-0.676	0.030	2.111	36.829	81.1	7.2	26.7	2018.07.10–2018.10.19
2018/07/24	ETH3	18.121	0.228	0.030	17.585	-0.299	0.016	1.775	37.169	171.5	6.7	23.8	2018.07.10–2018.10.19
2018/07/24	Carrara	18.389	-0.031	0.029	17.859	-0.552	0.014	2.097	37.384	125.9	7.3	27.9	2018.07.10–2018.10.19
2018/07/25	ETH2	-11.257	-0.900	0.025	-10.981	-0.621	0.030	-10.007	20.270	-8.5	5.7	20.8	2018.07.10–2018.10.19
2018/07/26	MuStd	23.537	0.375	0.023	22.914	-0.234	0.025	1.666	42.545	-11.8	6.1	22.8	2018.07.10–2018.10.19
2018/07/27	ETH3	18.157	0.167	0.042	17.704	-0.278	0.019	1.806	37.237	-123.5	5.4	19.6	2018.07.10–2018.10.19
2018/07/29	MuStd	23.718	0.353	0.043	23.081	-0.269	0.024	1.706	42.709	-22.2	6.7	25.0	2018.07.10–2018.10.19
2018/07/29	ETH1	17.844	-0.154	0.034	17.337	-0.653	0.034	2.125	36.938	86.8	5.4	20.4	2018.07.10–2018.10.19
2018/07/30	ETH3	18.275	0.215	0.030	17.776	-0.275	0.020	1.821	37.291	36.6	6.8	24.9	2018.07.10–2018.10.19
2018/07/31	Carrara	18.435	-0.084	0.036	17.974	-0.535	0.044	2.128	37.453	-67.7	6.0	22.8	2018.07.10–2018.10.19
2018/07/31	MuStd	23.788	0.375	0.055	23.170	-0.228	0.044	1.694	42.768	-63.5	5.9	22.2	2018.07.10–2018.10.19
2018/08/01	ETH1	17.835	-0.175	0.024	17.327	-0.674	0.020	2.130	36.944	57.9	5.6	20.2	2018.07.10–2018.10.19
2018/08/02	ETH3	18.413	0.212	0.036	17.899	-0.293	0.030	1.773	37.479	49.0	5.5	19.7	2018.07.10–2018.10.19
2018/08/03	Carrara	18.452	-0.076	0.034	17.953	-0.566	0.023	2.127	37.464	4.9	6.4	24.7	2018.07.10–2018.10.19
2018/08/04	ETH2	-11.648	-0.933	0.024	-11.347	-0.629	0.016	-10.031	19.929	32.3	8.3	31.5	2018.07.10–2018.10.19
2018/08/05	ETH3	18.294	0.241	0.025	17.755	-0.288	0.024	1.821	37.283	68.3	5.5	20.0	2018.07.10–2018.10.19
2018/08/05	MuStd	24.094	0.415	0.038	23.434	-0.230	0.027	1.696	43.032	-1.9	6.7	23.8	2018.07.10–2018.10.19
2018/08/06	ETH1	17.921	-0.166	0.048	17.414	-0.664	0.025	2.149	37.002	0.7	6.9	24.9	2018.07.10–2018.10.19
2018/08/07	ETH2	-11.794	-0.951	0.036	-11.467	-0.620	0.015	-10.026	19.793	-23.3	7.1	24.3	2018.07.10–2018.10.19
2018/08/08	ETH3	18.378	0.242	0.035	17.847	-0.279	0.021	1.832	37.355	43.3	7.5	27.3	2018.07.10–2018.10.19
2018/08/08	ETH2	-11.542	-0.941	0.045	-11.250	-0.647	0.029	-9.982	19.997	-2.1	7.5	27.4	2018.07.10–2018.10.19
2018/08/09	MuStd	23.771	0.420	0.018	23.086	-0.248	0.015	1.646	42.752	49.4	5.6	20.9	2018.07.10–2018.10.19
2018/08/09	Carrara	18.511	-0.049	0.049	17.980	-0.570	0.018	2.133	37.490	19.5	6.4	24.6	2018.07.10–2018.10.19
2018/08/10	ETH3	18.229	0.194	0.044	17.727	-0.300	0.028	1.794	37.292	-2.4	7.7	28.0	2018.07.10–2018.10.19
2018/08/11	Carrara	18.441	-0.058	0.028	17.920	-0.570	0.021	2.142	37.420	0.5	5.6	21.2	2018.07.10–2018.10.19
2018/08/13	ETH1	17.788	-0.183	0.040	17.297	-0.665	0.011	2.153	36.882	-41.0	5.6	20.6	2018.07.10–2018.10.19
2018/08/13	ETH2	-11.717	-0.923	0.044	-11.435	-0.638	0.032	-9.996	19.815	94.7	5.0	20.0	2018.07.10–2018.10.19
2018/08/13	ETH3	18.172	0.222	0.027	17.652	-0.289	0.023	1.791	37.210	15.1	7.8	28.5	2018.07.10–2018.10.19
2018/08/14	MuStd	23.957	0.432	0.062	23.278	-0.231	0.020	1.699	42.874	37.2	6.3	23.0	2018.07.10–2018.10.19
2018/08/15	Carrara	18.542	-0.004	0.056	17.947	-0.587	0.023	2.134	37.473	139.4	6.6	25.0	2018.07.10–2018.10.19
2018/08/15	ETH1	17.859	-0.104	0.018	17.262	-0.691	0.017	2.150	36.877	175.2	7.9	29.4	2018.07.10–2018.10.19
2018/08/16	Carrara	18.508	-0.027	0.041	17.954	-0.570	0.020	2.132	37.464	29.8	5.6	21.3	2018.07.10–2018.10.19

2018/08/17	ETH3	18.330	0.256	0.027	17.769	-0.295	0.025	1.823	37.302	72.0	7.5	27.3	2018.07.10–2018.10.19
2018/08/17	ETH2	-11.755	-0.965	0.039	-11.418	-0.624	0.022	-10.016	19.837	-41.9	5.9	22.2	2018.07.10–2018.10.19
2018/08/18	ETH3	18.277	0.249	0.033	17.742	-0.277	0.013	1.816	37.263	64.4	5.7	20.5	2018.07.10–2018.10.19
2018/08/19	Carrara	18.533	-0.005	0.046	17.961	-0.566	0.029	2.132	37.467	88.9	5.6	21.4	2018.07.10–2018.10.19
2018/08/19	ETH3	18.331	0.254	0.033	17.767	-0.300	0.018	1.827	37.301	66.9	6.5	23.8	2018.07.10–2018.10.19
2018/08/19	ETH1	17.937	-0.162	0.052	17.413	-0.677	0.035	2.171	36.993	9.7	5.9	21.7	2018.07.10–2018.10.19
2018/08/21	ETH4	-11.490	-0.711	0.032	-11.189	-0.406	0.024	-10.090	19.924	23.7	5.5	20.3	2018.07.10–2018.10.19
2018/08/22	Carrara	18.445	0.021	0.056	17.840	-0.573	0.027	2.102	37.382	155.6	7.3	27.8	2018.07.10–2018.10.19
2018/08/22	ETH3	18.246	0.303	0.036	17.648	-0.285	0.023	1.792	37.201	147.0	6.2	22.5	2018.07.10–2018.10.19
2018/08/23	ETH1	17.768	-0.131	0.025	17.227	-0.663	0.034	2.107	36.854	61.5	5.7	19.6	2018.07.10–2018.10.19
2018/08/23	ETH4	-11.621	-0.744	0.043	-11.266	-0.385	0.036	-10.060	19.795	-45.7	6.2	25.4	2018.07.10–2018.10.19
2018/08/24	MuStd	23.673	0.470	0.043	22.911	-0.276	0.010	1.619	42.631	160.8	8.1	30.0	2018.07.10–2018.10.19
2018/08/25	Carrara	18.550	0.011	0.045	17.951	-0.577	0.023	2.132	37.468	122.4	5.5	20.6	2018.07.10–2018.10.19
2018/08/25	ETH3	18.295	0.280	0.040	17.709	-0.295	0.019	1.801	37.264	112.7	5.6	20.0	2018.07.10–2018.10.19
2018/08/26	ETH1	17.800	-0.129	0.040	17.254	-0.664	0.041	2.125	36.867	78.5	6.3	22.9	2018.07.10–2018.10.19
2018/08/26	MuStd	23.850	0.413	0.039	23.177	-0.245	0.029	1.687	42.799	-20.7	5.6	20.2	2018.07.10–2018.10.19
2018/08/27	Carrara	18.488	-0.033	0.035	17.969	-0.542	0.026	2.123	37.460	-10.2	6.6	24.8	2018.07.10–2018.10.19
2018/08/28	ETH3	18.426	0.245	0.046	17.895	-0.276	0.020	1.837	37.396	17.4	7.0	26.0	2018.07.10–2018.10.19
2018/08/29	ETH3	18.468	0.276	0.049	17.902	-0.280	0.028	1.868	37.376	32.4	6.2	22.4	2018.07.10–2018.10.19
2018/08/30	Carrara	18.572	-0.016	0.038	18.009	-0.569	0.020	2.134	37.516	40.0	6.8	26.1	2018.07.10–2018.10.19
2018/08/31	ETH2	-11.591	-0.937	0.038	-11.274	-0.616	0.022	-10.019	19.979	45.0	5.6	19.8	2018.07.10–2018.10.19
2018/09/03	ETH3	18.290	0.198	0.043	17.798	-0.284	0.023	1.820	37.323	17.8	6.5	23.4	2018.07.10–2018.10.19
2018/09/04	ETH1	17.844	-0.178	0.016	17.348	-0.666	0.012	2.159	36.928	110.8	9.3	32.6	2018.07.10–2018.10.19
2018/09/04	ETH3	18.219	0.170	0.038	17.750	-0.290	0.028	1.796	37.304	-12.0	5.7	20.2	2018.07.10–2018.10.19
2018/09/06	ETH1	17.795	-0.201	0.035	17.353	-0.635	0.014	2.143	36.918	-51.5	5.3	19.7	2018.07.10–2018.10.19
2018/09/06	Carrara	18.535	-0.100	0.025	18.048	-0.578	0.019	2.142	37.557	-9.9	5.6	20.8	2018.07.10–2018.10.19
2018/09/07	ETH3	18.186	0.188	0.027	17.712	-0.277	0.038	1.790	37.259	-18.8	6.3	22.6	2018.07.10–2018.10.19
2018/09/08	ETH1	17.833	-0.160	0.020	17.319	-0.666	0.022	2.124	36.934	70.5	8.4	30.8	2018.07.10–2018.10.19
2018/09/08	ETH2	-11.823	-0.923	0.029	-11.545	-0.641	0.020	-10.045	19.755	41.7	5.7	20.1	2018.07.10–2018.10.19
2018/09/09	ETH4	-11.864	-0.733	0.028	-11.544	-0.409	0.017	-10.094	19.571	-42.9	5.4	19.8	2018.07.10–2018.10.19
2018/09/10	ETH2	-11.890	-0.956	0.043	-11.566	-0.628	0.019	-10.063	19.738	-32.6	5.4	19.4	2018.07.10–2018.10.19
2018/09/10	ETH4	-11.779	-0.703	0.046	-11.482	-0.403	0.039	-10.105	19.638	40.5	5.7	20.8	2018.07.10–2018.10.19
2018/09/11	Carrara	18.339	-0.072	0.036	17.816	-0.585	0.026	2.084	37.389	23.4	5.5	20.5	2018.07.10–2018.10.19
2018/09/12	MuStd	23.854	0.413	0.045	23.180	-0.245	0.018	1.645	42.843	38.6	5.7	20.4	2018.07.10–2018.10.19
2018/09/12	ETH3	18.255	0.282	0.035	17.665	-0.297	0.022	1.774	37.248	154.2	6.8	24.2	2018.07.10–2018.10.19
2018/09/13	ETH2	-11.359	-0.895	0.034	-11.135	-0.668	0.018	-10.016	20.169	125.9	7.9	27.0	2018.07.10–2018.10.19
2018/09/14	Carrara	18.435	-0.025	0.039	17.860	-0.589	0.016	2.089	37.432	113.1	5.5	20.3	2018.07.10–2018.10.19
2018/09/15	Carrara	18.486	-0.026	0.036	17.961	-0.542	0.010	2.114	37.460	19.2	5.5	20.1	2018.07.10–2018.10.19
2018/09/15	ETH1	17.701	-0.170	0.031	17.220	-0.642	0.021	2.106	36.828	-25.8	5.8	20.3	2018.07.10–2018.10.19
2018/09/16	MuStd	23.867	0.406	0.036	23.197	-0.249	0.034	1.676	42.834	-8.7	6.2	22.0	2018.07.10–2018.10.19
2018/09/16	ETH3	18.208	0.232	0.052	17.701	-0.265	0.024	1.768	37.258	0.5	5.4	18.7	2018.07.10–2018.10.19
2018/09/17	Carrara	18.491	-0.022	0.064	17.909	-0.593	0.030	2.104	37.470	56.1	5.6	20.6	2018.07.10–2018.10.19
2018/09/17	ETH2	-11.596	-0.922	0.058	-11.301	-0.624	0.032	-10.031	19.971	47.7	6.9	24.5	2018.07.10–2018.10.19
2018/09/18	Carrara	18.377	-0.042	0.061	17.841	-0.568	0.032	2.096	37.384	-5.8	5.6	20.6	2018.07.10–2018.10.19

2018/09/19	ETH3	18.194	0.258	0.032	17.648	-0.279	0.025	1.761	37.224	58.1	5.6	19.3	2018.07.10–2018.10.19
2018/09/20	Carrara	18.499	-0.040	0.036	17.983	-0.547	0.028	2.129	37.472	-6.1	6.1	22.9	2018.07.10–2018.10.19
2018/09/20	ETH3	18.420	0.273	0.027	17.864	-0.273	0.026	1.815	37.382	70.9	6.7	21.9	2018.07.10–2018.10.19
2018/09/20	ETH2	-11.547	-0.917	0.063	-11.269	-0.637	0.029	-9.976	19.962	95.5	5.4	19.2	2018.07.10–2018.10.19
2018/09/21	ETH1	17.829	-0.139	0.071	17.302	-0.657	0.027	2.110	36.921	17.8	5.6	20.3	2018.07.10–2018.10.19
2018/09/22	Carrara	18.444	-0.009	0.039	17.890	-0.553	0.023	2.098	37.416	54.9	5.9	21.7	2018.07.10–2018.10.19
2018/09/23	ETH3	18.285	0.251	0.036	17.721	-0.304	0.020	1.783	37.302	42.5	6.1	21.4	2018.07.10–2018.10.19
2018/09/23	ETH1	17.776	-0.099	0.046	17.201	-0.665	0.020	2.103	36.835	81.0	6.0	21.2	2018.07.10–2018.10.19
2018/09/24	MuStd	24.005	0.437	0.039	23.268	-0.283	0.022	1.697	42.919	76.3	5.6	19.3	2018.07.10–2018.10.19
2018/09/24	Carrara	18.522	0.038	0.025	17.920	-0.553	0.024	2.092	37.452	159.1	6.3	22.0	2018.07.10–2018.10.19
2018/09/25	ETH3	18.347	0.279	0.089	17.757	-0.301	0.024	1.773	37.345	119.2	6.7	23.2	2018.07.10–2018.10.19
2018/09/26	ETH1	17.815	-0.143	0.043	17.289	-0.660	0.018	2.108	36.913	29.6	6.5	23.2	2018.07.10–2018.10.19
2018/09/27	ETH2	-11.532	-0.902	0.047	-11.268	-0.635	0.014	-10.048	20.032	111.1	5.6	20.2	2018.07.10–2018.10.19
2018/09/28	ETH4	-11.481	-0.744	0.044	-11.174	-0.433	0.027	-10.067	19.943	-5.9	6.1	20.2	2018.07.10–2018.10.19
2018/09/28	ETH2	-11.368	-0.932	0.070	-11.074	-0.634	0.020	-10.022	20.202	33.2	5.2	17.9	2018.07.10–2018.10.19
2018/09/29	ETH3	18.312	0.306	0.036	17.719	-0.276	0.023	1.773	37.283	141.3	6.1	21.7	2018.07.10–2018.10.19
2018/09/29	Carrara	18.459	0.054	0.033	17.852	-0.543	0.035	2.076	37.389	143.6	6.5	24.6	2018.07.10–2018.10.19
2018/10/02	Carrara	18.548	0.008	0.045	17.953	-0.577	0.014	2.132	37.470	120.1	6.9	26.1	2018.07.10–2018.10.19
2018/10/02	ETH1	17.859	-0.093	0.041	17.250	-0.691	0.023	2.150	36.865	163.5	6.8	25.5	2018.07.10–2018.10.19
2018/10/02	ETH2	-11.522	-0.996	0.043	-11.146	-0.617	0.023	-9.941	20.033	-102.5	5.6	18.7	2018.07.10–2018.10.19
2018/10/03	ETH3	18.228	0.200	0.051	17.732	-0.287	0.027	1.741	37.337	-80.8	5.5	19.3	2018.07.10–2018.10.19
2018/10/04	ETH2	-11.724	-0.913	0.051	-11.446	-0.632	0.025	-10.025	19.826	121.0	6.1	22.9	2018.07.10–2018.10.19
2018/10/04	ETH4	-11.687	-0.739	0.037	-11.380	-0.429	0.016	-10.070	19.733	31.4	5.8	21.7	2018.07.10–2018.10.19
2018/10/05	ETH3	18.129	0.217	0.042	17.628	-0.275	0.013	1.715	37.247	-63.9	5.3	19.3	2018.07.10–2018.10.19
2018/10/06	MuStd	24.030	0.446	0.036	23.301	-0.267	0.011	1.722	42.911	22.3	9.4	33.8	2018.07.10–2018.10.19
2018/10/10	Carrara	18.548	0.052	0.053	17.925	-0.559	0.022	2.128	37.429	167.6	7.6	29.7	2018.07.10–2018.10.19
2018/10/10	ETH2	-11.590	-1.004	0.054	-11.223	-0.633	0.022	-9.977	20.007	-93.7	5.8	20.7	2018.07.10–2018.10.19
2018/10/11	MuStd	23.622	0.396	0.040	22.964	-0.247	0.021	1.599	42.675	-105.4	5.5	21.0	2018.07.10–2018.10.19
2018/10/12	Carrara	18.462	0.021	0.068	17.874	-0.557	0.030	2.106	37.395	82.9	6.4	24.8	2018.07.10–2018.10.19
2018/10/12	ETH1	17.931	-0.098	0.037	17.363	-0.656	0.021	2.149	36.944	73.8	6.5	24.7	2018.07.10–2018.10.19
2018/10/13	ETH3	18.361	0.241	0.033	17.840	-0.271	0.012	1.805	37.366	-36.6	6.1	24.9	2018.07.10–2018.10.19
2018/10/13	ETH2	-11.637	-0.919	0.068	-11.361	-0.639	0.031	-10.041	19.935	105.6	5.7	21.4	2018.07.10–2018.10.19
2018/10/14	ETH4	-11.782	-0.794	0.035	-11.405	-0.412	0.021	-10.069	19.691	-61.4	5.2	19.3	2018.07.10–2018.10.19
2018/10/14	ETH2	-11.872	-0.979	0.065	-11.557	-0.660	0.027	-10.048	19.764	26.8	7.8	28.6	2018.07.10–2018.10.19
2018/10/14	ETH1	17.689	-0.124	0.051	17.138	-0.666	0.025	2.095	36.781	50.1	8.0	27.5	2018.07.10–2018.10.19
2018/10/15	Carrara	18.584	0.054	0.039	17.968	-0.551	0.015	2.114	37.477	144.5	5.4	20.7	2018.07.10–2018.10.19
2018/10/16	ETH3	18.310	0.314	0.028	17.684	-0.300	0.035	1.779	37.266	128.8	5.8	20.8	2018.07.10–2018.10.19
2018/10/17	Carrara	18.433	-0.009	0.062	17.854	-0.578	0.037	2.086	37.417	53.0	6.3	24.3	2018.07.10–2018.10.19
2018/10/17	MuStd	23.955	0.460	0.046	23.210	-0.267	0.019	1.678	42.863	67.7	6.5	23.7	2018.07.10–2018.10.19
2018/10/18	ETH1	17.810	-0.133	0.036	17.253	-0.680	0.019	2.124	36.881	48.3	6.3	22.2	2018.07.10–2018.10.19
2018/10/19	ETH2	-11.506	-0.932	0.058	-11.248	-0.672	0.030	-9.922	19.965	96.4	7.7	26.9	2018.07.10–2018.10.19
2018/10/19	Carrara	18.579	0.013	0.044	17.975	-0.580	0.024	2.123	37.505	109.2	7.0	26.3	2018.07.10–2018.10.19
2018/10/20	MuStd	23.927	0.401	0.033	23.257	-0.253	0.017	1.706	42.868	-76.0	6.4	23.4	2018.07.10–2018.10.19
2018/10/21	ETH3	18.250	0.241	0.065	17.684	-0.315	0.021	1.787	37.272	25.8	6.5	22.2	2018.07.10–2018.10.19

2018/10/21	ETH1	17.832	-0.109	0.042	17.246	-0.684	0.029	2.141	36.863	82.8	7.4	26.5	2018.07.10–2018.10.19
2018/10/21	ETH2	-11.907	-0.994	0.045	-11.561	-0.645	0.015	-10.046	19.743	-14.6	6.1	21.6	2018.07.10–2018.10.19

ID	Sample	Weight (mg)	d45	d45 SD	d46	d46 SD	d47	d47 SD	d48	d48 SD	d49	d49 SD
2019-01-09 01:13 CET	ETH2	10.0	-5.5	0.0	-5.2	0.0	-11.439	0.0130	-10.433	0.0430	7.051	2.7
2019-01-09 05:27 CET	ETH2	10.7	-5.6	0.0	-5.2	0.0	-11.531	0.0210	-10.502	0.0800	8.910	2.6
2019-01-09 09:44 CET	ETH4	11.000	-5.6	0.0	-5.3	0.0	-11.344	0.0180	-10.445	0.0800	6.520	2.7
2019-01-09 14:20 CET	ETH4	9.700	-5.6	0.0	-5.5	0.0	-11.548	0.0240	-10.897	0.0730	3.750	2.3
2019-01-10 03:23 CET	Carrara	9.8	6.4	0.0	11.9	0.0	17.808	0.0330	23.468	0.0730	-33.855	3.3
2019-01-15 03:03 CET	Carrara	9.5	6.4	0.0	12.1	0.0	18.003	0.0320	23.689	0.0560	-35.827	3.4
2019-01-19 19:43 CET	Carrara	9.8	6.5	0.0	12.1	0.0	18.123	0.0320	23.787	0.0910	12.768	1.6
2019-01-19 23:59 CET	Carrara	9.7	6.4	0.0	12.0	0.0	17.970	0.0250	23.688	0.0700	12.261	1.1
2019-01-27 01:34 CET	Carrara	10.1	6.4	0.0	12.0	0.0	17.918	0.0270	23.505	0.1020	11.534	1.6
2019-01-30 06:18 CET	Carrara	9.8	6.4	0.0	12.0	0.0	17.961	0.0410	23.634	0.0990	10.849	1.4
2019-01-10 07:39 CET	ETH1	9.4	6.3	0.0	11.4	0.0	17.090	0.0250	22.333	0.0880	-33.226	2.9
2019-01-10 11:55 CET	ETH1	9.6	6.4	0.0	11.6	0.0	17.405	0.0180	22.733	0.0820	-34.629	2.6
2019-01-14 09:17 CET	ETH4	9.660	-5.5	0.0	-5.3	0.0	-11.332	0.0220	-10.617	0.1120	6.196	3.6
2019-01-18 13:30 CET	ETH4	9.530	-5.6	0.0	-5.4	0.0	-11.526	0.0280	-10.792	0.0780	-3.368	1.2
2019-01-19 06:45 CET	ETH4	9.530	-5.6	0.0	-5.3	0.0	-11.387	0.0230	-10.569	0.0670	-4.666	1.6
2019-01-21 15:30 CET	ETH4	9.590	-5.7	0.0	-5.5	0.0	-11.663	0.0340	-10.910	0.0930	-5.072	1.3
2019-01-22 13:01 CET	ETH1	9.8	6.4	0.0	11.5	0.0	17.357	0.0120	22.630	0.0650	13.151	1.2
2019-01-22 21:35 CET	ETH1	9.7	6.5	0.0	11.6	0.0	17.398	0.0280	22.696	0.0940	11.788	1.6
2019-01-24 05:40 CET	ETH4	9.740	-5.6	0.0	-5.2	0.0	-11.323	0.0260	-10.391	0.0750	-4.027	1.4
2019-01-26 13:08 CET	ETH1	10.4	6.4	0.0	11.4	0.0	17.217	0.0240	22.396	0.0950	11.296	1.3
2019-01-26 17:17 CET	ETH1	10.0	6.4	0.0	11.4	0.0	17.258	0.0220	22.420	0.1070	11.385	0.8
2019-01-29 08:19 CET	ETH4	9.460	-5.6	0.0	-5.4	0.0	-11.455	0.0220	-10.656	0.0820	-3.614	1.4
2019-01-29 17:57 CET	ETH1	10.0	6.4	0.0	11.4	0.0	17.208	0.0180	22.449	0.0990	11.503	1.9
2019-01-31 23:55 CET	ETH1	10.4	6.4	0.0	11.5	0.0	17.320	0.0210	22.529	0.1450	11.233	1.4
2019-01-11 07:19 CET	ETH2	12.8	-5.5	0.0	-5.1	0.0	-11.327	0.0250	-10.261	0.0930	9.959	2.6
2019-01-11 11:32 CET	ETH2	10.7	-5.5	0.0	-5.3	0.0	-11.525	0.0140	-10.579	0.0700	9.977	3.6

2019-01-14 04:59 CET	ETH3	9.0	6.0	0.0	11.7	0.0	17.490	0.0280	23.125	0.1090	-37.017	4.2
2019-01-17 02:47 CET	ETH2	9.7	-5.6	0.0	-5.4	0.0	-11.647	0.0180	-10.734	0.0760	-3.655	1.2
2019-01-17 15:45 CET	ETH2	9.7	-5.6	0.0	-5.4	0.0	-11.684	0.0340	-10.770	0.0610	-3.875	1.5
2019-01-20 17:19 CET	ETH2	10.9	-5.5	0.0	-5.2	0.0	-11.428	0.0190	-10.381	0.0710	-4.745	1.3
2019-01-26 00:41 CET	ETH2	10.3	-5.6	0.0	-5.3	0.0	-11.624	0.0290	-10.681	0.0860	-4.797	1.4
2019-01-30 10:28 CET	ETH2	9.9	-5.6	0.0	-5.2	0.0	-11.531	0.0430	-10.455	0.0950	-3.394	3.2
2019-01-18 09:12 CET	ETH3	9.7	6.1	0.0	11.8	0.0	17.751	0.0280	23.289	0.0940	12.701	1.8
2019-01-21 06:19 CET	ETH3	9.5	6.2	0.0	11.8	0.0	17.783	0.0240	23.402	0.0640	12.655	1.5
2019-01-23 06:11 CET	ETH3	9.5	6.2	0.0	11.9	0.0	17.887	0.0260	23.599	0.1110	12.488	1.3
2019-01-30 23:01 CET	ETH3	9.9	6.1	0.0	11.9	0.0	17.810	0.0240	23.415	0.1220	11.247	1.7
2019-02-02 00:49 CET	ETH3	10.0	6.1	0.0	11.8	0.0	17.783	0.0240	23.314	0.0510	10.918	1.1
2019-02-02 04:58 CET	ETH3	10.8	6.2	0.0	11.9	0.0	17.789	0.0410	23.447	0.0690	11.520	1.0
2019-02-02 13:20 CET	ETH2	9.8	-5.6	0.0	-5.4	0.0	-11.686	0.0340	-10.815	0.1070	-4.966	0.7
2019-02-02 17:29 CET	ETH2	9.9	-5.6	0.0	-5.3	0.0	-11.642	0.0230	-10.655	0.0690	-4.544	1.4
2019-02-02 21:38 CET	ETH1	10.0	6.5	0.0	11.5	0.0	17.358	0.0260	22.552	0.0990	9,48	3.0
2019-02-03 01:47 CET	ETH1	10.5	6.4	0.0	11.5	0.0	17.305	0.0280	22.521	0.0880	10.360	1.6
2019-02-03 05:56 CET	ETH1	10.7	6.5	0.0	11.5	0.0	17.336	0.0210	22.512	0.0790	10.473	2.0
2019-02-03 18:25 CET	ETH4	10.480	-5.6	0.0	-5.0	0.0	-11.089	0.0130	-9.933	0.0570	-3.478	1.2
2019-02-04 02:46 CET	Carrara	10.6	6.4	0.0	12.0	0.0	17.916	0.0160	23.524	0.0670	11.194	1.6
2019-02-04 06:55 CET	Carrara	9.9	6.5	0.0	12.0	0.0	17.937	0.0360	23.539	0.1250	10.885	1.4
2019-02-04 11:27 CET	Carrara	9.9	6.5	0.0	12.0	0.0	17.964	0.0220	23.586	0.0410	11.963	1.9
2019-02-04 15:36 CET	ETH3	10.1	6.2	0.0	11.9	0.0	17.852	0.0270	23.478	0.0610	11.339	1.5
2019-02-05 04:14 CET	ETH3	9.7	6.2	0.0	11.8	0.0	17.813	0.0300	23.356	0.1180	10.812	1.8
2019-02-05 08:25 CET	ETH3	10.4	6.1	0.0	11.8	0.0	17.758	0.0290	23.356	0.0930	9.820	2.9
2019-02-05 12:35 CET	ETH3	9.9	6.1	0.0	11.8	0.0	17.756	0.0260	23.345	0.0820	11.857	2.8
2019-02-06 00:54 CET	Carrara	9.6	6.5	0.0	12.0	0.0	17.987	0.0280	23.614	0.0930	10.891	0.9
2019-02-06 13:20 CET	ETH2	10.8	-5.6	0.0	-5.2	0.0	-11.540	0.0380	-10.494	0.0700	-3.899	2.2
2019-02-07 02:11 CET	ETH1	10.4	6.5	0.0	11.6	0.0	17.425	0.0310	22.686	0.0730	10.872	1.9
2019-02-07 14:59 CET	Carrara	9.9	6.5	0.0	12.0	0.0	17.972	0.0220	23.590	0.0890	11.033	2.3
2019-02-08 03:34 CET	ETH3	9.9	6.2	0.0	11.9	0.0	17.858	0.0230	23.542	0.0780	12.212	1.6
2019-02-09 04:33 CET	ETH1	10.9	6.5	0.0	11.5	0.0	17.318	0.0270	22.491	0.1040	10.652	1.7

2019-02-09 17:00 CET	ETH2	10.1	-5.6	0.0	-5.2	0.0	-11.491	0.0330	-10.447	0.1160	-5.379	2.1
2019-02-10 05:27 CET	ETH3	9.8	6.1	0.0	11.8	0.0	17.696	0.0220	23.402	0.0710	12.309	1.4
2019-02-10 17:52 CET	ETH1	10.1	6.3	0.0	11.5	0.0	17.193	0.0340	22.547	0.0670	10.258	1.3
2019-02-11 02:10 CET	ETH2	10.4	-5.5	0.0	-5.1	0.0	-11.312	0.0310	-10.202	0.0790	-5.428	1.7
2019-02-11 21:11 CET	ETH3	9.9	6.1	0.0	11.9	0.0	17.814	0.0220	23.498	0.0610	12.839	1.3
2019-02-12 09:40 CET	ETH1	10.1	6.4	0.0	11.5	0.0	17.339	0.0350	22.570	0.0720	11.108	1.3
2019-02-12 23:02 CET	ETH3	10.9	6.1	0.0	11.9	0.0	17.839	0.0330	23.455	0.0720	11.566	1.8
2019-02-13 11:28 CET	ETH2	9.9	-5.5	0.0	-5.0	0.0	-11.279	0.0290	-10.054	0.0750	-5.494	1.1
2019-02-14 08:14 CET	ETH4	9.300	-5.6	0.0	-5.2	0.0	-11.283	0.0310	-10.395	0.0660	-5.515	1.3
2019-02-14 20:37 CET	ETH1	11.0	6.4	0.0	11.5	0.0	17.350	0.0240	22.660	0.0420	12.161	1.4
2019-02-15 09:15 CET	Carrara	9.4	6.4	0.0	12.0	0.0	17.997	0.0190	23.744	0.1070	13.530	1.5
2019-02-16 04:32 CET	ETH3	10.7	6.1	0.0	11.8	0.0	17.768	0.0260	23.442	0.0910	11.768	1.7
2019-02-17 05:26 CET	ETH2	9.9	-5.5	0.0	-5.0	0.0	-11.162	0.0240	-9.947	0.0750	-4.556	1.5
2019-02-17 17:53 CET	ETH1	10.1	6.4	0.0	11.5	0.0	17.320	0.0250	22.603	0.0630	12.881	1.6
2019-02-18 06:20 CET	ETH2	10.0	-5.5	0.0	-4.9	0.0	-11.040	0.0290	-9.792	0.1010	-5.588	1.5
2019-02-20 20:15 CET	ETH1	10.6	6.4	0.0	11.5	0.0	17.329	0.0210	22.560	0.0960	12.823	1.1
2019-02-21 00:24 CET	ETH2	10.9	-5.4	0.0	-4.9	0.0	-11.061	0.0170	-9.896	0.1050	-4.907	1.5
2019-03-01 09:32 CET	Carrara	10.100	6.4	0.0	11.9	0.0	17.884	0.0210	23.172	0.0760	12.948	1.4
2019-03-01 13:41 CET	Carrara	8.100	6.4	0.0	12.0	0.0	17.922	0.0260	23.214	0.0920	14.327	1.5
2019-03-02 02:11 CET	Carrara	5.470	6.4	0.0	12.0	0.0	17.942	0.0310	23.334	0.0770	14.420	2.1
2019-03-02 06:21 CET	Carrara	3.210	6.4	0.0	12.0	0.0	17.963	0.0260	23.341	0.0790	18.717	1.7
2019-03-02 10:28 CET	Carrara	10.870	6.4	0.0	11.8	0.0	17.669	0.0240	22.913	0.1200	12.129	1.5
2019-03-02 14:46 CET	Carrara	7.980	6.4	0.0	12.0	0.0	17.903	0.0250	23.379	0.0770	13.923	1.5
2019-03-02 18:52 CET	Carrara	5.290	6.4	0.0	12.0	0.0	17.914	0.0300	23.301	0.0730	14.848	0.8
2019-03-02 23:01 CET	Carrara	2.960	6.4	0.0	12.0	0.0	17.977	0.0130	23.442	0.0860	19.096	0.8
2019-03-03 03:21 CET	Carrara	8.110	6.4	0.0	11.8	0.0	17.683	0.0290	22.998	0.1230	12.938	1.1
2019-03-03 07:30 CET	ETH1	10.1	6.4	0.0	11.4	0.0	17.271	0.0320	22.239	0.0530	11.812	0.6
2019-03-03 11:42 CET	ETH1	11.0	6.4	0.0	11.4	0.0	17.274	0.0280	22.233	0.0810	11.774	1.7
2019-03-03 15:46 CET	ETH2	10.7	-5.5	0.0	-5.3	0.0	-11.533	0.0270	-10.513	0.0900	-4.104	1.7
2019-03-03 20:01 CET	ETH2	10.7	-5.5	0.0	-5.2	0.0	-11.448	0.0310	-10.368	0.1010	-5.190	1.9
2019-03-04 00:15 CET	ETH2	10.0	-5.5	0.0	-5.2	0.0	-11.424	0.0320	-10.674	0.0690	-5.002	1.5

2019-03-04 04:25 CET	ETH1	10.7	6.4	0.0	11.4	0.0	17.219	0.0290	22.236	0.0420	11.497	1.2
2019-03-04 08:28 CET	ETH1	10.0	6.4	0.0	11.4	0.0	17.223	0.0220	22.290	0.0610	12.452	1.0
2019-03-04 12:45 CET	ETH2	10.9	-5.5	0.0	-5.2	0.0	-11.424	0.0320	-10.674	0.0690	-5.002	1.5
2019-03-05 02:55 CET	ETH2	9.9	-5.5	0.0	-5.2	0.0	-11.498	0.0300	-10.636	0.0650	-4.269	1.0
2019-03-05 06:59 CET	ETH1	10.0	6.4	0.0	11.3	0.0	17.108	0.0210	22.573	0.1010	12.434	1.3
2019-03-05 11:09 CET	ETH3	10.3	6.1	0.0	11.8	0.0	17.729	0.0140	23.747	0.1140	13.862	1.8
2019-03-06 01:02 CET	ETH3	9.9	6.1	0.0	11.8	0.0	17.731	0.0180	23.713	0.0830	13.085	1.7
2019-03-06 05:11 CET	Carrara	9.6	6.4	0.0	12.1	0.0	18.078	0.0290	24.260	0.1030	13.406	1.1
2019-03-06 09:29 CET	Carrara	10.3	6.4	0.0	12.2	0.0	18.149	0.0210	24.414	0.0970	13.624	1.1
2019-03-06 13:38 CET	ETH1	10.3	6.4	0.0	11.5	0.0	17.321	0.0270	22.939	0.1050	12.450	1.1
2019-03-07 06:24 CET	ETH1	10.3	6.4	0.0	11.4	0.0	17.251	0.0270	22.806	0.1280	12.522	1.0
2019-03-07 10:34 CET	ETH2	10.1	-5.5	0.0	-5.2	0.0	-11.474	0.0260	-10.616	0.1360	-5.869	1.5
2019-03-07 14:45 CET	ETH2	9.5	-5.6	0.0	-5.4	0.0	-11.628	0.0180	-10.869	0.0980	-5.158	1.6
2019-03-08 07:28 CET	ETH4	9.5	-5.6	0.0	-5.3	0.0	-11.334	0.0200	-10.670	0.0960	-5.704	1.4
2019-03-08 11:34 CET	ETH4	10.1	-5.6	0.0	-5.4	0.0	-11.439	0.0330	-10.914	0.1270	-4.845	1.7
2019-03-09 00:09 CET	ETH3	9.6	5.9	0.0	11.5	0.0	17.296	0.0310	23.280	0.0730	13.518	0.9
2019-03-09 04:13 CET	ETH3	10.4	6.1	0.0	11.8	0.0	17.685	0.0360	23.770	0.0780	13.234	1.3
2019-03-09 08:24 CET	ETH1	9.6	6.4	0.0	11.4	0.0	17.201	0.0240	22.806	0.0970	13.330	1.9
2019-03-09 12:39 CET	ETH1	9.9	6.4	0.0	11.4	0.0	17.213	0.0250	22.822	0.0960	13.160	1.3
2019-03-09 20:52 CET	ETH2	11.9	-5.5	0.0	-5.1	0.0	-11.371	0.0280	-10.480	0.1000	-6.016	1.8
2019-03-10 09:21 CET	ETH3	11.0	6.1	0.0	11.8	0.0	17.618	0.0320	23.704	0.0700	13.712	0.8
2019-03-10 21:53 CET	ETH1	9.6	6.4	0.0	11.4	0.0	17.230	0.0280	22.852	0.0810	12.870	1.7
2019-03-11 10:19 CET	ETH2	10.3	-5.6	0.0	-5.2	0.0	-11.507	0.0250	-10.717	0.0380	-4.476	1.8
2019-03-12 13:05 CET	ETH3	9.8	6.1	0.0	11.8	0.0	17.765	0.0210	23.890	0.0920	15.294	1.3
2019-03-13 10:09 CET	ETH1	10.2	6.4	0.0	11.5	0.0	17.336	0.0250	23.019	0.0610	13.855	0.9
2019-03-14 09:25 CET	ETH2	10.6	-5.6	0.0	-5.3	0.0	-11.558	0.0180	-10.824	0.0690	-6.263	1.5
2019-03-14 13:32 CET	ETH1	10.7	6.4	0.0	11.5	0.0	17.362	0.0300	23.084	0.1010	13.108	2.2
2019-03-15 02:00 CET	ETH3	11.1	6.2	0.0	11.8	0.0	17.784	0.0240	23.882	0.0940	13.369	1.6
2019-03-16 18:11 CET	ETH1	9.9	6.4	0.0	11.4	0.0	17.260	0.0280	22.501	0.0830	13.727	1.5
2019-03-17 06:37 CET	ETH2	10.0	-5.5	0.0	-5.0	0.0	-11.245	0.0120	-10.060	0.0750	-6.251	1.6
2019-03-17 19:04 CET	ETH3	10.1	6.1	0.0	11.8	0.0	17.730	0.0280	23.469	0.0830	15.381	1.6

2019-03-18 07:30 CET	ETH1	10.2	6.4	0.0	11.4	0.0	17.263	0.0280	22.534	0.0660	13.614	1.7
2019-03-19 04:18 CET	ETH2	10.6	-5.5	0.0	-5.2	0.0	-11.491	0.0280	-10.487	0.1160	-6.308	2.4
2019-03-19 20:58 CET	ETH3	9.7	6.1	0.0	11.8	0.0	17.718	0.0300	23.405	0.0650	14.558	1.3
2019-03-20 09:24 CET	ETH1	10.3	6.4	0.0	11.4	0.0	17.235	0.0130	22.505	0.0930	13.851	1.3
2019-03-21 06:11 CET	ETH2	9.7	-5.5	0.0	-5.1	0.0	-11.332	0.0290	-10.233	0.0610	-6.817	1.5
2019-03-22 04:15 CET	ETH1	10.2	6.4	0.0	11.5	0.0	17.363	0.0230	22.747	0.0940	14.257	1.5
2019-03-23 01:41 CET	ETH2	10.0	-5.5	0.0	-5.1	0.0	-11.379	0.0210	-10.335	0.0710	-6.647	1.9
2019-03-23 14:10 CET	ETH3	10.0	6.1	0.0	11.8	0.0	17.684	0.0180	23.439	0.0980	14.734	2.1
2019-03-24 02:35 CET	ETH1	9.9	6.4	0.0	11.4	0.0	17.171	0.0230	22.455	0.0980	13.522	1.2
2019-03-24 15:00 CET	ETH3	9.8	6.1	0.0	11.8	0.0	17.705	0.0170	23.452	0.0780	15.584	2.1
2019-03-25 15:57 CET	ETH4	10.1	-5.6	0.0	-5.2	0.0	-11.305	0.0230	-10.458	0.1540	-6.102	2.0
2019-03-25 03:28 CET	ETH2	10.5	-5.6	0.0	-5.2	0.0	-11.508	0.0280	-10.546	0.0830	-6.174	2.4
2019-03-26 08:36 CET	ETH3	9.6	6.1	0.0	11.9	0.0	17.759	0.0230	23.635	0.0740	14.908	1.5
2019-03-27 15:59 CET	ETH1	10.1	6.4	0.0	11.4	0.0	17.199	0.0320	22.509	0.1250	13.959	1.6
2019-03-28 08:35 CET	ETH2	9.5	-5.6	0.0	-5.2	0.0	-11.483	0.0160	-10.486	0.1100	-6.801	1.3
2019-03-29 05:25 CET	ETH3	9.8	5.9	0.0	11.7	0.0	17.423	0.0290	23.276	0.1220	14.068	1.4
2019-03-30 02:58 CET	ETH1	9.8	6.3	0.0	11.3	0.0	16.978	0.0280	22.420	0.0730	13.501	1.7
2019-03-30 15:24 CET	ETH2	9.7	-5.5	0.0	-5.2	0.0	-11.439	0.0250	-10.413	0.0740	-6.463	1.5
2019-03-31 04:50 CEST	ETH3	10.0	6.1	0.0	11.8	0.0	17.637	0.0250	23.411	0.0960	14.565	1.5
2019-03-31 17:15 CEST	ETH1	9.8	6.4	0.0	11.4	0.0	17.270	0.0300	22.673	0.0830	14.210	1.6
2019-04-01 05:52 CEST	ETH2	10.1	-5.5	0.0	-5.1	0.0	-11.374	0.0220	-10.296	0.1110	-6.519	1.7
2019-04-02 02:37 CEST	ETH3	9.9	6.1	0.0	11.9	0.0	17.765	0.0270	23.587	0.1010	13.939	2.2
2019-04-02 19:16 CEST	ETH1	10.3	6.4	0.0	11.5	0.0	17.265	0.0260	22.668	0.1010	13.586	1.4
2019-04-03 11:53 CEST	ETH2	10.1	-5.6	0.0	-5.2	0.0	-11.457	0.0370	-10.428	0.0650	-7.252	1.7
2019-04-04 08:38 CEST	ETH1	10.9	6.5	0.0	11.5	0.0	17.359	0.0290	22.763	0.0680	13.656	2.3
2019-04-04 12:53 CEST	ETH2	10.1	-5.5	0.0	-5.1	0.0	-11.352	0.0290	-10.341	0.0600	-7.861	1.5
2019-04-05 09:39 CEST	ETH3	10.3	6.1	0.0	11.9	0.0	17.782	0.0200	23.645	0.1070	13.953	2.5
2019-04-06 02:20 CEST	ETH4	10.1	-5.6	0.0	-5.4	0.0	-11.506	0.0280	-10.785	0.0700	-6.949	1.5
2019-04-06 06:26 CEST	ETH1	10.6	6.4	0.0	11.5	0.0	17.275	0.0260	22.651	0.0990	12.619	1.3
2019-04-06 18:54 CEST	ETH2	10.9	-5.5	0.0	-5.2	0.0	-11.432	0.0200	-10.466	0.0660	-6.615	1.2
2019-04-07 07:20 CEST	ETH3	10.3	6.1	0.0	11.8	0.0	17.675	0.0160	23.454	0.0540	13.334	1.6

2019-04-07 19:45 CEST	ETH1	10.9	6.4	0.0	11.5	0.0	17.306	0.0270	22.798	0.1140	14.445	1.9
2019-04-08 08:35 CEST	ETH2	9.4	-5.6	0.0	-5.1	0.0	-11.395	0.0220	-10.353	0.0920	-5.688	1.3
2019-04-09 05:24 CEST	ETH3	9.9	6.1	0.0	11.8	0.0	17.662	0.0220	23.521	0.1010	13.879	2.0
2019-04-10 02:05 CEST	ETH1	9.7	6.4	0.0	11.5	0.0	17.266	0.0290	22.752	0.0680	13.596	2.6
2019-04-10 22:59 CEST	ETH2	9.7	-5.6	0.0	-5.2	0.0	-11.522	0.0230	-10.583	0.1080	-7.123	1.3
2019-04-11 11:25 CEST	ETH3	9.7	6.1	0.0	11.8	0.0	17.653	0.0300	23.643	0.0630	14.169	2.0
2019-04-12 08:06 CEST	ETH4	10.7	-5.6	0.0	-5.4	0.0	-11.491	0.0290	-10.793	0.1140	-8.512	1.7
2019-04-12 21:58 CEST	Carrara	9.7	6.4	0.0	12.2	0.0	18.135	0.0250	24.258	0.1070	14.625	1.7
2019-04-13 10:24 CEST	ETH2	10.7	-5.6	0.0	-5.3	0.0	-11.554	0.0180	-10.671	0.0520	-7.615	1.4
2019-04-13 22:50 CEST	ETH3	9.9	6.1	0.0	11.8	0.0	17.716	0.0290	23.540	0.0590	14.318	1.8
2019-04-14 11:15 CEST	ETH1	10.7	6.4	0.0	11.5	0.0	17.291	0.0310	22.778	0.0690	13.275	1.6
2019-04-14 23:42 CEST	ETH4	10.2	-5.6	0.0	-5.4	0.0	-11.464	0.0270	-10.848	0.0780	-6.146	2.1
2019-04-15 13:22 CEST	ETH2	10.7	-5.5	0.0	-5.2	0.0	-11.476	0.0140	-10.524	0.0730	-7.086	2.0
2019-04-16 02:08 CEST	ETH1	10.5	6.5	0.0	11.5	0.0	17.318	0.0270	22.773	0.1090	13.570	1.4
2019-04-16 06:21 CEST	ETH2	10.2	-5.3	0.0	-4.8	0.0	-10.757	0.0280	-9.598	0.1180	-6.833	2.0
2019-04-16 23:06 CEST	ETH3	10.0	6.1	0.0	11.9	0.0	17.738	0.0270	23.658	0.1380	15.015	1.4
2019-04-17 03:15 CEST	Carrara	10.0	6.4	0.0	12.1	0.0	18.015	0.0290	24.099	0.0890	13.403	1.5
2019-04-17 11:32 CEST	ETH1	10.6	6.4	0.0	11.5	0.0	17.308	0.0220	22.808	0.0940	15.288	1.4
2019-04-18 04:06 CEST	ETH2	9.9	-5.5	0.0	-5.2	0.0	-11.479	0.0130	-10.552	0.1150	-7.710	1.7
2019-04-18 16:38 CEST	ETH3	10.0	6.1	0.0	11.8	0.0	17.766	0.0300	23.685	0.1540	13.483	1.3
2019-04-19 05:05 CEST	ETH4	9.9	-5.6	0.0	-5.1	0.0	-11.199	0.0210	-10.263	0.0970	-6.808	1.8
2019-04-19 09:13 CEST	ETH1	10.0	6.3	0.0	11.3	0.0	17.053	0.0210	22.461	0.0660	13.711	1.4
2019-04-19 21:41 CEST	ETH2	10.3	-5.6	0.0	-5.2	0.0	-11.465	0.0310	-10.498	0.0700	-6.162	1.7
2019-04-20 22:34 CEST	ETH1	10.6	6.5	0.0	11.7	0.0	17.547	0.0250	23.161	0.0460	13.428	1.0
2019-04-22 00:39 CEST	ETH3	10.3	6.1	0.0	11.8	0.0	17.759	0.0300	23.640	0.1150	13.713	1.4
2019-04-22 13:07 CEST	ETH1	10.3	6.4	0.0	11.6	0.0	17.389	0.0240	22.978	0.1010	13.494	1.2
2019-04-22 21:24 CEST	ETH4	10.1	-5.6	0.0	-5.4	0.0	-11.482	0.0220	-10.836	0.1020	-6.636	1.7
2019-04-23 01:33 CEST	ETH2	11.2	-5.6	0.0	-5.2	0.0	-11.439	0.0350	-10.440	0.1330	-7.135	1.5
2019-04-23 14:06 CEST	ETH3	11.0	6.1	0.0	11.8	0.0	17.736	0.0360	23.590	0.1060	14.225	1.1
2019-04-24 11:11 CEST	ETH1	9.4	6.4	0.0	11.4	0.0	17.254	0.0270	22.679	0.0660	12.746	1.5
2019-04-25 03:57 CEST	ETH2	9.9	-5.6	0.0	-5.1	0.0	-11.355	0.0170	-10.305	0.0840	-7.639	1.4

2019-04-25 20:35 CEST	ETH3	10.2	6.1	0.0	11.9	0.0	17.775	0.0160	23.723	0.0940	13.485	1.0
2019-04-26 09:01 CEST	ETH1	10.3	6.4	0.0	11.5	0.0	17.313	0.0420	22.851	0.0800	13.937	1.9
2019-04-26 23:41 CEST	ETH1	10.4	6.5	0.0	11.5	0.0	17.321	0.0250	22.741	0.0720	13.685	1.5
2019-04-27 03:50 CEST	ETH2	10.5	-5.5	0.0	-5.3	0.0	-11.544	0.0260	-10.707	0.0780	-7.923	2.4
2019-04-27 16:26 CEST	ETH3	10.4	6.1	0.0	11.8	0.0	17.652	0.0290	23.579	0.0740	14.069	2.0
2019-04-28 05:03 CEST	ETH1	10.2	6.4	0.0	11.4	0.0	17.238	0.0200	22.661	0.0830	13.495	1.2
2019-04-28 09:15 CEST	Carrara	10.1	6.4	0.0	12.1	0.0	17.979	0.0260	24.029	0.0610	14.159	1.7
2019-04-28 17:37 CEST	ETH2	9.7	-5.2	0.0	-4.6	0.0	-10.573	0.0180	-9.331	0.0640	-6.352	1.5
2019-04-28 21:47 CEST	ETH4	10.8	-5.4	0.0	-5.0	0.0	-10.971	0.0280	-10.156	0.0840	-7.165	1.6
2019-04-29 06:11 CEST	ETH3	11.4	6.1	0.0	11.7	0.0	17.596	0.0140	23.400	0.0600	12.809	1.1
2019-04-30 07:53 CEST	ETH1	10.5	6.4	0.0	11.4	0.0	17.274	0.0140	22.735	0.1340	13.731	1.8
2019-05-01 00:48 CEST	ETH2	9.6	-5.5	0.0	-4.9	0.0	-11.150	0.0260	-9.980	0.1260	-7.503	1.0
2019-05-01 13:27 CEST	ETH3	10.0	6.1	0.0	11.7	0.0	17.615	0.0230	23.422	0.0960	13.409	1.7
2019-05-02 02:08 CEST	ETH4	9.4	-5.6	0.0	-5.2	0.0	-11.219	0.0270	-10.409	0.0910	-6.891	1.5
2019-05-02 23:39 CEST	ETH1	9.5	6.4	0.0	11.4	0.0	17.262	0.0340	22.673	0.1020	12.926	1.6
2019-05-03 12:26 CEST	ETH2	9.5	-5.5	0.0	-5.1	0.0	-11.383	0.0250	-10.434	0.0600	-7.064	1.6
2019-05-04 07:00 CEST	ETH3	9.6	6.1	0.0	11.8	0.0	17.679	0.0290	23.669	0.0530	13.658	2.1
2019-05-04 19:54 CEST	ETH4	9.6	-5.6	0.0	-4.9	0.0	-10.983	0.0190	-9.847	0.1230	-5.972	1.6
2019-05-05 00:16 CEST	Carrara	9.6	6.3	0.0	12.0	0.0	17.804	0.0300	23.888	0.0530	13.021	2.0
2019-05-05 08:54 CEST	ETH1	11.0	6.4	0.0	11.3	0.0	17.106	0.0280	22.459	0.0650	12.728	1.4
2019-05-05 21:57 CEST	ETH2	10.1	-5.5	0.0	-5.0	0.0	-11.217	0.0360	-10.076	0.0820	-9.064	1.5
2019-05-06 11:04 CEST	ETH3	9.9	6.1	0.0	11.8	0.0	17.708	0.0220	23.673	0.0810	13.953	1.9
2019-05-07 04:25 CEST	ETH1	9.6	6.5	0.0	11.5	0.0	17.329	0.0240	22.784	0.1050	12.503	1.5
2019-05-07 08:35 CEST	ETH2	11.3	-5.5	0.0	-5.0	0.0	-11.230	0.0220	-10.216	0.0800	-8.269	1.4
2019-05-08 02:03 CEST	ETH3	9.6	6.2	0.0	11.8	0.0	17.756	0.0250	23.629	0.1090	14.053	2.2
2019-05-08 15:28 CEST	ETH1	10.1	6.4	0.0	11.5	0.0	17.279	0.0290	22.740	0.1180	13.662	1.8
2019-05-09 09:33 CEST	ETH2	10.8	-5.5	0.0	-5.1	0.0	-11.368	0.0380	-10.358	0.0760	-8.052	1.8
2019-05-10 20:00 CEST	ETH1	10.3	6.3	0.0	11.5	0.0	17.241	0.0250	22.917	0.1570	14.314	1.9
2019-05-11 00:08 CEST	ETH2	9.5	-5.5	0.0	-4.9	0.0	-11.211	0.0240	-9.979	0.0760	-5.083	1.9
2019-05-11 04:18 CEST	ETH3	10.5	6.1	0.0	11.9	0.0	17.747	0.0250	23.929	0.1130	15.589	1.5
2019-05-11 08:25 CEST	ETH4	10.5	-5.6	0.0	-5.0	0.0	-11.154	0.0200	-10.147	0.0810	-5.555	1.8

2019-05-11 12:32 CEST	Carrara	9.7	6.3	0.0	12.1	0.0	17.916	0.0260	24.180	0.0990	14.631	1.6
2019-05-11 16:42 CEST	ETH1	10.5	6.4	0.0	11.7	0.0	17.464	0.0200	23.208	0.0930	14.544	2.2
2019-05-11 20:50 CEST	ETH2	10.6	-5.6	0.0	-5.0	0.0	-11.260	0.0190	-10.085	0.0970	-7.809	1.5
2019-05-12 00:59 CEST	ETH3	9.9	6.1	0.0	12.0	0.0	17.804	0.0200	23.969	0.0610	15.455	1.7
2019-05-12 05:07 CEST	ETH4	10.9	-5.6	0.0	-5.0	0.0	-11.104	0.0240	-10.124	0.1250	-5.686	1.6
2019-05-12 09:16 CEST	Carrara	10.4	6.3	0.0	12.2	0.0	17.982	0.0290	24.309	0.0640	15.738	1.7
2019-05-12 13:24 CEST	ETH1	9.9	6.4	0.0	11.5	0.0	17.252	0.0190	22.831	0.0800	15.519	1.2
2019-05-12 17:33 CEST	ETH2	10.5	-5.5	0.0	-5.0	0.0	-11.327	0.0250	-10.240	0.0820	-5.623	2.0
2019-05-12 21:43 CEST	ETH3	10.1	6.1	0.0	11.9	0.0	17.788	0.0150	23.885	0.0650	15.459	1.6
2019-05-13 01:51 CEST	ETH4	9.6	-5.6	0.0	-4.9	0.0	-11.081	0.0250	-9.889	0.0520	-5.596	1.8
2019-05-13 05:59 CEST	Carrara	10.3	6.3	0.0	12.0	0.0	17.759	0.0250	23.909	0.0820	14.470	1.9
2019-05-13 22:49 CEST	ETH1	10.2	6.4	0.0	11.6	0.0	17.336	0.0240	22.960	0.1040	15.094	1.0
2019-05-14 02:58 CEST	ETH2	10.3	-5.6	0.0	-5.1	0.0	-11.426	0.0200	-10.209	0.1090	-5.779	1.7
2019-05-14 07:08 CEST	ETH3	9.9	6.1	0.0	11.9	0.0	17.738	0.0270	23.890	0.1130	15.528	2.0
2019-05-14 11:17 CEST	ETH4	9.7	-5.6	0.0	-5.0	0.0	-11.137	0.0210	-10.011	0.1040	-5.285	1.9
2019-05-15 16:08 CEST	Carrara	9.9	6.2	0.0	12.0	0.0	17.708	0.0240	23.931	0.1050	14.996	2.0
2019-05-16 23:25 CEST	ETH2	11.6	-5.6	0.0	-5.0	0.0	-11.367	0.0240	-10.211	0.0760	-6.797	0.7

ID	D47 (raw)	D47 SD (raw)	D48 (raw)	D48 SD (raw)	D49 (raw)	D49 SD (raw)	d13C	d13C SD	d18O	d18O SD	Aqui	ETF period
2019-01-09 01:13 CET	-0.656	0.014	-0.0110	0.0450	23.5	2.773	-9.880	0.000	19.910	0.0	10	2019.01.09–2019.03.22
2019-01-09 05:27 CET	-0.670	0.020	-0.0450	0.0820	25.5	2.648	-9.940	0.000	19.890	0.0	10	2019.01.09–2019.03.22
2019-01-09 09:44 CET	-0.421	0.022	0.0810	0.0770	23.1	2.749	-9.960	0.000	19.860	0.0	10	2019.01.09–2019.03.22
2019-01-09 14:20 CET	-0.414	0.025	0.0210	0.0730	20.7	2.291	-9.980	0.000	19.650	0.0	10	2019.01.09–2019.03.22
2019-01-10 03:23 CET	-0.567	0.036	-0.5090	0.0760	-62.5	3.182	2.160	0.000	37.480	0.0	10	2019.01.09–2019.03.22
2019-01-15 03:03 CET	-0.561	0.029	-0.5620	0.0570	-64.7	3.28	2.220	0.000	37.620	0.0	10	2019.01.09–2019.03.22
2019-01-19 19:43 CET	-0.567	0.030	-0.5830	0.0910	-17.7	1.509	2.280	0.000	37.680	0.0	10	2019.01.09–2019.03.22
2019-01-19 23:59 CET	-0.560	0.024	-0.5130	0.0660	-18.0	1.052	2.210	0.000	37.600	0.0	10	2019.01.09–2019.03.22
2019-01-27 01:34 CET	-0.562	0.025	-0.5550	0.1000	-18.6	1.583	2.230	0.000	37.530	0.0	10	2019.01.09–2019.03.22

2019-01-30 06:18 CET	-0.572	0.041	-0.5400	0.0970	-19.3	1.337	2.220	0.000	37.580	0.0	10	2019.01.09–2019.03.22
2019-01-10 07:39 CET	-0.658	0.024	-0.5720	0.0870	-60.8	2.816	2.080	0.000	36.940	0.0	10	2019.01.09–2019.03.22
2019-01-10 11:55 CET	-0.656	0.016	-0.5390	0.0780	-62.6	2.501	2.210	0.000	37.130	0.0	10	2019.01.09–2019.03.22
2019-01-14 09:17 CET	-0.419	0.021	-0.0120	0.1100	22.8	3.656	-9.910	0.000	19.820	0.0	10	2019.01.09–2019.03.22
2019-01-18 13:30 CET	-0.427	0.028	0.0500	0.0790	13.4	1.254	-9.980	0.000	19.690	0.0	10	2019.01.09–2019.03.22
2019-01-19 06:45 CET	-0.446	0.022	0.0250	0.0700	11.8	1.62	-9.950	0.000	19.820	0.0	10	2019.01.09–2019.03.22
2019-01-21 15:30 CET	-0.436	0.033	0.0430	0.0940	11.9	1.37	-10.060	0.000	19.640	0.0	10	2019.01.09–2019.03.22
2019-01-22 13:01 CET	-0.675	0.012	-0.5100	0.0630	-16.1	1.165	2.250	0.000	37.060	0.0	10	2019.01.09–2019.03.22
2019-01-22 21:35 CET	-0.685	0.025	-0.5320	0.0920	-17.6	1.509	2.260	0.000	37.100	0.0	10	2019.01.09–2019.03.22
2019-01-24 05:40 CET	-0.428	0.029	0.0570	0.0740	12.3	1.392	-9.980	0.000	19.900	0.0	10	2019.01.09–2019.03.22
2019-01-26 13:08 CET	-0.677	0.025	-0.4850	0.0920	-17.7	1.256	2.240	0.000	36.930	0.0	10	2019.01.09–2019.03.22
2019-01-26 17:17 CET	-0.665	0.021	-0.5600	0.1070	-17.7	0.775	2.220	0.000	36.980	0.0	10	2019.01.09–2019.03.22
2019-01-29 08:19 CET	-0.428	0.021	0.0700	0.0810	13.0	1.385	-9.970	0.000	19.750	0.0	10	2019.01.09–2019.03.22
2019-01-29 17:57 CET	-0.660	0.016	-0.5510	0.0940	-17.5	1.826	2.150	0.000	36.990	0.0	10	2019.01.09–2019.03.22
2019-01-31 23:55 CET	-0.667	0.023	-0.5610	0.1380	-17.9	1.312	2.230	0.000	37.030	0.0	10	2019.01.09–2019.03.22
2019-01-11 07:19 CET	-0.669	0.025	-0.0610	0.0940	26.2	2.621	-9.870	0.000	20.020	0.0	10	2019.01.09–2019.03.22
2019-01-11 11:32 CET	-0.668	0.015	-0.0290	0.0660	26.6	3.638	-9.890	0.000	19.840	0.0	10	2019.01.09–2019.03.22
2019-01-14 04:59 CET	-0.258	0.028	-0.3720	0.1050	-64.7	4.049	1.770	0.000	37.240	0.0	10	2019.01.09–2019.03.22
2019-01-17 02:47 CET	-0.682	0.021	-0.0580	0.0740	12.9	1.17	-9.930	0.000	19.780	0.0	10	2019.01.09–2019.03.22
2019-01-17 15:45 CET	-0.659	0.034	0.0180	0.0610	12.8	1.504	-9.930	0.000	19.720	0.0	10	2019.01.09–2019.03.22
2019-01-20 17:19 CET	-0.679	0.016	-0.0540	0.0690	11.4	1.321	-9.890	0.000	19.960	0.0	10	2019.01.09–2019.03.22
2019-01-26 00:41 CET	-0.675	0.028	-0.0430	0.0830	11.7	1.444	-9.940	0.000	19.800	0.0	10	2019.01.09–2019.03.22
2019-01-30 10:28 CET	-0.680	0.044	-0.0150	0.0990	12.9	3.26	-9.940	0.000	19.900	0.0	10	2019.01.09–2019.03.22
2019-01-18 09:12 CET	-0.251	0.030	-0.4370	0.0920	-16.8	1.768	1.910	0.000	37.360	0.0	10	2019.01.09–2019.03.22
2019-01-21 06:19 CET	-0.270	0.024	-0.3960	0.0640	-16.9	1.427	1.920	0.000	37.390	0.0	10	2019.01.09–2019.03.22
2019-01-23 06:11 CET	-0.266	0.026	-0.3880	0.1070	-17.3	1.278	1.930	0.000	37.490	0.0	10	2019.01.09–2019.03.22
2019-01-30 23:01 CET	-0.252	0.027	-0.4260	0.1200	-18.3	1.628	1.910	0.000	37.410	0.0	10	2019.01.09–2019.03.22
2019-02-02 00:49 CET	-0.253	0.025	-0.4680	0.0500	-18.6	1.065	1.910	0.000	37.380	0.0	10	2019.01.09–2019.03.22
2019-02-02 04:58 CET	-0.279	0.038	-0.3930	0.0710	-18.1	0.932	1.920	0.000	37.410	0.0	10	2019.01.09–2019.03.22
2019-02-02 13:20 CET	-0.677	0.034	-0.0870	0.1050	11.7	0.733	-9.950	0.000	19.750	0.0	10	2019.01.09–2019.03.22
2019-02-02 17:29 CET	-0.676	0.024	-0.0110	0.0680	12.0	1.376	-9.950	0.000	19.800	0.0	10	2019.01.09–2019.03.22

2019-02-02 21:38 CET	-0.670	0.024	-0.5740	0.1000	-19.7	2.96	2.250	0.000	37.050	0.0	10	2019.01.09–2019.03.22
2019-02-03 01:47 CET	-0.678	0.030	-0.5250	0.0890	-18.8	1.569	2.250	0.000	37.010	0.0	10	2019.01.09–2019.03.22
2019-02-03 05:56 CET	-0.663	0.020	-0.5510	0.0780	-18.7	1.963	2.250	0.000	37.020	0.0	10	2019.01.09–2019.03.22
2019-02-03 18:25 CET	-0.425	0.012	0.0680	0.0610	12.4	1.249	-9.970	0.000	20.130	0.0	10	2019.01.09–2019.03.22
2019-02-04 02:46 CET	-0.572	0.017	-0.5570	0.0620	-18.9	1.532	2.230	0.000	37.540	0.0	10	2019.01.09–2019.03.22
2019-02-04 06:55 CET	-0.576	0.034	-0.5710	0.1200	-19.3	1.325	2.240	0.000	37.550	0.0	10	2019.01.09–2019.03.22
2019-02-04 11:27 CET	-0.563	0.022	-0.5570	0.0420	-18.2	1.839	2.230	0.000	37.570	0.0	10	2019.01.09–2019.03.22
2019-02-04 15:36 CET	-0.254	0.025	-0.4220	0.0580	-18.3	1.44	1.930	0.000	37.440	0.0	10	2019.01.09–2019.03.22
2019-02-05 04:14 CET	-0.251	0.030	-0.4720	0.1170	-18.8	1.752	1.920	0.000	37.410	0.0	10	2019.01.09–2019.03.22
2019-02-05 08:25 CET	-0.267	0.019	-0.4290	0.0920	-19.7	2.839	1.900	0.010	37.380	0.0	10	2019.01.09–2019.03.22
2019-02-05 12:35 CET	-0.265	0.024	-0.4030	0.0840	-17.7	2.694	1.920	0.000	37.370	0.0	10	2019.01.09–2019.03.22
2019-02-06 00:54 CET	-0.565	0.027	-0.5430	0.0950	-19.3	0.844	2.250	0.000	37.570	0.0	10	2019.01.09–2019.03.22
2019-02-06 13:20 CET	-0.670	0.035	-0.0340	0.0740	12.5	2.226	-9.950	0.000	19.890	0.0	10	2019.01.09–2019.03.22
2019-02-07 02:11 CET	-0.650	0.027	-0.5360	0.0640	-18.4	1.874	2.250	0.000	37.100	0.0	10	2019.01.09–2019.03.22
2019-02-07 14:59 CET	-0.569	0.021	-0.5770	0.0860	-19.2	2.221	2.230	0.000	37.580	0.0	10	2019.01.09–2019.03.22
2019-02-08 03:34 CET	-0.272	0.023	-0.3980	0.0770	-17.5	1.534	1.930	0.000	37.460	0.0	10	2019.01.09–2019.03.22
2019-02-09 04:33 CET	-0.662	0.026	-0.5380	0.1020	-18.5	1.649	2.250	0.000	37.000	0.0	10	2019.01.09–2019.03.22
2019-02-09 17:00 CET	-0.672	0.030	-0.0440	0.1140	10.9	2.151	-9.920	0.000	19.920	0.0	10	2019.01.09–2019.03.22
2019-02-10 05:27 CET	-0.268	0.021	-0.3950	0.0670	-17.2	1.318	1.830	0.000	37.390	0.0	10	2019.01.09–2019.03.22
2019-02-10 17:52 CET	-0.655	0.034	-0.5350	0.0660	-18.7	1.214	2.090	0.000	37.030	0.0	10	2019.01.09–2019.03.22
2019-02-11 02:10 CET	-0.647	0.030	-0.0640	0.0790	10.5	1.75	-9.900	0.000	20.060	0.0	10	2019.01.09–2019.03.22
2019-02-11 21:11 CET	-0.251	0.025	-0.3790	0.0580	-16.8	1.288	1.890	0.000	37.430	0.0	10	2019.01.09–2019.03.22
2019-02-12 09:40 CET	-0.658	0.036	-0.5470	0.0720	-18.1	1.233	2.220	0.000	37.050	0.0	10	2019.01.09–2019.03.22
2019-02-12 23:02 CET	-0.258	0.034	-0.4450	0.0660	-18.0	1.766	1.910	0.000	37.440	0.0	10	2019.01.09–2019.03.22
2019-02-13 11:28 CET	-0.660	0.027	-0.0500	0.0770	10.4	1.151	-9.930	0.000	20.130	0.0	10	2019.01.09–2019.03.22
2019-02-14 08:14 CET	-0.426	0.031	0.0110	0.0700	10.8	1.337	-9.960	0.000	19.920	0.0	10	2019.01.09–2019.03.22
2019-02-14 20:37 CET	-0.663	0.021	-0.4500	0.0440	-17.1	1.334	2.250	0.000	37.040	0.0	10	2019.01.09–2019.03.22
2019-02-15 09:15 CET	-0.544	0.019	-0.4570	0.1060	-16.8	1.492	2.220	0.000	37.600	0.0	10	2019.01.09–2019.03.22
2019-02-16 04:32 CET	-0.270	0.024	-0.3610	0.0870	-17.8	1.666	1.910	0.000	37.390	0.0	10	2019.01.09–2019.03.22
2019-02-17 05:26 CET	-0.655	0.026	-0.0640	0.0720	11.1	1.567	-9.880	0.000	20.190	0.0	10	2019.01.09–2019.03.22
2019-02-17 17:53 CET	-0.654	0.023	-0.4950	0.0610	-16.3	1.517	2.210	0.000	37.040	0.0	10	2019.01.09–2019.03.22

2019-02-18 06:20 CET	-0.652	0.026	-0.1090	0.0990	9.9	1.474	-9.860	0.000	20.290	0.0	10	2019.01.09–2019.03.22
2019-02-20 20:15 CET	-0.656	0.020	-0.4930	0.0950	-16.4	1.103	2.250	0.000	37.010	0.0	10	2019.01.09–2019.03.22
2019-02-21 00:24 CET	-0.661	0.014	-0.0340	0.1070	10.6	1.48	-9.770	0.000	20.200	0.0	10	2019.01.09–2019.03.22
2019-03-01 09:32 CET	-0.549	0.021	-0.8110	0.0760	-17.1	1.37	2.220	0.000	37.490	0.0	10	2019.01.09–2019.03.22
2019-03-01 13:41 CET	-0.532	0.027	-0.8230	0.0880	-15.8	1.473	2.210	0.000	37.520	0.0	10	2019.01.09–2019.03.22
2019-03-02 02:11 CET	-0.538	0.028	-0.7510	0.0740	-15.8	2.077	2.210	0.000	37.540	0.0	10	2019.01.09–2019.03.22
2019-03-02 06:21 CET	-0.514	0.024	-0.7580	0.0780	-11.6	1.69	2.200	0.000	37.550	0.0	10	2019.01.09–2019.03.22
2019-03-02 10:28 CET	-0.553	0.023	-0.7450	0.1210	-17.6	1.488	2.170	0.000	37.320	0.0	10	2019.01.09–2019.03.22
2019-03-02 14:46 CET	-0.558	0.024	-0.6720	0.0730	-16.2	1.442	2.210	0.000	37.520	0.0	10	2019.01.09–2019.03.22
2019-03-02 18:52 CET	-0.536	0.029	-0.7470	0.0740	-15.3	0.745	2.200	0.000	37.520	0.0	10	2019.01.09–2019.03.22
2019-03-02 23:01 CET	-0.512	0.011	-0.6770	0.0840	-11.3	0.728	2.200	0.000	37.560	0.0	10	2019.01.09–2019.03.22
2019-03-03 03:21 CET	-0.563	0.025	-0.7010	0.1240	-16.8	1.048	2.170	0.000	37.340	0.0	10	2019.01.09–2019.03.22
2019-03-03 07:30 CET	-0.682	0.032	-0.7580	0.0470	-17.3	0.573	2.240	0.000	36.990	0.0	10	2019.01.09–2019.03.22
2019-03-03 11:42 CET	-0.671	0.027	-0.7510	0.0830	-17.3	1.656	2.240	0.000	36.980	0.0	10	2019.01.09–2019.03.22
2019-03-03 15:46 CET	-0.663	0.026	0.0350	0.0900	12.3	1.694	-9.900	0.000	19.850	0.0	10	2019.01.09–2019.03.22
2019-03-03 20:01 CET	-0.652	0.030	-0.0010	0.1010	11.0	1.887	-9.920	0.000	19.940	0.0	10	2019.01.09–2019.03.22
2019-03-04 00:15 CET	-0.657	0.032	-0.2790	0.0700	11.2	1.523	-9.870	0.000	19.920	0.0	10	2019.01.09–2019.03.22
2019-03-04 04:25 CET	-0.669	0.028	-0.6920	0.0450	-17.5	1.197	2.210	0.000	36.950	0.0	10	2019.01.09–2019.03.22
2019-03-04 08:28 CET	-0.682	0.024	-0.6770	0.0610	-16.6	0.929	2.210	0.000	36.970	0.0	10	2019.01.09–2019.03.22
2019-03-04 12:45 CET	-0.657	0.032	-0.2790	0.0700	11.2	1.523	-9.870	0.000	19.920	0.0	10	2019.01.09–2019.03.22
2019-03-05 02:55 CET	-0.660	0.030	-0.1770	0.0650	12.1	1.023	-9.910	0.000	19.890	0.0	10	2019.01.09–2019.03.22
2019-03-05 06:59 CET	-0.675	0.020	-0.1980	0.0970	-16.4	1.237	2.190	0.000	36.870	0.0	10	2019.01.09–2019.03.22
2019-03-05 11:09 CET	-0.276	0.013	-0.0510	0.1080	-15.7	1.756	1.880	0.000	37.390	0.0	10	2019.01.09–2019.03.22
2019-03-06 01:02 CET	-0.267	0.021	-0.0200	0.0820	-16.4	1.602	1.910	0.000	37.350	0.0	10	2019.01.09–2019.03.22
2019-03-06 05:11 CET	-0.551	0.026	-0.1740	0.0970	-17.1	1.073	2.190	0.000	37.710	0.0	10	2019.01.09–2019.03.22
2019-03-06 09:29 CET	-0.548	0.019	-0.1570	0.1010	-17.0	1.093	2.190	0.000	37.780	0.0	10	2019.01.09–2019.03.22
2019-03-06 13:38 CET	-0.664	0.025	-0.1360	0.1050	-16.7	1.115	2.240	0.000	37.020	0.0	10	2019.01.09–2019.03.22
2019-03-07 06:24 CET	-0.679	0.026	-0.1520	0.1250	-16.6	0.956	2.240	0.000	36.960	0.0	10	2019.01.09–2019.03.22
2019-03-07 10:34 CET	-0.681	0.025	-0.2270	0.1410	10.3	1.494	-9.900	0.000	19.930	0.0	10	2019.01.09–2019.03.22
2019-03-07 14:45 CET	-0.650	0.021	-0.1780	0.1030	11.4	1.637	-9.940	0.000	19.770	0.0	10	2019.01.09–2019.03.18
2019-03-08 07:28 CET	-0.421	0.017	-0.1780	0.0950	10.7	1.44	-9.970	0.000	19.870	0.0	10	2019.01.09–2019.03.19

2019-03-08 11:34 CET	-0.413	0.035	-0.1960	0.1330	11.8	1.677	-9.970	0.000	19.760	0.0	10	2019.01.09–2019.03.20
2019-03-09 00:09 CET	-0.252	0.031	0.0480	0.0690	-15.3	0.917	1.710	0.000	37.100	0.0	10	2019.01.09–2019.03.21
2019-03-09 04:13 CET	-0.259	0.035	0.0370	0.0760	-16.2	1.288	1.850	0.000	37.350	0.0	10	2019.01.09–2019.03.22
2019-03-09 08:24 CET	-0.670	0.026	-0.1200	0.0980	-15.7	1.838	2.200	0.000	36.940	0.0	10	2019.01.09–2019.03.22
2019-03-09 12:39 CET	-0.663	0.028	-0.0910	0.0970	-15.9	1.279	2.210	0.000	36.940	0.0	10	2019.01.09–2019.03.22
2019-03-09 20:52 CET	-0.672	0.028	-0.2760	0.1050	10.0	1.814	-9.900	0.000	20.020	0.0	10	2019.01.09–2019.03.22
2019-03-10 09:21 CET	-0.260	0.033	0.0570	0.0680	-15.7	0.762	1.830	0.000	37.310	0.0	10	2019.01.09–2019.03.22
2019-03-10 21:53 CET	-0.678	0.027	-0.0840	0.0790	-16.2	1.696	2.230	0.000	36.950	0.0	10	2019.01.09–2019.03.22
2019-03-11 10:19 CET	-0.663	0.026	-0.2770	0.0400	11.8	1.779	-9.930	0.000	19.900	0.0	10	2019.01.09–2019.03.22
2019-03-12 13:05 CET	-0.251	0.022	0.0850	0.0920	-14.3	1.235	1.890	0.000	37.390	0.0	10	2019.01.09–2019.03.22
2019-03-13 10:09 CET	-0.666	0.023	-0.0810	0.0660	-15.4	0.862	2.250	0.000	37.030	0.0	10	2019.01.09–2019.03.22
2019-03-14 09:25 CET	-0.664	0.019	-0.2740	0.0700	10.1	1.544	-9.920	0.000	19.840	0.0	10	2019.01.09–2019.03.22
2019-03-14 13:32 CET	-0.672	0.031	-0.0840	0.1030	-16.2	2.117	2.240	0.000	37.070	0.0	10	2019.01.09–2019.03.22
2019-03-15 02:00 CET	-0.272	0.025	0.0850	0.0890	-16.2	1.532	1.930	0.000	37.390	0.0	10	2019.03.15–2019.05.16
2019-03-16 18:11 CET	-0.653	0.027	-0.4440	0.0810	-15.4	1.434	2.230	0.000	36.960	0.0	10	2019.03.15–2019.05.16
2019-03-17 06:37 CET	-0.669	0.013	-0.1130	0.0760	9.5	1.581	-9.910	0.000	20.160	0.0	10	2019.03.15–2019.05.16
2019-03-17 19:04 CET	-0.277	0.029	-0.2850	0.0790	-14.2	1.518	1.900	0.000	37.370	0.0	10	2019.03.15–2019.05.16
2019-03-18 07:30 CET	-0.675	0.027	-0.4490	0.0620	-15.5	1.698	2.240	0.000	36.980	0.0	10	2019.03.15–2019.05.16
2019-03-19 04:18 CET	-0.666	0.029	-0.0560	0.1200	10.0	2.392	-9.920	0.000	19.910	0.0	10	2019.03.15–2019.05.16
2019-03-19 20:58 CET	-0.271	0.031	-0.3100	0.0620	-15.0	1.287	1.900	0.000	37.350	0.0	10	2019.03.15–2019.05.16
2019-03-20 09:24 CET	-0.674	0.012	-0.4090	0.0930	-15.2	1.282	2.240	0.000	36.940	0.0	10	2019.03.15–2019.05.16
2019-03-21 06:11 CET	-0.659	0.030	-0.1040	0.0640	9.1	1.536	-9.920	0.000	20.060	0.0	10	2019.03.15–2019.05.16
2019-03-22 04:15 CET	-0.674	0.022	-0.4230	0.0890	-15.1	1.443	2.240	0.000	37.070	0.0	10	2019.03.15–2019.05.16
2019-03-23 01:41 CET	-0.656	0.019	-0.1200	0.0760	9.4	1.902	-9.920	0.000	20.020	0.0	10	2019.03.15–2019.05.16
2019-03-23 14:10 CET	-0.287	0.018	-0.2680	0.0940	-14.8	2.074	1.890	0.000	37.340	0.0	10	2019.03.15–2019.05.16
2019-03-24 02:35 CET	-0.684	0.022	-0.4120	0.0990	-15.5	1.136	2.210	0.000	36.920	0.0	10	2019.03.15–2019.05.16
2019-03-24 15:00 CET	-0.278	0.016	-0.2360	0.0750	-14.0	2.084	1.910	0.000	37.330	0.0	10	2019.03.15–2019.05.16
2019-03-25 15:57 CET	-0.433	0.022	-0.0400	0.1600	10.2	1.987	-9.970	0.000	19.910	0.0	10	2019.03.15–2019.05.16
2019-03-25 03:28 CET	-0.673	0.028	-0.1080	0.0830	10.1	2.429	-9.920	0.000	19.900	0.0	10	2019.03.15–2019.05.16
2019-03-26 08:36 CET	-0.271	0.023	-0.2040	0.0750	-14.7	1.451	1.880	0.000	37.410	0.0	10	2019.03.15–2019.05.16
2019-03-27 15:59 CET	-0.679	0.033	-0.3870	0.1250	-15.1	1.602	2.220	0.000	36.930	0.0	10	2019.03.15–2019.05.16

2019-03-28 08:35 CET	-0.663	0.016	-0.1360	0.1130	9.4	1.337	-9.950	0.000	19.950	0.0	10	2019.03.15–2019.05.16
2019-03-29 05:25 CET	-0.273	0.026	-0.2570	0.1190	-15.1	1.325	1.700	0.000	37.260	0.0	10	2019.03.15–2019.05.16
2019-03-30 02:58 CET	-0.666	0.029	-0.2950	0.0720	-15.2	1.656	2.080	0.000	36.840	0.0	10	2019.03.15–2019.05.16
2019-03-30 15:24 CET	-0.675	0.027	-0.0960	0.0770	9.7	1.53	-9.910	0.000	19.960	0.0	10	2019.03.15–2019.05.16
2019-03-31 04:50 CEST	-0.281	0.025	-0.2430	0.0970	-14.9	1.447	1.860	0.000	37.320	0.0	10	2019.03.15–2019.05.16
2019-03-31 17:15 CEST	-0.673	0.027	-0.3490	0.0840	-15.0	1.594	2.220	0.000	37.000	0.0	10	2019.03.15–2019.05.16
2019-04-01 05:52 CEST	-0.676	0.022	-0.1230	0.1140	9.5	1.767	-9.920	0.000	20.040	0.0	10	2019.03.15–2019.05.16
2019-04-02 02:37 CEST	-0.278	0.026	-0.2700	0.1030	-15.7	2.155	1.890	0.000	37.420	0.0	10	2019.03.15–2019.05.16
2019-04-02 19:16 CEST	-0.684	0.024	-0.3630	0.0980	-15.6	1.326	2.220	0.000	37.000	0.0	10	2019.03.15–2019.05.16
2019-04-03 11:53 CEST	-0.683	0.038	-0.1170	0.0690	8.9	1.764	-9.930	0.000	19.970	0.0	10	2019.03.15–2019.05.16
2019-04-04 08:38 CEST	-0.676	0.029	-0.3620	0.0690	-15.6	2.197	2.260	0.000	37.050	0.0	10	2019.03.15–2019.05.16
2019-04-04 12:53 CEST	-0.675	0.031	-0.1310	0.0630	8.1	1.504	-9.880	0.000	20.020	0.0	10	2019.03.15–2019.05.16
2019-04-05 09:39 CEST	-0.282	0.021	-0.2040	0.1010	-15.7	2.456	1.910	0.000	37.410	0.0	10	2019.03.15–2019.05.16
2019-04-06 02:20 CEST	-0.460	0.029	-0.0270	0.0710	9.7	1.532	-9.970	0.000	19.740	0.0	10	2019.03.15–2019.05.16
2019-04-06 06:26 CEST	-0.674	0.025	-0.3790	0.1020	-16.5	1.234	2.220	0.000	37.000	0.0	10	2019.03.15–2019.05.16
2019-04-06 18:54 CEST	-0.666	0.023	-0.1430	0.0700	9.5	1.218	-9.910	0.000	19.960	0.0	10	2019.03.15–2019.05.16
2019-04-07 07:20 CEST	-0.274	0.019	-0.1950	0.0540	-16.1	1.578	1.900	0.000	37.310	0.0	10	2019.03.15–2019.05.16
2019-04-07 19:45 CEST	-0.692	0.028	-0.2840	0.1130	-14.8	1.805	2.250	0.000	37.030	0.0	10	2019.03.15–2019.05.16
2019-04-08 08:35 CEST	-0.677	0.021	-0.1590	0.0950	10.4	1.32	-9.930	0.000	20.030	0.0	10	2019.03.15–2019.05.16
2019-04-09 05:24 CEST	-0.283	0.024	-0.2050	0.1020	-15.6	1.984	1.850	0.000	37.350	0.0	10	2019.03.15–2019.05.16
2019-04-10 02:05 CEST	-0.678	0.028	-0.3200	0.0650	-15.6	2.486	2.200	0.000	37.020	0.0	10	2019.03.15–2019.05.16
2019-04-10 22:59 CEST	-0.695	0.024	-0.1630	0.1120	9.1	1.275	-9.920	0.000	19.910	0.0	10	2019.03.15–2019.05.16
2019-04-11 11:25 CEST	-0.286	0.031	-0.1230	0.0580	-15.3	1.954	1.830	0.000	37.370	0.0	10	2019.03.15–2019.05.16
2019-04-12 08:06 CEST	-0.452	0.030	-0.0700	0.1180	8.1	1.692	-9.980	0.000	19.760	0.0	10	2019.03.15–2019.05.16
2019-04-12 21:58 CEST	-0.577	0.023	-0.3580	0.1060	-16.1	1.676	2.180	0.000	37.800	0.0	10	2019.03.15–2019.05.16
2019-04-13 10:24 CEST	-0.684	0.020	-0.1680	0.0530	8.7	1.421	-9.920	0.000	19.870	0.0	10	2019.03.15–2019.05.16
2019-04-13 22:50 CEST	-0.281	0.029	-0.2130	0.0610	-15.2	1.764	1.890	0.000	37.370	0.0	10	2019.03.15–2019.05.16
2019-04-14 11:15 CEST	-0.693	0.031	-0.2820	0.0690	-15.9	1.545	2.240	0.000	37.020	0.0	10	2019.03.15–2019.05.16
2019-04-14 23:42 CEST	-0.439	0.028	-0.0980	0.0800	10.5	2.179	-9.950	0.000	19.740	0.0	10	2019.03.15–2019.05.16
2019-04-15 13:22 CEST	-0.663	0.014	-0.1250	0.0740	9.1	2.07	-9.920	0.000	19.920	0.0	10	2019.03.15–2019.05.16
2019-04-16 02:08 CEST	-0.683	0.024	-0.2950	0.1100	-15.7	1.382	2.260	0.000	37.020	0.0	10	2019.03.15–2019.05.16

2019-04-16 06:21 CEST	-0.682	0.027	-0.1200	0.1200	8.2	1.996	-9.640	0.000	20.400	0.0	10	2019.03.15–2019.05.16
2019-04-16 23:06 CEST	-0.290	0.026	-0.1780	0.1380	-14.6	1.373	1.880	0.000	37.410	0.0	10	2019.03.15–2019.05.16
2019-04-17 03:15 CEST	-0.564	0.031	-0.3350	0.0900	-17.0	1.473	2.140	0.000	37.710	0.0	10	2019.03.15–2019.05.16
2019-04-17 11:32 CEST	-0.680	0.020	-0.2840	0.0910	-14.0	1.335	2.230	0.000	37.030	0.0	10	2019.03.15–2019.05.16
2019-04-18 04:06 CEST	-0.675	0.015	-0.1650	0.1180	8.5	1.753	-9.920	0.000	19.930	0.0	10	2019.03.15–2019.05.16
2019-04-18 16:38 CEST	-0.278	0.031	-0.1430	0.1510	-16.1	1.222	1.900	0.000	37.400	0.0	10	2019.03.15–2019.05.16
2019-04-19 05:05 CEST	-0.451	0.024	-0.0840	0.0970	9.2	1.807	-9.970	0.000	20.040	0.0	10	2019.03.15–2019.05.16
2019-04-19 09:13 CEST	-0.680	0.020	-0.3350	0.0640	-15.1	1.373	2.120	0.000	36.880	0.0	10	2019.03.15–2019.05.16
2019-04-19 21:41 CEST	-0.666	0.031	-0.1860	0.0750	10.0	1.702	-9.950	0.000	19.970	0.0	10	2019.03.15–2019.05.16
2019-04-20 22:34 CEST	-0.660	0.024	-0.3160	0.0440	-16.2	0.924	2.260	0.000	37.230	0.0	10	2019.03.15–2019.05.16
2019-04-22 00:39 CEST	-0.280	0.030	-0.1660	0.1150	-15.9	1.315	1.910	0.000	37.390	0.0	10	2019.03.15–2019.05.16
2019-04-22 13:07 CEST	-0.687	0.022	-0.3050	0.0990	-15.9	1.194	2.220	0.000	37.130	0.0	10	2019.03.15–2019.05.16
2019-04-22 21:24 CEST	-0.440	0.024	-0.0760	0.1020	10.0	1.691	-9.960	0.000	19.740	0.0	10	2019.03.15–2019.05.16
2019-04-23 01:33 CEST	-0.666	0.035	-0.1400	0.1340	9.0	1.519	-9.930	0.000	19.970	0.0	10	2019.03.15–2019.05.16
2019-04-23 14:06 CEST	-0.287	0.036	-0.2080	0.1040	-15.4	1.062	1.900	0.000	37.390	0.0	10	2019.03.15–2019.05.16
2019-04-24 11:11 CEST	-0.680	0.025	-0.3160	0.0650	-16.4	1.436	2.230	0.000	36.980	0.0	10	2019.03.15–2019.05.16
2019-04-25 03:57 CEST	-0.669	0.015	-0.1760	0.0840	8.3	1.392	-9.930	0.000	20.060	0.0	10	2019.03.15–2019.05.16
2019-04-25 20:35 CEST	-0.277	0.017	-0.1270	0.0920	-16.2	1.005	1.900	0.000	37.410	0.0	10	2019.03.15–2019.05.16
2019-04-26 09:01 CEST	-0.687	0.043	-0.2360	0.0810	-15.3	1.894	2.250	0.000	37.030	0.0	10	2019.03.15–2019.05.16
2019-04-26 23:41 CEST	-0.686	0.026	-0.3460	0.0750	-15.6	1.487	2.250	0.000	37.030	0.0	10	2019.03.15–2019.05.16
2019-04-27 03:50 CEST	-0.689	0.024	-0.1970	0.0800	8.4	2.434	-9.910	0.000	19.860	0.0	10	2019.03.15–2019.05.16
2019-04-27 16:26 CEST	-0.278	0.027	-0.1280	0.0730	-15.4	1.961	1.850	0.000	37.340	0.0	10	2019.03.15–2019.05.16
2019-04-28 05:03 CEST	-0.688	0.018	-0.3460	0.0830	-15.6	1.173	2.210	0.000	36.990	0.0	10	2019.03.15–2019.05.16
2019-04-28 09:15 CEST	-0.581	0.024	-0.3050	0.0610	-16.2	1.612	2.170	0.000	37.660	0.0	10	2019.03.15–2019.05.16
2019-04-28 17:37 CEST	-0.659	0.020	-0.1310	0.0690	8.4	1.553	-9.620	0.000	20.540	0.0	10	2019.03.15–2019.05.16
2019-04-28 21:47 CEST	-0.430	0.026	-0.0990	0.0840	8.6	1.676	-9.820	0.000	20.100	0.0	10	2019.03.15–2019.05.16
2019-04-29 06:11 CEST	-0.300	0.014	-0.1790	0.0610	-16.5	1.027	1.880	0.000	37.280	0.0	10	2019.03.15–2019.05.16
2019-04-30 07:53 CEST	-0.672	0.014	-0.2630	0.1310	-15.4	1.795	2.240	0.000	36.980	0.0	10	2019.03.15–2019.05.16
2019-05-01 00:48 CEST	-0.669	0.026	-0.1670	0.1310	8.1	1.035	-9.880	0.000	20.220	0.0	10	2019.03.15–2019.05.16
2019-05-01 13:27 CEST	-0.292	0.022	-0.1820	0.0970	-16.0	1.688	1.880	0.000	37.290	0.0	10	2019.03.15–2019.05.16
2019-05-02 02:08 CEST	-0.429	0.031	-0.0930	0.0930	9.3	1.51	-9.940	0.000	19.960	0.0	10	2019.03.15–2019.05.16

2019-05-02 23:39 CEST	-0.675	0.033	-0.3160	0.1010	-16.2	1.566	2.230	0.000	36.980	0.0	10	2019.03.15–2019.05.16
2019-05-03 12:26 CEST	-0.682	0.025	-0.2070	0.0610	9.0	1.594	-9.890	0.000	20.010	0.0	10	2019.03.15–2019.05.16
2019-05-04 07:00 CEST	-0.270	0.028	-0.1190	0.0520	-15.9	2.056	1.830	0.000	37.380	0.0	10	2019.03.15–2019.05.16
2019-05-04 19:54 CEST	-0.443	0.018	-0.0430	0.1240	9.7	1.617	-9.950	0.000	20.230	0.0	10	2019.03.15–2019.05.16
2019-05-05 00:16 CEST	-0.551	0.029	-0.2800	0.0530	-17.1	1.967	2.050	0.000	37.580	0.0	10	2019.03.15–2019.05.16
2019-05-05 08:54 CEST	-0.680	0.030	-0.3230	0.0610	-16.1	1.382	2.190	0.000	36.870	0.0	10	2019.03.15–2019.05.16
2019-05-05 21:57 CEST	-0.673	0.035	-0.1830	0.0850	6.6	1.494	-9.910	0.000	20.180	0.0	10	2019.03.15–2019.05.16
2019-05-06 11:04 CEST	-0.286	0.022	-0.1040	0.0790	-15.6	1.856	1.880	0.000	37.380	0.0	10	2019.03.15–2019.05.16
2019-05-07 04:25 CEST	-0.683	0.025	-0.3090	0.1020	-16.7	1.491	2.260	0.000	37.030	0.0	10	2019.03.15–2019.05.16
2019-05-07 08:35 CEST	-0.677	0.021	-0.1780	0.0830	7.5	1.384	-9.840	0.000	20.110	0.0	10	2019.03.15–2019.05.16
2019-05-08 02:03 CEST	-0.277	0.028	-0.1440	0.1100	-15.5	2.117	1.920	0.000	37.380	0.0	10	2019.03.15–2019.05.16
2019-05-08 15:28 CEST	-0.674	0.028	-0.2960	0.1180	-15.5	1.777	2.220	0.000	37.000	0.0	10	2019.03.15–2019.05.16
2019-05-09 09:33 CEST	-0.679	0.039	-0.1370	0.0780	7.9	1.828	-9.890	0.000	20.010	0.0	10	2019.03.15–2019.05.16
2019-05-10 20:00 CEST	-0.690	0.024	-0.2760	0.1590	-14.9	1.891	2.120	0.000	37.080	0.0	10	2019.03.15–2019.05.16
2019-05-11 00:08 CEST	-0.686	0.021	-0.1400	0.0790	10.6	1.936	-9.920	0.000	20.210	0.0	10	2019.03.15–2019.05.16
2019-05-11 04:18 CEST	-0.301	0.025	-0.0690	0.1120	-14.2	1.463	1.820	0.000	37.490	0.0	10	2019.03.15–2019.05.16
2019-05-11 08:25 CEST	-0.447	0.021	-0.1040	0.0830	10.4	1.831	-9.990	0.000	20.110	0.0	10	2019.03.15–2019.05.16
2019-05-11 12:32 CEST	-0.588	0.024	-0.2590	0.0950	-15.8	1.55	2.060	0.000	37.710	0.0	10	2019.03.15–2019.05.16
2019-05-11 16:42 CEST	-0.695	0.020	-0.2950	0.0930	-15.1	2.141	2.190	0.000	37.240	0.0	10	2019.03.15–2019.05.16
2019-05-11 20:50 CEST	-0.686	0.019	-0.2030	0.0980	7.9	1.549	-9.950	0.000	20.190	0.0	10	2019.03.15–2019.05.16
2019-05-12 00:59 CEST	-0.297	0.020	-0.1340	0.0590	-14.4	1.669	1.820	0.000	37.540	0.0	10	2019.03.15–2019.05.16
2019-05-12 05:07 CEST	-0.445	0.025	-0.1340	0.1220	10.2	1.649	-9.970	0.000	20.130	0.0	10	2019.03.15–2019.05.16
2019-05-12 09:16 CEST	-0.604	0.025	-0.2290	0.0640	-14.8	1.617	2.090	0.000	37.760	0.0	10	2019.03.15–2019.05.16
2019-05-12 13:24 CEST	-0.685	0.016	-0.2870	0.0800	-13.7	1.151	2.170	0.000	37.040	0.0	10	2019.03.15–2019.05.16
2019-05-12 17:33 CEST	-0.692	0.025	-0.1830	0.0840	10.3	2.036	-9.920	0.000	20.100	0.0	10	2019.03.15–2019.05.16
2019-05-12 21:43 CEST	-0.283	0.016	-0.1210	0.0670	-14.3	1.551	1.840	0.000	37.490	0.0	10	2019.03.15–2019.05.16
2019-05-13 01:51 CEST	-0.458	0.025	-0.0350	0.0510	10.2	1.799	-10.010	0.000	20.200	0.0	10	2019.03.15–2019.05.16
2019-05-13 05:59 CEST	-0.592	0.025	-0.3110	0.0880	-15.7	1.815	2.020	0.000	37.600	0.0	10	2019.03.15–2019.05.16
2019-05-13 22:49 CEST	-0.697	0.025	-0.3060	0.1020	-14.3	0.976	2.190	0.000	37.120	0.0	10	2019.03.15–2019.05.16
2019-05-14 02:58 CEST	-0.708	0.020	-0.1140	0.1100	10.2	1.733	-9.980	0.000	20.080	0.0	10	2019.03.15–2019.05.16
2019-05-14 07:08 CEST	-0.300	0.027	-0.1030	0.1090	-14.2	1.978	1.810	0.000	37.490	0.0	10	2019.03.15–2019.05.16

2019-05-14 11:17 CEST	-0.459	0.019	-0.0820	0.1050	10.6	1.971	-10.030	0.000	20.160	0.0	10	2019.03.15–2019.05.16
2019-05-15 16:08 CEST	-0.583	0.026	-0.2840	0.1040	-15.1	1.98	1.960	0.000	37.600	0.0	10	2019.03.15–2019.05.16
2019-05-16 23:25 CEST	-0.687	0.025	-0.1700	0.0770	9.1	0.662	-9.970	0.000	20.110	0.0	10	2019.03.15–2019.05.16

Sample data – S.5.IV

Date	Sample	δ47 (raw) (‰)	Δ47 (raw) (‰)	SD Δ47 (raw) (‰)	δ47 (bgcorr) (‰)	Δ47 (bgcorr) (‰)	SD Δ47 (bgcorr) (‰)	δ13C CO2 (‰ VPDB)	δ18O CO2 (‰ VSMOW)	Diff Bellow (mV)	Weight (g)	Pressure Bellow (mBar)	ETF period
MAT 253													
6/7/2017	2017-AM-011	2.530	-0.274	0.026	2.487	-0.311	0.024	-8.032	-8.019	-10.8	10.9	33.8	2017.01.06–2017.07.10
6/7/2017	2017-AM-018	2.712	-0.222	0.037	2.652	-0.276	0.020	-7.311	-7.300	-31.2	10.2	18.3	2017.01.06–2017.07.10
6/7/2017	2017-AM-029	3.554	-0.283	0.036	3.532	-0.299	0.027	-7.048	-7.038	76.7	10.2	28.5	2017.01.06–2017.07.10
6/8/2017	2017-AM-022	3.629	-0.231	0.028	3.557	-0.297	0.028	-6.947	-6.937	-36.9	11.1	21.5	2017.01.06–2017.07.10
6/8/2017	2017-AM-011	2.373	-0.293	0.040	2.360	-0.301	0.026	-8.068	-8.055	105.0	7.7	24.8	2017.01.06–2017.07.10
6/9/2017	2017-AM-018	2.663	-0.309	0.024	2.621	-0.346	0.018	-7.293	-7.283	43.6	13.3	25.5	2017.01.06–2017.07.10
6/9/2017	2017-AM-029	3.475	-0.292	0.021	3.438	-0.324	0.027	-7.044	-7.033	83.6	8.8	25.3	2017.01.06–2017.07.10
7/4/2017	2017-AM-022	3.564	-0.255	0.037	3.485	-0.328	0.031	-6.906	-6.896	-28.0	12.0	23.8	2017.01.06–2017.07.10
7/4/2017	2017-AM-011	2.519	-0.264	0.021	2.461	-0.316	0.028	-8.018	-8.005	-15.3	7.3	22.7	2017.01.06–2017.07.10
7/5/2017	2017-AM-018	2.580	-0.303	0.021	2.555	-0.323	0.015	-7.289	-7.278	54.5	12.3	22.7	2017.01.06–2017.07.10
7/5/2017	2017-AM-029	3.442	-0.299	0.050	3.428	-0.308	0.025	-7.021	-7.011	50.8	10.6	26.2	2017.01.06–2017.07.10
7/5/2017	2017-AM-022	3.495	-0.260	0.024	3.435	-0.314	0.025	-6.928	-6.918	12.9	10.1	19.7	2017.01.06–2017.07.10
7/6/2017	2017-AM-011	2.402	-0.262	0.055	2.357	-0.301	0.016	-8.055	-8.042	-7.3	7.4	23.7	2017.01.06–2017.07.10
7/6/2017	2017-AM-018	2.579	-0.310	0.024	2.519	-0.365	0.017	-7.278	-7.268	-8.8	13.5	26.4	2017.01.06–2017.07.10
7/6/2017	2017-AM-022	3.496	-0.282	0.046	3.464	-0.308	0.022	-6.926	-6.916	69.3	12.3	23.2	2017.01.06–2017.07.10
7/6/2017	2017-AM-011	2.338	-0.307	0.043	2.331	-0.308	0.024	-8.065	-8.052	89.4	8.2	25.9	2017.01.06–2017.07.10
7/7/2017	2017-AM-018	2.694	-0.304	0.029	2.653	-0.340	0.013	-7.256	-7.246	1.9	12.8	24.8	2017.01.06–2017.07.10
7/8/2017	2017-AM-029	3.666	-0.260	0.029	3.619	-0.302	0.016	-7.020	-7.009	24.6	11.0	31.1	2017.01.06–2017.07.10
7/8/2017	2017-AM-018	2.677	-0.306	0.047	2.654	-0.324	0.026	-7.286	-7.275	31.2	12.8	25.0	2017.01.06–2017.07.10
7/8/2017	2017-AM-022	3.531	-0.262	0.023	3.470	-0.317	0.015	-6.936	-6.926	-5.3	11.8	23.8	2017.01.06–2017.07.10
7/9/2017	2017-AM-029	3.543	-0.273	0.038	3.494	-0.317	0.027	-7.017	-7.007	51.1	9.8	29.1	2017.01.06–2017.07.10
7/9/2017	2017-AM-020	4.393	-0.329	0.040	4.392	-0.325	0.029	-6.648	-6.639	226.6	13.0	37.2	2017.01.06–2017.07.10
7/10/2017	2017-AM-026	4.849	-0.308	0.043	4.794	-0.357	0.023	-6.081	-6.073	44.8	13.9	34.4	2017.01.06–2017.07.10
7/11/2017	2017-AM-013	3.197	-0.292	0.026	3.179	-0.304	0.015	-7.746	-7.733	97.8	13.0	28.3	2017.01.06–2017.07.10
7/15/2017	2017-AM-020	4.324	-0.232	0.027	4.242	-0.308	0.019	-6.631	-6.621	-10.3	8.2	23.1	2017.07.14–2017.11.13
7/15/2017	2017-AM-026	4.748	-0.277	0.033	4.657	-0.362	0.016	-6.100	-6.092	-46.1	8.6	20.8	2017.07.14–2017.11.13
7/16/2017	2017-AM-013	3.153	-0.279	0.024	3.119	-0.307	0.011	-7.767	-7.755	87.3	10.2	21.4	2017.07.14–2017.11.13
7/18/2017	2017-AM-013	3.513	-0.230	0.028	3.410	-0.327	0.017	-7.699	-7.687	-68.1	10.5	20.8	2017.07.14–2017.11.13
7/19/2017	2017-AM-020	4.828	-0.301	0.034	4.791	-0.332	0.025	-6.564	-6.555	121.9	10.6	28.7	2017.07.14–2017.11.13
7/19/2017	2017-AM-026	4.812	-0.312	0.071	4.767	-0.351	0.020	-6.105	-6.097	41.2	10.9	21.0	2017.07.14–2017.11.13
7/20/2017	2017-AM-028	2.931	-0.421	0.095	2.987	-0.360	0.016	-7.222	-7.211	353.9	11.9	38.4	2017.07.14–2017.11.13
7/20/2017	2017-AM-013	3.363	-0.254	0.060	3.333	-0.278	0.025	-7.679	-7.666	70.6	11.3	25.6	2017.07.14–2017.11.13
7/20/2017	2017-AM-020	4.288	-0.290	0.034	4.253	-0.320	0.014	-6.625	-6.615	61.8	12.0	33.8	2017.07.14–2017.11.13
7/21/2017	2017-AM-026	4.781	-0.317	0.021	4.721	-0.371	0.012	-6.064	-6.056	59.8	12.1	29.1	2017.07.14–2017.11.13
7/21/2017	2017-AM-013	3.264	-0.210	0.034	3.192	-0.276	0.026	-7.759	-7.746	-40.0	10.3	20.4	2017.07.14–2017.11.13
7/24/2017	2017-AM-020	4.600	-0.166	0.026	4.483	-0.276	0.024	-6.612	-6.603	-79.9	10.7	15.3	2017.07.14–2017.11.13
7/27/2017	2017-AM-028	2.869	-0.327	0.037	2.862	-0.330	0.018	-7.247	-7.236	132.8	10.1	33.7	2017.07.14–2017.11.13

7/27/2017	2017-AM-026	4.777	-0.309	0.029	4.694	-0.386	0.019	-6.073	-6.065	-2.8	10.9	26.5	2017.07.14–2017.11.13
7/28/2017	2017-AM-028	2.922	-0.333	0.033	2.913	-0.337	0.025	-7.257	-7.246	136.4	10.4	32.1	2017.07.14–2017.11.13
7/29/2017	2017-AM-024	4.427	-0.353	0.030	4.385	-0.391	0.019	-6.556	-6.546	90.2	31.5	23.7	2017.07.14–2017.11.13
7/29/2017	2017-AM-028	3.198	-0.279	0.035	3.159	-0.314	0.027	-7.202	-7.192	-11.5	7.7	25.1	2017.07.14–2017.11.13
7/29/2017	2017-AM-013	3.312	-0.269	0.038	3.274	-0.301	0.020	-7.709	-7.696	36.2	12.6	26.3	2017.07.14–2017.11.13
7/30/2017	2017-AM-028	3.019	-0.302	0.036	2.998	-0.317	0.034	-7.229	-7.218	74.2	7.2	23.9	2017.07.14–2017.11.13
7/30/2017	2017-AM-024	4.533	-0.304	0.021	4.439	-0.393	0.021	-6.526	-6.517	-16.2	30.2	23.2	2017.07.14–2017.11.13
7/30/2017	2017-AM-020	4.323	-0.287	0.033	4.287	-0.318	0.029	-6.630	-6.620	70.6	11.4	33.3	2017.07.14–2017.11.13
7/31/2017	2017-AM-028	3.230	-0.198	0.043	3.129	-0.293	0.015	-7.201	-7.190	-104.9	6.6	15.3	2017.07.14–2017.11.13
8/1/2017	2017-AM-024	4.472	-0.337	0.042	4.418	-0.386	0.021	-6.541	-6.532	61.2	27.9	20.9	2017.07.14–2017.11.13
10/22/2017	2017-AM-019	3.530	-0.271	0.028	3.477	-0.319	0.010	-7.191	-7.180	13.5	9.9	23.2	2017.07.14–2017.11.13
10/22/2017	2017-AM-025	4.262	-0.327	0.047	4.231	-0.353	0.021	-6.594	-6.585	90.2	10.6	27.9	2017.07.14–2017.11.13
10/22/2017	2017-AM-016	3.819	-0.315	0.047	3.807	-0.322	0.013	-7.066	-7.055	117.3	10.2	21.5	2017.07.14–2017.11.13
4/17/2018	2017-AM-016	4.157	-0.141	0.024	4.019	-0.273	0.018	-6.879	-6.869	-84.0	11.7	25.9	2018.03.07–2018.04.27
4/17/2018	2017-AM-019	3.626	-0.162	0.023	3.513	-0.269	0.015	-7.151	-7.141	-32.1	13.1	30.9	2018.03.07–2018.04.27
4/17/2018	2017-AM-025	4.492	-0.181	0.041	4.378	-0.289	0.027	-6.422	-6.413	52.6	12.0	32.0	2018.03.07–2018.04.27
4/28/2018	2017-AM-016	4.134	-0.175	0.027	4.010	-0.294	0.032	-6.880	-6.870	-49.6	11.2	24.1	2018.03.07–2018.04.27
8/4/2018	2017-AM-019	3.603	-0.151	0.044	3.488	-0.260	0.021	-7.156	-7.145	45.0	11.9	29.9	2018.07.10–2018.10.19
8/4/2018	2017-AM-016	4.212	-0.126	0.048	4.044	-0.288	0.029	-6.873	-6.863	115.3	11.7	26.6	2018.07.10–2018.10.19
8/5/2018	2017-AM-025	4.610	-0.147	0.019	4.477	-0.274	0.017	-6.421	-6.412	34.9	10.9	29.7	2018.07.10–2018.10.19
8/6/2018	2017-AM-019	3.574	-0.182	0.036	3.480	-0.271	0.015	-7.149	-7.139	-2.5	10.6	26.2	2018.07.10–2018.10.19
8/8/2018	2017-AM-016	4.179	-0.156	0.019	4.073	-0.255	0.025	-6.861	-6.851	-38.8	10.4	23.6	2018.07.10–2018.10.19
8/9/2018	2017-AM-025	4.670	-0.155	0.026	4.516	-0.303	0.021	-6.392	-6.383	62.2	10.5	27.9	2018.07.10–2018.10.19
8/9/2018	2017-AM-019	3.688	-0.129	0.035	3.512	-0.299	0.031	-7.137	-7.126	162.0	11.9	28.3	2018.07.10–2018.10.19
8/9/2018	2017-AM-016	4.151	-0.154	0.036	4.035	-0.265	0.025	-6.874	-6.864	-21.2	11.4	25.3	2018.07.10–2018.10.19
8/11/2018	2017-AM-025	4.653	-0.109	0.032	4.427	-0.329	0.025	-6.413	-6.404	176.3	10.8	29.1	2018.07.10–2018.10.19
8/14/2018	2017-AM-019	3.648	-0.130	0.035	3.491	-0.282	0.025	-7.153	-7.142	78.3	9.6	23.6	2018.07.10–2018.10.19
8/14/2018	2017-AM-025	4.679	-0.135	0.038	4.467	-0.340	0.027	-6.394	-6.385	140.9	8.4	22.3	2018.07.10–2018.10.19
8/16/2018	2018-AM-114	3.613	-0.182	0.027	3.494	-0.295	0.023	-6.905	-6.895	-11.8	11.7	25.5	2018.07.10–2018.10.19
8/16/2018	2018-AM-110	2.904	-0.234	0.026	2.797	-0.335	0.034	-7.503	-7.491	-6.6	11.2	22.7	2018.07.10–2018.10.19
8/17/2018	2018-AM-92a	3.297	-0.163	0.044	3.161	-0.293	0.019	-7.096	-7.085	86.9	13.4	21.5	2018.07.10–2018.10.19
8/17/2018	2018-AM-75a	4.210	-0.121	0.043	4.000	-0.325	0.024	-6.686	-6.677	174.0	12.2	20.9	2018.07.10–2018.10.19
8/18/2018	2018-AM-75a	4.216	-0.154	0.058	4.055	-0.309	0.033	-6.673	-6.663	68.5	12.5	21.4	2018.07.10–2018.10.19
8/18/2018	2018-AM-110	3.116	-0.223	0.041	3.007	-0.326	0.022	-7.437	-7.426	-7.2	10.6	20.8	2018.07.10–2018.10.19
8/19/2018	2018-AM-92a	3.265	-0.181	0.036	3.188	-0.253	0.019	-7.081	-7.071	-41.8	14.2	23.2	2018.07.10–2018.10.19
8/19/2018	2018-AM-114	3.648	-0.128	0.032	3.464	-0.306	0.016	-6.925	-6.915	162.3	10.5	23.2	2018.07.10–2018.10.19
8/31/2018	2018-AM-75a	4.137	-0.209	0.033	4.054	-0.285	0.069	-6.669	-6.659	-50.7	12.9	21.4	2018.07.10–2018.10.19
8/31/2018	2018-AM-92a	3.362	-0.188	0.023	3.283	-0.262	0.021	-7.080	-7.069	-23.1	13.4	20.6	2018.07.10–2018.10.19
9/11/2018	2018-AM-75a	4.181	-0.134	0.061	3.995	-0.314	0.038	-6.722	-6.712	119.3	13.6	22.1	2018.07.10–2018.10.19
9/11/2018	2018-AM-92a	3.387	-0.188	0.027	3.312	-0.258	0.029	-7.092	-7.081	-36.7	14.5	22.3	2018.07.10–2018.10.19
9/11/2018	2018-AM-110	3.058	-0.246	0.045	2.985	-0.312	0.017	-7.458	-7.447	-53.0	11.4	21.4	2018.07.10–2018.10.19
9/12/2018	2018-AM-114	3.782	-0.155	0.034	3.622	-0.309	0.025	-6.907	-6.897	92.2	9.7	19.2	2018.07.10–2018.10.19
9/13/2018	2018-AM-75a	4.393	-0.158	0.068	4.239	-0.305	0.025	-6.658	-6.649	19.8	12.0	19.0	2018.07.10–2018.10.19
9/13/2018	2018-AM-114	3.608	-0.193	0.054	3.491	-0.304	0.015	-6.911	-6.901	15.9	10.3	20.8	2018.07.10–2018.10.19

9/13/2018	2018-AM-92a	3.372	-0.160	0.033	3.239	-0.287	0.019	-7.086	-7.076	66.6	13.7	20.6	2018.07.10–2018.10.19
9/14/2018	2018-AM-110	3.054	-0.205	0.036	2.949	-0.305	0.024	-7.453	-7.442	26.4	11.2	20.2	2018.07.10–2018.10.19
9/15/2018	2018-AM-110	3.201	-0.150	0.031	3.039	-0.306	0.011	-7.418	-7.407	117.9	11.9	22.0	2018.07.10–2018.10.19
9/15/2018	2018-AM-114	3.782	-0.152	0.028	3.615	-0.313	0.025	-6.808	-6.799	121.5	11.5	23.9	2018.07.10–2018.10.19

ID	Sample	Weight (mg)	d47	d47 SD	d48	d48 SD	d49	D47 (raw)	D47 SD (raw)	D48 (raw)	D48 SD (raw)	D49 (raw)	d13C	d13C SD	d18O	d18O SD	Aqui	ETF period
2019-02-06 05:03 CET	2018-AM-92a	21.7	3.262	0.0200	11.934	0.0720	4.489	-0.274	0.020	-0.2960	0.0710	-4.9	-6.950	0.000	31.520	0.0	10	2019.01.09–2019.03.14
2019-02-07 23:22 CET	2017-AM-24	40.1	4.612	0.0180	13.360	0.1010	5.358	-0.289	0.017	-0.2620	0.0990	-6.1	-6.270	0.000	32.230	0.0	10	2019.01.09–2019.03.20
2019-02-09 08:42 CET	2018-AM-57	13.7	4.921	0.0290	13.500	0.0770	5.154	-0.256	0.030	-0.2620	0.0810	-6.7	-6.060	0.000	32.300	0.0	10	2019.01.09–2019.03.21
2019-02-09 12:52 CET	2017-AM-24	30.8	4.767	0.0200	13.630	0.0970	6.302	-0.273	0.021	-0.2310	0.0930	-5.4	-6.250	0.000	32.350	0.0	10	2019.01.09–2019.03.22
2019-02-09 21:09 CET	2018-AM-57	13.8	4.909	0.0240	13.553	0.1210	6.086	-0.255	0.023	-0.2350	0.1250	-5.7	-6.080	0.000	32.320	0.0	10	2019.01.09–2019.03.23
2019-02-10 01:18 CET	2018-AM-65a	16.0	4.240	0.0120	12.779	0.0680	4.993	-0.278	0.010	-0.2940	0.0660	-5.8	-6.380	0.000	31.950	0.0	10	2019.01.09–2019.03.24
2019-02-10 09:35 CET	2018-AM-65a	16.0	4.406	0.0250	12.961	0.1040	5.143	-0.266	0.024	-0.2680	0.0960	-5.9	-6.300	0.000	32.030	0.0	10	2019.01.09–2019.03.25
2019-02-10 13:44 CET	2018-AM-57	14.0	4.858	0.0260	13.444	0.0930	5.431	-0.270	0.020	-0.2700	0.0850	-6.3	-6.080	0.000	32.280	0.0	10	2019.01.09–2019.03.26
2019-02-10 22:01 CET	2018-AM-65a	15.5	4.243	0.0250	12.777	0.0790	4.647	-0.276	0.021	-0.2800	0.0780	-6.2	-6.370	0.000	31.940	0.0	10	2019.01.09–2019.03.27
2019-02-11 06:19 CET	2018-AM-65a	16.4	4.414	0.0420	12.965	0.1230	5.674	-0.284	0.044	-0.2910	0.1160	-5.4	-6.290	0.000	32.050	0.0	10	2019.01.09–2019.03.28
2019-02-12 05:31 CET	2018-AM-65a	15.8	4.342	0.0350	12.913	0.0590	4.510	-0.248	0.028	-0.2520	0.0560	-6.4	-6.350	0.000	32.000	0.0	10	2019.01.09–2019.03.29
2019-03-10 13:30 CET	2018-AM-37II	18.3	3.985	0.0330	12.704	0.0550	4.654	-0.273	0.033	0.0060	0.0560	-5.7	-6.450	0.000	31.760	0.0	10	2019.01.09–2019.03.30
2019-03-11 14:30 CET	2018-AM-57	17.0	4.074	0.0270	12.907	0.0700	5.479	-0.287	0.024	-0.0090	0.0720	-5.1	-6.450	0.000	31.870	0.0	10	2019.01.09–2019.03.31
2019-03-12 03:00 CET	2018-AM-37II	17.3	3.881	0.0270	12.418	0.1120	6.068	-0.273	0.028	-0.0980	0.1120	-4.1	-6.460	0.000	31.670	0.0	10	2019.01.09–2019.03.32
2019-03-13 14:43 CET	2018-AM-37II	16.9	3.937	0.0220	12.567	0.0840	6.104	-0.268	0.022	-0.0400	0.0860	-4.2	-6.460	0.000	31.710	0.0	10	2019.01.09–2019.03.33
2019-03-21 02:00 CET	2018-AM-37II	17.8	3.959	0.0160	12.519	0.1320	6.702	-0.289	0.017	-0.1760	0.1290	-3.7	-6.460	0.000	31.760	0.0	10	2019.03.15–2019.05.16
2019-03-24 06:43 CET	2018-AM-57	16.1	4.158	0.0260	12.862	0.0910	5.253	-0.288	0.027	-0.1660	0.0940	-5.5	-6.430	0.000	31.930	0.0	10	2019.03.15–2019.05.16

Δ47 soil temperature datasets – S.5.V

47-1/T² calibration:	Petersen *et. al.* 2019 [IUPAC]	**slope**	**intercept**	**AFF**
		0.0383	0.2580	0.088

$\delta^{18}O$ correction factor: +0.1

Sample ID	Age [Ma]	Date	Sample size [mg]	$\delta^{13}C_{V\text{-}PDB}$ [‰]	$\delta^{18}O_{V\text{-}SMOW}$ [‰]	$\delta^{47}{}_{raw\ bc}$ [‰]	$\Delta_{47raw\ bc}$ [‰]	Δ_{47} [‰]	se [‰]	T (Δ_{47})	n	residual slope*	slope	intercept		Time interval HG/25G
2017-AM-011	12.975	6/7/2017	10.9	-8.02	23.42	2.487	-0.311	0.701	0.008		5	-0.0002	1.0690	0.9441	1/6/2017	7/10/2017
		6/8/2017	7.7	-8.06	23.31	2.360	-0.301	0.711	0.008			-0.0002	1.0690	0.9441	1/6/2017	7/10/2017
		7/4/2017	7.3	-8.00	23.38	2.461	-0.316	0.695	0.009			-0.0002	1.0690	0.9441	1/6/2017	7/10/2017
		7/6/2017	7.4	-8.04	23.30	2.357	-0.301	0.711	0.005			-0.0002	1.0690	0.9441	1/6/2017	7/10/2017
		7/7/2017	8.2	-8.05	23.29	2.331	-0.308	0.703	0.007			-0.0002	1.0690	0.9441	1/6/2017	7/10/2017
			AV	-8.03	23.34		**AV**	0.704		**20 ± 1**						
			SD	0.02	0.06		**SD**	0.007								
							SE	0.003								

Sample ID	Age [Ma]	Date	Sample size [mg]	$\delta^{13}C_{V\text{-}PDB}$ [‰]	$\delta^{18}O_{V\text{-}SMOW}$ [‰]	$\delta^{47}{}_{raw\ bc}$ [‰]	$\Delta_{47raw\ bc}$ [‰]	Δ_{47} [‰]	se [‰]	T (Δ_{47})	n
2017-AM-013	13.075	7/11/2017	13.0	-7.73	23.82	3.179	-0.304	0.713	0.005		6
		7/16/2017	10.2	-7.75	23.79	3.119	-0.307	0.710	0.003		
		7/18/2017	10.5	-7.69	24.03	3.410	-0.327	0.688	0.005		
		7/20/2017	11.3	-7.67	23.89	3.333	-0.278	0.741	0.008		
		7/21/2017	10.3	-7.75	23.82	3.192	-0.276	0.743	0.008		
		7/29/2017	12.6	-7.70	23.88	3.274	-0.301	0.716	0.006		
			AV	-7.71	23.87		**AV**	0.718		**15 ± 3**	
			SD	0.04	0.09		**SD**	0.020			
							SE	0.008			

residual slope*	slope	intercept		Time interval HG/25G
-0.0003	1.0492	0.9429	7/14/2017	11/3/2017
-0.0003	1.0492	0.9429	7/14/2017	11/3/2017
-0.0003	1.0492	0.9429	7/14/2017	11/3/2017
-0.0003	1.0492	0.9429	7/14/2017	11/3/2017
-0.0003	1.0492	0.9429	7/14/2017	11/3/2017
-0.0003	1.0492	0.9429	7/14/2017	11/3/2017

Sample ID	Age [Ma]	Date	Sample size [mg]	$\delta^{13}C_{V\text{-}PDB}$ [‰]	$\delta^{18}O_{V\text{-}SMOW}$ [‰]	$\delta^{47}_{raw\ bc}$ [‰]	$\Delta_{47raw\ bc}$ [‰]	Δ_{47} [‰]	se [‰]	T (Δ_{47})	n					
2017-AM-016	13.320	10/22/2017	10.2	-7.05	23.81	3.807	-0.322	0.695	0.004		6	-0.0003	1.0492	0.9429	7/14/2017	11/3/2017
		4/17/2018	11.7	-6.87	23.79	4.019	-0.273	0.700	0.006			0.0000	1.1137	0.9159	3/7/2018	4/27/2018
		4/28/2018	11.2	-6.87	23.80	4.010	-0.294	0.677	0.010			0.0000	1.1137	0.9159	3/7/2018	4/27/2018
		8/4/2018	11.7	-6.86	23.82	4.044	-0.288	0.702	0.009			-0.0007	1.0970	0.9267	7/10/2018	10/19/2018
		8/8/2018	10.4	-6.85	23.81	4.073	-0.255	0.738	0.008			-0.0007	1.0970	0.9267	7/10/2018	10/19/2018
		8/9/2018	11.4	-6.86	23.79	4.035	-0.265	0.727	0.008			-0.0007	1.0970	0.9267	7/10/2018	10/19/2018
			AV	-6.90	23.80		**AV**	0.706		**19** ± **3**						
			SD	0.08	0.01		**SD**	0.022								
							SE	0.009								

Sample ID	Age [Ma]	Date	Sample size [mg]	$\delta^{13}C_{V\text{-}PDB}$ [‰]	$\delta^{18}O_{V\text{-}SMOW}$ [‰]	$\delta^{47}_{raw\ bc}$ [‰]	$\Delta_{47raw\ bc}$ [‰]	Δ_{47} [‰]	se [‰]	T (Δ_{47})	n					
2017-AM-018	13.415	6/7/2017	10.2	-7.30	22.84	2.652	-0.276	0.737	0.006		6	-0.0002	1.0690	0.9441	1/6/2017	7/10/2017
		6/9/2017	13.3	-7.28	22.87	2.621	-0.346	0.663	0.006			-0.0002	1.0690	0.9441	1/6/2017	7/10/2017
		7/5/2017	12.3	-7.28	22.77	2.555	-0.323	0.688	0.005			-0.0002	1.0690	0.9441	1/6/2017	7/10/2017
		7/6/2017	13.5	-7.27	22.77	2.519	-0.365	0.642	0.005			-0.0002	1.0690	0.9441	1/6/2017	7/10/2017
		7/7/2017	12.8	-7.25	22.86	2.653	-0.340	0.669	0.004			-0.0002	1.0690	0.9441	1/6/2017	7/10/2017
		7/8/2017	12.8	-7.28	22.87	2.654	-0.324	0.686	0.008			-0.0002	1.0690	0.9441	1/6/2017	7/10/2017
			AV	-7.27	22.83		**AV**	0.681		**28** ± **5**						
			SD	0.02	0.05		**SD**	0.032								
							SE	0.013								

Sample ID	Age [Ma]	Date	Sample size [mg]	$\delta^{13}C_{V\text{-}PDB}$ [‰]	$\delta^{18}O_{V\text{-}SMOW}$ [‰]	$\delta^{47}_{raw\ bc}$ [‰]	$\Delta_{47raw\ bc}$ [‰]	Δ_{47} [‰]	se [‰]	T (Δ_{47})	n					
2017-AM-019	13.487	10/22/2017	9.9	-7.18	23.60	3.477	-0.319	0.698	0.003		5	-0.0003	1.0492	0.9429	7/14/2017	11/3/2017
		8/4/2018	11.9	-7.15	23.51	3.488	-0.260	0.732	0.007			-0.0007	1.0970	0.9267	7/10/2018	10/19/2018
		8/6/2018	10.6	-7.14	23.51	3.480	-0.271	0.721	0.005			-0.0007	1.0970	0.9267	7/10/2018	10/19/2018
		8/9/2018	11.9	-7.13	23.56	3.512	-0.299	0.690	0.010			-0.0007	1.0970	0.9267	7/10/2018	10/19/2018
		8/14/2018	9.6	-7.14	23.54	3.491	-0.282	0.709	0.008			-0.0007	1.0970	0.9267	7/10/2018	10/19/2018
			AV	-7.15	23.54		**AV**	0.710		**18** ± **2**						

			SD	0.02	0.04		**SD**	0.017								
							SE	0.008								

Sample ID	Age [Ma]	Date	Sample size [mg]	$\delta^{13}C_{V\text{-}PDB}$ [‰]	$\delta^{18}O_{V\text{-}SMOW}$ [‰]	$\delta^{47}{}_{raw\ bc}$ [‰]	$\Delta_{47raw\ bc}$ [‰]	Δ_{47} [‰]	se [‰]	T (Δ_{47})	n					
2017-AM-020	13.607	7/9/2017	13.0	-6.64	23.99	4.392	-0.325	0.686	0.009		6	-0.0002	1.0690	0.9441	1/6/2017	7/10/2017
		7/15/2017	8.2	-6.62	23.81	4.242	-0.308	0.709	0.006			-0.0003	1.0492	0.9429	7/14/2017	11/3/2017
		7/19/2017	10.6	-6.55	24.31	4.791	-0.332	0.684	0.008			-0.0003	1.0492	0.9429	7/14/2017	11/3/2017
		7/20/2017	12.0	-6.62	23.82	4.253	-0.320	0.697	0.004			-0.0003	1.0492	0.9429	7/14/2017	11/3/2017
		7/24/2017	10.7	-6.60	24.00	4.483	-0.276	0.742	0.008			-0.0003	1.0492	0.9429	7/14/2017	11/3/2017
		7/30/2017	11.4	-6.62	23.76	4.287	-0.318	0.699	0.009			-0.0003	1.0492	0.9429	7/14/2017	11/3/2017
			AV	-6.61	23.95		**AV**	0.703		**20** ± **3**						
			SD	0.03	0.21		**SD**	0.021								
							SE	0.009								

Sample ID	Age [Ma]	Date	Sample size [mg]	$\delta^{13}C_{V\text{-}PDB}$ [‰]	$\delta^{18}O_{V\text{-}SMOW}$ [‰]	$\delta^{47}{}_{raw\ bc}$ [‰]	$\Delta_{47raw\ bc}$ [‰]	Δ_{47} [‰]	se [‰]	T (Δ_{47})	n					
2017-AM-022	13.758	7/8/2017	11.1	-6.94	23.42	3.557	-0.297	0.715	0.009		5	-0.0002	1.0690	0.9441	1/6/2017	7/10/2017
		7/4/2017	12.0	-6.90	23.34	3.485	-0.328	0.682	0.010			-0.0002	1.0690	0.9441	1/6/2017	7/10/2017
		7/5/2017	10.1	-6.92	23.29	3.435	-0.314	0.697	0.008			-0.0002	1.0690	0.9441	1/6/2017	7/10/2017
		7/7/2017	12.3	-6.92	23.31	3.464	-0.308	0.704	0.007			-0.0002	1.0690	0.9441	1/6/2017	7/10/2017
		7/8/2017	11.8	-6.93	23.34	3.470	-0.317	0.694	0.005			-0.0002	1.0690	0.9441	1/6/2017	7/10/2017
			AV	-6.92	23.34		**AV**	0.698		**22** ± **2**						
			SD	0.02	0.05		**SD**	0.012								
							SE	0.006								

Sample ID	Age [Ma]	Date	Sample size [mg]	$\delta^{13}C_{V\text{-}PDB}$ [‰]	$\delta^{18}O_{V\text{-}SMOW}$ [‰]	$\delta^{47}{}_{raw\ bc}$ [‰]	$\Delta_{47raw\ bc}$ [‰]	$\Delta_{47\ CDES\ 90\ °C}$ [‰]	se [‰]	T (Δ_{47})	n					
2017-AM-024	14.067	7/29/2017	31.5	-6.55	23.96	4.385	-0.391	0.622	0.006		5	-0.0003	1.0492	0.9429	7/14/2017	11/3/2017
		7/31/2017	26.7	-6.57	23.91	4.326	-0.380	0.633	0.008			-0.0003	1.0492	0.9429	7/14/2017	11/3/2017
		8/1/2017	27.9	-6.53	23.97	4.418	-0.386	0.627	0.006			-0.0003	1.0492	0.9429	7/14/2017	11/3/2017
		2/7/2019	40.1	-6.27	23.91	4.612	-0.289	0.677	0.005			0.0001	1.0038	0.8800	1/9/2019	3/14/2019

		2/9/2019	30.8	-6.25	24.03	4.767	-0.273	0.693	0.007			0.0001	1.0038	0.8800	1/9/2019	3/14/2019
			AV	-6.43	23.96		**AV**	0.651		**39** ± **6**						
			SD	0.16	0.05		**SD**	0.032								
							SE	0.014								

Sample ID	Age [Ma]	Date	Sample size [mg]	$\delta^{13}C_{V\text{-}PDB}$ [‰]	$\delta^{18}O_{V\text{-}SMOW}$ [‰]	$\delta^{47}{}_{raw\ bc}$ [‰]	$\Delta_{47raw\ bc}$ [‰]	Δ_{47} [‰]	se [‰]	T (Δ_{47})	n					
2017-AM-025	14.227	10/22/2017	10.6	-6.59	23.80	4.231	-0.353	0.662	0.007		6	-0.0003	1.0492	0.9429	7/14/2017	11/3/2017
		4/17/2018	12.0	-6.41	23.72	4.378	-0.289	0.682	0.008			0.0000	1.1137	0.9159	3/7/2018	4/27/2018
		8/5/2018	10.9	-6.41	23.80	4.477	-0.274	0.718	0.005			-0.0007	1.0970	0.9267	7/10/2018	10/19/2018
		8/9/2018	10.5	-6.38	23.84	4.516	-0.303	0.686	0.007			-0.0007	1.0970	0.9267	7/10/2018	10/19/2018
		8/11/2018	10.8	-6.40	23.80	4.427	-0.329	0.657	0.008			-0.0007	1.0970	0.9267	7/10/2018	10/19/2018
		8/14/2018	8.4	-6.38	23.83	4.467	-0.340	0.645	0.009			-0.0007	1.0970	0.9267	7/10/2018	10/19/2018
			AV	-6.43	23.80		**AV**	0.675		**30** ± **4**						
			SD	0.08	0.04		**SD**	0.026								
							SE	0.011								

Sample ID	Age [Ma]	Date	Sample size [mg]	$\delta^{13}C_{V\text{-}PDB}$ [‰]	$\delta^{18}O_{V\text{-}SMOW}$ [‰]	$\delta^{47}{}_{raw\ bc}$ [‰]	$\Delta_{47raw\ bc}$ [‰]	Δ_{47} [‰]	se [‰]	T (Δ_{47})	n					
2017-AM-026	14.350	7/10/2017	13.9	-6.07	23.87	4.794	-0.357	0.659	0.007		5	-0.0002	1.0672	0.9506	1/6/2017	7/10/2017
		7/15/2017	8.6	-6.09	23.76	4.657	-0.362	0.652	0.005			-0.0003	1.0492	0.9429	7/14/2017	11/3/2017
		7/19/2017	10.9	-6.10	23.86	4.767	-0.351	0.664	0.006			-0.0003	1.0492	0.9429	7/14/2017	11/3/2017
		7/21/2017	12.1	-6.06	23.80	4.721	-0.371	0.643	0.004			-0.0003	1.0492	0.9429	7/14/2017	11/3/2017
		7/27/2017	10.9	-6.07	23.79	4.694	-0.386	0.627	0.006			-0.0003	1.0492	0.9429	7/14/2017	11/3/2017
			AV	-6.08	23.82		**AV**	0.649		**40** ± **3**						
			SD	0.02	0.05		**SD**	0.015								
							SE	0.007								

Sample ID	Age [Ma]	Date	Sample size [mg]	$\delta^{13}C_{V\text{-}PDB}$ [‰]	$\delta^{18}O_{V\text{-}SMOW}$ [‰]	$\delta^{47}{}_{raw\ bc}$ [‰]	$\Delta_{47raw\ bc}$ [‰]	Δ_{47} [‰]	se [‰]	T (Δ_{47})	n					
2017-AM-028	14.476	7/20/2017	11.9	-7.21	23.18	2.987	-0.360	0.654	0.005		6	-0.0003	1.0492	0.9429	7/14/2017	11/3/2017

	7/27/2017	10.1	-7.24	23.05	2.862	-0.330	0.686	0.006		-0.0003	1.0492	0.9429	7/14/2017	11/3/2017	
	7/28/2017	10.4	-7.25	23.11	2.913	-0.337	0.678	0.008		-0.0003	1.0492	0.9429	7/14/2017	11/3/2017	
	7/29/2017	7.7	-7.19	23.28	3.159	-0.314	0.703	0.008		-0.0003	1.0492	0.9429	7/14/2017	11/3/2017	
	7/30/2017	7.2	-7.22	23.15	2.998	-0.317	0.699	0.011		-0.0003	1.0492	0.9429	7/14/2017	11/3/2017	
	7/31/2017	6.6	-7.19	23.23	3.129	-0.293	0.724	0.005		-0.0003	1.0492	0.9429	7/14/2017	11/3/2017	
		AV	-7.22	23.17		**AV**	0.691		**24 ± 3**						
		SD	0.02	0.08		**SD**	0.024								
						SE	0.010								

Sample ID	Age [Ma]	Date	Sample size [mg]	$\delta^{13}C_{V\text{-}PDB}$ [‰]	$\delta^{18}O_{V\text{-}SMOW}$ [‰]	$\delta^{47}{}_{raw\ bc}$ [‰]	$\Delta_{47raw\ bc}$ [‰]	Δ_{47} [‰]	se [‰]	T (Δ_{47})	n					
2017-AM-029	14.543	6/7/2017	10.2	-7.04	23.49	3.532	-0.299	0.713	0.009		5	-0.0002	1.0690	0.9441	1/6/2017	7/10/2017
		6/9/2017	8.8	-7.03	23.42	3.438	-0.324	0.686	0.008			-0.0002	1.0690	0.9441	1/6/2017	7/10/2017
		7/5/2017	10.6	-7.01	23.37	3.428	-0.308	0.704	0.008			-0.0002	1.0690	0.9441	1/6/2017	7/10/2017
		7/8/2017	11.0	-7.01	23.55	3.619	-0.302	0.711	0.005			-0.0002	1.0690	0.9441	1/6/2017	7/10/2017
		7/9/2017	9.8	-7.01	23.44	3.494	-0.317	0.695	0.009			-0.0002	1.0690	0.9441	1/6/2017	7/10/2017
			AV	-7.02	23.46		**AV**	0.702		**21 ± 2**						
			SD	0.01	0.07		**SD**	0.011								
							SE	0.005								

Sample ID	Age [Ma]	Date	Sample size [mg]	$\delta^{13}C_{V\text{-}PDB}$ [‰]	$\delta^{18}O_{V\text{-}SMOW}$ [‰]	$\delta^{47}{}_{raw\ bc}$ [‰]	$\Delta_{47raw\ bc}$ [‰]	Δ_{47} [‰]	se [‰]	T (Δ_{47})	n					
2018-AM-037II	15.325	3/10/2019	18.3	-6.45	23.44	3.985	-0.273	0.694	0.010		4	0.0001	1.0038	0.8800	1/9/2019	3/14/2019
		3/12/2019	17.3	-6.46	23.35	3.881	-0.273	0.694	0.009			0.0001	1.0038	0.8800	1/9/2019	3/14/2019
		3/13/2019	16.9	-6.46	23.39	3.937	-0.268	0.699	0.007			0.0001	1.0038	0.8800	1/9/2019	3/14/2019
		3/21/2019	17.8	-6.46	23.44	3.959	-0.289	0.692	0.005			0.0000	1.0096	0.8962	3/15/2019	5/16/2019
			AV	-6.46	23.41		**AV**	0.694		**23 ± 0**						
			SD	0.00	0.04		**SD**	0.003								
							SE	0.001								

Sample ID	Age [Ma]	Date	Sample size [mg]	$\delta^{13}C_{V\text{-}PDB}$ [‰]	$\delta^{18}O_{V\text{-}SMOW}$ [‰]	$\delta^{47}{}_{raw\ bc}$ [‰]	$\Delta_{47raw\ bc}$ [‰]	Δ_{47} [‰]	se [‰]	T (Δ_{47})	n					
2018-AM-057	15.060	2/9/2019	13.7	-6.06	23.98	4.921	-0.256	0.710	0.009		5	0.0003	1.0046	0.8803	1/9/2019	3/14/2019

	2/9/2019	13.8	-6.08	24.00	4.909	-0.255	0.711	0.007			0.0003	1.0046	0.8803	1/9/2019	3/14/2019
	2/10/2019	14.0	-6.08	23.96	4.858	-0.270	0.696	0.006			0.0003	1.0046	0.8803	1/9/2019	3/14/2019
	3/11/2019	17.0	-6.45	23.55	4.074	-0.287	0.679	0.008			0.0001	1.0038	0.8800	1/9/2019	3/14/2019
	3/24/2019	16.1	-6.43	23.61	4.158	-0.288	0.693	0.009			0.0000	1.0096	0.8962	3/15/2019	5/16/2019
		AV	-6.22	23.82		**AV**	0.698		**22**	± **2**					
		SD	0.20	0.22		**SD**	0.013								
						SE	0.006								

Sample ID	Age [Ma]	Date	Sample size [mg]	$\delta^{13}C_{V\text{-}PDB}$ [‰]	$\delta^{18}O_{V\text{-}SMOW}$ [‰]	$\delta^{47}{}_{raw\ bc}$ [‰]	$\Delta_{47raw\ bc}$ [‰]	Δ_{47} [‰]	se [‰]	T (Δ_{47})	n					
2018-AM-065a	14.760	2/10/2019	16.0	-6.38	23.63	4.240	-0.278	0.688	0.003		5	0.0001	1.0038	0.8800	1/9/2019	3/14/2019
		2/10/2019	16.0	-6.30	23.71	4.406	-0.266	0.700	0.008			0.0001	1.0038	0.8800	1/9/2019	3/14/2019
		2/10/2019	15.5	-6.37	23.62	4.243	-0.276	0.690	0.007			0.0001	1.0038	0.8800	1/9/2019	3/14/2019
		2/11/2019	16.4	-6.29	23.73	4.414	-0.284	0.682	0.014			0.0001	1.0038	0.8800	1/9/2019	3/14/2019
		2/12/2019	15.8	-6.35	23.68	4.342	-0.248	0.719	0.009			0.0001	1.0038	0.8800	1/9/2019	3/14/2019
		AV		-6.34	23.67		**AV**	0.696		**22**	± **2**					
		SD		0.04	0.05		**SD**	0.014								
							SE	0.006								

Sample ID	Age [Ma]	Date	Sample size [mg]	$\delta^{13}C_{V\text{-}PDB}$ [‰]	$\delta^{18}O_{V\text{-}SMOW}$ [‰]	$\delta^{47}{}_{raw\ bc}$ [‰]	$\Delta_{47raw\ bc}$ [‰]	Δ_{47} [‰]	se [‰]	T (Δ_{47})	n					
2018-AM-075a	14.340	8/17/2018	12.2	-6.68	23.63	4.000	-0.325	0.661	0.008		5	-0.0007	1.0970	0.9267	7/10/2018	10/19/2018
		8/18/2018	12.5	-6.66	23.66	4.055	-0.309	0.679	0.010			-0.0007	1.0970	0.9267	7/10/2018	10/19/2018
		8/31/2018	12.9	-6.66	23.63	4.054	-0.285	0.705	0.022			-0.0007	1.0970	0.9267	7/10/2018	10/19/2018
		9/11/2018	13.6	-6.71	23.65	3.995	-0.314	0.674	0.012			-0.0007	1.0970	0.9267	7/10/2018	10/19/2018
		9/13/2018	12.0	-6.65	23.83	4.239	-0.305	0.683	0.008			-0.0007	1.0970	0.9267	7/10/2018	10/19/2018
		AV		-6.67	23.68		**AV**	0.680		**28**	± **3**					
		SD		0.02	0.08		**SD**	0.016								
							SE	0.007								

Sample ID	Age [Ma]	Date	Sample size [mg]	$\delta^{13}C_{V\text{-}PDB}$ [‰]	$\delta^{18}O_{V\text{-}SMOW}$ [‰]	$\delta^{47}{}_{raw\ bc}$ [‰]	$\Delta_{47raw\ bc}$ [‰]	Δ_{47} [‰]	se [‰]	T (Δ_{47})	n					
2018-AM-092a	14.180	8/17/2018	13.4	-7.09	23.16	3.161	-0.293	0.695	0.006		6	-0.0007	1.0970	0.9267	7/10/2018	10/19/2018

	8/19/2018	14.2	-7.07	23.13	3.188	-0.253	0.740	0.006		-0.0007	1.0970	0.9267	7/10/2018	10/19/2018
	8/31/2018	13.4	-7.07	23.24	3.283	-0.262	0.730	0.007		-0.0007	1.0970	0.9267	7/10/2018	10/19/2018
	9/11/2018	14.5	-7.08	23.27	3.312	-0.258	0.735	0.009		-0.0007	1.0970	0.9267	7/10/2018	10/19/2018
	9/13/2018	13.7	-7.08	23.22	3.239	-0.287	0.702	0.006		-0.0007	1.0970	0.9267	7/10/2018	10/19/2018
	2/6/2019	21.7	-6.95	23.20	3.262	-0.274	0.693	0.006		0.0001	1.0038	0.8800	1/9/2019	3/14/2019
		AV	-7.06	23.21		**AV**	0.716		**16 ± 3**					
		SD	0.05	0.05		**SD**	0.021							
						SE	0.009							

Sample ID	Age [Ma]	Date	Sample size [mg]	$\delta^{13}C_{V\text{-}PDB}$ [‰]	$\delta^{18}O_{V\text{-}SMOW}$ [‰]	$\delta^{47}{}_{raw\ bc}$ [‰]	$\Delta_{47raw\ bc}$ [‰]	Δ_{47} [‰]	se [‰]	T (Δ_{47})	n					
2018-AM-110	13.885	8/16/2018	11.2	-7.49	23.23	2.797	-0.335	0.649	0.011		5	-0.0007	1.0970	0.9267	7/10/2018	10/19/2018
		8/18/2018	10.6	-7.43	23.37	3.007	-0.326	0.659	0.007			-0.0007	1.0970	0.9267	7/10/2018	10/19/2018
		9/11/2018	11.4	-7.45	23.36	2.985	-0.312	0.674	0.006			-0.0007	1.0970	0.9267	7/10/2018	10/19/2018
		9/14/2018	11.2	-7.44	23.31	2.949	-0.305	0.683	0.008			-0.0007	1.0970	0.9267	7/10/2018	10/19/2018
		9/15/2018	11.9	-7.41	23.37	3.039	-0.306	0.681	0.003			-0.0007	1.0970	0.9267	7/10/2018	10/19/2018
			AV	-7.44	23.33		**AV**	0.669		**32 ± 2**						
			SD	0.03	0.06		**SD**	0.014								
							SE	0.006								

Sample ID	Age [Ma]	Date	Sample size [mg]	$\delta^{13}C_{V\text{-}PDB}$ [‰]	$\delta^{18}O_{V\text{-}SMOW}$ [‰]	$\delta^{47}{}_{raw\ bc}$ [‰]	$\Delta_{47raw\ bc}$ [‰]	Δ_{47} [‰]	se [‰]	T (Δ_{47})	n					
2018-AM-114	13.805	8/16/2018	11.7	-6.89	23.31	3.494	-0.295	0.694	0.007		5	-0.0007	1.0970	0.9267	7/10/2018	10/19/2018
		8/19/2018	10.5	-6.91	23.31	3.464	-0.306	0.681	0.005			-0.0007	1.0970	0.9267	7/10/2018	10/19/2018
		9/12/2018	9.7	-6.90	23.45	3.622	-0.309	0.679	0.008			-0.0007	1.0970	0.9267	7/10/2018	10/19/2018
		9/13/2018	10.3	-6.90	23.32	3.491	-0.304	0.684	0.005			-0.0007	1.0970	0.9267	7/10/2018	10/19/2018
		9/15/2018	11.5	-6.80	23.36	3.615	-0.313	0.674	0.008			-0.0007	1.0970	0.9267	7/10/2018	10/19/2018
			AV	-6.88	23.35		**AV**	0.682		**27 ± 1**						
			SD	0.05	0.06		**SD**	0.007								

$\delta^{18}O$ and $\delta^{13}C$ of pedogenic carbonates supplementary data – S.5.VI

sample	Replicate measurement	Also measured for Δ_{47}	sample type	stratigraphic position	local magnetostrat.	Age (strictly based on Krijgsman *et. al.* 1997b)	Age (secondarily adjusted to Holbourn *et. al.* 2014)	$\delta^{13}C$	StDev $\delta^{13}C$	$\delta^{18}O$	StDev $\delta^{18}O$	$CaCO_3$	Spacing D47	$\delta^{13}C$	StDev $\delta^{13}C$	$\delta^{18}O$	StDev $\delta^{18}O$
				[m above base of Krijgsman *et. al.* 1997b]	Krijgsman *et. al.* 1997b	[Ma]	[Ma]	[‰, VPDB]	[‰, VPDB]	[‰, VSMOW]	[‰, VSMOW]	[‰wt.]	[m]	[‰, VPDB]	[‰, VPDB]	[‰, VSMOW]	[‰, VSMOW]
2018-AM-175			Caliche	237.1		12.847	12.910	-7.53	0.01	25.21	0.02	80.6					
2017-AM-011		x	Nodule	233.0		12.926	12.975	-8.19	0.03	23.67	0.05	77.6		-8.03	0.02	23.34	0.06
2017-AM-011	x	x	Nodule	233.0		12.926	12.975	-8.02	0.01	23.39	0.03	68.4	7.0				
2017-AM-012			Caliche	230.0		12.985	13.010	-7.68	0.02	23.91	0.05	50.1					
2017-AM-012	x		Caliche	230.0		12.985	13.010	-7.59	0.02	23.68	0.05	44.1					
2017-AM-013		x	Nodule	226.0		13.062	13.075	-7.76	0.01	24.19	0.02	52.2		-7.71	0.04	23.87	0.09
2017-AM-013	x	x	Nodule	226.0		13.062	13.075	-7.59	0.03	24.02	0.03	50.6	15.0				
2017-AM-014			Caliche	225.0	C5AAn	13.082	13.120	-7.23	0.02	24.00	0.06	44.7					
2017-AM-014	x		Caliche	225.0		13.082	13.120	-7.15	0.02	23.62	0.03	40.7					
2018-AM-162			Caliche	225.0		13.082	13.110	-7.56	0.03	23.59	0.04	45.6					
2018-AM-161			Caliche	224.5		13.091	13.120	-7.20	0.02	23.81	0.05	28.7					
2018-AM-150			Caliche	214.2		13.287	13.260	-7.76	0.02	23.69	0.04	60.6					
2018-AM-148			Caliche	213.0		13.310	13.285	-7.55	0.02	23.87	0.04	49.5					
2017-AM-016		x	Nodule	211.0		13.348	13.320	-7.20	0.02	23.98	0.05	58.5		-6.90	0.08	23.80	0.01
2017-AM-016	x	x	Nodule	211.0		13.348	13.320	-7.05	0.02	23.78	0.04	60.8	7.0				
2018-AM-144			Caliche	208.7	C5ABn	13.391	13.330	-7.67	0.02	23.52	0.03	58.1					
2018-AM-142			Caliche	207.2		13.418	13.365	-7.02	0.02	23.83	0.05	45.3					
2017-AM-018		x	Nodule	204.0		13.476	13.415	-7.33	0.03	23.13	0.05	50.3		-7.27	0.02	22.83	0.05
2017-AM-018	x	x	Nodule	204.0		13.476	13.415	-7.25	0.02	22.76	0.04	48.8	8.0				
2017-AM-019		x	Nodule	196.0		13.617	13.487	-7.33	0.03	23.72	0.03	72.1	4.0	-7.15	0.02	23.54	0.04
2018-AM-133			Caliche	195.1		13.633	13.530	-7.43	0.02	23.76	0.03	40.9					
2017-AM-020		x	Nodule	192.0		13.685	13.607	-6.70	0.02	24.18	0.05	75.5		-6.61	0.03	23.95	0.21

2017-AM-020	x	x	Nodule	192.0		13.685	13.607	-6.58	0.01	24.04	0.03	74.0	10.0			
2018-AM-127			Caliche	191.1		13.701	13.610	-7.28	0.02	23.87	0.03	48.5				
2018-AM-124			Caliche	185.7		13.789	13.748	-6.48	0.01	23.71	0.04	55.1				
2017-AM-021			Caliche	184.0		13.817	13.753	-7.04	0.02	23.87	0.05	46.1				
2017-AM-021	x		Caliche	184.0		13.817	13.753	-6.88	0.03	23.58	0.04	42.3				
2017-AM-022		x	Nodule	182.0		13.849	13.758	-6.95	0.02	23.66	0.03	45.7	5.1	-6.92	0.02	23.34	0.05
2017-AM-022	x	x	Nodule	182.0	C5ACn	13.849	13.758	-6.90	0.02	23.32	0.04	53.5				
2018-AM-119			Caliche	180.9		13.866	13.777	-6.90	0.03	23.47	0.03	49.2				
2018-AM-118			Caliche	179.8		13.884	13.779	-6.11	0.02	23.79	0.04	53.9				
2018-AM-114		x	Nodule	176.9		13.929	13.805	-7.04	0.02	23.32	0.03	56.2	3.9	-6.88	0.05	23.35	0.06
2018-AM-110		x	Nodule	173.0		13.988	13.885	-7.51	0.02	23.30	0.04	41.6	8.0	-7.44	0.03	23.33	0.06
2018-AM-107			Caliche	169.0		14.047	13.920	-7.47	0.02	23.64	0.04	36.4				
2018-AM-104			Caliche	166.3		14.088	13.990	-6.99	0.02	23.70	0.05	50.7				
2017-AM-024		x	Nodule	165.0		14.106	14.067	-6.51	0.03	24.17	0.06	18.7	6.8	-6.47	0.14	23.97	0.06
2018-AM-100			Caliche	163.0		14.135	14.100	-7.11	0.02	23.46	0.04	80.0				
2018-AM-094			Caliche	158.9		14.193	14.165	-6.95	0.02	23.47	0.03	52.1				
2018-AM-093			Caliche	158.9		14.194	14.170	-6.88	0.02	23.49	0.03	40.0				
2018-AM-092a		x	Nodule	158.2		14.203	14.180	-7.19	0.03	23.18	0.04	36.3	2.2	-7.06	0.05	23.21	0.05
2017-AM-025		x	Nodule	156.0		14.234	14.227	-6.67	0.02	24.04	0.05	59.2	8.7	-6.43	0.08	23.80	0.04
2017-AM-025	x	x	Nodule	156.0		14.234	14.227	-6.53	0.02	23.71	0.03	69.1				
2018-AM-080			Caliche	151.0		14.304	14.315	-6.74	0.02	23.39	0.04	45.4				
2018-AM-075a		x	Nodule	147.3		14.354	14.340	-7.05	0.01	23.46	0.02	47.0	1.3	-6.67	0.02	23.68	0.08
2018-AM-075a	x	x	Nodule	147.3	C5ADn	14.354	14.340	-6.81	0.02	23.55	0.03	37.3				
2018-AM-074			Caliche	146.3		14.368	14.347	-7.02	0.03	23.41	0.05	39.7				
2017-AM-026		x	Nodule	146.0		14.372	14.350	-6.11	0.02	24.15	0.04	61.0	8.0	-6.08	0.02	23.82	0.05
2017-AM-026	x	x	Nodule	146.0		14.372	14.350	-6.03	0.03	23.92	0.03	58.1				
2018-AM-073s			Caliche	144.3		14.395	14.360	-7.05	0.02	22.47	0.04	79.5				
2018-AM-035			Caliche	143.5		14.406	14.373	-6.67	0.03	23.85	0.03	49.5				
2018-AM-032			Caliche	142.1		14.425	14.421	-6.40	0.02	23.88	0.02	53.3				
2017-AM-028		x	Nodule	138.0		14.480	14.476	-7.31	0.02	23.53	0.05	81.7		-7.22	0.02	23.17	0.08
2017-AM-028	x	x	Nodule	138.0		14.480	14.476	-7.24	0.01	23.24	0.02	88.8				

2018-AM-026			Caliche	134.6		14.526	14.486	-6.47	0.02	23.81	0.05	88.1					
2018-AM-025			Caliche	134.5		14.527	14.503	-6.68	0.02	23.71	0.04	95.9					
2018-AM-022b			Caliche	133.2		14.545	14.520	-7.00	0.02	23.73	0.03	87.4					
2018-AM-022a			Caliche	133.2		14.545	14.520	-7.13	0.02	23.68	0.03	83.2					
2018-AM-021			Caliche	131.8		14.564	14.525	-6.91	0.03	23.61	0.04	77.2					
2018-AM-019			Caliche	131.0		14.575	14.529	-7.06	0.05	23.55	0.07	77.5					
2018-AM-017			Caliche	130.1		14.586	14.531	-6.86	0.03	23.66	0.05	78.1					
2017-AM-029		x	Nodule	129.0		14.602	14.543	-7.05	0.03	23.42	0.03	94.3	7.7	-7.02	0.01	23.46	0.07
2018-AM-013			Caliche	127.4		14.624	14.610	-6.61	0.02	23.54	0.05	65.8					
2018-AM-009a			Caliche	126.3		14.638	14.620	-6.50	0.01	23.55	0.03	79.9					
2018-AM-009b			Caliche	126.3		14.638	14.620	-6.70	0.03	23.52	0.05	71.6					
2018-AM-008			Caliche	125.2		14.653	14.626	-6.59	0.03	23.13	0.07	28.6					
2018-AM-003			Caliche	123.7		14.673	14.640	-6.38	0.02	23.46	0.06	65.5					
2018-AM-066			Caliche	123.2		14.681	14.670	-6.70	0.03	23.37	0.05	76.5					
2018-AM-065a		x	Nodule	121.3	C5Bn.1n	14.707	14.760	-6.71	0.04	23.64	0.07	69.3	24.5	-6.34	0.04	23.67	0.05
2018-AM-065a	x	x	Nodule	121.3		14.707	14.760	-6.64	0.02	23.59	0.03	53.3					
2018-AM-062			Caliche	106.2		14.922	14.890	-7.34	0.01	23.14	0.03	65.2					
2018-AM-061			Caliche	100.6		15.007	14.925	-7.19	0.03	23.31	0.04	80.8					
2018-AM-057	x	x	Nodule	96.8		15.066	15.060	-6.38	0.02	23.78	0.03	67.1	14.6	-6.22	0.20	23.82	0.22
2018-AM-057	x	x	Nodule	96.8		15.066	15.060	-6.76	0.01	23.56	0.04	75.5					
2018-AM-056			Caliche	96.1	C5Bn.2n	15.076	15.068	-6.92	0.02	23.64	0.05	60.5					
2018-AM-054			Caliche	95.1		15.092	15.078	-7.30	0.02	23.55	0.05	73.1					
2018-AM-052a			Caliche	92.9		15.128	15.106	-6.91	0.03	23.84	0.06	75.1					
2018-AM-051			Caliche	92.0		15.143	15.115	-6.82	0.03	23.44	0.03	69.3					
2018-AM-049			Caliche	90.6		15.165	15.161	-6.60	0.02	23.79	0.05	52.9					
2018-AM-044			Caliche	89.0		15.191	15.189	-6.70	0.02	23.50	0.05	54.2					
2018-AM-038			Caliche	84.3		15.270	15.303	-7.02	0.03	23.65	0.04	67.8					
2018-AM-039a			Caliche	84.2		15.271	15.312	-6.97	0.02	22.94	0.04	100.0					
2018-AM-037II		x	Nodule	82.2		15.306	15.325	-6.73	0.02	23.42	0.04	50.7		-6.46	0.00	23.41	0.04
2018-AM-036			Caliche	81.9		15.311	15.375	-6.87	0.03	23.47	0.04	56.8					

Lithology, magnetostratigraphy, and results – S.5.VII

Lithology, magnetostratigraphy of the Armantes section with measured soil temperatures, $\delta^{18}O$, and $\delta^{13}C$.

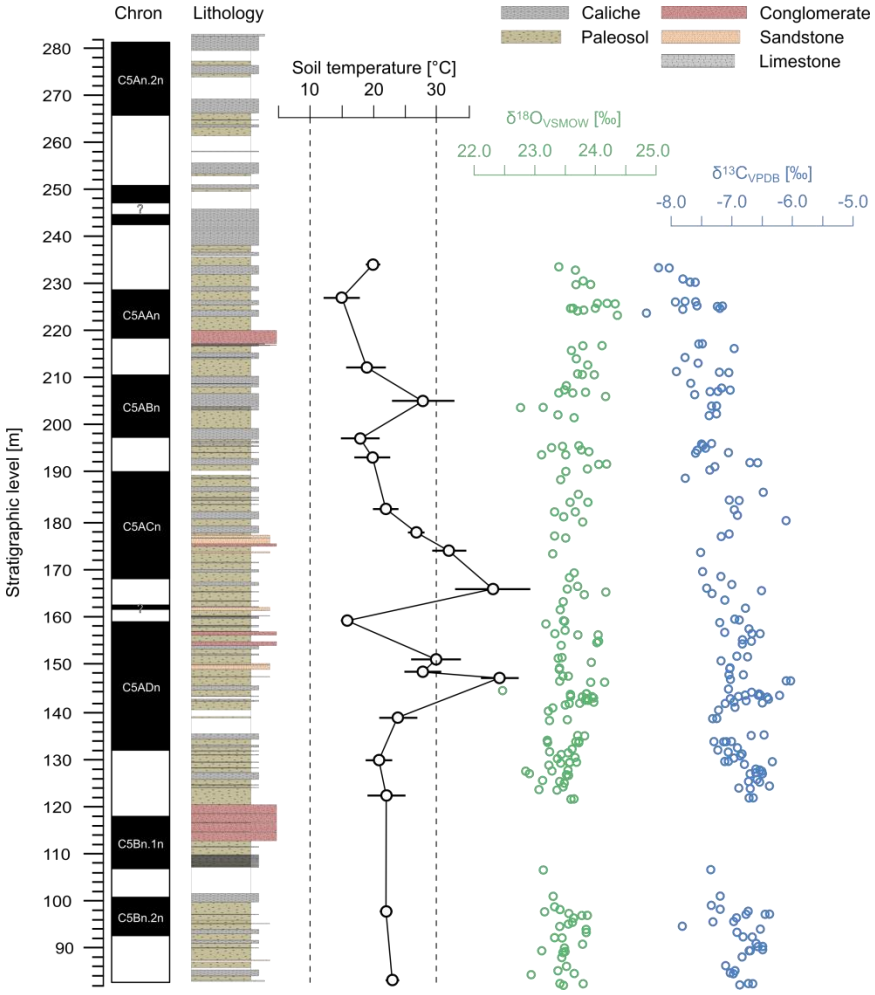

Supplementary figure 5.I: Stratigraphic profile relative to the original profile meters incl. the assigned chrons (Krijgsman *et al.*, 1997). The lithology is as follows whereas the relative abundance within the profile sampled for clumped isotope analyses (82.2 to 233.0 m) is given in brackets: Green: Paleosoil with red and white mottling, rootlets, and soil carbonates in a sandy matrix (23.9 %) Dark grey: Caliche banks, partly with nodular to porous structure and predominantly grey color (57.4 %). Light grey: carbonates from an aquatic facies (0.1 %). Yellow: Weakly cemented sandstone with carbonate components (3.0 %). Red: Conglomerate with sand to gravel sized carbonatic and siliciclastic components (8.2%). White: gap (7.4 %)

Appendix to chapter 6

Comparison of the lithology and magnetostratigraphy of the Aragon and Armantes sections (*S.6.I*). Measured and calculated data from equilibrated gases and empirical transfer functions (*S.6.II*), standard (*S.6.III*) and sample (*S.6.IV*) measurements including δ^{47} and raw Δ_{47} values. Overview on the Δ_{47} soil temperature datasets (*S.6.V*) and $\delta^{18}O$ and $\delta^{13}C$ of pedogenic carbonates (*S.6.VI*).

Comparison of the Lithology of Armantes and Aragon – S.6.I

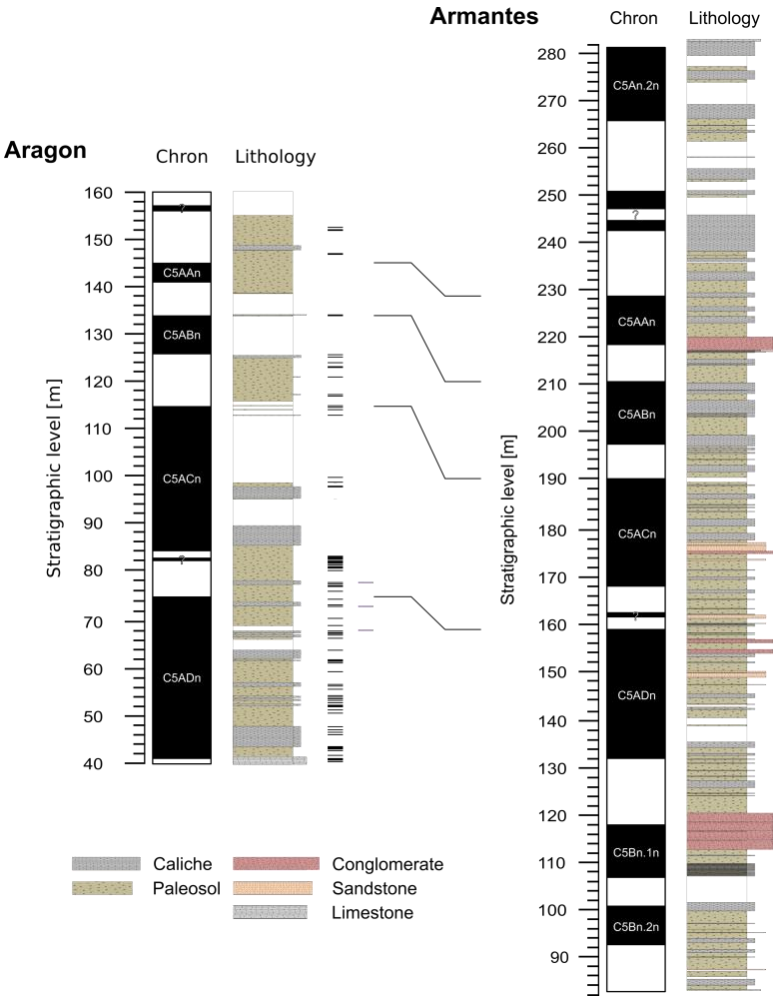

Supplementary figure 6.I: Comparison of the lithology and magnetostratigraphy of the sections Aragon (left) and Armantes (right). The correlations of the upper chron boundaries are indicated by black lines (middle). For Aragon, black horizontal lines indicate sample positions, purple horizontal lines indicate sampels measured for Δ_{47}.

Equilibrated gases and empirical transfer functions – S.6.II

Date	Sample	δ47 (raw) (‰)	Δ47 (raw) (‰)	SD Δ47 (raw) (‰)	δ47 (bgcorr) (‰)	Δ47 (bgcorr) (‰)	SD Δ47 (bgcorr) (‰)	δ13C CO2 (‰ VPDB)	δ18O CO2 (‰ VSMOW)	Diff Bellow (mV)	ETF period
7/11/2018	HG	-24.719	-1.425	0.027	-24.119	-0.811	0.019	-21.427	18.287	30.8	2018.07.10–2018.10.19
7/12/2018	HG	-26.397	-1.451	0.025	-25.775	-0.814	0.025	-22.850	17.996	128.5	2018.07.10–2018.10.19
7/13/2018	HG	-1.553	-0.800	0.023	-1.559	-0.805	0.023	-4.198	24.301	141.3	2018.07.10–2018.10.19
7/14/2018	HG	19.746	-0.303	0.024	19.225	-0.813	0.015	2.348	38.773	71.7	2018.07.10–2018.10.19
7/18/2018	HG	19.777	-0.319	0.022	19.244	-0.842	0.027	2.228	38.938	70.3	2018.07.10–2018.10.19
7/19/2018	HG	-23.678	-1.372	0.022	-23.121	-0.802	0.012	-20.486	18.372	95.1	2018.07.10–2018.10.19
7/23/2018	HG	-1.308	-0.849	0.026	-1.296	-0.838	0.024	-4.373	24.768	22.2	2018.07.10–2018.10.19
7/25/2018	HG	19.441	-0.305	0.038	18.882	-0.853	0.023	2.151	38.663	68.3	2018.07.10–2018.10.19
7/26/2018	HG	-26.936	-1.505	0.039	-26.269	-0.821	0.035	-23.014	17.657	37.2	2018.07.10–2018.10.19
7/31/2018	HG	-1.308	-0.818	0.029	-2.149	-0.823	0.023	-4.424	23.945	157.6	2018.07.10–2018.10.19
8/1/2018	HG	18.060	-0.335	0.062	17.547	-0.839	0.032	2.277	37.188	40.6	2018.07.10–2018.10.19
8/2/2018	HG	-24.150	-1.426	0.036	-23.543	-0.806	0.029	-20.675	18.129	62.0	2018.07.10–2018.10.19
8/6/2018	HG	-1.959	-0.807	0.024	-1.953	-0.801	0.023	-4.505	24.198	114.7	2018.07.10–2018.10.19
8/10/2018	HG	-23.387	-1.442	0.037	-22.765	-0.805	0.024	-20.541	18.794	18.1	2018.07.10–2018.10.19
8/13/2018	HG	19.599	-0.309	0.033	19.083	-0.815	0.015	2.358	38.622	-50.5	2018.07.10–2018.10.19
8/15/2018	HG	-1.180	-0.811	0.033	-1.186	-0.817	0.021	-3.958	24.454	81.1	2018.07.10–2018.10.19
8/16/2018	HG	-23.114	-1.399	0.050	-22.529	-0.801	0.029	-20.396	18.888	125.6	2018.07.10–2018.10.19
8/21/2018	HG	17.830	-0.300	0.046	17.289	-0.831	0.024	2.284	36.916	37.1	2018.07.10–2018.10.19
8/22/2018	HG	-1.140	-0.836	0.029	-1.139	-0.835	0.018	-4.015	24.575	34.5	2018.07.10–2018.10.19
8/23/2018	HG	-26.939	-1.523	0.033	-26.247	-0.813	0.029	-22.919	17.579	139.5	2018.07.10–2018.10.19
8/27/2018	HG	18.898	-0.213	0.054	18.286	-0.814	0.027	1.940	38.234	157.4	2018.07.10–2018.10.19
8/29/2018	HG	-27.787	-1.588	0.028	-27.016	-0.795	0.029	-23.206	17.056	61.8	2018.07.10–2018.10.19
9/3/2018	HG	-24.389	-1.359	0.048	-23.868	-0.826	0.041	-21.274	18.407	163.5	2018.07.10–2018.10.19
9/5/2018	HG	18.034	-0.345	0.032	17.561	-0.810	0.012	2.074	37.372	-2.6	2018.07.10–2018.10.19
9/10/2018	HG	-27.420	-1.556	0.043	-26.669	-0.786	0.035	-23.181	17.377	-32.5	2018.07.10–2018.10.19
9/12/2018	HG	-1.367	-0.820	0.036	-1.367	-0.819	0.031	-4.121	24.434	60.6	2018.07.10–2018.10.19
9/14/2018	HG	17.492	-0.316	0.071	16.961	-0.838	0.038	2.216	36.660	62.6	2018.07.10–2018.10.19
9/18/2018	HG	-1.145	-0.822	0.021	-1.167	-0.843	0.024	-4.051	24.591	78.0	2018.07.10–2018.10.19
9/19/2018	HG	-25.161	-1.452	0.046	-24.515	-0.790	0.033	-21.427	17.860	91.2	2018.07.10–2018.10.19
9/22/2018	HG	17.642	-0.271	0.052	17.077	-0.826	0.026	2.161	36.819	87.5	2018.07.10–2018.10.19
9/27/2018	HG	-1.453	-0.810	0.042	-1.476	-0.833	0.022	-4.410	24.619	82.3	2018.07.10–2018.10.19
9/28/2018	HG	17.385	-0.300	0.038	16.876	-0.800	0.011	1.909	36.838	25.4	2018.07.10–2018.10.19
10/1/2018	HG	-26.402	-1.535	0.064	-25.680	-0.794	0.010	-22.463	17.692	24.6	2018.07.10–2018.10.19
10/5/2018	HG	-0.842	-0.806	0.049	-0.870	-0.834	0.015	-4.031	24.861	61.9	2018.07.10–2018.10.19
10/9/2018	HG	18.102	-0.291	0.042	17.572	-0.811	0.020	2.245	37.217	-10.9	2018.07.10–2018.10.19
10/10/2018	HG	-25.852	-1.538	0.031	-25.133	-0.801	0.020	-22.106	17.907	50.4	2018.07.10–2018.10.19
10/10/2018	HG	-1.317	-0.819	0.030	-1.324	-0.827	0.025	-4.275	24.634	50.8	2018.07.10–2018.10.19
10/15/2018	HG	-1.463	-0.815	0.035	-1.484	-0.837	0.020	-4.191	24.401	88.5	2018.07.10–2018.10.19
10/17/2018	HG	-27.173	-1.549	0.048	-26.439	-0.796	0.028	-22.846	17.292	103.6	2018.07.10–2018.10.19
10/18/2018	HG	17.236	-0.237	0.051	16.597	-0.865	0.024	2.201	36.339	223.0	2018.07.10–2018.10.19

Date	Sample	δ47 (raw) (‰)	Δ47 (raw) (‰)	SD Δ47 (raw) (‰)	δ47 (bgcorr) (‰)	Δ47 (bgcorr) (‰)	SD Δ47 (bgcorr) (‰)	δ13C CO2 (‰ VPDB)	δ18O CO2 (‰ VSMOW)	Diff Bellow (mV)	ETF period
7/10/2018	25G	30.847	0.775	0.016	30.0179	-0.030	0.015	-4.312	55.419	85.1	2018.07.10–2018.10.19
7/17/2018	25G	31.478	0.829	0.024	30.6136	-0.010	0.022	-4.306	55.991	181.4	2018.07.10–2018.10.19
7/17/2018	25G	-29.801	-0.703	0.030	-29.0815	0.038	0.025	-40.646	31.561	95.6	2018.07.10–2018.10.19
7/19/2018	25G	-29.566	-0.730	0.029	-28.8339	0.024	0.022	-40.789	31.979	-24.8	2018.07.10–2018.10.19
7/25/2018	25G	30.652	0.822	0.021	29.7692	-0.035	0.013	-4.415	55.277	203.9	2018.07.10–2018.10.19
7/27/2018	25G	32.615	0.826	0.033	31.7188	-0.042	0.021	-4.191	57.022	108.4	2018.07.10–2018.10.19
7/30/2018	25G	31.908	0.827	0.033	31.0498	-0.006	0.033	-4.154	56.274	51.9	2018.07.10–2018.10.19
8/1/2018	25G	-29.701	-0.716	0.028	-28.9874	0.020	0.027	-40.634	31.666	169.4	2018.07.10–2018.10.19
8/7/2018	25G	31.447	0.870	0.035	30.5135	-0.036	0.022	-4.351	55.963	159.4	2018.07.10–2018.10.19
8/9/2018	25G	-29.655	-0.786	0.032	-28.8505	0.042	0.030	-40.767	31.921	-38.5	2018.07.10–2018.10.19
8/14/2018	25G	32.026	0.872	0.049	31.1118	-0.014	0.013	-4.169	56.360	44.2	2018.07.10–2018.10.19
8/17/2018	25G	-28.881	-0.766	0.050	-28.0878	0.051	0.030	-40.544	32.481	0.5	2018.07.10–2018.10.19
8/20/2018	25G	31.538	0.887	0.057	30.6013	-0.021	0.034	-4.300	55.984	90.5	2018.07.10–2018.10.19
8/24/2018	25G	-29.209	-0.836	0.030	-28.3974	0.000	0.015	-40.551	32.217	-19.6	2018.07.10–2018.10.19
8/30/2018	25G	31.406	0.920	0.049	30.4402	-0.017	0.028	-4.331	55.849	84.2	2018.07.10–2018.10.19
9/6/2018	25G	-29.364	-0.679	0.029	-28.7194	-0.015	0.025	-40.645	31.991	230.5	2018.07.10–2018.10.19
9/7/2018	25G	31.779	0.833	0.032	30.8864	-0.033	0.027	-4.294	56.277	79.0	2018.07.10–2018.10.19
9/11/2018	25G	-29.258	-0.743	0.053	-28.5418	-0.006	0.036	-40.713	32.238	111.3	2018.07.10–2018.10.19
9/13/2018	25G	32.332	0.847	0.044	31.4656	0.007	0.025	-4.230	56.755	-4.6	2018.07.10–2018.10.19
9/17/2018	25G	-29.711	-0.752	0.040	-28.9966	-0.016	0.028	-40.776	31.837	180.9	2018.07.10–2018.10.19
9/20/2018	25G	32.116	0.912	0.040	31.1474	-0.028	0.040	-4.278	56.519	73.1	2018.07.10–2018.10.19
9/24/2018	25G	-29.619	-0.773	0.057	-28.8582	0.010	0.017	-40.763	31.941	99.1	2018.07.10–2018.10.19

9/26/2018	25G	31.646	0.979	0.066	30.5896	-0.046	0.027	-4.361	56.060	240.9	2018.07.10–2018.10.19
10/2/2018	25G	-28.956	-0.775	0.018	-28.2168	-0.014	0.020	-40.546	32.414	148.5	2018.07.10–2018.10.19
10/4/2018	25G	32.703	0.911	0.027	31.7456	-0.017	0.021	-4.145	56.976	-4.1	2018.07.10–2018.10.19
10/11/2018	25G	-29.063	-0.768	0.047	-28.3169	0.000	0.025	-40.586	32.336	175.8	2018.07.10–2018.10.19
10/16/2018	25G	33.096	0.982	0.028	32.0210	-0.060	0.022	-3.865	57.016	177.3	2018.07.10–2018.10.19

from/until	**ETF*s**	
2018/07/10	**Slope:**	1.0970
2018/10/19	**Intercept:**	0.9267
	Residual slope**	-0.0007

Equilibrated gas line intercepts		
	Intercept	**Intended**
HG	-0.8205	0.0266
25G	-0.0062	0.9198

AFF Δ47	
25–90°C	0.088

AFF δ18O (Kim *et. al.* 2007)		
	calcite	**aragonite**
90	1.008128581	1.008541256
110	1.007608497	1.008049938

*) Empirical transfer function (ETF) applied during this study with slopes (m) and intercepts (b) of the empirical transfer functions in the form of y=m*x+b .

**) the residual slope is derived from the 25G and HG data. This correction step was performed even though the HGL slopes are below 0.001. This assures a precise data correction, especially for samples with extreme δ^{47} values. A slope of 0.0000 was chosen when the residual slope, within error, indistinguishable from 0.0000.

Standard data – S.6.III

Date	Sample	δ47 (raw) (‰)	Δ47 (raw) (‰)	SD Δ47 (raw) (‰)	δ47 (bgcorr) (‰)	Δ47 (bgcorr) (‰)	SD Δ47 (bgcorr) (‰)	δ13C CO2 (‰ VPDB)	δ18O CO2 (‰ VSMOW)	Diff Bellow (mV)	Weight (g)	Pressure Bellow (mBar)	ETF period
2018/07/11	ETH2	-11.649	-0.893	0.030	-11.416	-0.657	0.031	-9.988	19.846	157.7	6.8	26.1	2018.07.10–2018.10.19
2018/07/11	ETH2	-11.311	-0.916	0.027	-11.056	-0.658	0.035	-9.880	20.106	45.8	7.4	27.3	2018.07.10–2018.10.19
2018/07/11	ETH1	17.708	-0.202	0.038	17.223	-0.678	0.026	2.138	36.836	92.0	7.2	26.8	2018.07.10–2018.10.19
2018/07/12	ETH1	17.770	-0.205	0.023	17.298	-0.669	0.022	2.141	36.899	62.6	7.2	26.6	2018.07.10–2018.10.19
2018/07/12	ETH2	-11.673	-0.877	0.020	-11.430	-0.631	0.019	-10.033	19.850	130.3	6.5	25.0	2018.07.10–2018.10.19
2018/07/13	ETH2	-11.660	-0.916	0.026	-11.378	-0.631	0.012	-10.035	19.904	11.7	6.3	23.2	2018.07.10–2018.10.19
2018/07/17	ETH2	-11.766	-0.903	0.035	-11.517	-0.651	0.026	-10.017	19.766	123.5	7.1	26.5	2018.07.10–2018.10.19
2018/07/18	ETH2	-11.834	-0.901	0.019	-11.574	-0.638	0.016	-10.036	19.714	130.5	7.0	25.6	2018.07.10–2018.10.19
2018/07/18	ETH1	17.672	-0.191	0.019	17.205	-0.650	0.024	2.118	36.809	60.3	7.6	28.8	2018.07.10–2018.10.19
2018/07/18	ETH1	17.784	-0.185	0.023	17.305	-0.656	0.023	2.151	36.883	97.3	6.2	23.7	2018.07.10–2018.10.19
2018/07/18	ETH2	-11.790	-0.902	0.042	-11.563	-0.672	0.026	-10.030	19.753	187.7	7.8	29.0	2018.07.10–2018.10.19
2018/07/19	ETH1	17.857	-0.183	0.033	17.350	-0.681	0.023	2.159	36.946	121.7	5.7	22.0	2018.07.10–2018.10.19
2018/07/19	ETH1	17.918	-0.217	0.034	17.473	-0.654	0.032	2.162	37.038	-45.3	6.4	24.1	2018.07.10–2018.10.19
2018/07/19	ETH1	17.831	-0.186	0.020	17.335	-0.673	0.015	2.156	36.926	105.0	5.8	21.6	2018.07.10–2018.10.19
2018/07/20	ETH1	17.836	-0.184	0.018	17.351	-0.660	0.012	2.163	36.922	78.4	5.4	20.7	2018.07.10–2018.10.19
2018/07/20	ETH2	-11.707	-0.913	0.039	-11.441	-0.645	0.027	-9.998	19.817	45.2	5.7	21.5	2018.07.10–2018.10.19
2018/07/20	ETH2	-11.701	-0.911	0.028	-11.433	-0.640	0.023	-10.035	19.858	57.0	5.9	21.1	2018.07.10–2018.10.19
2018/07/21	ETH1	17.817	-0.192	0.034	17.334	-0.666	0.017	2.157	36.917	38.4	6.2	22.3	2018.07.10–2018.10.19
2018/07/21	ETH3	18.204	0.191	0.024	17.703	-0.301	0.014	1.800	37.264	60.6	6.8	24.6	2018.07.10–2018.10.19
2018/07/22	Carrara	18.402	-0.086	0.027	17.921	-0.559	0.016	2.119	37.432	-54.9	7.2	19.8	2018.07.10–2018.10.19
2018/07/22	MuStd	23.654	0.382	0.035	22.981	-0.276	0.025	1.645	42.676	192.7	6.7	25.2	2018.07.10–2018.10.19

2018/07/23	ETH1	17.683	-0.193	0.037	17.191	-0.676	0.030	2.111	36.829	81.1	7.2	26.7	2018.07.10–2018.10.19
2018/07/24	ETH3	18.121	0.228	0.030	17.585	-0.299	0.016	1.775	37.169	171.5	6.7	23.8	2018.07.10–2018.10.19
2018/07/24	Carrara	18.389	-0.031	0.029	17.859	-0.552	0.014	2.097	37.384	125.9	7.3	27.9	2018.07.10–2018.10.19
2018/07/25	ETH2	-11.257	-0.900	0.025	-10.981	-0.621	0.030	-10.007	20.270	-8.5	5.7	20.8	2018.07.10–2018.10.19
2018/07/26	MuStd	23.537	0.375	0.023	22.914	-0.234	0.025	1.666	42.545	-11.8	6.1	22.8	2018.07.10–2018.10.19
2018/07/27	ETH3	18.157	0.167	0.042	17.704	-0.278	0.019	1.806	37.237	-123.5	5.4	19.6	2018.07.10–2018.10.19
2018/07/29	MuStd	23.718	0.353	0.043	23.081	-0.269	0.024	1.706	42.709	-22.2	6.7	25.0	2018.07.10–2018.10.19
2018/07/29	ETH1	17.844	-0.154	0.034	17.337	-0.653	0.034	2.125	36.938	86.8	5.4	20.4	2018.07.10–2018.10.19
2018/07/30	ETH3	18.275	0.215	0.030	17.776	-0.275	0.020	1.821	37.291	36.6	6.8	24.9	2018.07.10–2018.10.19
2018/07/31	Carrara	18.435	-0.084	0.036	17.974	-0.535	0.044	2.128	37.453	-67.7	6.0	22.8	2018.07.10–2018.10.19
2018/07/31	MuStd	23.788	0.375	0.055	23.170	-0.228	0.044	1.694	42.768	-63.5	5.9	22.2	2018.07.10–2018.10.19
2018/08/01	ETH1	17.835	-0.175	0.024	17.327	-0.674	0.020	2.130	36.944	57.9	5.6	20.2	2018.07.10–2018.10.19
2018/08/02	ETH3	18.413	0.212	0.036	17.899	-0.293	0.030	1.773	37.479	49.0	5.5	19.7	2018.07.10–2018.10.19
2018/08/03	Carrara	18.452	-0.076	0.034	17.953	-0.566	0.023	2.127	37.464	4.9	6.4	24.7	2018.07.10–2018.10.19
2018/08/04	ETH2	-11.648	-0.933	0.024	-11.347	-0.629	0.016	-10.031	19.929	32.3	8.3	31.5	2018.07.10–2018.10.19
2018/08/05	ETH3	18.294	0.241	0.025	17.755	-0.288	0.024	1.821	37.283	68.3	5.5	20.0	2018.07.10–2018.10.19
2018/08/05	MuStd	24.094	0.415	0.038	23.434	-0.230	0.027	1.696	43.032	-1.9	6.7	23.8	2018.07.10–2018.10.19
2018/08/06	ETH1	17.921	-0.166	0.048	17.414	-0.664	0.025	2.149	37.002	0.7	6.9	24.9	2018.07.10–2018.10.19
2018/08/07	ETH2	-11.794	-0.951	0.036	-11.467	-0.620	0.015	-10.026	19.793	-23.3	7.1	24.3	2018.07.10–2018.10.19
2018/08/08	ETH3	18.378	0.242	0.035	17.847	-0.279	0.021	1.832	37.355	43.3	7.5	27.3	2018.07.10–2018.10.19
2018/08/08	ETH2	-11.542	-0.941	0.045	-11.250	-0.647	0.029	-9.982	19.997	-2.1	7.5	27.4	2018.07.10–2018.10.19
2018/08/09	MuStd	23.771	0.420	0.018	23.086	-0.248	0.015	1.646	42.752	49.4	5.6	20.9	2018.07.10–2018.10.19
2018/08/09	Carrara	18.511	-0.049	0.049	17.980	-0.570	0.018	2.133	37.490	19.5	6.4	24.6	2018.07.10–2018.10.19
2018/08/10	ETH3	18.229	0.194	0.044	17.727	-0.300	0.028	1.794	37.292	-2.4	7.7	28.0	2018.07.10–2018.10.19
2018/08/11	Carrara	18.441	-0.058	0.028	17.920	-0.570	0.021	2.142	37.420	0.5	5.6	21.2	2018.07.10–2018.10.19
2018/08/13	ETH1	17.788	-0.183	0.040	17.297	-0.665	0.011	2.153	36.882	-41.0	5.6	20.6	2018.07.10–2018.10.19
2018/08/13	ETH2	-11.717	-0.923	0.044	-11.435	-0.638	0.032	-9.996	19.815	94.7	5.0	20.0	2018.07.10–2018.10.19
2018/08/13	ETH3	18.172	0.222	0.027	17.652	-0.289	0.023	1.791	37.210	15.1	7.8	28.5	2018.07.10–2018.10.19
2018/08/14	MuStd	23.957	0.432	0.062	23.278	-0.231	0.020	1.699	42.874	37.2	6.3	23.0	2018.07.10–2018.10.19
2018/08/15	Carrara	18.542	-0.004	0.056	17.947	-0.587	0.023	2.134	37.473	139.4	6.6	25.0	2018.07.10–2018.10.19
2018/08/15	ETH1	17.859	-0.104	0.018	17.262	-0.691	0.017	2.150	36.877	175.2	7.9	29.4	2018.07.10–2018.10.19
2018/08/16	Carrara	18.508	-0.027	0.041	17.954	-0.570	0.020	2.132	37.464	29.8	5.6	21.3	2018.07.10–2018.10.19
2018/08/17	ETH3	18.330	0.256	0.027	17.769	-0.295	0.025	1.823	37.302	72.0	7.5	27.3	2018.07.10–2018.10.19
2018/08/17	ETH2	-11.755	-0.965	0.039	-11.418	-0.624	0.022	-10.016	19.837	-41.9	5.9	22.2	2018.07.10–2018.10.19
2018/08/18	ETH3	18.277	0.249	0.033	17.742	-0.277	0.013	1.816	37.263	64.4	5.7	20.5	2018.07.10–2018.10.19
2018/08/19	Carrara	18.533	-0.005	0.046	17.961	-0.566	0.029	2.132	37.467	88.9	5.6	21.4	2018.07.10–2018.10.19
2018/08/19	ETH3	18.331	0.254	0.033	17.767	-0.300	0.018	1.827	37.301	66.9	6.5	23.8	2018.07.10–2018.10.19
2018/08/19	ETH1	17.937	-0.162	0.052	17.413	-0.677	0.035	2.171	36.993	9.7	5.9	21.7	2018.07.10–2018.10.19
2018/08/21	ETH4	-11.490	-0.711	0.032	-11.189	-0.406	0.024	-10.090	19.924	23.7	5.5	20.3	2018.07.10–2018.10.19
2018/08/22	Carrara	18.445	0.021	0.056	17.840	-0.573	0.027	2.102	37.382	155.6	7.3	27.8	2018.07.10–2018.10.19
2018/08/22	ETH3	18.246	0.303	0.036	17.648	-0.285	0.023	1.792	37.201	147.0	6.2	22.5	2018.07.10–2018.10.19
2018/08/23	ETH1	17.768	-0.131	0.025	17.227	-0.663	0.034	2.107	36.854	61.5	5.7	19.6	2018.07.10–2018.10.19
2018/08/23	ETH4	-11.621	-0.744	0.043	-11.266	-0.385	0.036	-10.060	19.795	-45.7	6.2	25.4	2018.07.10–2018.10.19
2018/08/24	MuStd	23.673	0.470	0.043	22.911	-0.276	0.010	1.619	42.631	160.8	8.1	30.0	2018.07.10–2018.10.19

2018/08/25	Carrara	18.550	0.011	0.045	17.951	-0.577	0.023	2.132	37.468	122.4	5.5	20.6	2018.07.10–2018.10.19
2018/08/25	ETH3	18.295	0.280	0.040	17.709	-0.295	0.019	1.801	37.264	112.7	5.6	20.0	2018.07.10–2018.10.19
2018/08/26	ETH1	17.800	-0.129	0.040	17.254	-0.664	0.041	2.125	36.867	78.5	6.3	22.9	2018.07.10–2018.10.19
2018/08/26	MuStd	23.850	0.413	0.039	23.177	-0.245	0.029	1.687	42.799	-20.7	5.6	20.2	2018.07.10–2018.10.19
2018/08/27	Carrara	18.488	-0.033	0.035	17.969	-0.542	0.026	2.123	37.460	-10.2	6.6	24.8	2018.07.10–2018.10.19
2018/08/28	ETH3	18.426	0.245	0.046	17.895	-0.276	0.020	1.837	37.396	17.4	7.0	26.0	2018.07.10–2018.10.19
2018/08/29	ETH3	18.468	0.276	0.049	17.902	-0.280	0.028	1.868	37.376	32.4	6.2	22.4	2018.07.10–2018.10.19
2018/08/30	Carrara	18.572	-0.016	0.038	18.009	-0.569	0.020	2.134	37.516	40.0	6.8	26.1	2018.07.10–2018.10.19
2018/08/31	ETH2	-11.591	-0.937	0.038	-11.274	-0.616	0.022	-10.019	19.979	45.0	5.6	19.8	2018.07.10–2018.10.19
2018/09/03	ETH3	18.290	0.198	0.043	17.798	-0.284	0.023	1.820	37.323	17.8	6.5	23.4	2018.07.10–2018.10.19
2018/09/04	ETH1	17.844	-0.178	0.016	17.348	-0.666	0.012	2.159	36.928	110.8	9.3	32.6	2018.07.10–2018.10.19
2018/09/04	ETH3	18.219	0.170	0.038	17.750	-0.290	0.028	1.796	37.304	-12.0	5.7	20.2	2018.07.10–2018.10.19
2018/09/06	ETH1	17.795	-0.201	0.035	17.353	-0.635	0.014	2.143	36.918	-51.5	5.3	19.7	2018.07.10–2018.10.19
2018/09/06	Carrara	18.535	-0.100	0.025	18.048	-0.578	0.019	2.142	37.557	-9.9	5.6	20.8	2018.07.10–2018.10.19
2018/09/07	ETH3	18.186	0.188	0.027	17.712	-0.277	0.038	1.790	37.259	-18.8	6.3	22.6	2018.07.10–2018.10.19
2018/09/08	ETH1	17.833	-0.160	0.020	17.319	-0.666	0.022	2.124	36.934	70.5	8.4	30.8	2018.07.10–2018.10.19
2018/09/08	ETH2	-11.823	-0.923	0.029	-11.545	-0.641	0.020	-10.045	19.755	41.7	5.7	20.1	2018.07.10–2018.10.19
2018/09/09	ETH4	-11.864	-0.733	0.028	-11.544	-0.409	0.017	-10.094	19.571	-42.9	5.4	19.8	2018.07.10–2018.10.19
2018/09/10	ETH2	-11.890	-0.956	0.043	-11.566	-0.628	0.019	-10.063	19.738	-32.6	5.4	19.4	2018.07.10–2018.10.19
2018/09/10	ETH4	-11.779	-0.703	0.046	-11.482	-0.403	0.039	-10.105	19.638	40.5	5.7	20.8	2018.07.10–2018.10.19
2018/09/11	Carrara	18.339	-0.072	0.036	17.816	-0.585	0.026	2.084	37.389	23.4	5.5	20.5	2018.07.10–2018.10.19
2018/09/12	MuStd	23.854	0.413	0.045	23.180	-0.245	0.018	1.645	42.843	38.6	5.7	20.4	2018.07.10–2018.10.19
2018/09/12	ETH3	18.255	0.282	0.035	17.665	-0.297	0.022	1.774	37.248	154.2	6.8	24.2	2018.07.10–2018.10.19
2018/09/13	ETH2	-11.359	-0.895	0.034	-11.135	-0.668	0.018	-10.016	20.169	125.9	7.9	27.0	2018.07.10–2018.10.19
2018/09/14	Carrara	18.435	-0.025	0.039	17.860	-0.589	0.016	2.089	37.432	113.1	5.5	20.3	2018.07.10–2018.10.19
2018/09/15	Carrara	18.486	-0.026	0.036	17.961	-0.542	0.010	2.114	37.460	19.2	5.5	20.1	2018.07.10–2018.10.19
2018/09/15	ETH1	17.701	-0.170	0.031	17.220	-0.642	0.021	2.106	36.828	-25.8	5.8	20.3	2018.07.10–2018.10.19
2018/09/16	MuStd	23.867	0.406	0.036	23.197	-0.249	0.034	1.676	42.834	-8.7	6.2	22.0	2018.07.10–2018.10.19
2018/09/16	ETH3	18.208	0.232	0.052	17.701	-0.265	0.024	1.768	37.258	0.5	5.4	18.7	2018.07.10–2018.10.19
2018/09/17	Carrara	18.491	-0.022	0.064	17.909	-0.593	0.030	2.104	37.470	56.1	5.6	20.6	2018.07.10–2018.10.19
2018/09/17	ETH2	-11.596	-0.922	0.058	-11.301	-0.624	0.032	-10.031	19.971	47.7	6.9	24.5	2018.07.10–2018.10.19
2018/09/18	Carrara	18.377	-0.042	0.061	17.841	-0.568	0.032	2.096	37.384	-5.8	5.6	20.6	2018.07.10–2018.10.19
2018/09/19	ETH3	18.194	0.258	0.032	17.648	-0.279	0.025	1.761	37.224	58.1	5.6	19.3	2018.07.10–2018.10.19
2018/09/20	Carrara	18.499	-0.040	0.036	17.983	-0.547	0.028	2.129	37.472	-6.1	6.1	22.9	2018.07.10–2018.10.19
2018/09/20	ETH3	18.420	0.273	0.027	17.864	-0.273	0.026	1.815	37.382	70.9	6.7	21.9	2018.07.10–2018.10.19
2018/09/20	ETH2	-11.547	-0.917	0.063	-11.269	-0.637	0.029	-9.976	19.962	95.5	5.4	19.2	2018.07.10–2018.10.19
2018/09/21	ETH1	17.829	-0.139	0.071	17.302	-0.657	0.027	2.110	36.921	17.8	5.6	20.3	2018.07.10–2018.10.19
2018/09/22	Carrara	18.444	-0.009	0.039	17.890	-0.553	0.023	2.098	37.416	54.9	5.9	21.7	2018.07.10–2018.10.19
2018/09/23	ETH3	18.285	0.251	0.036	17.721	-0.304	0.020	1.783	37.302	42.5	6.1	21.4	2018.07.10–2018.10.19
2018/09/23	ETH1	17.776	-0.099	0.046	17.201	-0.665	0.020	2.103	36.835	81.0	6.0	21.2	2018.07.10–2018.10.19
2018/09/24	MuStd	24.005	0.437	0.039	23.268	-0.283	0.022	1.697	42.919	76.3	5.6	19.3	2018.07.10–2018.10.19
2018/09/24	Carrara	18.522	0.038	0.025	17.920	-0.553	0.024	2.092	37.452	159.1	6.3	22.0	2018.07.10–2018.10.19
2018/09/25	ETH3	18.347	0.279	0.089	17.757	-0.301	0.024	1.773	37.345	119.2	6.7	23.2	2018.07.10–2018.10.19
2018/09/26	ETH1	17.815	-0.143	0.043	17.289	-0.660	0.018	2.108	36.913	29.6	6.5	23.2	2018.07.10–2018.10.19

2018/09/27	ETH2	-11.532	-0.902	0.047	-11.268	-0.635	0.014	-10.048	20.032	111.1	5.6	20.2	2018.07.10–2018.10.19
2018/09/28	ETH4	-11.481	-0.744	0.044	-11.174	-0.433	0.027	-10.067	19.943	-5.9	6.1	20.2	2018.07.10–2018.10.19
2018/09/28	ETH2	-11.368	-0.932	0.070	-11.074	-0.634	0.020	-10.022	20.202	33.2	5.2	17.9	2018.07.10–2018.10.19
2018/09/29	ETH3	18.312	0.306	0.036	17.719	-0.276	0.023	1.773	37.283	141.3	6.1	21.7	2018.07.10–2018.10.19
2018/09/29	Carrara	18.459	0.054	0.033	17.852	-0.543	0.035	2.076	37.389	143.6	6.5	24.6	2018.07.10–2018.10.19
2018/10/02	Carrara	18.548	0.008	0.045	17.953	-0.577	0.014	2.132	37.470	120.1	6.9	26.1	2018.07.10–2018.10.19
2018/10/02	ETH1	17.859	-0.093	0.041	17.250	-0.691	0.023	2.150	36.865	163.5	6.8	25.5	2018.07.10–2018.10.19
2018/10/02	ETH2	-11.522	-0.996	0.043	-11.146	-0.617	0.023	-9.941	20.033	-102.5	5.6	18.7	2018.07.10–2018.10.19
2018/10/03	ETH3	18.228	0.200	0.051	17.732	-0.287	0.027	1.741	37.337	-80.8	5.5	19.3	2018.07.10–2018.10.19
2018/10/04	ETH2	-11.724	-0.913	0.051	-11.446	-0.632	0.025	-10.025	19.826	121.0	6.1	22.9	2018.07.10–2018.10.19
2018/10/04	ETH4	-11.687	-0.739	0.037	-11.380	-0.429	0.016	-10.070	19.733	31.4	5.8	21.7	2018.07.10–2018.10.19
2018/10/05	ETH3	18.129	0.217	0.042	17.628	-0.275	0.013	1.715	37.247	-63.9	5.3	19.3	2018.07.10–2018.10.19
2018/10/06	MuStd	24.030	0.446	0.036	23.301	-0.267	0.011	1.722	42.911	22.3	9.4	33.8	2018.07.10–2018.10.19
2018/10/10	Carrara	18.548	0.052	0.053	17.925	-0.559	0.022	2.128	37.429	167.6	7.6	29.7	2018.07.10–2018.10.19
2018/10/10	ETH2	-11.590	-1.004	0.054	-11.223	-0.633	0.022	-9.977	20.007	-93.7	5.8	20.7	2018.07.10–2018.10.19
2018/10/11	MuStd	23.622	0.396	0.040	22.964	-0.247	0.021	1.599	42.675	-105.4	5.5	21.0	2018.07.10–2018.10.19
2018/10/12	Carrara	18.462	0.021	0.068	17.874	-0.557	0.030	2.106	37.395	82.9	6.4	24.8	2018.07.10–2018.10.19
2018/10/12	ETH1	17.931	-0.098	0.037	17.363	-0.656	0.021	2.149	36.944	73.8	6.5	24.7	2018.07.10–2018.10.19
2018/10/13	ETH3	18.361	0.241	0.033	17.840	-0.271	0.012	1.805	37.366	-36.6	6.1	24.9	2018.07.10–2018.10.19
2018/10/13	ETH2	-11.637	-0.919	0.068	-11.361	-0.639	0.031	-10.041	19.935	105.6	5.7	21.4	2018.07.10–2018.10.19
2018/10/14	ETH4	-11.782	-0.794	0.035	-11.405	-0.412	0.021	-10.069	19.691	-61.4	5.2	19.3	2018.07.10–2018.10.19
2018/10/14	ETH2	-11.872	-0.979	0.065	-11.557	-0.660	0.027	-10.048	19.764	26.8	7.8	28.6	2018.07.10–2018.10.19
2018/10/14	ETH1	17.689	-0.124	0.051	17.138	-0.666	0.025	2.095	36.781	50.1	8.0	27.5	2018.07.10–2018.10.19
2018/10/15	Carrara	18.584	0.054	0.039	17.968	-0.551	0.015	2.114	37.477	144.5	5.4	20.7	2018.07.10–2018.10.19
2018/10/16	ETH3	18.310	0.314	0.028	17.684	-0.300	0.035	1.779	37.266	128.8	5.8	20.8	2018.07.10–2018.10.19
2018/10/17	Carrara	18.433	-0.009	0.062	17.854	-0.578	0.037	2.086	37.417	53.0	6.3	24.3	2018.07.10–2018.10.19
2018/10/17	MuStd	23.955	0.460	0.046	23.210	-0.267	0.019	1.678	42.863	67.7	6.5	23.7	2018.07.10–2018.10.19
2018/10/18	ETH1	17.810	-0.133	0.036	17.253	-0.680	0.019	2.124	36.881	48.3	6.3	22.2	2018.07.10–2018.10.19
2018/10/19	ETH2	-11.506	-0.932	0.058	-11.248	-0.672	0.030	-9.922	19.965	96.4	7.7	26.9	2018.07.10–2018.10.19
2018/10/19	Carrara	18.579	0.013	0.044	17.975	-0.580	0.024	2.123	37.505	109.2	7.0	26.3	2018.07.10–2018.10.19
2018/10/20	MuStd	23.927	0.401	0.033	23.257	-0.253	0.017	1.706	42.868	-76.0	6.4	23.4	2018.07.10–2018.10.19
2018/10/21	ETH3	18.250	0.241	0.065	17.684	-0.315	0.021	1.787	37.272	25.8	6.5	22.2	2018.07.10–2018.10.19
2018/10/21	ETH1	17.832	-0.109	0.042	17.246	-0.684	0.029	2.141	36.863	82.8	7.4	26.5	2018.07.10–2018.10.19
2018/10/21	ETH2	-11.907	-0.994	0.045	-11.561	-0.645	0.015	-10.046	19.743	-14.6	6.1	21.6	2018.07.10–2018.10.19

Sample data – S.6.IV

Date	Sample	δ47 (raw) (‰)	Δ47 (raw) (‰)	SD Δ47 (raw) (‰)	δ47 (bgcorr) (‰)	Δ47 (bgcorr) (‰)	SD Δ47 (bgcorr) (‰)	δ13C CO2 (‰ VPDB)	δ18O CO2 (‰ VSMOW)	Diff Bellow (mV)	weight	ETF period
8/5/2018	2017-AR-001	3.871	-0.180	0.037	3.759	-0.292	0.016	-6.804	31.7	13	13.5	2018.07.10–2018.10.19
8/5/2018	2017-AR-014	5.041	-0.127	0.027	4.868	-0.299	0.020	-6.541	32.6	47	11.8	2018.07.10–2018.10.19
8/5/2018	2017-AR-037	3.911	-0.105	0.028	3.748	-0.268	0.029	-7.191	32.0	111	12.1	2018.07.10–2018.10.19
8/10/2018	2017-AR-001	3.902	-0.145	0.025	3.727	-0.319	0.031	-6.814	31.7	140	10.7	2018.07.10–2018.10.19
8/10/2018	2017-AR-014	5.186	-0.116	0.046	4.979	-0.321	0.033	-6.519	32.7	131	12.6	2018.07.10–2018.10.19
8/11/2018	2017-AR-001	3.908	-0.147	0.027	3.760	-0.294	0.024	-6.823	31.7	78	10.5	2018.07.10–2018.10.19
8/14/2018	2017-AR-037	3.929	-0.130	0.037	3.779	-0.280	0.025	-7.176	32.1	73	15.4	2018.07.10–2018.10.19
8/15/2018	2017-AR-014	5.107	-0.113	0.026	4.954	-0.265	0.022	-6.557	32.6	24	12.8	2018.07.10–2018.10.19

8/18/2018	2017-AR-001	3.970	-0.159	0.052	3.852	-0.276	0.022	-6.814	31.8	28	11.1	2018.07.10–2018.10.19
8/19/2018	2017-AR-037	3.914	-0.125	0.029	3.774	-0.265	0.025	-7.170	32.0	26	13.3	2018.07.10–2018.10.19
8/19/2018	2017-AR-014	5.181	-0.141	0.050	5.026	-0.296	0.031	-6.545	32.7	-5	13.9	2018.07.10–2018.10.19
9/16/2018	2017-AR-001	3.934	-0.173	0.027	3.804	-0.303	0.025	-6.789	31.7	36	10.7	2018.07.10–2018.10.19
9/16/2018	2017-AR-037	3.912	-0.111	0.042	3.760	-0.263	0.026	-7.162	32.0	78	12.4	2018.07.10–2018.10.19
9/17/2018	2017-AR-014	5.153	-0.113	0.042	4.964	-0.301	0.026	-6.561	32.7	50	12.4	2018.07.10–2018.10.19

Δ47 soil temperature datasets – S.6.V

Δ47-1/T² calibration:	Petersen *et. al.* 2019 [IUPAC]	**slope**	**intercept**	**AFF**
		0.0383	0.2580	0.088

$\delta^{18}O$ correction factor: +0.1

Sample ID	Age [Ma]	Date	Sample size [mg]	$\delta^{13}C_{V\text{-}PDB}$ [‰]	$\delta^{18}O_{V\text{-}SMOW}$ [‰]	$\delta^{47}{}_{raw\ bc}$ [‰]	$\Delta_{47raw\ bc}$ [‰]	Δ_{47} [‰]	se [‰]	T (Δ_{47})	n	residual slope*	slope	intercept	Time interval HG/25G	
2017-AR-001	14.636	8/5/2018	13.5	-6.80	23.46	3.759	-0.292	0.698	0.005		5	-0.0007	1.0970	0.9267	7/10/2018	10/19/2018
	± 0.008	8/10/2018	10.7	-6.81	23.47	3.727	-0.319	0.667	0.010			-0.0007	1.0970	0.9267	7/10/2018	10/19/2018
		8/11/2018	10.5	-6.82	23.49	3.760	-0.294	0.695	0.008			-0.0007	1.0970	0.9267	7/10/2018	10/19/2018
		8/18/2018	11.1	-6.81	23.55	3.852	-0.276	0.715	0.007			-0.0007	1.0970	0.9267	7/10/2018	10/19/2018
		9/16/2018	10.7	-6.79	23.51	3.804	-0.303	0.686	0.008			-0.0007	1.0970	0.9267	7/10/2018	10/19/2018
			AV	-6.81	23.50		**AV**	0.692		**24 ± 3**						
			SD	0.01	0.04		**SD**	0.017								
							SE	0.008								

Sample ID	Age [Ma]	Date	Sample size [mg]	$\delta^{13}C_{V\text{-}PDB}$ [‰]	$\delta^{18}O_{V\text{-}SMOW}$ [‰]	$\delta^{47}{}_{raw\ bc}$ [‰]	$\Delta_{47raw\ bc}$ [‰]	Δ_{47} [‰]	se [‰]	T (Δ_{47})	n					
2017-AR-014	14.104	8/5/2018	11.8	-6.54	24.33	4.868	-0.299	0.690	0.006		5	-0.0007	1.0970	0.9267	7/10/2018	10/19/2018
	± 0.006	8/10/2018	12.6	-6.52	24.44	4.979	-0.321	0.666	0.010			-0.0007	1.0970	0.9267	7/10/2018	10/19/2018
		8/15/2018	12.8	-6.56	24.39	4.954	-0.265	0.727	0.007			-0.0007	1.0970	0.9267	7/10/2018	10/19/2018
		8/19/2018	13.9	-6.54	24.48	5.026	-0.296	0.694	0.010			-0.0007	1.0970	0.9267	7/10/2018	10/19/2018
		9/17/2018	12.4	-6.56	24.44	4.964	-0.301	0.688	0.008			-0.0007	1.0970	0.9267	7/10/2018	10/19/2018
			AV	-6.54	24.42		**AV**	0.693		**23 ± 3**						
			SD	0.02	0.06		**SD**	0.022								
							SE	0.010								

Sample ID	Age [Ma]	Date	Sample size [mg]	$\delta^{13}C_{V\text{-}PDB}$ [‰]	$\delta^{18}O_{V\text{-}SMOW}$ [‰]	$\delta^{47}{}_{raw\ bc}$ [‰]	$\Delta_{47raw\ bc}$ [‰]	Δ_{47} [‰]	se [‰]	T (Δ_{47})	n					
2017-AR-037	13.738	8/5/2018	12.1	-7.19	23.81	3.748	-0.268	0.724	0.009		4	-0.0007	1.0970	0.9267	7/10/2018	10/19/2018
	± 0.009	8/14/2018	15.4	-7.18	23.84	3.779	-0.280	0.710	0.008			-0.0007	1.0970	0.9267	7/10/2018	10/19/2018
		8/19/2018	13.3	-7.17	23.81	3.774	-0.265	0.727	0.008			-0.0007	1.0970	0.9267	7/10/2018	10/19/2018
		9/16/2018	12.4	-7.16	23.79	3.760	-0.263	0.730	0.008			-0.0007	1.0970	0.9267	7/10/2018	10/19/2018
			AV	-7.17	23.81		**AV**	0.723		**14 ± 1**						
			SD	0.01	0.02		**SD**	0.009								
							SE	0.004								

$\delta^{18}O$ and $\delta^{13}C$ of pedogenic carbonates supplementary data – S.6.VI

date	sample	Replicate measurement	Also measured for Δ_{47}	sample type	stratigraphic position	local magnetostrat.	Age (strictly based on Krijgsman *et. al.* 1994b)	$\delta^{13}C$	StDev $\delta^{13}C$	$\delta^{18}O$	StDev $\delta^{18}O$	$CaCO_3$
					[m above base of Krijgsman *et. al.* 1994b]	Krijgsman *et. al.* 1994b	[Ma]	[‰, VPDB]	[‰, VPDB]	[‰, VSMOW]	[‰, VSMOW]	[‰wt.]
8/16/2017	2017-AR-033			Caliche	134.2		13.362	-7.97	0.04	23.69	0.06	16.38
8/16/2017	2017-AR-032			Nodule	134.0	C5ABn	13.389	-8.02	0.04	23.51	0.04	38.57
8/16/2017	2017-AR-040			Caliche	121.1		13.664	-8.18	0.02	24.43	0.04	71.47
8/16/2017	2017-AR-039			Caliche	117.4		13.721	-8.14	0.02	24.42	0.06	69.93
8/16/2017	2017-AR-037		x	Nodule	115.1		13.738	-7.37	0.02	24.20	0.04	37.04
8/16/2017	2017-AR-036			Nodule	114.8	C5ACn	13.759	-8.25	0.01	23.36	0.05	59.63
8/16/2017	2017-AR-035			Nodule	114.3		13.766	-7.85	0.02	23.73	0.04	46.13
8/16/2017	2017-AR-034			Caliche	113.1		13.781	-7.86	0.02	23.68	0.04	42.12
8/16/2017	2017-AR-030			Nodule	98.9		13.935	-7.79	0.01	23.99	0.05	76.09
8/16/2017	2017-AR-029			Nodule	98.2		13.941	-7.48	0.02	24.42	0.04	78.70
8/16/2017	2017-AR-028			Caliche	98.0		13.943	-7.54	0.02	24.44	0.04	77.64
8/16/2017	2017-AR-031			Nodule	95.5		13.966	-7.68	0.02	23.70	0.04	68.75
8/16/2017	2017-AR-026			Nodule	83.5		14.079	-7.52	0.01	24.31	0.03	58.39
8/21/2017	2017-AR-025			Nodule	83.3		14.081	-7.55	0.01	23.45	0.04	50.33
8/16/2017	2017-AR-024			Nodule	83.1		14.082	-7.46	0.02	24.05	0.04	37.60
8/16/2017	2017-AR-023			Nodule	83.0		14.084	-7.43	0.01	24.06	0.06	48.63
8/16/2017	2017-AR-022			Nodule	82.8		14.086	-7.65	0.01	24.08	0.03	52.75
8/2/2018	2018-AR-040			Nodule	82.8		14.086	-6.38	0.02	23.96	0.04	78.12
8/21/2017	2017-AR-021			Nodule	82.5		14.089	-6.09	0.01	24.14	0.04	2.56
8/16/2017	2017-AR-020			Nodule	82.3		14.091	-7.44	0.01	24.02	0.05	66.57
8/16/2017	2017-AR-019			Nodule	82.1		14.092	-7.44	0.02	23.89	0.05	79.12
8/16/2017	2017-AR-018			Nodule	82.0		14.094	-6.48	0.02	24.26	0.04	41.64
8/16/2017	2017-AR-017			Nodule	81.6		14.097	-6.92	0.02	24.36	0.06	22.29
8/16/2017	2017-AR-016			Nodule	81.3		14.101	-6.64	0.03	24.33	0.06	18.43
8/16/2017	2017-AR-015			Nodule	81.1		14.102	-6.73	0.03	24.58	0.05	43.55
8/16/2017	2017-AR-014		x	Nodule	81.0		14.104	-6.78	0.02	24.68	0.05	44.81
8/2/2018	2018-AR-039			Nodule	80.5		14.109	-7.46	0.05	24.20	0.06	49.98
8/2/2018	2018-AR-038			Caliche	77.9		14.135	-5.66	0.03	24.56	0.04	66.83
8/2/2018	2018-AR-036a			Nodule	77.3		14.142	-6.56	0.01	24.29	0.04	82.86
8/2/2018	2018-AR-035			Nodule	76.1		14.154	-6.80	0.04	24.29	0.06	75.02
8/2/2018	2018-AR-034			Nodule	74.4	C5ADn	14.172	-7.24	0.03	24.36	0.07	55.40
8/2/2018	2018-AR-033			Caliche	73.3		14.185	-6.86	0.03	24.66	0.03	83.94
8/2/2018	2018-AR-032			Nodule	72.9		14.189	-6.85	0.02	24.22	0.09	32.79
8/2/2018	2018-AR-031			Nodule	70.4		14.217	-6.80	0.04	24.39	0.05	90.16
8/2/2018	2018-AR-030			Nodule	68.9		14.235	-6.41	0.02	24.34	0.05	74.24
8/2/2018	2018-AR-029			Caliche	67.7		14.249	-7.37	0.04	24.50	0.06	81.50
8/2/2018	2018-AR-028			Caliche	67.4		14.253	-6.93	0.02	24.69	0.04	92.91
8/2/2018	2018-AR-027			Nodule	67.2		14.255	-7.23	0.05	24.64	0.05	90.95
8/2/2018	2018-AR-026			Caliche	66.9		14.259	-6.33	0.04	24.65	0.04	65.19
8/2/2018	2018-AR-024			Caliche	63.7		14.298	-7.55	0.04	24.69	0.06	78.75
8/2/2018	2018-AR-023a			Nodule	61.7		14.324	-6.65	0.02	23.66	0.04	72.09

8/2/2018	2018-AR-020		Caliche	61.0	[redacted]	14.333	-6.70	0.05	24.16	0.08	69.63
8/2/2018	2018-AR-019		Nodule	59.2		14.357	-8.05	0.04	23.67	0.05	51.26
8/2/2018	2018-AR-018a		Nodule	56.5		14.393	-6.61	0.04	24.47	0.05	81.29
8/2/2018	2018-AR-017		Caliche	56.2		14.397	-7.06	0.02	23.74	0.04	50.44
8/2/2018	2018-AR-016a		Nodule	55.5		14.407	-7.66	0.05	24.03	0.06	76.54
8/2/2018	2018-AR-015a		Nodule	54.2		14.425	-7.52	0.02	24.03	0.04	79.50
8/2/2018	2018-AR-014		Caliche	53.9		14.430	-7.12	0.06	23.68	0.07	71.94
8/2/2018	2018-AR-013		Nodule	53.5		14.434	-7.12	0.04	23.95	0.08	64.00
8/2/2018	2018-AR-012		Caliche	53.2		14.439	-7.51	0.04	22.35	0.05	63.18
8/2/2018	2018-AR-011		Nodule	52.7		14.446	-7.26	0.03	23.20	0.05	78.71
8/2/2018	2018-AR-010		Caliche	52.2		14.453	-7.21	0.03	23.93	0.05	83.33
8/1/2018	2018-AR-009		Nodule	52.0		14.455	-7.84	0.06	22.76	0.06	83.40
8/1/2018	2018-AR-007		Nodule	51.2		14.467	-8.03	0.04	22.72	0.07	70.20
8/1/2018	2018-AR-006a		Nodule	50.5		14.476	-7.68	0.06	23.92	0.08	87.95
8/1/2018	2018-AR-008a		Nodule	51.8		14.457	-7.48	0.04	23.33	0.07	83.79
8/1/2018	2018-AR-005		Caliche	47.7		14.516	-7.94	0.05	23.92	0.06	81.77
8/1/2018	2018-AR-004		Caliche	43.5		14.575	-7.49	0.10	24.37	0.15	26.37
2/24/2018	2017-AR-007		Nodule	43.0		14.582	-7.55	0.01	22.77	0.03	52.15
8/1/2018	2018-AR-003a		Nodule	42.6		14.586	-7.68	0.06	23.92	0.09	46.79
8/1/2018	2018-AR-002b		Nodule	41.6		14.600	-6.66	0.09	25.02	0.13	11.42
2/24/2018	2017-AR-006		Nodule	40.8		14.612	-7.09	0.02	22.82	0.03	74.81
2/24/2018	2017-AR-005		Nodule	40.6		14.614	-7.39	0.01	22.40	0.04	76.41
2/24/2018	2017-AR-004		Nodule	40.3		14.618	-7.42	0.02	22.42	0.07	33.05
2/24/2018	2017-AR-003		Nodule	39.3		14.632	-7.14	0.01	22.44	0.03	47.43
2/24/2018	2017-AR-001	x	Nodule	39.0		14.636	-7.12	0.02	22.68	0.05	62.70

Digital annex

CD-ROM

(included in the printed version)